

# **TRIP STEELS AS SMART SENSOR ALLOYS**

**Clinton Bemont**

Submitted in fulfilment of the degree of

**Doctor of Philosophy**

College of Agriculture, Engineering and Science  
University of KwaZulu–Natal

2013

Supervisors:

Prof. Glen Bright,

Mechanical Engineering, University of KwaZulu–Natal.

Prof. Lesley Cornish,

Metallurgical and Materials Engineering, University of the Witwatersrand.

## Declaration

I, Clinton Pierre Bemont, declare that:

1. The research reported in this thesis, except where otherwise indicated, is my original research.
2. This thesis has not been submitted for any degree or examination at any other university.
3. This thesis does not contain other persons' data, pictures, graphs or other information, unless specifically acknowledged as being sourced from other persons.
4. This thesis does not contain other persons' writing, unless specifically acknowledged as being sourced from other researchers. Where other written sources have been quoted, then:
  - a. Their words have been re-written but the general information attributed to them has been referenced
  - b. Where their exact words have been used, then their writing has been placed in italics and inside quotation marks, and referenced.
5. This thesis does not contain text, graphics or tables copied and pasted from the Internet, unless specifically acknowledged, and the source being detailed in the thesis and in the References sections.

---

C. P. Bemont

As the candidate's Supervisor I agree / do not agree to the submission of this thesis.

---

Prof. G. Bright



## **Dedication**

For Nicole and Lily-April

## **Acknowledgements**

I would like to thank my PhD supervisors, Prof. Glen Bright at UKZN and Prof. Lesley Cornish at WITS, for supporting me over the last four years. Prof. Bright for his advice, inspiration and encouragement, and for the superb work environment he has facilitated for me and the other academics in my department. Prof. Cornish because, at a time when I was entirely isolated in the field of metallurgy and felt close to defeat, she engaged me, invigorated me and became my mentor and collaborator. Prof. Cornish is an academic in the truest sense, and yet always has time and energy to devote to her students.

I want to thank my colleagues at UKZN Department of Mechanical Engineering for offering me friendship and support, and most of all amusement. I am also grateful to Technische Universität Chemnitz for the opportunity to work there, and to my colleagues there, for their friendship and discourse. In addition, this work might not have commenced without the financial support received from the National Research Foundation via the Innovation Fund and technical contribution from Mintek.

I want to thank my parents and my two wonderful sisters for their support and their faith in me. Finally, to Nicole, who has stood by me, supported me and loved me steadfastly throughout; and to Lily-April, whose beautiful smile I have sometimes had to miss on this long road.

## Abstract

Upon deformation, TRIP steels undergo progressive irreversible transformation from paramagnetic austenite to more thermodynamically stable, ferromagnetic  $\alpha'$ -martensite. The change in magnetic permeability is readily detectable, and since TRIP steels also have excellent mechanical properties, this presents the opportunity for implementing cheap, robust structural health monitoring systems.

However, the extent of martensitic transformation in TRIP steels is affected not only by the degree of deformation, but by environmental temperature at the time of deformation and strain rate. This creates inherent inaccuracy when implementing TRIP steels as sensor materials. In this thesis it has been demonstrated that it is possible to design TRIP steels that are less susceptible to these factors, show good deformation induced transformation, and can function simultaneously as sensors and structural elements.

As-cast alloys were tested in compression, while annealed, hot-rolled and warm-rolled alloys were tested primarily in tension. There was considerable variation between alloys in rate of transformation with deformation. Martensitic transformation was evaluated magnetically and correlated with optical and scanning electron microscopy and X-ray diffraction results. Changes in magnetisation and magnetic permeability curves with deformation were characterised to ensure optimal electronic monitoring.

Equations from literature for determining characteristic transformation temperatures,  $M_s$  and  $M_{d30}$  were evaluated experimentally for the alloy range of interest, and the best equations were selected to aid in the design of high alloy TRIP steels exhibiting strong transformation and low temperature sensitivity. Temperature sensitivity between alloys was found to vary as predicted. Temperature sensitivity was also compared in annealed, hot rolled and warm rolled conditions; the annealed condition showed the lowest sensitivity, and this is thought to be related to lower dislocation densities.

Mining was targeted as a primary industry for application of these sensor systems because of the pressing need for greater safety and more efficient structural support at low cost. Two distinct devices for monitoring the structural health of mines were designed, built and tested, and a third was developed for the aerospace industry. Better understanding and control of the temperature sensitivity of martensitic transformation in TRIP steels is expected to aid not only structural health monitoring, but also the application of such materials to other areas of technology, such as sheet forming and high impact resistance applications.

Although there are limitations on the extent to which TRIP steel transformation characteristics can be controlled, it was shown that they can be manipulated to enable successful implementation of new alloys for smart load or damage sensors. Practical, robust, low cost structural health monitoring sensors based on the smart properties of TRIP steels were shown to be feasible.

# Contents

## TRIP Steels as smart sensor alloys

1.	Introduction .....	1
1.1	Aim.....	1
1.2	Hypothesis.....	1
1.3	Overview .....	1
1.4	Synopsis .....	2
2.	Understanding TRIP Steel.....	6
2.1	TRIP steel fundamentals .....	6
2.2	TRIP steel as a smart material.....	7
2.3	Some properties of steel .....	9
2.3.1	Steel phases and transformations .....	9
2.3.2	Plastic deformation in crystals .....	14
2.4	TRIP steel metallurgy .....	17
2.4.1	General effects of alloying elements.....	17
2.4.2	Deformation-induced transformation.....	19
2.4.3	The austenite to martensite transformation .....	28
2.4.4	Alloying chemistry for optimising the transformation.....	32
2.4.5	Schaeffler diagrams.....	36
2.4.6	Heat treatment, quenching and processing.....	38
2.5	The influence of temperature and strain rate on the transformation .....	42
2.6	Modelling the transformation.....	54
2.6.1	Overview of transformation modelling .....	54
2.6.2	Some earlier models.....	55
2.6.3	Investigation of a general model .....	57
2.7	Mechanical & physical properties of TRIP steels .....	59
2.8	Observing the transformation.....	64
2.8.1	Observing the transformation microscopically .....	64
2.8.2	Observing the transformation magnetically .....	73
2.9	Summary and analysis.....	78
3.	Material development and characterisation.....	85
3.1	Introduction.....	85
3.2	Alloy design overview .....	85
3.3	Alloy design methodology associated to transformation temperature sensitivity .....	87

3.3.1	Introduction .....	87
3.3.2	Theory .....	88
3.3.3	Summary .....	95
3.4	Cast alloy design, testing and analysis .....	95
3.4.1	Introduction .....	95
3.4.2	Methodology for the identification of relevant empirical formulae .....	98
3.4.3	Alloy fabrication .....	101
3.4.4	Experimental equipment and method .....	108
3.4.5	Compression testing results .....	109
3.4.6	Metallography .....	112
3.4.7	XRD .....	146
3.4.8	Temperature sensitivity .....	150
3.4.9	Effect of dislocation density .....	152
3.4.10	Effect of high strain rate .....	153
3.4.11	The effect cyclic loading .....	155
3.4.12	The effect of circuitous loading .....	156
3.4.13	Further analysis of compressive testing results .....	159
3.4.14	Conclusions and further work .....	171
3.5	Hot rolled tensile alloy .....	177
3.5.1	Introduction .....	177
3.5.2	Alloy investigation .....	177
3.5.3	Refining alloy transformation through theory and observation .....	183
3.5.4	Alloy design .....	186
3.5.5	Alloy fabrication .....	190
3.5.6	Experimental equipment and method .....	193
3.5.7	Alloy TRIP R comparison .....	194
3.5.8	Alloy DIN 1.4568 .....	195
3.5.9	Temperature sensitivity .....	197
3.5.10	Metallography .....	205
3.5.11	Conclusions and further work .....	228
3.6	Warm rolled tensile alloy .....	230
3.6.1	Introduction .....	230
3.6.2	Alloy design and production .....	230
3.6.3	Characterisation .....	231
3.6.4	Metallography .....	233
3.6.5	Conclusions and further work .....	234

3.7	Evaluating the TRIP steel transformation magnetically.....	235
3.7.1	Introduction.....	235
3.7.2	Determining hysteresis curves .....	236
3.7.3	Magnetisation curves .....	237
3.7.4	Conclusions .....	245
4.	Developing structural health monitoring devices.....	247
4.1	Introduction.....	247
4.2	Structural Health Monitoring .....	249
4.2.1	Introduction and objectives .....	249
4.2.2	Smart structural health monitoring technology .....	249
4.2.3	Smart SHM for South African mines .....	250
4.3	The Smart Rock Tendon .....	254
4.3.1	Introduction and objectives .....	254
4.3.2	Mechanical design.....	255
4.3.3	Inductive Coil design .....	257
4.3.4	Circuit.....	259
4.3.5	Experimental .....	260
4.3.6	Conclusion .....	264
4.4	The Smart Face Plate and Smart Load Cell .....	265
4.4.1	Introduction and objectives .....	265
4.4.2	Design .....	266
4.4.3	Experimental testing.....	269
4.4.4	Conclusions .....	272
4.5	Smart wing bolt.....	272
4.5.1	Introduction and objectives .....	272
4.5.2	Design .....	274
4.5.3	Experimental .....	276
4.5.4	Conclusion .....	278
5.	Conclusions .....	279
5.1	Cast alloys .....	279
5.2	Hot rolled alloys.....	281
5.3	Warm rolled alloys.....	282
5.4	Magnetics .....	283
5.5	Device development.....	283
5.5.1	Smart rock tendon .....	283
5.5.2	Smart face plate and smart load cell.....	284

5.5.3	Smart wing bolt .....	285
5.6	Overall Conclusion.....	285
6.	Works Cited.....	287
	Appendix 1 .....	304
A1.1.	Magnetic permeability and magnetisation .....	304
A1.2.	Electromagnetism and Inductance .....	306
A1.3.	Determining the true magnetisation curve .....	308
	Appendix 2.....	310
A2.1.	Circuit used in hand-held sensor interrogation device .....	310
	Appendix 3.....	311
A3.1.	Journal Paper 1 .....	312
A3.2.	Journal Paper 2.....	323
A3.3.	Journal Paper 3.....	330
A3.4.	List of associated conference papers.....	338

# **1. Introduction**

## **1.1 Aim**

To optimise high alloy TRIP steels to be applied in structural health monitoring sensor applications.

## **1.2 Hypothesis**

TRIP steels can be optimised for use as the core element of practical, low-cost deformation sensors.

## **1.3 Overview**

A smart material can respond to its environment by changing its properties in a beneficial manner. Very often, smart materials are capable of serving a dual purpose, one in a traditional manner and the other smart. TRIP steel is such a material. Its strength increases and its magnetic properties, among others, change in response to applied stress and strain. This project aimed to put these unusual properties to use in a practical manner by using a TRIP steel element to serve as a structural component while also monitoring the integrity of the structure. Mining was targeted as the primary industry for application of these sensors systems because of the pressing need for greater safety and more efficient structural support at low cost. However, with basic adaptations, the proposed sensors are likely to have broader application.

Early experimental investigations and literature reviews showed that not all of the properties of available TRIP steels were ideal for such sensors. In particular, their susceptibility to certain environmental factors during the transformation, and their lack of low strain sensitivity were considered problems. In order to develop such devices, it was therefore necessary to first investigate TRIP steels in an attempt to characterise and optimise their attributes wherever possible. Instrumentation capable of detecting and relaying the degree of transformation, while also being suitable for use in the harsh mining environment, also had to be implemented or developed. An understanding of the principles of mining and rock mechanics was necessary, since the devices were intended primarily for this very unique, unforgiving and insular environment.



The load sensor devices themselves were developed concurrently with the above tasks, utilising the best TRIP steel available at that point of the investigation. The project eventually lead to at least three distinct devices with adaptable functionality, discussed in Chapter 4.

## 1.4 Synopsis

This work is an investigation assessing the potential for Transformation Induced Plasticity (TRIP) steels to function as the primary sensor element of commercial smart structural health monitoring systems.

The layout of the work is somewhat unconventional in that no single experimental method chapter is included. The work is split between investigations into as-cast, hot worked and warm-worked TRIP steels. The experimental method for each of these materials was considerably different due to the fundamental differences in the materials and in their application. Each experimental method is thus discussed separately in a subsection of the relevant material group. Experimental methods each of the complete sensor devices utilising the various TRIP steels was again considerably different; this was due to the fundamental differences in the sensor designs and in their applications. Experimental methods for the testing of the sensor devices are therefore also included in the relevant sections.

Chapter 2:

Research in the metallurgically complex field of TRIP steel began in the 1960s and continues today. A review of the literature over much of this period was undertaken. The aim of this literature survey was to understand the mechanism of the transformation and the manner in which it may be influenced, with a view to improving and refining the transformation for the intended applications.

Section 2.4 to 2.6 and 3.3:

The focus of this work was empirical and experimental, rather than on the numerous recent attempts at mathematically modelling the transformation in a purely theoretical manner, an approach that has not yet been proven successful. However, certain theoretically based models were investigated and their results compared to empirical models and experimental data. A theory relating to the temperature sensitivity of TRIP steels was developed in Section 3.3.

## Section 2.8:

A brief literature survey regarding some of the more complex practical aspects of investigating the physical properties of TRIP steels has been included. These include revealing their complex microstructures and reliably detecting subtle changes in their magnetic permeability.

## Chapter 3:

The development and characterisation of TRIP steels for this work is discussed in Chapter 3. The aim of the work in this chapter was to develop TRIP steels that are optimised for smart deformation sensors.

## Section 3.2:

The general approach adopted for alloy design is discussed. The alloys were designed based on principles discussed in the literature survey, with a view to furthering the understanding of the influence of specific alloying elements and alloying element combinations on specific characteristics of the transformation.

## Section 3.3:

In order to better optimise TRIP steels for sensor applications, a theory was developed with a view to reducing the temperature sensitivity of the TRIP steel martensitic transformation. The influence of this theory on alloy design is then discussed. This work and experimental work from Section 3.5.9 was the primary source for journal paper 1 – The effect of transformation temperature on the rate of transformation in TRIP steels (Bemont, Cornish, & Bright, 2013). The paper is included in Appendix A3.1.

## Sections 3.4, 3.5 and 3.6:

The work on alloy design and characterisation is then divided into three parts: research on cast alloys (to be used in compression), Section 3.4; work on hot rolled alloys (to be used in tension), Section 3.5; and work on warm rolled alloys (also to be used in tension), Section 3.6.

Cast alloys were investigated first and that work is the primary source of journal paper 2 - The development of robust structural health monitoring sensors utilising TRIP steel (Bemont C. P., 2009). The paper is included in Appendix A3.2.

## Section 3.4.2 to 3.4.7:

There is currently not a significant body of research relating to TRIP steel alloys in their cast form. However, these alloys potentially possess beneficial properties for TRIP steel sensors

detecting compressive stresses in that their yield point is relatively lower and their detection range thus relatively larger. They are also cheap to produce and a complete device could potentially be manufactured in just one or two castings. A range of cast TRIP steels was thus designed and characterised.

#### Section 3.4.8 to 3.4.12:

While TRIP steels in an as-cast state were found to transform very strongly in compression, there were various hurdles to overcome if their application in load sensors was to become practical. These hurdles related to the altered response of the transformation under varying environmental and loading conditions, primarily temperature at time of deformation, rate of deformation and loading regime (continuously increasing versus interrupted). Each of these detrimental phenomena was investigated in the hope that a better understanding of their effect might lead to the ability to minimise it. The effects of environmental temperature at time of deformation and, by extension, rate of transformation were targeted.

#### Section 3.4.13

In order to properly design TRIP steel alloys for sensor applications, it is necessary to be able to predict the effect that the various alloying elements will have on  $M_s$  and  $M_d$  temperatures. Several empirical equations proposed in literature to predict  $M_s$  and  $M_{d30}$  were compared to experimental results for as-cast alloys to determine which were likely to most accurately predict  $M_s$  and  $M_{d30}$  in the alloy systems of interest. An analysis of these parameters was then shown to assist in the design of TRIP steel alloys with low temperature sensitivity.

#### Section 3.5.1 to 3.5.8:

Tensile transformation of hot rolled alloys was investigated. Alloy selection and design principles for these alloys were discussed. The processes and equipment involving their fabrication and testing was then discussed. The quasi-static, continuous transformation of several of these alloys was compared, and cyclic loading was also investigated.

#### Section 3.5.9 to 3.5.11:

The effects of deformation temperature on different alloys and on an alloy in different conditions were investigated, and their associated microstructures were examined. In order to test the theory developed in Section 3.3, a single alloy was compared in three different conditions: annealed, hot rolled and water-quenched, and warm-worked. This work also contributed to journal paper 1 (Bemont, Cornish, & Bright, 2013).

### Section 3.6:

Warm rolled alloys were investigated with a view to producing TRIP steel sensor alloys with mechanical properties similar to AISI 4340 alloy steel. This work and that in Section 4.4.4 were the primary source for journal paper 3 – The design and testing of sub-scale smart aircraft wing bolts (Vugampore & Bemont, The design and testing of subscale smart aircraft wing bolts, 2012). The paper is included in Appendix A3.3.

### Section 3.7:

Experimental investigation characterised the magnetisation curves of various TRIP steels. This is considered important for the optimal measurement of the transformation.

### Section 4.2:

Chapter four focuses on the utilisation of the cast and rolled TRIP steels previously investigated to produce structural health monitoring (SHM) devices. A brief literature survey examining methods and trends in structural health monitoring is included. The primary application for the devices based on the cast and hot-rolled alloys was envisaged to be in the South African mining industry. In order to design devices to be utilised in the very harsh and unique conditions found in mines (especially deep mines), it was considered necessary to gain an understanding of mining, mining support and rudimentary rock mechanics. A literature survey detailing this was undertaken and an abridged version is included.

### Section 4.3, Section 4.4 and Section 4.4.4:

The development of three structural health monitoring devices is discussed - the smart rock tendon based on hot rolled alloys, the smart face plate based on cast alloys and the smart wing bolt based on warm rolled alloys.

### Section 5:

Finally, conclusions for the major parts of this work are given in Sections 5.1 to 5.5. A general conclusion for the project as a whole is given in Section 5.6.

The published and submitted journal papers associated to this work are included in Appendix 3. A list of associated conference papers is also included in Appendix A3.4.

## **2. Understanding TRIP Steel**

### **2.1 TRIP steel fundamentals**

The TRIP (Transformation Induced Plasticity) effect was first noticed by Scheil in the 1930s (Scheil, 1932). However, it was not widely researched until the late 1960s when Zackay and his co-workers (Zackay et al., 1967) (Zackay, 1969) became interested in such steels for use as ultra-high strength structural steels that exhibit better toughness than high strength low alloy steels. The same phenomenon that imparts these superior mechanical properties to TRIP steel during deformation is responsible for its classification as a metastable strain memory alloy, a type of smart metal that can effectively memorise the peak deformation that it has been subjected to.

The mechanism for this strain memory is an irreversible crystal structure transformation when the material is deformed (Form & Baldwin, 1956). The initial austenitic structure is not ferromagnetic but the transformed martensitic structure is, thus a direct correlation exists between the extent of deformation-induced martensite in the material and its magnetic permeability. The degree to which the transformation has taken place therefore serves as a gauge of the maximum stress or strain to which the material has been subjected.

Shape memory alloys (SMAs) share certain characteristics with TRIP steels. SMAs form a different class of smart material, capable of returning to original dimensions upon heating after deformation (Smith & Hashemi, 2006). The fundamental difference between TRIP steels and SMAs is that in the case of SMAs, the transformation from austenite to martensite is directly and completely reversible, with no diffusion taking place. In the case of TRIP steels, upon reheating to the austenitic phase, the martensite will first temper to ferrite, as with ordinary steels, thus compromising the shape reversal. The gap between martensitic and austenitic temperatures in TRIP steels is usually also considerably greater than that in SMAs, this is beneficial because temperature stability is important for TRIP steels.

The change in magnetic permeability after deformation in TRIP steels can be readily converted to an electronic signal (Bressanelli & Moskowitz, 1966). Since TRIP steels are high strength, high toughness steels, they may be implemented as the foundation for smart reinforcing members that serve the dual purpose of being load bearing members and forming the basis of passive peak deformation sensors (Thompson & Westermo, 1992).

## 2.2 TRIP steel as a smart material

Smart materials include a broad range of materials that can usually be placed into one of two groups: materials whose physical properties can be manipulated via input conditions and materials that have the inherent ability to indicate the amount of damage they experience (Verma, Gupta, & Tirth, 2006). TRIP steels fall primarily into the second category. These materials are inherently capable of passively monitoring the peak damage that occurs within them, while also functioning as structural members. Passive monitoring here means that the damage level does not need to be continuously monitored or stored. TRIP steels are also smart in that they inherently strengthen themselves in a region of damage via a transformation to hard, strong martensite.

Maintenance, cost and reliability are potentially better for passive than for active monitoring methods. The TRIP steel records the peak damage so that it only needs to be interrogated when the peak damage data is required and continuous power is therefore not essential. The irreversible crystal transformation from non-ferromagnetic austenite to ferromagnetic martensite stores these data automatically since its extent is relative to the peak material deformation. The level of ferromagnetism that is detected can therefore be correlated to the maximum degree of deformation using a calibration curve defined for the particular alloy and specimen geometry in a manner similar that shown in Figure 2.1 (Verijenko, 2003). For a given specimen geometry, it is possible to manipulate this curve through alloy composition and processing to produce variation in both the transformation rate and range. Mechanical properties can also be manipulated. These transformation rates and ranges are in turn related to sensor resolution, accuracy, repeatability and monitoring range, and thus to the properties of potential smart structural health monitoring systems. These associations have been investigated by several authors (Jonson, 2003) (Thompson & Westermo, 1992) (Westermo, 1996).

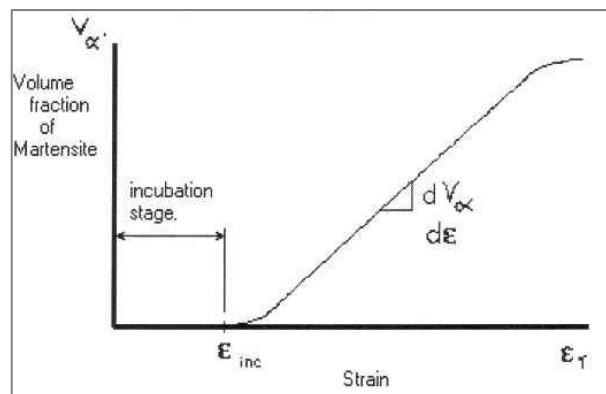


Figure 2.1: Generic strain-induced transformation curve, showing incubation strain (Jonson, 2003).

Figure 2.1 shows a generic transformation curve for a metastable sensor alloy (Jonson, 2003). The incubation strain corresponds to the point where the strain-induced transformation is triggered and thus to the lowest strain measurable via the martensitic transformation and for a given cross-sectional area, the lowest measurable load. This point can, to a degree, be shifted (it usually corresponds approximately to yield load) and the gradient of the curve, synonymous to the martensitic transformation rate, can also be adjusted (by alloy composition and processing) according to the requirements of an application, as will be discussed in Chapters 3 and 4. Naturally, there are significant physical limitations and the alloy composition and processing parameters may become considerably more expensive as these requirements become more inflexible. In many applications where the structural component being monitored is not pre-tensioned, a large incubation strain is problematic. Where the component is pre-tensioned, as with most bolting applications, an incubation strain would be beneficial, since the sensor resolution will effectively improve for a given strain monitoring range because the gradient of the strain versus martensitic volume curve would be steeper. In order for such sensors to operate, as with nearly all sensors, a certain amount of structural instability must be tolerable in the design (Jonson, 2003).

The crystal transformation can be monitored reasonably well in most metastable steel alloys. The paramagnetic fcc austenite has a very low magnetic permeability and the magnetic permeability can theoretically differ by up to five orders of magnitude from pure parent austenite to 100% ferromagnetic martensite (Jonson, 2003). However, in practice, complete transformation from pure austenite to pure martensite is not possible.

In order for it to be commercially viable though, the system must be cheap and the sensor must be reliable and repeatable, from transformation to detection to calibration. This is where alloy design and fabrication, physical sensor design and manufacture, and custom designed electronic magnetic-susceptibility monitors become vital. Various commercially available alloy steels were tested and analysed early in the project, but none were found to possess adequate properties for the proposed application. A TRIP steel, already produced specifically for smart load sensors in mines by Mintek, Randburg, as part of this project (De R. , 2003), was also tested. This material was shown to be significantly superior to commercially available materials, but needed to be further characterised and optimised. The customised design of TRIP steel alloys was therefore fundamental to the project.

## 2.3 Some properties of steel

### 2.3.1 Steel phases and transformations

The crystal transformation from austenite to martensite that occurs in TRIP steels is not unique to TRIP steels. In fact, similar transformations can be made to occur in almost any steel, as well as numerous other materials (Askeland, 1988). However, in almost all of these materials this transformation only takes place due to a change in temperature and is not advanced by external deformation. In order to understand the crystal transformation that takes place in TRIP steel due to deformation, it is necessary to first have an understanding of the more common crystallographic transformations that occur in iron and steel.

Iron is a relatively dense metal, it is ferromagnetic below 770°C, and is allotropic (Askeland, 1988). Its equilibrium crystal structures are face-centred cubic (fcc) and body-centred cubic (bcc). Pure iron at ambient temperature has a bcc structure referred to as  $\alpha$ -ferrite. At just over 900°C, it transforms into an fcc structure called  $\gamma$ -austenite, then at about 1400°C, just before its melting point of 1538°C, it becomes bcc again, this structure is referred to as  $\delta$ -ferrite.

Many of the beneficial and interesting properties of iron and steel, such as the broad range of properties attainable through heat treatment, relate to the differences between these crystal structures. Due to its configuration, the sides of the fcc unit cell are about 25% larger than those of the bcc unit cell. The larger fcc unit cell contains a total of four atoms in a close-packed configuration, while the bcc unit cell contains only two. The different atomic configurations mean that while the bcc unit cell has more potential sites where interstitial atoms can be stored (octahedral and tetrahedral), those sites present in the fcc unit cell (octahedral) are large enough to accommodate the interstitial atoms with much less severe deformation of the fcc lattice. This is significant, because it means that very many more interstitial atoms (such as carbon and nitrogen) may be stored in solid solution in the fcc structure. The fcc and bcc structures also have different densities, theoretically varying by approximately 8% (Smith & Hashemi, 2006).

Iron in its pure form is relatively soft and malleable, but not very strong; it has very few practical applications. Mostly it is used as steel which is an iron-carbon alloy and for commercial purposes can be defined as having a carbon content of between 0.005% and 2% by weight. In solid steel, carbon is principally found in two forms, either in solid solution within the bcc and fcc iron crystal structures, or as a carbide. The ratio of these two forms can be controlled by the carbon and other alloy content as well as by heat treatment. Carbides may be iron carbides ( $\text{Fe}_3\text{C}$ ), known as cementite, carbides of alloying elements such as titanium ( $\text{TiC}$ ) or chromium ( $\text{M}_{23}\text{C}_6$ ,  $\text{M}_3\text{C}_2$  and others), or mixed metal carbides (Askeland, 1988).



Due to its efficient fcc crystal structure, austenite has the ability to hold up to 2wt% carbon interstitially, a relatively large amount. Ferrite's bcc structure can hold considerably less, a maximum of only 0.02wt% (Askeland, 1988). Thus, when cooling from austenite to ferrite, carbon has a propensity to diffuse out of the lattice, and carbides are formed. The effects of carbon proportion in an iron-carbon alloy are illustrated by the iron-carbon equilibrium phase diagram, Figure 2.2 (Tisza, 2001). At the eutectoid composition, austenite decomposes to form ferrite and cementite in a particular configuration, referred to as pearlite. At hypoeutectoid compositions ferrite is formed before eutectoid composition is attained, and at hypereutectoid compositions, cementite is formed prior to pearlite. Cementite is harder and stronger but much less ductile than ferrite. Pearlite generally has good mechanical properties and even these can be varied by altering its inter-lamellar spacing (the spacing between ferrite and cementite plates) via the cooling rate. It is because of these and other similar effects that it is possible to greatly vary the properties of steels by altering their carbon contents and the processing they receive.

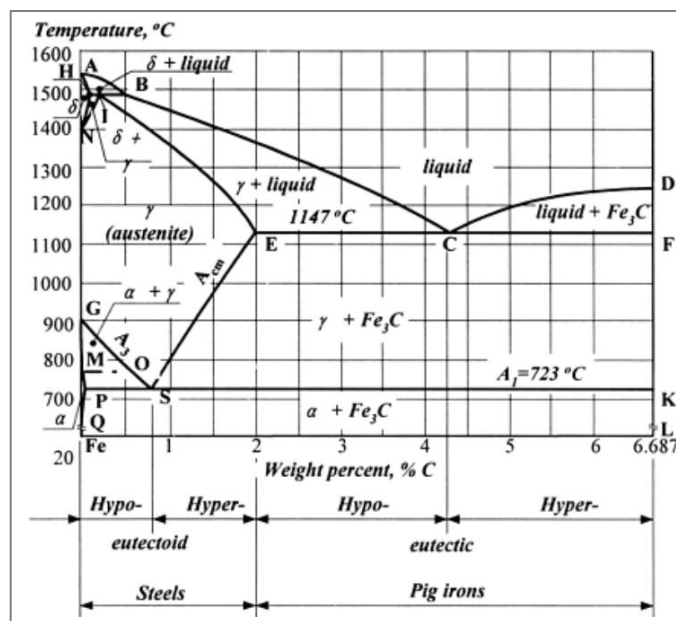


Figure 2.2: Iron – carbon phase diagram (Tisza, 2001)

However, these processes require diffusion, and diffusion requires time at raised temperatures for the carbon to move in or out of the lattice structure. Thus, when the steel is cooled very quickly from  $\gamma$ -austenite, for example at 1000°C per minute, there is a complete suppression of carbide formation as there is not time for diffusion to occur and the ferrite structure is thus forced to store the carbon atoms in solution in its very small interstitial sites (Smith & Hashemi, 2006) (Totten, 2007). Instead of carbide formation, a body-centred tetragonal (bct) martensitic structure forms spontaneously from a diffusionless phase transformation when the austenite's fcc microstructure becomes suddenly unstable below the critical temperature (Totten, 2007).

The required rate of cooling is highly dependent on the alloying elements present. The bcc martensite phase is symbolised by  $\alpha'$ . Martensitic transformations are solid-state diffusionless phase transformations. The chemical composition of the parent phase, austenite, and the product phase, martensite, is identical (Bhadeshia & Edmonds, 1979a). The rate of growth of martensitic plates has been determined by resistivity experiments to be as high as 1100m/s (Bunshah, 1953). This very high growth rate is one of the reasons why martensitic transformations are particularly difficult to investigate and why theories remain vague (Hedström, 2005). Variation in composition also has a significant effect on the martensitic transformation. Certain alloyed steels produce another martensitic phase known as epsilon martensite ( $\epsilon$ ) (Porter et al., 2009). This phase has a hexagonal close packed (hcp) crystal structure and is formed in a similar manner to  $\alpha'$ . It is sometimes formed as a precursor to  $\alpha'$  (Maxwell et al., 1974).

Martensite is an extremely hard phase. In plain carbon steels it is metastable at room temperature and is thus not shown on the equilibrium phase diagram. In alloy steels the stability of martensite depends on the alloying elements, this will be elaborated on in Section 2.4.4 and 2.4.5. Martensite is ferromagnetic, as is ferrite, while austenite is paramagnetic. The hcp  $\epsilon$  phase is anti-ferromagnetic. Where ferromagnetic materials show a significant increase in magnetic flux density with increasing magnetic field strength, paramagnetic materials show only a very small increase in magnetic permeability, similar to that of free space and anti-ferromagnetic materials show a (usually small) drop in magnetic permeability (Cullity, 1972).

It was shown by Bain (Bain, 1924), as early as the 1920s that martensite consisted of carbon dispersed atomically as an interstitial solid solution in a tetragonal ferrite crystal. In steel with less than about 0.2wt% carbon, a supersaturated bcc martensite microstructure forms. Martensitic transformation begins at the  $M_s$  (martensite start) temperature and continues until the  $M_f$  (martensite finish) temperature, below which a small percentage of retained austenite remains. The reaction is athermal as it depends only on temperature, not on diffusion, as with the transformation to ferrite (Totten, 2007) (Bhadeshia, 2001a). Unlike in diffusive transformations, no individual atom departs more than a fraction of a nanometre from its previous neighbours, as they all shift in unison and the reaction proceeds rapidly, at speeds often approaching the speed of sound in steel (Zackay et al., 1962).

Bain showed that the fcc or bcc austenite to bcc or bct martensite transformation can be related by a homogenous deformation (Bain, 1924). The Bain strain consists of a contraction of the parent lattice along the  $a_3$  axis and equal expansions along the  $a_1$  and  $a_2$  axes, as depicted in Figure 2.3 (Bhadeshia, 2001b).

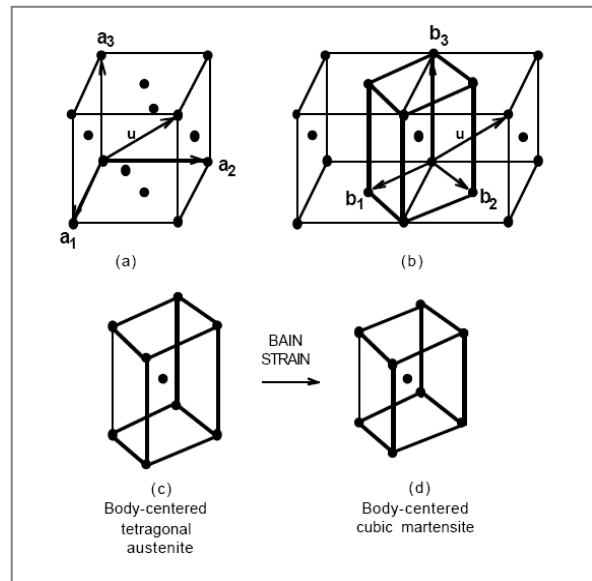


**Figure 2.3: (a) Conventional FCC austenite unit cell, (b) Relation between FCC and BCT austenite unit cells, (c) BCT austenite unit cell. (d) Bain strain deforming the BCT austenite unit cell into a BCC or BCT martensite unit cell (Bhadeshia, 2001b).**

When martensite plates form from austenite, there is a volume expansion of between 1% and 4% in practice (Hedström, 2005), causing deformation of the parent lattice (Suzuki & Wuttig, 1972). The austenite must deform to accommodate the lower density martensite through the generation and movement of dislocations and this may further aid martensite formation (Fahr, 1971) (Turteltaub & Suiker, 2005). As these martensite plates form, they eventually surround and isolate small pools of austenite. Eventually, for the remaining austenite to transform, the martensite must deform. Since the martensite is strong and brittle, it resists the transformation and the existing martensite may crack, or if the driving force for the transformation is not large enough, the austenite remains trapped in the structure as retained austenite (Askeland, 1988). Heating to a relatively low temperature can reduce residual matrix stresses and may partially temper the martensite, thereby allowing further austenite to martensite transformation. It is well known that martensite morphology is affected by carbon content (Kelly & Nutting, 1960). The austenite to martensite transformation is discussed in some detail in Section 2.4.3.

There also exists an intermediate cooling rate where neither pearlite nor martensite forms from the austenite. Instead, cementite precipitates as discrete rounded particles, aggregating in finely dispersed lath shapes within a ferrite matrix. This arrangement of ferrite and cementite is called bainite. Bainite is commonly divided into two broad types, upper and lower bainite. This is because its microstructure shows two distinct morphologies arising from different mechanisms, depending on transformation temperature (Bain & Davenport, 1930) (Askeland, 1988).

The time-temperature-transformation (TTT) diagram, also referred to as the isothermal transformation diagram (IT), along with the continuous cooling transformation (CCT) diagram, is typically used to illustrate the dependence of a steel's microstructure on cooling temperature, sequence and rate (Askeland, 1988). A TTT diagram for eutectic steel is shown in Figure 2.4. At any particular temperature, the rate at which the austenite transforms to a mixture of ferrite and cementite is described by a sigmoidal-type TTT curve depicting the incubation time required for nucleation of new phases.

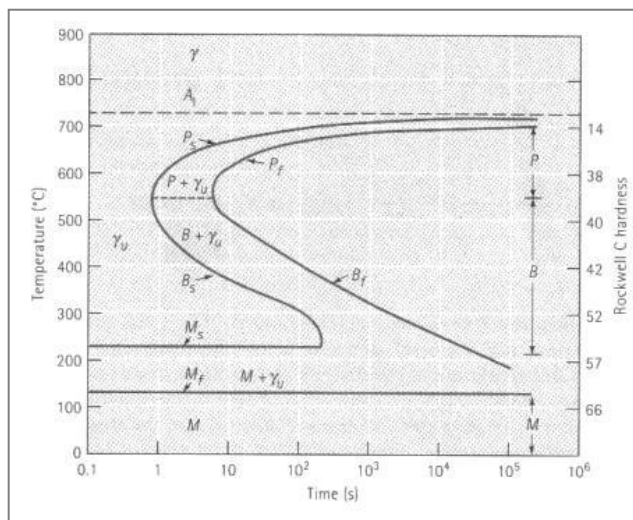


**Figure 2.4: TTT curve for eutectoid steel (Askeland, 1988).**

Simple TTT diagrams, such as the one above for plain carbon steels without significant alloying elements, exhibit a well-defined “C” shape, where the nose of the curve represents the temperature at which the transformation occurs most rapidly. Both above and below this temperature, the transformation is slower. Above this temperature, near the  $A_{c1}$  temperature (eutectoid temperature), the atoms move readily in solid solution, but the driving force for the transformation is low. Below this temperature, the driving force for the reaction increases but the process is impeded by the lack of diffusivity of the rate-controlling element, in this case, carbon (Askeland, 1988).

At some even lower temperature (below  $M_s$ ), a point is reached where atoms cannot diffuse a significant distance. It is at these low temperatures that only martensite can form from austenite because the process must be effectively diffusionless. As discussed above, bainite forms at temperatures slightly above those required to form martensite. Bainite formation involves only short distance (relatively low temperature) diffusion, resulting in its extremely finely dispersed microstructure of cementite within ferrite. Some dispute still remains in the literature as to whether bainite is a variation of martensite or of ferrite formed isothermally at lower temperatures (Stumpf, 2010).

Alloying elements have a broad range of effects on the TTT diagram. The nose of the TTT curve may be moved up, down, left or right. Most substitutional alloying elements move the nose to the right, thus making the alloy more hardenable. Certain elements, specifically molybdenum or chromium, may even split the TTT nose in two, which produces a “metastable bay” and is useful when bainite is desired. TTT diagrams for the new alloys produced in this work were of course not available. TTT type diagrams are less frequently utilised for austenitic alloys such as type 301 and 304 stainless steels because no ferrite transformation takes place upon cooling. Martensitic start and finish temperatures are of primary relevance for these alloys, although a cooling rate sufficiently rapid to suppress carbide formation is also important. A TTT type diagram, more correctly called a time-temperature-sensitisation (TTS) diagram, representing the formation of grain boundary carbides in type 304 stainless steel alloys, is shown in Figure 2.5 (Shields, J., 2010).

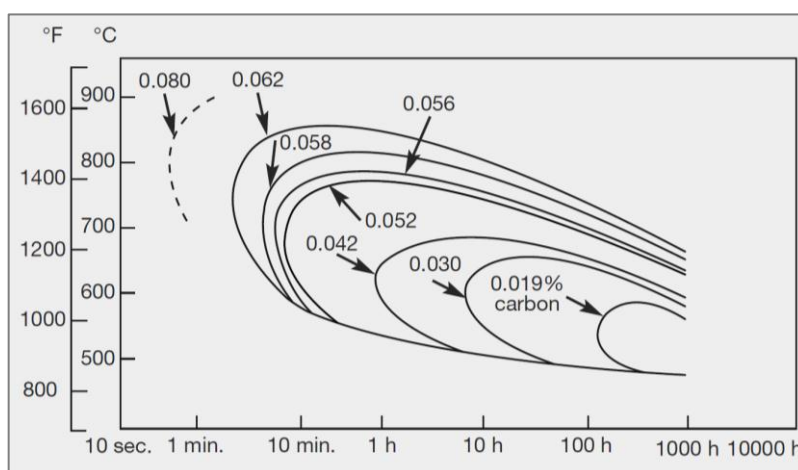


Figure 2.5: TTS diagram showing sensitisation by carbide precipitation in type 304 stainless steels for a variety of carbon contents (Shields, J., 2010).

### 2.3.2 Plastic deformation in crystals

Plastic deformation in crystals occurs by shear processes such as dislocation slip, stacking faults, twinning or occasionally by the migration of vacancy sites. Crystal structure, amount of deformation, mode of deformation, and temperature and rate of deformation are factors that affect the type of deformation structure formed (ASM International, 2005). Except in the case of hcp metals (usually at low temperature and/or elevated strain rates), twins ordinarily play only a minor role in plastic flow, while stacking faults significantly impact the work-hardening of metals that have close-packed (e.g. fcc) structures. Grain size also significantly affects plastic deformation, as described by the Hall-Petch effect (Hall, 1951) (Petch, 1953). Grain boundaries are disruptions and act as defects within the crystal lattice. The boundaries thus provide a source of strengthening by pinning dislocation movement at ambient temperatures. Since grain

boundaries have high disorder (such as vacancies and dislocations), diffusion occurs at considerably higher rates there, particularly at low temperatures (Thelning, 1984). It is partly for this reason that substitutional and interstitial atoms are found here in a higher concentration, and precipitation of particles such as carbides often occur primarily on grain boundaries.

Metallic bonding, combined with dislocations, allow metals to deform in shear by slip mechanisms at relatively low stresses. Without these and similar mechanisms, metal crystals would have to deform by shear motion of a complete slip plane. Stresses of 10 to 30 GPa would be required to accomplish this (ASM International, 2005). During slip, only a relatively small number of atomic bonds are required to break at a time, as the slip plane propagates through the lattice via dislocations. In practice, huge numbers of dislocations act together, with dislocations present before deformation (many often formed during cooling) multiplying to form new dislocations, and working together as the material changes shape via slip.

Slip will occur only in specific directions or on specific planes within a crystal structure (Smith & Hashemi, 2006). It is most likely to occur between close-packed crystal planes in fcc or hcp structures, or between the closest-packed planes present in other crystal structures, because atomic movement is thereby minimised. The number of expected slip planes thus depends on the crystal structure of the material. The fcc and hcp crystal systems have planes that are packed as closely (efficiently) as is possible, bcc systems do not have close-packed planes but do of course have closest packed planes. In hcp systems there is only one set of close-packed planes with three unique directions and thus relatively few potential slip systems exist. It is for this reason that twinning commonly occurs at relatively low strains in hcp materials. Conversely, the fcc system has four sets of differently oriented close-packed planes and hence many more slip systems.

In a similar manner to a grain boundary, a twin boundary is a surface defect (Smith & Hashemi, 2006). However, in the case of twinning, there is a mutual orientation across the boundary. Twins are produced during crystal growth (annealing twins) as well as during plastic deformation (deformation twins or mechanical twins). Deformation twinning involves shear displacement similar to slip. However, where in slip the atoms on one side of a slip plane all move an equal distance and crystal orientation remains everywhere unchanged, in twinning the atoms move distances proportional to their distance from the twin plane. A comparison between slip and twinning, showing the manner in which crystal orientation in the band of deformation is altered, is depicted in Figure 2.6 (Doitpoms, 2012). The twin boundary is an atomic plane that

conforms exactly to the crystal lattices on both its sides, and these crystal lattices may be regarded as the mirror image of one another.

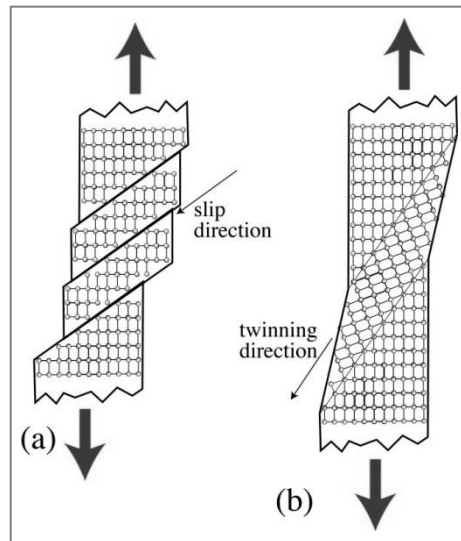


**Figure 2.6: Schematic comparison between deformation by (a) slip and (b) twinning (Doitpoms, 2012).**

While cases of mechanical twinning in fcc materials are well documented, they are generally considered to twin with considerable difficulty and only in exceptional cases because of the many possible close-packed slip opportunities available (Cahn, 1964) (Chin, 1973). Many hcp materials, however, twin with considerable ease (some are even known to twin during mechanical polishing). Certain bcc materials, particularly tin, are also known to mechanically twin very easily.

Strain rates commonly utilised in tensile testing ( $10^{-2}$  to  $10^{-3} \text{ min}^{-1}$ ) will not usually cause twinning at room temperature (Hall, 1954). High rates of deformation are known to favour twinning. When twinning does occur at room temperature and at low strain rates, this will usually happen only after the material has work-hardened due to slip and where the crystal orientation happens to favour twinning.

Other types of planar defect encouraged by plastic deformation is stacking faults. These defects are essentially associated to the sequence of stacking planes within close-packed crystal structures. Both fcc and hcp lattices are formed from identical close-packed planes, however the stacking of these planes relative to one another varies (Barrett, 1949). Once the first two close-packed planes are laid down, there are two possible positions in which the following plane might be equally efficiently placed. The first two planes are stacked in the same way for fcc and hcp. However, in the case of fcc, the third plane is placed over the other possible position, whereas in the hcp case the third plane is placed in a position identical to the first. Thus fcc

planes are denoted to stack in the sequence ABCABCABC, whereas hcp planes stack ABABAB. Occasionally atoms in an fcc structure will stack in a thin layer of the hcp form, ABABAB (usually only a few atomic planes thick). Such a planar defect in the structure is called a stacking fault.

Stacking faults may be produced during grain growth, or on formation and propagation of a partial dislocation (Shockley et al., 1952). A full dislocation moves lattice points one full lattice position in the slip direction and thus cannot produce a stacking fault because it leaves behind a perfect structure. If stacking faults can be made to occur easily in a metal then they are said to have low stacking fault energy. Addition of alloying elements to a metal changes the stacking fault energy (Roser, 1963). The stacking fault energy relates to the surface energy introduced by the stacking fault and depends on the fault-width and the repulsive energy between dislocation pairs within the material.

The fault usually extends over relatively large distances in one direction within the plane, but is narrow in the other. The width is usually larger when the fcc and hcp allotropes of the material are of similar free energy (Talonien, 2007). At the boundaries at the extents of a stacking fault, a special type of dislocation, called a partial dislocation, is present to switch from hcp to fcc (Whelan et al., 1957). Stacking fault formation and stacking fault energy significantly influences the nature of plastic deformation and work-hardening in fcc metals, as well as static and dynamic recrystallization (Smallman & Ngan, 2011).

## **2.4 TRIP steel metallurgy**

### **2.4.1 General effects of alloying elements**

Each of the more than 10 alloying elements potentially used in TRIP steel have a distinct influence on the steels properties and microstructure and on the temperature, holding time, and cooling rates at which microstructures change. Transformation temperatures may be altered, solution and diffusion rates modified, and they may compete with other elements in forming intermetallic compounds, carbides and nitrides (Allegheny Ludlum Steel Corporation, 1959). More specifically, alloying elements are added to provide solid solution strengthening of ferrite, precipitation of alloy carbides other than  $\text{Fe}_3\text{C}$ , improve corrosion resistance and other special characteristics, and also improve hardenability by moving the TTT nose to longer times as already discussed.



TRIP steels comprise a broad range of chemical compositions (Section 2.4.4). The main alloying elements are chromium, nickel and manganese, but many other elements contribute to the steels diverse properties. Chromium imparts good corrosion resistance to TRIP steels, and when present in excess of 11wt%, the material can be considered a stainless steel (Askeland, 1988). Nickel increases ductility and toughness and reduces corrosion rate. Nickel also increases yield strength by solid solution strengthening (Thelning, 1984). Manganese can also increase strength by increasing the solubility of nitrogen. Silicon helps to inhibit carbide formation (which can stabilise high carbon austenite, although it is considered a ferrite-stabiliser); it also prevents carburising and oxidation at high temperatures and is beneficial for corrosion resistance. Aluminium and phosphorus can also inhibit carbide formation in carbon-rich austenite (Chatterjee, 2006) and aluminium can increase the material's strength. Molybdenum substantially increases corrosion resistance, while also increasing strength and promoting secondary phases.

Carbon substantially increases strength and hardness by interstitial solid solution strengthening, while decreasing toughness (Thelning, 1984). It is kept at low levels in TRIP steels since it is an exceptionally powerful austenite-stabiliser and at room temperature it can readily stabilise austenite to the point where no transformation will occur (Schaeffler, 1949). Carbon can also form chromium carbides, depleting the material of chromium, and thus altering transformation characteristics and reducing corrosion resistance. Nitrogen is also a powerful austenite-stabiliser. Nitrogen enhances the strength of steel by interstitial solid solution strengthening, while preventing localised corrosion but reducing toughness. Concentrations of up to 0.25% can as much as double the yield strength of Cr-Ni austenitic steel (Bhadeshia, 2005).

Titanium and other strong carbide-formers, such as niobium, stabilize the steel and prevent chromium carbide precipitation, and the associated depletion of chromium from the grains (Thelning, 1984). They also lower the effective carbon content and reduce martensite hardness. Cobalt increases the hardness and tempering resistance of martensite. Sulphur substantially increases machinability, but reduces corrosion resistance, ductility, formability and weldability.

The contribution of specific elements to the properties of stainless steels have been extensively explored in prior literature and this has led to some well-known empirical models some of which will be discussed in Section 2.4.2. The following empirical models predict tensile and yield strengths from material composition and grain size (Kerr et al., 1999):

$$\text{Tensile strength (MPa)} = 470 + 600(\%N + 0.02) + 14\%Mo + 1.5\delta + 8d^{-0.5}$$

$$\text{Yield strength (MPa)} = 120 + 210\sqrt{(\%N+0.02)} + 2\%Cr + 2\%Mn + 14\%Mo + 10\%Cu + \delta(6.15 - 0.054\delta) + (7+35(N+0.02))d^{-0.5}$$

Equations 2.1 and 2.2

where  $d$  is the grain size in mm and  $\delta$  is the delta ferrite content (in vol. %), and alloy contents are in weight percent.

It is seen from Equations 2.1 and 2.2 that grain size has an inverse influence on tensile and yield strength. This effect is discussed in relation to TRIP steel sensor elements in Section 2.4.2.

Figure 2.7 shows the effect that various alloying elements have on steel hardness, although there are frequently complex interactions between certain alloying elements which are not accounted for here (Bain, 1939). Hardness is approximately proportional to tensile strength. An increased tensile strength may improve the range of the sensor, particularly if the yield strength is not increased proportionately.

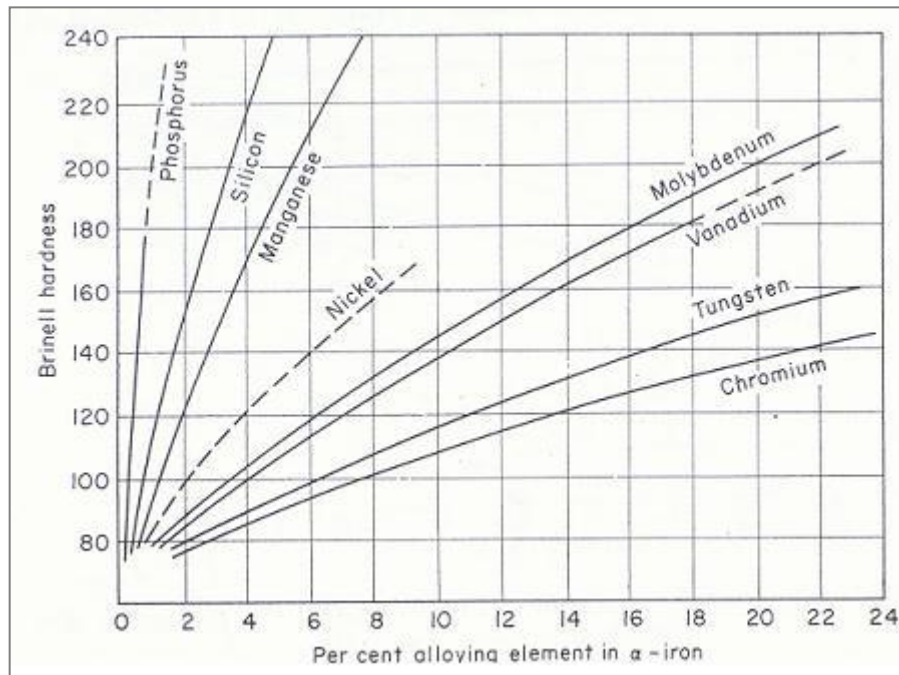


Figure 2.7: The effect of various alloying elements on the hardness of steels (Bain, 1939).

#### 2.4.2 Deformation-induced transformation

In austenitic stainless steel alloys, the  $M_s$  temperature is below operating temperature. However, applying a deformation to certain metastable austenitic steels at room temperature (above  $M_s$ ) can initiate the austenite to martensite transformation. This phenomenon, with the associated paramagnetic to ferromagnetic change, forms the foundation for the application of TRIP steels in smart structural health monitoring sensors. The temperature above which deformation-

induced martensite cannot form is referred to as  $M_d$ , depicted on the TTT curve sketch in Figure 2.8 (Askeland, 1988). Generally, the speed of the martensitic transformation due to a given amount of deformation increases as the temperature drops and  $M_s$  is approached, and decreases as  $M_d$  is approached at increasing temperatures. Ferrite and carbides do not form, even after holding for extended periods of time in TRIP alloys because there is not enough driving force for these transformations below  $M_d$  temperature.

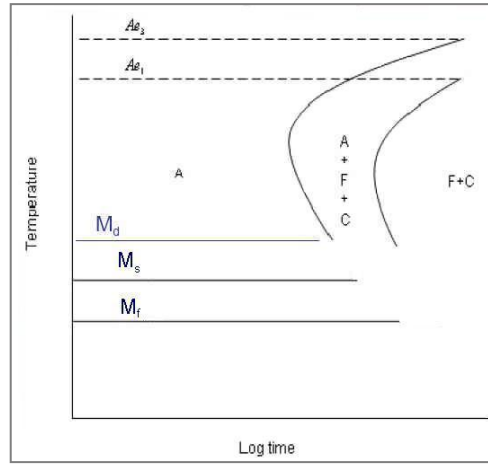


Figure 2.8: TTT-curve depicting  $M_d$  (Askeland, 1988).

There has been more than one empirical equation proposed to predict  $M_s$  temperature in austenitic stainless steels when there has been no plastic deformation. For example that developed by Andrews (Andrews, 1965):

$$M_s (^{\circ}\text{C}) = 539 - 423\%C - 30.4\%Mn - 17.7\%Ni - 12.1\%Cr - 7.5\%Mo \quad (\text{wt}\%)$$

Equation 2.3

Other such equations intended for similar alloy compositions give substantially different results when applied to the same TRIP steel composition, for example that developed by Hull (Hull, 1973):

$$M_s = 1482 - 2390\%C - 3720\%N - 54\%Mn - 59\%Ni - 47\%Cr - 37\%Si - 56\%Mo - 180\%Ti \quad (\text{wt}\%)$$

Equation 2.4

or that originating from Cina via Krupp (Cina, 1954) (Krupp et al., 2008):

$$M_s = 1305 - 1667(\%C + \%N) - 33\%Mn - 61\%Ni - 42\%Cr - 28\%Si \quad (\text{wt}\%)$$

Equation 2.5

Since the  $M_d$  temperature is difficult to measure experimentally, Angel introduced another parameter, called  $M_{d30}$  (Angel, 1954). This is defined as the temperature where the material develops 50% martensite at a true strain of 30%. Although Hull's formula for  $M_s$  was used in this work (Equation 2.4), his formula for  $M_d$  was not, since  $M_{d30}$  is considered a better, more

measurable gauge of stability for metastable stainless steels.  $M_{d30}$  can be determined by Angel's empirical formula (Angel, 1954):

$$M_{d30} = 413 - 462\%C + \%N - 9.2\%Si - 8.1\%Mn - 13.7\%Cr - 9.5\%Ni - 18.5\%Mo \quad (\text{wt}\%)$$

**Equation 2.6**

Other authors have since proposed modified empirically determined equations to predict  $M_{d30}$ . The following equation for  $M_{d30}$  was proposed by Pickering (Pickering, 1978):

$$M_{d30} = 497 - 20Ni - 13.7Cr - 8.1Mn - 9.2Si - 18.75Mo - 462(C+N) \quad (\text{wt}\%)$$

**Equation 2.7**

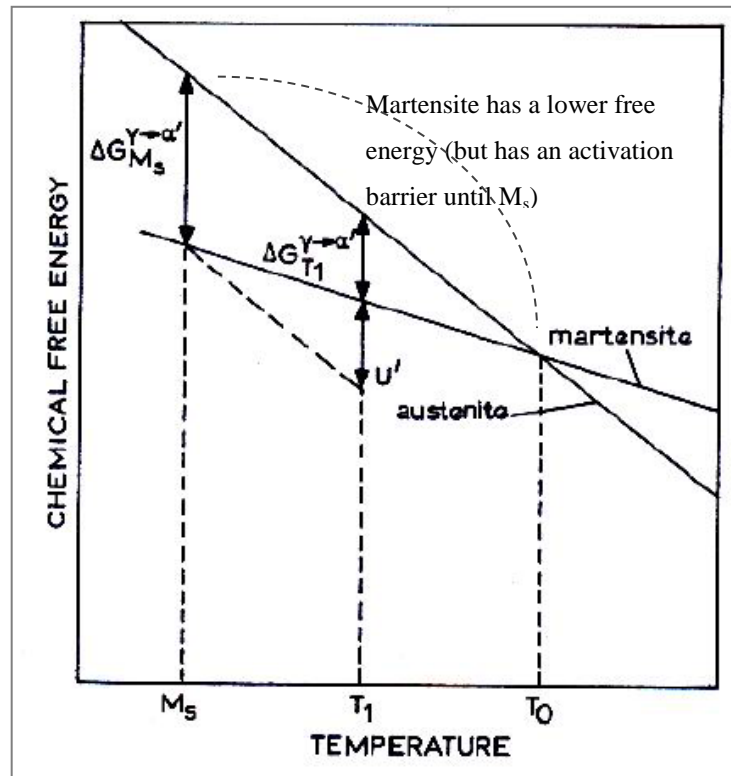
The following equation for  $M_{d30}$  was proposed by Nohara (Nohara et al., 1978):

$$M_{d30} = 551 - 29Ni - 14Cr - 8.1Mn - 9.2Si - 18.5Mo - 29Cu - 462C \quad (\text{wt}\%)$$

**Equation 2.8**

Similar to  $M_s$ , there have been a number of empirically-determined formulae proposed to predict  $M_{d30}$  within similar composition ranges; these all give different results. All such equations imply that more alloying additives produce more stable austenite, reducing the transformation to martensite. Further empirical equations for  $M_s$  or  $M_{d30}$  have been developed, but the above equations were selected for investigation here based mainly on their relevance to the alloy system of interest, and also on their prevalence in that literature.

It is held that the chemical driving force for the martensitic transformation decreases approximately linearly as temperature increases (Patel & Cohen, 1953) (Porter et al., 2009). However, as discussed, applied mechanical loading can contribute to the driving force necessary to start the transformation (McCoy et al., 1970). It is therefore possible for martensite to nucleate above  $M_s$  if there is enough mechanical driving force. Thus, in order for the transformation to proceed in the temperature range between  $M_s$  and  $M_d$ , it is necessary to induce the remainder of the driving force mechanically via external loading, as depicted in Figure 2.9 (Porter et al., 2009). In this diagram  $\Delta G_{M_s}$  and  $\Delta G_{T_1}$  are the free energy changes that would result from transformation from austenite ( $\gamma$ ) to  $\alpha'$ -martensite at martensite start temperature and at temperature  $T_1$  respectively. The thermodynamic contribution from the applied mechanical load is  $U'$ .



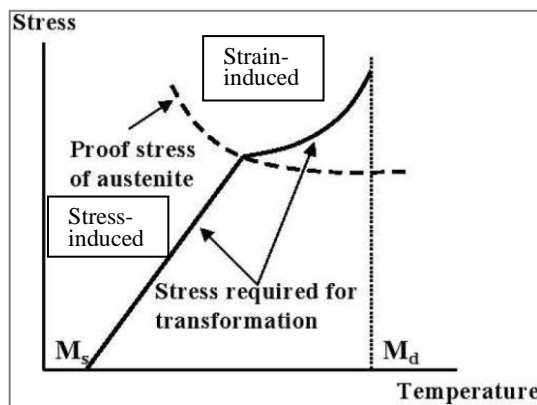
**Figure 2.9: Schematic of the free energy change between austenite and martensite as a function of temperature and applied mechanical load (Porter et al., 2009).**

Figure 2.9 illustrates how the free energy of austenite and martensite changes with temperature (Tamura, 1982) (Porter et al., 2009). The temperature,  $T_0$ , at which the two phases have equal free energy is clearly depicted. The martensite phase is thermodynamically favoured everywhere below this temperature. However, because energy is required for the nucleation of martensite and because martensite stores energy in the form of strain (estimated to be about 600 J/mol (Christian, 1979), primarily due to the excess carbon atoms stored within the ferrite matrix), the transformation will not take place until there exists an extra driving force, as depicted in the diagram by the free energy  $\Delta G_{M_s}$ . This occurs at temperature  $M_s$  or at any temperature  $T_1$  below temperature  $T_0$  if an extra driving force ( $U'$ ) is imposed via an applied mechanical deformation, to make up the difference between  $\Delta G_{M_s}$  and  $\Delta G_{T_1}$ .

Different martensite morphologies have been observed to result from the differing contributors to the transformation - thermal, stress and strain (Olson & Azrin, 1978) (Maxwell et al., 1974). Regarding the mechanically-induced types, it is useful to distinguish between stress-assisted and strain-induced martensite (Olson & Cohen, 1975). The terminology is somewhat arbitrary, because it is the local state of stress that induces transformation in both cases (Bhandarkar et al., 1972).

Stress-assisted martensite describes martensite formed under an applied stress by thermodynamically assisting the transformation of previously formed nucleation sites through elastic deformation; the same sites that would trigger spontaneous transformation on cooling to  $M_s$  (Stringfellow et al., 1992) (Bhadeshia, 1982). The martensite formed is usually of a similar morphology to thermally-induced martensite. Stress-assisted martensite can also form in austenite that has already undergone extensive plastic strain. It can form above, as well as below, the  $M_s$  temperature.

When the stress required for transformation exceeds the yield strength of the austenite, then plastic strain precedes the transformation and the transformation is referred to as being strain-induced (Olson & Cohen, 1972). Yielding decreases the amount of stress that would otherwise be required, as is represented in Figure 2.10 (Stumpf, 2010).



**Figure 2.10: Stress required to induce martensitic transformation at different temperatures (Stumpf, 2010).**

Strain-induced martensite is different because new nucleation sites for martensite, for example shear band intersections, can be formed as a direct consequence of the plastic deformation and associated faulting (Olson & Cohen, 1975) (Lecroisey & Pineau, 1972) (Manganon & Thomas, 1970), thereby greatly promoting the transformation. Strain-induced martensite produces overwhelmingly more rapid transformation than stress-induced martensite does (Christian, 1979). Strain-induced martensite has the same crystal structure as that of normal martensite, but its morphology, distribution, temperature dependence and other characteristics are different (Maxwell et al., 1974). A sigmoidal shaped stress-strain curve often indicates a significant degree of strain-induced martensite formation (Biggs & Knutsen, 1995). It is noteworthy for the current alloy design that extensive faulting (due to excessive applied strain during operation or for example during warm or cold rolling) may mechanically stabilise austenite against transformation (Bhadeshia & Edmonds, 1979b). This is because it is difficult for martensite to propagate across faults and discontinuities (Chatterjee et al., 2006). It has been shown that

ageing type treatments have a similar negative effect on the transformation (Basuki & Aernoudt, 1999).

Figure 2.11 shows how  $\Delta G$  (the difference between the free energy of austenite and martensite) varies with temperature and nickel composition for 316L type stainless steel (Basuki & Aernoudt, 1999). Very high strains are required for transformation in these alloys at room temperature. It is significant that the curves of all compositions shown have a similar gradient, implying that nickel content does not impact the rate of change of  $\Delta G$  with temperature in these alloys. It is hoped that this rate of change of  $\Delta G$  with temperature might be reduced in certain other alloys by altering alloy content or processing.

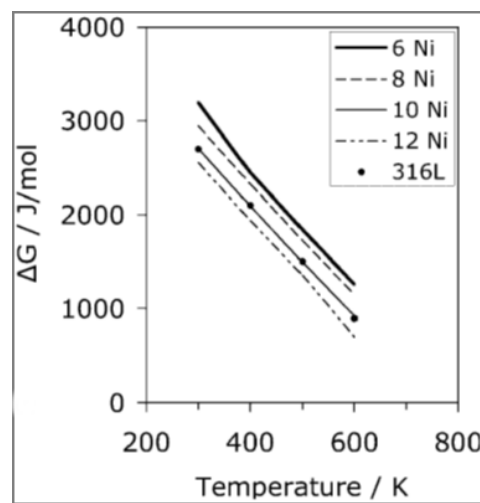


**Figure 2.11:  $\Delta G$  versus temperature for various 316L type stainless steels (Basuki & Aernoudt, 1999).**

It has been shown that near  $M_s$  stress-assisted martensite is responsible for significant transformation but near  $M_d$ , inelastic-strain-induced martensite is overwhelmingly dominant (Fahr, 1971) (Bressanelli & Moskowitz, 1966). A temperature  $M_s^\sigma$  may be defined below which applied elastic stresses assist the spontaneous growth of pre-existing nuclei, as in stress-assisted martensite (Leal & Guimarães, 1981).

During the formation of stress-assisted martensite, slip in the austenite may be a consequence of plastic strain during the formation (and expansion) of martensite from the denser austenite. Maxwell and co-workers found that stress-assisted martensite formed in certain alloys with high nickel contents as a result of the interaction of the externally applied stress with the strain resulting from prior martensitic transformation, giving a combined energetic contribution to the driving force for the martensite transformation (Maxwell et al., 1974). However this investigation was confined to Fe-Ni-C alloys with extremely high nickel contents and nickel equivalents, all well in excess of 30, with chromium equivalents around zero, that were

compared to Fe-Ni-Cr-C-Mn-Si-Co alloys of very high nickel and chromium equivalents (chromium favours the bcc phase). It was noted that the total martensitic transformation of the Fe-Ni-C alloys was small compared to that in the TRIP steels. This stress-assisted martensite appears to be the same plate martensite formed spontaneously when these alloys are cooled below  $M_s$ , which has also been found by other authors (Olson & Azrin, 1978). However, as the transformation temperature increases above  $M_s$  towards  $M_d$ , the stress-assisted martensite plates were observed to become finer and less regular in shape (Maxwell et al., 1974). Generally, the amount of stress-assisted martensite formed also decreases with increasing temperature and there comes a point,  $M_s^\sigma$ , well below  $M_d$  where no stress-assisted martensite is observed to form.

Strain-induced martensite is formed by a mechanism requiring plastic strain to the parent austenite (Turteltaub & Suiker, 2005), as shown in Figure 2.10 (Stumpf, 2010). Some authors have found that the morphology of stress-induced martensite is often lath-like, whereas that of strain-induced martensite is often plate-like (Maxwell et al., 1974). Strain-induced martensite forms in elongated clusters or sheaves of parallel laths whose formation and orientation is related to the slip occurring in the parent austenite. Martensite laths are frequently located at the intersection of two shear deformation bands in the austenite as shown in Figure 2.12, Figure 2.13 and Figure 2.14 (Spencer K. et al., 2009). In these bands, the deformation can occur via formation of  $\epsilon$ -martensite platelets, twinning of the austenite or by the gliding of dissociated dislocations. Thompson found that in the several TRIP steel alloys, deformation assisted (strain-induced)  $\alpha'$  only formed at  $\epsilon$ -band intersections (Thompson, 1986).

The plate and lath martensites normally have the same crystal structure, but their morphology, distribution and temperature dependence are different. The extensive transformation observed in a wide range of TRIP steel alloys researched by Maxwell and co-workers was shown to result almost solely in strain-induced martensite (Maxwell et al., 1974).



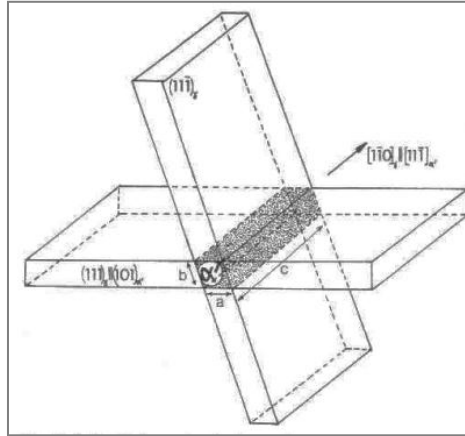


Figure 2.12: A lath of martensite located at the intersection of two deformation bands (Spencer K. et al., 2009).

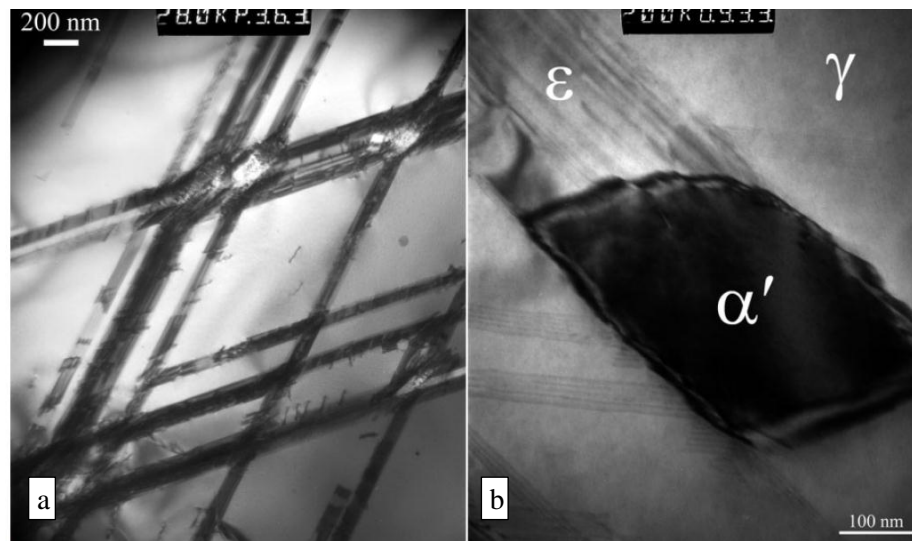


Figure 2.13: Martensite embryos, white in (a), dark in (b), at the intersection of bands of  $\epsilon$  martensite (Spencer K. et al., 2009).

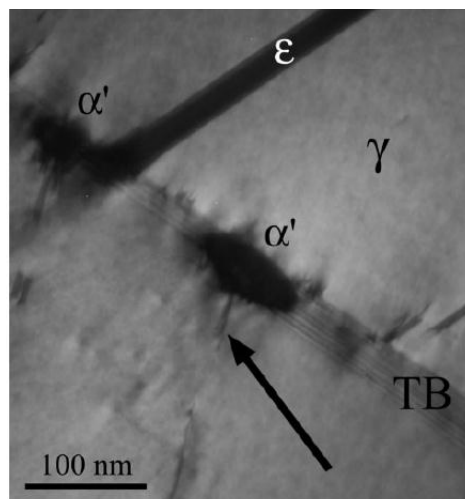


Figure 2.14: Image of martensite forming on annealing twin boundary (TB) intersected by  $\epsilon$  phase and by slip band (indicated by arrow). Sample deformed 5% at 77K (Spencer K. et al., 2009).

As the austenite grain size decreases below about 10  $\mu\text{m}$ , the interfacial energy required during the formation of a martensite plate within an austenitic grain increases exponentially (Wang &

van der Zwaag, 2001). At some point (austenite grain sizes below approximately  $0.01\ \mu\text{m}$ ), transformation into martensite does not occur at all, due to the extreme levels of driving force necessary for the transformation to take place (Wang & van der Zwaag, 2001). This is undoubtedly exacerbated by the many grain boundaries that form barriers to the transformation. Figure 2.15 illustrates how martensite plate growth is hindered by other martensite plates or by high angle austenite grain boundaries (Porter et al., 2009). According to basic theory, larger austenitic grain sizes allow the growth of larger martensite laths, and a greater volume fraction of martensite is thus transformed (Nishiyama, 1978).



**Figure 2.15:** Schematic diagram showing the growth of  $\alpha'$  martensite plates and the manner in which their growth is hindered by other martensite plates or high angle grain boundaries (Porter et al., 2009).

Figure 2.16 shows a material that was quenched from different austenitization holding temperatures (Chatterjee & Bhadeshia, 2006). Austenite grain size is expected to increase with increasing austenitization temperature. It is noted that progressively smaller martensite laths are formed as the austenitizing temperature (and thus prior austenite grain size) decreases.

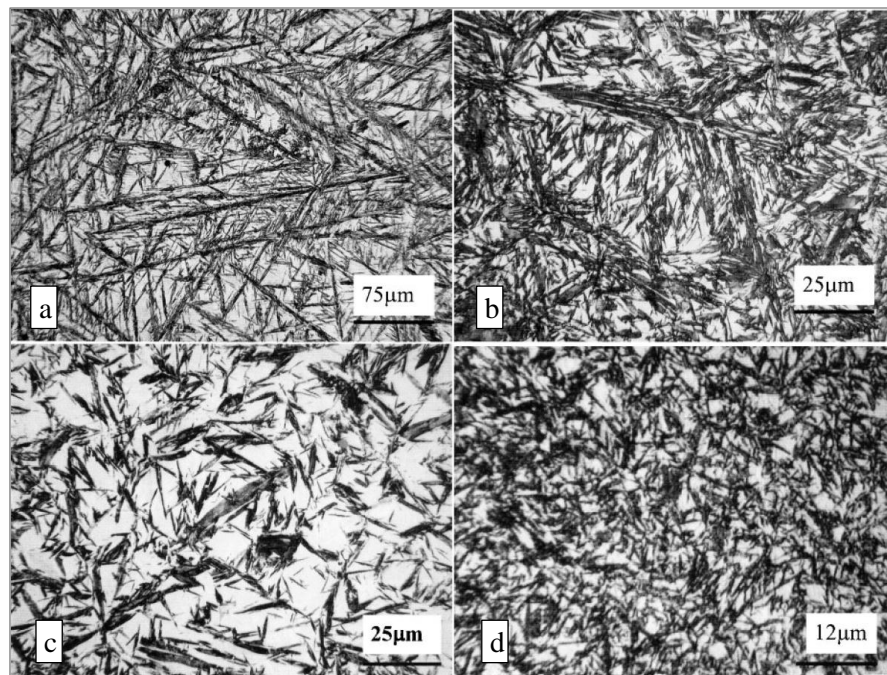


**Figure 2.16:** Micrographs showing the martensitic structure of one material quenched from different austenitizing temperatures (a) 1200°C, (b) 1100°C, (c) 1000°C, (d) 950°C (Chatterjee & Bhadeshia, 2006).

### 2.4.3 The austenite to martensite transformation

There exists a temperature,  $T_0$ , where austenite and ferrite of identical composition have equivalent free energy, as was shown in Figure 2.9 (Porter et al., 2009). Thermodynamically, diffusionless transformation is possible anywhere below  $T_0$ . Yet, Zener (Zener, 1946) and Cohen (Cohen et al., 1950) noted that martensite only forms at an undercooling significantly below  $T_0$ . Thus, it was hypothesised that this extra undercooling was needed to overcome the strain energy and to a lesser extent, change in interface energy, during the formation of the martensite plates.

According to Ko and Cottrell (Ko & Cottrell, 1952), a coherent nucleus may develop into either martensite or bainite below  $M_s$ , this depends on the driving force available for transformation. However, optical microscopy observations have shown that bainite sheaves form at a considerably slower rate than do martensite plates (Bhadeshia & Christian, 1990) (Bhadeshia, 2001c). Bainite requires the diffusion of carbon from martensite (Ko & Cottrell, 1952) and thus cannot form at temperatures as low as martensite. Martensitic transformation will occur, provided that the rate of cooling is high enough to prevent alternative transformations involving diffusion (Porter & Easterling, 1993). Some authors believe that in certain circumstances, diffusion of the interstitial (not substitutional) solutes is still possible even at temperatures as low as  $-60^\circ\text{C}$  (Callister & Rethwisch, 2012) (Sherif, 2003).

Since martensite can form at very low temperatures, any process which is a part of its formation does not rely on thermal activation (Bhadeshia, 2001a). For example, the interface connecting the martensite with the parent phase must be able to move easily at such temperatures, without any significant help from thermal agitation. Since the interface must have high mobility at low temperatures with high velocities, it cannot be incoherent. It must therefore be semi- or fully coherent (Christian & Knowles, 1981). This is experimentally verified by the observation that scratch marks across a martensite plate in an austenite lattice change their direction, but remain continuous (Wayman, 1965).

Fully coherent interfaces are only possible when the parent and product lattices can be related by a strain which is an invariant-plane strain (IPS) (Christian, 1975). This means that during the non-diffusive, displacive transformation into the martensite crystal, there must exist a plane which remains undistorted and unrotated from the previous state, as illustrated in Figure 2.17 (Bhadeshia, 2001b). Such a transformation is possible during the fcc to hcp transformation, but an fcc austenite lattice cannot be transformed into a bcc martensite lattice by such a strain.

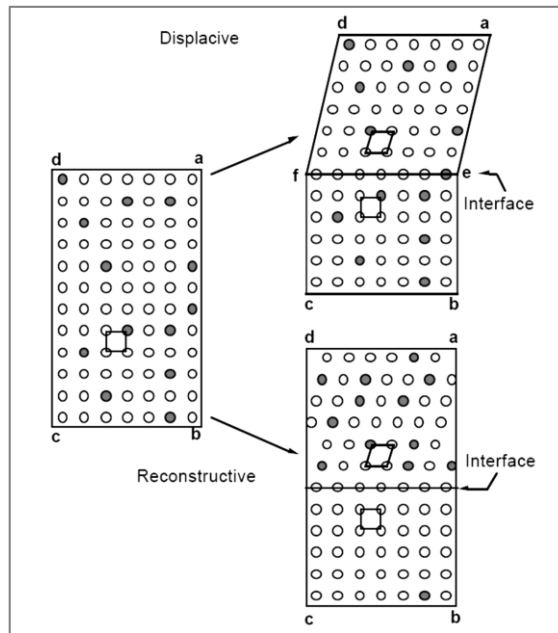


**Figure 2.17: Diffusional transformation mechanism versus shear transformation mechanism (Bhadeshia, 2001b).**

When full coherency between the parent and martensite lattices is not possible, then the only alternative for the interface to be highly mobile at low temperatures (be glissile) is semi-coherency (Bhadeshia, 2001b). The transformation strain relating the two lattices must be an invariant-line strain (ILS) and the invariant-line must lie in the interface plane. The interface between the newly forming phase and the parent phase is called the ‘habit plane’. An ILS is equivalent to two IPSs with the second necessarily intersecting the first and the line of intersection remaining undistorted and unrotated.

When an ILS is applied to the fcc lattice, it generates the bcc martensite lattice in the experimentally observed atomic orientation relation (Bhadeshia, 2001b). However, the shape deformation that accompanies the formation of bcc martensite from fcc austenite was experimentally found to be an invariant-plane strain (Machlin & Cohen, 1951) (Machlin & Cohen, 1952) (Mackenzie, 1957). This is clear due to the existence of an atomic correspondence between the parent and product lattices; it can be observed that a particular atom in the product lattice occupied a particular corresponding site in the parent lattice.

As previously stated, an ILS can be imagined to consist of two homogeneous IPSs (Bhadeshia, 2001b). If the shape change due to the second ILS was rendered invisible on a macroscopic scale due to some inhomogeneous lattice-invariant deformation (a deformation that does not alter the lattice structure), then the observed macroscopic shape change would be solely due to the first IPS only and therefore have the characteristics of an invariant-plane strain.

Ordinary slip does not change the nature of the lattice and is one form of a lattice-invariant deformation (Christian, 1975). Hence, slip deformation on specific crystal planes and in a direction parallel to the interface would make the shape change due to the second IPS invisible on a macroscopic scale, as illustrated in Figure 2.18 (Bhadeshia, 2001b). Twinning deformation also does not change the nature of the lattice (although unlike slip, it does reorientate it). Slip or twinning could cause the shape illustrated in Figure 2.18 (c) to be deformed in such a way as to correspond macroscopically to that Figure 2.18 (b) without changing its bcc nature.

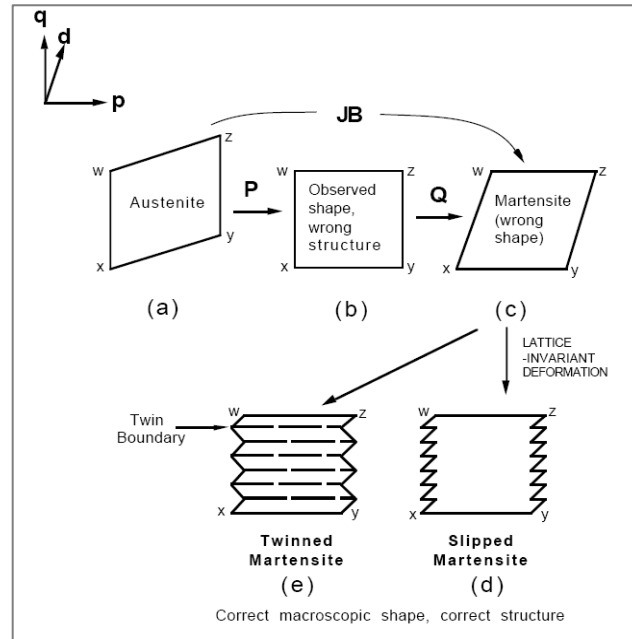


**Figure 2.18: Schematic illustration of the phenomenological theory of martensite. (a) the fcc austenite crystal, (c), (d), (e) represent bcc structures, (b) has a structure in between fcc and bcc (Bhadeshia, 2001b) after Bain (Bain, 1924).**

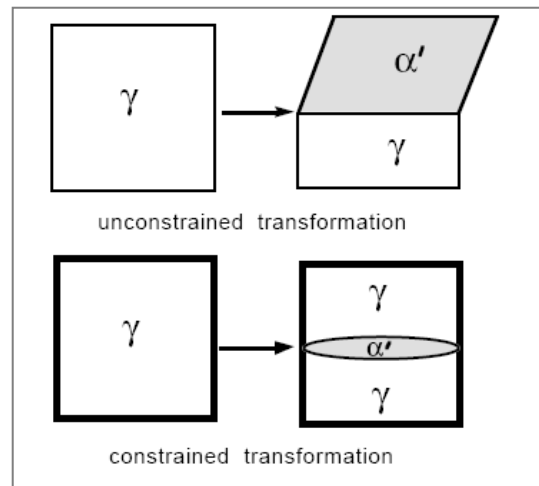
Thus, the martensitic transformation occurs via a Bain distortion and a shear deformation (slip or twinning) at the austenite-martensite interface (Bhadeshia, 2001b). All of the changes necessary for the fcc to bcc transformation to occur arise simultaneously at the moving interface. The fcc lattice changes into the bcc lattice as the interface progresses. The theory simply provides an understanding of the process, without being precisely certain of the path it follows.

The observation that the martensite forms in a displacive, diffusionless manner has some interesting consequences. The formation of martensite in a constrained environment must, due to its IPS shape deformation, create stresses within the parent lattice and dislocations if it cannot be elastically accommodated (Bhadeshia, 2004). The strain energy per unit volume of material due to the elastic distortion, is approximately given by (Eshelby, 1957) (Christian, 1958) (Christian, 1979):

$$E = \frac{c}{r} \mu (s^2 + \partial^2)$$

**Equation 2.9**

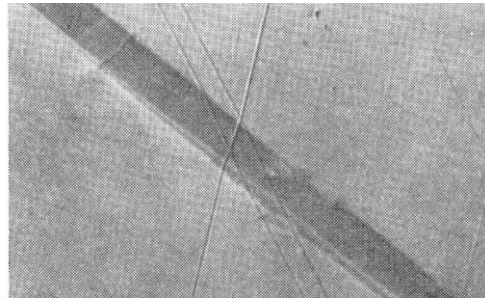
where  $\mu$  is the shear modulus of the parent lattice,  $c/r$  is the thickness to length ratio of the martensite plate and  $s$  and  $\delta$  are the shear and dilatational components of the shape deformation strain ( $\delta$  being much smaller than  $s$ ). It follows that martensite must always have a thin plate morphology, to minimize the  $c/r$  ratio, in order to minimize  $E$ . Thus, when martensite forms in a constrained environment, it grows in the shape of a thin lenticular plate or lath. The previously mentioned habit plane is then less clear, because the interface is curved on a macroscopic scale, as shown in Figure 2.19 (Bhadeshia, 2001b).



**Figure 2.19: The habit plane of martensite under conditions of unconstrained and constrained transformation, respectively (Bhadeshia, 2001b).**

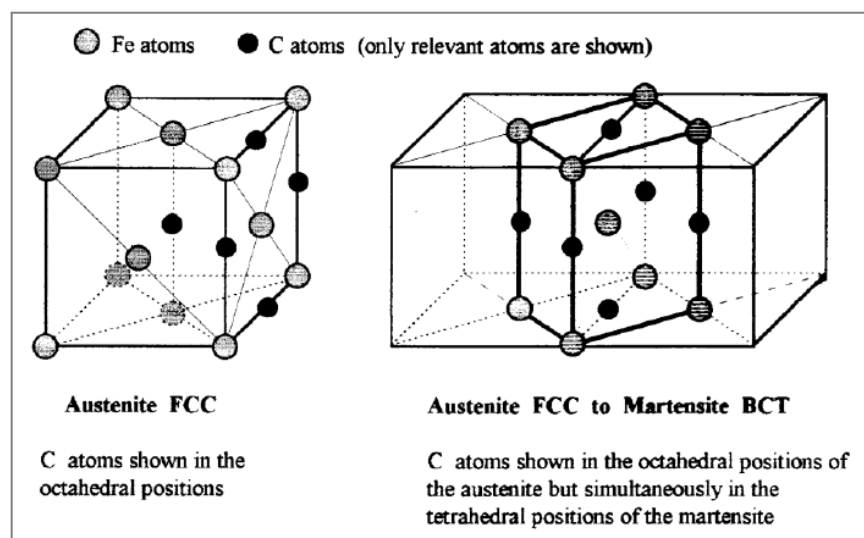
It is also interesting that when martensite forms due to an applied external deformation, the orientation of the crystals do not form randomly (Kundu & Bhadeshia, 2006). There is always an orientation relationship between the parent austenite and the martensite. There are 24 possible crystallographic orientations of martensite that can occur (Bhadeshia, 2002) and it is those that best accommodate the applied stress that will form (Bhadeshia, 1982). Martensitic plates commonly form at about  $45^\circ$  to either side of the axis of a uniaxial deformation.

Figure 2.20 shows how a scratch on the surface of an austenitic grain was displaced, without losing continuity when a martensitic plate was formed within (Wayman, 1965). This observation was fundamental to the early development of theories of martensitic transformations described in this section.



**Figure 2.20: Displacement of scratched due to the shape change caused by the formation of a martensite plate in Fe-7.9%Cr-1.11%C steel (Wayman, 1965).**

During the austenite to martensite transformation, carbon atoms move only a very short distance and remain in contact with their neighbouring atoms (thus, their relative position does not change) (Bowles, 1951). The carbon atoms occupy random positions along the  $\langle 100 \rangle$  directions in the austenite lattice. These carbon atoms become automatically ordered in that they occupy non-random positions in forming the tetragonal martensite lattice, as represented in Figure 2.21 (Bowles & Wayman, 1972) (Stumpf, 2010).



**Figure 2.21: A representation of the relationship of the carbon atom positions in the austenite lattice structure and their automatically ordered placement in the martensite lattice unit cell (Stumpf, 2010) after Bain (Bain, 1924).**

#### 2.4.4 Alloying chemistry for optimising the transformation

Steels making up the strain memory alloy group are very varied in their chemistry. They range from relatively simple alloys of the Fe-Ni-C group to alloys including various combinations of carbon, chromium, nickel, manganese, silicon, aluminium, nitrogen, molybdenum, phosphorus, cobalt, copper, titanium and niobium (Cina, 1954) (Cina, 1958) (Fahr, 1971) (Bhandarkar et al., 1972) (Olson & Azrin, 1978) (Hedström, 2005) (Krupp et al., 2008). Properties relating directly to the austenitic-martensitic transformation will be discussed here and other properties will be discussed in Section 2.4.5.

The level of stability of austenite at the operating temperature in any TRIP steel alloy is fundamental to its strain memory properties (Zackay et al., 1967) (Thompson, 1986). Alloying elements alter the equilibrium phase diagram by either expanding the austenite field (promoting formation of austenite) or by contracting the austenite field (promoting ferrite formation) (Andrews, 1965). Andrews proposed that the effects of alloying elements on the binary iron-carbon phase diagram may be divided into four main categories, defined as: open and closed austenite field systems and expanded and contracted austenite field systems (Andrews, 1965), as represented in Figure 2.22.

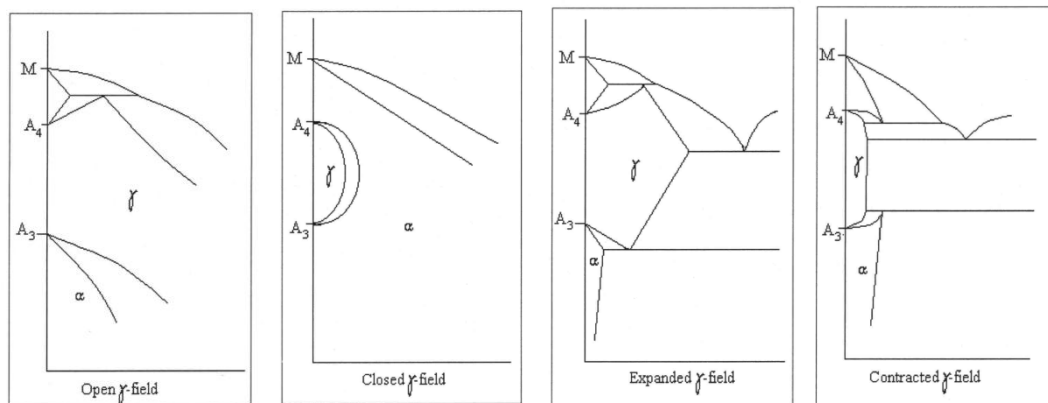


**Figure 2.22: A graphical representation of four categories of iron-carbon-alloy phase diagrams: open-field, closed-field, expanded-field and contracted-field austenite field systems (Andrews, 1965).**

Certain alloying elements promote an open austenite field. They stabilise austenite at room temperature and promote austenite formation over wider compositional limits. Elements that can act as austenite-stabilisers include nickel, manganese and cobalt, and the noble metals, ruthenium, rhodium, palladium, osmium, iridium, and platinum (Andrews, 1965). Although manganese can be a very weak  $\delta$ -ferrite former (Whittenberger et al., 1957), either nickel or manganese or a combination, added in sufficient quantities, can eliminate bcc ferrite entirely at room temperature in exchange for fcc austenite (Bhadeshia, 2005).

As will be seen from the Schaeffler diagram in Section 2.4.5, nickel depresses  $M_s$  temperature. Pineau & Pelloux showed that a 2.5% increase in the nickel content can produce a 150°C suppression in the  $M_s$  temperature (Pineau & Pelloux, 1974). Figure 2.23 shows the effect of manganese with carbon as an austenite-stabiliser and Figure 2.24 that of chromium with carbon (Bain, 1939). Bain found nickel and cobalt to have a similar effect to manganese and believed this to be due to all these elements not being more soluble in ferrite than in austenite, while also not being strongly carbide forming (Bain, 1939). It was later determined that manganese is not as powerful an austenitic stabiliser as nickel, but about half as effective (Schaeffler, 1949) (Schmid & Knutsen, 1992). However, manganese is much cheaper and has other possible beneficial properties (Lefevre et al., 1974), to be discussed in Sections 2.5 and 2.6. The relative



effectiveness of elements acting as ferrite or austenite formers in steels is shown in Figure 2.25 (Andrews, 1965).

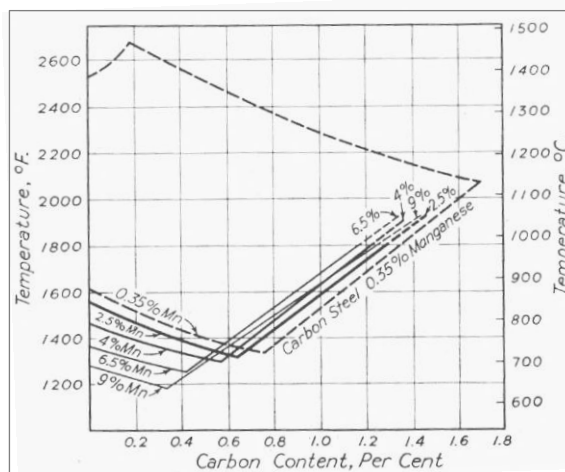


Figure 2.23: Effect of manganese with carbon on the austenite field (Bain, 1939), nickel and cobalt were found to have a similar effect.

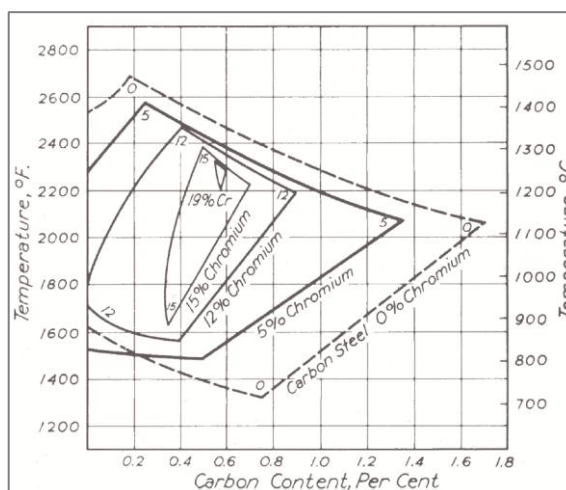


Figure 2.24: Effect of chromium with carbon on the austenite field (Bain, 1939).

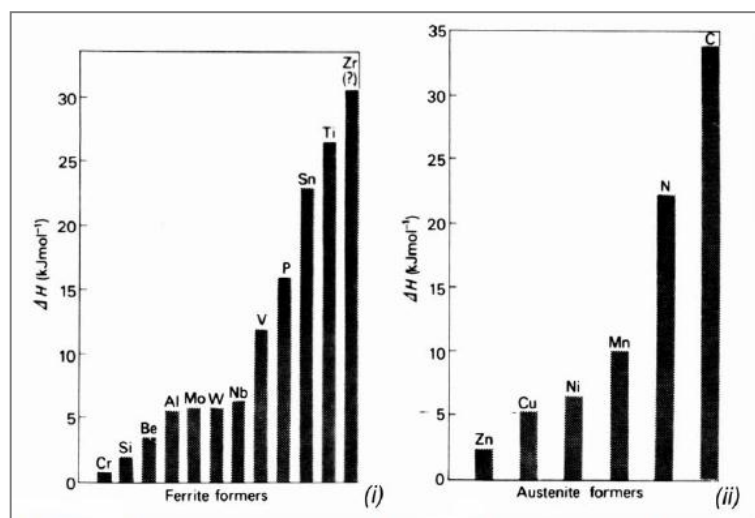


Figure 2.25: Relative effectiveness of (i) ferrite formers and (ii) austenite formers in the Fe-C system (Andrews, 1965).

Some elements, such as the interstitial elements carbon and nitrogen, promote an expanded austenite field. They also promote austenite stability, but because of the formation of compounds (carbides and nitrides) and because of their limited solubility in austenite and in ferrite, the field is cut short (Jeong & Matlock, 1993). This effect is shown in Figure 2.22 (c). Copper, zinc and gold also fall into this group. Substantial research has gone into the replacement or partial replacement of nickel by nitrogen in austenitic stainless steels, as nitrogen is an extremely cheap austenitic stabiliser (Reed, 1989) (Biggs & Knutsen, 1995) (Sumita et al., 2004). It has been found that similar properties can be attained with work hardening, but that higher nitrogen levels may cause martensite embrittlement.

Some elements reduce the stability of austenite, while promoting the formation of bcc ferrite. These elements can cause the austenite field to contract and close, and the ferrite  $\alpha$  and  $\delta$  phases to become continuous, as in Figure 2.22 (b) (Andrews, 1965). Elements in this category include silicon, aluminium, beryllium, phosphorus and the strong carbide-formers, chromium, molybdenum, titanium and vanadium. A carbide-forming element may be incorporated into austenitic alloys to promote certain properties, in spite of their effect on the austenite field. For example, chromium may be selected for its corrosion resistance or for its carbide formation, it can increase yield strength when combined with thermo-mechanical processing (Thelning, 1984) (Sumita et al., 2004) (Stumpf, 2010). Although chromium alone favours the formation of ferrite, when added to a steel containing nickel, it can retard the kinetics of the  $\gamma \rightarrow \alpha$  transformation, thus making it easier to retain austenite at room temperature, as represented on the Schaeffler diagram (Section 2.4.5, Figure 2.26) (Schaeffler, 1949).

The last group of elements are those that strongly contract the austenite field without causing the ferrite and austenite phases to become continuous. These elements include boron, as well as the other carbide-formers, tantalum, niobium, and zirconium. Niobium may be added in small quantities to promote grain refinement (Padilha et al., 2005).

Silicon is believed to suppress cementite formation (at about 1.5wt%), possibly due to extremely low silicon solubility in cementite, and thus causes more carbon to be retained in austenite, thereby stabilising high carbon austenite (Pichler et al., 1998) (Chatterjee & Bhadeshia, 2006) (Bhadeshia, 2002). It has been shown that aluminium can have a similar effect (Mahieu et al., 2002).

Many of the above properties are surmised in the Schaeffler diagram that will be examined in Section 2.4.5.

### 2.4.5 Schaeffler diagrams

The effects of various alloying elements on the stability of the austenite field in relation to iron have been discussed in Section 2.4.4. These effects are relatively simple when only one alloying element is added. In practice though, strain memory alloys usually contain several alloying elements in order to attain the required characteristics, as already discussed. The interaction of these different alloying elements creates considerable complexity. However, the general effect on phase stability can be understood by examining the Schaeffler diagram shown in Figure 2.26 (Schaeffler, 1949), or the Schaeffler-De Long diagram (De Long, 1974). These were originally developed for analysing weld metal composition after melting and rapid cooling.

The diagram functions by dividing the alloying elements through varying equivalences to nickel or chromium in terms of phase stabilisation. These equivalents are first calculated from equations that weight the contributions of the individual elements. The alloying elements are divided into ferrite-stabilisers and austenite-stabilisers, where Cr and Si are generally ferrite-stabilisers and Ni, Mn and C are austenite-stabilisers. There have been some significant alterations to the original weightings. For example, nitrogen, which can have dramatic effects, was not originally included by Schaeffler but was later added by De Long (Davis, 1994).

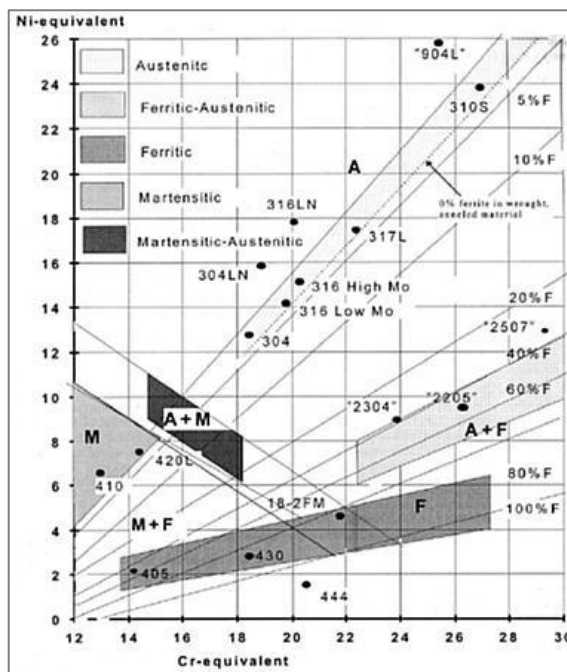


Figure 2.26: The Schaeffler diagram, developed by Schaeffler and modified by De Long to predict room temperature phases in a wide range of alloy steels (De Long, 1974).

The original equations for the chromium equivalent and nickel equivalent by Schaeffler are:

$$\text{Cr}_{\text{eq}} = \% \text{Cr} + \% \text{Mo} + 1.5\% \text{Si} + 0.5\% \text{Nb} \quad (\text{wt}\%)$$

$$\text{Ni}_{\text{eq}} = \% \text{Ni} + 30\% \text{C} + 0.5\% \text{Mn} \quad (\text{wt}\%)$$

Equations 2.10 and 2.11

The chromium equivalent and nickel equivalent are commonly calculated by giving each element an equivalent weighting in terms of its effect as a ferrite-stabiliser or austenite-stabiliser compared to chromium or nickel respectively (De Long, 1974). They were modified by De Long as follows:

$$\text{Cr}_{\text{eq}} = \% \text{Cr} + \% \text{Mo} + 1.5\% \text{Si} + 2\% \text{Ti} + 0.5\% \text{Nb} \quad (\text{wt}\%)$$

$$\text{Ni}_{\text{eq}} = \% \text{Ni} + 30\% \text{C} + 0.5\% \text{Mn} + 0.5\% \text{Cu} + 0.5\% \text{Co} + 25\% \text{N} \quad (\text{wt}\%)$$

**Equations 2.12 and 2.13**

However, there have been a number of proposals for modification to these weighting equations (Hull, 1973), due to the empirical nature of the Schaeffler diagram and the great variation in alloys it attempts to cover. For example, the flowing chromium equivalent equation is also used by some authors (Schneider, 1960) (Klueh & Mazaisz, 1990):

$$\text{Cr}_{\text{eq}} = \% \text{Cr} + 2\% \text{Si} + 1.5\% \text{Mo} + 5\% \text{V} + 5.5\% \text{Al} + 1.75\% \text{Nb} + 1.5\% \text{Ti} + 0.75\% \text{W} \quad (\text{wt}\%)$$

**Equation 2.14**

As seen from the Schaeffler-De Long diagram, nickel, manganese, carbon and nitrogen are the primary austenite-stabilisers (De Long, 1974). Chromium and silicon are the primary ferrite-stabilisers, although at a nickel equivalent of 10wt% or more, they work to stabilise austenite up to a chromium equivalent of 16wt%. Silicon can sometimes help to stabilise carbon-rich austenite by inhibiting carbide formation. Aluminium and phosphorus can also inhibit carbide formation in carbon-rich austenite.

The Schaeffler-De Long diagram illustrates which elements stabilise the various crystal structures and for a given alloy composition, what the expected crystal structure will be (De Long, 1974). The influence that certain alloying elements have on the diagram has been the subject of significant discussion. For example, the austenite-stabilising effect of manganese has more recently been considered by certain authors to be less than that estimated on the Schaeffler-De Long diagram (Davis, 1994) (Lampman, 1997). Some of these authors believe that the stabilizing effects of manganese are dependent on temperature. Specifically, it is believed that at high temperatures, manganese is a ferrite-stabiliser, while at lower temperatures it is an austenite-stabiliser (Lampman, 1997). It was largely for this reason that the WRC-1992 diagram was developed (Kotecki & Siewert, 1992); this diagram is considered to be more accurate than the Schaeffler diagrams, but does not take any account of manganese, as seen in Figure 2.27. Since manganese is of considerable interest in this work and since the transformations of interest occur at low temperature, the Schaeffler-De Long diagram will be utilized.

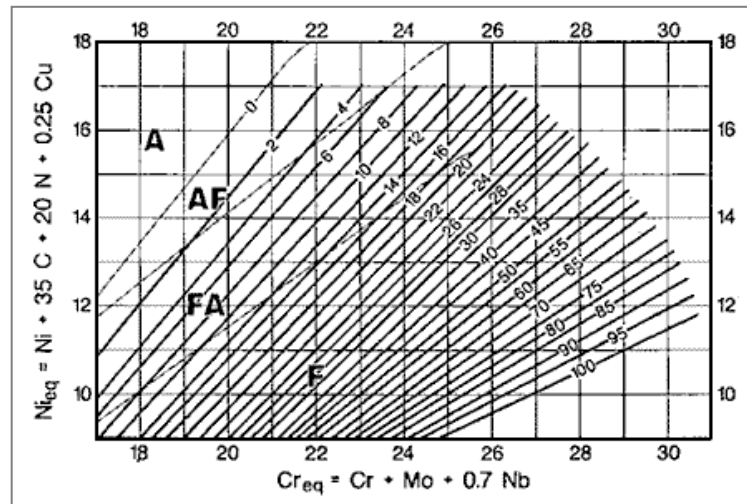


Figure 2.27: WRC-1992 Constitution Diagram for stainless steel weld metals (Kotecki & Siewert, 1992).

#### 2.4.6 Heat treatment, quenching and processing

Heat treatment of steels can alter a very broad range of properties. These include mechanical properties, physical properties such as resistance or magnetic permeability and microstructure conditions such as grain size, precipitation, phase or homogeneity.

Not all of these effects can be discussed here, but heat treatments can be broadly categorised into annealing, quenching and tempering, precipitation hardening (ageing), and case hardening. Annealing may be further categorised into several types whose effects vary drastically. These are illustrated in Figure 2.28 (Smith & Hashemi, 2006) and include (Thelning, 1984) (Higgins, 1994):

- Homogenising: A casting is brought to a significantly elevated temperature to allow for the reduction or elimination of chemical segregation and dendritic structures.
- Austenitizing: The casting is heated into the austenitic region to allow for the formation of austenite, before quenching or rapid cooling.
- Normalizing: The casting is heated to above the upper critical transformation temperature ( $Ac_3$ ) of the casting, and is held until austenite formation is completed. The casting is then removed from the furnace at temperature and cooled in moving or still air conditions.
- Full annealing: This process may be applied to any carbon steel. Hypo-eutectoid steels are heated to about  $50^\circ\text{C}$  above the  $Ac_3$  temperature and hyper-eutectic steels are heated to  $30^\circ\text{C}$  above  $Ac_1$ , since heating above this temperature would form coarse cementite. This is followed by slow cooling, usually in a furnace. The resulting structure is soft, coarse-grained, stress free, easily machinable and ductile. This may be followed by a quench and temper hardening process.

- Process annealing: An imprecise term, sometimes also called intermediate annealing or subcritical annealing. It consists of a stress-relieving heat treatment cycle that restores some of the ductility to a workpiece, often in order to allow it be worked further without breaking.
- Spheroidizing anneal: A prolonged annealing treatment, at a temperature just below  $Ac_1$ . Used to improve machining or cold forming properties of pearlitic steels. No phase change occurs but the cementite layers change into a globular form within the ferritic matrix. This structure may then be reverted back to pearlite via austenitization.

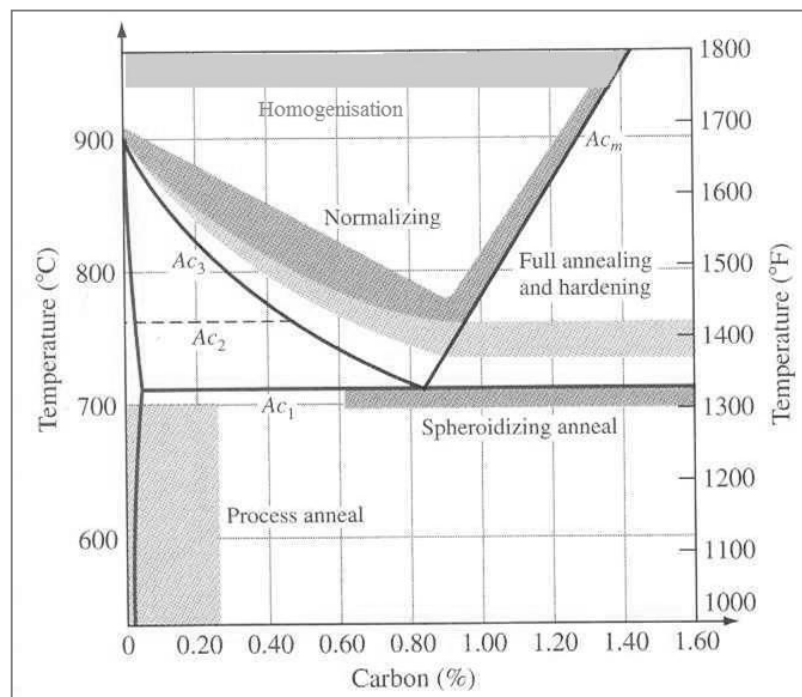


**Figure 2.28: Some common annealing processes and temperatures for carbon steels. (Smith & Hashemi, 2006).**

Quenching and tempering refers to a heat treatment where the steel is quenched rapidly from austenite to form hard, brittle martensite, which is then tempered by heating to a relatively low temperature to allow diffusion. This is usually between 150° and 650°C, and the range between 300°C and 500°C is usually avoided due to potential embrittlement (Totten, 2007). The tempering process produces ferrite finely interspersed with cementite of a form similar to but not the same as pearlite or bainite. Some fine martensite will usually remain after tempering. Precipitation hardening a steel is similar to tempering.

The quenching and tempering process is largely inapplicable to the current work since high alloy TRIP steels with an austenitic structure are implemented. However, some martensite or ferrite will likely be present in the structure before deformation (Maxwell et al., 1974). It may

be preferable to have this as martensite rather than as ferrite, since martensite is more likely to encourage further martensite formation by growth or provision of nucleation sites.

Grain size is generally easily increased via heat treatment. Grains size tends to increase at high temperatures and longer times. Grain size can be reduced through cold work and dynamic recrystallization, and sometimes through heat treatment. For most engineering applications at ambient temperatures, a fine grain size is ideal since this usually increases yield strength and toughness, while often not significantly impacting ductility. The Hall-Petch relationship describes the manner in which yield strength, is related to grain size (Hall, 1951) (Petch, 1953).

Most steel forms are shaped through hot working where the material is deformed above its recrystallization temperature. Hot working usually increases the strength, ductility and toughness of an alloy. This occurs primarily through grain refinement during dynamic recrystallization, reduction or closing of pores and reorientation of inclusions.

High chromium content in steels promotes grain growth at high temperature. This effect is offset when nickel is included, since nickel promotes grain refinement (Higgins, 1994). Chromium readily forms carbides at high temperature (between 425°C and 900°C) (Douthett, 1991). This means that certain regions will become depleted in chromium. Elements such as titanium or niobium (which have greater affinity than chromium for carbon) may be added since the formation of the titanium or niobium carbides will slow or prevent formation of chromium carbides via carbon depletion. Alternatively, rapid quenching from the austenitic region means that carbides do not have a chance to form. High alloy TRIP steels essentially never leave their austenitic region, even at room temperature, and are thus not susceptible to this phenomenon, since carbon remains in solution within the austenite matrix.

Homogenisation of stainless steels to remove alloy segregation and dendritic structures is carried out at temperatures at or above 1100°C for at least two hours (Douthett, 1991). Austenitic steels are usually annealed between about 1050°C - 1100°C and stress relieved at about 900°C. Stress relieving of austenitic stainless steels is usually only necessary when parts are subjected to conditions conducive to stress corrosion or intergranular corrosion. The level of stress relief is primarily proportional to temperature and not holding time. Since full stress relieving generally requires slow cooling, sensitization by chromium carbide formation and associated intergranular corrosion may again become a problem. Heating in the range between 540°C to 925°C (or slow cooling through this region) may form the hard, brittle sigma phase.

Heating in the annealing range will revert the microstructure to chromium carbide and sigma phase. Long annealing should dissolve some ferrite, if present. Solution annealing is usually carried out at 1095°C for more than half an hour, up to several hours (Douthett, 1991). With niobium-stabilised alloys, a further stabilizing treatment should be carried out at between 870°C and 925°C in order to precipitate niobium carbides.

Cold or warm working, where a material is deformed below its recrystallization temperature, significantly increases the yield strength and often also increases the tensile strength of a material, while the ductility decreases (Askeland, 1988). The strengthening takes place due to an increase in dislocation concentration. These dislocations are accompanied by strain fields in their vicinity and they act to prevent slip, the mechanism by which metals usually deform plastically. When TRIP steel alloys are warm-worked, it is important to avoid carbide precipitation as well as  $\alpha'$  martensite formation. Figure 2.29 is used to determine optimal warm working temperatures (Padilha et al., 2003).

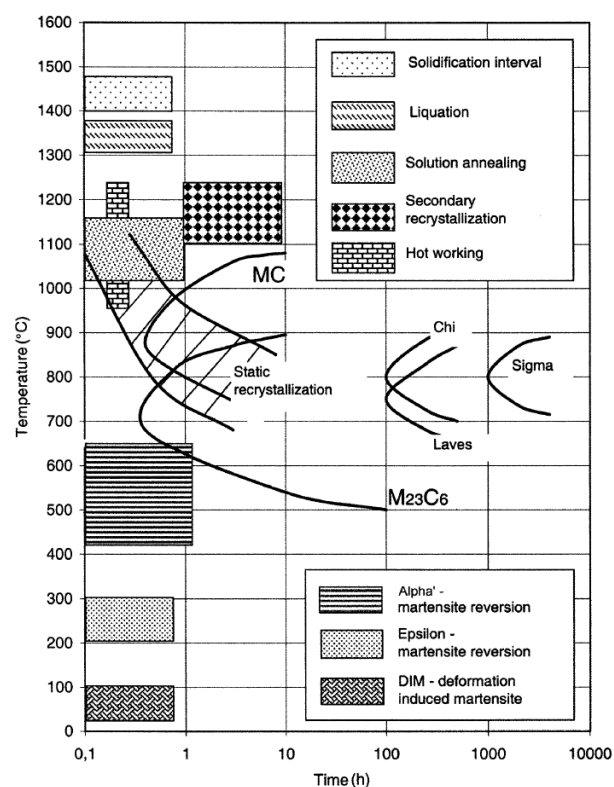
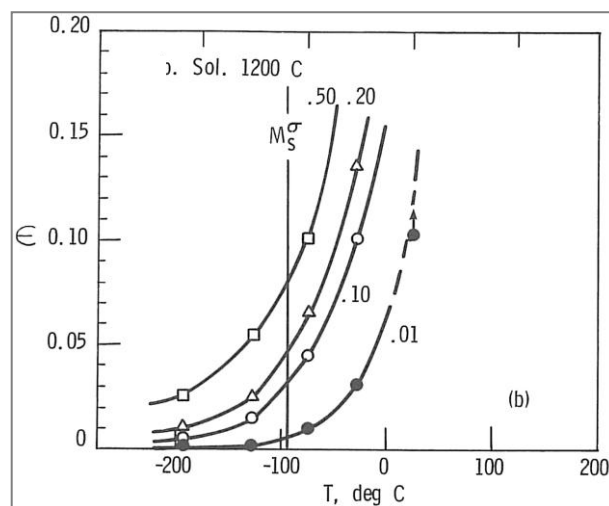


Figure 2.29: Transformations occurring in austenitic stainless steels (Padilha et al., 2003).



## 2.5 The influence of temperature and strain rate on the transformation

The quantity of martensite formed at a given stress or strain in a particular TRIP steel and the repeatability thereof is of particular concern. It has been shown that specimen temperature at time of deformation has an effect on the quantity of martensite formed at a given stress or strain (Fahr, 1971). Figure 2.30 shows a greater strain being required to induce a given amount of martensite in this alloy, as temperature increases (Olson & Azrin, 1978).



**Figure 2.30: Temperature dependence of tensile plastic strain required to give fixed volume fractions of martensite as shown. Fe-0.27C-0.78Mn-2.13Si-8.06Ni-9.11Cr-4.05Mo TRIP steel solution treated at 1200°C. (Olson & Azrin, 1978)**

From just before  $M_s^\sigma$ , the temperature where transformation is considered to change from stress-assisted to strain-induced, the transformation kinetics are seen to become more temperature sensitive (Olson & Azrin, 1978). However, Maxwell and co-workers found that strain-induced martensite is less temperature-sensitive than stress-induced martensite (Maxwell et al., 1974). Figure 2.31 shows the transformation of martensite with true strain at a variety of temperatures in a 29wt% nickel, 0.2wt%C alloy (Maxwell et al., 1974).

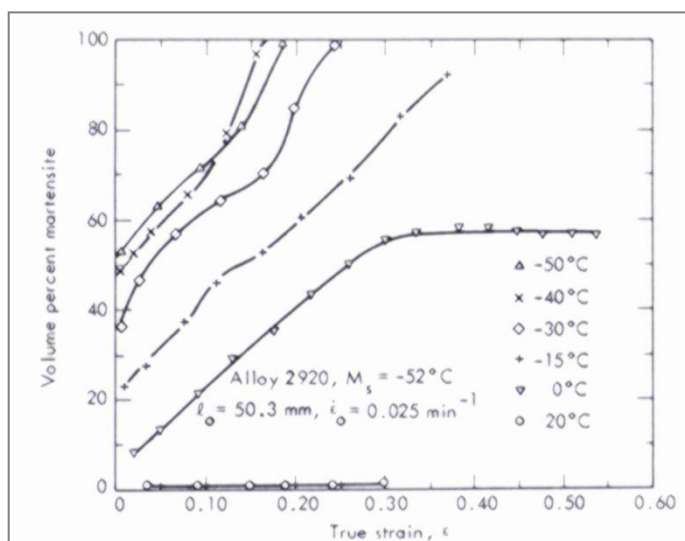


**Figure 2.31: Proportion martensite versus true strain for an Fe-Ni-C alloy of 29Ni, 0.2C, where  $M_s = -52^{\circ}\text{C}$  (Maxwell et al., 1974).**

The amount of martensite formed decreases with both increasing temperature and strain-rate (Form & Baldwin, 1956). It has been shown that the influence of strain rate on martensite formation is closely related to that of temperature (Bressanelli & Moskowitz, 1966) (Andrade-Campos et al., 2008) (Powell et al., 1958) (Olson & Azrin, 1978). In the same way that higher temperatures result in less martensite formation for a given strain, higher strain rates result in less martensite formation than lower strain rates do, particularly during strain-induced transformation, as shown in Figure 2.32 (Bressanelli & Moskowitz, 1966). Higher strain rates increase the specimen temperature more than lower strain rates, as shown in Figure 2.33 (Bressanelli & Moskowitz, 1966). It is thus believed that the effect of higher strain rates decreasing martensite formation is due principally to the higher specimen temperatures induced at these strain rates due to internal adiabatic heating. The temperature increases due to adiabatic heating are substantial and easily measured. The effect is more pronounced at lower temperatures than at higher temperatures, relative to  $M_d$ . This is because at lower temperatures, more martensite is produced and thus, due to the release of chemical free energy in the transformation, more heat energy is released more rapidly. The temperature difference between high and low strain rate specimens tested at lower temperatures was greater than for specimens tested at higher temperatures (Bressanelli & Moskowitz, 1966).

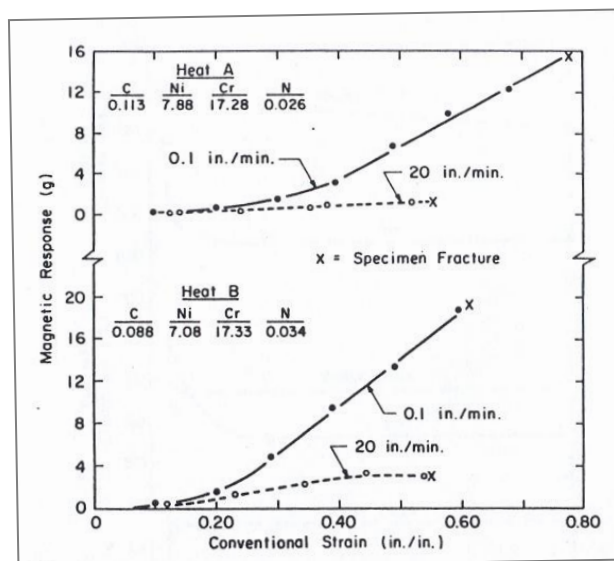


Figure 2.32: Effect of test speed on martensite formation (magnetic response) during testing (Bressanelli & Moskowitz, 1966).

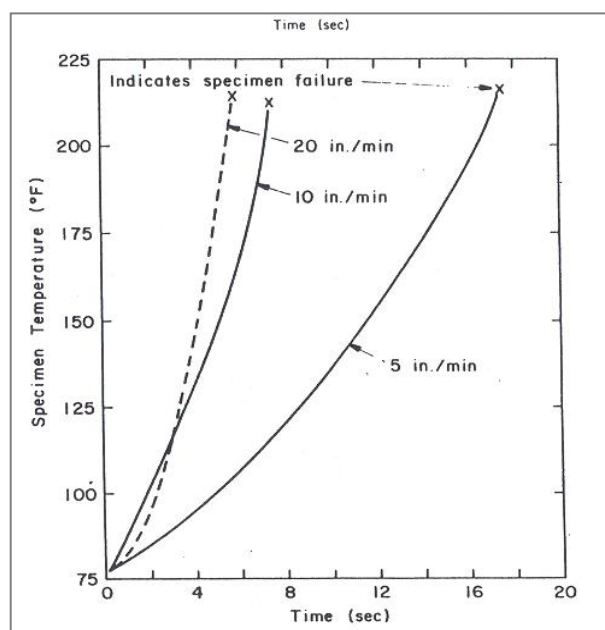
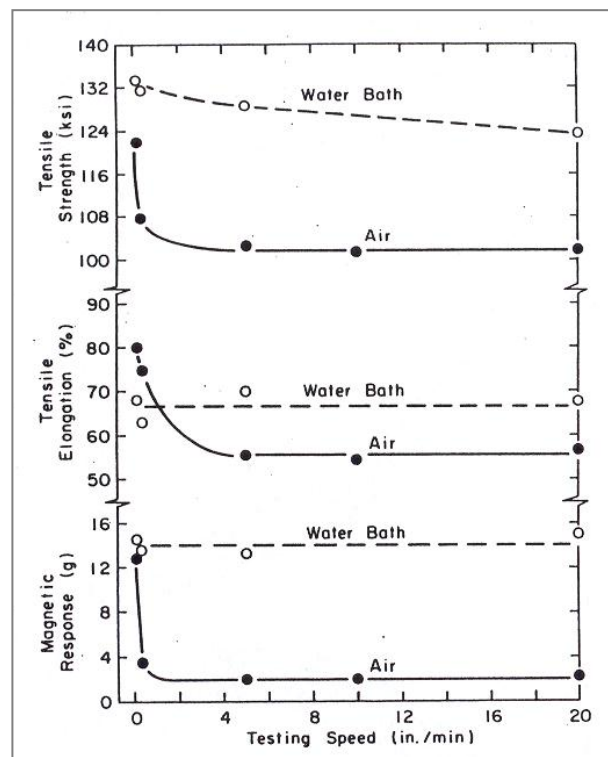


Figure 2.33: Time-Temperature profiles for specimen heating at various testing speeds (Bressanelli & Moskowitz, 1966).

In order to determine and explain the effects of test speed on the tensile properties of metastable austenitic stainless steels, Bressanelli and Moskowitz compared thin wire specimens tested in water baths to those tested in air (Bressanelli & Moskowitz, 1966). All steels in the study were considered fully austenitic prior to tensile testing and all had a fine grain size (smaller than ASTM 7). The steels formed no detectable martensite when cooled to  $-70^{\circ}\text{C}$ , the lowest test temperature used in the study, or when deformed at above  $260^{\circ}\text{C}$ , considered as  $M_d$  temperature.

The relative amounts of martensite formed during tensile testing were determined by measuring change in magnetic response (Bressanelli & Moskowitz, 1966). An analytical balance was used to determine the force required to separate the specimen from the pull of a magnet. The highly cold worked nature of the tensile specimens made direct correlation of magnetic response with metallographic measurement of martensite very difficult. This was due to the resultant highly distorted, fine microstructure of the samples making it difficult to identify distinct phases accurately. Magnetic response and X-ray diffraction were thus utilised instead. As seen in Figure 2.32, a lower strain rate resulted in a higher amount of martensite formation for a given strain (elongation) than a higher strain rate did when tested in air. Higher strain rates result in more adiabatic heating in the tensile test specimens as demonstrated in Figure 2.33 (note that the specimen strained at 20 in/min probably had a delayed temperature reading response due to this higher strain rate). It was concluded that these increased temperatures led to the observed lower rate of transformation (Bressanelli & Moskowitz, 1966).

The work-hardening coefficient of the material,  $w$ , generally decreased with increasing test speed. The specimens tested at a faster speed in water showed much higher martensite contents than specimens tested at the same speed in air, as shown in Figure 2.34 (Bressanelli & Moskowitz, 1966). Results were almost constant over a broad range of testing speeds when tested in the water bath.



**Figure 2.34: Comparison of tensile properties and transformation at higher speeds for specimens from heat A tested in air and in a water bath (Bressanelli & Moskowitz, 1966).**

It can be concluded that speed does not directly affect tensile elongation or magnetic response (martensitic transformation). It was concluded that the more uniform results obtained in the water bath were due to the reduction of adiabatic specimen heating via rapid heat transfer from the specimen during testing. Heat within the thin wire specimens was dissipated into the water quickly enough for the specimen temperature to remain significantly more stable. It was thus concluded that the effect on tensile properties (and associated martensitic transformation) is related to increased temperature (Bressanelli & Moskowitz, 1966).

Figure 2.35 illustrates how when test specimens of 301 stainless steel were immersed in a bath at 20°C, there was no drastic change in the level of transformation with strain-rate variation over two orders of magnitude ( $6 \times 10^{-3} \text{ min}^{-1}$  to  $600 \times 10^{-3} \text{ min}^{-1}$ ) (Powell et al., 1958). It is expected that the strain-rate effect would have been more severe if the tests had been carried out in air. However, these specimens were relatively thick, at 9.5mm diameter, and thus the water would be expected to have a reduced effect on adiabatic heating. It should be noted that even the maximum strain rate shown here ( $600 \times 10^{-3} \text{ min}^{-1}$  or  $0.01 \text{ s}^{-1}$ ) was not substantially high; strain rates up to  $10 \text{ s}^{-1}$  may be of interest in the current research.

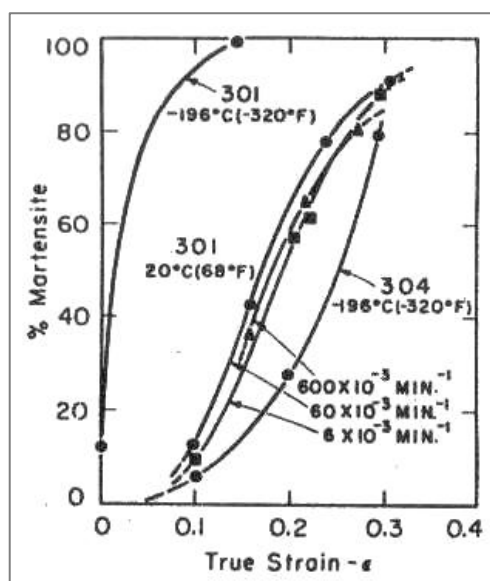


Figure 2.35: Volume percent martensite produced by tensile deformation in alloys AISI 301 and in AISI 304 at various strain rates (Powell et al., 1958).

Temperature and strain rate sensitivity might be reduced by manipulating composition and processing parameters. In certain TRIP steels, in particular the Fe-Cr-Mn group, it is possible to form intermediate  $\epsilon$  martensite from the parent austenite prior to  $\alpha'$ -martensite formation (previously discussed in Section 2.4.2). This is because the driving force required for  $\epsilon$  martensite is lower in these materials (Christian, 1979). The  $\gamma \rightarrow \alpha'$ ,  $\gamma \rightarrow \epsilon$  and  $\epsilon \rightarrow \alpha'$  transformation temperature for Fe-Mn binary alloys are represented in Figure 2.36.

Transformation of  $\gamma \rightarrow \varepsilon$  might be achieved prior to installation, by applying temperatures below operating temperature, by pre-straining or through pre-straining while at low temperatures.

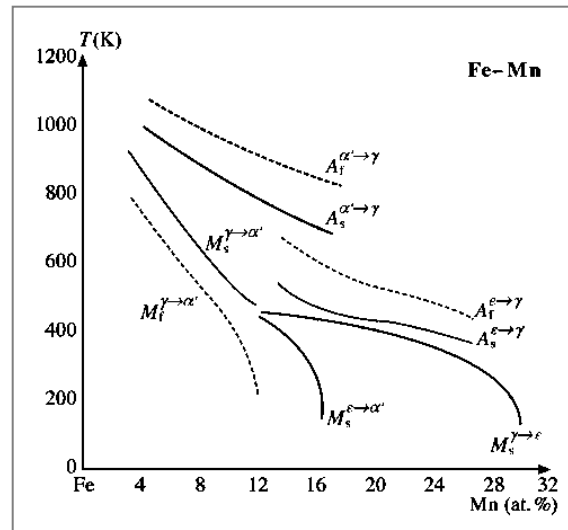


Figure 2.36: Transformation temperatures of Fe-Mn alloys (Christian, 1979).

Hexagonally close packed (hcp)  $\varepsilon$  martensite is of intermediate thermodynamic stability and is antiferromagnetic in the range of room temperature (Bracke et al., 2006) or paramagnetic according to Abrassart (Abrassart, 1973). Practically, there is little difference between antiferromagnetic and a paramagnetic material since neither are significantly magnetically permeable.

It was previously hypothesised and more recently experimentally shown that  $\varepsilon$  forms ahead of  $\alpha'$  as a result of cold work in some TRIP steel type alloys (Otte, 1957) (Cina, 1958) (Mostafa et al., 2007). Walters and Wells, Cina and to some extent Otte agree that Mn is the primary element producing these effects, and that high levels of carbon can suppress  $\varepsilon$  formation in Fe-Mn alloys (Walters & Wells, 1936) (Cina, 1958) (Otte, 1957). Cina showed that carbon simply lowers the  $M_s$  and  $M_d$  temperatures and does not in fact truly suppress  $\varepsilon$  formation. Some authors believe that in high Cr or high Mn alloys the  $\alpha'$  formation proceeds through the sequence fcc  $\rightarrow$  hcp  $\rightarrow$  bcc, while another has proposed that the fcc  $\rightarrow$  bcc transition is instead only stimulated by presence of the hcp martensite phase, although this was shown to be unlikely (Maxwell et al., 1974) (Hull, 1973) (De et al., 2004) (Das et al., 2008). While  $\varepsilon$ -martensite contributes to strain hardening, it has been shown that it does not increase ductility (Bracke, et al., 2006). It has been shown that Fe-Ni alloys do not form  $\varepsilon$ -martensite, and only Fe-Ni-Cr alloys of at least 24% to 28% combined Ni and Cr content will form  $\varepsilon$ -martensite (Otte, 1957) (Cina, 1958).

It has been documented that differences in strain induced martensite transformation behaviour can be largely attributed to changes in the austenite's intrinsic stacking fault energy (SFE) (Dunning, 1969) (Bracke et al., 2006) (Samek et al., 2006). A low intrinsic SFE implies that stacking faults will form readily in the austenite. In fcc metals, stacking faults originate from the dissociation of a perfect dislocation (Bracke et al., 2006). An intrinsic stacking fault is essentially a thin, four lattice-plane thick  $\epsilon$ -martensite crystal, and is thus a possible  $\epsilon$ -martensite nucleation site. Otte (Otte, 1957) stated that the hcp structure may be thought of as an ordered arrangement of stacking faults and thus the susceptibility to faulting may be reflected by the formation of an hcp structure. In the case of hcp platelets, nucleation is achieved by the propagation of intrinsic stacking faults on every other (111)  $\gamma$  plane (Kelly, 1965) (Lecroisey & Pineau, 1972) and in the case of twins, on each (111)  $\gamma$  plane (via a lattice invariant shear) (Hirthe & Lothe, 1968). The influence of an alloying element on the SFE is not unambiguous, it depends on the type and concentration of the other alloying elements (Dunning, 1969) (Bracke et al., 2006). Low SFE austenite favours martensitic transformation, while high SFE austenite favours mechanical twinning instead. Mechanical twinning generally promotes high elongation, as does the  $\gamma \rightarrow \alpha'$  transformation, while the  $\gamma \rightarrow \epsilon$  transformation is not considered to substantially improve elongation (Grassel, 1997).

Otte noted that in the compositional range studied, Cr and Mn lower the austenite stacking fault energy, though a combination of Cr and Mn promote  $\epsilon$  martensite stacking faults, he concluded that they were not a source of nucleation for bcc martensite (Otte, 1957). Contrary to this, several later authors concluded that stacking faults may be a source of nucleation for bcc martensite (Abrassart et al., 1970) (Fahr, 1971) (Olson & Cohen, 1975).

As previously discussed (Section 2.4.2),  $\alpha'$  may nucleate at austenite slip band intersections, with nucleation within macroscopic shear band intersections being predominant in most TRIP alloys, in the manner shown in Figure 2.37 (Bracke et al., 2006). The  $\epsilon$  is just one type of shear band whose intersections may nucleate  $\alpha'$  (for example, mechanical twins or dense stacking fault bundles may do the same) (Olson & Cohen, 1975). It seems that these other forms of shear band nucleation occur through a wider range of intrinsic SFEs. Abrassart's observation was that plastic deformation in TRIP steel is achieved through a combination of the processes of mechanical twinning, propagation of stacking faults and formation of  $\epsilon$ -martensite (Abrassart, 1973).

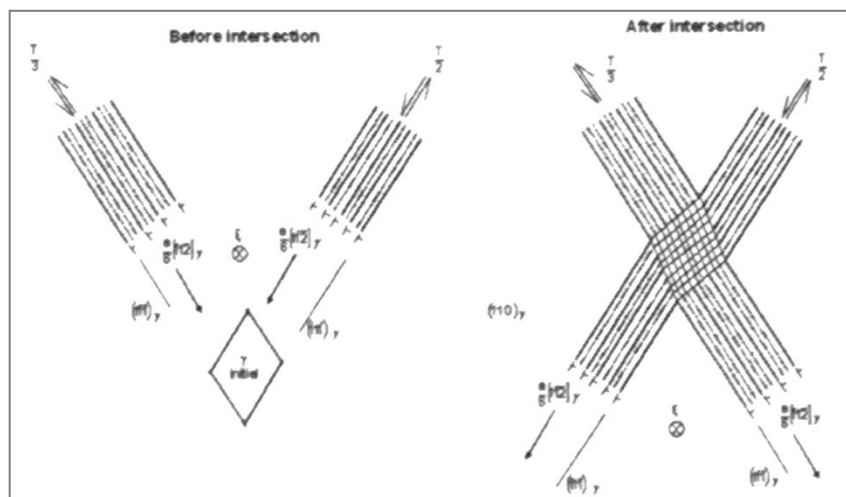


**Figure 2.37: Schematic illustration of the nucleation of  $\alpha'$  martensite at the intersection of deformation bands in austenite (Bracke et al., 2006).**

As discussed, there is believed to be an association between the formation of stress-induced martensite and the prior presence of  $\epsilon$ -martensite and mechanical twins. The level of nucleation stress required for the elastic stress-induced  $\gamma \rightarrow \alpha'$  transformation (at temperatures where this occurs, near  $M_s$ ) is directly dependant on the stress required to propagate planar defects in austenite (Abrassart, 1973). Dislocation strain energy assisted transformation nucleation theory suggests that martensitic nucleation is dependent on dislocation density (Porter et al., 2009). It has been suggested that the nucleation of elastic stress-induced  $\alpha'$  arises more readily if planar defects are in greater number and/or if existing or new planar defects can propagate more freely, as is the case in low stacking fault energy austenites (Andrews, 1965) (Hull, 1973) (Parker, 1997). Stacking fault energy is a function of composition and temperature. Alloys exhibiting a larger difference between  $M_d$  and  $M_s$  temperatures have lower stacking fault energy austenites. This is believed to be because a low SFE raises  $M_d$  without as significantly impacting  $M_s$ , although some alloys such as silicon and aluminium have been shown to both increase SFE and decrease  $M_s$  and others, such as manganese to decrease SFE and increase  $M_s$  (Effenberg, 2008).

It is widely held that manganese reduces the SFE of steels, although some authors have found the opposite effect in high alloy steels, specifically those with high aluminium contents (Frommeyer et al., 2003) (Mazancová et al., 2009). At manganese contents above approximately 10% to 15%, it is believed that  $\epsilon$ -martensite is formed prior to  $\alpha'$  formation, and can be formed on simply water quenching from austenitization temperature to room temperature, as shown in Table 2.1 (Cina, 1958) (Skroc, 2010). Otte concluded that in type 304 (or 18/8) stainless steel alloys (Fe-Cr-Ni with low Mn and C) total transformation to  $\epsilon$  martensite could not be achieved by any available method, and no  $\epsilon$  martensite formed spontaneously on cooling (Otte, 1957). However, he showed that very light low-temperature



deformation would produce  $\epsilon$ , while some further deformation would produce  $\epsilon$  and  $\alpha'$ . It was noted that  $\epsilon$  phase formed before  $\alpha'$  formation.

Cina investigated manganese, nickel and chromium alloy steels, with the amounts of these alloying elements varying between 0% and 20% (Cina, 1958). Not all of the alloys investigated by Cina are included here. The alloys were each subjected to one of three different heat treatments, as denoted in Table 2.1 (Cina, 1958). The first consisted of a ten minute anneal at 1050°C and then water quenching. The second was the same as the first, but followed with ten minutes at -196°C. The third followed that of the first by heavy cold working of about 50%. The notation in the last three columns of Table 2.1 represents the qualitative extent of each phase found to be present by X-ray diffraction as follows (Cina, 1958):

**Table 2.1: Constitution of plain Fe-Mn alloys (Cina, 1958).**

Series	Alloy number	Alloy %Mn	Treatment	Intensity of X-ray diffraction patterns		
				$\gamma$	$\epsilon$	$\alpha'$
(a)	i	5	10 min at 1050°C, water quench	0	0	S
	ii	10	10 min at 1050°C, water quench	VW	W	M/S
	iii	15	10 min at 1050°C, water quench	M	M/S	VW
	iv	20	10 min at 1050°C, water quench	M	M/S	0
(b)	i	10	As (a), 10 min at -196°C	0	W	M/S
	ii	15	As (a), 10 min at -196°C	M	M/S	VW
	iii	20	As (a), 10 min at -196°C	M	M/S	W
(c)	i	10	As (a), heavy cold work	0	0	S
	ii	15	As (a), heavy cold work	0	VW	M
	iii	20	As (a), heavy cold work	VW	W	M

Key: 0 = none; VW = very weak; W = weak; M = medium; M/S = medium-strong; S = strong

Cina assumed that increasing manganese content allowed  $\epsilon$  to form more readily by depressing the  $M_s$  of the  $\gamma \rightarrow \alpha'$  transformation. As seen in Table 2.1, heavy cold work in the 10wt% Mn alloy (c-i) caused all of the  $\gamma$  and  $\epsilon$  to transform to  $\alpha'$  (Cina, 1958). In the 15wt% Mn alloy (c-ii), all of the  $\gamma$  and most of the  $\epsilon$  transformed and in the 20wt% Mn alloy (c-iii), most of the  $\gamma$  and  $\epsilon$  transformed. It was further shown that replacing up to 10wt% Mn with nickel (series d, Table 2.2) in the 20wt% Mn alloy still allowed  $\epsilon$  to be formed, but that the amount of  $\epsilon$  decreased in favour of  $\gamma$  and to some extent  $\alpha'$ , in proportion to the amount of Ni added. Table 2.2 shows that this trend was continued after the low temperature and cold work treatment (series e and f), and that proportion of  $\alpha'$  increased as manganese was replaced with nickel, but with lesser effect after cold work (Cina, 1958).

**Table 2.2: Constitution of Fe-Mn-Ni alloys (Cina, 1958).**

Series	Alloy number	Alloy wt% Mn	Alloy wt% Ni	Treatment	Intensity of X-ray diffraction patterns		
					$\gamma$	$\epsilon$	$\alpha'$
(d)	i	20	-	10 min at 1050°C, water quench	M	M/S	0
	ii	15	5	10 min at 1050°C, water quench	M	M/S	VW
	iii	10	10	10 min at 1050°C, water quench	S	VW	W/M
	iv	5	15	10 min at 1050°C, water quench	M	0	S
(e)	i	20	-	As (a), 10 min at -196°C	M	M/S	W
	ii	15	5	As (a), 10 min at -196°C	M	M/S	W
	iii	10	10	As (a), 10 min at -196°C	M/S	VW	M
	iv	5	15	As (a), 10 min at -196°C	W	0	S
(f)	i	20	-	As (a), heavy cold work	VW	W	M
	ii	15	5	As (a), heavy cold work	VW	W	M
	iii	10	10	As (a), heavy cold work	M	0	M
	iv	5	15	As (a), heavy cold work	0	0	M/S

Key: 0 = none; VW = very weak; W = weak; M = medium; M/S = medium-strong; S = strong

Table 2.3 shows that replacement of up to 10wt% Mn by Cr (series g) had a similar effect on structure to replacement by Ni, except that a greater relative amount of  $\epsilon$  was observed (Cina, 1958). Heavy cold work caused complete transformation from  $\gamma$  and  $\epsilon$  to  $\alpha'$  (series i), except in the 15wt% Cr alloy, where transformation to  $\alpha'$  was already completed thermally (series h).

**Table 2.3: Constitution of Fe-Mn-Cr alloys (Cina, 1958).**

Series	Alloy number	Alloy wt% Mn	Alloy wt% Cr	Treatment	Intensity of X-ray diffraction patterns		
					$\gamma$	$\epsilon$	$\alpha'$
(g)	i	20	-	10 min at 1050°C, water quench	M	M/S	0
	ii	15	5	10 min at 1050°C, water quench	M	M+	M
	iii	10	10	10 min at 1050°C, water quench	0	W	S
	iv	5	15	10 min at 1050°C, water quench	0	0	M/S
(h)	i	20	-	As (a), 10 min at -196°C	M	M/S	W
	ii	15	5	As (a), 10 min at -196°C	W/M	M+	M
	iii	10	10	As (a), 10 min at -196°C	0	W	M
	iv	5	15	As (a), 10 min at -196°C	0	0	M/S
(i)	i	20	-	As (a), heavy cold work	VW	W	M
	ii	15	5	As (a), heavy cold work	0	0	M/S
	iii	10	10	As (a), heavy cold work	0	0	M/S
	iv	5	15	As (a), heavy cold work	0	0	M/S

Key: 0 = none; VW = very weak; W = weak; M = medium; M/S = medium-strong; S = strong

Cina's work shows that, in 20wt% Mn alloys, carbon content should be kept below 0.2wt% to avoid excessive depression of the  $M_d$  and  $M_s$  points of the  $\gamma \rightarrow \epsilon$  transformation (sometimes referred to as  $E_d$  and  $E_s$  with regards to  $\gamma \rightarrow \epsilon$ ) (Cina, 1958). However, the effect of increased carbon content could be offset somewhat, according to the Schaeffler equations (Schaeffler, 1949), by reducing the manganese content. Cobalt is regarded as a  $\gamma$ -stabiliser in Fe-Cr-Ni alloys, as can be seen from the  $Ni_{eq}$  in the Schaeffler diagram. However, Cina found that in combination with Mn in relatively high contents (5wt% to 10wt% Co, 10wt% to 15wt% Mn),

Co favours the formation of  $\alpha'$  (Cina, 1954). Adding Co or Cr to Fe-Mn alloys was generally shown also to suppress  $\epsilon$  formation in favour of  $\alpha'$ . Ni suppressed  $\epsilon$  in favour of  $\gamma$ .

Otte found that Cr and Mn had a strong effect in promoting stacking fault formation in austenite (Otte, 1957). He found that nickel had a drastically lesser effect. No hcp structure was found in the Fe-Ni system as in Fe-Mn system. It was also found that adding Cr to Fe-Ni alloys in the stainless steel composition range caused an hcp structure to appear. Further, he found that the addition of Cr to basic Fe-C alloys resulted in stacking faults upon quenching, whereas addition of Ni to basic Fe-C alloys did not produce stacking faults without deformation. Further, he found that addition of sufficient quantities of carbon to Fe-Mn alloys eliminated the hcp structure, as in Hadfield's steel composition (Hadfield, 1888), where only stacking faults were found (Otte, 1957). A similar effect was found in stainless steels, however an hcp structure may still form after deformation with up to 0.1wt% carbon present.

Cina found that in Fe-18Cr+8Ni alloys (304 type), the hcp phase was formed during low temperature deformation and this phase was finally transformed to  $\alpha'$  by further transformation until  $\epsilon$  was eliminated beyond about 25% deformation (Cina, 1958).

Otte also found that a 17/7 alloy was substantially more easily transformed to what was considered 100 percent martensite than were the 18/8 alloys (Otte, 1957). Otte and Cina both found that a lesser amount of transformation was generally found in alloys quenched from higher austenitization temperatures (1320°C as opposed to 1100°C) (Cina, 1954).

Abrassart examined two different TRIP steels that were subjected to prior deformation at various temperatures above  $M_d$  (Abrassart, 1973). It was found that when deformed well above  $M_d$ , there were very few planar defects formed and that there was segregation of impurities on the dislocations. Such segregation of impurities reduces the ability of planar defects to propagate under stress. On the other hand, when prior deformed at a temperature just above  $M_d$ , a large number of planar defects were formed. This material then transformed to martensite under elastic stress considerably more readily than the material prior deformed at a higher temperature. Although the materials were not tested without prior deformation, it may be concluded that the presence and propagation of planar deformations such as mechanical twins and  $\epsilon$ -martensite encourage stress-induced  $\alpha'$  formation, thereby promoting earlier transformation before yield as well as potentially lower sensitivity to temperature.

Dunning and Thompson concluded that sensor alloys which are based on carbon-free chemical formulations display reduced strain rate effects (Dunning & Thompson, 1995). In that study, the difference in strain rate was noted as only one order of magnitude, yet a significant variation in results was apparent. This assertion demonstrates that the level of insensitivity to temperature and strain rate required for the purposes of the current work is considerably greater than for some previous work. The use of TRIP steels as strain sensor materials means that the extent of transformation directly impacts the functioning of the proposed devices and reduced susceptibility to such phenomenon is thus required.

Data obtained from the numerical model by Sherif, examined in Section 2.6.3, infers that a reduction in carbon content from 0.12wt% to 0.6wt% does indeed reduce the temperature susceptibility of the martensitic transformation, as shown in Figure 2.38 (Sherif, 2003). The same model inferred that a reduction in manganese content would have little effect on temperature sensitivity.

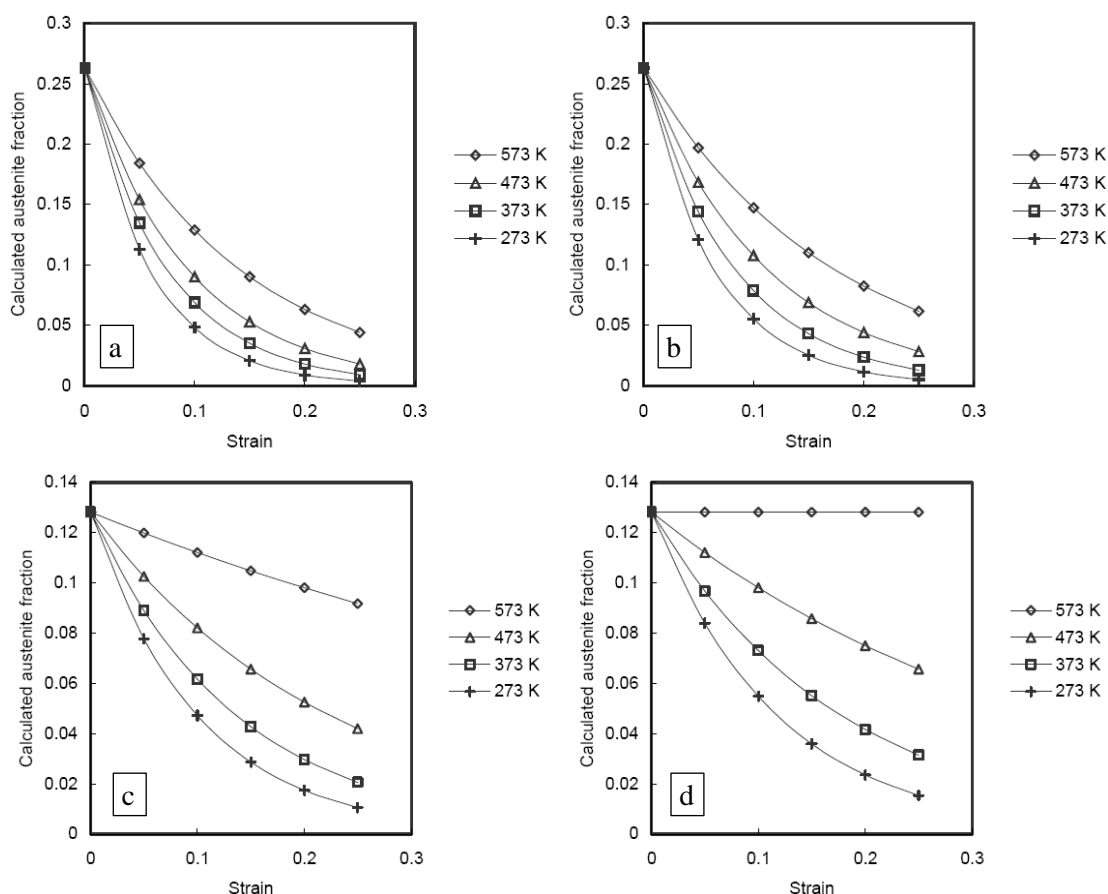


**Figure 2.38: The effect of decreasing carbon content on transformation temperature dependence in TRIP assisted Fe-xC-xMn-2Si steels, according to the transformation model by Sherif: (a) 0.6wt% C, 0.5wt% Mn; (b) 0.6wt% C, 2.5wt% Mn; (c) 1.2wt% C, 0.5wt% Mn; (d) 1.2wt% C, 2.5wt% Mn (Sherif, 2003).**

## 2.6 Modelling the transformation

### 2.6.1 Overview of transformation modelling

Several attempts have been made to theoretically model or simulate various aspects of the  $\gamma \rightarrow \alpha'$  transformation, with varying degrees of success (Stringfellow, 1991) (Guenin, 1995) (Wen et al., 1996) (Sherif et al., 2004) (Turteltaub & Suiker, 2005) (Dan, 2007) (Li et al., 2007) (Kouznetsov & Geers, 2008) (Creuziger & Foecke, 2010). All of these models rely in some way on constants that must be determined experimentally for a narrow range of alloy compositions, and are thus at least semi-empirical in nature. This is because of the complexity of inter-relations between the numerous factors that affect the transformation. Factors such as the interactions of the various elements with one another, effects that change with grain size and shape, internal stresses and strains, temperature and strain rate, defects, and the impact of different phases (which can be at least four) on one another and on the driving energy for the transformation.

Unfortunately, as yet, even models that might be shown to make accurate predictions for a particular set of alloys cannot be utilised to predict alloy properties over the broad range of compositions available without first physically fabricating multiple such alloys and testing them to determine the relevant constants. These constants are often not trivial to determine and require specialised equipment and considerable effort. Thus, their application to alloy design in the current project is severely limited. Very few of the models that have been formulated have attempted to incorporate factors such as strain rate, and again, none are accepted to have been entirely successful. Virtually all models examined have been formulated for hot or warm-worked material deformed in tension. At any rate, there currently exists no model that is accepted to accurately describe the martensitic transformation over a broad range of compositions.

All of these factors mean that the models found in literature to describe the deformation-induced martensitic transformation of TRIP steels were not considered directly beneficial to alloy design for this work. These issues do not however render such models completely useless for the purposes of alloy design. They might be utilised to investigate the manner in which alteration of specific factors is expected to affect transformation characteristics. Several models were thus examined to this end, and one in particular (in Section 2.6.3) was found to be of interest due to its potential application to a broad range of compositions and its incorporation of temperature at time of deformation.

### 2.6.2 Some earlier models

Olson and Cohen concluded that the temperature sensitivity of the transformation kinetics might be reduced by decreasing the fcc, bcc and hcp entropy differences via alloy composition (Olson & Cohen, 1975). They formulated the following model to predict the fraction of martensite formed by strain-induced nucleation. The model is based on the premise that shear band formation and intersection (in the form of  $\epsilon$ , twins or stacking faults) is the predominant origin of martensitic transformation (this model was later expanded by Stringfellow (Stringfellow, 1991)):

$$f^{\alpha'} = 1 - \exp\{-\beta [1 - \exp(-\alpha \cdot \epsilon)]^n\} \quad \text{Equation 2.15}$$

where:

$\alpha$  is a strain-independent constant and represents the rate of shear-band formation at low strains and will be temperature sensitive due to its dependence on stacking fault energy.

$\epsilon$  is the true strain

$n$  is a fixed exponent derived from experimental results, and

$$\beta = \frac{\bar{v}^{\alpha'} \cdot K}{(\bar{v}^{sb})^n} \cdot p \quad \text{Equation 2.16}$$

where:

$\bar{v}^{\alpha'}$  is the average volume of a martensitic unit (lath)

$\bar{v}^{sb}$  is the average shear band volume

$p$  is the probability that a shear-band intersection will generate a martensitic embryo

$K = \pi^2 \cdot d^2 / 16$ , where  $d$  is the average diameter of the shear plates ( $\approx$  austenitic grain size).

Thus, the transformation is related to strain by the temperature dependant parameters  $\alpha$  and  $\beta$  and the fixed exponent,  $n$ . The  $\beta$  factor represents the probability,  $p$ , that an intersection will form a martensite embryo. This probability depends on the chemical driving force for the reaction, which is linearly related to the temperature (and  $p$  will approach 1 at low temperatures).

Olson and Cohen fitted Equation 2.15 to experimental data from Angel for stainless steels of the SAE 304 type (Angel, 1954) (Olson & Cohen, 1975). An exponent of  $n = 4.5$  was found and the derived values of  $\alpha$  and  $\beta$  are plotted versus temperature in Figure 2.39.

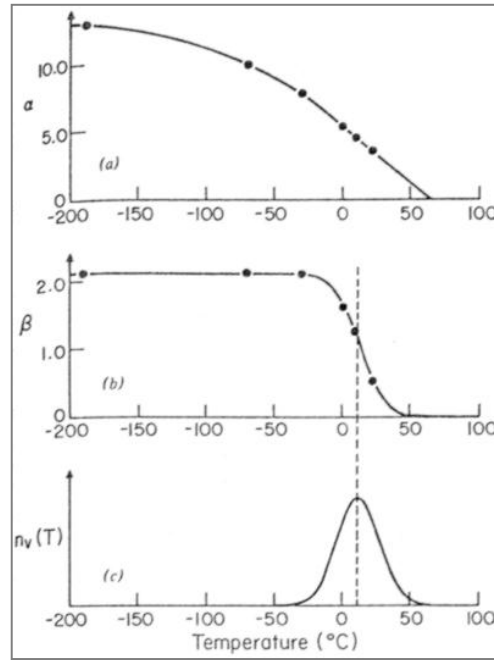


**Figure 2.39: Temperature dependence for the kinetic parameters of the model derived by Olson and Cohen for martensitic nucleation (Olson & Cohen, 1975). (a)  $\alpha$  parameter, representing the rate of shear-band formation. (b)  $\beta$  parameter, representing the probability of an intersection forming a martensitic embryo. (c)  $n_v(T)$ , the Gaussian distribution of intersection potencies with respect to temperature, giving the best fit for the temperature dependence of  $\beta$  in (b).**

Figure 2.39 shows that the temperature dependence for both  $\alpha$  and  $\beta$  is large in the vicinity of room temperature; this is especially apparent in Figure 2.39 (c), which represents the temperature dependence of parameter  $\beta$  (Olson & Cohen, 1975). It is clear that  $\beta$  shows greater temperature sensitivity than  $\alpha$  at room temperature. Olson and Cohen state that the most obvious manner in which temperature sensitivity might be reduced would be by taking advantage of the flat portion of the  $\beta$  curve (Olson & Cohen, 1975). This might be done by moving the shear band intersection potency distribution to higher temperatures by adjusting  $\Delta G^{\gamma \rightarrow \alpha'}$ , which might be achieved by increasing the transformation enthalpy change,  $\Delta H^{\gamma \rightarrow \alpha'}$ . However, Olson and Cohen advised against this, due to the softening effects (early plastic yielding) that would be expected to be associated to this increase in room temperature driving force (Olson & Cohen, 1975). In the non-flat region of the  $\beta$  curve, temperature sensitivity may be reduced by stretching out the intersection potency distribution (and thus reducing the peak) in temperature through a reduction in entropy difference between austenite and martensite ( $\Delta S^{\gamma \rightarrow \alpha'}$ ).

The temperature dependence of the  $\alpha$  parameter may be reduced by decreasing the temperature dependence of stacking fault energy, by reducing the entropy difference between  $\gamma$  and  $\epsilon$  ( $\Delta S^{\gamma \rightarrow \epsilon}$ ). However, this will only apply where  $\epsilon$  is the predominant type of shear band, which is usually the case at relatively low temperatures and in low SFE TRIP steels (Olson & Cohen,

1975). Olson and Cohen concluded that while their model is an over-simplification of an extremely complex problem, the model does seem to accurately represent (via the  $\alpha$  and  $\beta$  parameters) the quantitative role of the factors most important in governing the temperature dependence of the strain-induced transformation kinetics (Olson & Cohen, 1975).

However, according to Lacroisey and Pineau (Lacroisey & Pineau, 1972), temperature drastically increased the intrinsic stacking fault energy of the austenite in all of the chromium-bearing alloys which they investigated (including a wide range of materials in the Fe-Ni-Cr-C group from 0wt% Cr to 17.8wt% Cr, although none conformed to SAE 304). Thus, the effect of chromium is questionable, or rather the effect of the combination of nickel and chromium together is questionable.

Thompson found apparent strain rate insensitivity for Fe-Mn-Cr-Si-C alloy at room temperature with a strain rate ranging from 0.002 to 20 min<sup>-1</sup> (Thompson, 1986). Since manganese reduces austenite stacking fault energy,  $\epsilon$  might be formed before  $\alpha'$  (this may be encouraged by, for example, low temperature processing). It may be that this reduces temperature sensitivity and encourages transformation. However,  $E_s$ , the temperature at which  $\epsilon$  forms isothermally, appears to be coincident with  $M_s$  in Fe-Ni-Cr-C alloys and early formation of  $\epsilon$  is thus not possible in these alloys. The most significant compositional alteration regarding reducing temperature and strain rate sensitivity thus seems to be the substitution of manganese for nickel.

### 2.6.3 Investigation of a general model

Sherif and co-workers attempted to create a single model for the quantitative representation of the strain-induced transformation of retained austenite in a broad range of low alloy TRIP-assisted steels (Sherif, 2003) (Sherif et al., 2004). The results showed good correlation to experimental data from other literature, as reviewed by Sherif (Sherif, 2003). The model is interesting because it has the potential to be applicable to a broader range of alloys with relatively less experimental input. While it does include experimentally determined constants, it also factors in the material's Gibbs free energy change,  $\Delta G^{\gamma \rightarrow \alpha'}$ , as determined by modern computer software packages, specifically MTDATA (Metallurgical and Thermochemical DATAbank), for each specific material composition.

In order to derive the model, it was assumed that above  $M_s$ , the change in the fraction of martensite per unit of strain was proportional to the remaining volume of austenite, thus

$$\frac{dV_a}{d\epsilon} = k \cdot V_\gamma$$

**Equation 2.17**



It is then assumed that the volume of martensite is equal to the change in the volume of austenite ( $V_a = V_\gamma^0 - V_\gamma$ ) and thus,

$$\ln V_\gamma^0 - \ln V_\gamma = k.$$

**Equation 2.18**

This equation, originally proposed by Sugimoto and co-workers (Sugimoto et al., 1992), is well recognized, but the constant,  $k$ , is applicable only for the specific alloy for which it was determined. Sherif then hypothesized that in order to make this model more generally applicable,  $k$  should be expressed as a function of chemical composition of the austenite and deformation temperature (Sherif et al., 2004). Both of these effects are inherent to the chemical free energy change,  $\Delta G^{\alpha\gamma} = -\Delta G^{\gamma\alpha}$  (the free energy change must be negative for the martensitic transformation to take place). It is then assumed that  $k$  is proportional to the driving force,  $k = k_I \cdot \Delta G^{\alpha\gamma}$ , thus,

$$\ln V_\gamma^0 - \ln V_\gamma = k_I \cdot \Delta G^{\alpha\gamma} \cdot \varepsilon$$

**Equation 2.19**

$k_I$  was determined to be 0.00446 mol/J from analysis with experimental data for TRIP assisted steels of compositions shown in Table 2.4 (Sherif et al., 2004).  $\Delta G^{\alpha\gamma}$  was determined from MTDATA. This model was found to give good results within the alloy range investigated, as illustrated in Figure 2.40.

**Table 2.4: Chemical composition (wt%) and temperature ranges of steels used to determine  $k_I$  (Sherif, 2003).**

$C_\gamma$	$\bar{C}$	Mn	Si	Cr	Ni	Temp (K)
0.73 – 1.83	0.13 – 0.60	0.80 – 1.66	0.38 – 2.00	0.00 – 0.17	0.00 – 0.16	293 - 423

\* $C_\gamma$  is the carbon content in austenite,  $\bar{C}$  is the average carbon concentration in the steel.

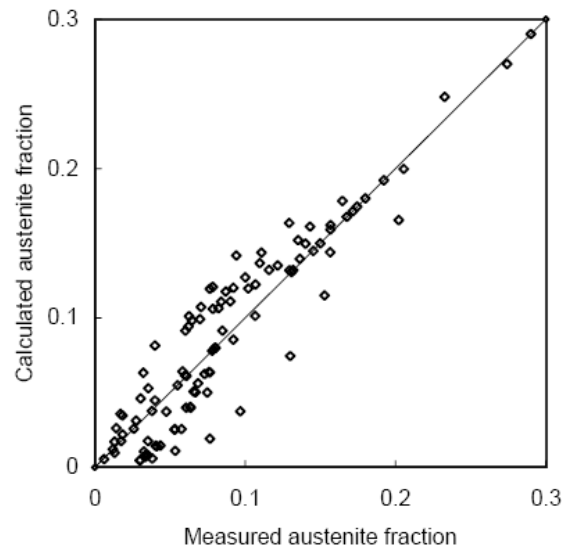


**Figure 2.40: Plot of the analysis based on Equation 2.19, where the line represents the ideal case where predicted and measured values are identical; coefficient of correlation 0.9 (Sherif, 2003).**

## 2.7 Mechanical & physical properties of TRIP steels

TRIP steels were originally developed as ultra-high strength alloys with superior ductility and toughness to traditional ultra-high strength alloys, as shown in Figure 2.41 (Skroc, 2010). They show impressive mechanical properties that can be manipulated by composition and processing parameters. Many of these superior properties relate directly to the transformation that gives them their smart sensing capability. One reason for this is that the austenite to martensite transformation absorbs a great deal of energy during fracture (Antolovich & Singh, 1971). The transformation also delays necking, since the material in the region of onset of necking will transform to hard, strong martensite, thus preventing necking.

Tensile properties of cold or warm-worked TRIP steel grades are substantially better than those of hot worked grades. Unworked, cast TRIP steels can only be utilised in compression. The strongest TRIP steels are stronger than HSLA (high strength low alloy) steels and their ductility and energy absorption capabilities make them good candidates for many applications. Figure 2.41 compares the ultimate tensile strength and elongation of TRIP steel to various structural steels (Skroc, 2010). Figure 2.42 compares the yield strength and elongation of TRIP steel to various structural steels (Thompson & Westermo, 1994).

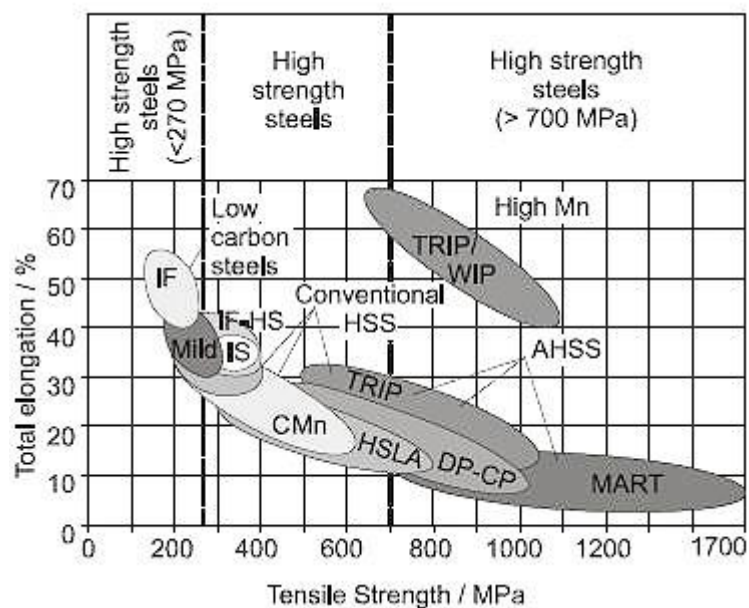


Figure 2.41: Mechanical properties of some TRIP steels compared to some common structural steels (Skroc, 2010).

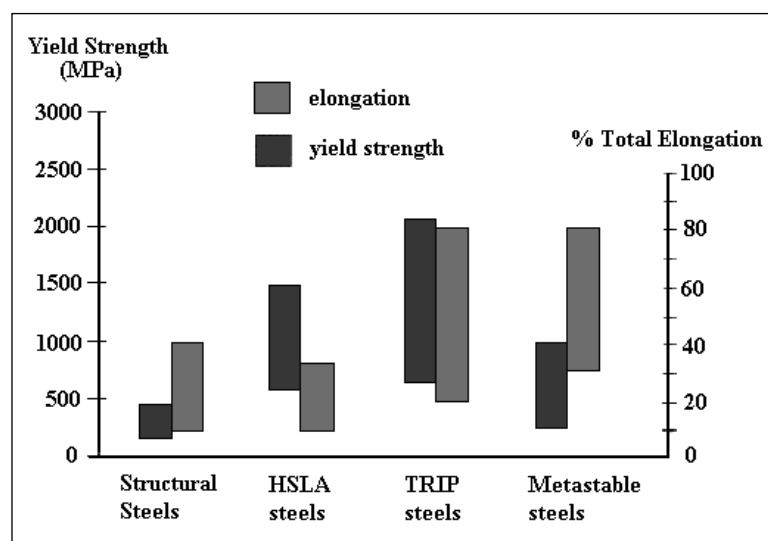
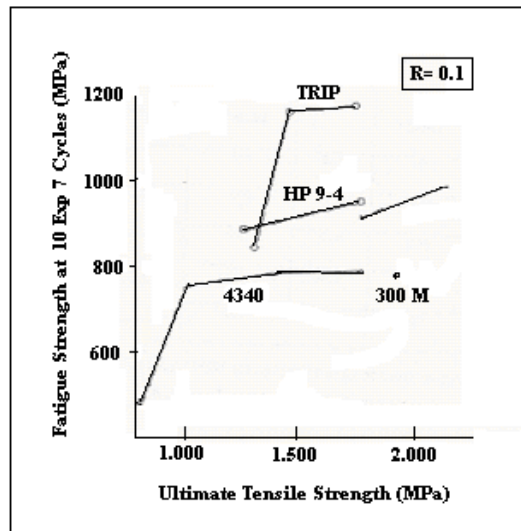


Figure 2.42: Comparison of strength and ductility for various grades of steel (Thompson & Westermo, 1994).

TRIP steels also show excellent fatigue strength properties, again this is influenced by the austenite to martensite transformation (Krupp et al., 2001). The propagation of fatigue cracks is reduced by the development of hard, strong martensite in the crack-tip region, and is possibly aided by the accompanying volume change. The fatigue strength and ultimate tensile strength of TRIP steels is compared to other structural steels in Figure 2.43 (Olson et al., 1980). The impact toughness properties of TRIP steels are also impressive, again due to the martensitic transformation (Zhang & Kelly, 2002).



**Figure 2.43: High-Cycle Fatigue Properties of TRIP Steel and High Performance Structural Steels (Olson et al., 1980)**

The impressive mechanical properties exhibited by TRIP steels are also partly due to the composite effect of the (often fine) multi-phase microstructure, the hard martensite in a softer austenite matrix (Tomota et al., 1976) (Bhadeshia & Edmonds, 1979a). Work by Chatterjee and co-workers implies that variation in plate size of the martensite formed due to deformation may further improve the composite effect, as in Figure 2.44 (Chatterjee & Bhadeshia, 2006). The variation in plate size was shown to be greater for strain-induced martensites than for thermally-induced martensites. The strain-induced phase transformation is primarily responsible for the impressive ductility and elongation properties (Zackay et al., 1967) (Sherif, 2003). The high strength can be attributed to work hardening, carbide precipitation and dislocation pinning (Maxwell et al., 1974).

The austenite to martensite transformation contributes to strain hardening because martensite is a hard, high strength phase and because it causes an effective decrease in grain size (Bressanelli & Moskowitz, 1966). Its structure is inherently fine grained due to its high rate of nucleation and due to its growth being contained inside prior austenite grains (Zackay et al., 1962). As shown in Figure 2.44 and Figure 2.45, the newly formed martensitic plates generally have smaller size as the transformation process proceeds (Otte, 1957) (Perlade et al., 2003) (Porter et al., 2009). This is due to the austenite grains being partitioned by previously transformed martensitic plates (Perlade et al., 2003).



**Figure 2.44: Martensite plate formation within an austenite particle. As the transformation to martensite proceeds, the size of newly formed martensitic plates decreases (Perlade et al., 2003).**



**Figure 2.45: An Fe-30%Ni-0.3%C alloy showing typical lens shaped (lenticular) martensite plates with retained austenite between (Otte, 1957).**

The transformation from fcc to hcp and bcc occurs as a means to accomplish plastic deformation and reduce energy. It occurs in bands that cut across the austenite grains, reducing the effective grain size, increasing strain hardening and acting as obstacles to slip, thereby serving to strengthen the material (Gerberich et al., 1971) (Bhandarkar et al., 1972). Martensite formed from plastically deformed austenite is generally stronger than that formed thermally (Zackay et al., 1962).

As the material begins to yield and enters plasticity, the phase transformation is triggered, or enhanced if it had already begun. Jonson (Jonson, 2003) stated that during tensile testing, the transformation initiates inhomogeneously along the gauge length of a tensile specimen. In conventional steels, once a mechanical instability initiates during plastic deformation, any further straining leads to the initiation of localised necking. In TRIP steels though, as deformation occurs in particular regions, transformation to martensite occurs there and thus these regions become stronger than the rest of the gauge length, inhibiting necking (Matsumura et al., 1987) (Sugimoto et al., 1993). Eventually, after the transformation to hard martensite has progressed along the entire gauge length to a significant degree, the specimen begins deforming homogeneously and failure occurs. This process delays (or even prevents) necking and increases

ultimate tensile strength (UTS) and elongation. Specimen elongations may be as high as 40 to 60 % for materials with yield strengths of 1380 MPa (Jonson, 2003) and 25% for materials with tensile strengths of around 2000 MPa (Maxwell et al., 1974).

As discussed in this section, the impressive energy absorption properties, toughness, strength and ductility shown by TRIP steels are largely attributed to the transformation and the resultant ability of the material to absorb energy beyond necking initiation throughout its entire gauge length, not only within the necking volume as with conventional steels. The greatest ductility has been found to occur in these materials when the martensitic transformation occurs at an optimum rate (Tamura, 1982). This rate of transformation, for a given composition, is dependent on temperature and therefore also strain rate. Maximum elongation has been found to occur when martensite formation is well distributed over the full range of deformation, rather than very rapidly during the early stages of deformation or in very small amounts during the final stages. It has been found that the first of these phenomena usually occur when the operating temperature is just above the  $M_s$  temperature and the second just below  $M_d$  temperature. Thus, peak elongation and ductility occur somewhere between the  $M_s$  and  $M_d$  temperatures (Tamura, 1982).

Deformation-induced martensitic transformation greatly affects tensile properties, and different grades, such as the austenitically stable 310S and the metastable 301, have completely different behavior during tensile loading. A greater proportion of alloying elements (especially interstitials like C and N) will increase the solid solution strengthening and thus yield strength. High enough alloy contents will also mean a more stable alloy, with less or no martensitic transformation.

The lower strength hot worked TRIP steels generally also show good corrosion resistance; they often qualify as stainless steels and exhibit corrosion properties similar to the 300 series stainless steels due to their large proportion of chromium (usually between 11% and 18%) and other elements that promote reduced corrosion (Baghdasarian & Ravitz, 1975). These TRIP steels are also weldable as they are not warm or cold worked (Ambekar, 1970). The higher strength cold or warm rolled TRIP steels are not considered weldable because the process of welding alters the worked microstructure in the heat affected zone of the weld.

## 2.8 Observing the transformation

In order to properly understand TRIP steels and to enable the design and testing of new alloys, it is essential to be able to observe the transformation in a qualitative and quantitative manner. In order to make practical use of the smart properties of TRIP steel, it was necessary to be able to efficiently measure the transformation. This section is devoted to understanding the methods that are used to interpret and measure the TRIP steel transformation. Optical microscopy, Scanning Electron Microscopy (SEM) and magnetic measurement are the primary focus. X-Ray Diffraction (XRD) is also investigated. Transmission Electron Microscopy (TEM) was not utilised because a broad understanding of the microstructure was of key relevance to this work. Electron Backscatter Diffraction (EBSD) was not locally available at the time the work was performed.

Talonen and co-workers (Talonen et al., 2004) found that Satmagan, magnetic balance and density measurements gave repeatable results for martensite content. XRD results were found to be affected by preferred orientation of grains (discussed further in Section 3.4.7) but averaging of several peaks gave reasonable reliability. Talonen found optical metallography to be time consuming and inaccurate for quantification, although it did give useable qualitative results.

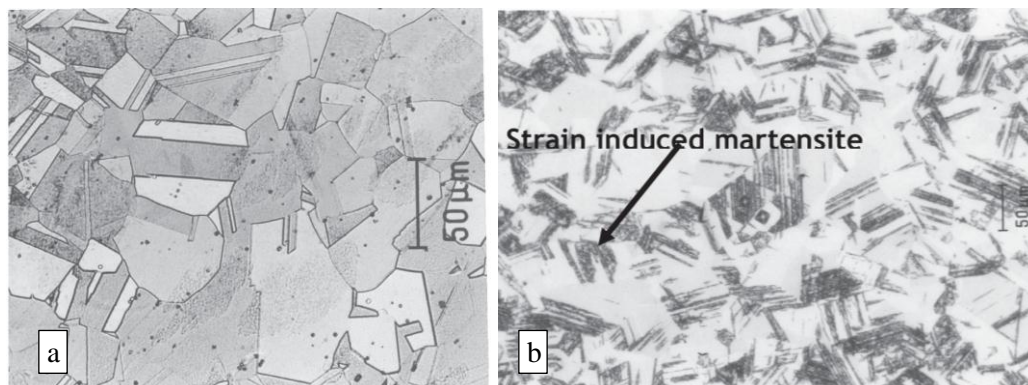
### 2.8.1 Observing the transformation microscopically

Microstructures in multi-phase steels are often complex and usually difficult to properly analyse quantitatively and even qualitatively, particularly after deformation (Maxwell et al., 1974) (Zaefferer et al., 2004) (Petrov et al., 2007). In this section, the microstructures and morphologies of TRIP steels and their phases are described.

Martensite produced by plastic strain above  $M_s$  has a much more irregular shape than ordinary plate martensite formed thermally below  $M_s$ , and the sizes of the  $\alpha'$  domains are smaller than the austenite grains (Cina, 1954) (Otte, 1957). Transformation initiates preferentially at twin or grain boundaries and  $\alpha'$  often grows parallel to active austenitic slip planes (Lecroisey & Pineau, 1972). High temperatures or large deformations lead to smaller martensitic lath dimensions, the width of a lath can decrease from about  $5\mu\text{m}$  (quenched) to  $0.1\mu\text{m}$  (Lecroisey & Pineau, 1972). Direct correlation of magnetic response with metallographic measurement of martensite is extremely difficult because of the heavily deformed nature of the microstructure (Bressanelli & Moskowitz, 1966).

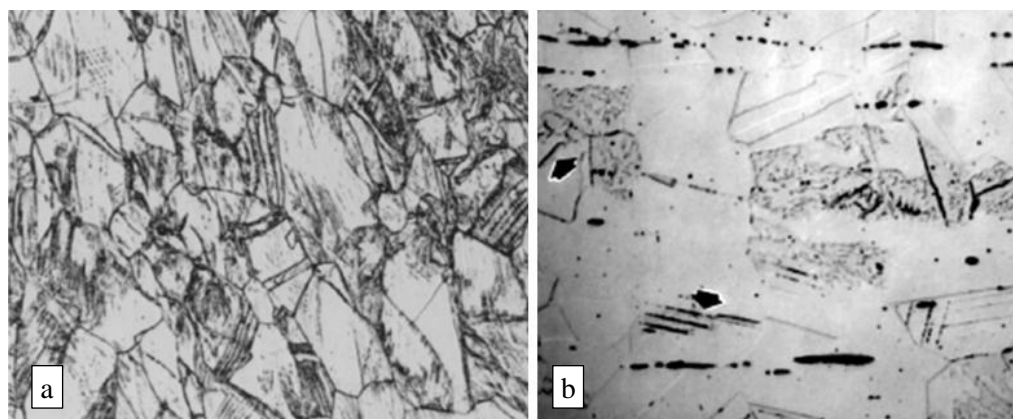
Figure 2.46 shows an austenitic alloy of an undisclosed composition (Moema et al., 2008). The left image shows the material in an annealed state, revealing a characteristic fully austenitic

microstructure, with substantial twinning. The right image, taken from the same material in a strained condition reveals that substantial strain-induced plate martensite has developed within the austenitic grains. It reveals how the plate martensite is usually confined to the prior austenite grain in which it grows, while it can cross twin boundaries.



**Figure 2.46:** Austenitic stainless steel alloy in annealed condition (a), and strained condition (b) (Moema et al., 2008).

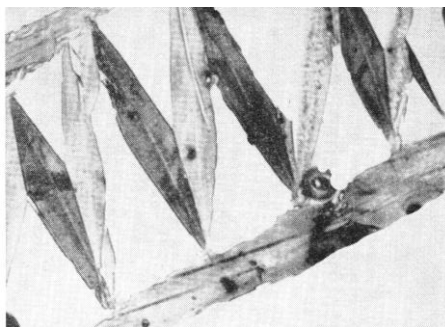
Figure 2.47 shows the austenitic microstructures of an undeformed high alloy TRIP steel (Maxwell et al., 1974). Figure 2.47 (a) shows the high density of slip bands in an austenitic structure due to its low stacking fault energy. Figure 2.47 (b) shows martensite, indicated by arrows, that has formed within an undeformed austenite structure.



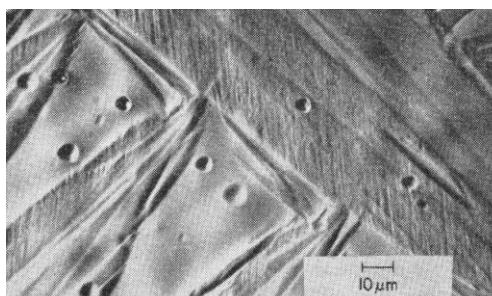
**Figure 2.47:** Heavily faulted undeformed austenite (a), martensite in an undeformed parent austenite structure, as indicated by arrows (b) (Maxwell et al., 1974).

Figure 2.48 shows the well-recognised manner in which martensitic plates form autocatalytically (burst martensite) (Wayman, 1965). This plate martensite is lenticular, internally twinned martensite with a midrib (Maxwell et al., 1974). Figure 2.49 shows an optical micrograph of the internally twinned structure of martensite in a Fe-33.2%Ni alloy (Wayman, 1965). Figure 2.50 shows the dislocation structure of a Fe-9%Ni alloy, recrystallized at 500°C and deformed 10% (Wayman, 1965).





**Figure 2.48: Typical array of plates produced by the burst transformation to martensite. (Wayman, 1965)**



**Figure 2.49: Optical micrograph of Fe-33.2%Ni alloy showing the internal twinning of the martensitic plates. (Wayman, 1965)**

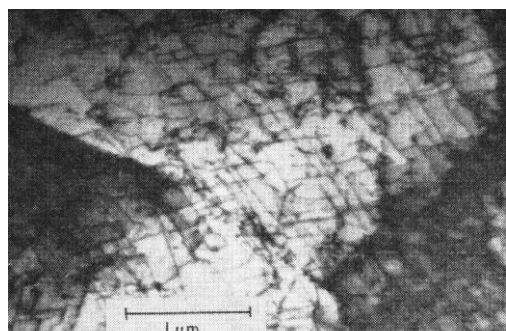


**Figure 2.50: Dislocation configuration of Fe-9%Ni recrystallized at 500°C and deformed 10%. (Wayman, 1965)**

Strain-induced martensite has been shown to form along the slip bands of austenite in TRIP steels as sheaves of fine parallel laths less than 5 μm wide, strung out along the planes of the austenite (Freiwillig et al., 1976) (Suzuki et al., 1977) (Hedström, 2005). The slip bands have been shown to be very uniformly spaced (Maxwell et al., 1974).

Otte (Otte, 1957) stated that deformation makes it difficult to distinguish microstructures and also distorts XRD results. Such difficulty in interpreting TRIP steel microstructures still persists today (Zaefferer et al., 2004) (Petrov et al., 2007). Otte also stated that, even in undeformed material, it is sometimes difficult to discern  $\epsilon$  from slip lines using XRD. Figure 2.51 shows the fully martensitic microstructure of a commercial 18/9 alloy deformed 78% at -196°C (Otte, 1957). Figure 2.52 shows the same alloy in an undeformed state and deformed 5% and 9% also at -196°C (Otte, 1957).



**Figure 2.51:** A commercial 18/9 stainless steel deformed 78% at  $-196^{\circ}\text{C}$  showing a fully martensitic microstructure (image width,  $90\text{ }\mu\text{m}$ ) (Otte, 1957).

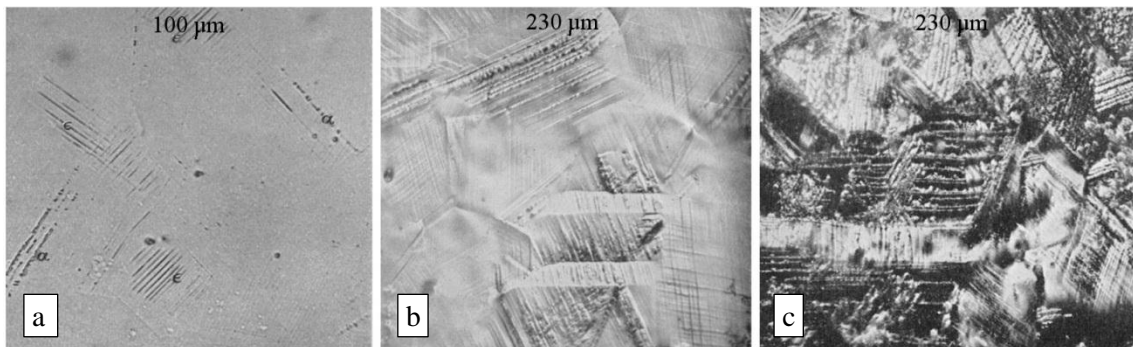
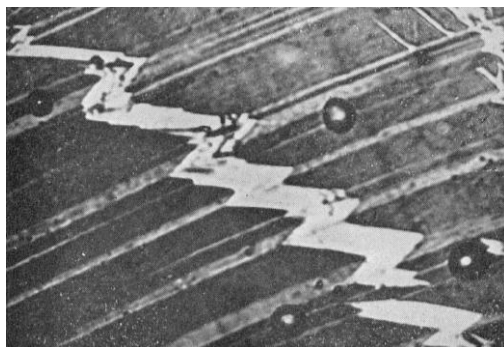


**Figure 2.52:** A commercial 18/9 stainless steel alloy undeformed (a), deformed 5% (b), deformed 9% (c) all at  $-196^{\circ}\text{C}$  (image widths shown) (Otte, 1957).

Figure 2.53 shows how  $\alpha'$  martensite plates are commonly prevented from growing across strain markings (possibly representing slip planes) (Otte, 1957). Figure 2.54 shows how, when a martensite plate crosses strain markings, the plate is altered to the twin position within the marking (Otte, 1957). This suggests that the strain markings are the result of austenite twinning.

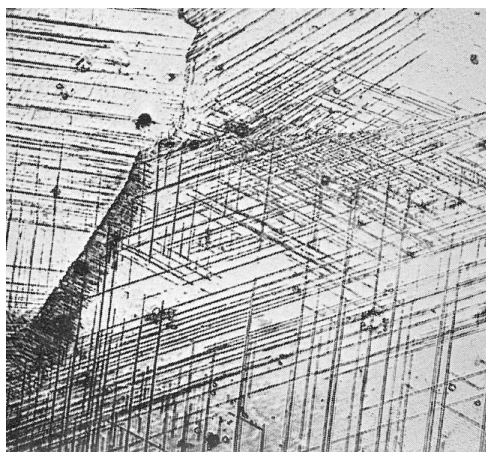


**Figure 2.53:** Micrograph of 5% nickel, 1.5% carbon alloy at  $1175\times$ , deformed at room temperature and then cooled to  $-56^{\circ}\text{C}$  (image width,  $90\text{ }\mu\text{m}$ ) (Otte, 1957).



**Figure 2.54: Micrograph of 5% nickel, 1.5% carbon alloy at 2650x, deformed at room temperature and then cooled to  $-56^{\circ}\text{C}$  (image width,  $30\text{ }\mu\text{m}$ ) (Otte, 1957).**

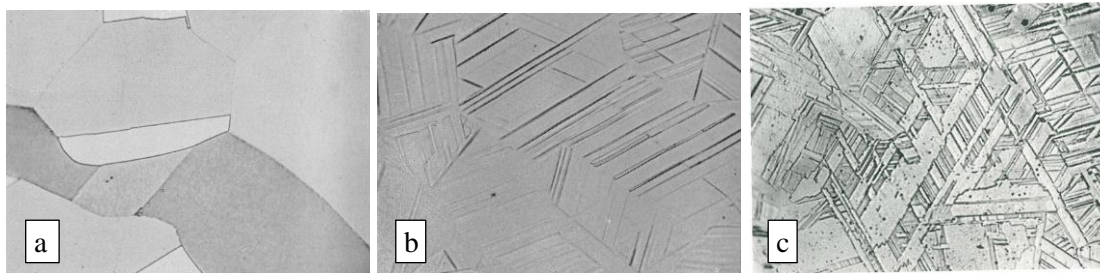
X-ray diffraction showed that the markings in the sample in Figure 2.55, with 6% deformation at  $-269^{\circ}\text{C}$ , were not martensite (Otte, 1957). The author thus considered it likely that the markings represented stacking faults.



**Figure 2.55: Micrograph of a 12% manganese, 1.2% carbon steel at 470x, deformed 6% at  $-269^{\circ}\text{C}$  (image width,  $180\text{ }\mu\text{m}$ ) (Otte, 1957).**

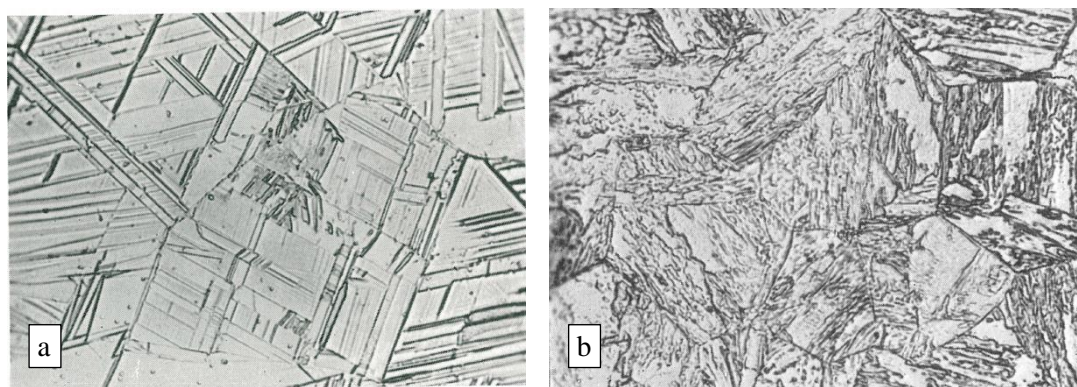
Figure 2.56 to Figure 2.61 comprise a selection of micrographs from work by Cina showing various extents and forms of martensite occurring in a variety of different composition high alloy TRIP steels (Cina, 1958). These images are included because they show a manner in which TRIP steel microstructures vary with composition, temperature and cold work. The micrographs shown here are also discussed in Section 2.5 and detailed in Table 2.1 to Table 2.3. All samples were annealed at  $1050^{\circ}\text{C}$  for 10 minutes and then water quenched; some were processed further, as specified.

Figure 2.56 shows the effect of carbon on the microstructure of a 20wt% manganese steel. With 0.42wt% carbon, the microstructure is fully austenitic (Figure 2.56 (a)) (Cina, 1958). When carbon was reduced to 0.19wt%, a substantial proportion of  $\epsilon$ -martensite was present in the microstructure (Figure 2.56 (b)), and when reduced to approximately 0wt%, a very significant proportion of  $\epsilon$ -martensite was found to be present (Figure 2.56 (c)) (Cina, 1958).



**Figure 2.56:** Micrograph of 20% manganese steels with (a) 0.42% carbon (fully austenitic), (b) 0.19% C (austenite with  $\epsilon$ -martensite), (c) ~0% carbon (austenite with  $\epsilon$ -martensite), annealed at 1050°C and water quenched (image width, 55  $\mu\text{m}$ ) (Cina, 1958).

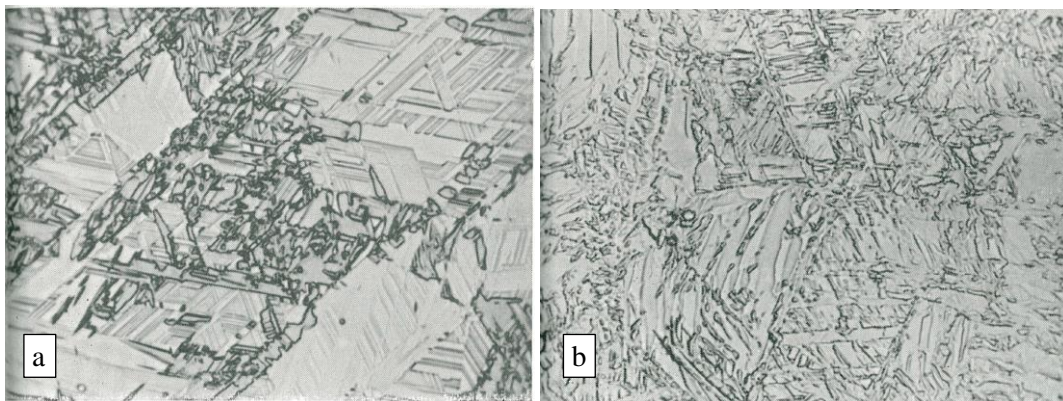
Figure 2.57 shows the effect of reducing the manganese content from 20wt% to 15wt% and to 5wt%. The microstructure of the 15wt% manganese sample (Figure 2.57 (a)) is similar to that of 20wt% manganese (Figure 2.56 (c)), but includes some  $\alpha'$  martensite. At 5wt% manganese (Figure 2.57 (b)), the sample is full  $\alpha'$  martensite, with no sign of austenite or  $\epsilon$ -martensite seen in XRD (Table 2.1) (Cina, 1958).



**Figure 2.57:** Micrograph of steels annealed at 1050°C and water quenched (a) 15% manganese showing austenite,  $\epsilon$ -martensite and some  $\alpha'$  martensite and (b) 5% manganese steel showing only  $\alpha'$  martensite (image width, 55  $\mu\text{m}$ ) (Cina, 1958).

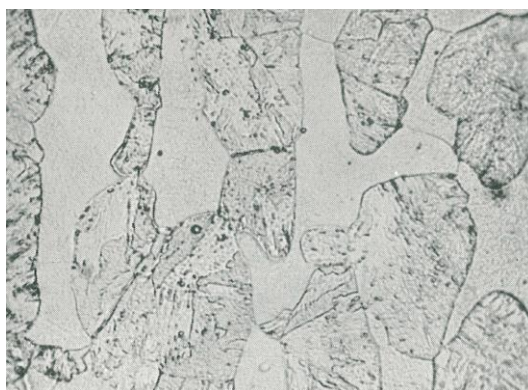
Figure 2.58 (a) shows the microstructure of a 15% manganese, 5% chromium steel with no deformation. The microstructure showed approximately equal proportions of austenite,  $\epsilon$ -martensite and  $\alpha'$  martensite (Cina, 1958), where the 20wt% manganese alloy showed no  $\alpha'$  martensite. Figure 2.58 (b) shows the same alloy after heavy cold work at room temperature. The microstructure was found to be full  $\alpha'$  martensite, where the microstructure of the 20wt% manganese alloy showed some austenite, and particularly  $\epsilon$ -martensite, in its microstructure after the same treatment (Cina, 1958).





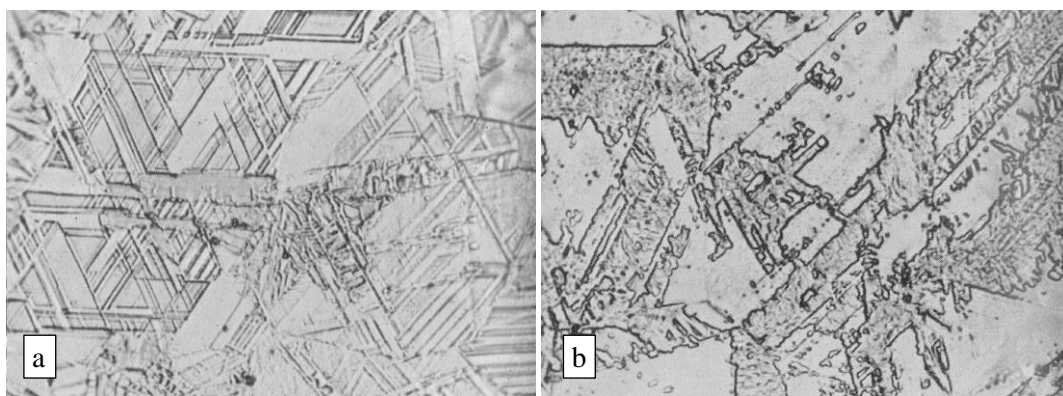
**Figure 2.58:** Micrograph of 15% manganese, 5% chromium steel, annealed at 1050°C and water quenched, (a) austenite,  $\epsilon$ -martensite and  $\alpha'$  martensite, (b) after heavy cold work at room temperature, (image width, 55  $\mu\text{m}$ ) (Cina, 1958).

Upon increasing the proportion of chromium to 15wt%, with 5wt% manganese, the microstructure after annealing and water quenching consisted of pools of  $\alpha'$  martensite in a  $\delta$ -ferrite matrix (Figure 2.59) (Cina, 1958). At 10wt% chromium and 10wt% manganese,  $\delta$ -ferrite was not present.



**Figure 2.59:** Micrograph of 5% manganese, 15% chromium steel, annealed at 1050°C and water quenched, showing  $\alpha'$  martensite and ferrite (image width, 55  $\mu\text{m}$ ) (Cina, 1958).

Substitution of manganese for nickel increased the  $\alpha'$  martensite content in a similar manner to chromium. The microstructures including nickel are shown in Figure 2.60 (a) and (b) (Cina, 1958).



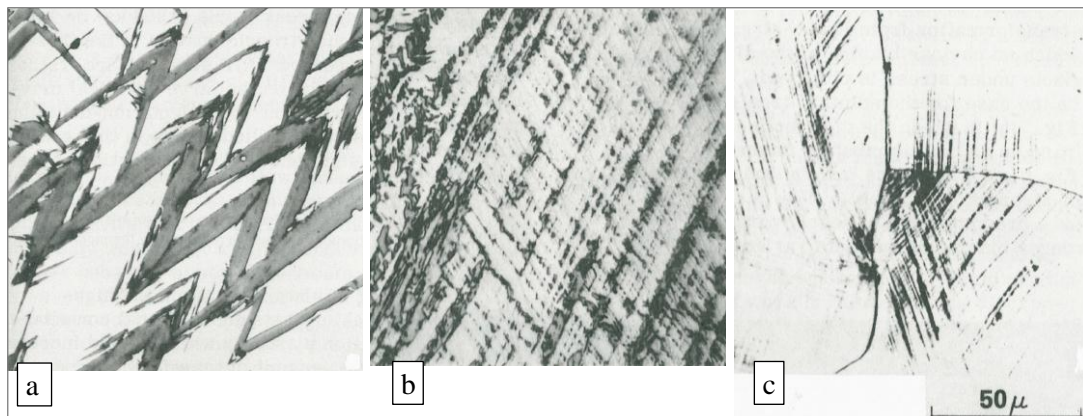
**Figure 2.60:** Micrograph of steels annealed at 1050°C and water quenched (a) 15% manganese, 5% nickel steel showing austenite,  $\epsilon$ -martensite and  $\alpha'$  martensite; (b) 10% manganese, 10% nickel steel showing only austenite and  $\alpha'$  martensite, (image width, 55  $\mu\text{m}$ ) (Cina, 1958).

Figure 2.61 shows the microstructure of the 15wt% manganese steel in Figure 2.57 (a) after heavy cold work at room temperature (Cina, 1958). Before deformation, austenite,  $\epsilon$ -martensite and a small amount of  $\alpha'$  martensite were present. After deformation the microstructure was mostly  $\alpha'$  martensite, with a small amount of  $\epsilon$ -martensite.



**Figure 2.61: Micrograph of 15% manganese steel, annealed at 1050°C and water quenched then heavily cold worked at room temperature,  $\epsilon$ -martensite and  $\alpha'$  martensite (image width, 55  $\mu\text{m}$ ) (Cina, 1958).**

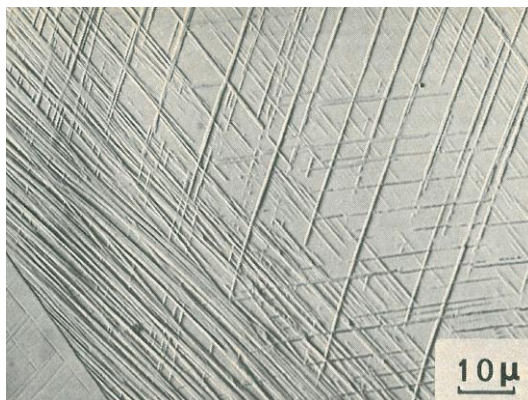
Figure 2.62 shows the difference in morphology between isothermally-induced martensite (a) and deformation-induced martensite (b and c) in the same material at different temperatures (Olson & Azrin, 1978). The amount of deformation was not disclosed.



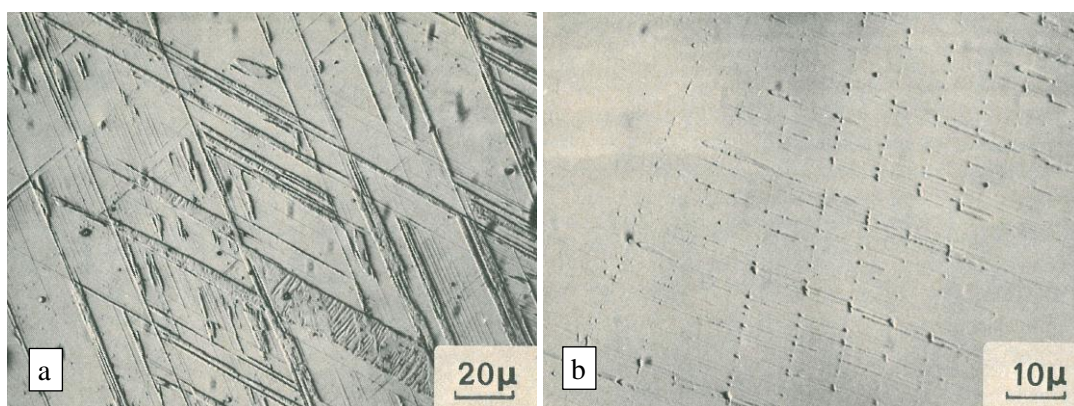
**Figure 2.62: Morphology of 9% chromium, 8% nickel martensite formed by isothermal holding at -196°C (a), deformation at -28°C (b), deformation at 25°C (c) (Olson & Azrin, 1978).**

Figure 2.63 shows parallel markings of  $\epsilon$ -martensite platelets (as confirmed by X-ray diffraction) present in certain grains in 18wt% chromium, 7wt% nickel steel after quenching to room temperature from 1150°C (Abrassart, 1973). Figure 2.64 shows a similar morphology in the same steel quenched to -196°C, but X-ray diffraction showed the martensite produced to be  $\alpha'$  martensite. Figure 2.65 shows the same material again strained 20% at 500°C, too high to form martensite, with the deformation structure of slip lines apparent and strained 20% at 110°C with  $\epsilon$  martensite platelets and possibly mechanical twins.





**Figure 2.63:** Morphology of 18% chromium, 7% nickel steel quenched to room temperature (Abrassart, 1973).



**Figure 2.64:** Morphology of 18% chromium, 7% nickel steel quenched to  $-196^{\circ}\text{C}$ , (a) general morphology and (b)  $\alpha'$  forming at the intersection of  $\epsilon$  platelets (Abrassart, 1973).

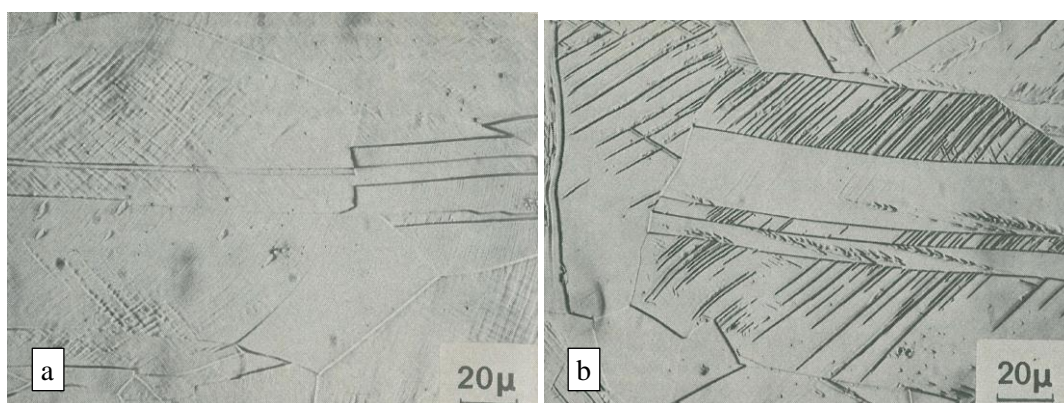


**Figure 2.65:** Morphology of 18% chromium, 7% nickel steel strained 20%, (a) at  $500^{\circ}\text{C}$ , (b) at  $110^{\circ}\text{C}$  (right) (Abrassart, 1973).

Lecroisey and Pineau found that in Fe, 7.2wt%Cr, 17.3wt%Ni, 0.25wt%C TRIP steel, upon deformation above  $M_s$ , two types of martensite occurred, as shown in Figure 2.66 (Lecroisey & Pineau, 1972). The first was plate-like martensite, which they considered similar to that obtained by quenching, but with smaller plate size and more irregular interfaces. The second was a lath martensite, located at the intersection between an austenite deformation twin and

either an active slip plane or another deformation twin. Lath martensite occurred when twinning in the prior austenite was extensive, which occurred primarily at temperatures below room temperature in this alloy.

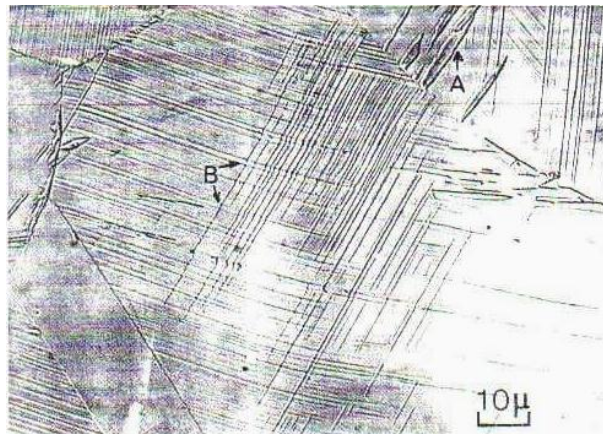


**Figure 2.66: Plate (A) and Lath (B) martensite (dark regions/lines) formed during 10% plastic deformation at -196°C in a Fe-7.2%Cr-17.3%Ni-0.25%C TRIP steel (Lecroisey & Pineau, 1972).**

Figure 2.67 shows the morphology of two distinct types of plate martensite, thin plate martensite (a) and lenticular plate martensite (b) (Shibata et al., 2008). Martensite autocatalysis, where a growing plate of martensite spurs the growth of another, upon reaching a barrier plate, is evident in both images.

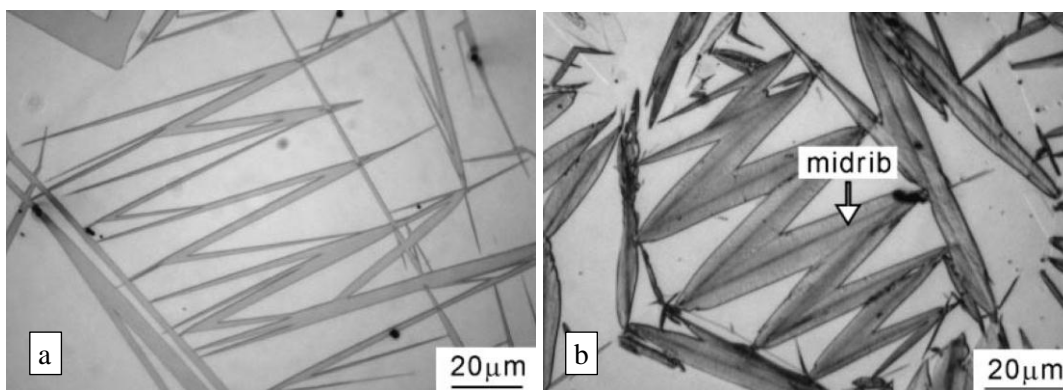


**Figure 2.67: Thin plate martensite (a) vs. lenticular plate martensite (b) (Shibata et al., 2008).**

### 2.8.2 Observing the transformation magnetically

For sensor development, as well as for alloy investigation, some method of magnetic permeability monitoring would need to be implemented. This form of monitoring was chosen because a system reliable and repeatable in a wide range of environments would be implemented using relatively inexpensive, portable, robust yet precise equipment. For methods giving immediate outputs, magnetic permeability is by far the one most commonly used in literature (Olson & Azrin, 1978) (Jonson, 2003) (Zhao et al., 2002) (Radu et al., 2005) (Kaneko et al., 2007) (Bigdeli Karimi et al., 2007) (Mészáros, 2008). The magnetic permeability change



during the materials' transformation is also relatively greater than the changes in other physical properties such as electrical resistance or density.

There are many possible methods of monitoring magnetic permeability, some of which were investigated with regards to practical TRIP steel smart sensors in Section 4.4. However, in order to devise any magnetic permeability monitoring method that functions in a reliable and repeatable fashion and has good sensitivity, it was required to first gain a deeper understanding of what exactly was being measured.

### **2.8.2.1 Magnetism and TRIP steel**

All matter exhibits magnetic properties. When placed in an inhomogeneous magnetic field, matter is either attracted or repelled in the direction of the field. This property is described by the magnetic susceptibility or magnetic permeability of the matter. The term permeability is usually used when referring to ferromagnetic materials, such as iron, that have very high magnetic susceptibility (relative to the field). The dimensionless term, relative permeability is also frequently used. This term relates the absolute permeability of a material to that of a vacuum. In qualitative terms, magnetic susceptibility and magnetic permeability can be used interchangeably.

When a TRIP steel's crystal structure transforms under deformation, it changes from paramagnetic to ferromagnetic, low permeability to high permeability. Most materials fall into only one of five magnetic groups and are not capable of switching between these. The three most common are diamagnetism, paramagnetic and ferromagnetism; the final two groups are ferrimagnetism and antiferromagnetic. The magnetic properties of materials are dependant almost entirely on the magnetic effects of their atoms' electrons, their spin and their orbital motion (Chabay & Sherwood, 2007). In solid materials, the orbital moments are strongly coupled to the crystal lattice parameters and are therefore unable to change direction under the influence of an applied magnetic field (Cullen & Clark, 1977) (Yardley, 2003). Since there is a lack of influence of the orbital moments, changing magnetic moments in stable solids is considered to be due to electron spin only.

The spin quantum number can only take one of the two values,  $+\frac{1}{2}$  or  $-\frac{1}{2}$  (Pauli, 1926). The Pauli exclusion principle permits each energy state to contain up to two electrons. If only one electron is present then its spin moment will contribute to the overall spin moment of the atom. If present, the second electron must have an antiparallel spin to the first, and so their spins will cancel out, resulting in no net moment. Elements that have a large number of unpaired spins are more likely to show strong magnetic properties.

It has been known for many years that the magnetic properties of steels depend on their composition and heat treatment, because of the associated variation in crystal structure (Curie 1898). Atomic magnetic moments will align preferentially along particular crystal directions, while other directions are particularly unfavourable. The orbital moments are thus constrained in particular directions by the crystal lattice, and because there is an interaction between electron spin and these orbital moments (Brooks, 1940), the geometry of the crystal structure influences the behaviour of the spins and thus the magnetic permeability of the material. In bcc iron crystals, unlike in fcc crystals, the cube edges are aligned in the easy directions, thus favouring ferromagnetism (Honda & Kaya, 1926).

Diamagnetic materials are those where the atoms have no net orbital or spin magnetism because the angular momentum of each electron is opposite to that of its neighbour (Srinivas, 2007). When any material is exposed to a magnetic field, electrons in orbit planes at right angles to the magnetic field will change momentum a tiny amount. This behaviour is present in all materials, but is usually relatively insignificant in materials where paramagnetic or ferromagnetism is present. In diamagnetic materials, the net magnetic moments then cease to cancel completely. The molecules then acquire an induced magnetic moment opposite to that of the applied field. A magnet will thus very weakly repel diamagnetic materials.

In atoms where the electron spins do not all cancel each other out, the atom has a magnetic dipole moment. When these atoms are placed into a magnetic field, the atomic dipoles tend to line up with the field. This characteristic is called paramagnetic. These materials are attracted to a magnet, but the effect is almost as feeble as in diamagnetism. The reason for this is that the alignment process is seriously disturbed by thermal agitation (Brailsford et al., 1948). Figure 2.68 shows schematic magnetisation curves (also called B-H curves) for a vacuum, a diamagnetic material, a paramagnetic material and a ferromagnetic material. The gradient of the free space curve corresponds to the fundamental physical constant  $\mu_0$ , the magnetic permeability of a vacuum.

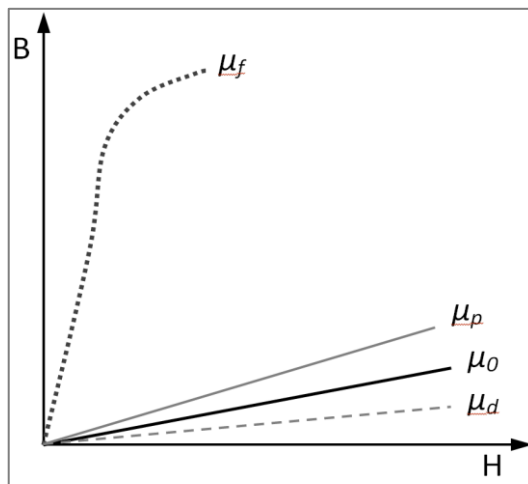


**Figure 2.68:** Schematic magnetisation curves of various material categories:  $\mu_0$ , free space;  $\mu_d$ , diamagnetic material;  $\mu_p$ , paramagnetic material;  $\mu_f$ , ferromagnetic material. B represents flux density and H magnetic field strength.

In a few materials, notably iron, nickel, cobalt and some of their alloys, as well as some manganese alloys, the atomic dipoles line up with each other in rigid parallelism, in spite of thermal energy (Elmen, 1935). This occurs through a special interaction called an exchange coupling that cannot be explained with classical physics. It causes these materials to be capable of producing an extremely large magnetic field under certain circumstances. These ferromagnetic materials do not naturally produce this magnetic field because although there exist regions called domains within the material's crystals in which the atomic dipole alignment is essentially perfect, these domains are normally oriented in random directions (Katz & Semat, 1958). This causes the material to have no significant net magnetic field. When an external magnetic field is applied, the magnetic domains are encouraged to align and a magnetic field much larger than the applied magnetic field can be produced as shown in Figure 2.69 (Gaita, 2004).

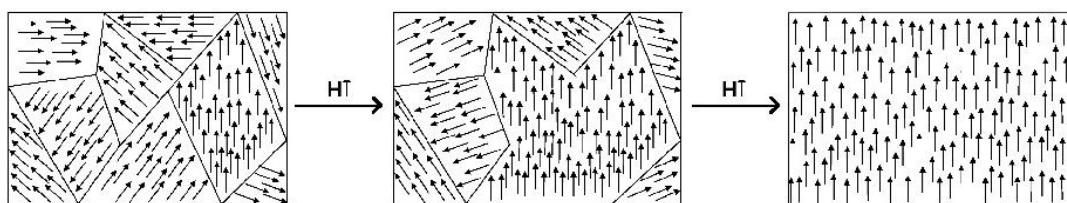


**Figure 2.69:** Left illustration shows magnetic domains randomly oriented with no net magnetic field. Centre and right illustrations show magnetic domains that have been increasingly aligned as an applied magnetic field increases in strength. (Gaita, 2004)

Figure 2.70 shows the magnetisation curve (sometimes called a saturation curve) for pure iron (Clarke, 2008). It is notable that the y-axis (flux density) scale is in Tesla, not millitesla as with the magnetisation curves for paramagnetic and diamagnetic materials and for a vacuum. This curve shows the manner in which the flux density within the iron core increases as the field strength is increased. The fact that this is not a straight line relationship shows that the magnetic permeability,  $\mu$ , of the ferromagnetic iron core changes as the flux density increases.

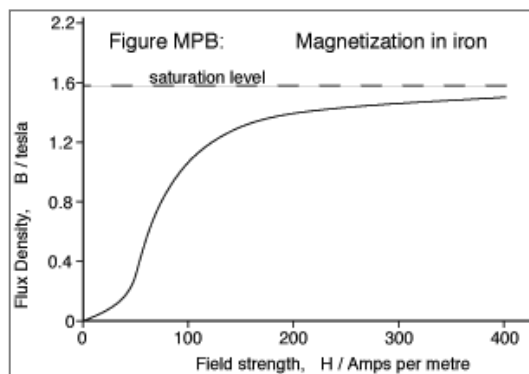


Figure 2.70: The magnetisation curve for pure iron (Clarke, 2008).

Four regions are distinct in Figure 2.70 (Clarke, 2008):

- Close to the origin there is a slow rise due to reversible growth of the domain alignment and the magnetic permeability of the core remains low.
- A long fairly straight region shows irreversible growth of the domain alignment.
- The gradient begins to decrease, representing domain rotation.
- An almost flat region with a very low gradient, corresponds to paramagnetic behaviour and finally  $\mu_0$ . At this point, the core is saturated and the flux in the iron core cannot grow faster than in free space.

Magnetic permeability is defined as the ratio of flux density to field strength ( $\mu = B/H$ ) for a particular material. The magnetic permeability curve shown in Figure 2.71 is derived from the preceding magnetisation curve and the relation  $\mu = B/H$  (Clarke, 2008). It shows, for a typical iron core, how the magnetic permeability changes with increasing field strength, peaking well before magnetic saturation. For a vacuum, diamagnetic material or a paramagnetic material the magnetisation curve is a straight line, and therefore the magnetic permeability is a constant ( $\mu_0$  in the case of a vacuum).

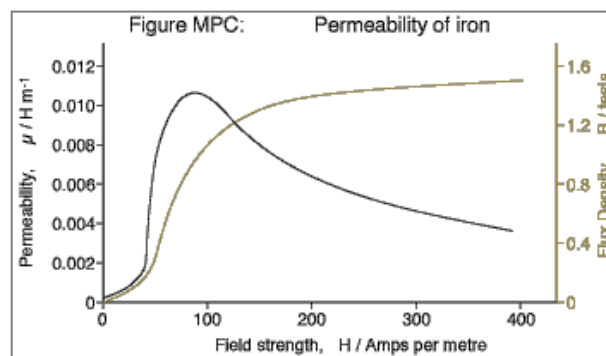
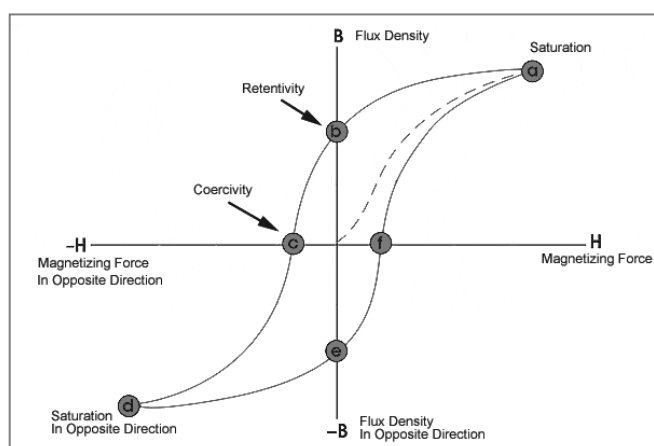


Figure 2.71: Magnetic permeability curve and corresponding magnetisation curve (orange) for pure iron (Clarke, 2008).

TRIP steels exhibit the rare characteristic that their magnetisation and permeability curves change dramatically as the crystal structure transformation from fcc to bcc takes place due to deformation. The measurement of these changes is thus a good way to monitor the fcc to bcc transformation.

It may be seen from Figure 2.72 that the magnetisation curves of ferromagnetic materials do not retrace themselves as the external magnetic field is increased and then decreased (NDT Resource Center, 2012). This effect is called magnetic hysteresis. When the applied field is removed, the domains usually do not lose all of their alignment and a permanent magnet results (retentivity). In order to reduce the domain alignment so that the internal magnetic field equates to zero once again, a reverse magnetic field must be applied (coercivity). At the Currie temperature, about  $770^{\circ}\text{C}$  for iron, the exchange coupling ceases to exist and most of these materials become effectively paramagnetic (Gao & Sammes, 2000).



**Figure 2.72: The magnetic hysteresis loop for a typical ferromagnetic material (NDT Resource Center, 2012).**

## 2.9 Summary and analysis

Figure 2.15 showed that the size of the martensitic plates formed is generally proportional to that of the prior austenitic grains (Porter, Easterling, & Sherif, Phase transformations in metals and alloys, 2009). Grain boundaries can act as barriers to martensite plate propagation. Thus, concerning the effect of austenite grain size for the present work, large blocky grains may be preferable, as they should give a more rapid transformation, particularly early on (Nishiyama, Fine, Meshii, & Wayman, 1978) (Wang & van der Zwaag, 2001). It is likely that nucleation across grain boundaries is possible, due to imposed deformation, although grain boundaries will substantially hinder martensitic plate growth (Guimaraes & Gomes, 1978) (Christian, Thermodynamics and kinetics of martensite, 1979). Fewer grain boundaries may result in fewer

martensite nucleation sites, although the primary mechanism for martensite nucleation is considered to be on slip bands and stacking faults (Olson & Cohen, 1975). Stacking faults may not directly create  $\alpha'$  nucleation sites in the compositions of interest, but instead create  $\varepsilon$  nucleation sites, which in turn nucleate  $\alpha'$ .

A coarse grain size usually results in reduced yield strength at ambient temperature, which will also reduce the incubation strain before transformation begins; this would be beneficial to the functioning of a sensor. If the material's tensile strength is not equally reduced, as is expected to be the case particularly when deformed in compression, then this will also increase the useable range of the sensor.

Some martensite or ferrite will be present in the austenitic structure of most TRIP steels prior to deformation. It is likely better to have martensite than ferrite, since martensite is more likely to encourage further martensite formation by growth or nucleation, and because the presence of ferrite may imply the presence of carbides as well (Guimaraes & Gomes, 1978).

Maximum elongation has been found to occur when martensite formation is well distributed over the full range of deformation, rather than very rapidly during the early stages of deformation, or in very small amounts during the final stages. It has been found that the first of these phenomena usually occur when the operating temperature is just above the  $M_s$  temperature and the second just below the  $M_d$  temperature. Thus, peak elongation and ductility, and the most constant rate of transformation, occur somewhere between the  $M_s$  and  $M_d$  temperatures (Fahr, 1971).

Cold or warm working, and even hot working, considerably increases the expense of an alloy and also adds extra variables, with the potential to negatively impact repeatability. The yield point of the alloy is also increased, particularly for cold and warm working, which will increase the incubation period before transformation for the TRIP sensor alloy (Askeland, 1988).

It has been shown that near  $M_s$ , stress-assisted martensite is primarily responsible for the transformation, but near  $M_d$ , inelastic-strain-induced martensite dominates (Fahr, 1971) (Bressanelli & Moskowitz, 1966).  $M_s^\sigma$ , a temperature between  $M_s$  and  $M_d$ , may be defined below which stress-assisted martensite formation is significant (Leal & Guimarães, 1981). Olson and Azrin found that solution treated material exhibited stress-assisted martensite formation more readily than warm-rolled material (Olson & Azrin, 1978). However, prior warm rolling was shown to increase  $M_d$  as well as  $M_s^\sigma$  temperatures well above those for the solution

treated material, when tested in tension. In compression, it is likely that even solution treated material will exhibit these effects to an extent, since cold working will occur during deformation.

It was considered that for the current work, it might be beneficial, for certain applications where a pre-tension cannot be applied, to design alloys such that the operating temperature was between  $M_s$  and  $M_s^\sigma$ , in order to obtain stress-assisted transformation before yield. However, Olson and Azrin showed that for their 0.19wt% and 0.27wt% carbon solution treated alloys, which were of similar compositional range to those proposed for the current work (Fe-xC-0.78Mn-2.13Si-8.06Ni-9.11Cr-4.05Mo), only one percent transformation occurred by 0.02 offset yield stress (Olson & Azrin, 1978). While warm working at 450°C to 78 percent reduction increased the temperature range under which stress-assisted nucleation occurred, again only one percent transformation was observed at yield. This low level of transformation would not be useful in practical sensor applications, because it is difficult to accurately and repeatably detect a fraction of a percent change in martensite content outside of laboratory conditions.

Even if substantial transformation could be obtained before yield, design of a sensor alloy to function within the stress-induced transformation range may increase susceptibility to temperature variation, since stress-induced transformation will cease outside of this usually narrow temperature range (Leal & Guimarães, 1981). All applications envisaged will at any rate incorporate a pre-tension, meaning that sensors may be pre-tensioned up to or near to their yield, eliminating the initial incubation period at any rate.

On cursory inspection, Figure 2.31 seems to show that, in high nickel alloys, the sensitivity to temperature is less severe at lower temperatures, closer to  $M_s$  (Maxwell, Goldberg, & Shyne, Influence of martensite formed during deformation on the mechanical behaviour of Fe-Ni-C alloys, 1974). However, on closer examination of Figure 2.31, the rate of transformation with strain is approximately identical at all temperatures. Only the amount of martensite at zero strain, before deformation begins, is different. This implies that the authors have incorrectly stated  $M_s$  to be lower than it is.

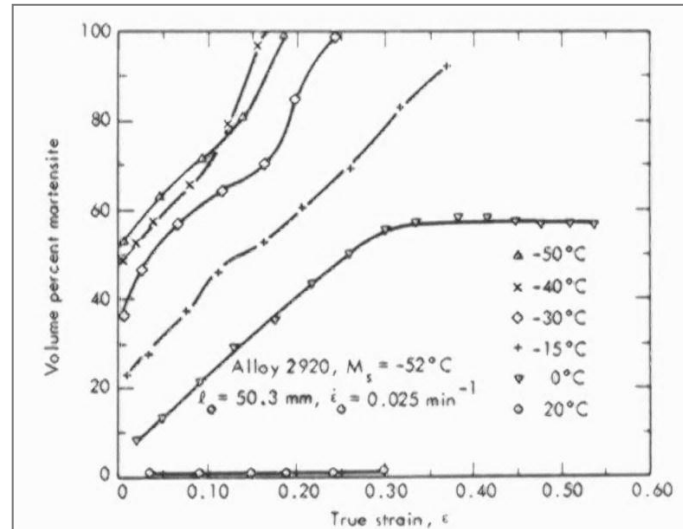


**Figure 2.31: Percent martensite versus true strain for an Fe-Ni-C alloy of 29Ni, 0.2C, where  $M_s = -52^\circ\text{C}$  (Maxwell, Goldberg, & Shyne, 1974).**

In the work by Olson and Azrin, it is noteworthy that in Figure 2.73 from just below  $M_s^\sigma$ , increasing temperatures caused the transformation kinetics to become significantly more temperature sensitive (Olson & Azrin, Transformation behavior of TRIP steels, 1978). This implies that TRIP steel elements for a sensor should be designed to function in the range between  $M_s$  to  $M_s^\sigma$  if temperature sensitivity is to be minimised.

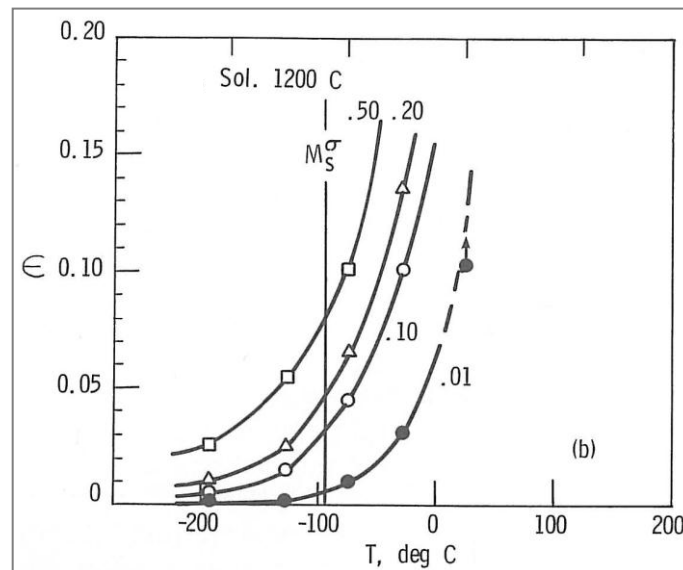


**Figure 2.73: Temperature dependence of tensile plastic strain required to give fixed volume fractions of martensite in 1470K solution treated Fe-0.27C-0.78Mn-2.13Si-8.06Ni-9.11Cr-4.05Mo TRIP steel (Olson & Azrin, Transformation behavior of TRIP steels, 1978).**

It was noted in Section 2.5 that annealed alloys function more consistently at temperatures near  $M_s$  than do the warm-worked alloys. Thus, such alloys may be beneficial for operation in the region between  $M_s$  and  $M_s^\sigma$ , where it has been observed that less temperature dependence is expected.



As discussed in Section 2.5, adiabatic heating during rapid deformation drastically alters the transformation rate. The effect is more pronounced at lower temperatures than at higher temperatures, relative to  $M_d$ . This is because at lower temperatures, more martensite is produced and thus, due to the release of chemical free energy in the transformation, more heat energy is released more rapidly. The temperature difference between high and low strain rate specimens tested at lower temperatures is thus greater than for those tested at higher temperatures (Nanga, Pineau, Tanguy, Naze, & Santacreu, 2009).

Since the  $\varepsilon$  phase has an energy between  $\gamma$  and  $\alpha'$ , the difference between the gradients of the  $\varepsilon$  and the  $\alpha'$  free energy curves should be small. Temperature sensitivity of the  $\varepsilon \rightarrow \alpha'$  transformation should thus be lower. It is possible that the nucleation of ferromagnetic  $\alpha'$  from  $\varepsilon$  martensite might be only minimally sensitive to temperature and strain rate. It has been found that in certain alloys with martensite already in excess of 50%, martensitic transformation due to deformation is almost entirely independent of temperature (Maxwell, Goldberg, & Shyne, Influence of martensite formed during deformation on the mechanical behaviour of Fe-Ni-C alloys, 1974).

Stacking fault energy is a function of composition and temperature (Gallagher, 1970). Alloys exhibiting a larger difference between  $M_d$  and  $M_s$  temperatures usually have lower stacking fault energy austenites. This is believed to be because a low SFE raises  $M_d$  without as significantly impacting  $M_s$ , although some alloys such as silicon and aluminium have been shown to both increase SFE and decrease  $M_s$  and others, such as manganese to decrease SFE and increase  $M_s$  (Effenberg, 2008). The level of nucleation stress required for elastic stress-induced  $\gamma \rightarrow \alpha'$  transformation (at temperatures where this occurs, near  $M_s$ ) is directly dependant on the stress required to propagate planar defects in austenite (Abrassart, Stress-induced  $\gamma \rightarrow \alpha'$  transformation in two carbon stainless steels. Application to TRIP steels., 1973).

As discussed in Section 2.5, the level of insensitivity to temperature and strain rate required for the purposes of the current work is considerably greater than for most previous work. There, the aim was to reduce variation in mechanical properties during processes such as forming and shaping. The use of TRIP steels as strain sensors means that the extent of transformation directly impacts the functioning of the proposed devices, and greater insusceptibility to such phenomenon is thus required.

Data obtained from the numerical model by Sherif infers that a reduction in carbon content from 0.12wt% to 0.6 wt% reduces the temperature susceptibility of the martensitic transformation, as

shown in Figure 2.38 (Sherif, 2003). It has been suggested, as discussed in Section 2.5, that warm working TRIP steel increases the density of  $\alpha'$  nucleation sites (Ghosh & Olson, 1994) (Spencer, Embury, Conlon, Veron, & Brechet, 2004) (Krupp, West, & Christ, 2008).

The  $\beta$  parameter in Equation 2.15 (Section 2.6.2) represents the probability that a shear band intersection will produce a martensitic embryo. Equation 2.16, which defines  $\beta$ , implies that one way to reduce the temperature sensitivity of martensitic nucleation may be to reduce the multiplication factors of the temperature sensitive probability constant,  $p$ . Since martensite laths are essentially one-dimensional,  $\dot{\nu}^{\alpha'}$  is proportional to  $d$  (average austenite grain diameter), shear band plates are essentially two-dimensional and thus  $\dot{\nu}^{\text{sb}}$  is proportional to  $d^2$ , and  $K$  is proportional to  $d^2$ . Thus,  $\beta \approx d \cdot p$

Therefore, according to this model, reducing austenite grain size would reduce sensitivity to temperature via a reduction of the gradient of the curve representing  $\beta$  in Figure 2.39 (b), but would also reduce the rate of transformation and the maximum proportion of martensite possible, because this is determined by  $\beta$  in the model (Olson & Cohen, 1975). High chromium content is known to promote grain growth, particularly when nickel is not present.

Another possibility to reduce temperature sensitivity would be to design an alloy so that it operates in the region where  $p \approx 1$ , where the  $\beta$  curve is flat in Figure 2.39 (b) (Olson & Cohen, 1975). This might be achieved by decreasing the alloy content such that  $M_s$  is increased to near the operating temperature, while ensuring that  $M_s$  does not approach the operating temperature. Olson and Cohen warned against this, due to the softening effects (early plastic yielding occurring via stress-assisted transformation) that would be expected to be associated to this increase in room temperature driving force (Olson & Cohen, 1975).

For the present work, a reduced yield point is of secondary concern, but is expected to actually be beneficial. If the transformation properties are thus improved, then it would be considered doubly positive. However, the stress-assisted plastic yielding that is expected to contribute under these conditions will show different transformation kinetics to those examined in the Olson and Cohen model (Section 2.6.2) and thus different potential temperature sensitivities.

In order to maximise the rate of transformation,  $\alpha$  could be maximised. The rate of shear band formation is represented by  $\alpha$ , and this is accepted to increase with decreasing SFE (Yang, Zhang, Xu, & Meyers, 2008). SFE is known to decrease with decreasing temperature (Lecroisey & Pineau, 1972) (Remy, 1977).

Figure 2.39 (a) implies that reduced SFE (equivalent to reduced temperature in the figure) is expected to decrease the temperature sensitivity of  $\alpha$  in Equation 2.15 (Olson & Cohen, 1975). This may be achieved by reducing the entropy difference between  $\gamma$  and  $\epsilon$  via composition. However, this will only apply where  $\epsilon$  is the predominant type of shear band, which is usually the case at relatively low temperatures or in low SFE TRIP steels. Increased manganese content, and in particular substitution of manganese for nickel, is widely held to reduce SFE in austenitic stainless steels, as discussed in Section 2.5 (Frommeyer, Br  x, & Neumann, 2003) (Mazancov  , Schindler, & Mazanec, 2009). Lecroisey and Pineau's work on Ni-Cr-C alloys of between 0wt% and 18wt% chromium showed that the SFE of these alloys is extremely temperature sensitive (Lecroisey & Pineau, 1972). Thompson found apparent strain rate and temperature insensitivity in alloys in which manganese is substituted for nickel (Thompson, 1986). However, Woodcock found theoretically that the enthalpy difference between fcc and hcp phases does not vary with temperature (Woodcock, 1997).

The model by Sherif, investigated in Section 2.6.3, is based on premises mutual to TRIP and TRIP assisted steels (Sherif, 2003). However, there are several fundamental differences between the TRIP and TRIP-assisted transformations, such as the phases present and the extent of retained austenite. Sherif's model has not been tested on high alloy TRIP steels. The proportionality constant is determined from experimental data for low alloy TRIP assisted steels, and thus is not relevant to high alloy TRIP steels. The model is thus not yet useful for designing high alloy TRIP steels. Sherif also shows that the model is imprecise when the constant is determined for a broad alloy range (Sherif, 2003). There is not a large body of published literature including experimental data representing the transformation of high alloy TRIP steels in the composition range of interest. Thus, such a proportionality constant cannot easily be determined. It may be useful to determine this constant for a specific alloy set in the future.

### 3. Material development and characterisation

#### 3.1 Introduction

The principal aim of this work was to characterise TRIP steel alloys with a view to the development of new alloys optimised for use as cheap structural health monitoring sensor elements. The work up to this point consists primarily of a literature review and an analysis of that literature. The compilation of the literature review is unique to the stated aims of this project and often attempts to place facts in a newly relevant context. The following sections are the author's attempt to build on this work.

Some of the following sections include both experimental methods and results. This is because the work was often iterative, requiring adaptation of techniques and experimental approaches often dictated by previous results.

#### 3.2 Alloy design overview

It was anticipated that TRIP steel alloy composition formulation and processing could be refined in order to attain TRIP steels that showed greater, more easily detectable and repeatable transformation and less sensitivity to uncontrollable conditions, such as environmental temperature and strain rate, or some balance between these two ideals. To attain this, it was necessary to rely to some extent on models and formulae that describe the characteristics of the transformation. All the models and formulae found in literature to describe characteristics of the TRIP transformation were at least partially empirical. Several that were proposed to determine  $M_{d30}$  or  $M_s$  in the compositional range of interest, include empirically determined variables already established for hot worked material. Since several such formulae were proposed by different authors for the same alloy groups (Section 2.6, Table 3.2, Table 3.3) and since each author utilised limited experimental results from literature to verify their formula, it was necessary to test these formulae, by way of experimentation, to determine which most accurately described the alloy group of interest and would thus be most beneficial in future alloy design (Section 3.3.2 for methodology).

It was hoped that experimental results might also be utilised to establish the empirically determined variables required for the more recently developed models discussed in Section 2.6.

However, before this could become a possibility, it was necessary to design the alloys by more fundamental means.

Schaeffler diagrams were used to approximate the proportions of different phases within the material and to roughly predict the propensity to form other phases during deformation. The  $M_s$  temperature of the alloy in relation to operating temperature can give clues about its austenitic stability and thus its tendency to transform. As discussed in Section 3.4.1, there are several different formulae that have been proposed for  $M_s$  and the results of these different formulae vary considerably. Also previously discussed, the  $M_{d30}$  temperature can be used in a similar fashion, but again, several substantially different formulae have been proposed for  $M_{d30}$ .

Certain elements used in the material composition commonly have specific effects on the characteristics of the material's transformation. The elemental composition of the material can also be used to qualitatively predict mechanical and physical property variations, some of which have an indirect influence on the character of the material's martensitic transformation. A degree of trial and error is inevitably involved when employing such empirical methods, especially with multiple alloying elements.

The tensile and compressive alloy designs were undertaken separately. There are fundamental differences in their application and processing and in the mode of deformation. It has been found that when transformation under tensile and compressive deformation are compared for a given material at a given strain, tensile extension produces a greater amount of martensite (Powell et al., 1958) (Stringfellow et al., 1992). A material deformed in compression will also tend to show a higher ultimate strength than when deformed in tension, thereby often increasing its useful range. As discussed in the chapters describing the proposed applications in detail, it is simple to build in fail-safe mechanisms for situations where the compressive TRIP specimen may reach its ultimate strength. On the other hand, failure of a tensile TRIP element will usually result in complete mechanical failure of the device. Specific applications may be better served either by tensile or by compressive TRIP steel elements for these and other reasons that will be discussed in the following sections.

The ultimate tensile strength of a TRIP steel utilised in tension must therefore defined by the application (the maximum over-load strength required). Sometimes even the extent of strain shortly after yield will be a fundamental limiting design factor. On the other hand, it is usually beneficial for a TRIP specimen utilised in compression to have the lowest possible yield strength, as this is usually accompanied by improved early transformation, a smaller incubation

period and a wider useful range. TRIP steel to be utilised in tension must of course be worked in some way to attain the required tensile properties. This can be a costly process, especially when production is in small quantities.

As discussed in Section 2.5, it was known that temperature and strain rate, among other environmental factors, would impact transformation and thus repeatability. An attempt was made to further understand this phenomenon with a view to reducing it.

### **3.3 Alloy transformation temperature sensitivity**

In this section the effect of transformation temperature on the rate of transformation in TRIP steels is examined primarily in terms of free energy diagrams. The differences between diffusional and non-diffusional phase transformations are considered.

The work in Section 3.3, along with that in Section 3.4.2, Section 3.4.8, Section 3.4.9 and Section 3.5.9 constituted journal paper 1 (The effects of transformation temperature on the rate of transformation in TRIP steels), included as submitted in Appendix 3 (Bemont et al., 2013).

#### **3.3.1 Introduction**

The austenite to martensite transformation occurring during the deformation of TRIP steel is well known to be temperature sensitive (Bressanelli & Moskowitz, 1966). However, this effect has not been extensively investigated. The effect of transformation temperature is often not accounted for when researching new applications for TRIP steels and has not as yet been widely investigated in the literature. The purpose of this investigation was to better understand this characteristic and if possible to uncover methods for its minimisation.

Attempts to characterise or model this effect have not been demonstrated to be successful outside of a narrow range of alloys. The investigation stems from research into the development of TRIP steel based load sensors and the obvious need for the minimisation of transformation temperature sensitivity in such applications. However, transformation temperature sensitivity is relevant to many applications. It is hoped that a greater understanding of temperature sensitivity in high alloy, high transformation TRIP steels might aid the understanding of these characteristics in a wider range of TRIP and TRIP assisted steels.

### 3.3.2 Theory

It is well known that an austenite to martensite transformation begins in many steels upon rapidly quenching to a temperature specific to the alloy, known as  $M_s$ , and that upon reaching a lower temperature,  $M_f$ , the transformation to martensite is complete (with some retained austenite permanently remaining). At any intermediate temperature, a specific amount of martensite is permanently formed and will not change without a further reduction in temperature. The transformation occurs extremely rapidly due to its diffusionless nature.

It is interesting to consider the martensitic transformation in terms of free energy diagrams. First the case of a diffusional transformation is considered, as depicted in Figure 3.1. During diffusional transformation, a phase will either develop gradually as temperature decreases ( $\alpha \rightarrow \beta$  in  $T_2 \rightarrow T_3 \rightarrow T_4$ ), or may form at one temperature such as eutectoid temperature ( $\alpha \rightarrow \gamma$  in  $T_4 \rightarrow T_5$ ). In all cases, compositional change between phases via diffusion is necessary and quasi-equilibrium is ultimately thus maintained.

Diffusionless transformations occur extremely rapidly and undergo no composition change. A free energy diagram for a diffusionless austenitic to martensitic transformation is shown in Figure 3.2. For the composition of interest, at some temperature  $T_0$ , the austenitic and martensitic phases have the same Gibbs free energy ( $G$ ). However, in order for the transformation from austenite to martensite to proceed, it is necessary to overcome certain retarding forces associated primarily with surface formation (of the new phase) and also with lattice strain. This means that further cooling to  $T_4$  ( $M_s$ ) is required so that an extra driving force for the transformation,  $\Delta G^{\gamma \rightarrow \alpha'}$  is present before transformation will proceed.

Once  $M_s$  is reached, a very small amount of austenite will transform into martensite. But in order for transformation to proceed and produce more martensite, temperature must be further reduced.

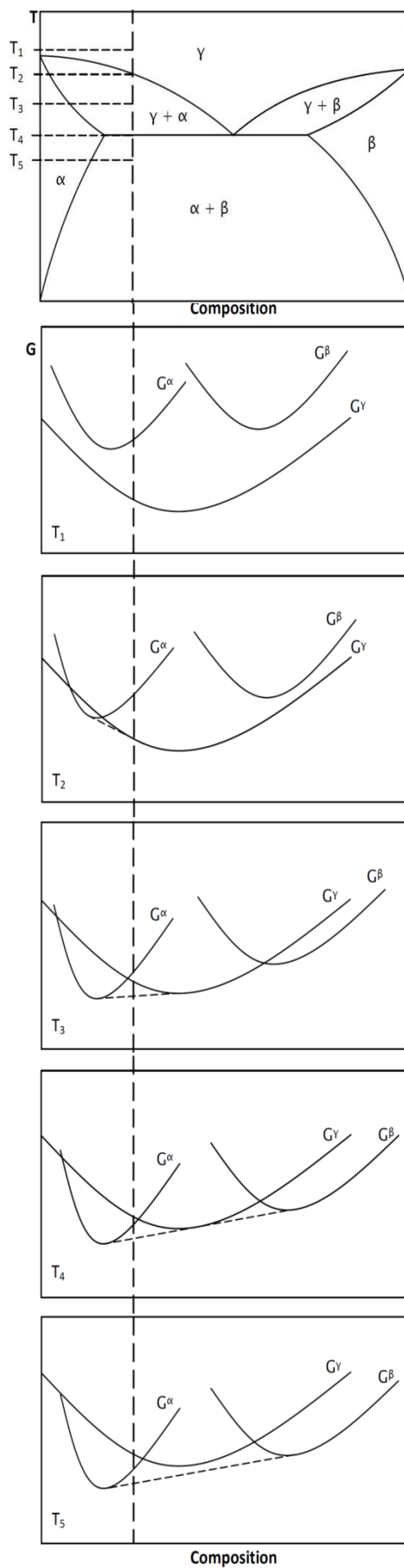
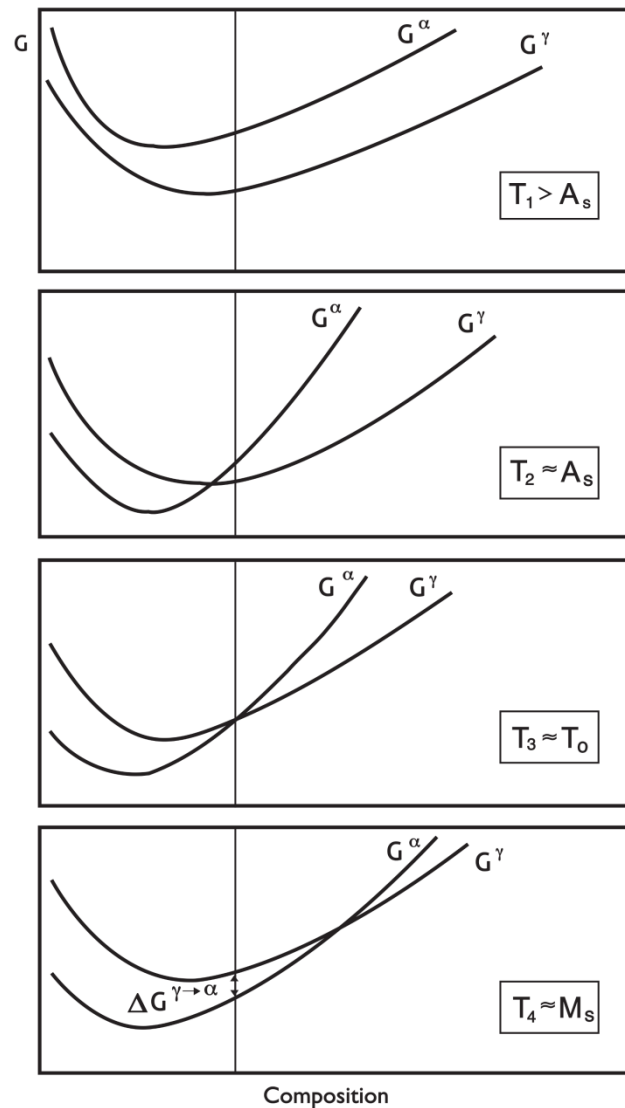


Figure 3.1: Gibbs free energy diagrams for a material undergoing phase change due to diffusion (Bemont et al., 2013). Based on work by A. H. Cottrell (Cottrell, 1955).





**Figure 3.2:** Gibbs free energy diagrams for a material undergoing a diffusionless phase change (Bemont et al., 2013).

The fact that the transformation does not occur entirely (or even primarily) at any distinct temperature, but rather over a range of temperatures, must be due to one or more of the following:

- Inherent variation in magnitude of the driving or retarding forces in different regions of the material.
- Increasing lattice strains in the austenite lattice as martensite volume fraction increases.
- Change in magnitude of the driving or retarding forces at the austenite martensite interface as a martensite plate grows.
- Differences in heterogeneous nucleation site potential.

If transformation occurs over a range of temperatures due to differences in heterogeneous nucleation site potential, then there must also be a mechanism preventing existing martensite grains from growing continuously larger.

Small particle experiments in which submicron single crystal particles were cooled have shown that even at 4K, with undercooling of 300K, some particles remain untransformed (Perepezko et al., 2002). This implies that the reason that transformation occurs over a range of temperatures is related primarily to heterogeneous nucleation, rather than to variations in surface or strain energy retarding forces.

A single plate of martensite in steels is known to grow to its full size in  $10^{-5}$  to  $10^{-7}$  s at constant temperature (Nishiyama et al., 1978). This implies that neither strain induced in the austenitic lattice, nor changes in the austenite martensite interface are fundamentally responsible for the continually increasing driving force required. In fact, the strain induced in the austenitic lattice by the growth of a martensitic plate is even known to encourage martensitic nucleation or growth in other orientations, known as autocatalysis (Olson & Cohen, 1972). At any rate, the maximum growth of any martensite plate is limited by its morphology and the size of the prior austenite grains. Again, this implies that the increase in required driving force for the transformation to proceed is primarily due to a variation in heterogeneous nucleation site activation energies, rather than due to changing surface or strain energy retarding forces.

It has previously been approximated that the critical energy required to form a homogeneous martensite nucleus in austenite is too large for thermal fluctuations alone to overcome (Porter et al., 2009). Thus, from the above argument, it is hypothesised that different driving forces (different temperatures) will be required to activate different pre-existing or autocatalytically induced potential nucleation site configurations, depending on the activation energy required. This will then lead to transformation over a range of temperatures, as occurs in practice. The lack of increased driving force for nucleation relative to growth during diffusionless transformation is also relevant here, since otherwise wide-spread instantaneous nucleation would be expected with associated growth. This is again due to the lack of compositional change as opposed to the diffusional case where the driving force for nucleation can be considerably greater than that for growth. Figure 3.3 depicts the substantially increased driving force present for nucleation in diffusional transformations.

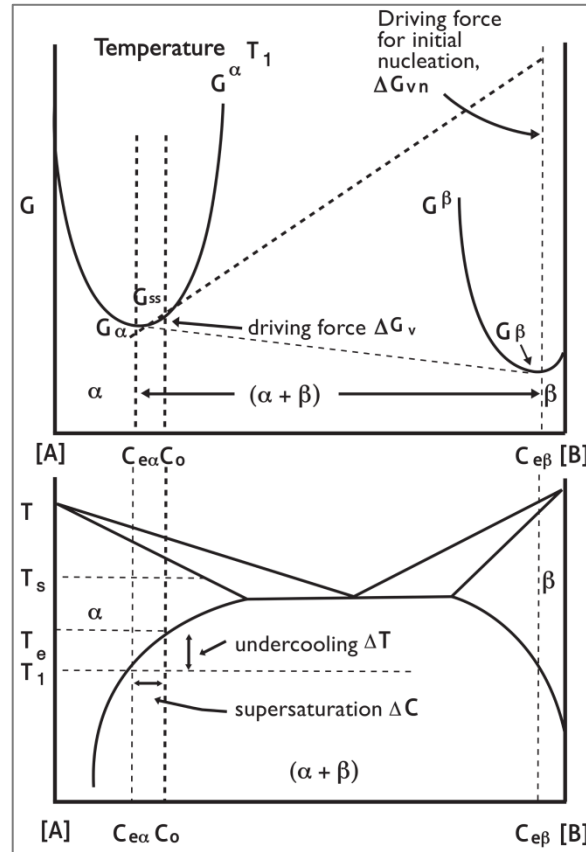


**Figure 3.3: Schematic relationship between the driving force  $\Delta G_v$ , the supersaturation  $\Delta c$ , and the undercooling  $\Delta T$  for a diffusional transformation (Porter et al., 2009).**

This result is thus in agreement with the view that the austenite to martensite transformation is nucleation-controlled. It corresponds more specifically with the dislocation strain energy assisted transformation nucleation theory (dislocation nucleation theory) in which the nucleation barrier to form a coherent nucleus is reduced by a favourable interaction with the elastic strain field of a dislocation, allowing a very broad range of potential favourable interactions (Porter et al., 2009). It also corresponds with the theory that  $\alpha'$ -martensite nucleates at shear band intersections (Suzuki et al., 1977) (Brooks et al., 1979). Since the characteristics of the austenite to martensite transformation are dependent on martensitic nucleation, this suggests that they are also dependent on dislocation density. Moreover, new potential nucleation or autocatalysis sites may be formed during the growth of new martensite plates. The strain energy generated as the transformation progresses is unlikely to contribute to controlling nucleation. This is because, as already discussed, strain would be expected to actually encourage nucleation in certain orientations, at least until very large and wide-spread austenitic lattice strains occur.

Some understanding of the progression of the martensitic transformation with temperature reduction is expected to be helpful in designing alloys to be less temperature sensitive during deformation-induced transformation. If an alloy was designed such that it had large numbers of

nucleation sites within a narrow range of activation energies near to  $M_s$ , then  $M_f$  would be expected to be relatively close to  $M_s$ , as depicted in Figure 3.4(a). Relatively high temperature sensitivity would be expected, since a small change in temperature of deformation will result in a large change in the proportion of nuclei activated.

In Figure 3.4, the deformation-induced transformation is represented as progressing from 0% to 100% between the upper and lower dotted lines respectively. These lines represent the energy contribution required from deformation for the transformation to progress to the specified level at the temperature of interest. When considering deformation-induced transformation, a deformation energy contribution that induces about 50% transformation into the alloy in Figure 3.4(a) at standard test temperature ( $T_1$ ) requires a smaller temperature change to instead attain either zero or complete transformation than the alloy in Figure 3.4(b) which has a lower  $M_f$  temperature, with  $M_s$  and  $T_0$  remaining unchanged.  $\Delta G_{M_s}$  remains approximately constant between the alloys, as is believed to be the case (Porter et al., 2009). This implies relatively greater transformation temperature sensitivity for the alloy in Figure 3.4(a). The alloy in Figure 3.4(b) is also expected to transform more gradually over a larger deformation range. However, the maximum extent of transformation should be about the same for the two alloys represented by Figure 3.4 (a) and Figure 3.4(b) (similar amounts of retained austenite) and a more gradual transformation is even likely to be beneficial. It is also observed that transformation should begin sooner in whichever alloy has test temperature  $T_1$  closest to  $M_s$ .

Reducing the gradient of the difference between the free energy curves by separating  $M_f$ ,  $M_s$  and  $T_0$  should also reduce temperature sensitivity. This is illustrated when comparing Figure 3.4 (b) and (c), where only  $T_0$  moves while  $M_s$  and  $M_f$  remain constant and  $\Delta G_{M_s}$  again remains approximately constant. The alloy in Figure 3.4(c) shows slightly less temperature sensitivity than that in Figure 3.4(b). Figure 3.4(d) represents the most likely scenario, where the temperature differences between  $M_f$ ,  $M_s$ ,  $M_d$  and  $T_0$  all increase. Clearly, temperature sensitivity is substantially reduced for the alloy represented in Figure 3.4(c), while rate of transformation with deformation is likely to either decrease or remain the same, but may also increase, depending of the extent of reduction in gradient.

From the above analysis of energy diagrams and dislocation nucleation theory, it is clear that no TRIP steel alloy can be made to be completely temperature insensitive during deformation-induced  $\gamma \rightarrow \alpha'$  transformation. This is because under a given deformation, at a lower temperature, a greater proportion of the nucleation sites present will be activated as martensitic nuclei, since the driving force for transformation is larger.

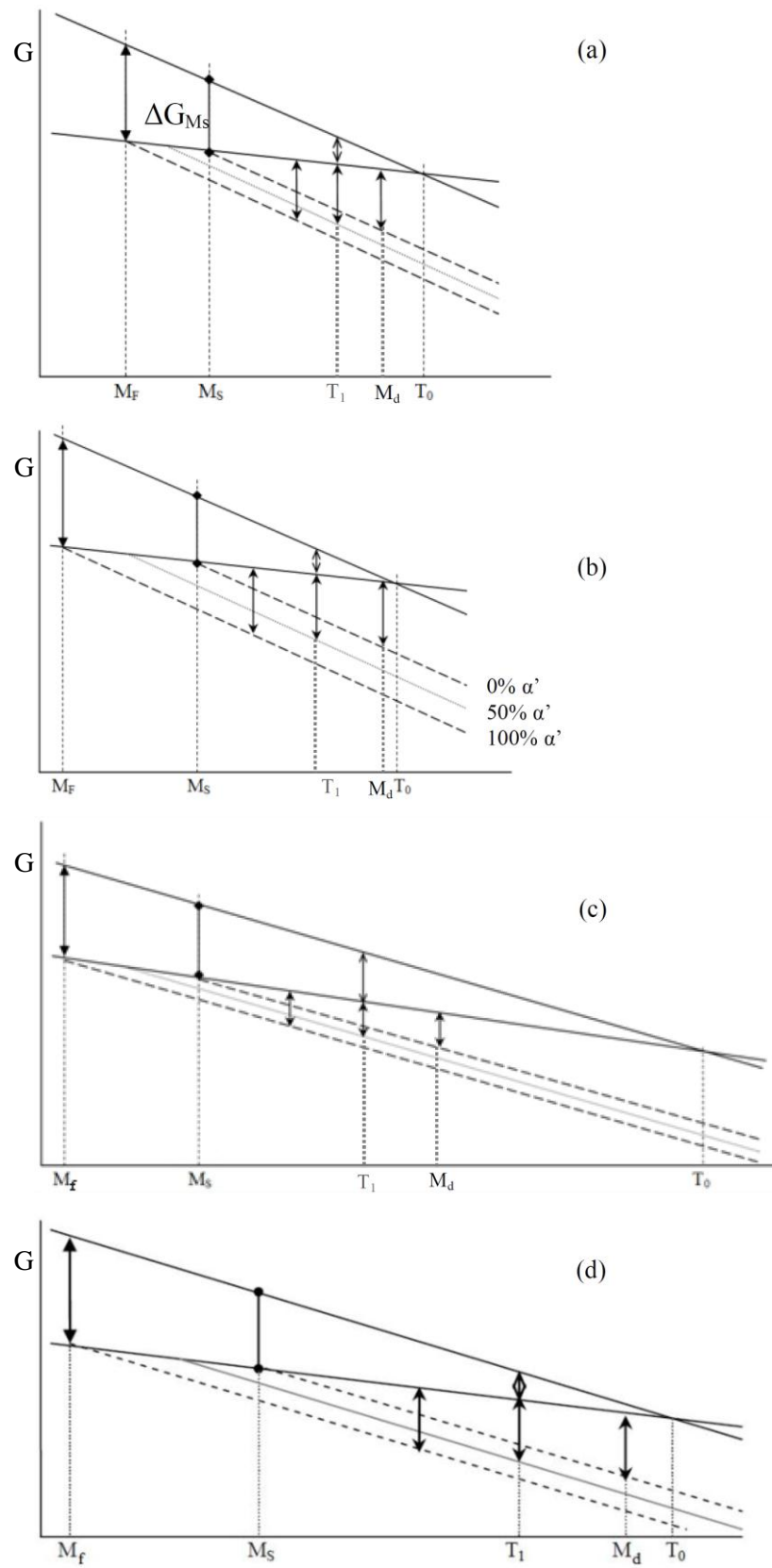


Figure 3.4: Schematic diagrams representing free energy versus temperature for the austenite to martensite transformation, showing how transformation temperature sensitivity varies as  $M_F$ ,  $M_S$  and  $T_0$  change (Bemont et al., 2013).

### 3.3.3 Summary

An energy diagram approach has been used to reach the hypothesis that the transformation temperature sensitivity of TRIP steel alloys can be minimised by manipulating  $M_f$ ,  $M_s$  and  $M_d$  temperatures and dislocation density through alloy composition and processing control. It is apparent that while no TRIP steel alloy can be made to be completely temperature insensitive during deformation-induced  $\gamma \rightarrow \alpha'$  transformation, it is possible to reduce temperature sensitivity by design via alloy composition and dislocation density.

## 3.4 Cast alloy design, testing and analysis

### 3.4.1 Introduction

The work in Section 3.4 was the primary origin of journal paper 2 (The development of robust structural health monitoring sensors utilising TRIP steel), included in Appendix 3, and is the sole work of the author (Bemont, 2009). The compressive alloy was to be applied as-cast or cast and heat treated in order to substantially reduce the material cost, particularly in low volume production. Potentially near-complete smart load cells might be cast directly, reducing costs even further. It was hoped that the cast material would also exhibit a low yield point, allowing for a broader range of stress measurement.

It was hypothesised that because the cast alloys would exhibit substantially lower yield points but not substantially lower UTS values in compression, they would be likely to have another advantage over wrought alloys in that their sensor range would be greater.

A comparison of results for the same cast TRIP steel ("Alloy D" of composition 0.22wt% C, 2.34wt% Mn, 0.7wt% Si, 8.98wt% Cr, 10.7wt% Ni) deformed in compression and in tension are shown in Figure 3.5. Although this material gave good transformation in compression, it was not strong enough in tension even to properly develop the transformation.

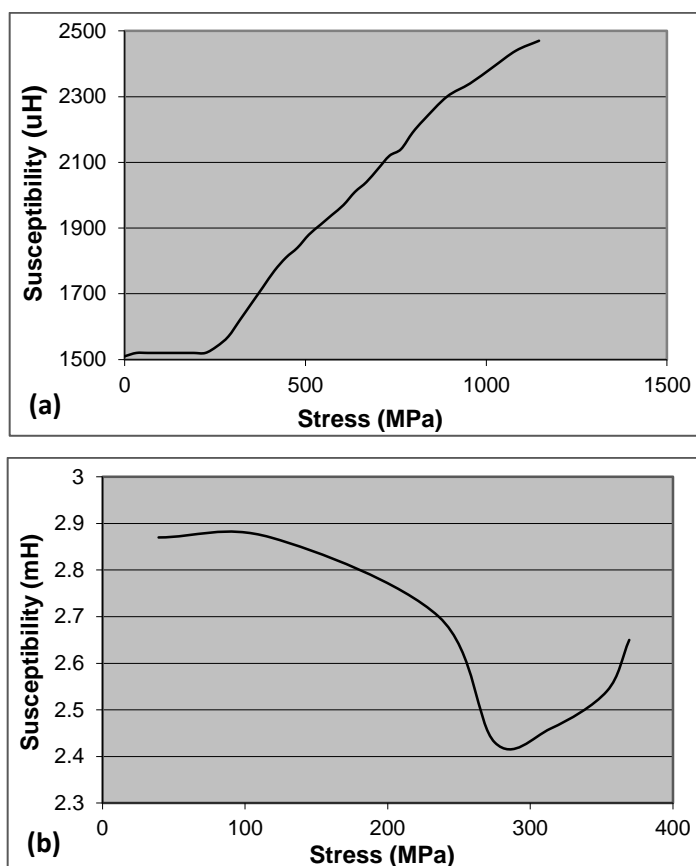


**Figure 3.5:** The above two graphs show cast TRIP steel alloy D deformed (a) in compression (20mm diameter specimen, 200 turn coil) and (b) in tension (20mm diameter specimen, 600 turn coil).

The mode of deformation occurring on a crystallographic level is different when a material is deformed in compression or tension, thus it is possible that a composition functioning well in tension may not do so when utilised in compression. It could also not be assumed that a material exhibiting optimum characteristics in compression would also do so in tension. The two cases were thus dealt with separately. More detail regarding their alloy design, fabrication and testing is given in the following chapters.

No as-cast metastable alloys were available to purchase and no information was found regarding such alloys in literature. The approach to alloy design was described in the previous chapter. Several alloys were designed with a view to gaining a better understanding of how different compositions affect the transformation in cast material. Three main alloy groups of the same Schaeffler nickel equivalents and chromium equivalents were chosen. These alloy groups were selected within a region of the Schaeffler diagram previously found in the literature (Section 2.5) and in preliminary experimentation to give good transformation. They were also selected, where possible, to have a relatively high UTS and low yield strength, and to have good corrosion resistance. These three groups are shown in the Schaeffler diagram in Figure 3.6. Within these groups, different alloy combinations were utilised to obtain the specified nickel

and chromium equivalents, so that the effect of the different alloying elements might be analysed independently of the alloy's position on the Schaeffler diagram (its phase stability). The proposed alloy groups are shown in Table 3.1.

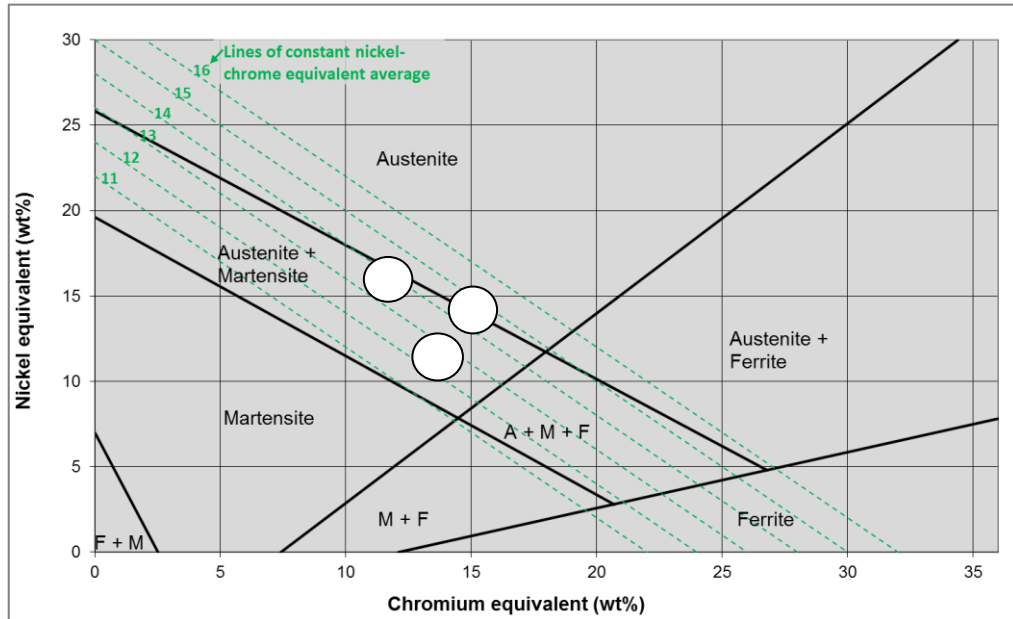


Figure 3.6: Schaeffler diagram showing the proposed alloy groupings (Bemont, 2009) (modified from Radu, originating from Schaeffler (Radu et al., 2005) (Schaeffler, 1949)).

Table 3.1: Proposed alloy compositions (in wt%)

Alloy	C	Cr	Mn	Ni	Si	Ti	Fe	Ni <sub>eq</sub>	Cr <sub>eq</sub>
1A	0	13	0	11	0	0	Bal.	11	13
1B	0.02	13	0	10.4	0	0	Bal.	11	13
1C	0.1	12.25	0	8	0.5	0	Bal.	11	13
1D	0.1	12.25	6	5	0.5	0	Bal.	11	13
1E	0.02	11.5	0	11	0	0.75	Bal.	11	13
2A	0	11	0	13	0	0	Bal.	13	11
2B	0.1	10.25	0	10	0.5	0	Bal.	13	11
2C	0.1	10.25	8	6	0.5	0	Bal.	13	11
2D	0.02	9.5	0	13	0	0.75	Bal.	13	11
3A	0	14	0	13	0	0	Bal.	14	13
3B	0.1	13.25	0	10	0.5	0	Bal.	14	13
3C	0.1	13.25	8	6	0.5	0	Bal.	14	13
3D	0.02	12.5	0	13	0	0.75	Bal.	14	13
4	0.2	13.5	9	0.5	0.4	0	Bal.	11	14
5	0.13	13	12	4.1	0.4	0	Bal.	14	13.5



The data resulting from these experiments would also be utilised to determine which of the empirical formulae for  $M_s$  and  $M_{d30}$ , discussed in Section 2.4.2 and listed in Table 3.2, most accurately fitted the current alloys. Data from these tests might also be utilised later to aid in the determination of the empirical constants required for theoretical transformation models, such as those discussed in Section 2.6.

**Table 3.2: Various empirically determined formulae to describe  $M_s$  temperature for the alloy range of interest in weight % alloy composition (Cina, 1954) (Stuhlmann, 1959) (Andrews, 1965) (Hull, 1973) (Brooks, 1996) (Krupp et al., 2008).**

$M_s$ Andrews	$539 - 17.7.Ni - 12.1.Cr - 30.4.Mn - 7.5.Mo - 423.C$
$M_s$ Cina	$1305 - 61.Ni - 42.Cr - 33.Mn - 28.Si - 1667.(C+N)$
$M_s$ Stuhlmann	$550 - 17.Ni - 20.Cr - 40.Mn - 10.Mo - 350.C$
$M_s$ Hull	$1482 - 59.Ni - 47.Cr - 54.Mn - 37.Si - 56.Mo - 180.Ti - 2390.C - 3720.N$

**Table 3.3: Various empirically determined formulae to describe  $M_{d30}$  temperature for the alloy range of interest in weight % alloy composition (Angel, 1954) (Pickering, 1978) (Nohara et al., 1978) (Hedström, 2005).**

$M_{d30}$ Angel	$413 - 9.5.Ni - 13.7.Cr - 8.1.Mn - 18.5.Mo - 9.2.Si - 462.(C+N)$
$M_{d30}$ Pickering	$497 - 20.Ni - 13.7.Cr - 8.1.Mn - 9.2.Si - 18.75.Mo - 462.(C+N)$
$M_{d30}$ Nohara	$551 - 29.Ni - 14.Cr - 8.1.Mn - 9.2.Si - 18.5.Mo - 29.Cu - 462.C$

The work in Section 3.3, along with that in Section 3.4.2, Section 3.4.8, Section 3.4.9 and Section 3.5.9 constituted journal paper 1 (The effects of transformation temperature on the rate of transformation in TRIP steels), included as submitted in Appendix 3 (Bemont et al., 2013).

### 3.4.2 Methodology for the identification of relevant empirical formulae

In order to test whether TRIP steel alloys could be designed to reduce their temperature and strain rate sensitivity by adjusting  $M_f$ ,  $M_s$ ,  $M_d$  and  $T_0$  temperature, as suggested in Section 3.3.2, a range of special alloys should have been designed according to these parameters. However, no fundamental models are known that can be relied upon to predict these parameters accurately for the high alloy stainless TRIP steels of interest. All of these parameters are hard to measure experimentally, although it can be seen from Table 3.2 that there has been substantial experimental work done to empirically model  $M_s$  and  $M_{d30}$  (where  $M_{d30}$  is the temperature at which 50% martensite is attained at 30% strain). Thus, to test the hypothesis and also for the result to be useful in alloy design, it will be necessary to be able to predict at least some of the alloys' temperature parameters using empirical models.

Several empirical models for  $M_s$  and  $M_{d30}$  are found in the literature for materials close to the alloy range of interest (Angel, 1954) (Hull, 1973) (Pickering, 1978) (Nohara et al., 1978) (Capdevila et al., 2002) (Krupp et al., 2008). However, there is significant variation between

these models, and it was not known which might most accurately represent the alloy range being investigated. Very little experimental work has been performed on high alloy TRIP steels in compression. Several experimental alloys were cast with a view to determining which of the empirical equations were most relevant, and also the manner in which alloy composition affects the rate of transformation with deformation in the alloys (Bemont, 2009). If specific empirical equations could be identified to be suitable predictors, then they might also be used to estimate the  $M_s$  and  $M_{d30}$  of these or new alloys (at least relative to each other) and thereby to test the above hypotheses relating these intrinsic temperature parameters to an alloy's temperature sensitivity.

As discussed in Section 3.3, the thermally-induced martensite transformation temperature,  $M_s$  and the upper limit temperature of the deformation-induced martensite,  $M_d$  (or associated  $M_{d30}$ ) are taken to be related to the rate of transformation and to the thermal stability of the transformation.  $\Delta G_{Ms}$  is the Gibbs free energy for martensitic transformation to begin, as specified in Figure 3.7.  $\Delta G_{Ms}$  is considered to be approximately constant within a range of alloys (Porter et al., 2009). It is thus inferred from Figure 3.7 (which originates from journal paper 1, Appendix 3) that when the free energy curve of martensite is shifted downwards (orange line)  $M_s$  and  $M_{d30}$  both increase in temperature in equal amounts and  $V'$  (the deformation energy contribution required for the transformation to occur at ambient temperature) is reduced. When the free energy curve of martensite is tilted (blue line),  $M_s$  and  $M_{d30}$  again increase in temperature, but with  $M_{d30}$  increasing less rapidly than  $M_s$ .  $V'$  is again reduced. Similar changes occur when the austenite free energy curve is shifted.

It can be concluded that changes in  $M_s$  and/or  $M_{d30}$  are expected to result in an associated change in the rate of transformation with deformation at a given temperature, such as ambient temperature (since  $V'$  changes). Since several empirical equations have been proposed by various authors (Table 3.2) to determine  $M_s$  and  $M_{d30}$  in the alloy range of interest (although none specifically for compression), it is proposed that this principle can be used to test which of these empirical equations best describe the transformation by plotting experimentally measured transformation data against the predicted  $M_s$  and  $M_{d30}$  temperatures and then statistically analysing the quality of the linear fit.

It can also be inferred from Figure 3.7 that when the difference between  $M_s$  and  $M_{d30}$  is altered, then  $V'$  is proportionately altered. Thus, the differences between various combinations of proposed empirical equations for  $M_s$  and  $M_{d30}$  can be analysed for linear fit to experimentally measured transformation.

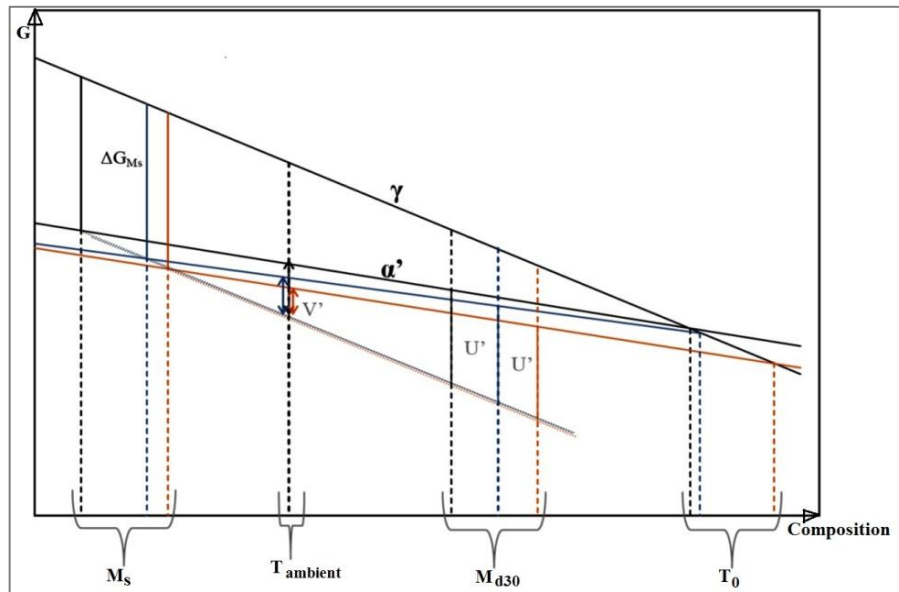


**Figure 3.7: Transformation temperature sensitivity effect of shifting the austenite-martensite free energy curves.**

Further to this, it can be inferred from Figure 3.8 that when the gradient of the difference between the free energy curve for martensite and that for austenite is reduced, then a shift in ambient temperature will less severely affect the magnitude of  $U'$  and will thus reduce the impact on the rate of transformation (assuming again that  $\Delta G_{Ms}$  and  $\Delta G_{Mf}$  are approximately constant). Thus, determining empirical equations that approximate  $M_s$  and  $M_{d30}$  may aid the design of alloys with reduced temperature and strain-rate sensitivity.

Thus, if formulae that approximate  $M_s$  and  $M_{d30}$  in the alloy system of interest can be identified, then these formulae might be beneficial to optimise the alloys using two of the principle objectives for implementing TRIP steel as smart sensor alloys.

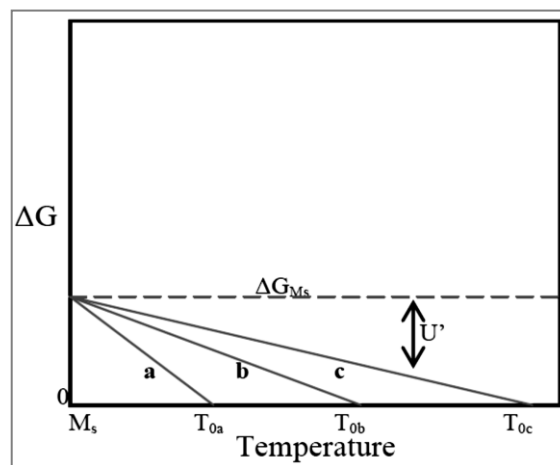


**Figure 3.8: Schematic illustration representing the difference in energy between austenite and martensite with temperature. Lines a, b and c represent the manner in which a smaller gradient of change between austenite and martensite free energy reduces the effect of temperature change on the transformation deformation energy required ( $U'$ ).**

As discussed in Section 2.5 (particularly the work of Otte and Cina), various authors have found that manganese significantly influences the transformation by decreasing stacking fault energy and promoting the  $\gamma \rightarrow \epsilon$  transformation (Otte, 1957) (Cina, 1958). It is proposed that manganese may thereby be beneficial in that it may separate  $M_d$  and  $M_s$  as described in Section 2.5, and thus reduce temperature sensitivity in the manner outlined in this section. The casting of high manganese alloys proved to be difficult in the arc-furnace but two alloys of over 10wt% manganese were produced, as shown in Table 3.5 and Table 3.7 of Section 3.4.3.

### 3.4.3 Alloy fabrication

The special alloys melted for compressive analysis were produced using various different methods. Initially, it was attempted to melt alloys in the induction furnace shown in Figure 3.9. This furnace required significant repair and upgrading and the frame and tilt-mechanism among other components were designed and implemented as part of this project. Experts from Columbus Stainless assisted with practical training in the process of casting ingots in small research inductance furnaces. A 5kg crucible was utilised. However, it was found to be extremely difficult to attain a specified composition with any level of accuracy. This was believed to be at least partly due to the furnace not operating an inert gas or vacuum.

Thus, Mintek (Randburg) vacuum cast five alloys in 2kg ingots. The designation of these alloys begins with “V”. They were cast in much larger ingots than the alloys that were cast in a small research vacuum arc furnace, to be discussed later in this section. These alloys were normalised for one hour at 1150°C.



**Figure 3.9: Induction furnace and tilt mechanism: (a) At the start of a melt, without the mould in place, (b) Melt progressing, unmelted metal flakes can still be seen and (c) Melt almost ready to be poured, temperature being monitored with a high-temperature thermocouple.**

The alloys produced by induction melting are shown in Table 3.4, and Alloy TRIP M is included. Alloy TRIP M was produced by Mintek as part of an earlier phase of this project. It was induction cast and then hot rolled at a temperature between 1000°C and 1200°C. Alloy TRIP M was then annealed for one hour at 1150°C and furnace cooled. This alloy is referred to as Alloy HM.

**Table 3.4: Compositions of the induction furnace cast alloys, analysed by spark-spectroscopy (wt%).**

		<b>V2</b>	<b>V4</b>	<b>V5</b>	<b>V6</b>	<b>TRIP M / HM</b>
<b>ELEMENT</b>						
<b>Carbon</b>		0.15	0.179	0.189	0.142	0.2
<b>Manganese</b>		6.12	5.67	4.88	5.28	8.9
<b>Sulphur</b>		0.012	0.014	0.013	0.014	0.015
<b>Phosphorus</b>		0.019	0.023	0.023	0.023	0.016
<b>Silicon</b>		0.81	0.77	0.63	0.98	0.56
<b>Chromium</b>		12.2	12.71	12.33	12.42	13.66
<b>Molybdenum</b>		0.01	<	0	<	<
<b>Nickel</b>		3.59	3.16	3.24	2.78	0.27
<b>Copper</b>		0.01	0.01	0.01	0.01	0.07
<b>Aluminium</b>		0.005	<	<	0.01	<
<b>Vanadium</b>		<	<	<	<	<
<b>Niobium</b>		0.006	<	<	<	<
<b>Titanium</b>		<	<	<	<	<
<b>Iron</b>		Matrix	Matrix	Matrix	Matrix	Matrix
<b>Nickel equivalent</b>		11.2	11.4	11.4	9.685	10.72
<b>Chromium equivalent</b>		13.4	13.9	13.3	13.89	14.5
<b>Equivalent average</b>		12.3	12.6	12.3	11.7875	12.6

The special alloys other than the group designated “V” were cast using the VTD arc-furnace in Figure 3.10 at TUC (Technische Universität Chemnitz, Germany). This furnace had to be adapted from a dental prosthesis casting furnace and required significant modification before it could be reliably used for casting TRIP steel research ingots. Modifications included upgrading vacuum pump filters, updating software code and modifying the tilting mechanism and tray shown in Figure 3.11. Crucible design was also a significant hurdle since a long, bar-shaped specimen was required that could be easily machined into three eight millimetre diameter compressive test specimens. Optimum length to diameter ratio of the ingot had to be established, largely through trial and error, because the maximum melt mass was approximately 90 grams and thus a too large diameter would not produce an ingot long enough to obtain three specimens, while a too small diameter would produce porosity in the specimen and other casting problems. To ensure that specimens were porosity-free, many were cast, and then sectioned and

examined in multiple locations, with crucible modifications made where necessary, before final specimen casting. The final crucible and process of removal is shown in Figure 3.12. Final ingot dimensions were approximately 55 mm total length with a 10 mm diameter (Figure 3.13). These ingots were then machined into 3 test specimens of 11 mm x 8 mm diameter.

The furnace has a maximum charge size of about 120 grams. The furnace melted the material in a vacuum or inert gas (argon) environment in its upper chamber. The furnace was programmed with the required environment, current and melting time. The programme was set to first evacuate the furnace and then pressurise with argon gas. The ideal melting current and time was found to be 105 seconds at 135 A. The alloying elements were placed in the required proportion on a small crucible-tray below the electrode (Figure 3.14). The door was then sealed and the program started. Once the melting process had been completed, the crucible-tray immediately tipped, dropping the molten alloy into the casting-crucible that was placed in the chamber below, as shown in Figure 3.14. Unfortunately, although the furnace was able to accept over 100 grams of charge, it was found that with the drop-cast TRIP alloys, the maximum useable casting mass was approximately 80 to 90 grams for repeatable results.



Figure 3.10: Arc-furnace used to produce the majority of the special cast alloys at TUC.





**Figure 3.11: Purpose designed tipping crucible tray.**



**Figure 3.12: Purpose designed casting mould placed in lower furnace chamber. Images from left to right show the empty mould, a mould into which a melt has been drop-cast, the lug on the mould base used to aid removal of the ingot, the mould with the ingot removed.**

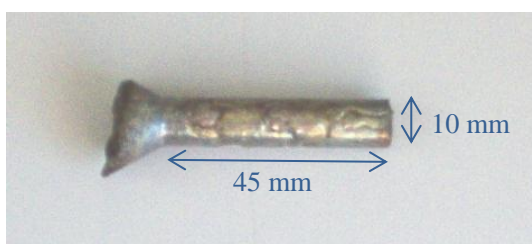


**Figure 3.13: Relevant ingot dimensions of inductance furnace cast specimens.**



**Figure 3.14: Drop-casting mechanism by which the furnace releases the melt from the upper chamber tipping crucible tray into the casting crucible in the lower chamber.**

The copper moulds have a melting temperature of 1084°C, considerably below that of the alloy TRIP steels, which is of the order of 1500°C. However, due to copper's very high heat capacity and conductivity, and due to the relatively large mass of the mould, it was able to withstand the process undamaged. The arc-furnace was deemed to thoroughly homogenise the alloy during melting due to the very high temperature gradient and arc impingement causing a considerable mixing effect. The transformation characteristics of specimen-portions further homogenised at 1100°C for one hour were compared to those directly from the furnace, and were found to be near identical. In order to achieve good uniformity in the casting, the casting crucible was also heated to approximately 400°C prior to casting. Temperatures higher than this were liable to cause damage to the casting surface of the crucible.

Extremely pure forms of the alloying elements, between 99.2wt% and 99.9wt%, were purchased in powder, granular or fine chip form. For each alloy, the relevant alloying elements were carefully measured out on a balance in the correct proportions. This mixture was then placed on the furnace tipping crucible and the casting process described above initiated. Unfortunately, it was found that carbon and manganese, in particular, showed a tendency to be lost during melting. This was most likely due largely to arc sublimation. If an alloy was analysed and found to be considerably low in an element, the ingot was remelted with more of that element added. With practice, the correct amount of extra carbon and manganese was added in order to more closely obtain the required composition. However, precise control of the full elemental composition in the castings was never achieved.

The level of ferromagnetism obtained during slow-cooling or quenching in water was shown to be the same for a variety of alloys (approximately zero). Thus, in order to optimise repeatability and time, all ingots were allowed to cool in the furnace to approximately 400°C, and were then water-quenched upon removal from the furnace at approximately 400°C.

Three specimens were sectioned and half of each given homogenising/austenitizing heat-treatments in a Strohlrin Instruments CTF tube furnace, to investigate how this might affect transformation. Specimens were held at 1150°C for between 10 minutes and 72 hours (furnace cooled). Testing showed that, apart from strength reduction, such heat treatments had little effect on the basic room-temperature strain versus transformation characteristics. The effect of long-annealing was later investigated in detail on alloys subjected to tensile deformation, discussed in Section 3.5.9.

An attempt was made to melt specimens in the evacuated-chamber induction furnace in Figure 3.15. This process may have resulted in more precisely controllable compositions, but it was unsuccessful as the furnace did not impart enough power to fully melt the high-alloy TRIP steels.





**Table 3.6: Nickel and chromium equivalents and empirically calculated  $M_s$  and  $M_{a30}$  results for alloy DIN 1.4301 and special TRIP steel alloys A1 to B2 (wt%).**

ALLOY:	1.4301	A1	A1c	A3a	A3b	A3d	A3e	A4	A5	B1	B2
Ni equivalent = Ni + 30(C + N) + 0.5Mn + 0.5(Cu + Co);      Cr equivalent = Cr + 1.5 Si + Mo + 2Ti + 0.5Nb											
Ni <sub>eq</sub>	11.0	13.5	31.9	14.3	13.7	14.7	23.3	12.9	16.5	16.1	14.1
Cr <sub>eq</sub>	20.7	14.9	12.3	13.5	13.8	13.6	14.4	14.5	21.8	11.4	12.5
Eq <sub>ave</sub>	15.8	14.2	22.1	13.9	13.7	14.2	18.9	13.7	19.1	13.8	13.3
Andrews: Ms (°C)											
	79	119	-99	132	143	131	0.4	6.7	-18	116	-61
Cina: Ms (°C)											
	-200	-148	-1013	-107	-75	-127	-629	-81	-612	-152	-68
Hull: Ms (°C)											
	-186	-15	-1367	-11	0.7	-90	-809	-106	-516	-9.5	-216
Angel: Md30 (°C)											
	9.9	76	-175	86	84	66	-76	72	-48	99	64
Pickering: Md30 (°C)											
	3.6	17	-221	35	48	35	-110	58	-136	17	78
Nohara: Md30 (°C)											
	-28	-48	-292	-28	-4.8	-12	-158	25	-230	-71	73

**Table 3.7: Compositions of special TRIP steel alloys B3 to N1 (wt%).**

[illegible]

**Table 3.8: Nickel and chromium equivalents and empirically calculated  $M_s$  and  $M_{d30}$  results for special TRIP steel alloys B3 to N1 (wt%).**

ALLOY:	B3	B4c	C1a	C2	C2b	C3	C4c	M1a	M1b	N1
Ni equivalent = Ni + 30(C + N) + 0.5Mn + 0.5(Cu + Co); Cr equivalent = Cr + 1.5 Si + Mo + 2Ti + 0.5Nb										
Ni eq	13.9	15.0	14.7	12.0	15.0	12.1	15.4	12.7	11.7	14.3
Cr eq	14.2	13.4	15.0	14.8	15.5	14.7	13.9	14.6	14.7	14.5
Eq_ave	14.0	14.2	14.8	13.4	15.2	13.4	14.7	13.7	13.2	14.4
Andrews: $M_s$ (°C)										
	111	109	97	158	109	-9.4	98	-60	-55	-118
Cina: $M_s$ (°C)										
	-121	-171	-219	-18	204	-43	-215	-38	5.7	-161
Hull: $M_s$ (°C)										
	-21	-41	-95	72	-196	-132	-85	-339	-270	-390
Angel: $M_{d30}$ (°C)										
	82	81	62	92	34	63	71	19	34	20
Pickering: $M_{d30}$ (°C)										
	30	11	-5.2	64	9.2	78	-3.8	100	114	56
Nohara: $M_{d30}$ (°C)										
	-33	-71	-81	20	-47	71	-86	149	163	68

#### 3.4.4 Experimental equipment and method

Quasi-static compression testing was performed in the following manner. Specimens were placed in a jig including a 3000 turn inductance coil, between two compression platens inside a calibrated Instron 5500R universal testing machine. Ambient air temperature was maintained at 23°C in the room by an air-conditioner. The platens were purpose-made and the bottom one to which the coil was fixed was manufactured from ferromagnetic hardened steel, while the top one was manufactured from paramagnetic 316 stainless steel.

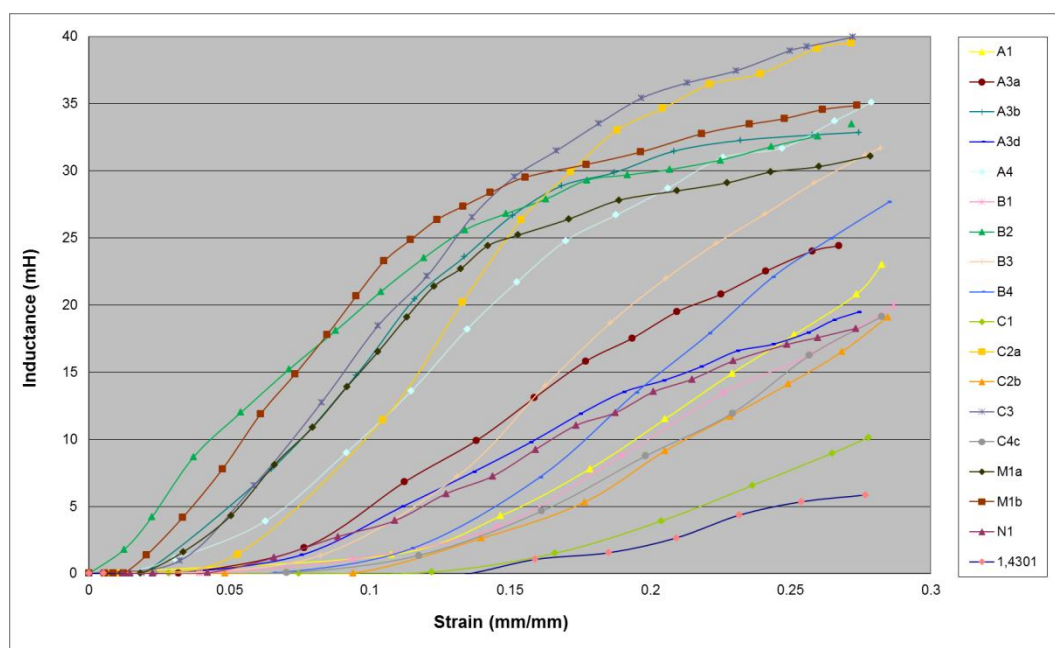
Molybdenum disulphide-based grease was used to lubricate the interface between the TRIP steel test specimens and the compression platens in order to reduce barrelling of the specimens. Initially, a Toptronic T24 LCR inductance meter was modified to incorporate an analogue BNC output so that the data could be digitally logged (via a WaveBook/615 analogue to digital converter). Later, a Tecpel LCR612 digital logging inductance meter was used for most of the work.

Inductance readings were taken on each specimen before placing it into the jig, and also after placing it into the jig and closing the platens with no load. After testing, each specimen was measured in a similar manner. During testing, engineering stress, engineering strain and inductance data were digitally logged throughout.

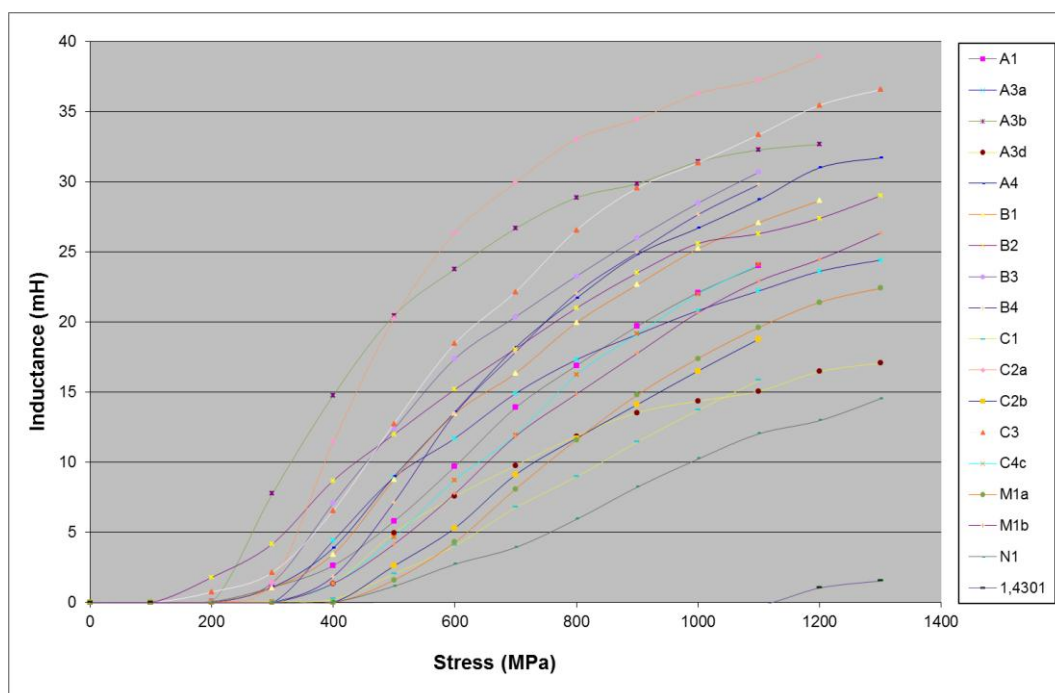
### 3.4.5 Compression testing results

Figure 3.16 and Figure 3.17 depict the inductance-strain and inductance-stress curves respectively for the alloys shown in Table 3.5 and Table 3.7, Section 3.4.3. All of these alloys were produced in the VDC laboratory arc-furnace (Section 3.4.3) as part of the second overall alloy batch. Compressive testing was performed quasi-statically ( $0.01 \text{ s}^{-1}$ ) at  $23^\circ\text{C}$ . Each plot represents the average of two or three tests from specimens cut from the same ingot. This was usually the maximum number of specimens available from the small ingots. In general, good repeatability was attained between specimens from the same ingot. This is portrayed in Figure 3.18, where two individual plots are shown for each alloy. The variation between plots for specimens from the same ingot (usually less than 1% strain) was considered negligible in comparison to other factors. It is likely that these variations occurred primarily due to difficult to control variations in test conditions. The three alloys in Table 3.5 and Table 3.6 with an average nickel equivalent and chromium equivalent above 19 were excluded since they were produced through alloying error; alloys in this composition range were not intended.

As described in Section 3.4.3, porosity was a problem in early ingots. A small amount of porosity was suspected in some test specimens, and specimens in which porosity was found during machining were excluded. Significant porosity would be expected to result in variation between specimens from the same ingot, which was not observed. In order to allow comparison between alloys, these plots show change in inductance on their y-axes instead of absolute inductance. However, the range of absolute starting inductances was relatively narrow and was between 92.7 and 95 for all alloys other than M1b, which was 95.5 and B2 which was 98.



**Figure 3.16: Strain versus inductance for the different experimental alloys, with offset zeroed. Specimens deformed under continuous, quasi-static loading conditions to a peak of approximately 28% strain.**



**Figure 3.17:** Stress versus inductance for the different experimental alloys, with offset zeroed, to 1300 MPa. Specimens deformed under continuous, quasi-static loading.

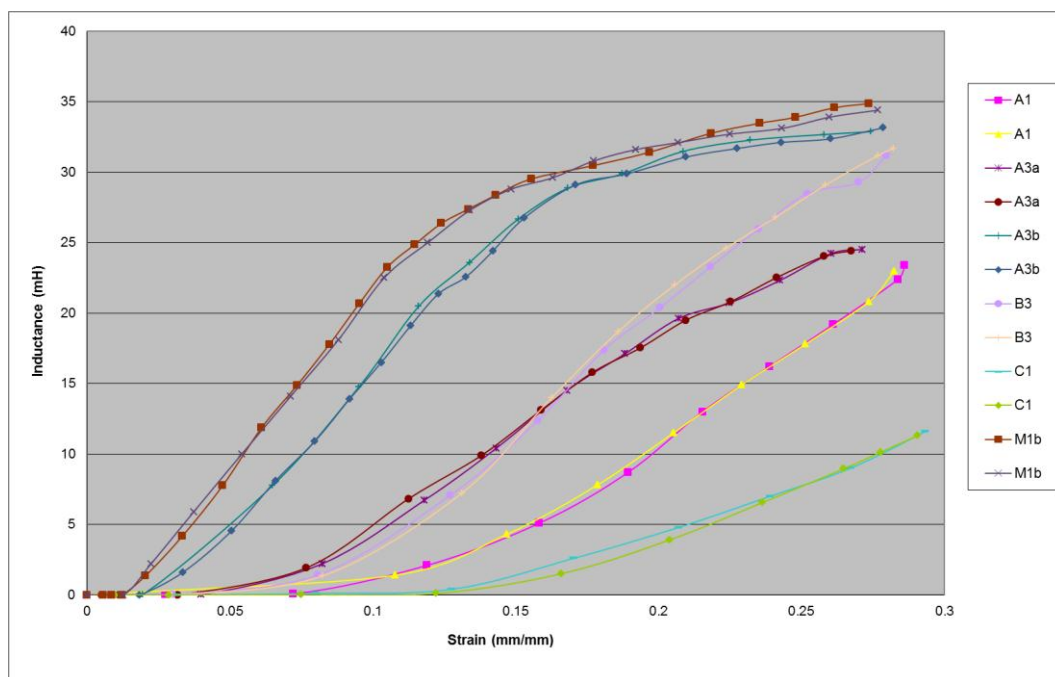


**Figure 3.18:** Repeatability of a selection of the alloys shown in Figure 3.16.

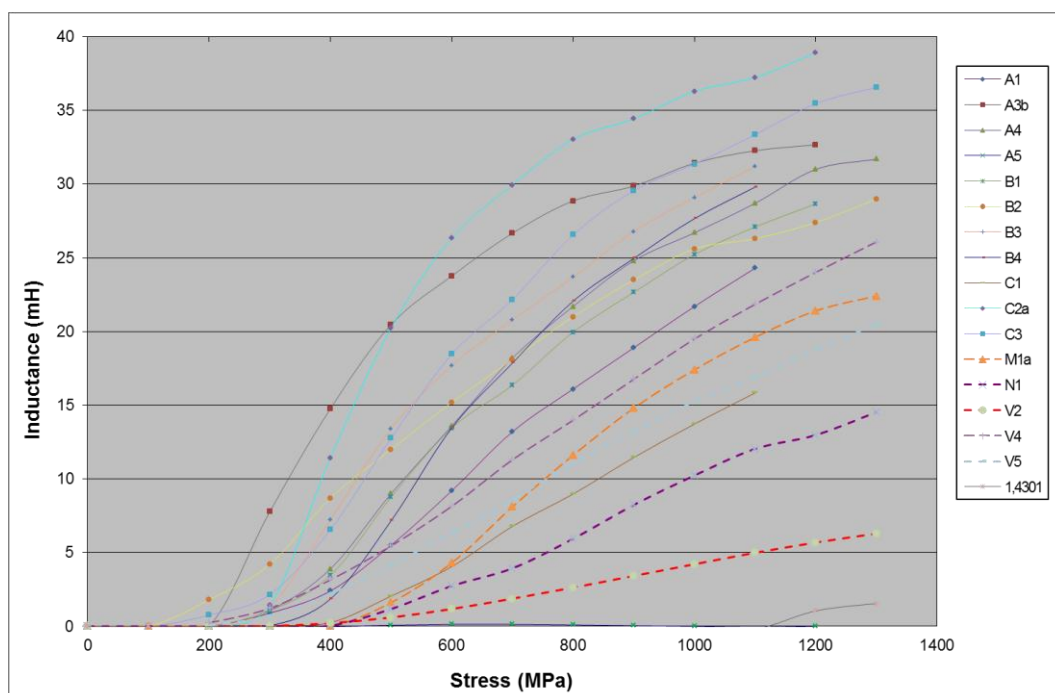


**Figure 3.19: Comparison of selected cast alloys produced in-house and those produced for the project at Mintek, offset zeroed, to 1300 MPa (specimen dimensions, 8mm diameter x 11mm). Curves are the average of at least two tests on specimens from the same ingot.**

The curves in Figure 3.16 to Figure 3.19 characterise the relative extent of transformation exhibited by various alloys during quasi-static compressive transformation. They also show the manner in which certain alloys begin their transformation sooner than others, while some that show rapid early transformation slow their transformation by about 15% strain. It is apparent from Section 3.3.2 that some of the same properties that result in high transformation may result in greater fundamental temperature and strain rate susceptibility. Thus, optimum alloys showing both high transformation and low temperature susceptibility were sought in the following sections, particularly Section 3.4.8 and Section 3.4.13.

Table 3.9 gives an overview of the extent of transformation for the arc-melted alloys tested in compression. Starting inductance, finishing inductance and change in inductance are tabulated.

**Table 3.9: Overall starting inductance, finishing inductance and inductive change in alloys tested in compression at 28% deformation.**

Alloy	1.4301	A1	A1c	A3a	A3b	A3d	A3e	A4	A5
mH start	94.7	92.7	93.0	93.2	93.4	93.1	93.4	95.0	98.4
mH finish	100.5	115.9	93.2	117.7	126.0	112.0	96.9	130.1	97.7
Δ mH	6	23	0	25	33	19	3	35	-0
Alloy	B1	B2	B3	B4	C1	C2a	C2b	C3	C4c
mH start	92.6	99.5	93.16	93.14	92.5	93.3	92.9	94.6	93.0
mH finish	113.7	132.9	124.6	120.8	104.1	132.8	112.0	134.5	113
Δ mH	21	33	31	28	12	40	19	40	20
Alloy	M1	M1b	N1						
mH start	93.7	96.6	93.0						
mH finish	124.8	131.2	109.6						
Δ mH	31	35	17						

### 3.4.6 Metallography

#### 3.4.6.1 Sample preparation

Samples of each alloy were prepared for microscopic examination from the undeformed composition analysis specimen and from a 28% deformed compression test specimen. These were first sectioned with coolant on a low speed cut-off saw, ensuring that a minimum amount of deformation was applied to the structure. Specimens were then mounted in Struers Multifast Black Bakelite resin using a Struers Labopress 3 hot specimen mounting press. They were then ground and polished on a Struers Tegrapol 11 semi-automatic grinding and polishing machine.

Specimens were then viewed on a Nikon Eclipse MA200 inverted optical metallurgical microscope. Figure 3.20 and Figure 3.21 show undeformed Alloy B3 in the as-polished condition at 50 times and 500 times magnification respectively. Figure 3.22 shows the same alloy as in Figure 3.20, also at 50 times magnification but polished with a final chemical polishing step using Struers OP-S solution on an MD Chem polishing disk.



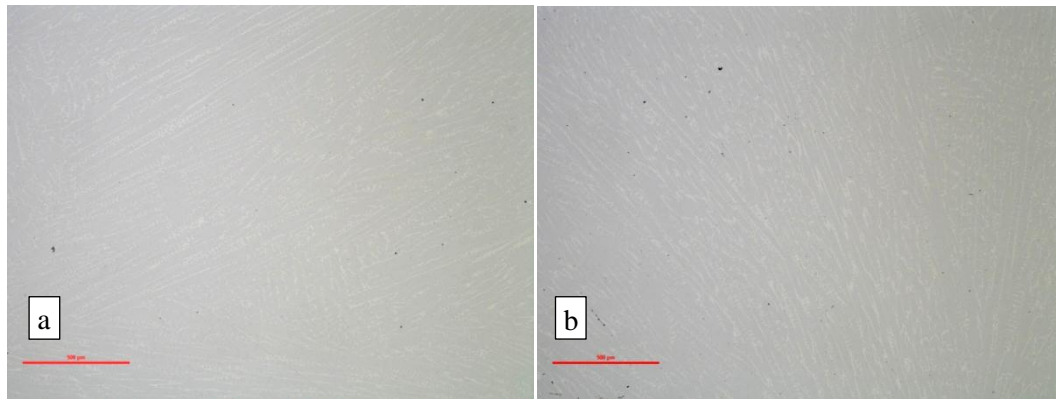


**Figure 3.20:** As polished, alloy B3, optical image, scale bar represents 500 $\mu$ m: (a) undeformed, (b) deformed 28%. Minimal phase differentiation.

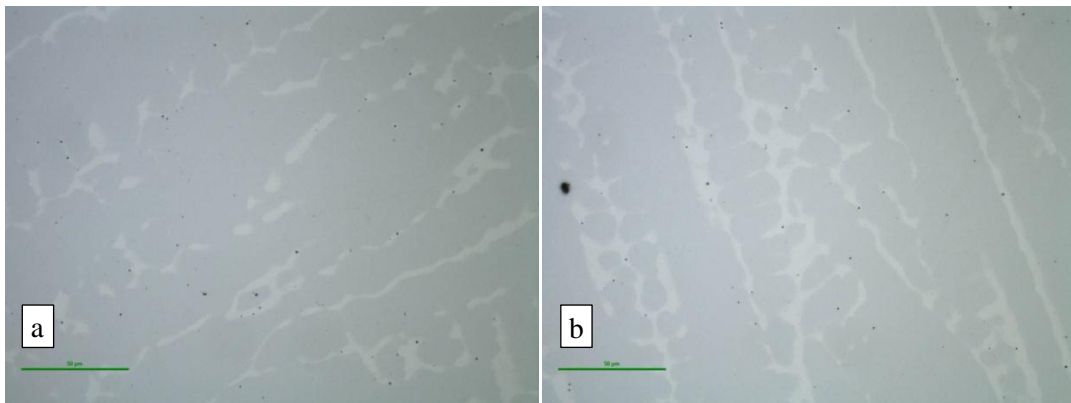


**Figure 3.21:** As polished, alloy B3, optical image, scale bar represents 50 $\mu$ m: (a) undeformed, (b) deformed 28%. Minimal phase differentiation.

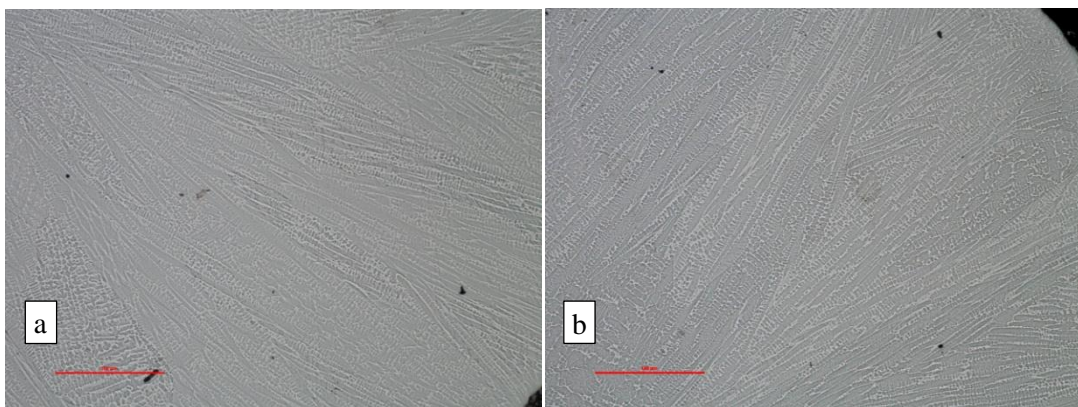


**Figure 3.22:** As-polished including final chemical polishing step, alloy B3, optical image, scale bar represents 500 $\mu$ m: (a) undeformed, (b) deformed 28%. Some phase differentiation.

It is possible that mechanical polishing may introduce surface artefacts through deformation induced transformation at the surface. Electro-polishing specimens using an ATM Kristall 620 electrolytic polisher and etcher was thus undertaken. Electrolytes used for electro-polishing and electro-etching of stainless steels are shown in Table 3.10. The perchloric acid based electrolyte suggested by Hedström (Hedström, 2005) was used for electro-polishing at the voltage, current



and time suggested. A comparison between mechanical polishing and electro-polishing was made. First, an undeformed specimen of Alloy A1a was mechanically ground and polished and then etched in the etchant selected in Section 3.4.6.2. The same alloy was then mechanically ground to 9  $\mu\text{m}$  and then electro-polished and etched in the same etchant. The result is shown in Figure 3.23. It was observed that the extent of the dark martensite phase was similar for both methods of surface preparation, implying that mechanical polishing did not introduce significant surface artefacts.

Figure 3.24 shows a deformed specimen of Alloy C1 electro-polished in a similar manner. This result was considered unsuccessful because a heavily etched surface was revealed. Another electrolyte, based on oxalic acid (Small et al., 2008), was also attempted, but proved similarly unsuccessful. Proper electro-polishing of highly multi-phase structures is known to be difficult to achieve. Maxwell and co-workers (Maxwell et al., 1974) compared the microstructures of mechanically polished and electro-polished TRIP steel specimens of various alloys and found that mechanical polishing did not introduce increased surface artefacts.

**Table 3.10: Electrolytes used by previous authors on stainless type TRIP steels.**

Author	Electropolish / Electroetch electrolytes
(Bracke et al., 2006)	Electropolish: 90ml distilled water, 730ml ethanol, 100ml butylcellosolve, 78ml perchloric acid Electroetch: 1.2% $\text{K}_2\text{S}_2\text{O}_8$ , 0.5% $\text{NH}_4\text{HF}_2$ , aqueous solution
(Hedström, 2005)	Electropolish for TEM / EBSD: 12V; 1A–1.5A in 125 ml perchloric acid; 200 ml ethanol and 800ml methanol Electropolish for optical microscopy as above and then etch in: 10% HCl; 0.25% Sodium bisulfite and 89.75% $\text{H}_2\text{O}$

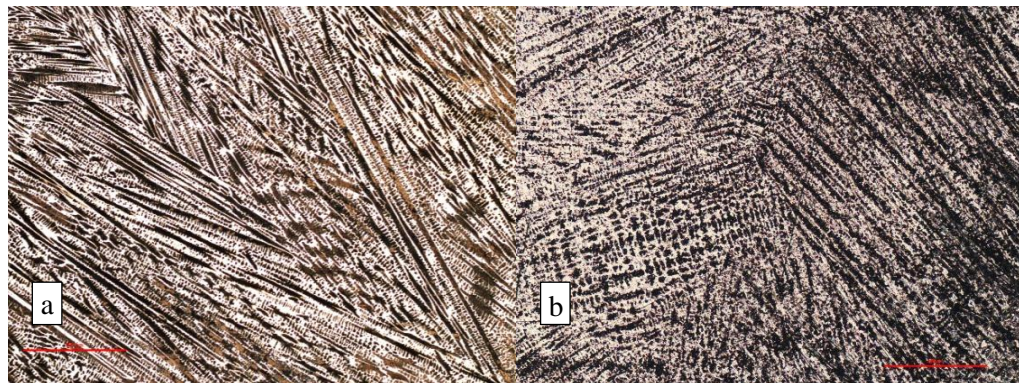


**Figure 3.23: Alloy A3a undeformed, optical image, scale bar represents 500 $\mu\text{m}$ : (a) mechanically polished and chemically etched, (b) mechanically polished to 9  $\mu\text{m}$ , electro-polished, chemically etched. Showing similar phase differentiation and extents of dark martensite in a light austenite matrix.**

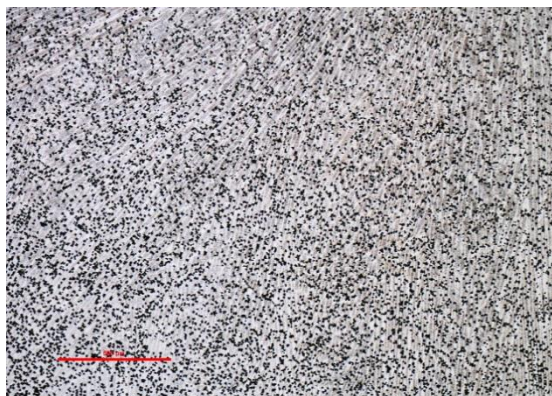


**Figure 3.24: Specimen C1 in a deformed condition, optical image, mechanically polished and then electro-polished in a perchloric acid based electrolyte. Electro-polishing could not be made to produce an even surface in preparation for etching. Scale bar represents 500 $\mu$ m.**

### 3.4.6.2 Etching

It proved challenging to properly etch the highly multi-phase TRIP steel microstructures. Some relevant electrolytic etches are shown in Table 3.10 and chemical etchants are shown in Table 3.11. After much experimentation with these etchants, one similar to some of Beraha's reagents, formulated by Olson and Azrin (Olson & Azrin, 1978) (Table 3.11), was found to be best for viewing the various alloys' microstructure. Etching time had to be varied from alloy to alloy due to variations in composition. According to the ASM Handbook, volume 9, etchants based on sulphite coatings such as Beraha's reagent darken martensite, while austenite remains white or yellow and ferrite is coloured blue (Vander Voort & Beuhler, 2004).

It was considered that a low temperature temper, at around 200°C, would potentially allow for differentiation of austenite and martensite by nital. Tempering alone might be enough to differentiate austenite and martensite in SEM since martensite grains would develop surface relief due to fine carbide precipitation.

Other than the etchant suggested by Olson and Azrin, the etchants in Table 3.11 were found not to reveal microstructures well across the range of the TRIP steel alloys (Olson & Azrin, 1978). Based on the above etchants and on a general review of literature relating to the etching of stainless steels, some other etchant formulations were attempted.

**Table 3.11: Etchants used by previous authors on stainless type TRIP steels.**

Author	Etchant
Otte (Otte, 1957)	45% HCl; 5% HNO <sub>3</sub> ; 50% Methanol
Olson and Azrin (Olson & Azrin, 1978)	0.5 g sodium metabisulphite; 33ml HCl; 167 ml H <sub>2</sub> O
Suggestion by lab technician at TUC	100 ml H <sub>2</sub> O; 100 ml HCl; 10 ml H <sub>2</sub> SO <sub>4</sub> ; pickling inhibitor* 0.3 ml; bring to 50°C, use at room temperature.
Kalling (ASM) (Vander Voort, 2004)	Kalling's no. 1 or Kalling's no. 2 (CuCl <sub>2</sub> , HCl, Ethanol)
Klemm II (ASM) (Vander Voort, 2004)	Pre-etch the sample with a 5% Nital in HPLC (high performance liquid chromatography) methanol mixture. 25 g sodium thiosulphate and 5 g potassium metabisulphite in 50 ml of distilled water.
Beraha's reagent (ASM) (For TRIP: Dimatteo, et al.)	20 ml HCl, 0.5 – 1g Potassium metabisulphite, 100ml water Immerse & agitate (Dimatteo et al., 2006)
De, similar to LePera's reagent (De et al., 2003)	1 <sup>st</sup> 4% Picral, 2 <sup>nd</sup> (carefully) 2% aq. sodium metabisulphite

Specifically, the TUC etchant in Table 3.11 was modified to include 5% HNO<sub>3</sub>. This etchant was used as-is, as well as followed by a solution of 1g sodium metabisulphite per 100ml water. An electro-etch suggested for multi-phase stainless steels in the ASM Handbook (Vander Voort, 2004), with electrolyte consisting of 60% HNO<sub>3</sub> and water (Table 3.12), was also attempted.

Some optical images comparing the effects of various etchants are shown in Figure 3.25 to Figure 3.28. Etchants 1 and 2 as listed in Table 3.12 were found to incompletely etch the martensite phase (Figure 3.25 and Figure 3.26). Electro-etching as specified in etchant 3 in Table 3.12 clearly revealed the martensitic phase (Figure 3.28), but the result was not as finely resolved as with the etch suggested by Olson and Azrin (Figure 3.27) (Olson & Azrin, 1978).

**Table 3.12: Further chemical and electrolytic etchants tested.**

	Etchant
<b>1.</b>	100ml H <sub>2</sub> O; 100ml HCl; 10ml HNO <sub>3</sub> ; 10ml H <sub>2</sub> SO <sub>4</sub> ; pickling inhibitor 0.3ml; bring to 50°C, use at room temperature (Struers) (Geels, 2007).
<b>2.</b>	As in 1, then 1g sodium metabisulphite in H <sub>2</sub> O (Struers) (Geels, 2007).
<b>3.</b>	Electrolytic etch: 60% HNO <sub>3</sub> ; 40% water (ASM Handbook) (Vander Voort, 2004)

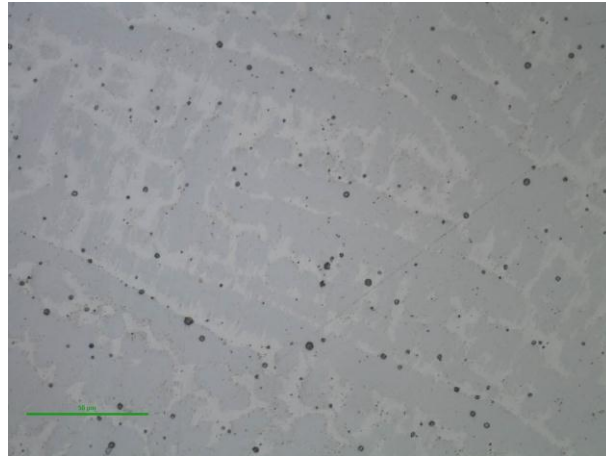


**Figure 3.25:** Cross-section of Specimen C2, deformed 28%, etched in etchant Table 3.12, number 1. Dark martensite phase is not appropriately revealed in optical image. Scale bar represents 50μm.

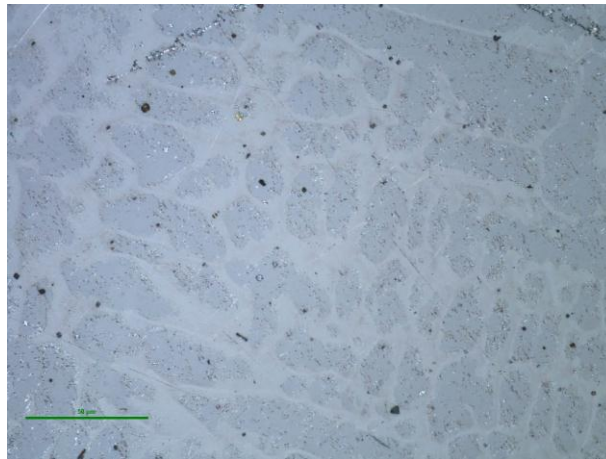


**Figure 3.26:** Cross-section of Specimen C2, deformed 28%, etched in etchant Table 3.12, number 2. Dark martensite phase is not properly revealed in optical image. Scale bar represents 50μm.



**Figure 3.27:** Cross-section of Specimen C2, deformed 28%, etched in the etchant suggested by Olson and Azrin (Table 3.11). Dark martensite phase is clearly revealed in optical image, with fine surface relief visible. Scale bar represents 50μm.



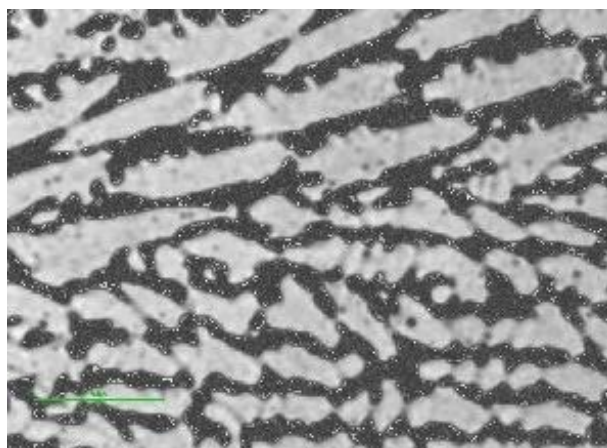


**Figure 3.28: Cross-section of Specimen C2, deformed 28%, electro-etched in etchant Table 3.12, number 3. Dark martensite phase is clearly revealed in optical image, but does not appear as finely resolved as in Figure 3.27. Scale bar represents 50 $\mu$ m.**

A Gatan Model 683 Met-Etch ion beam etcher was also used to etch some specimens for comparison. The results from this process were similar to those with the etchant suggested by Olson and Azrin, but the process was considerably slower and more difficult to control from specimen to specimen, and fine martensite surface relief was not as well revealed (Olson & Azrin, 1978).

### 3.4.6.3 Microstructures

The optical micrographs were obtained using a Nikon MA200 inverted metallurgical microscope. SEM microscopy was performed using a Zeiss Ultra FEG-SEM. Optical and SEM micrographs of the cast alloys were taken in a pre-deformation state and deformed 28% in compression. The micrographs are shown in Figure 3.29 to Figure 3.92. Specimens were cross-sectioned unless otherwise specified. All specimens were prepared as described in Section 3.4.6.1 and etched using the etchant suggested by Olson and Azrin (Table 3.11), as tested and discussed in Section 3.4.6.2. Austenite appeared light (white or off-white) while martensite plates and laths appeared dark.

The extent of the change in transformation, measured inductively, is listed in the caption for each specimen for comparative purposes, and also listed in Table 3.9. Before deformation, most specimens showed an inductance between 92.5 mH and 94 mH (Table 3.9). Specimen B2 showed the highest pre-deformation inductance of 99.5 mH. Peak increases in inductance after deformation varied considerably from alloy to alloy, from no increase for Alloy A1c, up to 40 mH for Alloy C3.

Since coil inductance in air was 92.1 mH, this implies that minimal levels of ferrite and martensite were present before deformation. This is contrary to most of the micrographs of the pre-deformation samples, where dark areas likely being martensite, were typically seen. These dark areas may signify the presence of thermally-induced deformation structures,  $\epsilon$  martensite or  $\alpha'$  martensite (described in Section 2.8.1). However, particularly in specimens showing low pre-deformation inductance such as A3a, A3b, B3, B4 and C2, the dark areas may also signify that deformation-induced martensite was formed on the surface during preparation. All specimens were sectioned on a low-speed cut-off saw under only their own mass, and as illustrated in Figure 3.23, electro-polishing did not substantially reduce this phenomenon.

It is likely that the cast alloys, particularly those that show strong transformation, may be highly sensitive to deformation during sectioning and grinding, compared to hot or warm formed alloys, because their yield strength and associated stress at first transformation was lower. This may result in deeper sub-surface deformation artefacts during sectioning and grinding which was not readily removed by electro-polishing. However, distinct differences in microstructure were apparent between alloys before and after compressive deformation. These differences were observed to be closely associated to the extent of transformation measured by the inductive change. A comparison between these microstructures is therefore relevant. Also of interest is the distinct difference in morphology in the martensite produced in the different alloys.

Alloy DIN 1.4301 underwent a small inductive change, 6 mH. Pre-deformation inductance was marginally higher than in air, at 95 mH (Table 3.6), and this may relate to apparent dispersed ferrite in the pre-deformation microstructure. This is confirmed by the Schaeffler diagram because, with nickel and chromium equivalents of 11 and 21 respectively (Table 3.9), it predicts approximately 15% ferrite. The microstructures of this material are shown in an undeformed and deformed state at various magnifications in Figure 3.29 to Figure 3.32. Figure 3.38 shows the formation of dark martensite in the deformed microstructure of Figure 3.29 (b) as compared to Figure 3.29 (a). A very small amount of isolated  $\alpha'$  lath martensite, with signs of twinning, was revealed in the pre-deformation microstructure (Figure 3.30 (a) and Figure 3.32 (a)). In Figure 3.32 (b) the post-deformation microstructure appeared to show isolated  $\alpha'$  martensite possibly originating largely in prior  $\epsilon$  martensite platelets. The microstructure in Figure 3.32 was reminiscent of that in Figure 2.62 and Figure 2.64 by Olson and Azrin (Olson & Azrin, 1978).

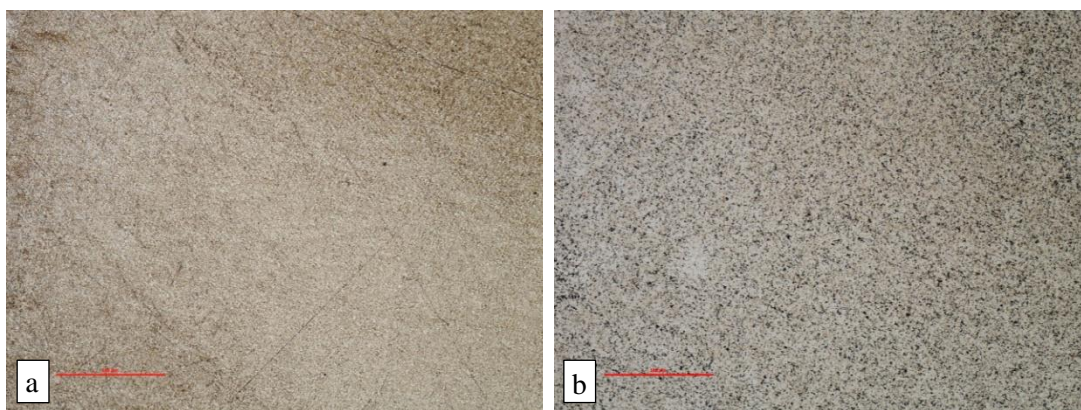


**Figure 3.29: Alloy 1.4301, (a) pre-deformation, (b) deformed 28% in compression; inductive change 6 mH. Optical microscopy image; scale bar represents 500 $\mu$ m. Dark martensite in light austenite matrix.**

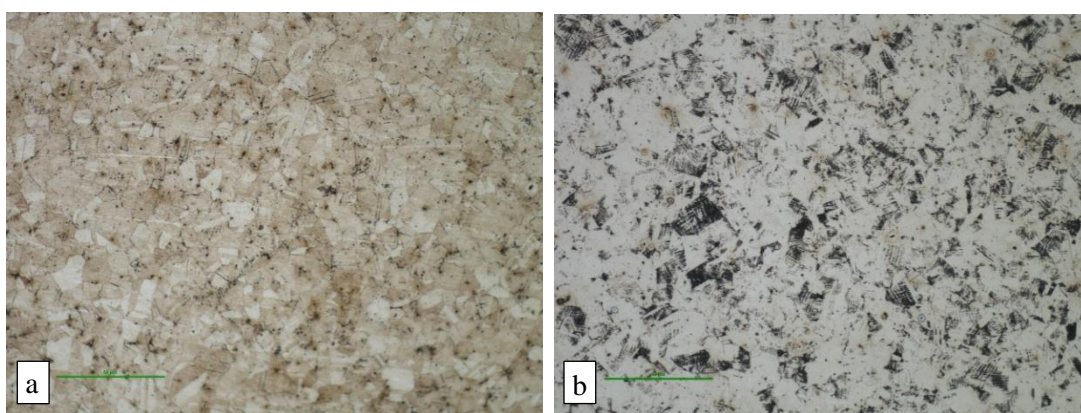


**Figure 3.30: Alloy 1.4301, (a) pre-deformation, (b) deformed 28% in compression; inductive change 6 mH. Optical microscopy image; scale bar represents 50 $\mu$ m. Dark martensite in light austenite matrix.**

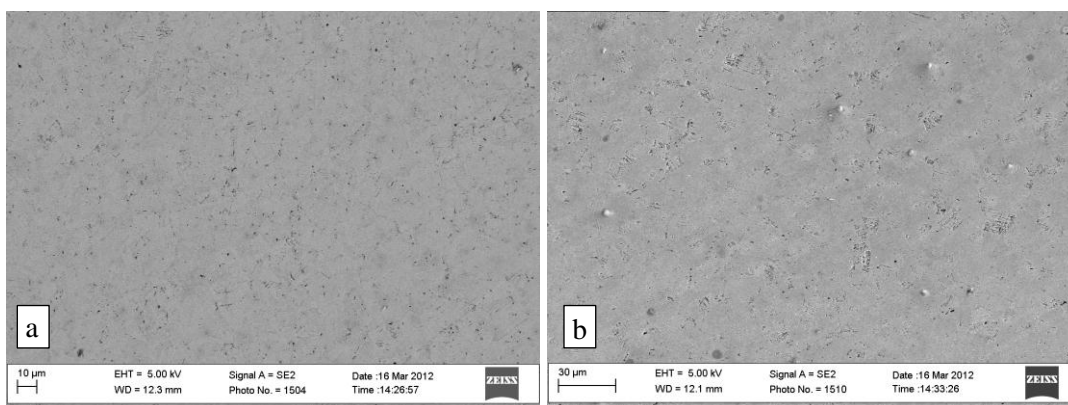


**Figure 3.31: Alloy 1.4301, (a) pre-deformation, (b) deformed 28% in compression; inductive change 6 mH. SEM-SE image. Darker martensite in light austenite matrix.**



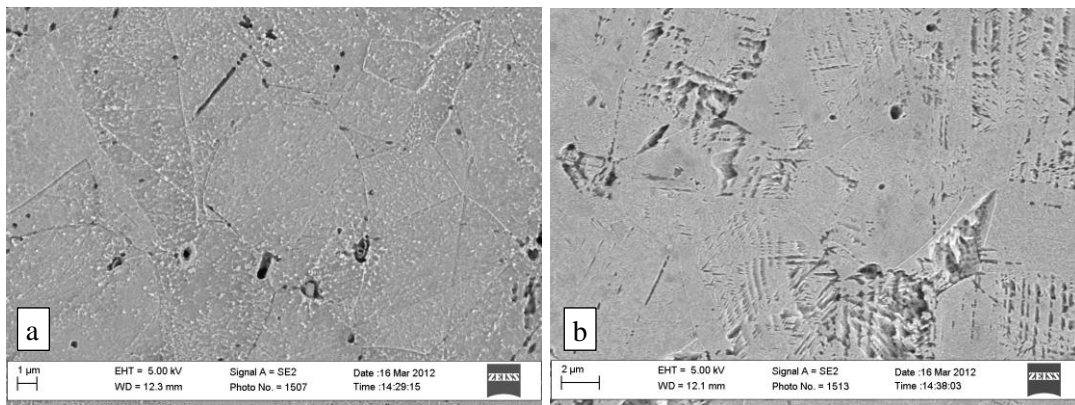


**Figure 3.32: Alloy 1.4301, (a) pre-deformation, (b) deformed 28% in compression; inductive change 6 mH. SEM-SE image. Darker, etched martensite in light austenite matrix.**

Alloy A1c underwent almost no inductive change (0.2 mH). The microstructures of this material are shown in an undeformed and deformed state at various magnifications in Figure 3.33 to Figure 3.36. No martensite or faulting was revealed in the pre-deformation microstructure (part (a) of Figure 3.33 to Figure 3.36), whereas the post-deformation microstructure showed extensive slip and deformation most clearly observed in the optical micrographs in Figure 3.33 (b) and Figure 3.34 (b). Figure 3.35 (b) and Figure 3.36 (b) showed traces of martensite formation, primarily with an  $\epsilon$  martensite morphology; they also revealed that most of the dark etched areas in the optical micrographs are likely due to deformation structures rather than martensite (Figure 3.35 (b)).

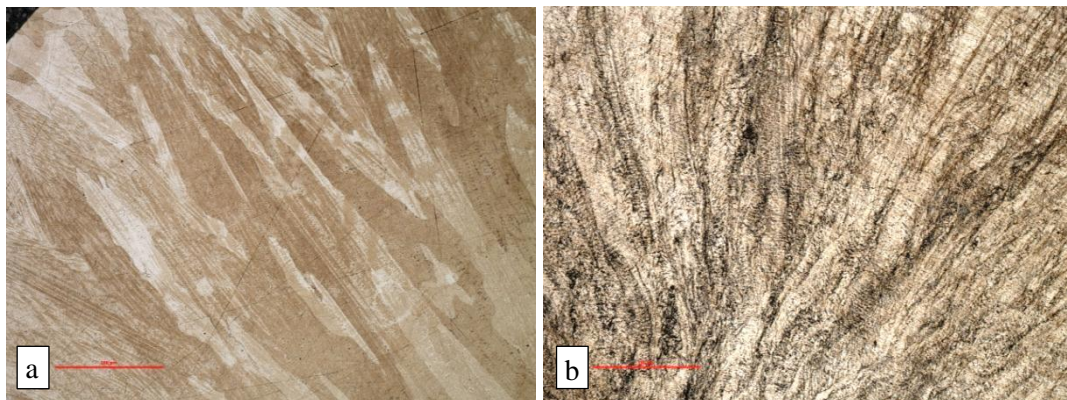


**Figure 3.33: Alloy A1c, (a) pre-deformation, (b) deformed 28% in compression; inductive change 0 mH. Optical microscopy image; scale bar represents 500μm. Dark martensite in light austenite matrix.**



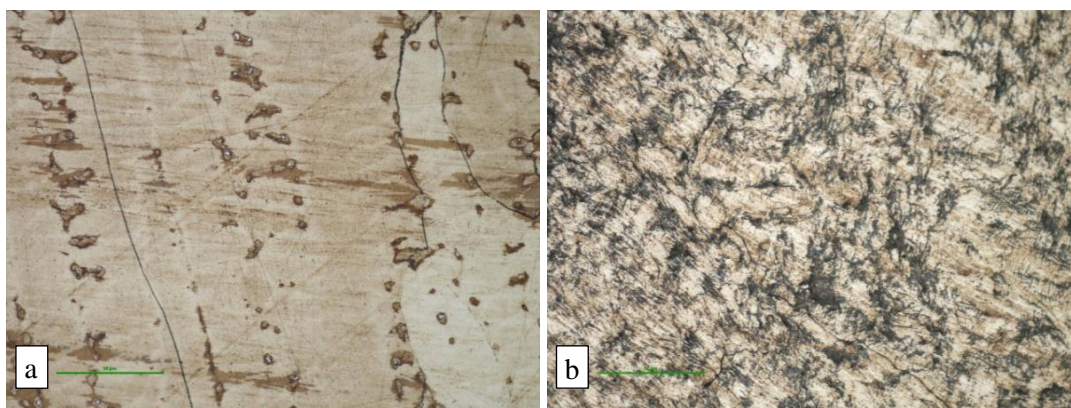


**Figure 3.34: Alloy A1c, (a) pre-deformation, (b) deformed 28% in compression; inductive change 0 mH. Optical microscopy image; scale bar represents 50μm. Dark martensite in light austenite matrix.**

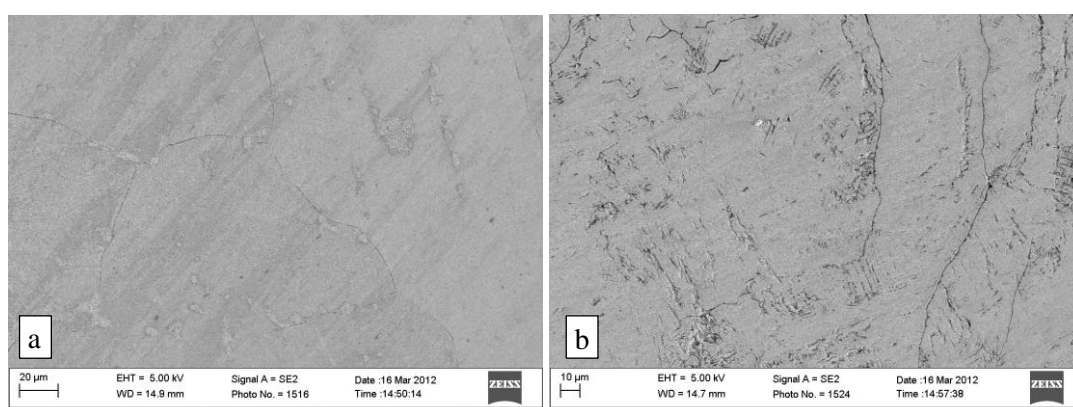


**Figure 3.35: Alloy A1c, (a) pre-deformation, (b) deformed 28% in compression; inductive change 0 mH. SEM-SE image. Dark martensite in light austenite.**

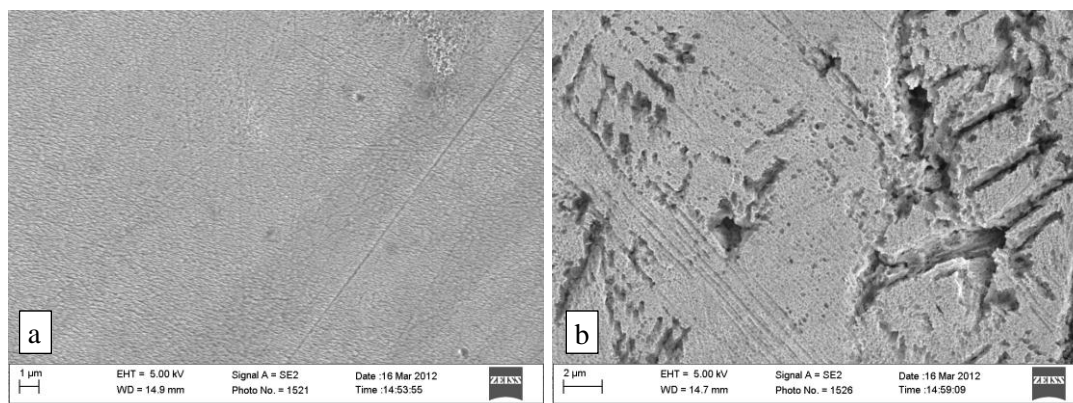


**Figure 3.36: Alloy A1c, (a) pre-deformation, (b) deformed 28% in compression; inductive change 0 mH. SEM-SE image. Dark, coarse martensite in smoother, lighter austenite matrix.**

Alloy A3a underwent a large inductive change, 25 mH. The microstructures of this material are shown in an undeformed and deformed state at various magnifications in Figure 3.37 to Figure 3.40. Considerable martensite was revealed at all of these magnifications in the pre-deformation microstructure (Figure 3.37 (a) to Figure 3.40 (a)). The post-deformation microstructure was similar, particularly at low magnification (Figure 3.37 (b)). However, at higher magnifications it was clear that the martensite was present in greater proportion in the deformed sample, which



was also revealed in the low-magnification image upon closer inspection (Figure 3.37 (b) to Figure 3.40 (b)). It is likely that much of the martensite in the pre-deformation sample was produced during sample preparation. This was verified by the low pre-deformation inductance of 92.6 mH (Table 3.9). Signs of slip associated to the directionality of the martensitic growth may be present in the post-deformation microstructure (centre-right, Figure 3.38 (b)).

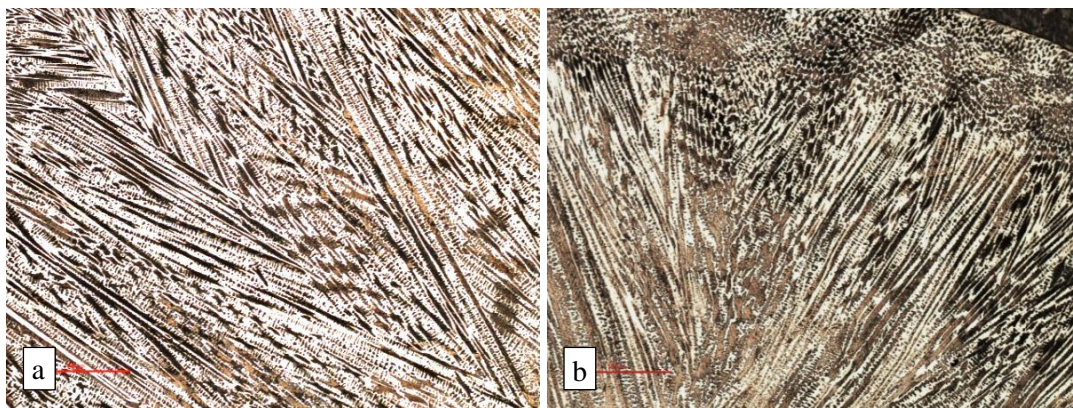


**Figure 3.37: Alloy A3a, (a) pre-deformation, (b) deformed 28% in compression; inductive change 25 mH. Optical microscopy image; scale bar represents 500μm. Dark martensite in light austenite matrix.**

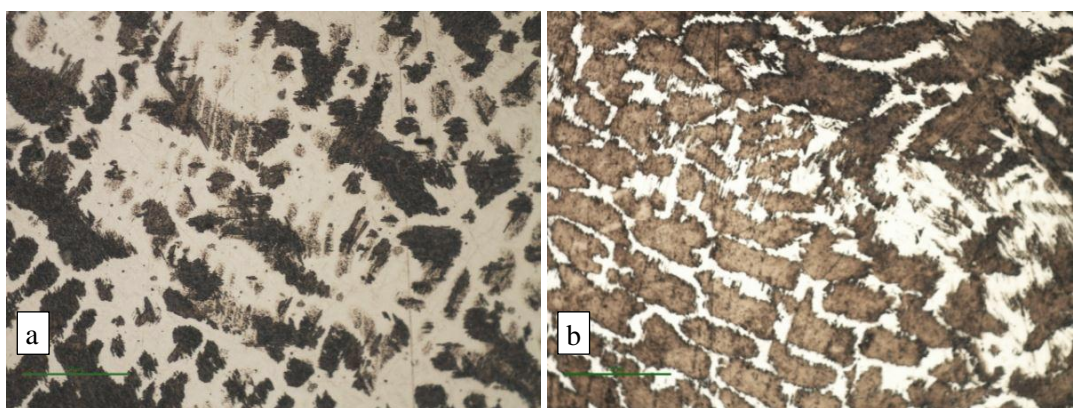


**Figure 3.38: Alloy A3a, (a) pre-deformation, (b) deformed 28% in compression; inductive change 25 mH. Optical microscopy image; scale bar represents 50μm. Dark martensite in light austenite matrix.**

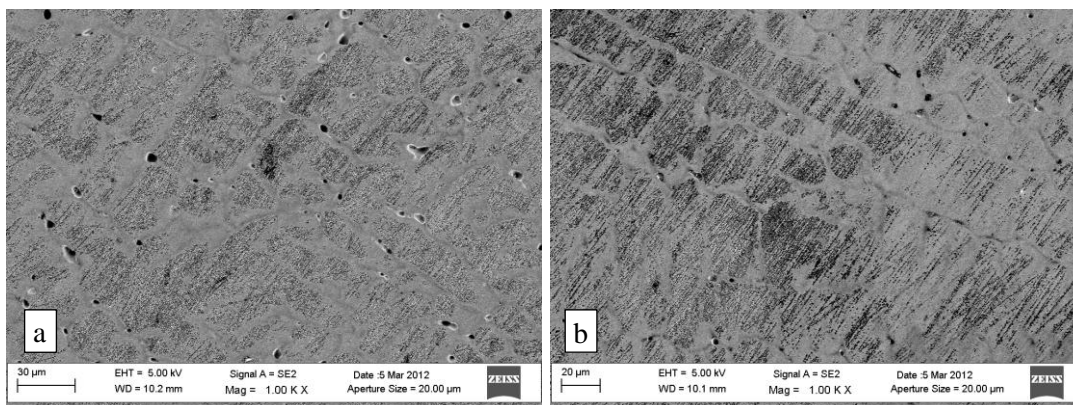


**Figure 3.39: Alloy A3a, (a) pre-deformation, (b) deformed 28% in compression; inductive change 25 mH. SEM-SE image. Dark martensite in light austenite matrix.**



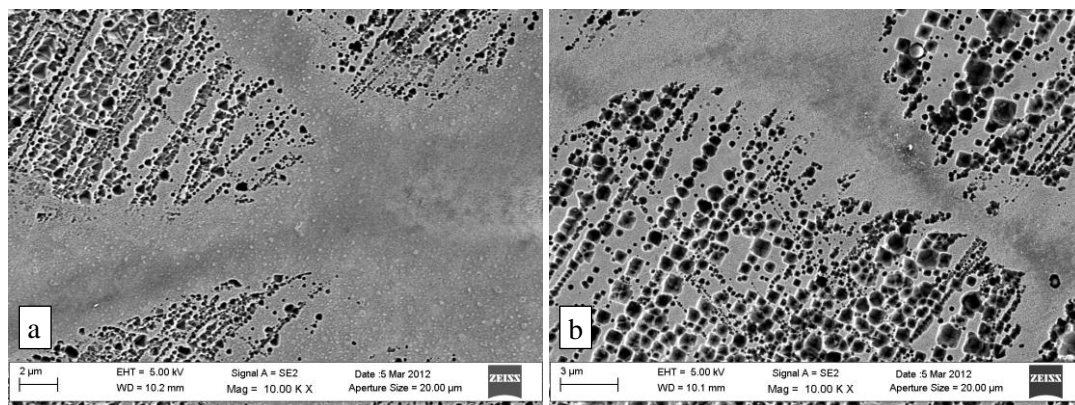


**Figure 3.40: Alloy A3a, (a) pre-deformation, (b) deformed 28% in compression; inductive change 25 mH. SEM-SE image. Dark martensite in light austenite matrix.**

Alloy A3b underwent a medium inductive change, 33 mH. The microstructures of this material are shown in an undeformed and deformed state at various magnifications as specified in Figure 3.41 to Figure 3.44. It revealed considerable  $\alpha'$  lath martensite in the pre-deformation microstructure, seen particularly clearly in Figure 3.42 (a). The post-deformation microstructure was similar but showed more dark  $\alpha'$  lath martensite (Figure 3.41 (b)), with higher magnification images also revealing different surface morphology (Figure 3.43 and Figure 3.44), possibly related to the higher proportion of martensite. It is likely that much of the martensite in the pre-deformation sample was produced during sample preparation. This was verified by the low pre-deformation inductance of 93 mH (Table 3.9).

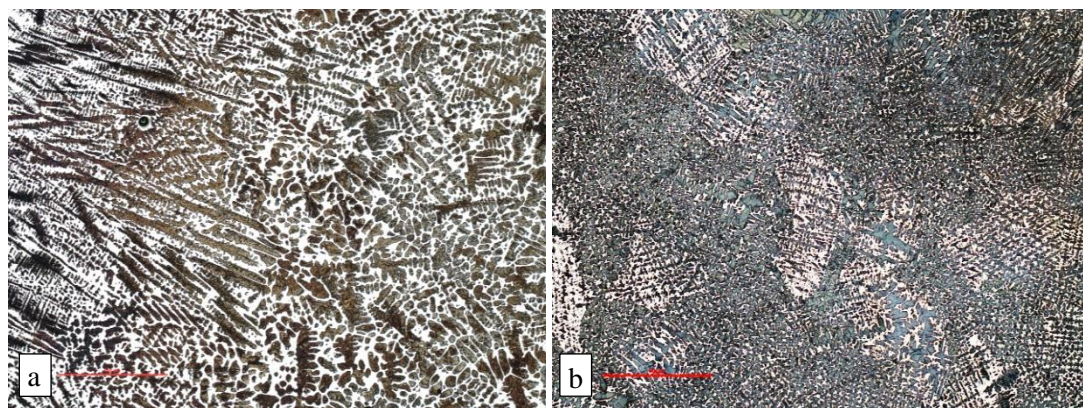


**Figure 3.41: Alloy A3b, (a) pre-deformation, (b) deformed 28% in compression; inductive change 33 mH. Optical microscopy image; scale bar represents 500μm. Dark martensite, light austenite.**



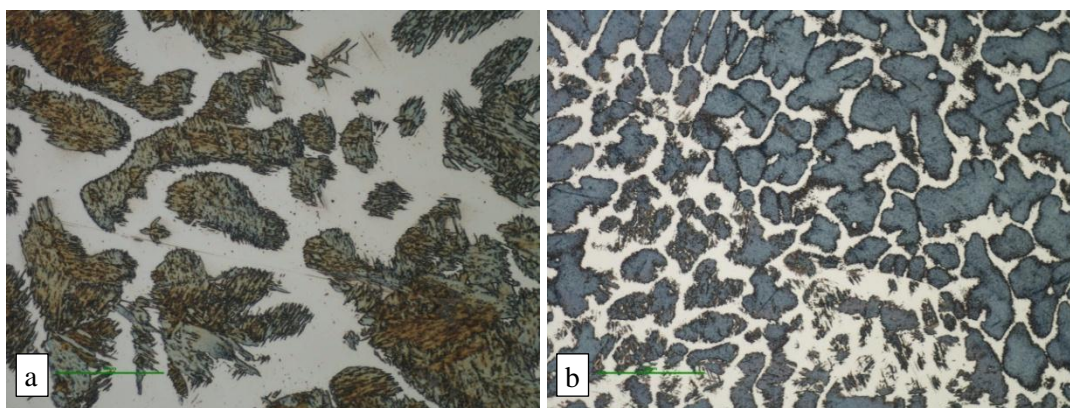


**Figure 3.42: Alloy A3b, (a) pre-deformation, (b) deformed 28% in compression; inductive change 33 mH. Optical microscopy image; scale bar represents 50μm. Dark martensite in light austenite matrix.**

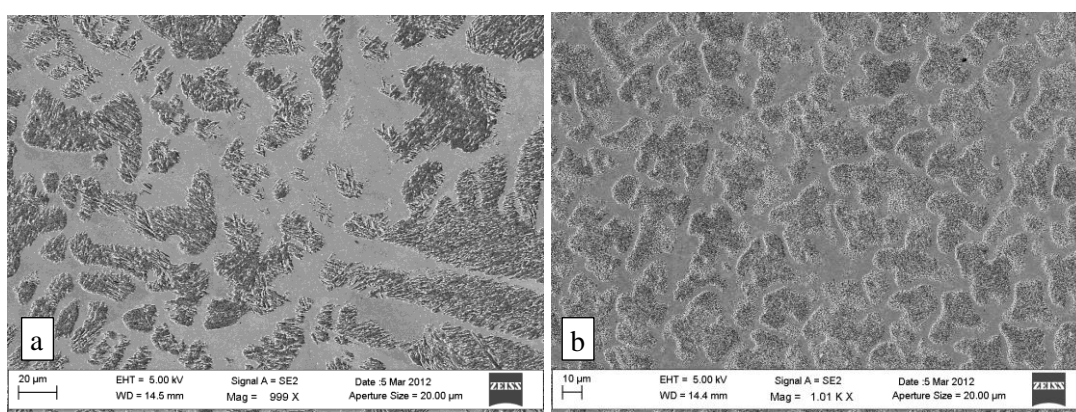


**Figure 3.43: Alloy A3b, (a) pre-deformation, (b) deformed 28% in compression; inductive change 33 mH. SEM-SE image. Coarse, darker martensite in light austenite matrix.**

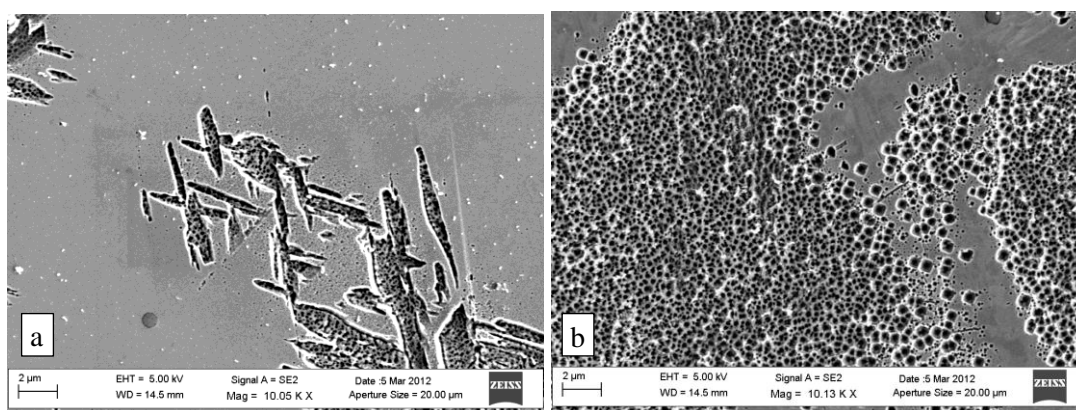


**Figure 3.44: Alloy A3b, (a) pre-deformation, (b) deformed 28% in compression; inductive change 33 mH. SEM-SE image. Dark  $\alpha'$  martensite, showing a somewhat plate-like morphology in the undeformed structure, in a light austenite matrix.**

Figure 3.45 and Figure 3.46 show SEM images for Alloy A3d. This alloy underwent an inductive change of 19 mH. These images revealed a similar microstructure and evolution with deformation to Alloy A3b, with a similar martensite morphology (Figure 3.43 compared to Figure 3.45), but a slightly smaller change in martensite proportion.

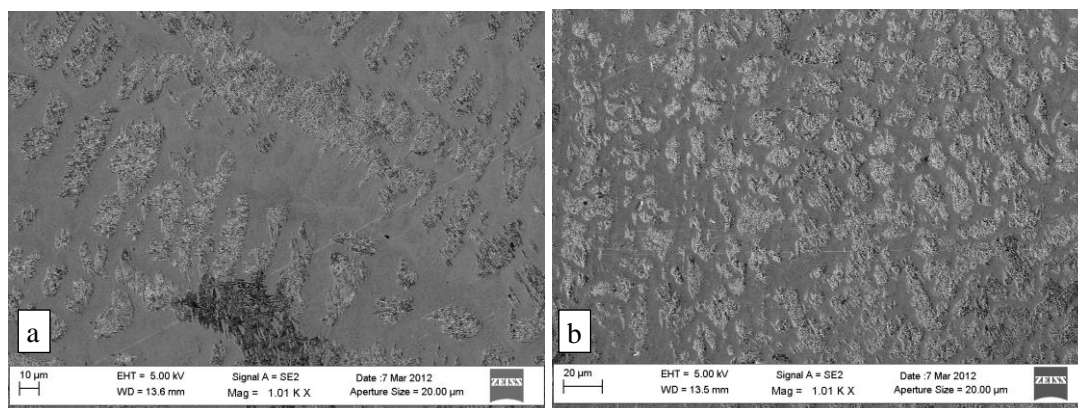


**Figure 3.45: Alloy A3d, (a) pre-deformation, (b) deformed 28% in compression; inductive change 19 mH. SEM-SE image. Light coarse martensite in darker austenite matrix.**

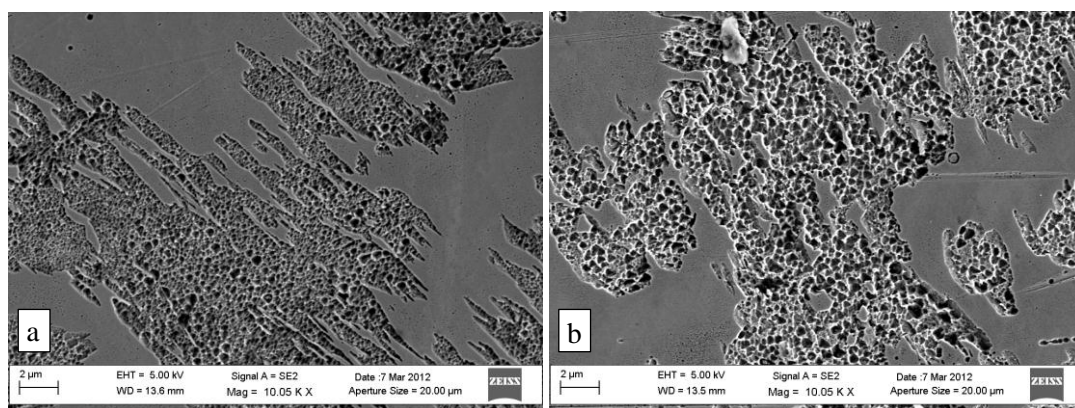


**Figure 3.46: Alloy A3d, (a) pre-deformation, (b) deformed 28% in compression; inductive change 19 mH. SEM-SE image. Etched, dark martensite in smooth, lighter austenite matrix.**

Alloy A3e underwent a small inductive change of 3 mH. The microstructures of this material are shown in an undeformed and deformed state at various magnifications in Figure 3.47 to Figure 3.51. It had isolated regions of dense  $\alpha'$  martensite (Figure 3.47 (a) and Figure 3.48 (a)), and distinct  $\epsilon$  martensite plates in the pre-deformation microstructure (Figure 3.49 (a)). The post-deformation microstructure showed a distinctly greater degree of dark martensite at low magnification (Figure 3.47 (b)). Micrographs at 100x magnification are included (Figure 3.48) because they revealed that a large portion of the dark phase may represent  $\epsilon$  martensite platelets, not  $\alpha'$  martensite, although  $\alpha'$  martensite was also present after deformation (Figure 3.50 (b) and Figure 3.51 (b)). This may explain the relatively small inductive change observed during compressive deformation.



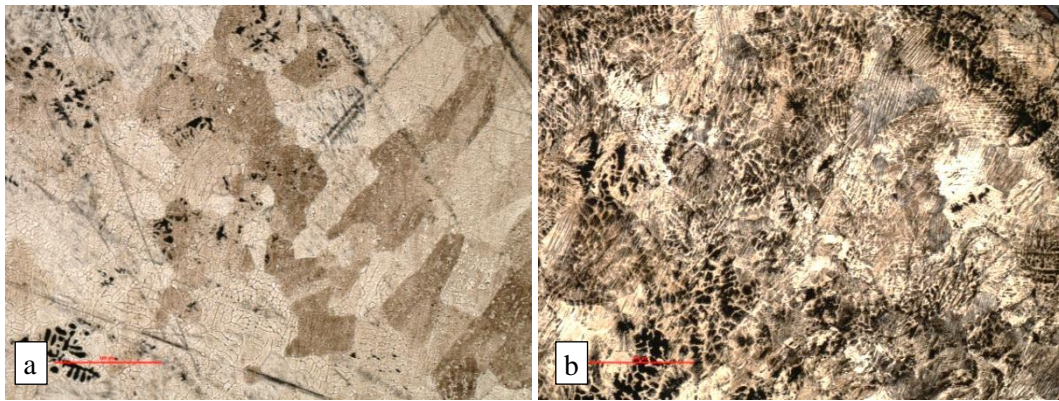


**Figure 3.47: Alloy A3e, (a) pre-deformation, (b) deformed 28% in compression; inductive change 3 mH. Optical microscopy image; scale bar represents 500 $\mu$ m. Dark martensite in light austenite matrix.**

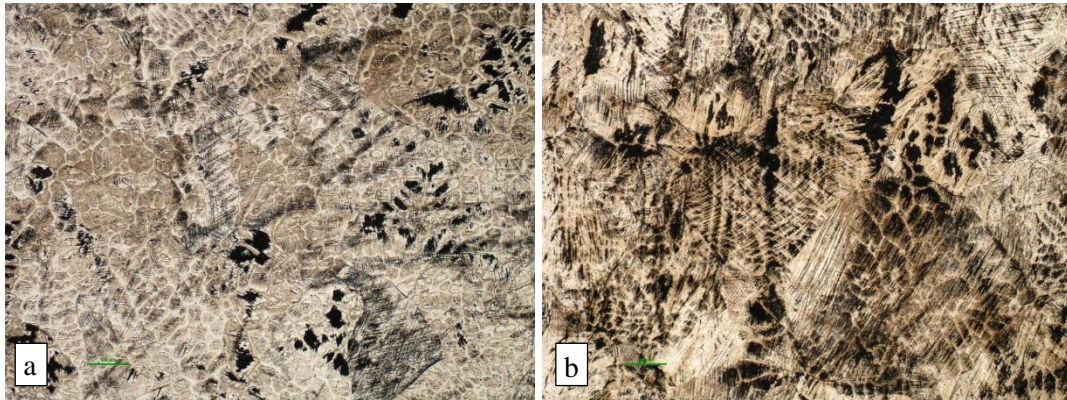


**Figure 3.48: Alloy A3e, (a) pre-deformation, (b) deformed 28% in compression; inductive change 3 mH. Optical microscopy image; scale bar represents 100 $\mu$ m. Dark martensite in light austenite matrix.**

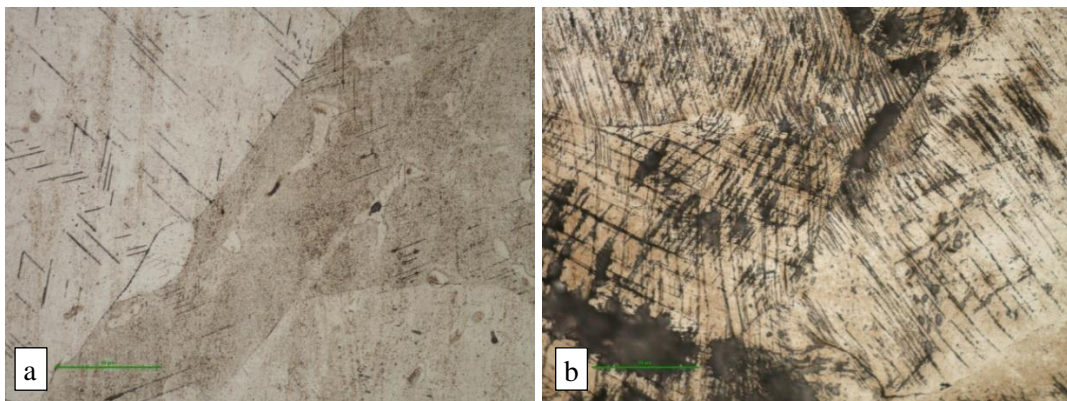


**Figure 3.49: Alloy A3e, (a) pre-deformation, (b) deformed 28% in compression; inductive change 3 mH. Optical microscopy image; scale bar represents 50 $\mu$ m. Dark plate martensite in light austenite matrix.**

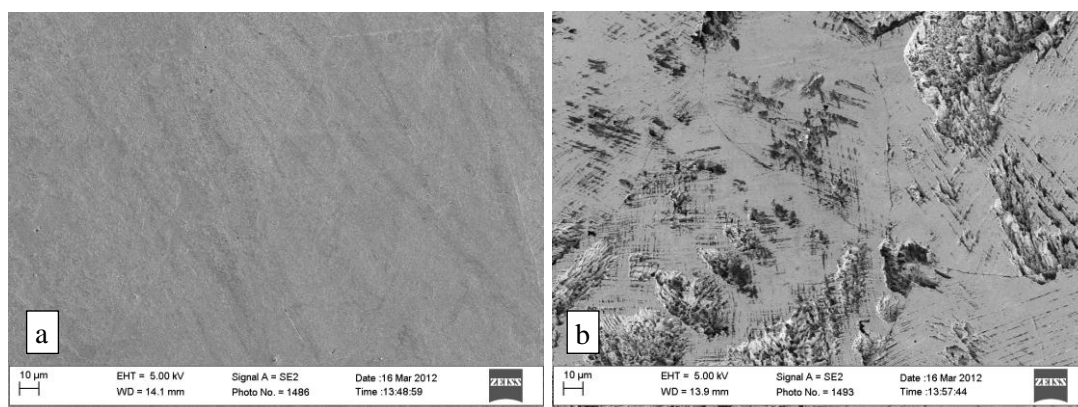


**Figure 3.50: Alloy A3e, (a) pre-deformation, (b) deformed 28% in compression; inductive change 3 mH. SEM-SE image. Dark martensite in light austenite matrix.**

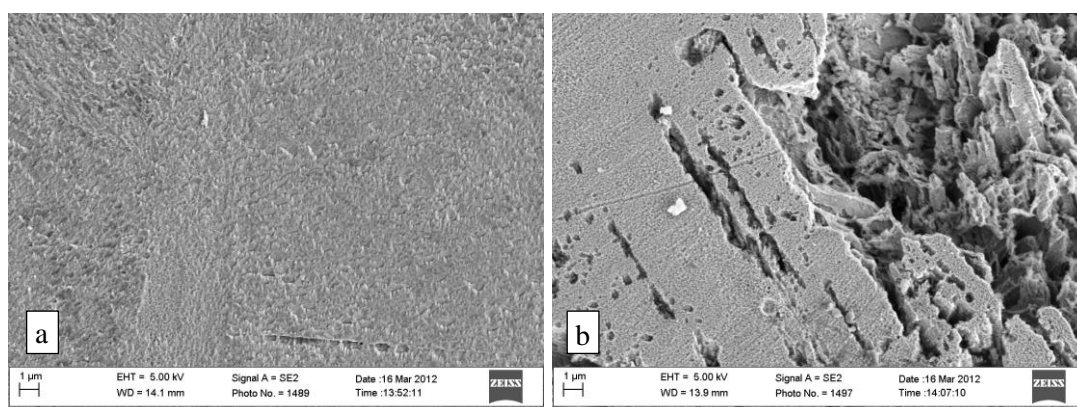


**Figure 3.51: Alloy A3e, (a) pre-deformation, (b) deformed 28% in compression; inductive change 3 mH. SEM-SE image. Coarse martensite in smoother, lighter austenite matrix.**

Alloy A4 underwent a very large inductive change, 35 mH. The microstructures of this material are shown in undeformed and deformed states at various magnifications in Figure 3.52 to Figure 3.57. It revealed dark regions of martensite (and possibly ferrite) in a dendritic pattern in its austenitic pre-deformation microstructure (Figure 3.52 (a)). The occurrence of martensitic dendrites (which were formerly austenite) may not be due to preparation but rather be related to slight inhomogeneity of the microstructure upon solidification, with regions of reduced alloying elements in solution. This is made more likely considering the alloy's very low nickel and chromium equivalents placing it well within the austenite-martensite region of the Schaeffler diagram (Table 3.6, Figure 2.26) and a slightly raised pre-deformation inductance of 95 mH (Table 3.9). In comparing Figure 3.52 (b) to Figure 3.53, there is a clear orientation effect, as expected, regarding the dendrites and the sectioning direction.

The microstructure showed extensive increase in  $\alpha'$  martensite from before to after deformation (Figure 3.52, Figure 3.57). Figure 3.57 shows lath and plate martensite, with the proportion of plate martensite in particular increasing after deformation. The hatched plate martensite



structure revealed in Figure 3.57 (b) may be linked to prior  $\epsilon$  martensite, particularly since this is a high manganese alloy (Table 3.5).

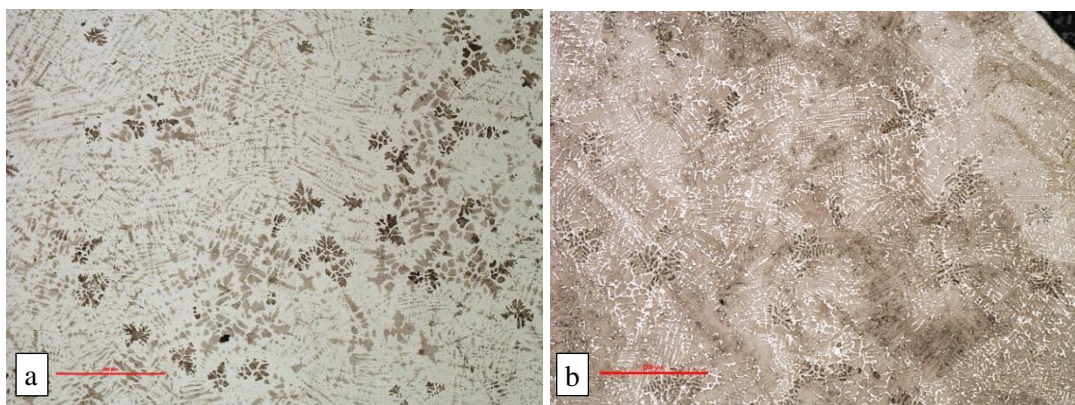


**Figure 3.52: Alloy A4 sectioned longitudinally, (a) pre-deformation, (b) deformed 28% in compression; inductive change 35 mH. Optical microscopy image; scale bar represents 500μm. Darker martensite in light austenite matrix.**

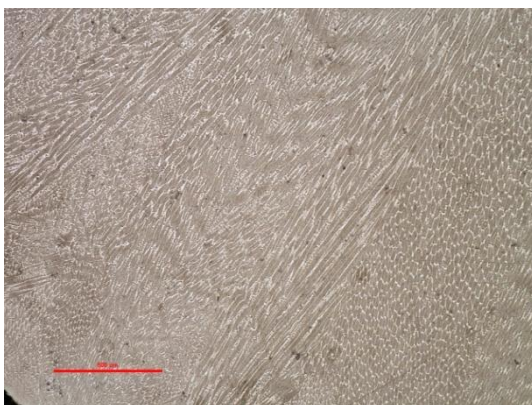


**Figure 3.53: Alloy A4 deformed 28% in compression and cross-sectioned; inductive change 35 mH. Optical microscopy image; scale bar represents 500μm. Darker martensite in light austenite matrix.**

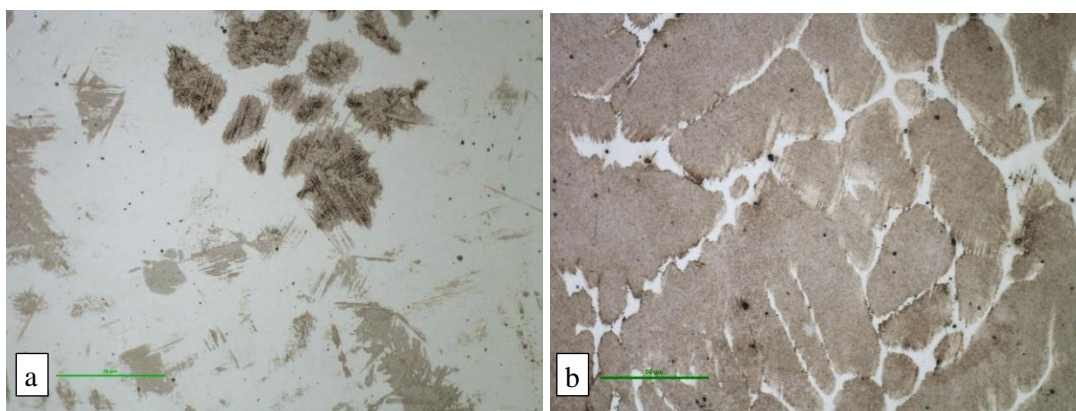


**Figure 3.54: Alloy A4, (a) pre-deformation, (b) deformed 28% in compression, sectioned longitudinally; inductive change 35 mH. Optical microscopy image; scale bar represents 50μm. Darker martensite in light austenite matrix.**



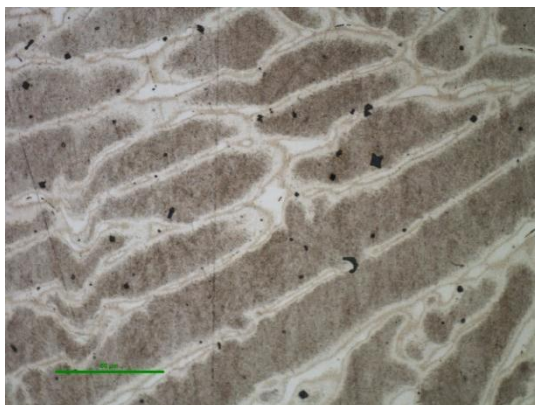


**Figure 3.55:** Alloy A4 deformed 28% in compression and cross-sectioned; inductive change 35 mH. Optical microscopy image; scale bar represents 50 $\mu$ m. Darker martensite in light austenite matrix.

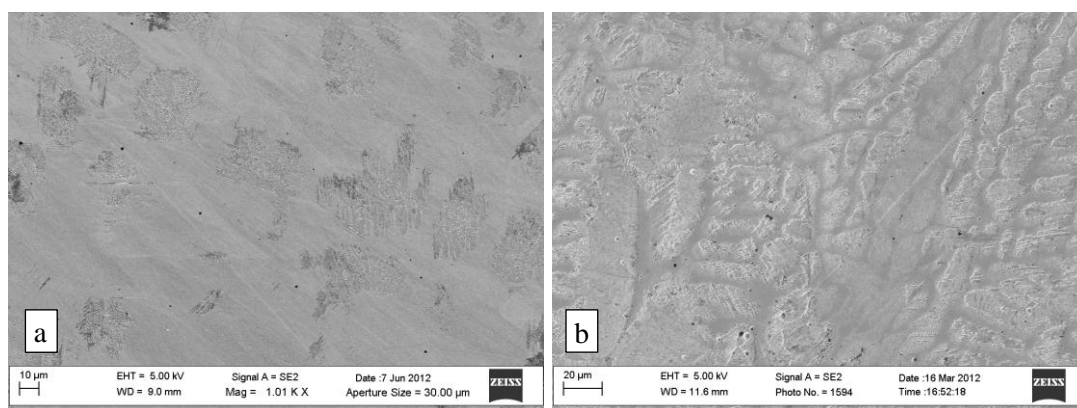


**Figure 3.56:** Alloy A4 sectioned longitudinally, (a) pre-deformation, (b) deformed 28% in compression; inductive change 35 mH. SEM-SE image. Light coarse martensite in darker, smooth austenite matrix.

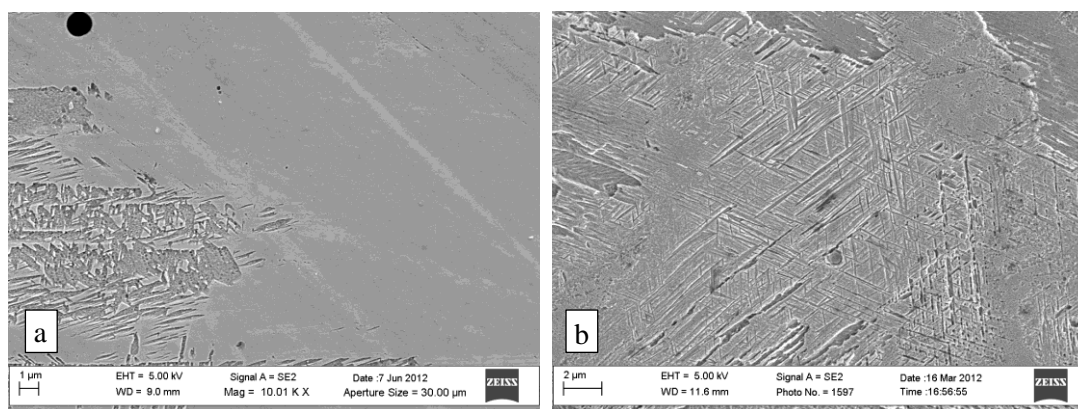


**Figure 3.57:** Alloy A4, longitudinal, (a) pre-deformation, (b) deformed 28% in compression; inductive change 35 mH. SEM-SE image. Darker lath and plate martensite in light, smooth austenite matrix.

Alloy B2 underwent a very large inductive change of 33 mH. The microstructures of Alloy B2 are shown in an undeformed and deformed state at various magnifications in Figure 3.58 to Figure 3.61. Extensive martensite plates were revealed in both the pre-deformation and post-deformation microstructures (Figure 3.58), but the proportion of martensite plates was

considerably higher post-deformation (Figure 3.58 and Figure 3.59). Many of these plates may represent  $\epsilon$  martensite that transformed (particularly post-deformation) into  $\alpha'$  martensite, as revealed at high magnification both optically (Figure 3.59) and on the SEM (Figure 3.61 (b)).

Pre-deformation martensite (Figure 3.58) was likely only partly due to preparation, because the alloy had extremely low nickel and chromium equivalents, placing it well within the austenite-martensite region on the Schaeffler diagram (Table 3.6), and the specimen showed a high pre-deformation inductance of 97.7 mH (Table 3.9). The microstructure showed an extensive increase in  $\alpha'$  plate martensite post-deformation (Figure 3.59 and Figure 3.60).

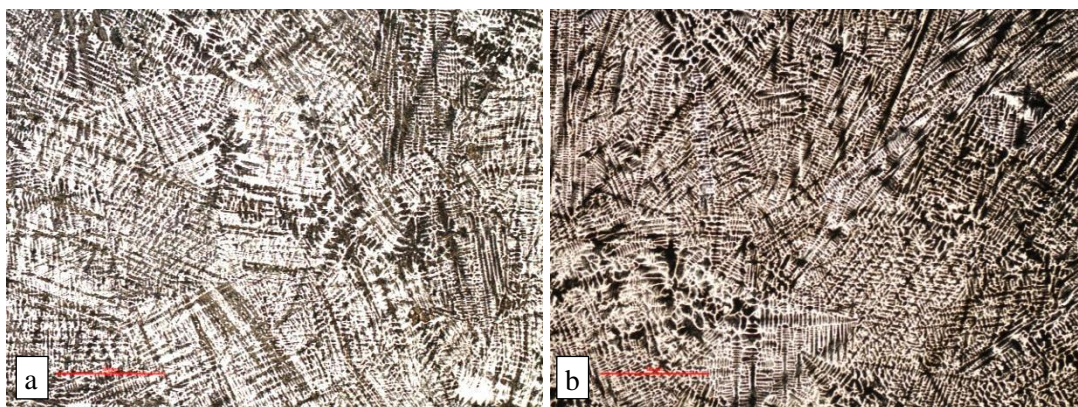


**Figure 3.58: Alloy B2, (a) pre-deformation, (b) deformed 28% in compression; inductive change 33 mH. Optical microscopy image; scale bar represents 500 $\mu$ m. Dark martensite in light austenite matrix.**

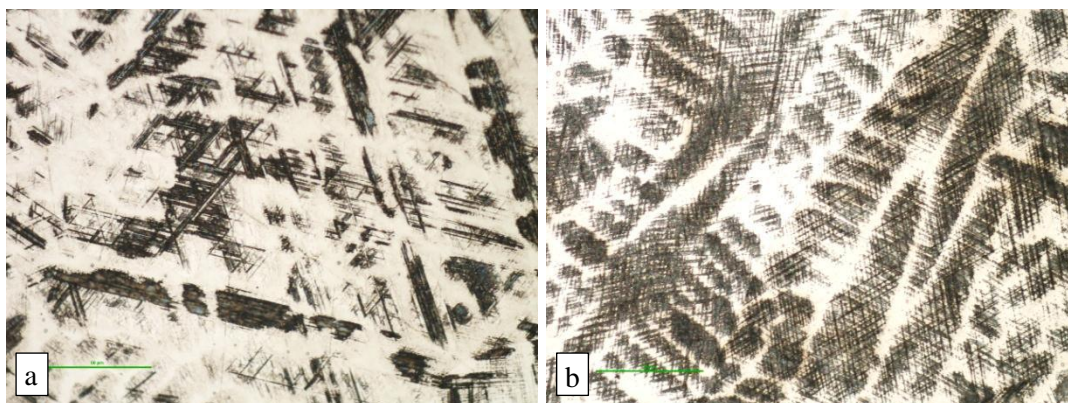


**Figure 3.59: Alloy B2, (a) pre-deformation, (b) deformed 28% in compression; inductive change 33 mH. Optical microscopy image; scale bar represents 50 $\mu$ m. Dark plate martensite in light austenite matrix.**



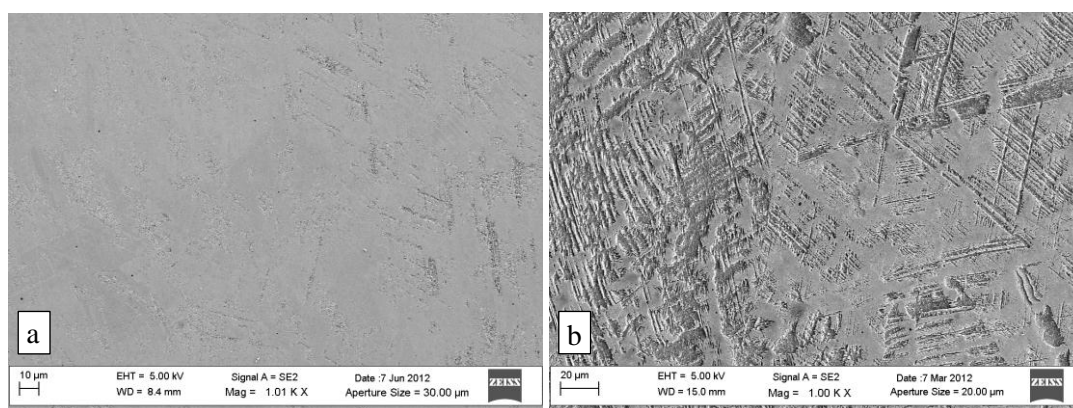


**Figure 3.60: Alloy B2, (a) pre-deformation, (b) deformed 28% in compression; inductive change 33 mH. SEM-SE image. Darker plate martensite in light austenite matrix.**

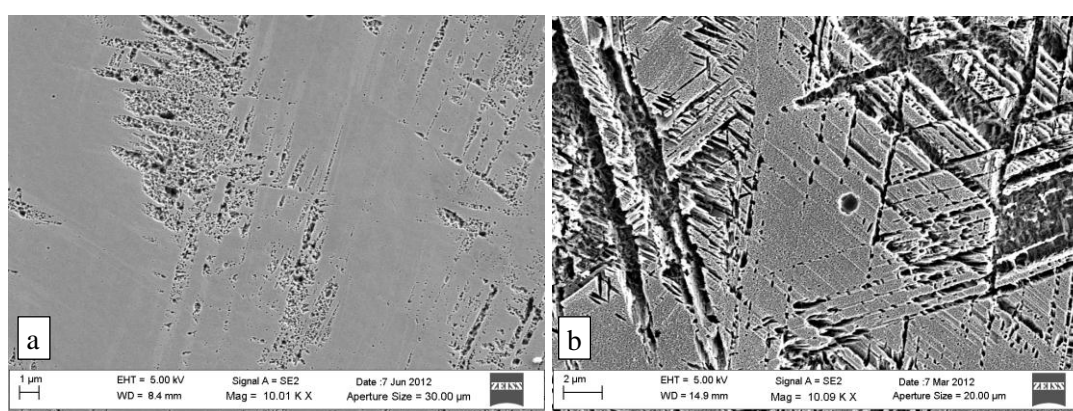


**Figure 3.61: Alloy B2, (a) pre-deformation, (b) deformed 28% in compression; inductive change 33 mH. SEM-SE image. Dark plate and lath martensite in light austenite matrix.**

Alloy B3 showed a similar microstructure both pre- and post-deformation (Figure 3.62 to Figure 3.65) to that of Alloy A3a (Figure 3.37 to Figure 3.40). It also underwent a similarly large inductive change of 31 mH. Alloy B3 had considerable  $\alpha'$  lath martensite in the pre-deformation microstructure, with no obvious  $\epsilon$  martensite morphology (Figure 3.63 (a) and Figure 3.65 (a)). The post-deformation microstructure was similar to the pre-deformation microstructure, particularly at low magnification (Figure 3.62 (b)). However, at higher magnification (Figure 3.63), it was clear that the martensite was considerably more densely distributed in the deformed sample. This was also revealed at lower-magnification (Figure 3.62) upon closer inspection.

There was some evidence of  $\epsilon$  martensite stimulating  $\alpha'$  martensite growth in the post-deformation microstructure (Figure 3.65 (b)). It is likely that much of the martensite in the pre-deformation sample was produced during sample preparation. This was verified by the low pre-deformation inductance of 93.1 mH (Table 3.9) as well as the alloy composition's position within the austenitic region of the Schaeffler diagram (Table 3.8).

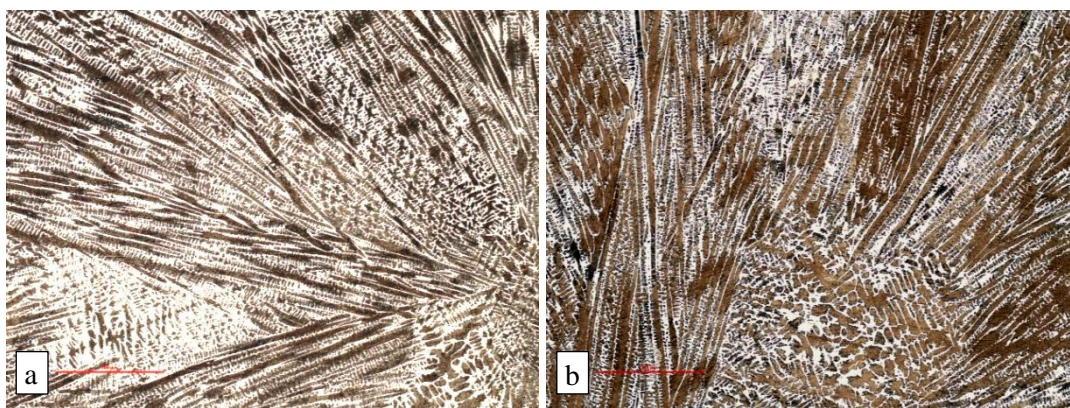


**Figure 3.62: Alloy B3, (a) pre-deformation, (b) deformed 28% in compression; inductive change 31 mH. Optical microscopy image; scale bar represents 500 $\mu$ m. Dark martensite in light austenite matrix.**

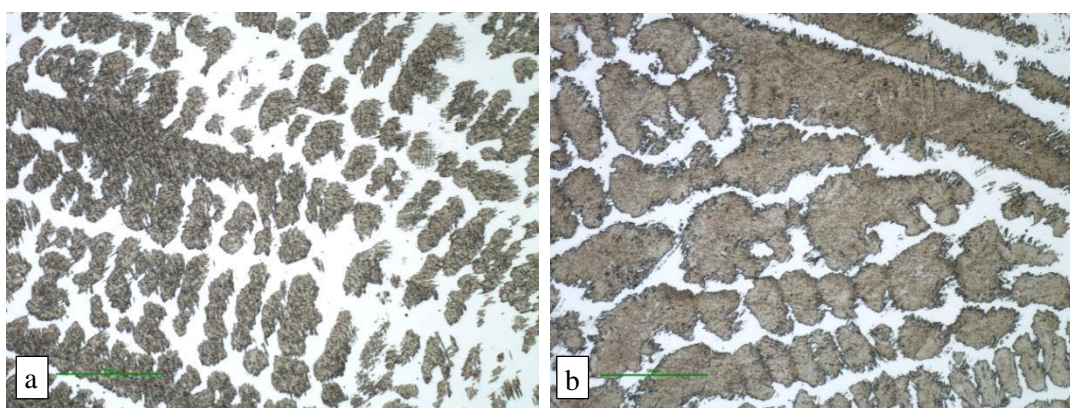


**Figure 3.63: Alloy B3, (a) pre-deformation, (b) deformed 28% in compression; inductive change 31 mH. Optical microscopy image; scale bar represents 50 $\mu$ m. Dark martensite in light austenite matrix.**

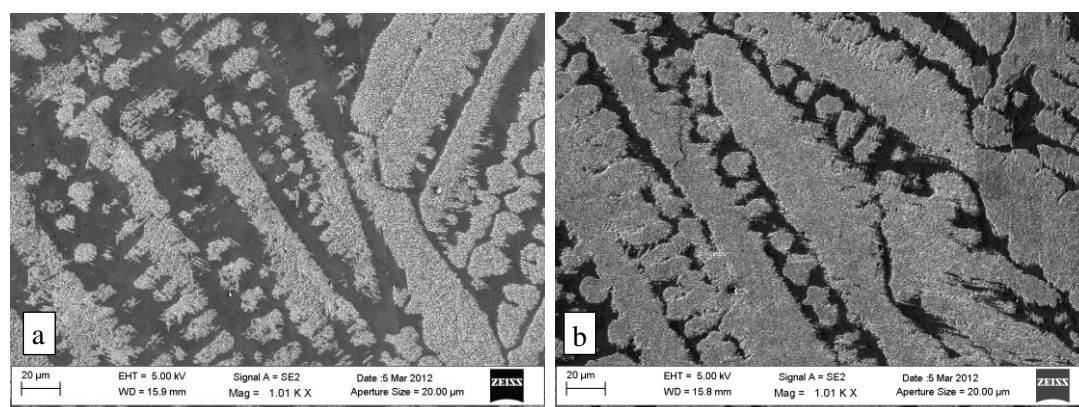


**Figure 3.64: Alloy B3, (a) pre-deformation, (b) deformed 28% in compression; inductive change 31 mH. SEM-SE image. Coarse, lighter martensite in smooth, dark austenite matrix.**



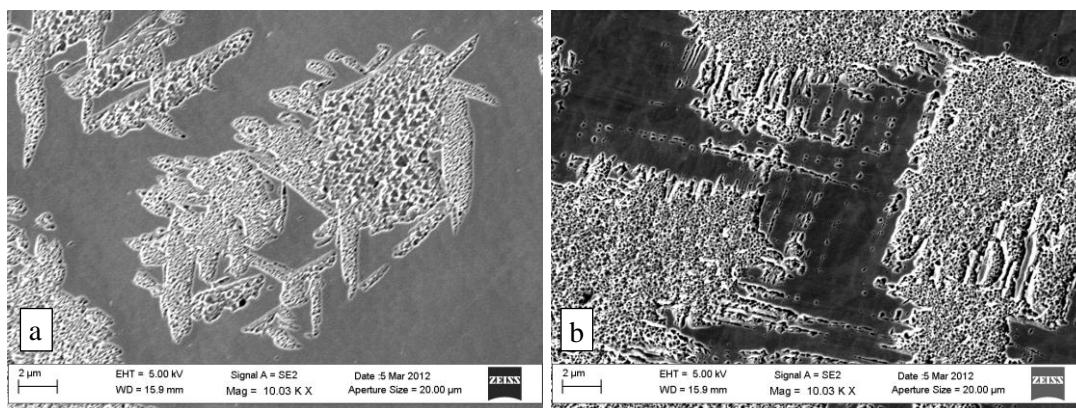


**Figure 3.65: Alloy B3, (a) pre-deformation, (b) deformed 28% in compression; inductive change 31 mH. SEM-SE image. Coarse, lighter martensite in smooth, dark austenite matrix.**

The microstructure of Alloy B4 (Figure 3.66 to Figure 3.69) showed an evolution with deformation similar to that of Alloys A3a, A3b, A3d and B3. The surface morphology of the martensite after deformation was more uniform than before (Figure 3.67 (b) and Figure 3.68 (b)), likely associated to the greater proportion of martensite present. It was noted that all alloys showing this type of microstructure were high in nickel and low in carbon and manganese. Alloy B4 also underwent a large inductive change of 28 mH (Table 3.9), similar in magnitude to that of Alloys A3a, A3b, A3d and B3.

The pre-deformation microstructure shows austenite dendrites that have partially transformed to martensite (Figure 3.66 (a)). It is likely that much of the martensite in the pre-deformation sample (Figure 3.66) was produced during sample preparation. This was verified by the low pre-deformation inductance of 93.1 mH (Table 3.9), as well as the alloy's position within the austenitic region of the Schaeffler diagram (Table 3.8).

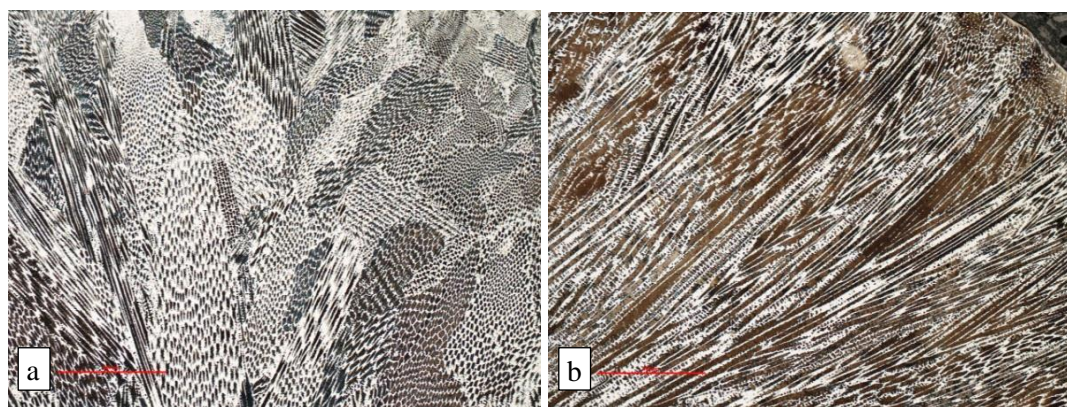


**Figure 3.66: Alloy B4, (a) pre-deformation, (b) deformed 28% in compression; inductive change 28 mH. Optical microscopy image; scale bar represents 500μm. Dark martensite in light austenite matrix.**



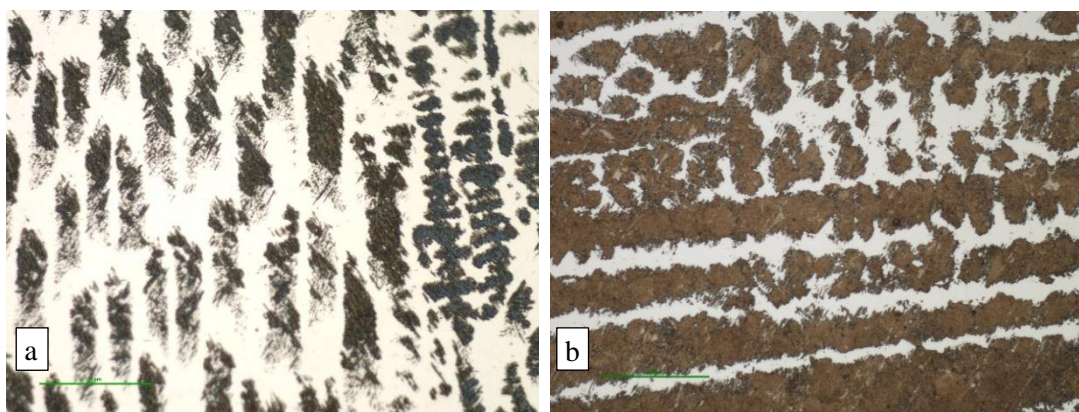


**Figure 3.67: Alloy B4, (a) pre-deformation, (b) deformed 28% in compression; inductive change 28 mH. Optical microscopy image; scale bar represents 50μm. Dark martensite in light austenite matrix.**

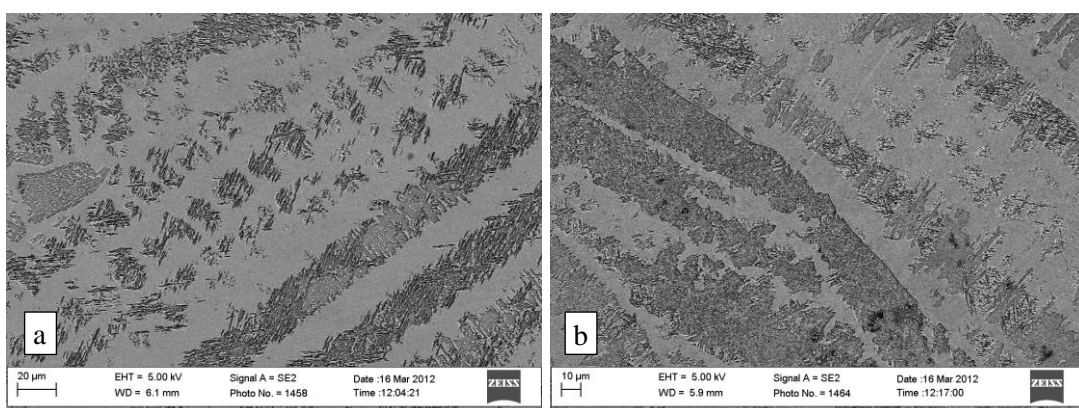


**Figure 3.68: Alloy B4, (a) pre-deformation, (b) deformed 28% in compression; inductive change 28 mH. SEM-SE image. Coarse, darker martensite in smooth, light austenite matrix.**

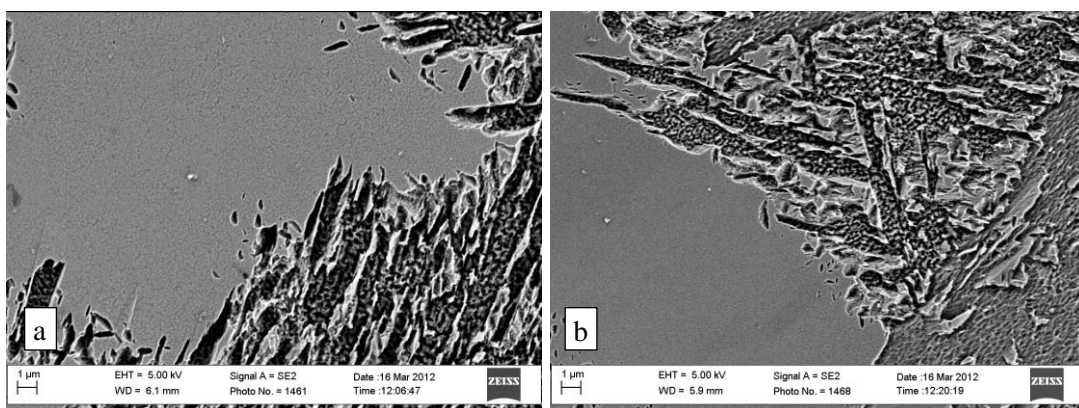


**Figure 3.69: Alloy B4, (a) pre-deformation, (b) deformed 28% in compression; inductive change 28 mH. SEM-SE image. Etched, darker martensite in smooth, light austenite matrix.**

Alloy C1 underwent a medium-low inductive change of 12 mH. It showed a pre-deformation microstructure similar to that seen in several previous pre-deformation samples, particularly Alloy B4 (Figure 3.66). However, the post-deformation microstructure showed a very distinctive microstructural evolution, with repeated attempts at preparing and etching (including with different etchants) confirming a distinctive speckled microstructure (Figure 3.70 (b) and

Figure 3.71 (b)). These markings were found to also be present in much smaller size and extent in the pre-deformation microstructure (Figure 3.71 (a)).

The high magnification SEM images in Figure 3.73 show two different etched morphologies that are both assumed to be martensite. The first, present in considerably larger proportion in the undeformed specimen, presents as relatively large islands of a lightly etched, coarse surface (Figure 3.72 (a) and Figure 3.73 (a)). The second presents as deeply pitted regions present in the centre of the islands in the pre-deformation microstructure (Figure 3.72 (a) and Figure 3.73 (a)) that have apparently grown to largely consume the islands after deformation (Figure 3.72 (b) and Figure 3.73 (b)).

The first martensite morphology was similar to that observed in Alloys B3 and B4 (Figure 3.65 and Figure 3.69). The second was more similar to that of Alloy A3e or possibly B2 (Figure 3.51 (b) and Figure 3.61 (b) respectively). Both morphologies possibly increase in extent from before deformation to after deformation, but more so the second (Figure 3.71). It is thus hard to draw a conclusion as to which accounts for the moderate to low increase in magnetic permeability. However, since specimens of Alloy C1 had the lowest pre-deformation magnetic permeability of all the alloys (barely above that of air, Table 3.9) and a high nickel-chromium equivalent (Table 3.8), it seems likely that the second morphology is responsible for the increase in magnetic permeability. Thus, the first morphology was then likely introduced primarily through preparation.

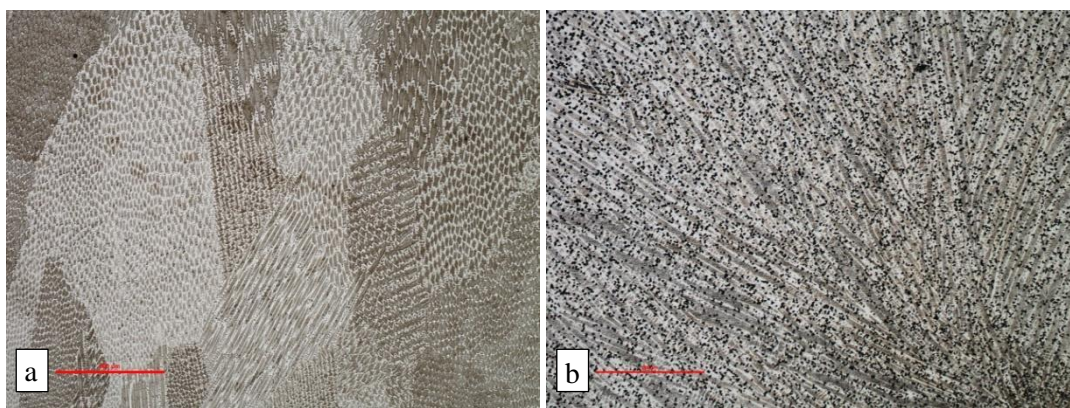


**Figure 3.70: Alloy C1, (a) pre-deformation, (b) deformed 28% in compression; inductive change 12 mH. Optical microscopy image; scale bar represents 500 $\mu$ m. Dark martensite of two morphologies in light austenite matrix.**



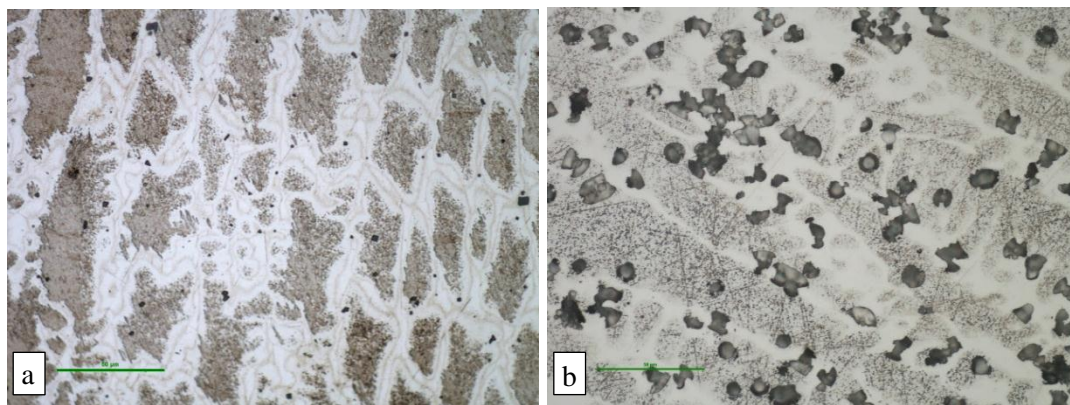


**Figure 3.71: Alloy C1, (a) pre-deformation, (b) deformed 28% in compression; inductive change 12 mH. Optical microscopy image; scale bar represents 50μm. Dark martensite of two morphologies in light austenite matrix.**

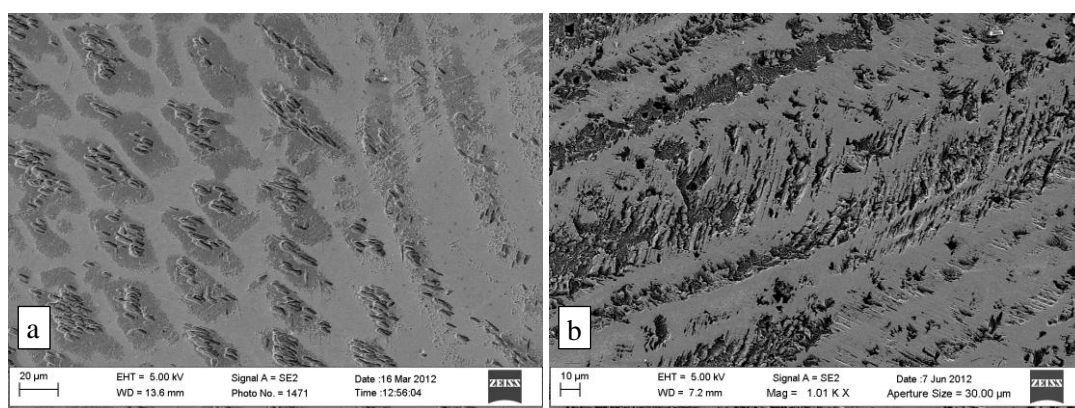


**Figure 3.72: Alloy C1, (a) pre-deformation, (b) deformed 28% in compression; inductive change 12 mH. SEM-SE image. Dark martensite in lighter, smooth austenite matrix.**

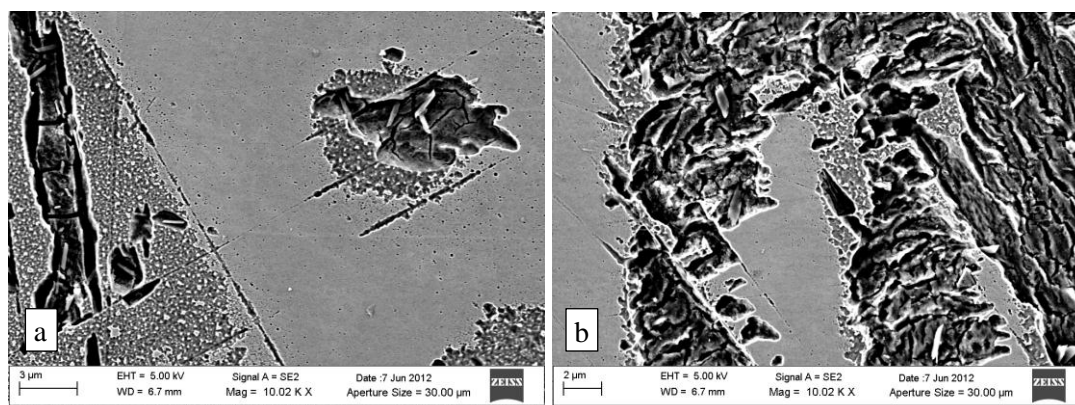


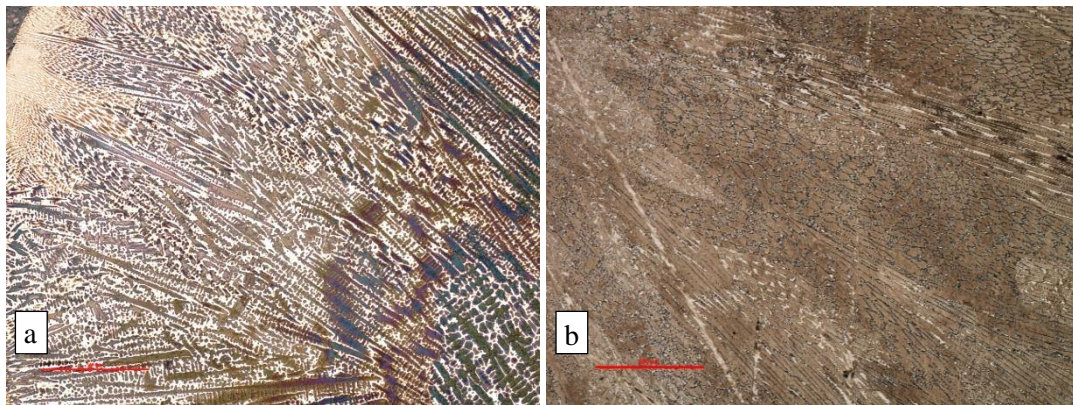
**Figure 3.73: Alloy C1, (a) pre-deformation, (b) deformed 28% in compression; inductive change 12 mH. SEM-SE image. Etched martensite of two lath-type morphologies in lighter, smooth austenite matrix.**

Alloy C2 revealed an almost identical microstructure pre- and post-deformation to Alloys A3a, A3, A3d, B3, B4. This alloy, along with Alloy C3 had the largest inductive change of all alloys, 40 mH. The microstructures of this material are shown in an undeformed and deformed state at various magnifications in Figure 3.74 to Figure 3.78. The post-deformation microstructure was almost entirely martensitic (Figure 3.74 (b) and Figure 3.77 (b)), with isolated regions of retained austenite.

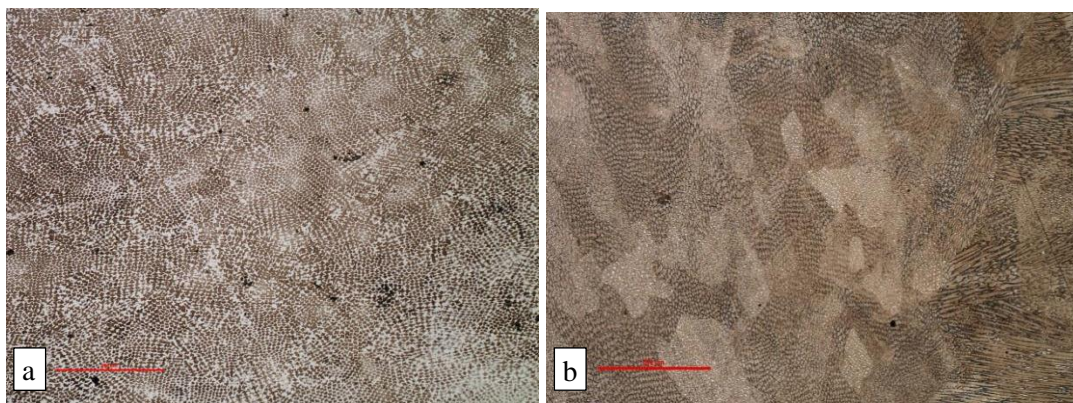


Figure 3.74 and Figure 3.75 show the difference in observed microstructure between a sample that has been cross-sectioned and one that has been longitudinally-sectioned, respectively. While the microstructures were similar regarding martensite extent and high magnification morphology, the dendrites were more apparent in the cross-sectioned specimen (Figure 3.74) and were clearly pared along their length in the longitudinally-sectioned specimen (Figure 3.75).

While martensite was likely formed during preparation, it is probable that some was already present prior to preparation, since the alloy had a slightly raised starting inductance (Table 3.9) and was well within the austenite-martensite region in the Schaeffler diagram (Table 3.8).



**Figure 3.74: Alloy C2, (a) pre-deformation, (b) deformed 28% in compression; inductive change 40 mH. Optical microscopy image; scale bar represents 500 $\mu$ m. Dark martensite, light austenite.**



**Figure 3.75: Alloy C2, sectioned longitudinally, (a) pre-deformation, (b) deformed 28% in compression; inductive change 40 mH. Optical microscopy image; scale bar represents 500 $\mu$ m. Dark martensite in light austenite matrix.**



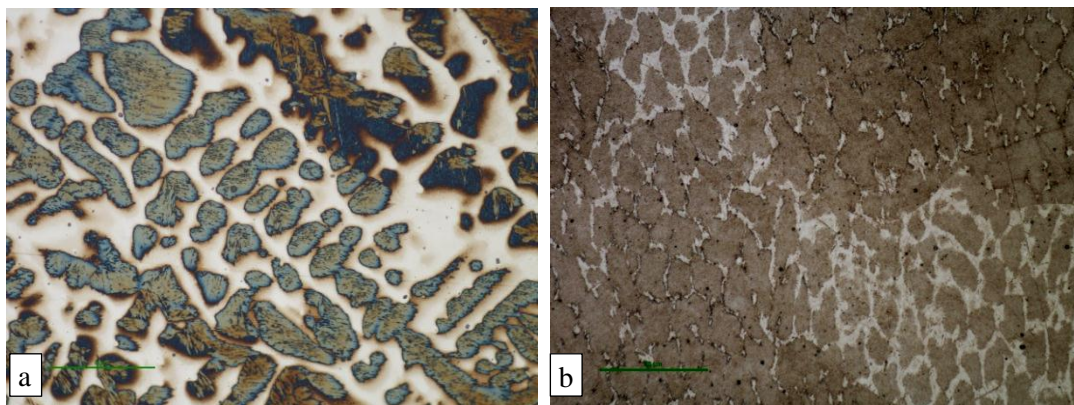


**Figure 3.76: Alloy C2, (a) pre-deformation, (b) deformed 28% in compression; inductive change 40 mH. Optical microscopy image; scale bar represents 50 $\mu$ m. Dark martensite in light austenite matrix.**

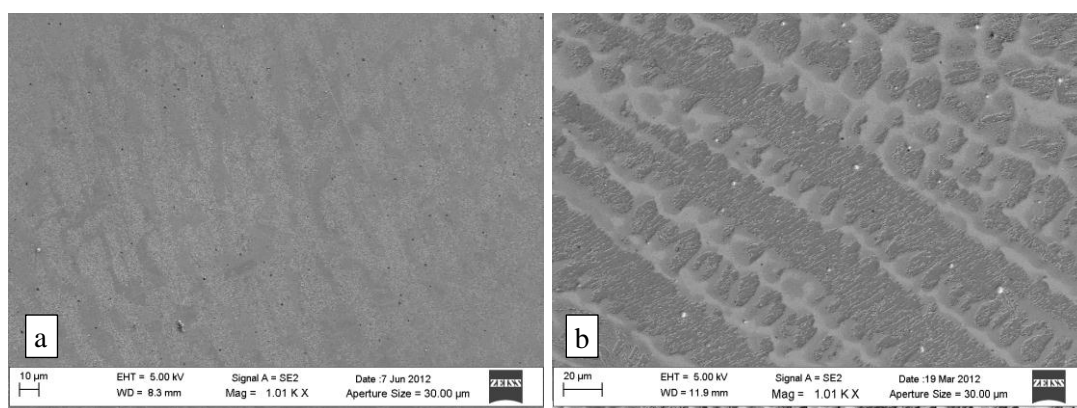


**Figure 3.77: Alloy C2, (a) pre-deformation, (b) deformed 28% in compression; inductive change 40 mH. SEM-SE image. Darker, etched martensite in lighter austenite matrix.**

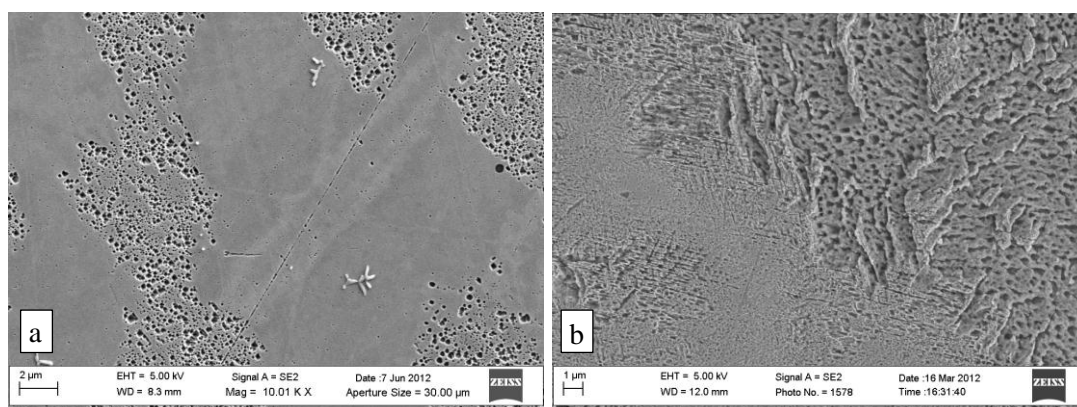


**Figure 3.78: Alloy C2, (a) pre-deformation, (b) deformed 28% in compression; inductive change 40 mH. SEM-SE image. Darker etched lath martensite in lighter austenite matrix.**

The microstructures of Alloy C3 are shown in an undeformed and deformed state at various magnifications in Figure 3.79 to Figure 3.84. Alloy C3, along with Alloy C2 had the largest inductive change of all alloys, 40 mH. At low magnification, Alloy C3 showed similar microstructural evolution to Alloy C2 (Figure 3.79 and Figure 3.80). However, at higher magnification (Figure 3.81 and Figure 3.84), the microstructure was different from that of Alloy

C2, and in fact similar to that of Alloy B2 (Figure 3.59, Figure 3.60 and Figure 3.61). There were signs of  $\epsilon$  martensite and some  $\alpha'$  martensite pre-deformation (Figure 3.81 (a), Figure 3.82, Figure 3.84 (a)), and extensive slip, faulting and  $\alpha'$  martensite post-deformation (Figure 3.81 (b), Figure 3.82). Pre-deformation martensite was likely not primarily due to preparation, since the alloy showed a slightly raised pre-deformation inductance of 94.5 mH (Table 3.8) and was well within the austenite-martensite region on the Schaeffler diagram (Table 3.9). Figure 3.84 shows a combination of lath and plate martensite.

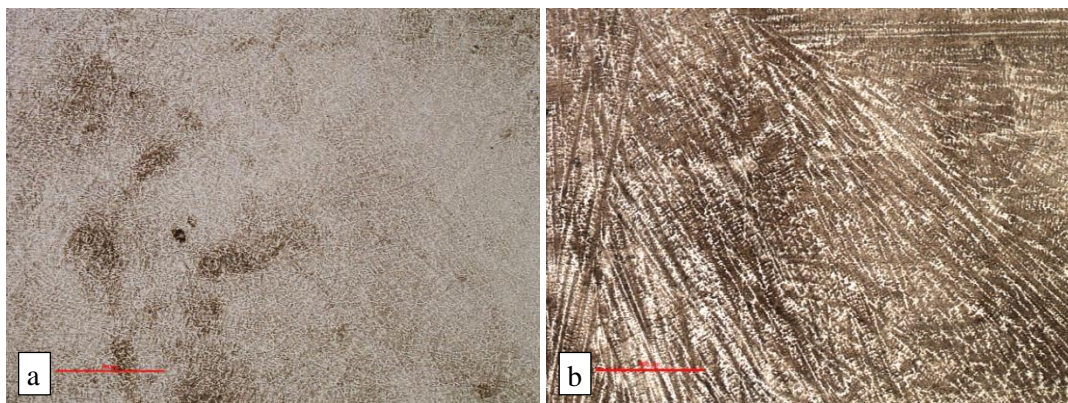


**Figure 3.79: Alloy C3, (a) pre-deformation, (b) deformed 28% in compression, showing an inductive change of 40 mH. Optical microscopy image; scale bar represents 500 $\mu$ m. Darker martensite in lighter austenite matrix.**

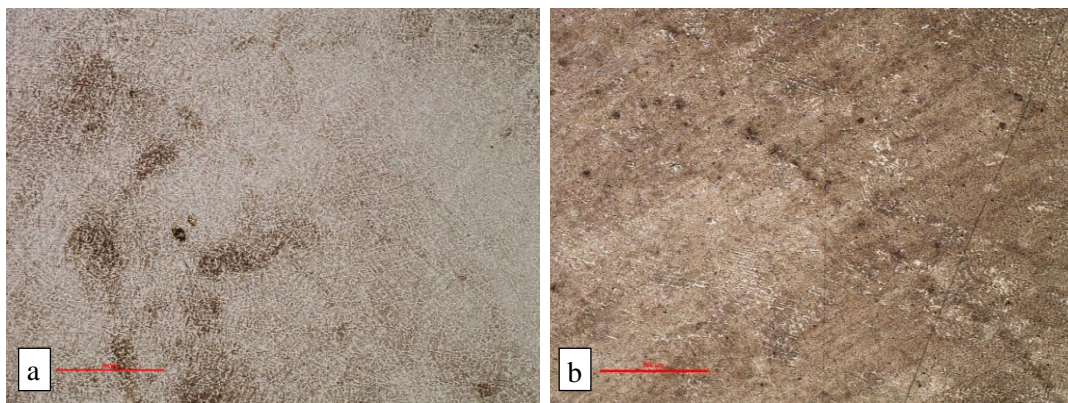


**Figure 3.80: Alloy C3, (a) pre-deformation, (b) deformed 28% in compression, sectioned longitudinally, showing an inductive change of 40 mH. Optical microscopy image; scale bar represents 500 $\mu$ m. Dark martensite, light austenite.**



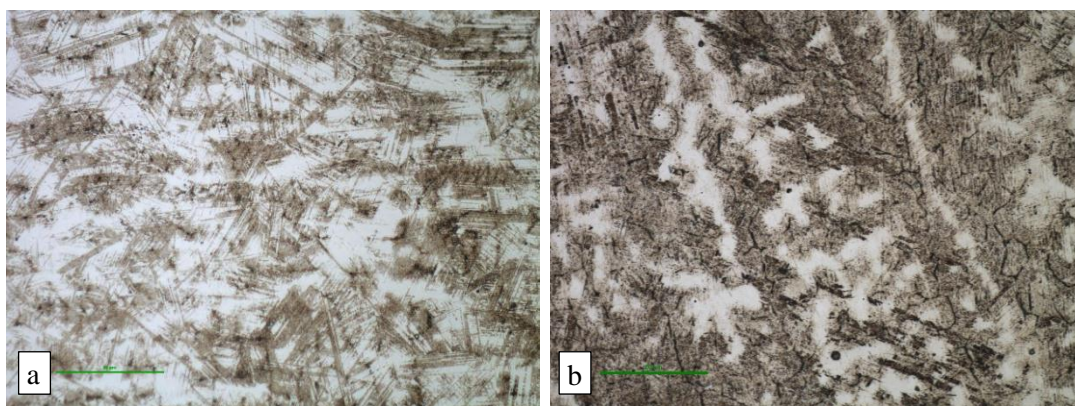


**Figure 3.81: Alloy C3, (a) pre-deformation, (b) deformed 28% in compression; inductive change 40 mH. Optical microscopy image; scale bar represents 50μm. Dark martensite, light austenite.**

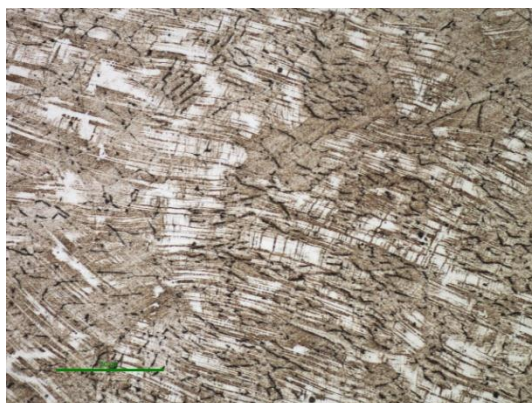


**Figure 3.82: Alloy C3, deformed 28% in compression, sectioned longitudinally; inductive change 40 mH. Optical microscopy image; scale bar represents 50μm. Dark martensite, light austenite, heavily faulted matrix.**

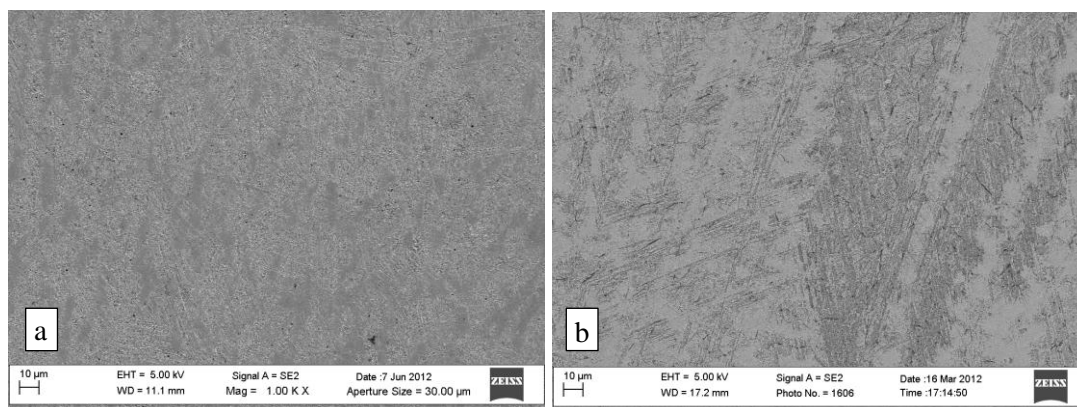


**Figure 3.83: Alloy C3, (a) pre-deformation, (b) deformed 28% in compression; inductive change 40 mH. SEM-SE image. Darker, more etched martensite in light austenite matrix.**



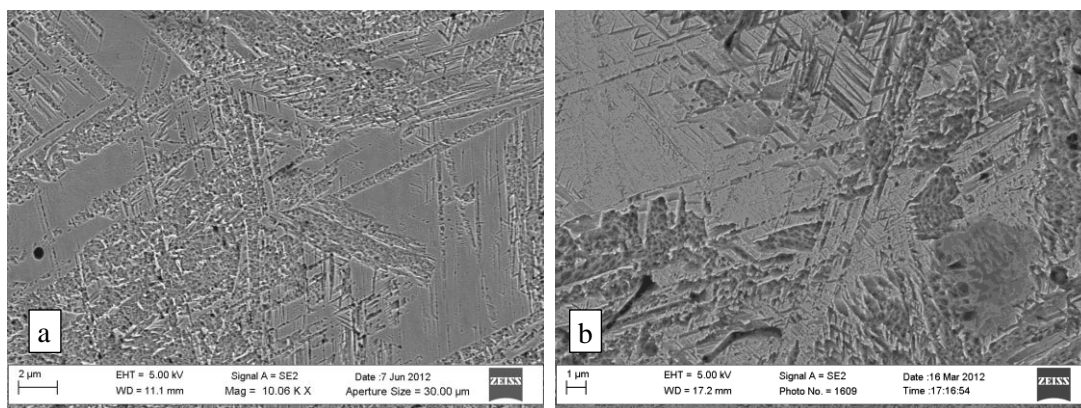


**Figure 3.84: Alloy C3, (a) pre-deformation, (b) deformed 28% in compression; inductive change 40 mH. SEM-SE image. Darker, etched martensite in light austenite matrix; showing lath and plate martensite.**

Alloy M1 underwent a large inductive change, 31 mH. The microstructures of this material are shown in an undeformed and deformed state at various magnifications in Figure 3.85 to Figure 3.88. The pre-deformation microstructure showed finely dispersed ferrite or  $\alpha'$  martensite in twinned austenite (Figure 3.86 (a) and Figure 3.87 (a)). This corresponds to the alloy's slightly raised pre-deformation inductance of 95.5 mH. The post-deformation microstructure showed extensive  $\alpha'$  martensite (Figure 3.85 (a)), with signs of  $\epsilon$  martensite (Figure 3.86 (b) and Figure 3.87 (b)).

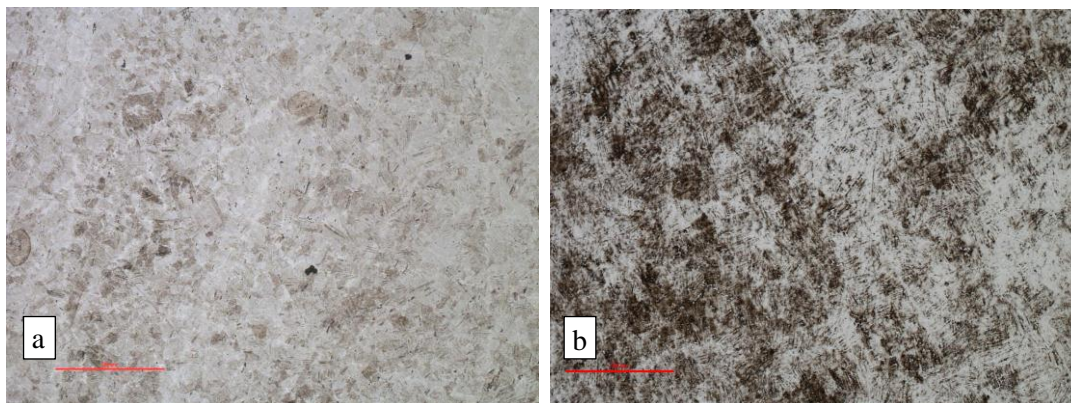


**Figure 3.85: Alloy M1, (a) pre-deformation, (b) deformed 28% in compression; inductive change 31 mH. Optical microscopy image; scale bar represents 500 μm. Dark martensite in light austenite matrix.**

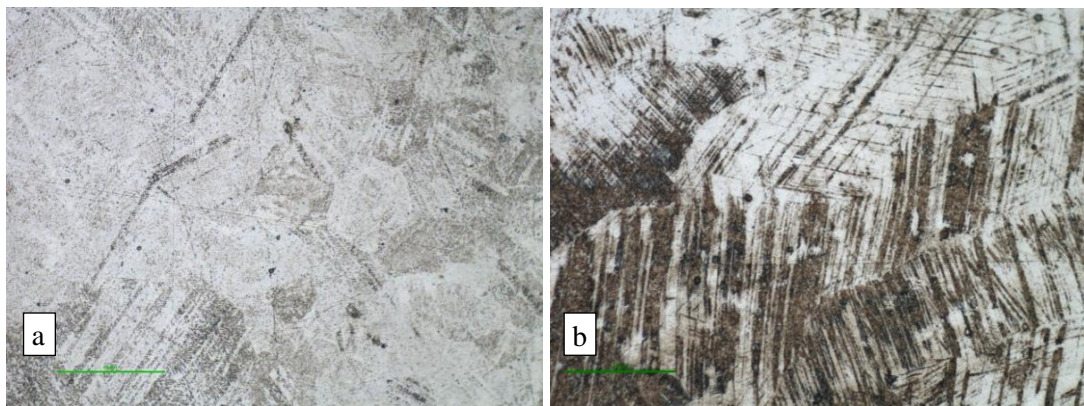


**Figure 3.86: Alloy M1, (a) pre-deformation, (b) deformed 28% in compression; inductive change 31 mH. Optical microscopy image; scale bar represents 50 μm. Dark martensite in light austenite matrix.**

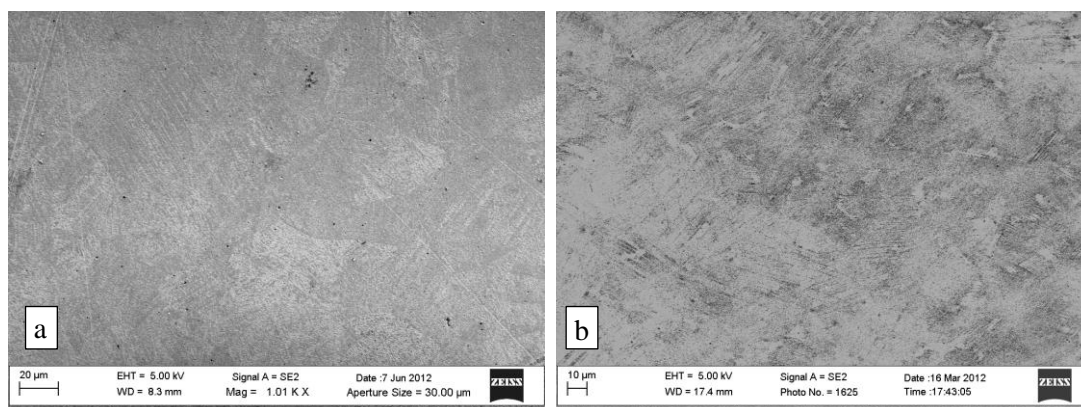


**Figure 3.87: Alloy M1, (a) pre-deformation, (b) deformed 28% in compression; inductive change 31 mH. SEM-SE image. Darker martensite in light austenite matrix.**

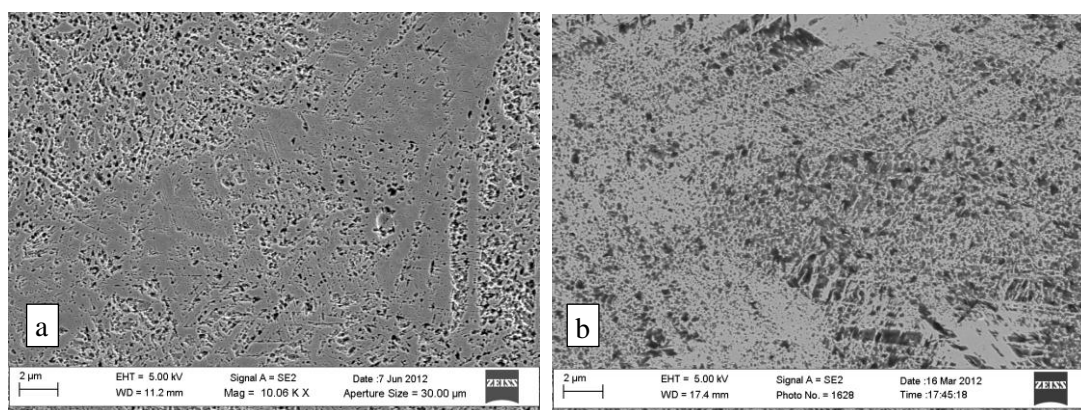


**Figure 3.88: Alloy M1, (a) pre-deformation, (b) deformed 28% in compression; inductive change 31 mH. SEM-SE image. Dark lath martensite in light austenite matrix.**

Alloy N1 underwent a medium inductive change of 17 mH. The microstructures of this material are shown in an undeformed and deformed state at various magnifications in Figure 3.89 to Figure 3.92. The pre-deformation microstructure revealed  $\epsilon$  martensite within a light brown dendritic structure (Figure 3.89 (a) and Figure 3.90 (a)). Prior to deformation the alloy showed a low inductance, near to that of air. Thus the light brown dendrites may be primarily the result of surface martensite formation during sample preparation.

The light brown dendrites are fewer in the post-deformation microstructure (Figure 3.89 and Figure 3.90). This may be due to the greater proportion of hard martensite offering the surface some protection from deformation. The post-deformation microstructure showed a considerably increased number of  $\alpha'$  martensite plates (Figure 3.90). At high magnification, the deformation induced martensite had a dispersed lath-like  $\alpha'$  martensite structure (Figure 3.92 (b)). In some regions, particularly those most densely transformed, the  $\alpha'$  martensite appears to have originated in shear bands. and (Figure 3.90 (b) and Figure 3.91 (b)).



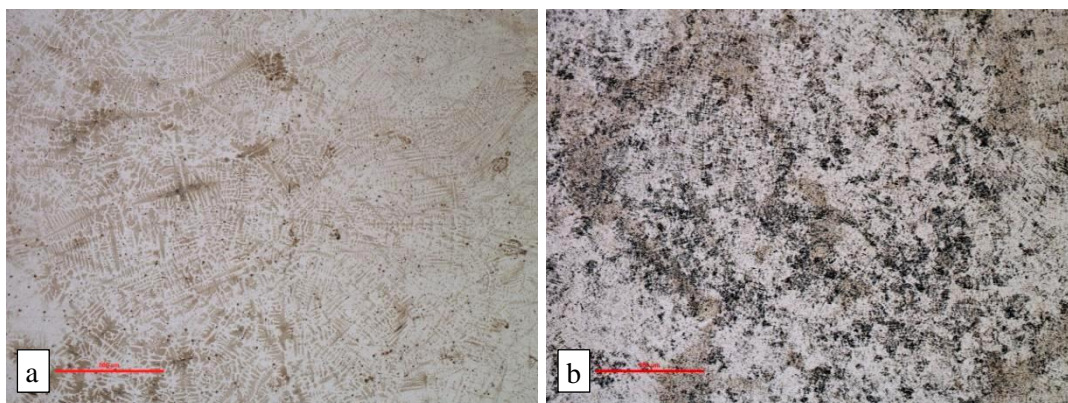


**Figure 3.89: Alloy N1, (a) pre-deformation, (b) deformed 28% in compression; inductive change 17 mH. Optical microscopy image; scale bar represents 500μm. Dark martensite in light austenite matrix.**

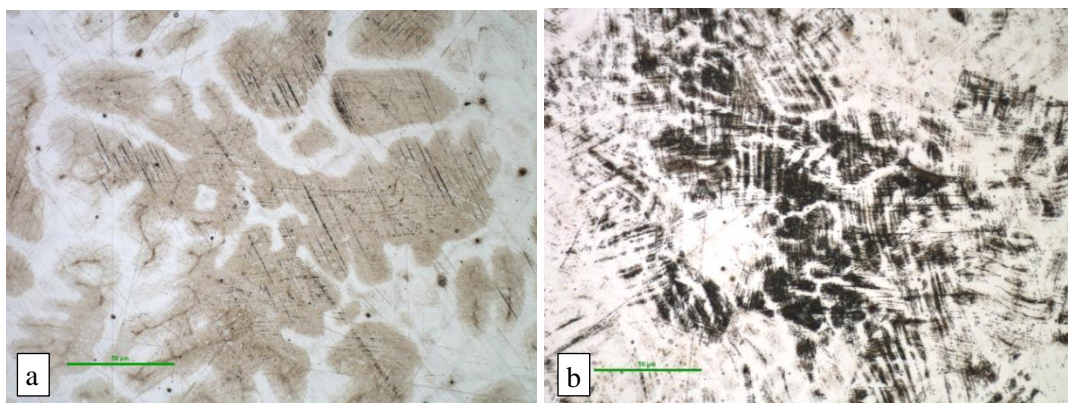


**Figure 3.90: Alloy N1, (a) pre-deformation, (b) deformed 28% in compression; inductive change 17 mH. Optical microscopy image; scale bar represents 50μm in both images. Dark martensite in light austenite matrix.**

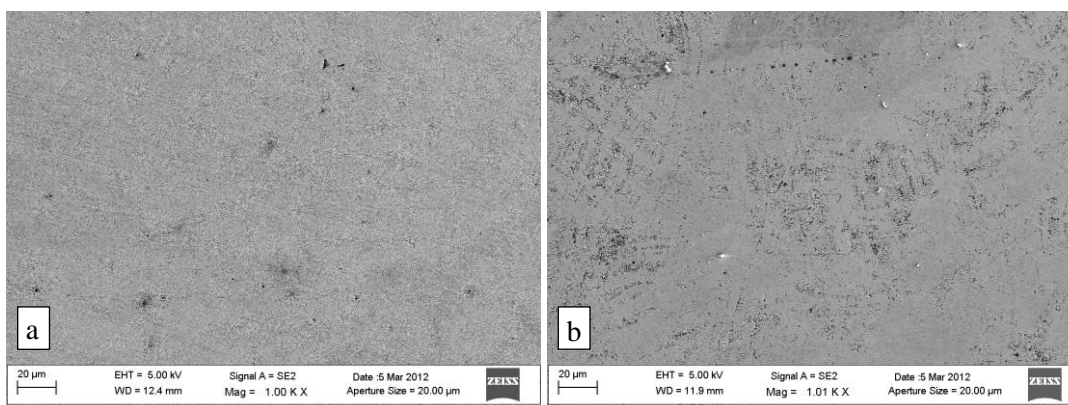


**Figure 3.91: Alloy N1, (a) pre-deformation, (b) deformed 28% in compression; inductive change 17 mH. SEM-SE image. Darker etched martensite in light austenite matrix.**

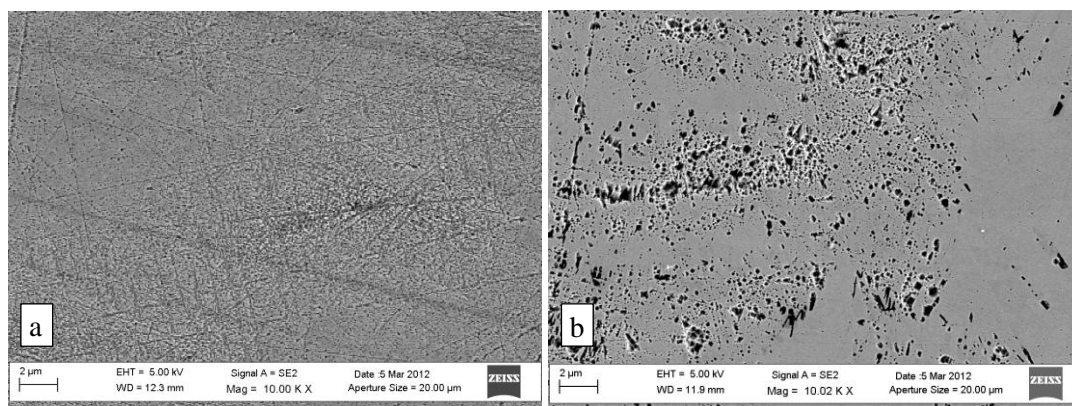


**Figure 3.92: Alloy N1, (a) pre-deformation, (b) deformed 28% in compression; inductive change 17 mH. SEM-SE image. Dark etched martensite in smooth, light austenite matrix.**

#### 3.4.6.4 Assessment of microstructures

All of the arc-cast alloys showed a dendritic structure. They exhibit varying degrees of dark martensite that has developed in the austenite dendrites. In the case of undeformed samples, this martensite has developed during either cooling or specimen preparation. In the case of deformed samples, the martensite has developed primarily during deformation.

Alloys high in manganese showed  $\epsilon$  martensite morphology in their undeformed microstructure and a propensity towards growing this plate-type hatched martensite during deformation, which probably began as  $\epsilon$  martensite and evolved into  $\alpha'$  martensite. This was exemplified in the microstructures of Alloys B2, M1 and N1, (although Alloy N1 showed only average transformation). These three alloys also had the highest levels of manganese of all the alloys, at over 10%. This observation corresponds to the theory that replacing nickel with manganese reduces stacking fault energy, as discussed in Section 2.5.

Low carbon and manganese predicts a microstructure of lath-type  $\alpha'$  martensite islands as in Alloys A3, B3, B4 and C2. These low carbon, low manganese alloys were also apparently most susceptible to forming martensite during preparation. This may be associated with their different martensite morphology than that of the high manganese alloys. The high manganese alloys apparently contained some harder non-ferromagnetic  $\epsilon$  martensite plates prior to deformation. The plates may reduce these alloys' propensity to forming martensite during surface preparation, because the hard martensite plates may act as reinforcement to the softer austenite phase. Alternatively, the plate martensite that formed first in the high manganese alloys may have had less propensity to form during the type of deformation applied in sample preparation. The high manganese alloys did not however show a later start to transformation during compressive testing.



Microstructures of all alloys from both before and after deformation showed combinations of austenite and martensite. Although a few alloys, for example Alloy A3b, showed signs of ferrite, it is improbable that it was ferrite that was observed. Alloys that were found during compressive testing to exhibit a large change in magnetic permeability were generally seen to exhibit considerably increased proportions of martensite after deformation. However, there was not a clearly defined relationship between microstructure and magnetic permeability. This was also found by previous authors, as discussed in Section 2.8 (Maxwell et al., 1974) (Zaefferer et al., 2004) (Petrov et al., 2007). It is probably due to the localised and two-dimensional nature of the visual inspection (although representative areas were selected as far as possible), as well as small variations in etching contrast and microscope operation, and the highly multi-phase nature of TRIP steels. It was probably for these same reasons that software based phase image analysis was not successful. The grain structure both of as-cast and of deformed specimens varied with sectioning direction as expected, with cross-sections exhibiting columnar austenite grains towards the surface and longitudinal sections showing equiaxed grains.

#### **3.4.7 XRD**

The XRD analyses were carried out on a PANalytical X'Pert Pro at the Technische Universität Chemnitz in Germany by a technician skilled in phase analysis of polycrystalline metals. Since the XRD analyses were performed only for verification and comparison to the other phase analysis methods used, the technician, using PANalytical Highscore Plus software, was relied upon to provide an approximate quantitative analysis from the results.

As with all experiments, results were hampered by the very small quantity of each material available. X-ray diffraction analysis was performed on samples of Alloys A4, C3 and N1 and the results are shown in Figure 3.93 to Figure 3.95 and in Table 3.13. Samples from microscopic analysis were utilised, one cross-section from the as-cast specimen and one from the deformed compression test specimen.

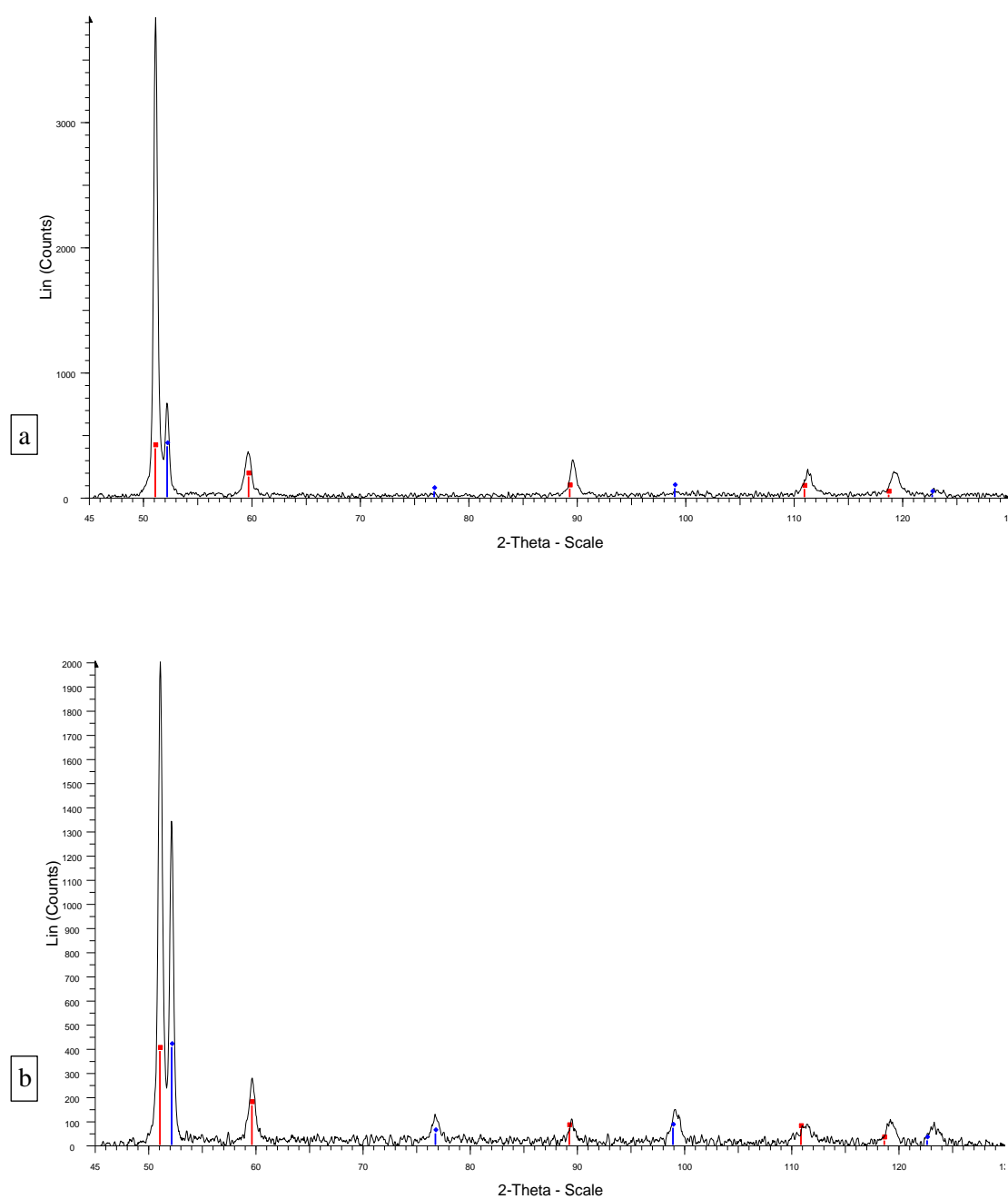


**Figure 3.93: Alloy A4, (a) undeformed (86% austenite) (b) deformed 28% (54% austenite). Red bars represent austenite peaks, blue bars represent ferrite/martensite peaks.**

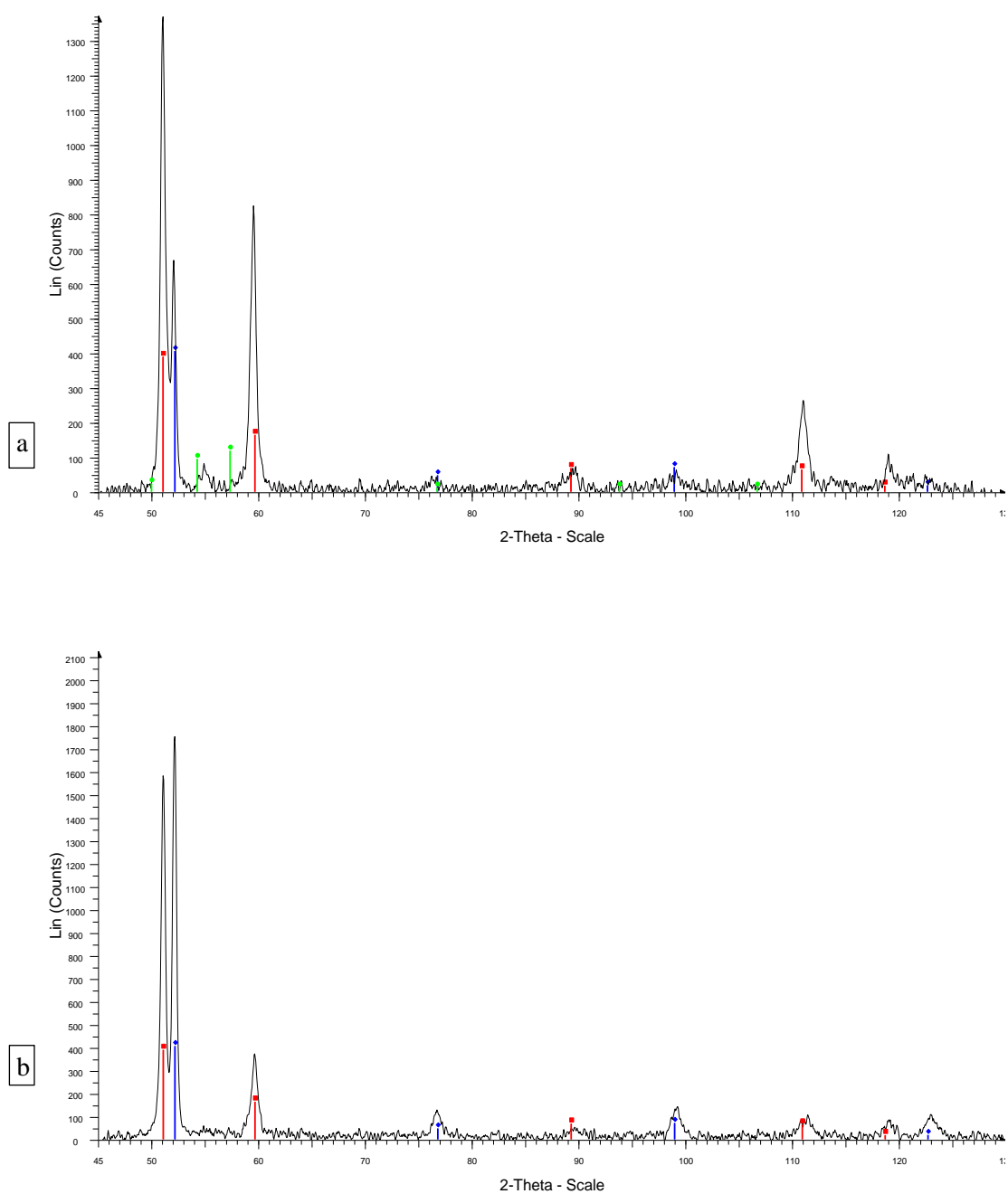


**Figure 3.94: Specimen C3 (a) undeformed (72% austenite) (b) deformed 28% (44% austenite). Red bars represent austenite peaks, blue bars represent ferrite/martensite peaks, green bars represent hexagonal close-packed peaks.**

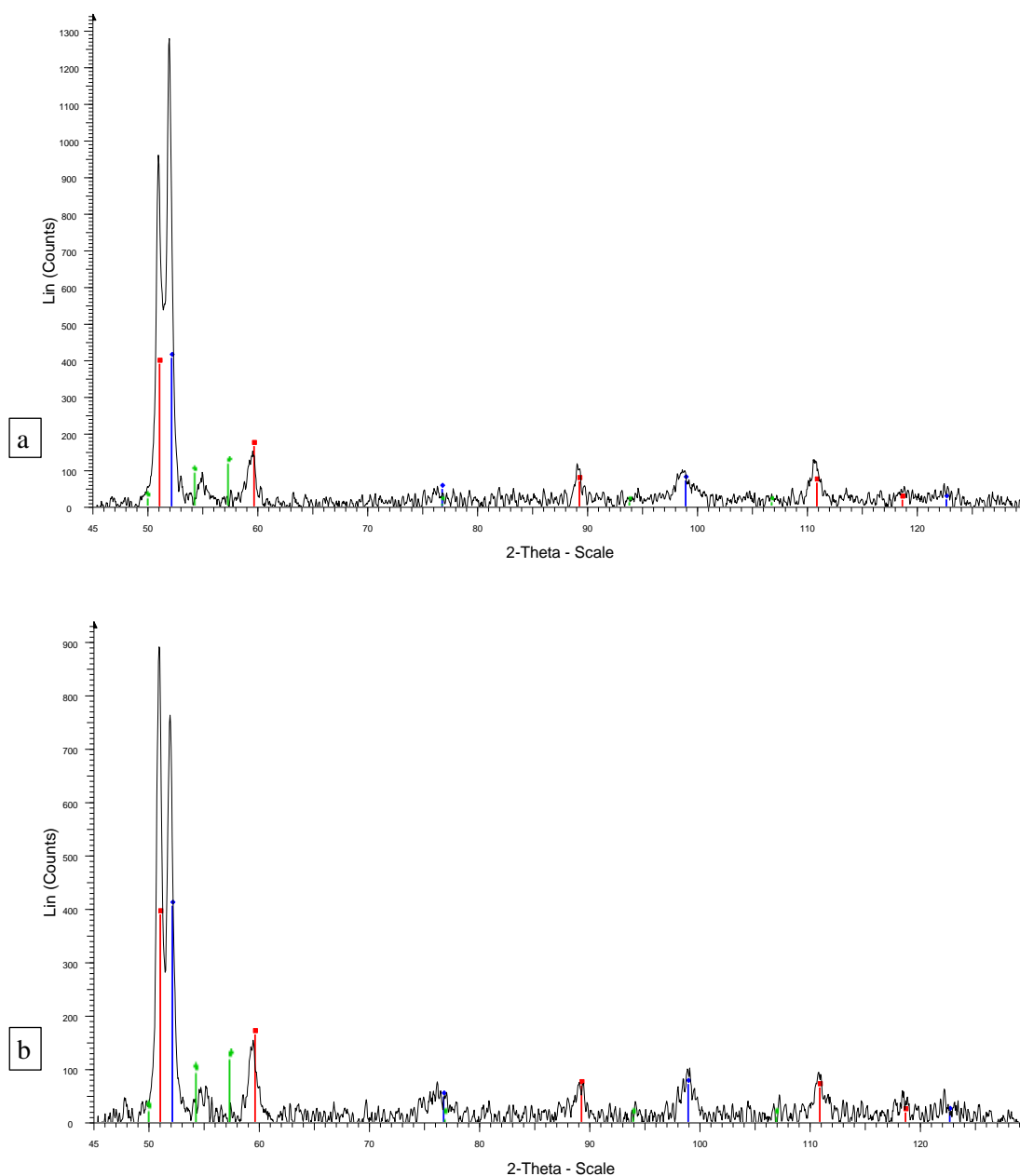


**Figure 3.95: Specimen N1 (a) undeformed (52% austenite) (b) deformed 28% (38% austenite). Red bars represent austenite peaks, blue bars represent ferrite/martensite peaks, green bars represent hexagonal close-packed peaks.**

**Table 3.13: Estimated % non-austenite change in various alloys during deformation to 28% strain.**

Material	Est. start % non- $\gamma$	Est. finish % non- $\gamma$	Est. increase % non- $\gamma$
C3	28	56	28
A4	14	46	32
N1	48	62	14

X-ray diffraction (XRD) data were shown to broadly correlate with inductance measurements, although the relationship was not precise or considered to be quantitatively accurate. This result

reinforces what previous experimenters have found, that it is difficult to determine quantitative strain-induced martensite proportions via XRD (Otte, 1957) (Talonen et al., 2004) (Petrov et al., 2007). These difficulties are believed to be due to texture, the highly multi-phase nature of TRIP steels and the heavily distorted structure present after deformation. Although hcp  $\epsilon$  martensite is expected to be present in all of the tested alloys since they all have high manganese contents, the amount of  $\epsilon$  martensite was expected to be relatively very small and likely unquantifiable.

Differentiation between ferrite (bcc) and martensite (bct) orientations is often difficult to determine using XRD (Mayr et al., 2010). The difference in peak positions for these two phases varies with interstitial (carbon) level because low carbon martensite approaches a bcc structure. All three alloys had low levels of carbon, about 0.1wt%, making differentiation even more difficult. A small amount of peak broadening may be observed when comparing the undeformed specimens to the deformed specimens.

Alloy N1 showed signs of hcp martensite phase being present after deformation, this can be seen in increased counts at the  $2\theta$  angles marked by green bars in Figure 3.95 (b), although the increase is only marginally above background. This corresponds to the hypothesis that high manganese levels promote  $\epsilon$  martensite (Section 2.5). When phase analysis was performed with hcp phase included, it was found to be present in similarly small quantities (approximately 3%) both before and after deformation.

#### 3.4.8 Temperature sensitivity

Temperature at time of measurement was shown to have no significant effect on results. This was verified between  $-20^{\circ}\text{C}$  and  $120^{\circ}\text{C}$  (Section 3.7.3). Cyclic temperature change at constant stress was also shown to have no significant effect. Specimens of Alloy HM were cycled between  $-40^{\circ}\text{C}$  and  $80^{\circ}\text{C}$  for approximately 100 cycles, with no observable change in inductive output. However, temperature at time of deformation was shown to have a significant effect.

Compressive temperature testing was conducted on cast Alloy V2 between  $25^{\circ}\text{C}$  and  $90^{\circ}\text{C}$  and on Alloy HM between  $-15^{\circ}\text{C}$  and  $90^{\circ}\text{C}$ . If a sensor based on Alloy V2 was programmed to assume an average between  $25^{\circ}\text{C}$  and  $90^{\circ}\text{C}$ , then as seen in Figure 3.96, Alloy V2 would produce a precision of  $\pm 19\%$  at a peak stress reading of 800 MPa when it was unknown at what temperature between  $25^{\circ}\text{C}$  and  $90^{\circ}\text{C}$  the load occurred. Each curve shown in Figure 3.96 was the average of three tests and variation between tests was less than 2%, which is considered negligible in comparison to variation with temperature.

However, such a broad temperature range is unlikely to be encountered in underground mining applications (where average rock temperature is often between 40°C and 60°C and variation is less than 10°C year round (Florides & Kalogirou, 2005) (Minnie, 2005) (Oelofse, 2005) or in certain civil applications. Over a transformation temperature variation between 40°C and 65°C, Alloy V2 would produce a precision of  $\pm 10\%$  at a stress reading of 800 MPa. Precision over various temperature ranges are listed in Table 3.14.

**Table 3.14: Precision over various temperature ranges for Alloy V2 tested in compression.**

<b>Temperature Range:</b>	<b>25°C - 40°C</b>	<b>40°C - 65°C</b>	<b>40°C - 90°C</b>	<b>25°C - 90°C</b>
<b>Precision at 800 MPa:</b>	$\pm 7\%$	$\pm 10\%$	$\pm 14\%$	$\pm 19\%$

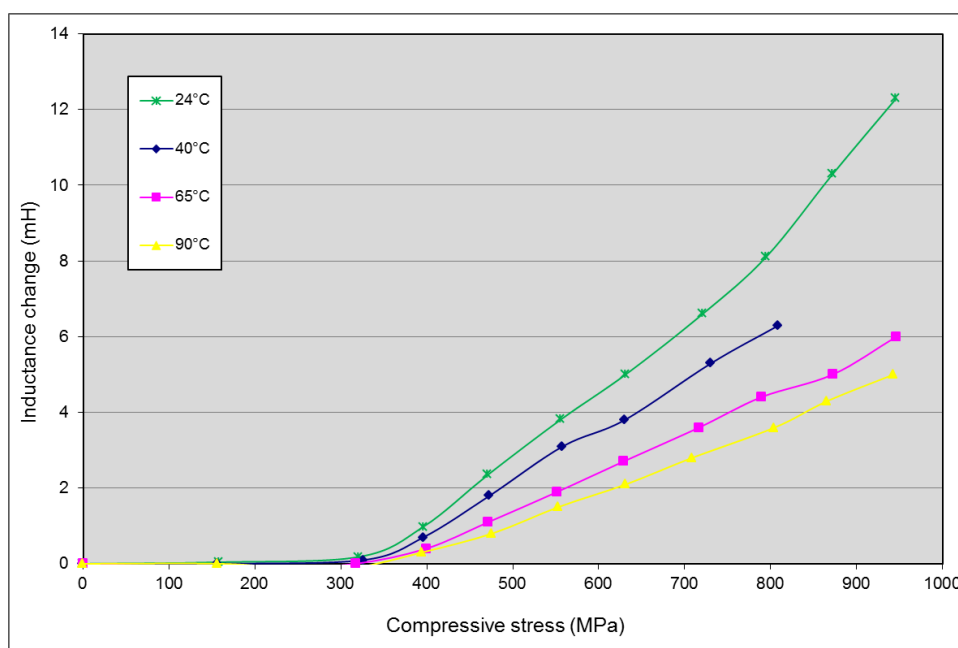


**Figure 3.96: Change in transformation levels with stress due to transformation temperature variation for Alloy V2 (Bemont, 2009).**

A registered output will always predict a lower load than the true historical peak load when the temperature was higher than expected at the time of deformation. A higher load will always be predicted when the temperature during deformation was below that expected.

Compressive temperature testing was also conducted on Alloy HM between -15°C and 90°C. If a sensor based on Alloy HM was programmed to assume an average between 25°C and 90°C (as with sensor Alloy V2), then as seen in Figure 3.97, Alloy HM would produce a precision of  $\pm 13\%$  at a peak stress reading of 1100 MPa when it is unknown where between 25°C and 90°C



the load occurred. Each curve shown in Figure 3.96 is the average of three tests and variation between tests was less than 2%, considered minor in comparison to variation with temperature. Precision over various temperature ranges are listed in Table 3.15.

**Table 3.15: Precision over various temperature ranges for Alloy HM tested in compression.**

Temperature Range:	25°C - 45°C	45°C - 90°C	25°C - 90°C	-15°C to 90°C
Precision at 1100 MPa:	±5%	±9%	±13%	±17%

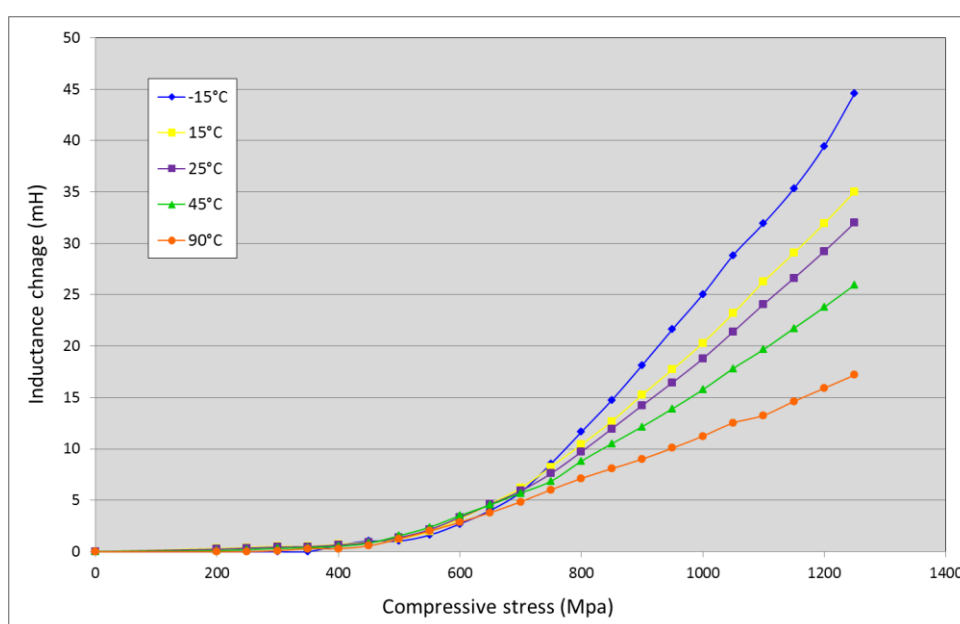


**Figure 3.97: Change in transformation levels with stress due to transformation temperature variation for Alloy HM.**

### 3.4.9 Effect of dislocation density

Finally, an attempt was made to examine the effects of material condition and associated implicit changes in dislocation density on transformation temperature sensitivity. Alloy TRIP M was utilised in a hot rolled and water-quenched state and in a fully annealed state (1150°C for 2 hours and furnace cooled). Hot rolling was performed between 1000°C and 1200°C. The hot rolled austenitic samples were expected to have a higher dislocation density than annealed samples (Singhal, 1971) (Rowcliffe & Nicholson, 1972) (Suh et al., 2002). Results are shown in Figure 3.98, where each curve is the average of three tests. Repeated tests of the same alloy under the same conditions gave near identical results, with a maximum total error of about 1% strain above 20% strain. Error was small compared to variation with temperature.

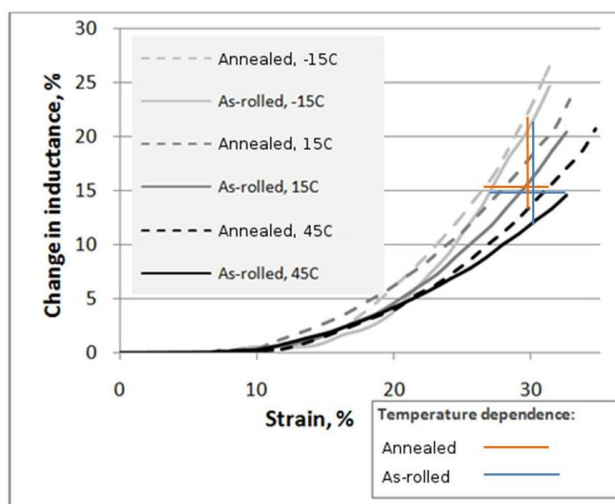


**Figure 3.98:** Strain versus transformation curves for alloy TRIP M in a hot-rolled and water-quenched state and in a fully annealed state, tested at  $-15^{\circ}\text{C}$ ,  $15^{\circ}\text{C}$  and  $45^{\circ}\text{C}$  (Bemont et al., 2013).

The annealed material showed a slightly more rapid transformation with deformation. This may be due to its larger austenite grain size (as seen when comparing Figure 3.158 with Figure 3.170). Slightly less temperature sensitivity was exhibited by the annealed material. At 30% strain, the difference in temperature sensitivity between the two materials was about 2 mH change in inductance over  $60^{\circ}\text{C}$  (9% for the annealed material and 10% for the as-rolled material), this was statistically significant at the  $p = 0.05$  level, compared to the test repeatability error. The difference in temperature sensitivity at 15 mH was 1% strain over  $60^{\circ}\text{C}$ , also statistically significant at  $p = 0.05$ . It correlates with the hypothesis that a higher dislocation density is expected to increase  $M_f$  and thereby increase temperature sensitivity, as discussed in Section 3.3.2.

Similar testing was conducted in tension on alloy TRIP M in annealed, hot-worked and warm-worked conditions. These tests were performed on annealed, hot-rolled and warm-rolled alloys and are discussed in Section 3.5.9.

#### 3.4.10 Effect of high strain rate

As previously discussed, extent of transformation at a particular strain is affected by strain rate, as well as by environmental temperature (Section 2.5). Higher strain rates are believed to cause microscopic heating within the highly strained regions of the material's crystal structure, which does not have time to dissipate during transformation (Bressanelli & Moskowitz, 1966). It was proposed that the reduced transformation at higher strain rates is thus due to the influence of this temperature increase (Bressanelli & Moskowitz, 1966). It is thus expected that an alloy with lower temperature transformation sensitivity will also exhibit less strain rate sensitivity. Figure 3.99 and Figure 3.100 were from one set of high strain rate deformation tests performed on an MTS 312.21 with 100 l/min hydraulic power pack and hydraulic accumulators. A second and

similar test was performed and results were closely comparable. The testing was performed on Alloy HM (composition Table 3.4), which was annealed at 1150°C for one hour and furnace cooled. The specimens were 16.3 mm long and 8 mm in diameter. In each case, displacement, load and inductance were plotted on the top, middle and bottom curves respectively. The second set of curves shows a magnified portion of the first. On the displacement curve 1 mm is represented by 0.1 volts. On the load curve, 10 kN is represented by 1 volt. On the inductance curve, 1 henry is represented by 1 volt.

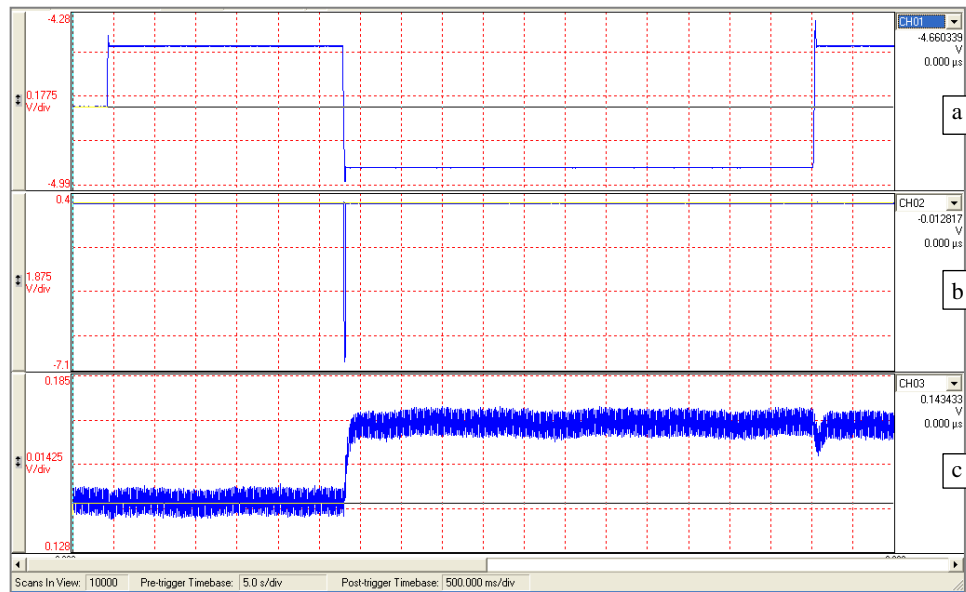


**Figure 3.99:** An example of the Labview result from a high strain rate test. The x-axis measures time in 0.5 seconds per division for all three graphs. The y-axes are: (a) displacement; (b) load; (c) inductance / comparative magnetic permeability.

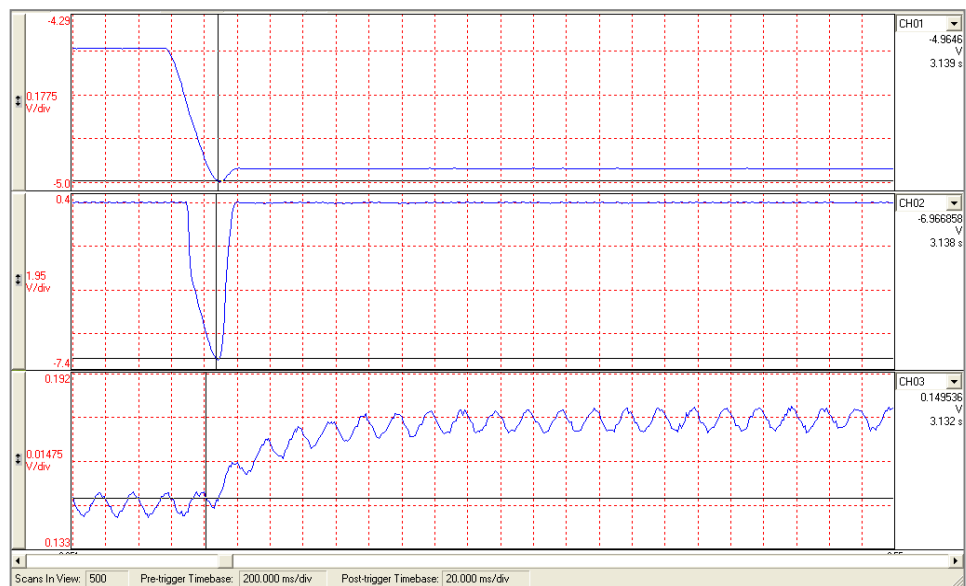


**Figure 3.100:** The same set of graphs as in Figure 3.99 with the x-axis (time) magnified. A displacement of 3.2 mm was thus applied to the 16.3 mm long specimen in 17 ms, equating to a speed of 190 mm/s and strain rate of  $11 \text{ s}^{-1}$ . Y-axes same as in Figure 3.99.

It can be seen that a deformation of 3.2 mm was applied in 17 milliseconds, attaining about 1300 MPa. The total loading time was about 300 ms and peak load was maintained only instantaneously. Deformation was measured only from when load began to increase. Average deformation speed was approximately 190 mm/s, the maximum strain was 0.2 mm/mm and the average strain rate was  $11 \text{ s}^{-1}$ . The measured inductance was 148 mH before deformation and increased by 29 mH after deformation. This compares to a change of approximately 32 mH at 0.2 mm/mm strain during quasi-static ( $0.001 \text{ s}^{-1}$ ), room temperature testing. Thus, the higher strain rate was apparently responsible for an approximately 10% reduction in transformation. If a quasi-static strain rate ( $0.001 \text{ s}^{-1}$ ) calibration curve was used to convert the rapidly deformed material's inductance reading to a strain reading, this scenario would result in an output reading approximately 20% below the true peak load. However, this is an unlikely scenario in that as well as the load being applied extremely rapidly, it is applied for an almost instantaneous period. Further testing showed that when a rapidly applied load is maintained, the effect is not as severe. An increase in strain rate of one or even two orders of magnitude above quasi-static ( $0.001 \text{ s}^{-1}$ ) did not significantly impact results relative to quasi-static variation (Table 3.16). This is probably due to frictional heating having an exponentially greater impact on localised specimen temperature as strain rate increases.

**Table 3.16: Effect of strain rate on Alloy HM at 20% strain. Tests conducted at room temperature with specimens immersed in heat conductive paste.**

Test strain rate ( $\text{s}^{-1}$ )	Inductance change at 20% strain (mH)	Deviation in inductance change vs. Quasi-static	Resulting equivalent strain output error
0.001	32	0%	0%
0.01	32	0%	0%
0.1	32	0%	0%
11	29	-10%	-20%

Strain rate will therefore have a considerable effect on a device's effective resolution in an environment where the strain rate is completely unpredictable. However, when the strain rate is known to be within a limited range, the resolution is significantly better.

#### **3.4.11 The effect cyclic loading**

No change in inductance was detected during cyclic loading on Alloy HM within the full elastic zone for more than 10 000 cycles conducted on an MTS 312.21. Low strain-rate ( $0.1 \text{ s}^{-1}$ ) cyclic loading into the plastic zone (700 MPa) for 20 cycles showed insignificant deviation from quasi-static results relative to single-load quasi-static repeatability ( $\pm 1\%$  of stress).

### 3.4.12 The effect of circuitous loading

Applying load cycles other than continuously increasing led to unexpected results. In Figure 3.101, a specimen of Alloy V5 was repeatedly loaded to a local peak stress, fully unloaded and then reloaded to a higher local peak stress. This loading regime is referred to as circuitous loading.

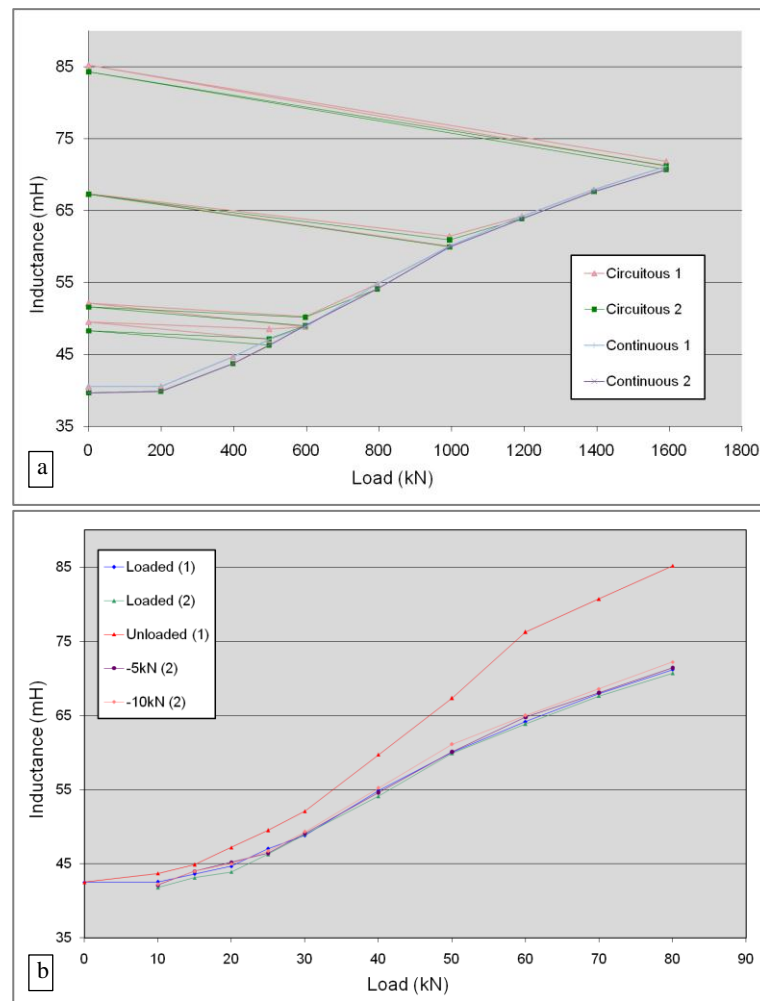


**Figure 3.101: (a) Inductive output versus load during circuitous loading on Alloy V5, including plots of continuously loaded specimens, for comparison; (b) the effect on sensor resolution, showing the potential range of implied stress for a particular measured inductive output (Bemont, 2009).**

It is notable that the profile of the transformation curve is very close to that of its continuously loaded counterpart. However, releasing the load increased the inductance reading, thus mimicking an increase in load from the standpoint of the inductance measurement. This effect was not as prominent in tension as in compression. Considering the magnetic path length of the inductor increases and the magnetically permeable volume within the inductive coil decreases

(due to the regaining of the specimen's elastic strain), the increase in inductance is contrary to expectation. It is possible that the reason for this phenomenon is a small change in the lattice parameters within the material's crystal structure.

According to the circuitous loading curve shown for Alloy V5 at 500 MPa, the additional error due to this phenomenon is 10%, at 650 MPa it is 13% and by 1000 MPa it is over 25%. The inaccuracies due to this phenomenon are in one direction only; the load interpreted from the proposed device may register above the true peak historical load, but never below.

Figure 3.101 (b) depicts the same set of data, but illustrates more clearly how the resolution of the device was affected by more clearly depicting the potential range of implied stress for a particular measured inductive output. It is notable that up to 30% of the load can be released with little effect on the output; only drastically reduced loads substantially affect output readings.

It can be seen from Figure 3.102 that Alloy HM was considerably less susceptible to this circuitous loading phenomenon. Up to 700 MPa, there was almost no error and at 1000 MPa it produced less than 5% error, in a single direction only. Only well beyond 1000 MPa, where it is unlikely to be utilised, did the error become significant. It is currently inconclusive whether this lower susceptibility to circuitous loading was due to microstructural condition, composition or a combination of both. However, the material also showed low early load sensitivity (it has a large incubation period) and had a relatively small useful range.



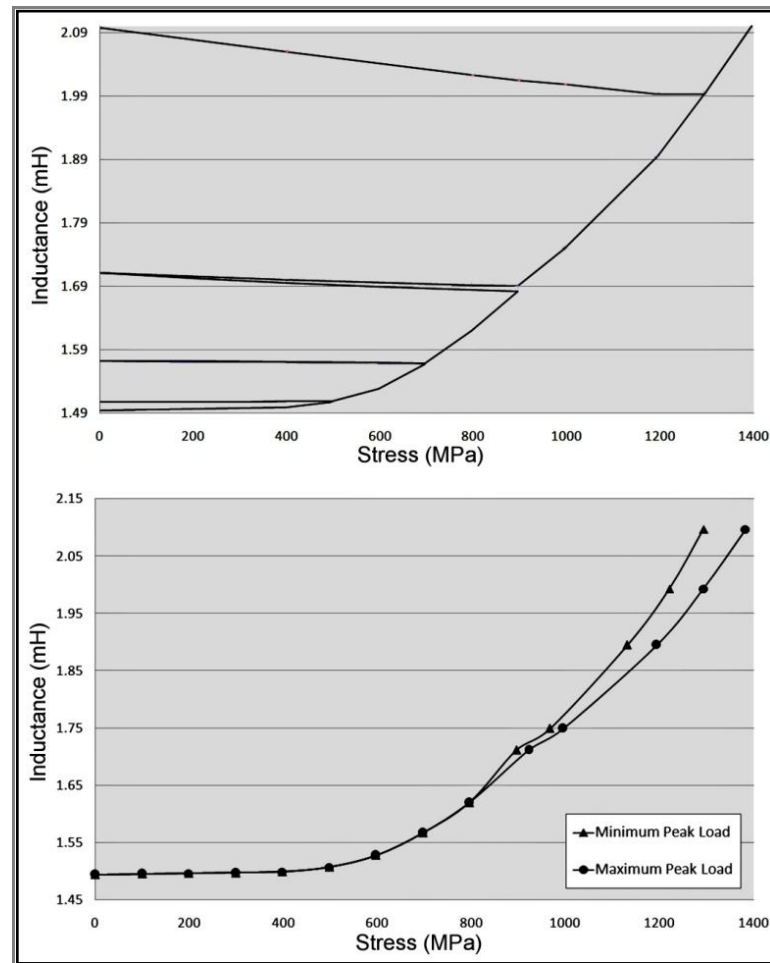


**Figure 3.102: Inductive output of Alloy HM is plotted against load during circuitous loading in a similar manner as was done using Alloy V5 in Figure 3.101 (Bemont, 2009).**

Maxwell and co-workers noted that magnetic permeability could be affected by applied stress directly, without any phase transformation (Maxwell et al., 1974). However, their research showed that releasing the load before taking each magnetic permeability reading using a transformer type monitoring method did not have any apparent effect when compared to uninterrupted tests. In the current experiments, a similar effect was observed in that releasing and then re-applying the load did not change the resultant inductance (Figure 3.101 and Figure 3.102). However, while the load was released, particularly from very high stresses, inductance readings were falsely raised. Olson and co-workers postulated that, in a fashion similar to nickel, the magnetic permeability of martensite has a plastic strain dependence, particularly at high strains (Olson & Azrin, 1978). While the permeability change was not the result of plastic strain but rather of elastic strain in the current work, it is probable that the deformation of the martensitic lattice causes a similar effect whether it is elastically or plastically strained, thereby accounting for the perceived increase in magnetic permeability. This also explains the steeper incline of the curve as the load is released from higher stresses where more martensite is present.

### 3.4.13 Further analysis of compressive testing results

In this section, compression test transformation results were analysed for the various cast alloys in the manner proposed in Section 3.4.2. The three alloys in Table 3.5 and Table 3.6 with an average nickel equivalent and chromium equivalent above 19 (A1c, A3e, A5) were excluded since they were produced through alloying error; alloys in this compositional range were not intended. The two plots shown in Figure 3.103 and Figure 3.104 illustrate that there was no apparent trend when change in inductance at 25% strain was plotted against the average of the nickel and chromium contents. However, a strong linear relationship was shown when total change in inductance was plotted against the average of the nickel equivalent and chromium equivalent (coefficient of correlation 0.9). This is relevant because the nickel and chromium equivalents are directly related to the stability of the austenite and martensite phases on the Schaeffler diagram (Figure 2.26). The averaged nickel and chromium equivalents allow us to relate these results to the Schaeffler diagram.

The observation of a trend with degree of transformation at 25% strain versus the nickel and chromium equivalent average, and no trend when plotted against the simple nickel and chromium content, is indicative that the Schaeffler diagram is functioning as expected. It is also indicative that it may be used as an alloy design instrument and that the approach taken here in attempting to identify valid empirical formulae is relevant. A strong coefficient of correlation of 0.8 was again obtained when change in inductance was plotted against transformation at a stress of 900 MPa, instead of at a strain of 25% (plot not shown).

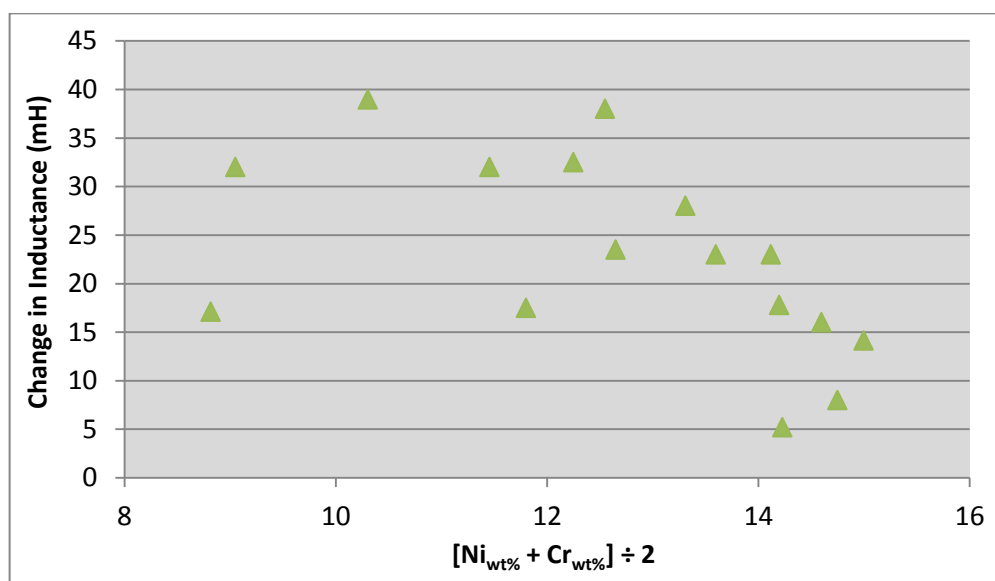


**Figure 3.103:** Change in inductance plotted against the average of each alloy's nickel and chromium contents. The coefficient of correlation of data to a linear fit was 0.4.

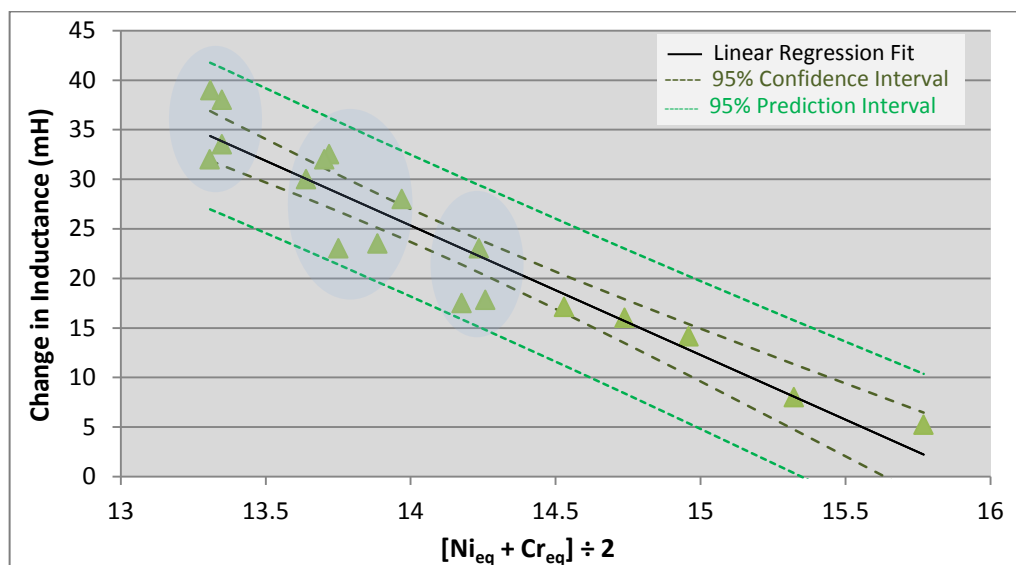


**Figure 3.104: Change in inductance plotted against the average of each alloy's nickel and chromium equivalents (average of nickel and chromium equivalent above 16 not shown). Coefficient of correlation of data to a linear fit was 0.9.**

Formulae predicting  $M_{d30}$  and  $M_s$  that were found in the literature to be relevant for the alloy range are shown in Table 3.3. Figure 3.105 plots the values calculated from the empirical formula for  $M_{d30}$  developed by Pickering (Pickering, 1978) for the respective alloys against their change in inductance at 25% strain. The plot shows a good coefficient of correlation to a linear relationship of 0.8. The plot in Figure 3.106 is for the formula for  $M_{d30}$  developed by Angel (Angel, 1954) against change in inductance at 25% strain. The plot shows a very weak linear relationship, with a coefficient of correlation of 0.4.

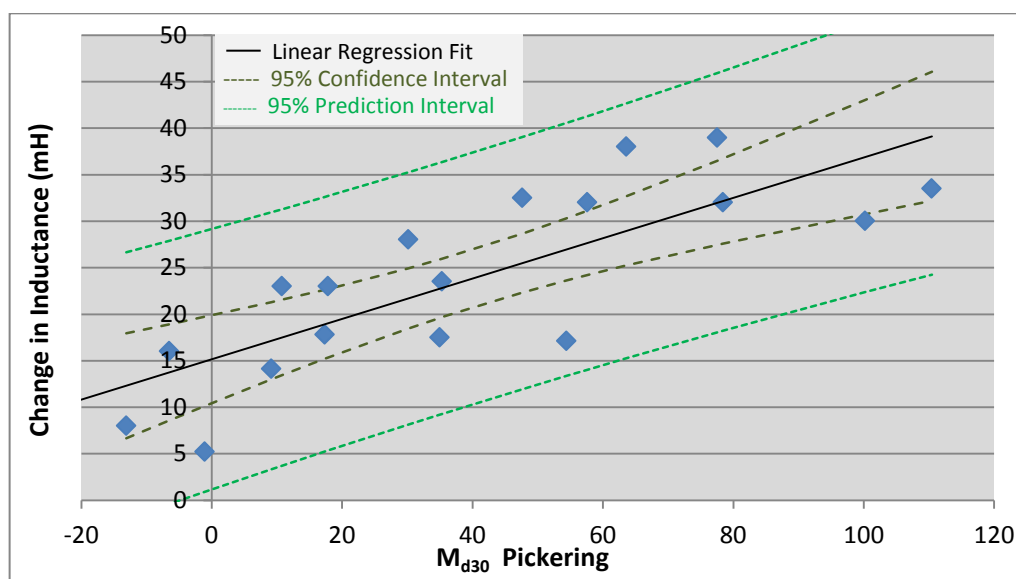


**Figure 3.105: Formula for  $M_{d30}$  proposed by Pickering (Pickering, 1978), showing strong evidence of a linear relationship when plotted against change in inductance. Coefficient of correlation of data to a linear fit was 0.8.**

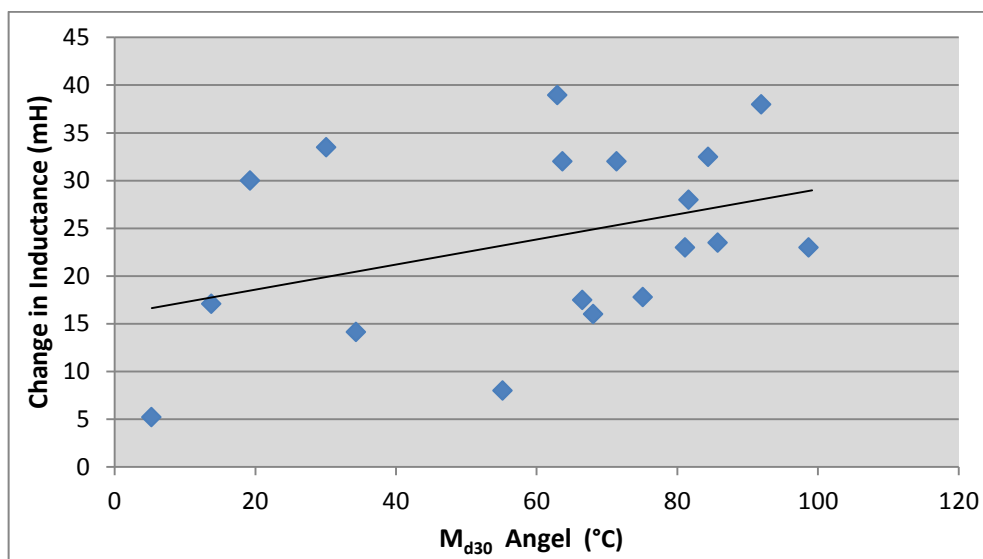


**Figure 3.106:** Formula for  $M_{d30}$  developed by Angel (Angel, 1954), showing some signs of a linear relationship with change in inductance. Coefficient of correlation of data to a linear fit was 0.4.

In Figure 3.107, the formula for  $M_{d30}$  by Nohara (Nohara et al., 1978) is plotted against change in inductance at 25% strain. It shows a some linear relationship to the change in inductance (and associated magnetic permeability) of the tested alloys, with a coefficient of correlation of 0.6. The predicted  $M_{d30}$  temperatures were distinctly low, although it was primarily a trend that was of interest, rather than absolute temperature values.

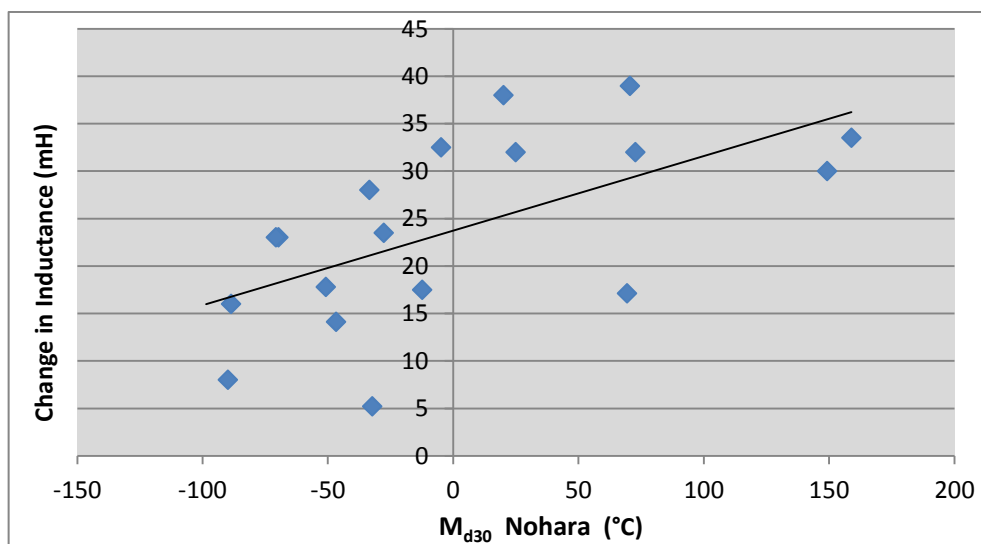


**Figure 3.107:** Formula for  $M_{d30}$  proposed by Nohara (Nohara et al., 1978), showing some signs of a linear relationship with change in inductance. Coefficient of correlation of data to a linear fit was 0.6.

Since the formulae developed by Pickering (Pickering, 1978), Angel (Angel, 1954) and Nohara (Nohara et al., 1978) are empirical, the possibility of adjusting them to more accurately predict the transformation in the current alloys was considered. When an average between that by

Pickering and that by Nohara was taken, there was no improvement. However, when an average between the formula by Pickering and that by Angel was plotted, the result showed a strong linear relationship, with a higher coefficient of correlation (0.95) than either formula alone. Figure 3.108 plots an average of the  $M_{d30}$  temperatures predicted by Angel and by Pickering against change in inductance at 25% strain.

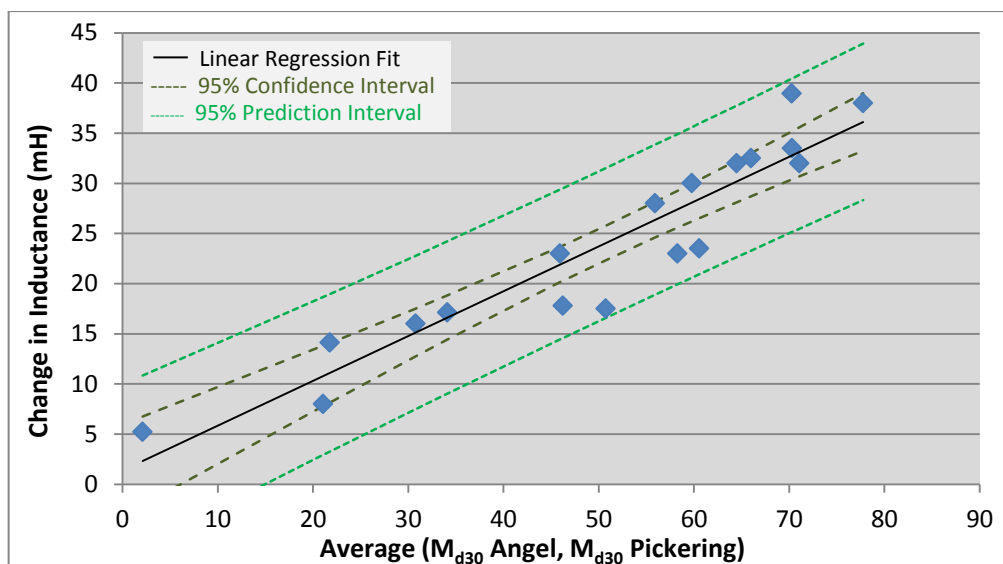


Figure 3.108: Average of  $M_{d30}$  from the formulae developed by Angel (Angel, 1954) and that developed by Pickering (Pickering, 1978), plotted against transformation at 25% strain. Coefficient of correlation of data to a linear fit was 0.9.

Results from empirical and partly empirical formula for  $M_s$  temperature by Cina, Andrews, Hull, Capdevila et al., Stuhlmann and Brooks were tested for linear relationships to degree of transformation in the same way that those for  $M_{d30}$  temperature were tested (Cina, 1954) (Stuhlmann, 1959) (Andrews, 1965) (Hull, 1973) (Brooks, 1996) (Capdevila et al., 2002). The plot in Figure 3.109 represents the values calculated for each alloy from the empirical formula for  $M_s$  proposed by Cina, plotted against the respective alloy's change in inductance at 25% strain. The plot showed a linear relationship with a good coefficient of correlation of 0.9.

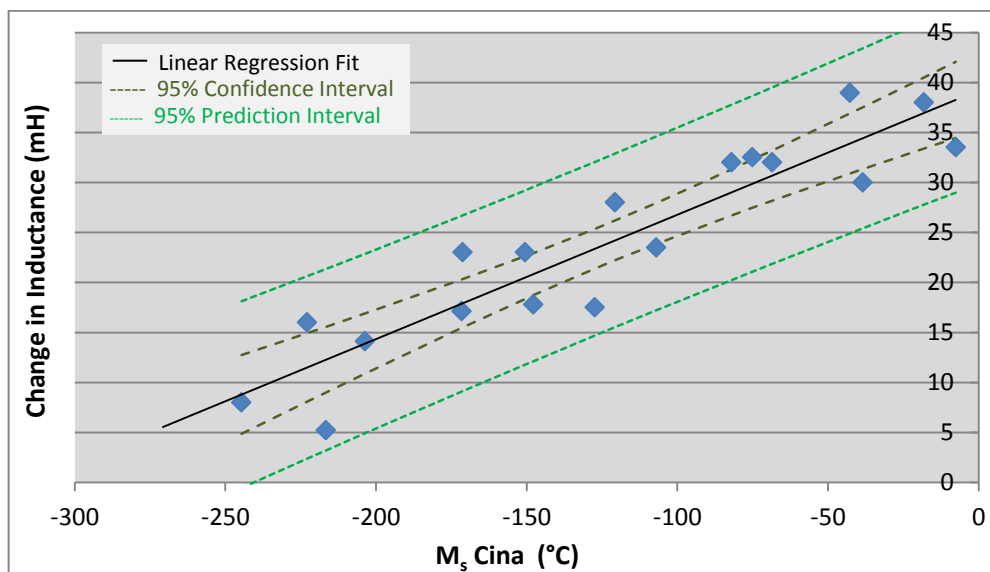


Figure 3.109: Formula for  $M_s$  proposed by Cina (Cina, 1954), showing strong evidence of a linear relationship to transformation, with coefficient of correlation 0.9 (Bemont et al., 2013).

The plot using the formula by Hull showed no significant linear relationship, with a coefficient of correlation of only 0.3 (Figure 3.110) (Hull, 1973). The plots using formulae by Capdevila et al., Stuhlmann, and Brooks showed no discernible relationship to the degree of transformation for the alloys tested (Capdevila et al., 2002) (Stuhlmann, 1959) (Andrews, 1965) (Brooks, 1996). The plot for the formulae by Capdevila in Figure 3.111 is an examples of one that showed no discernible linear relationship to change in inductance at 25%.

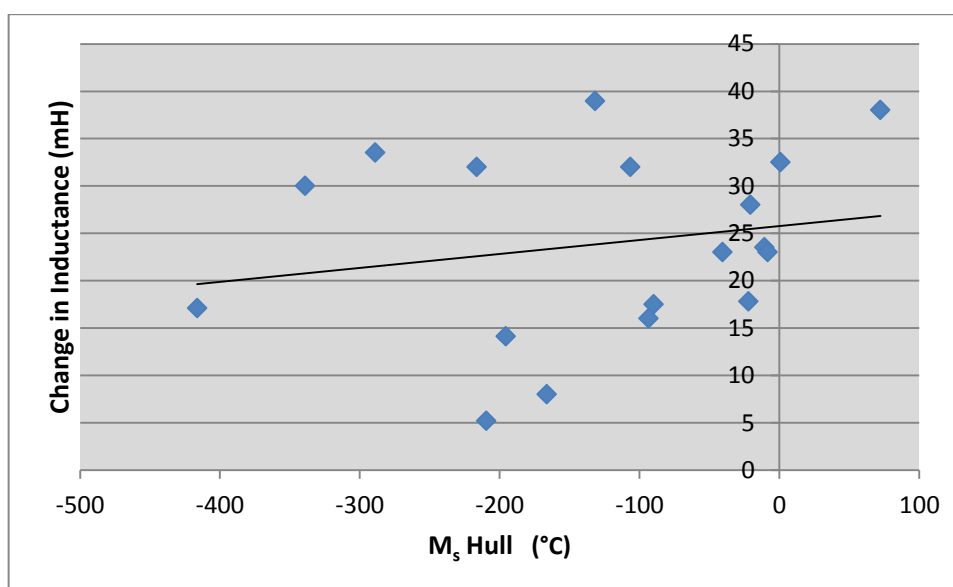


Figure 3.110: Formula for  $M_s$  proposed by Hull (Hull, 1973) showing no significant sign of a linear relationship to transformation, with coefficient of correlation 0.3.



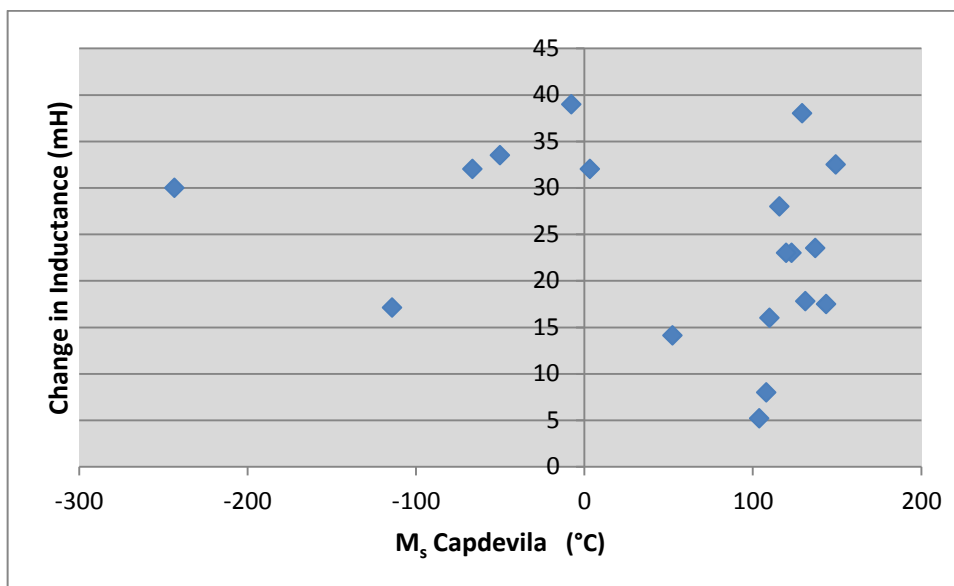


Figure 3.111: Formula for  $M_s$  proposed by Capdevilla (Capdevilla et al., 2002), showing no significant relationship to transformation.

The plot using the formula by Andrews (Andrews, 1965), shown in Figure 3.112, also showed no significant linear relationship to transformation on initial inspection. However, the alloys fell into two distinct groups in this plot and it was determined that these groups were split between those alloys with high manganese (group A, more than 6%) and those with low manganese (group B, less than 1%). Within these groups, there were strong linear relationships to transformation at 25% deformation, as shown in Figure 3.112.

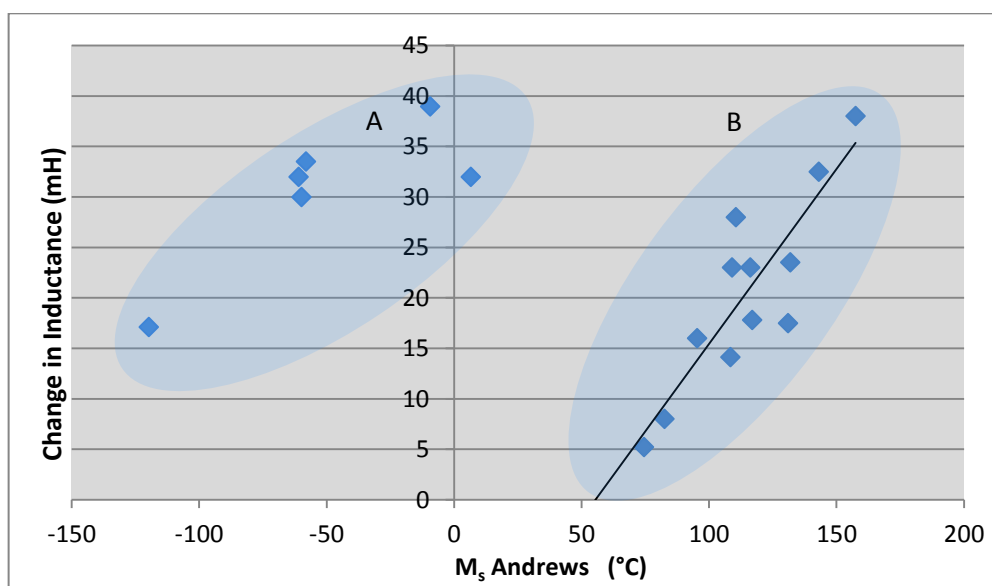


Figure 3.112: The formula for  $M_s$  proposed by Andrews (Andrews, 1965) showed no significant relationship to transformation for the full batch of alloys. However, when split into high manganese (A) and low manganese (B) groups, each group inferred strong linear relationship.

The bar graph in Figure 3.113 shows the  $M_{s\_Cina}$  and  $M_{d30\_Pickering}$  temperature range for the cast alloys tested in compression. Group A includes the inductance furnace cast alloys, cast early in the project. Alloy V6 (Table 3.4) was not included because it showed no significant deformation induced transformation, its  $M_{s\_Cina}$  temperature was well above its  $M_{d30\_Pickering}$  temperature (25°C).

Group B includes the arc-furnace cast alloys, those primarily analysed in this section. A comparison between the alloys, particularly within group B, shows that those exhibiting high levels of transformation generally had  $M_s$  and  $M_{d30}$  closer together than those exhibiting poor transformation. In comparing the formulae for  $M_{s\_Cina}$  and  $M_{d30\_Pickering}$ , the reasons for this became apparent since a three to four times more rapid decrease in  $M_s$  than in  $M_{d30}$  was expected with increasing alloy content. Thus, the difference between  $M_{s\_Cina}$  and  $M_{d30\_Pickering}$  became larger as more alloying elements were added, reducing temperature sensitivity. However, as seen from the Schaeffler diagram, an addition of alloying elements also rapidly increased austenite stability in this alloy range, thus impeding transformation.

In Figure 3.114, the difference between  $M_{s\_Cina}$  and  $M_{d30\_Pickering}$  was plotted against the change in inductance at 25% strain for the alloys tested. It clearly shows a strong linear relationship, with a coefficient of correlation above 0.9. A narrower temperature band between  $M_s$  and  $M_{d30}$  generally corresponded to a more rapid transformation. According to theory proposed in Section 3.3.2, this is probably detrimental for producing an alloy that shows good transformation while also being insusceptible to environmental temperature fluctuation.

Manganese reduces  $M_{s\_Cina}$  at four times the rate that it reduces  $M_{d30\_Pickering}$ , whereas other alloying elements reduce  $M_{s\_Cina}$  at about three times the rate that they reduce  $M_{d30\_Pickering}$ . Thus, manganese may be utilised to increase the difference between  $M_s$  and  $M_d$  more quickly than other alloying elements. Additionally, manganese also increases the austenite stability half as fast as nickel does according to the Schaeffler equations. Thus, for the combination of these two characteristics, manganese is again identified as an ideal candidate alloying element.

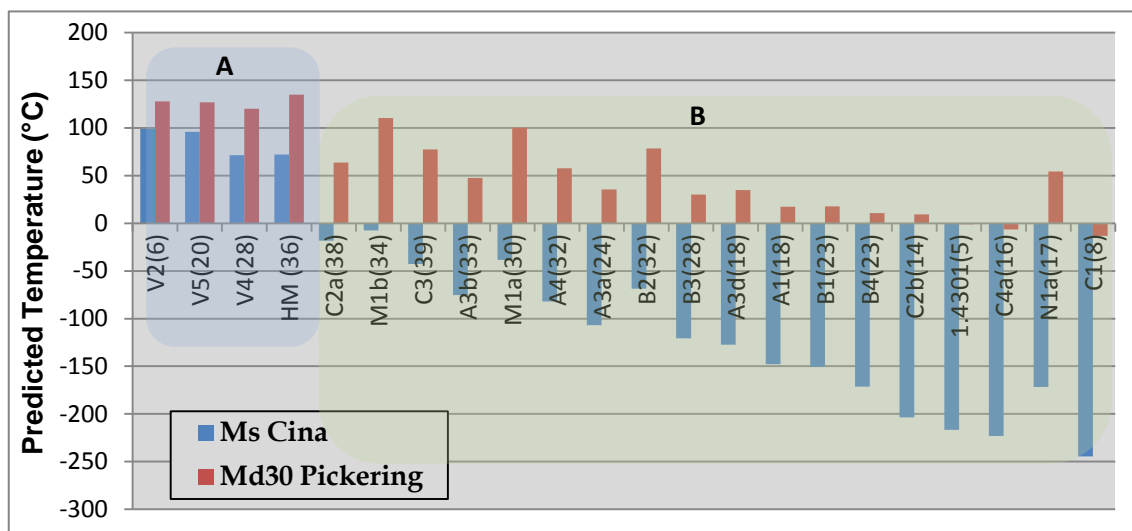


Figure 3.113: Bar graph showing temperature difference between  $M_{s\_Cina}$  and  $M_{d30\_Pickering}$  (in increasing order) for compressive alloys. Group A includes the early inductance-furnace cast alloys. Group B includes the arc-furnace cast alloys.

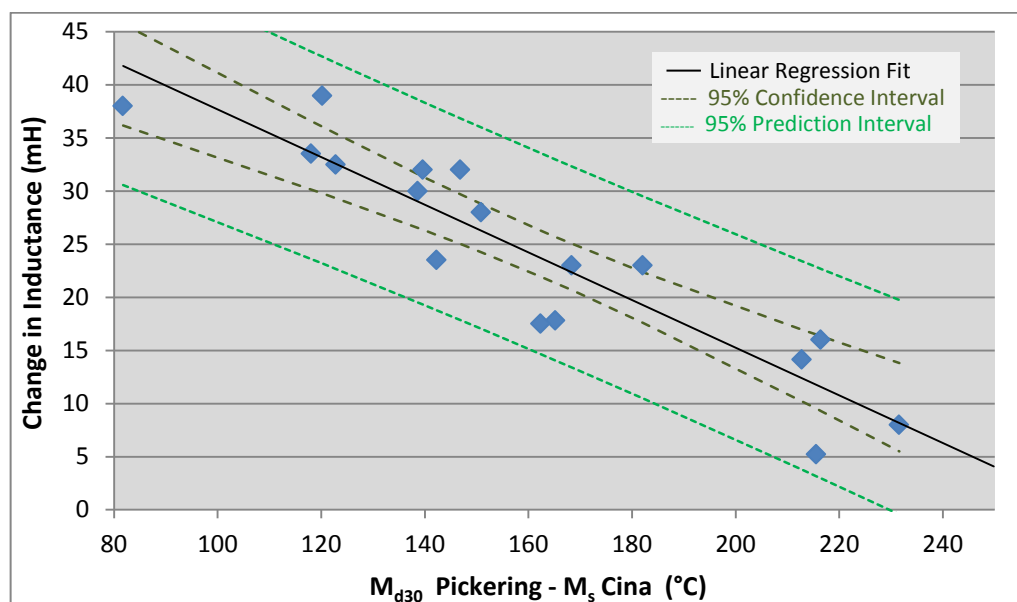


Figure 3.114: Difference between an alloy's  $M_{d30\_Pickering}$  and  $M_{s\_Cina}$  temperatures, showing overwhelming evidence of a linear relationship to change in inductance (transformation) during deformation to 25% strain. Coefficient of correlation of data, 0.9 (Bemont et al., 2013).

Figure 3.115 shows the same properties for a narrower range of alloys. Alloys that underwent a good inductive change while also having a large difference between  $M_{s\_Cina}$  and  $M_{d30\_Pickering}$  temperatures were included. Alloy V2 and Alloy HM (group A) were also included since temperature testing had previously been undertaken on these alloys.

Of the group B alloys in Figure 3.115, the best performing alloys, were high in manganese. All of the high manganese alloys also showed a large difference between their  $M_s$  and  $M_{d30}$  temperatures. Of these, all but one alloy (N1) also showed strong transformation. Comparing

this plot to the transformation versus deformation plot in Figure 3.16 showed that alloys with early transformation (low incubation strain) have their  $M_s$  temperature closer to ambient temperature.

When environmental temperature is above  $M_d$  or below  $M_s$ , then transformation sensitivity would clearly be affected, since it would respectively either cease or occur partially spontaneously. Thus positioning the operating temperature range away from both  $M_s$  and  $M_{d30}$  was expected to reduce the effect of temperature on transformation. After considering all of these factors, Alloy B2 showed good overall transformation, early transformation, ambient temperature between  $M_s$  and  $M_{d30}$  and a large difference between  $M_s$  and  $M_{d30}$ , and is probably the best of these alloys to implement in compressive strain sensors.

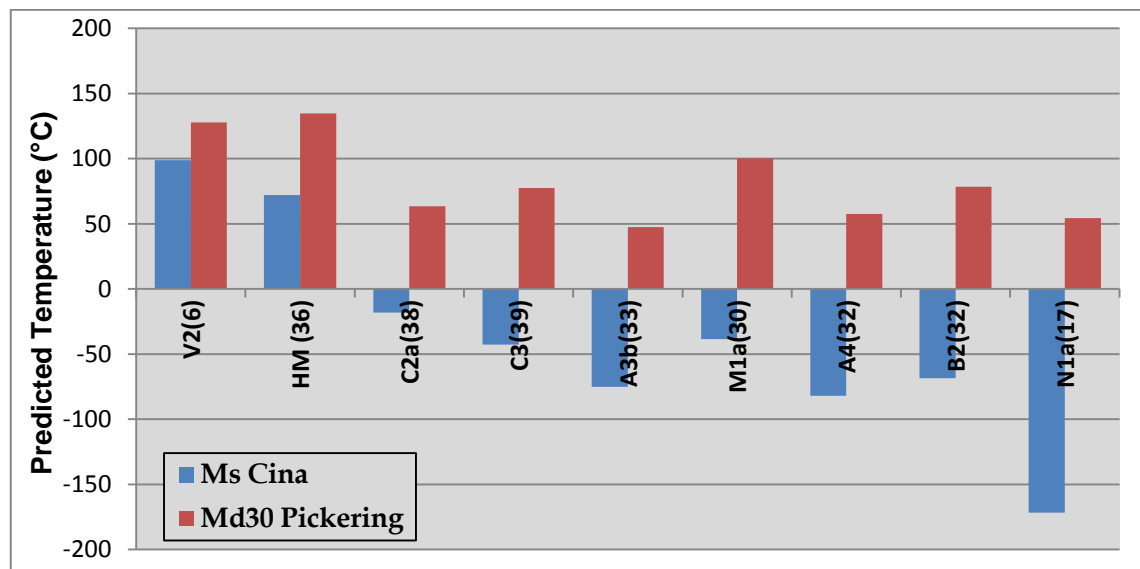
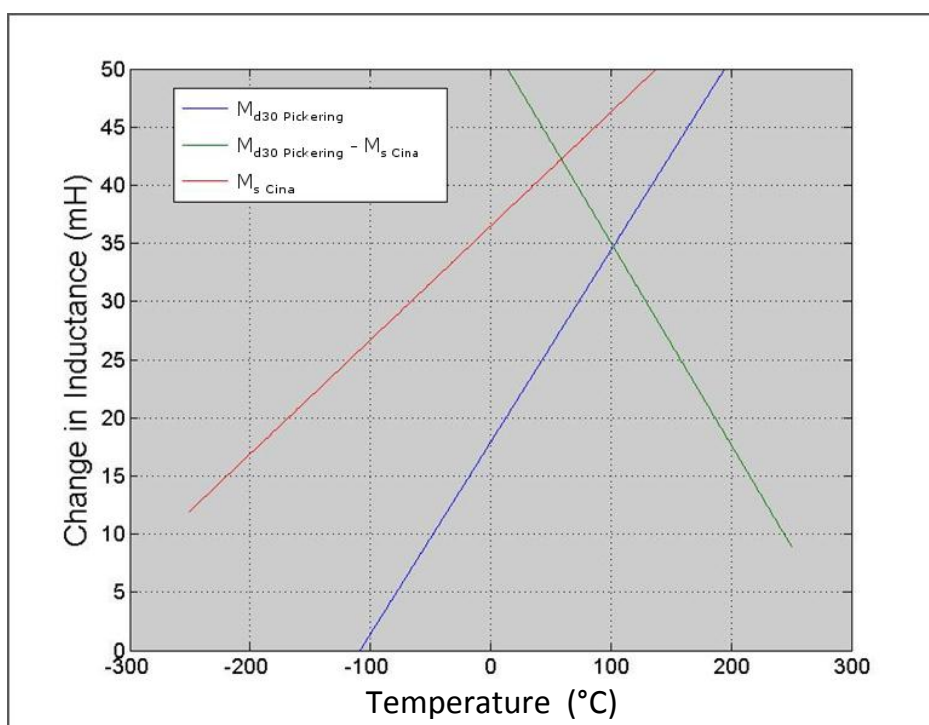


Figure 3.115: Bar graph showing temperature difference between  $M_s$  Cina and  $M_{d30}$  Pickering (in increasing order) for a selection of alloys, showing the alloy's total inductive change in brackets.

The magnitude of the difference between these predicted temperatures ( $M_{d30\_Pickering}$  and  $M_{s\_Cina}$ ) and the observed change in inductance also showed a strong inverse linear relationship with relatively small standard error. A smaller difference ( $M_{d30} - M_s$ ) predicted a better transformation. However, as discussed in Section 3.3.2, it is hypothesised that when  $M_s$  and  $M_{d30}$  are close together, a change in environmental temperature will more severely affect rate of transformation. This is because the free energy difference between austenite and martensite will vary more slowly with temperature when  $M_s$  and  $M_{d30}$  are far apart as in part (d) in Figure 3.4, Section 3.3.2. Thus, the deformation energy ( $U$ ) required to initiate the transformation will also vary more slowly with temperature.

A quandary thus exists in that improving rate of transformation is predicted to generally increase temperature susceptibility. Thus, a compromise must be reached. An alloy that operates near its  $M_{d30}$  temperature is not expected for this reason alone to be highly temperature susceptible, as long as the  $M_d$  temperature is never exceeded. An alloy operating below its  $M_s$  temperature is not expected, for this reason alone, to be highly temperature susceptible, although a reduction in temperature to below all previous temperatures would be expected to produce some martensite (the quantity produced would depend also on  $M_f$  temperature). It may be deduced from the gradients of the linear regression plots shown in Figure 3.116 (originating from the arc-furnace cast alloy data) that increasing  $M_{d30}$  temperature more rapidly improves transformation than does increasing  $M_s$  temperature. Thus, increasing  $M_{d30}$  temperature while holding  $M_s$  temperature constant, or even increasing it by a similar absolute amount, may improve temperature sensitivity without negatively affecting transformation, as depicted in Figure 3.116. This proposition is also supported by the energy diagram theory, part (d) in Figure 3.4, Section 3.3.2.



**Figure 3.116: Linear regression fits for  $M_{d30}$  Pickering, for  $M_s$  Cina and for the difference between  $M_{d30}$  Pickering and  $M_s$  Cina.**

Since the alloy will usually be utilised at, or slightly above, room temperature, to reduce temperature susceptibility,  $M_s$  should thus be as far below and  $M_{d30}$  as far above this temperature as feasible. The proportion of elements that reduce  $M_s$  faster relative to  $M_{d30}$  might be increased. Considering ratios, manganese reduces  $M_s$  relative to  $M_{d30}$  approximately 30% faster than other elements. Increasing manganese content with the aim of reducing the effect of

temperature and strain rate on the transformation is in line with some other empirical and theoretical conclusions derived via different routes (Section 2.6) (Olson & Cohen, 1975).

An increase in carbon or nitrogen content is similarly inferred to reduce  $M_s$  15% faster than average relative to  $M_{d30}$ . However, carbon and nitrogen have other effects on alloy properties, some of which may be detrimental to the transformation. They are expected to increase yield strength and will rapidly increase Schaeffler nickel equivalent. As previously mentioned, such detrimental effects of carbon may be observed in the current experimental data where alloys that are otherwise similar show slower transformation when they have higher carbon contents.

The above analysis is based on all deformed specimens having undergone a similar extent of compressive deformation, approximately 25%. However, casting porosity was of concern since it may reduce the level of true deformation in the structure. In order to test the significance of this effect, similar analyses were performed relating specimen stress to transformation, instead of specimen strain. It is expected that stress would be minimally affected by porosity compared to strain, since a significantly porous region would be expected to collapse in compression, and become effectively solid before attaining a given stress. Sectioning of specimens during machining and microscopic examination revealed no porosity.

Plots comparing stress instead of strain to transformation were performed and showed very similar trends to the strain-transformation plots. The same empirical equations were identified as being most relevant. It is also significant that specimens from the same ingot gave similar results. If porosity was significant, then certain parts of an ingot would be expected to be substantially more porous than others, as found during early ingot design, where porosity was nearly always found lower down in the upright-cast ingot bar. Thus, specimens machined from different parts of the same ingot would be expected to give different results at a particular strain if significant porosity was present.

Figure 3.117 shows a plot of an average of the  $M_{d30}$  temperature predicted by Angel and by Pickering versus change in inductance at 900 MPa compressive stress (Angel, 1954) (Pickering, 1978). This plot is similar to that observed in Figure 3.108 at 25% strain, and shows a similarly high coefficient of correlation to a linear relationship of 0.9.



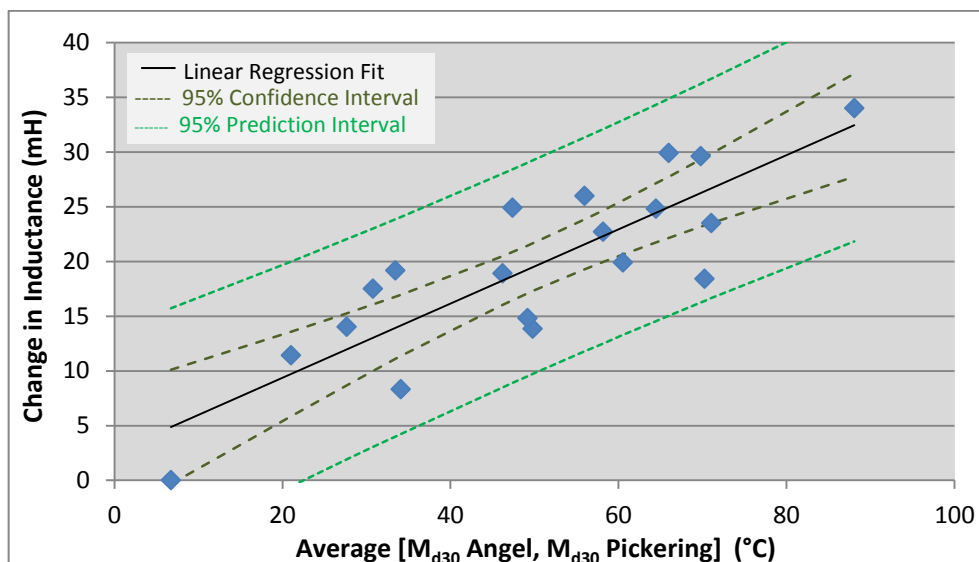


**Figure 3.117:** Plot of an average of the  $M_{d30}$  temperature predicted by Angel (Angel, 1954) and by Pickering (Pickering, 1978) versus change in inductance at 900 MPa compressive stress. Coefficient of correlation of data, 0.9.

Figure 3.118 shows an average of  $M_{s\text{Cina}}$  (Cina, 1954) versus change in inductance at 900 MPa. Coefficient of correlation to a linear relationship is 0.7. The plot for  $M_s$  temperature predicted by Andrews (Andrews, 1965) versus change in inductance at 900 MPa again showed two distinct alloy groups, which each showed a strong linear relationship with change in inductance at 900 MPa.

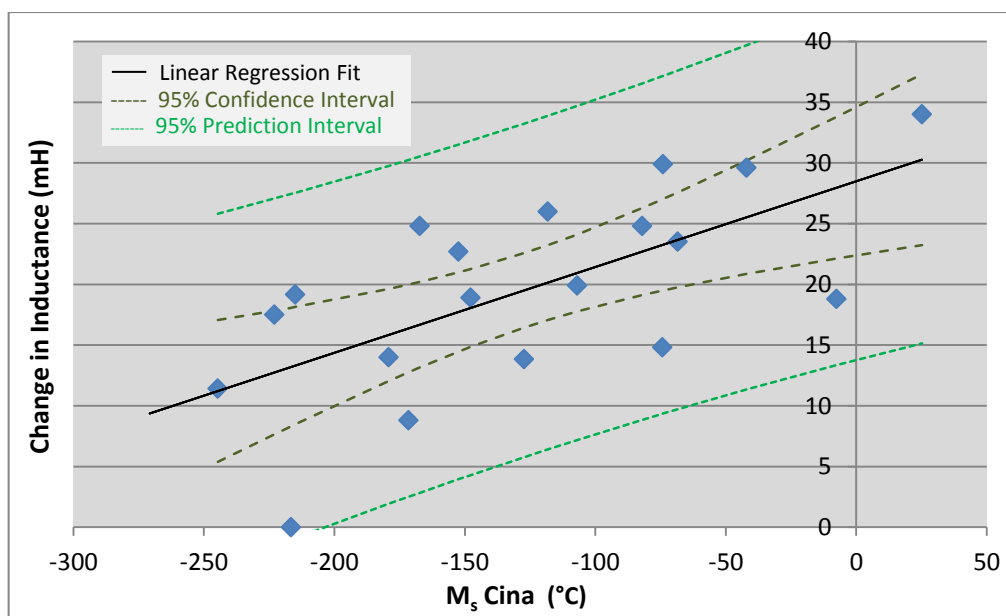


**Figure 3.118:** Plot of an average of the  $M_s$  temperature predicted by Cina (Cina, 1954) versus change in inductance at 900 MPa compressive stress. Coefficient of correlation of data, 0.7.

#### 3.4.14 Conclusions and further work

It was anticipated that alloy composition and processing could be refined in order to optimise cast compressive TRIP steels for sensor applications. Such TRIP steels should show greater, more easily detectable and repeatable transformations, and less sensitivity to uncontrollable conditions, such as environmental temperature and strain rate, or a balance between these two ideals.

An energy diagram approach was used to reach the hypothesis that the transformation temperature sensitivity of TRIP steel alloys could be minimised by manipulating  $M_f$ ,  $M_s$  and  $M_d$  through alloy composition and processing control (Section 3.3.2). In order to allow the design of alloy compositions according to this hypothesis, empirical equations to determine  $M_s$  and  $M_{D30}$  temperatures for the alloy group of interest needed to be identified. Since these parameters were shown to also directly influence the rate of transformation with deformation, it was proposed that the relevance of the equations might be identified via the analysis of alloy transformation data (Section 3.4.2).

Initially, several alloy compositions were carefully planned, with small compositional tolerances, to allow the interpretation of the effects of individual alloying elements and of position on the Schaeffler diagram, as well as to test which empirical equations found in the literature for  $M_{d30}$  and  $M_s$  were most appropriate for the targeted alloys. In practice, the alloys could not be cast with the level of composition accuracy required. However, while not precise, compositional spread and variation was close to that targeted, and this meant that analyses similar to those planned could be performed.

It was decided that alloys used in compression should, if possible, be applied in an as-cast or at most, a cast and heat-treated state, in order to substantially reduce the material cost, particularly in low volume production, as opposed to utilising the material hot or cold worked, as is usually done. Potentially near-complete smart load cells might then be cast directly, reducing costs even further.

There were no easily obtainable as-cast metastable alloys available to purchase and no information was found regarding such alloys. It was hypothesised that because the cast alloys would exhibit substantially lower yield points but not substantially lower UTS values in compression, they would be likely to have another advantage over wrought alloys in that their range would be greater. When the first as-cast alloys were tested in compression, this was substantiated.

Alloy transformation test results showed that there was a wide variation in the rate of transformation of the various alloys (Section 3.4.5). Some alloys transformed very slowly initially, but continued to transform steadily (e.g. Alloys A4 and C2a), while others never attained high levels of transformation (e.g. Alloy N1). Other alloys transformed rapidly and then transformation slowed notably at high strains (e.g. Alloy M1a). Specimens cut from the same ingot were found to show very good repeatability.

Casting porosity was of concern since certain ingots were found to have high porosity early on. However, alteration of the drop-casting mould, melting time and other parameters reduced this. This was later verified through comparison of strain versus transformation and stress versus transformation curves, as well as by microstructure examination.

Results of metallographic examination corresponded to the inductance measurements, as discussed in Section 3.4.6. Alloys that had a strong tendency to form  $\alpha'$  from  $\gamma$  were seen to exhibit considerably increased proportions of martensite in their microstructures after compressive deformation. XRD results also generally corresponded to inductance measurements but were not considered accurate quantitatively (Section 3.4.7).

The effects of temperature fluctuation on the apparatus and on the TRIP steel specimens was measured (Section 3.4.8). Temperature fluctuation at time of measurement between -20°C and 120 °C was found not to affect inductance readings. Temperature cycling of Alloy HM between -40°C and 80°C was found to produce no transformation after 100 cycles.

Specimen temperature at the time of deformation is well known to affect transformation (Bressanelli & Moskowitz, 1966) (Olson & Cohen, 1975) (Section 2.5 and Section 2.6). This phenomenon was studied on two alloys. Alloys V2 and HM were selected primarily due to their availability. Most other alloys had been manufactured in very small quantities due to the equipment available (Section 3.4.3).

Temperature testing on Alloy V2 revealed considerably larger errors over a given temperature range compared to alloy TRIP M. Total error between 25°C and 90°C was  $\pm 19\%$  for Alloy V2 compared to  $\pm 13\%$  for Alloy HM. Over the temperature fluctuation of a few degrees expected to occur in underground mines (Florides & Kalogirou, 2005) (Minnie, 2005) (Oelofse, 2005), errors due to temperature are expected to be less than  $\pm 5\%$ . However, most other applications

will be subject to considerably greater temperature fluctuations. Alloy HM showed an error of  $\pm 17\%$  between  $-15^{\circ}\text{C}$  and  $90^{\circ}\text{C}$ .

In conclusion, the analysis of alloys in this section established that the empirical equation by Pickering (Pickering, 1978) was most likely to be a good predictor of  $M_{d30}$  temperature and that the empirical equation by Cina (Cina, 1954) was most likely to be a good predictor of  $M_s$  temperature. Alloy V2 showed an  $M_{s\_Cina}$  of  $99^{\circ}\text{C}$  and an  $M_{d30\_Pickering}$  of  $128^{\circ}\text{C}$ . These two formulae were only shown to have relevance after the transformation temperature testing was already conducted on this alloy. It is notable that the gap between these two characteristic temperatures was small, only  $29^{\circ}\text{C}$  and that the testing temperatures were below or closely approaching  $M_s$ .

As illustrated in Figure 3.115, many other alloys exhibiting good transformation performance had considerably larger differences between their  $M_{s\_Cina}$  and  $M_{d30\_Pickering}$ , of  $100^{\circ}\text{C}$  to  $170^{\circ}\text{C}$ . For some of those alloys (Alloy B2 in particular), an operating range of  $-5^{\circ}\text{C}$  to  $40^{\circ}\text{C}$  would fall in the middle of their  $M_s - M_{d30}$  range. These predicted values may well imply considerably less temperature sensitivity in such alloys than was found in Alloy V2. Alloy HM (abbreviated to “HM” in Figure 3.115) was also found to have a relatively small difference between  $M_{s\_Cina}$  and  $M_{d30\_Pickering}$ , although it was double that of Alloy V2. It was found to exhibit substantially lower temperature sensitivity than Alloy V2. It is thus possible that two of the more temperature sensitive alloys were inadvertently selected for this testing.

Analysis of the effects of high strain rate, conducted on Alloy HM, was as expected in that it was similar to the effect of increasing specimen temperature (Section 3.4.10). At a strain rate of  $11\text{ s}^{-1}$  (equivalent to  $190\text{ m/s}$ ), transformation was reduced by approximately 10% compared to the quasi-static scenario ( $0.001\text{ s}^{-1}$ ). Unfortunately, due to the gradient of the inductance (transformation) versus strain curve being less than 1, this 10% reduction in transformation would translate into a 20% error in the output strain or load reading from a TRIP steel based sensor device. Under less severe strain rate increases of one or two orders of magnitude (as opposed to four), the impact on the degree of transformation can be expected to be significantly lower. This is probably due to frictional heating having an exponentially greater impact on localised specimen temperature as strain rate increases.

Cyclic load testing on Alloy HM within the full elastic zone for more than 10 000 cycles revealed no change in inductance (Section 3.4.11). Cyclic loading into the plastic zone revealed no significant increase in transformation upon repeated cycling to a set stress.

The effects of circuitous loading on the transformation were initially examined on Alloy V5 (Section 3.4.12). From these results, the effects of circuitous loading was found to be severe. However, experimentation utilising Alloy HM found these effects to be drastically lower, with the effect insignificant below about 750 MPa (Section 3.4.12). This phenomenon is not well understood, but may relate to the effects of elastic loading on the magnetic properties of the material's crystal structure. It is also possible that these effects are related to experimental setup, and the manner in which the compression platens and TRIP steel element move in relation to the sensor coil when load is applied and released elastically. It was attempted to minimise such phenomena by using non-magnetically permeable platens and by altering platen, coil and element geometry in the test rig, as well as in sensor devices. However, the effect could not be completely prevented. It is believed that the effect would also occur in commercialised sensor devices that operate in compression, and must therefore be accounted for.

Table 3.17 and Table 3.18 reflect the predicted errors accumulated from various characteristics of TRIP steel transformation and thereby give an estimated overall precision for the proposed sensor elements. This precision would eventually translate into instrument resolution. Table 3.17 estimates the worst case scenario, while Table 3.18 estimates a more likely scenario in a mining environment. Some errors are not accumulative, for example the error due to a released load is always positive, but error due to a high strain-rate is always negative.

**Table 3.17: Precision of proposed TRIP steel sensor elements - probable scenario for a range of engineering infrastructure.**

	<b>Quasi-static</b> (room temp, continuous)	<b>Temperature</b> (100°C fluctuation)	<b>Strain rate</b> (4 orders of magnitude)	<b>Circuitous</b> <b>loading</b> (complete release)	<b>Cyclic</b> <b>loading</b>	<b>Overall</b> <b>Precision /</b> <b>Resolution</b>
<b>Error</b> (% of Stress)	±1	±17	-10	+5	±1	<b>+28, -23</b>

**Table 3.18: Precision of proposed TRIP steel sensor elements - estimated scenario for a deep mining application.**

	<b>Quasi-static</b> (room temp, continuous)	<b>Temperature</b> (20°C fluctuation)	<b>Strain rate</b> (2 to 3 orders of magnitude)*	<b>Circuitous</b> <b>loading</b> (complete release)	<b>Cyclic</b> <b>loading</b>	<b>Overall</b> <b>Precision /</b> <b>Resolution</b>
<b>Error</b> (% of Stress)	±1	±5	Negligible	+3	Negligible	<b>+9, -6</b>

\*For the smart face plate, as discussed in Section 4.3.6.

Since several formulae for  $M_{d30}$  and  $M_s$  were proposed by different authors for the range of alloys of interest (Section 2.6), and since each author utilised limited experimental results from literature to verify their formula, it was necessary to test these formulae by way of experimentation, to determine which most accurately describe the current alloy group. The analyses applied to determine whether empirical equations might be relevant for predicting properties of the alloy system showed that the equation for  $M_{d30}$  temperature by Pickering (Pickering, 1978) and that for  $M_s$  by Cina (Cina, 1954) were most likely to be relevant (Section 3.4.13). This same result was attained when analysing for transformation at constant strain or at constant stress.

In utilising  $M_{d30}$  Pickering and  $M_s$  Cina to determine the likely temperature sensitivity of the various alloys, according to the proposed energy diagram theory (Section 3.3.2), certain alloys were identified as likely to show good transformation characteristics as well as lower temperature sensitivity and thus also lower strain rate sensitivity. When other important characteristics such as early transformation was included, Alloys A3, B2, B3 and C2 performed best, with Alloy A4 also performed very well. Alloys B3 and C2 showed a large difference between their  $M_s$  and  $M_{d30}$  temperatures and although their  $M_{d30}$  temperatures were only marginally above room temperature, this implies that their  $M_d$  temperatures should be well above room temperature. However, the absolute accuracy of the predicted  $M_{d30}$  and  $M_s$  temperatures are unknown. Alloy C2 also tied for highest transformation at 25% strain with Alloy C3.

Alloy transformation performance was also used in an attempt to analyse for individual elemental contributions, as originally intended (Section 3.4.1). Alloys M1b and C3 showed very similar nickel and chromium equivalents through significantly different compositions, as did Alloys B3, N1a and C2, as well as Alloys A3d and B4. Carbon, manganese and nickel are the primary differentiating elements, with chromium also varying significantly, but to a lesser extent. The assessment showed that higher carbon alloys tended to result in lower transformation at a given stress or strain. This is as expected, since carbon tends to increase strength, thus impairing dislocation movement and nucleation sites for transformation.

Alloys high in manganese tended to show slightly lower transformations than similar alloys with more nickel. Although the high manganese alloys did not show the largest difference between  $M_{d30}$  and  $M_s$  temperatures, five of the six high manganese alloys were in the group of alloys selected for possessing a good combination of high transformation and a large difference between  $M_{d30}$  and  $M_s$  temperatures (Figure 3.115), implying low temperature sensitivity. It is



proposed that manganese may be beneficial in that it may separate  $M_d$  and  $M_s$  as described in Section 2.5, and thus reduce temperature sensitivity.

The effect of annealing on an alloy's transformation temperature sensitivity was also investigated. It slightly reduced temperature sensitivity, in line with the hypothesis that annealing reduces dislocation density, thereby reducing  $M_f$ .  $M_s$  would be largely unchanged during annealing, due to there remaining a small number of dislocations or otherwise favourable low energy nucleation sites. Thus, since  $M_s$  and  $M_f$  would separate, temperature sensitivity would be reduced.

The magnitude of the difference between the  $M_{d30\_Pickering}$  and  $M_{s\_Cina}$  predicted temperatures showed a strong linear relationship with relatively small standard error to the observed change in inductance. A smaller difference between  $M_{d30}$  and  $M_s$  predicts a better transformation, but possibly also greater temperature sensitivity.

In the future,  $M_s$  and  $M_{d30}$  temperatures might be directly measured to determine the accuracy of the empirical equations, and also to properly test the hypothesis that alloys with greater differences between  $M_s$  and  $M_{D30}$  will show less transformation temperature sensitivity.

Warm compressive deformation (warm meaning well below austenitizing temperature, but above  $M_d$ ) may serve to strengthen the austenite by a combination of dislocation generation and carbide precipitation (Zackay et al., 1967). The fine carbide precipitates found in TRIP steels would be expected to increase the dislocation concentration, thus promoting the deformation-induced transformation.

Significant further experimental work is required to establish the absolute accuracy of the identified empirical equations in the alloy range of interest. Further experimental work will also be required to determine to what extent the above approach can be utilised to reduce transformation temperature sensitivity. Utilising the current results, it will be possible to meaningfully improve the resolution and range of the devices through further alloy refinement.

### **3.5 Hot rolled tensile alloy**

#### **3.5.1 Introduction**

The aim of the tensile alloy design was to produce a TRIP steel alloy to form a smart sensor element within a rock reinforcement tendon as described in Section 4.3. Alloys utilised in tension require hot or warm work to obtain the necessary tensile strength, as demonstrated in Figure 3.5 where an as cast alloy was tested in tension with very poor results. As was done for compression testing, it was attempted to use tensile test specimens of similar physical dimensions to those that would be required for implementation of the practical application envisaged.

Specimens took the form of standard tensile test specimens according to ISO 6892-1 and 6892-2. It was thus not possible to melt alloys for tensile applications in the small arc-furnace that was used for melting most of the compressive alloys. Even the UKZN inductance furnace, at a maximum of 7kg, was considered small for the application, since a full set of test specimens was required from a single melt because it is not possible to obtain the identical composition in a second melt.

The work in Section 3.3, along with that in Section 3.4.2, Section 3.4.8, Section 3.4.9 and Section 3.5.9 constituted journal paper 1 (The effects of transformation temperature on the rate of transformation in TRIP steels), included as submitted in Appendix 3 (Bemont et al., 2013).

#### **3.5.2 Alloy investigation**

The fundamental concepts on which the tensile alloys were selected and designed were similar to those used for the compression alloys. A similar set of design criteria and empirical formulae were utilised, described in Sections 3.2 and 3.3. In designing and selecting a TRIP steel alloy to be utilised in tension as a deformation sensor, theory and empirical formulae from the literature were combined with practical experimentation. In order to be successful in the intended application as the smart element in a mining bolt, the new material would need to display early transformation, strong transformation over a wide range of stress, as well as the lowest possible environmental temperature and strain-rate sensitivity. It should also have mechanical properties at least equivalent to the HSLA alloys widely used in structural reinforcement.

The transformation curves of available metastable alloy steels were measured in order to gain a practical understanding of the material and transformation characteristics. Alloys tested in this

fashion included ANSI 304 stainless steel, DIN 1.4301 stainless steel and TRIP M. Alloys were tested in a hot rolled and water-quenched condition. TRIP M was later also tested in various other conditions (Section 3.5.9). TRIP M was produced by Mintek early in this project, while the other materials were purchased commercially from steel suppliers in South Africa and Germany. The compositions of the alloys tested are shown in Table 3.19.

Specimens with a gauge length of 50mm and diameter of 12mm were deformed at an ambient temperature of 23°C in quasi-static tensile loading. An inductance meter with digital data-logger output (Tecpel LCR 612) coupled to an inductance coil of 4000 turns placed around the specimen was used to detect the change in magnetic permeability during deformation. Alloy AISI 304 was found to give consistent transformation when specimens originated from a single batch, but significantly varying results when purchased from different suppliers. The characteristic transformation curves detected in this manner were then plotted, as shown in Figure 3.119. Three tests were performed for each alloy but only the most divergent two of these are shown. Alloy DIN 1.4301 showed no transformation.

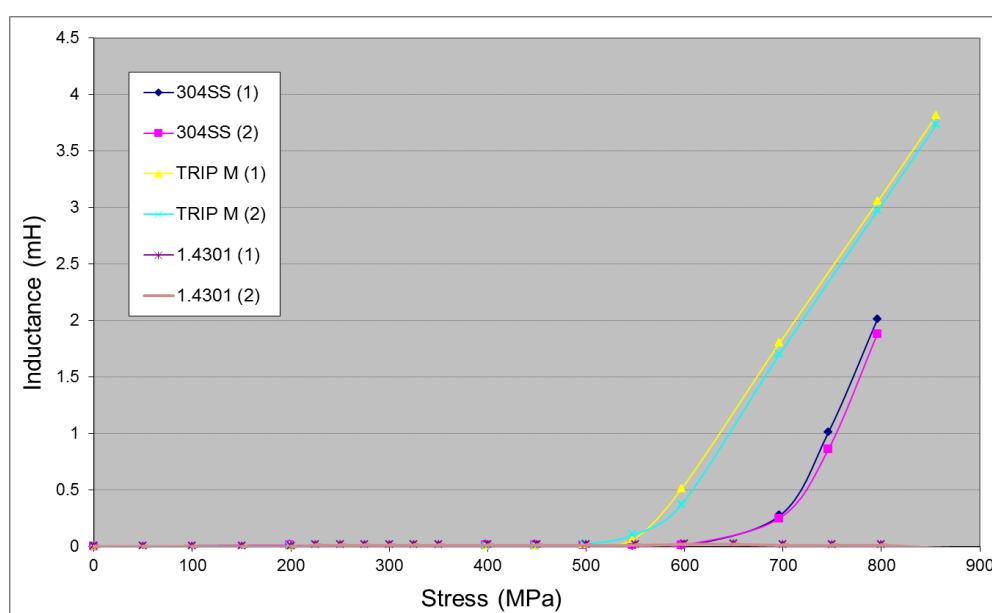


**Figure 3.119: Transformation curves of available tensile TRIP alloys that were quasi-statically tested prior to alloy design.**

The materials analysed were assessed according to their transformation curves and their positions on the Schaeffler diagram (Schaeffler, 1949), shown in Figure 3.120. It is observed from the Schaeffler diagram that those alloys with lower chromium equivalents (further left), and those with lower average chromium and nickel equivalents, showed better transformation. This would be expected until the parent microstructure develops significant levels of thermally induced martensite.

Early analysis was also attempted according to the Alloys' predicted  $M_s$  and  $M_{d30}$  temperatures (Cina, 1954) (Angel, 1954) (Stuhlmann, 1959) (Andrews, 1965) (Hull, 1973) (Pickering, 1978) (Nohara et al., 1978) (Capdevila et al., 2002). The empirical and semi-empirical equations from literature that were used to assess  $M_s$  and  $M_{d30}$  temperatures were the same as those used for the as-cast alloys in Section 3.4 and can be found in Table 3.2 and Table 3.3 respectively.

For the alloys tested, Table 3.19 shows the alloy compositions, nickel and chromium equivalents and empirically predicted  $M_s$  and  $M_{d30}$  temperatures as specified. It was observed that those alloys with higher  $M_{d30}$  temperatures generally showed better transformation. The only alloy with all empirically predicted  $M_{d30}$  temperatures substantially below room temperature, Alloy 1.4301, was also the only alloy that showed no transformation, as would be expected. Alloy 304, with predicted  $M_{d30}$  temperatures in the region of room temperature, showed minimal transformation.

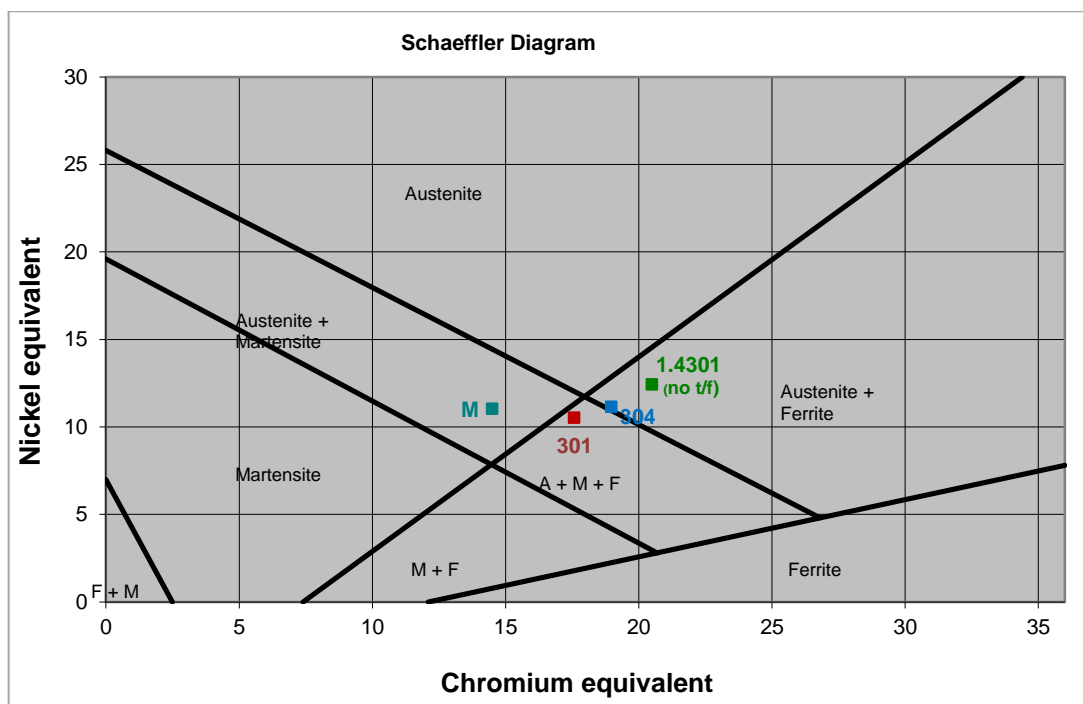


Figure 3.120: A Schaeffler-type diagram predicting the phases of the tested alloys.

**Table 3.19: Elemental compositions of the tested alloys in order of level of transformation, results of empirical and semi-empirical formulae used.**

<b><i>Alloy:</i></b>	<b>TRIP M</b>	<b>304</b>	<b>1.4301</b>
<b><i>Transformation</i></b> <b><i>(Max <math>\Delta</math> Inductance):</i></b>	3.8 (mH)	1.9 (mH)	0 (mH)
<b><i>Element:</i></b>			
<b>C</b>	0.20	0.06	0.07
<b>Ni</b>	0.27	8.51	9.30
<b>Mn</b>	8.90	1.80	2.00
<b>Cr</b>	13.66	18.00	19.00
<b>Si</b>	0.56	0.65	1.00
<b>Mo</b>	0.00	0.00	0.00
<b>Al</b>	0.00	0.00	0.00
<b>Fe</b>	<b>balance</b>	<b>balance</b>	<b>balance</b>
<b>Cr<sub>eq</sub></b>	14.50	18.98	20.50
<b>Ni<sub>eq</sub></b>	10.72	11.12	12.40
<b>eq<sub>ave</sub></b>	12.61	15.05	16.45
<b>M<sub>d30</sub> Angel</b>	53.65	38.66	6.61
<b>M<sub>d30</sub> Pickering</b>	130.70	27.90	-12.70
<b>M<sub>d30</sub> Nohara</b>	182.29	5.32	-42.44
<b>M<sub>s</sub> Andrews</b>	13.78	91.74	54.08
<b>M<sub>s</sub> Cina</b>	72.03	-142.73	-270.99
<b>M<sub>s</sub> Hull</b>	-155.27	-123.57	-272.00
<b>M<sub>s</sub> Stuhlmann</b>	-153.79	-46.62	-92.60
<b>M<sub>s</sub> Capdevila</b>	297.16	380.98	343.84

Lecroisey and Pineau studied several metastable alloys for which they experimentally estimated  $M_s$  temperature as well as  $M_{d30}$  temperature (Lecroisey & Pineau, 1972). Table 3.20 compares their measured results to those predicted by the previously discussed empirical equations (Table 3.2 and Table 3.3).

**Table 3.20: Comparison between the experimentally measured results of Lecroisey and Pineau (grey) and the empirical formulae for  $M_{d30}$  and  $M_s$  temperatures, as specified in Table 3.2 and Table 3.3.**

<b>Alloy number:</b>	<b>1</b>	<b>2</b>	<b>3</b>	<b>4</b>	<b>5</b>	<b>6</b>	<b>7</b>	<b>8</b>	<b>9</b>	<b>10</b>
<b>Composition:</b>										
<b>C</b>	0.15	0.01	0.25	0.00	0.01	0.10	0.00	0.01	0.14	0.02
<b>Ni</b>	18.00	19.60	17.30	11.00	12.00	11.20	11.20	12.50	30.80	30.80
<b>Mn</b>	0.00	0.00	0.00	0.00	0.00	0.00	0.00	0.00	0.00	0.00
<b>Cr</b>	7.20	6.90	4.50	15.60	17.80	15.70	15.50	15.90	0.00	0.00
<b>Si</b>	0.00	0.00	0.00	0.00	0.00	0.00	0.00	0.00	0.00	0.00
<b>Mo</b>	0.00	0.00	0.00	0.00	0.00	0.00	0.00	0.00	0.00	0.00
<b>Fe Balance</b>										
<b>Cr<sub>eq</sub></b>	7.20	6.90	4.50	15.60	17.80	15.70	15.50	15.90	0.00	0.00
<b>Ni<sub>eq</sub></b>	22.50	19.78	24.80	11.09	12.24	14.20	11.32	12.80	35.00	31.40
<b>eq<sub>ave</sub></b>	14.85	13.34	14.65	13.35	15.02	14.95	13.41	14.35	17.50	15.70
<b>M<sub>d30</sub> Angel</b>	74.06	129.50	71.50	93.39	51.44	45.31	92.40	71.80	55.72	111.16
<b>M<sub>d30</sub> Pickering</b>	-30.94	7.70	-26.15	61.89	9.44	11.71	58.80	24.55	-183.68	-128.24
<b>M<sub>d30</sub> Nohara</b>	-141.10	-116.77	-129.20	12.21	-49.90	-39.80	7.35	-38.72	-406.88	-351.44
<b>Measured <math>M_d</math> (Lecroisey &amp; Pineau)</b>	-5.00	60	40.00	150.00	50.00	60.00	150.00	80.00	0.00	5.00
<b>M<sub>s</sub> Andrews</b>	69.83	106.05	72.59	154.27	107.84	108.49	151.52	121.13	-65.38	-14.62
<b>M<sub>s</sub> Cina</b>	-345.45	-190.40	-356.05	-26.20	-187.94	-204.30	-35.87	-141.97	-807.18	-607.14
<b>M<sub>s</sub> Hull</b>	-276.90	-13.04	-347.70	92.63	-81.72	-155.70	83.14	-26.70	-669.80	-383.00
<b>M<sub>s</sub> Stuhlmann</b>	47.50	76.70	78.40	49.95	-12.80	10.60	48.20	16.00	-22.60	19.40
<b>M<sub>s</sub> Capdevila</b>	355.93	375.61	361.32	441.85	404.16	408.29	439.12	412.16	210.56	246.87
<b>Measured <math>M_s</math> (Lecroisey &amp; Pineau)</b>	-90.00	-25.00	-90.00	-10.00	-65.00	-269.00	-20.00	-95.00	-45.00	-25.00

Figure 3.121 and Figure 3.122 plot the predicted and the experimentally determined  $M_{d30}$  and  $M_s$  temperatures for more ready comparison. These plots exclude Lecroisey and Pineau's alloy number nine and number ten since the composition of these alloys included no chromium and extremely high nickel (over 30%), compositions which were well outside of the current alloy range of interest.  $M_{d30}$  temperature as determined by the empirical equations showed a definite relation to the  $M_d$  temperature determined experimentally. Note that an alloy's  $M_{d30}$  temperature must be lower than its  $M_d$  temperature, since  $M_d$  temperature represents the highest temperature under which deformation-induced transformation will occur, whereas  $M_{d30}$  represents the temperature at which 30% strain will induce 50% transformation. Thus, from Figure 3.121, the empirical equation by Pickering (Pickering, 1978) for  $M_{d30}$  seems to have the highest probability of correctness for the alloy range of interest; it shows an identical trend to that of Lecroisey & Pineau's measured values, but at a lower temperature. This is the same equation that was determined to be most relevant for the as-cast alloys deformed in compression, which were in a similar alloy range (Section 3.4.13). It was seen that an average between the equation



by Pickering and that by Angel (Angel, 1954) would still more closely predict  $M_d$ . This same average was found to have the best possible relevance for the as-cast alloys.

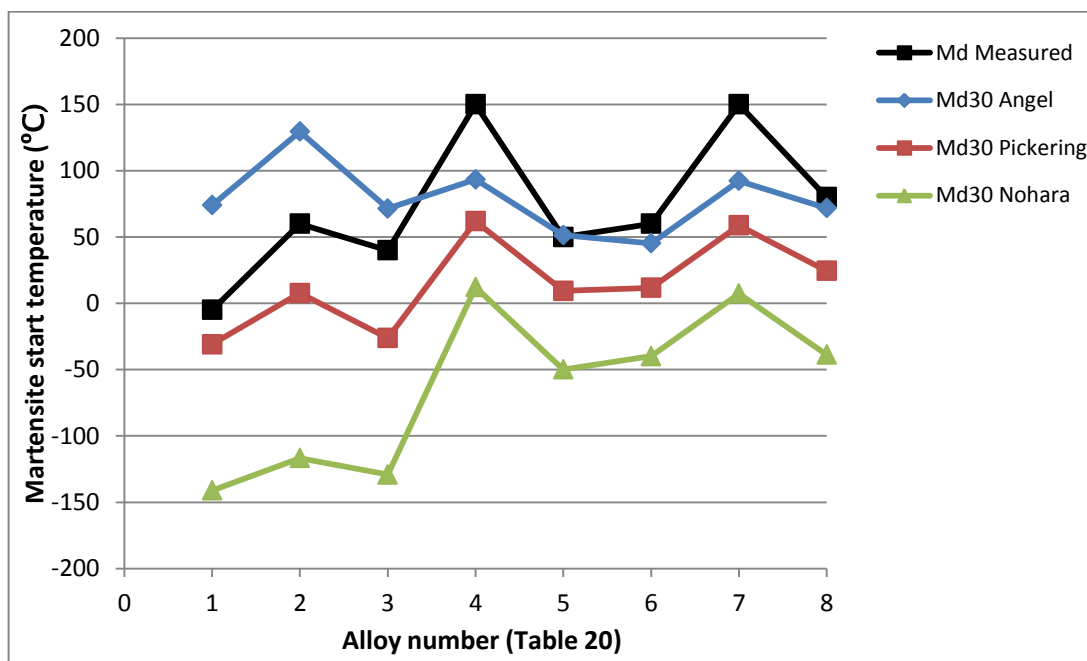


Figure 3.121: Empirically predicted  $M_{d30}$  temperatures (Table 3.20) compared to  $M_d$  temperatures experimentally measured by Lecroisey and Pineau (Lecroisey & Pineau, 1972).

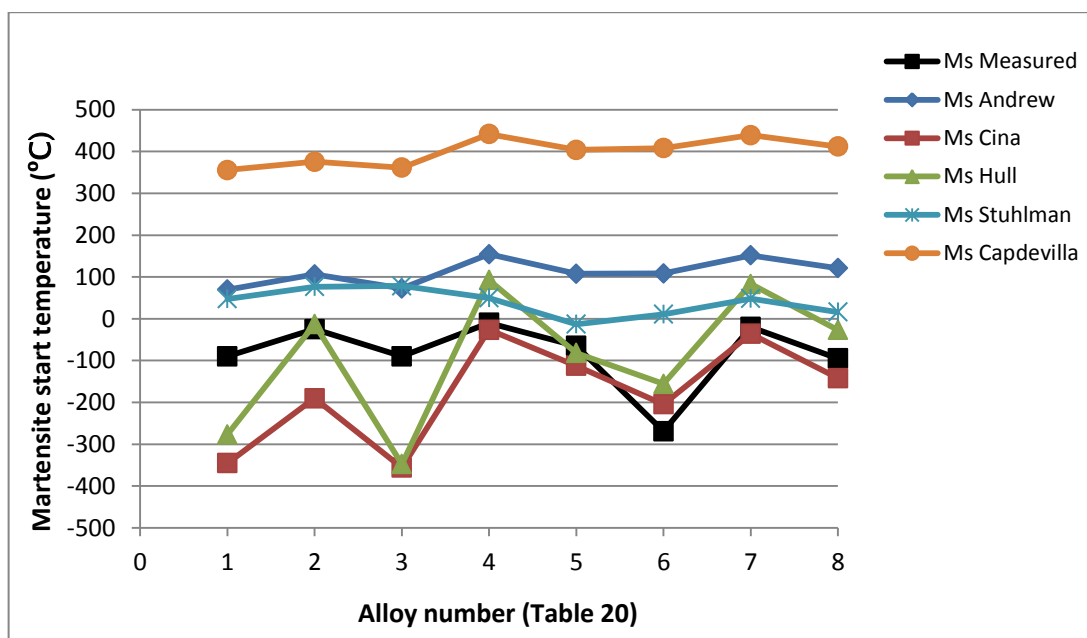


Figure 3.122: Empirically predicted  $M_s$  temperatures (Table 3.20) compared to  $M_s$  temperatures experimentally measured by Lecroisey and Pineau (Lecroisey & Pineau, 1972).

The  $M_s$  temperatures predicted by Cina bear the clearest relation to Lecroisey & Pineau's measured values for  $M_s$  (Cina, 1954). Results of the other formulae for  $M_s$ , other than that by Hull (Hull, 1973), show little relation to those measured  $M_s$  temperatures.

The  $M_s$  temperatures predicted from the formula proposed by Capdevila (Capdevila et al., 2002) showed considerable deviation from the  $M_s$  temperatures measured by Lecroisey and Pineau (Lecroisey & Pineau, 1972). They also did not show a similar trend to the measured results and were thus disregarded. The formulae proposed by Andrews (Andrews, 1965) and by Stuhlmann (Stuhlmann, 1959) gave somewhat accurate results relative to Lecroisey and Pineau's measured results, and showed some signs of predicting a similar trend. Alloys 4 to 8 are within the current alloy range of interest. The formula proposed by Cina (Cina, 1954), and to a lesser extent that by Hull (Hull, 1973), closely track Lecroisey and Pineau's measured results. That proposed by Cina also shows a relationship to the transformation results in that a raised  $M_{s\_Cina}$  temperature also corresponds to greater transformation.

During testing of the as-cast alloys in compression, the Cina formula for  $M_s$  temperature (Cina, 1954) was also found to be the most promising empirical predictor within the current alloy range. All of the above results imply that within the range of alloys tested, a lower level of alloying elements generally resulted in better transformation. It was hoped that even if the empirical formulae did not give precise  $M_s$  and  $M_{d30}$  temperatures, they could be helpful in deciphering the best metastable alloy compositions for the proposed application by identifying relative trends. The above analysis demonstrates a good likelihood of this.

### 3.5.3 Refining alloy transformation through theory and observation

AISI 304 and AISI 301 have been widely researched for their properties as metastable alloys (Bressanelli & Moskowitz, 1966) (Olson & Cohen, 1975) (Olson & Azrin, 1978) (Schmid & Knutsen, 1992) (Talonon, 2007) (Andrade-Campos et al., 2008) (Ryoo et al., 2011) (Larour et al., 2013). AISI 301 displays considerably better transformation properties than AISI 304 at room temperature. This is in agreement with the results in Table 3.19 and with the empirical formulae analysed. Powell et al., studied an AISI 301 material which exhibited considerable martensitic transformation during deformation (Powell et al., 1958), reaching about 90% martensite by 0.3 strain at 20°C. More recent research showed considerably lower levels of transformation for similar material, specifically approximately 40% martensite at 0.3 strain at 20°C (Schmid & Knutsen, 1992).

Quantifying the true martensite content of TRIP steel is extremely difficult, a relative comparison is usually easier and more relevant. It is possible that some authors have simply shown the maximum levels of transformation achieved as near 100% martensite (accounting for some retained austenite), when in reality the level may be considerably less. Hedström (Hedström, 2005) found that an AISI 301 stainless TRIP steel alloy with almost no warm rolling

reduction showed approximately 5% martensite before deformation increasing to a maximum of approximately 30% martensite during deformation (Figure 3.123).

Although warm-worked AISI 301 type materials display reasonable total transformation, this transformation occurs over a narrow range of deformation stress, which is not ideal for the proposed sensor applications. It was also found to be surprisingly difficult to obtain AISI 301 stainless steel, both in South Africa and abroad. A small batch of material claimed to be AISI 301 was imported from Taiwan, but analysis found it to be AISI 304. In these applications, it will usually be necessary to be able to apply the sensor over a broad range of stress and strain, enabling a broad range of measurement. Transformation should begin as early as possible. Warm working should not be utilised for the rock reinforcement tendon alloy since it substantially increases expense.

The phenomena of “strain-assisted” martensitic transformation occurring beyond yield, and that of “stress-assisted” transformation occurring prior to yield are well documented, Section 2.4.2. In designing TRIP steel alloys for sensors, it would be beneficial to produce TRIP steels that enable detection at low levels of deformation. Thus, the new alloys must either show stress-assisted martensitic transformation, or have an extremely low yield point, or a combination of these. As previously discussed, it is believed that the prior presence of  $\epsilon$ -martensite promotes the formation of stress-assisted  $\alpha'$  martensite before yield (Christian, 1979). As discussed in Section 2.5, it is believed that  $\epsilon$ -martensite provides increased  $\alpha'$  martensite nucleation site density, while also retarding  $M_s^{\alpha'}$ . Thus, possibly due to their forming a quasi-stable intermediate phase,  $\epsilon$ -martensite nuclei may transform more readily into  $\alpha'$  martensite via deformation rather than via temperature reduction. Thus, incubation strain, as well as temperature sensitivity, may be reduced.

The level of transformation induced during stress-assisted transformation, before yield, is usually very small relative to that induced by strain-induced transformation after yield (Bressanelli & Moskowitz, 1966) (Fahr, 1971). In order for the alloy to display significant transformation before yield, it is beneficial to design it with  $M_s$  temperature near the operating temperature. However, such stress-assisted transformation near to  $M_s$  in warm-worked alloys has been shown to be highly temperature sensitive, as discussed in Section 2.4.2, and thus should not be relied upon for a sensor material. As testing temperatures become substantially above  $M_s$ , plastic deformation must occur before martensitic transformation (Maxwell et al., 1974). Reducing the yield strength of a TRIP steel sensor material via correct composition and processing remains a feasible solution to realizing early transformation.

Olson and Cohen concluded that decreasing the fcc, bcc and hcp entropy differences (within an operational temperature range) through proper compositional control could reduce the temperature sensitivity of the martensitic transformation (and thus also strain rate sensitivity) (Olson & Cohen, 1975). As discussed in Section 2.6, they hypothesised that this could theoretically be achieved by replacing nickel with chromium and manganese. Alloys with large differences between their  $M_s$  and  $M_d$  temperatures (equating to lower entropy differences between phases) have been shown to have lower stacking fault energy austenite (Lecroisey & Pineau, 1972). This should then facilitate martensite formation via nuclei originating from austenite stacking faults. Temperature and strain rate dependence might thereby decrease, as well as reducing the incubation strain of the  $\alpha'$  martensite transformation (Hull, 1973).

Since the driving force required for  $\epsilon$ -martensite is lower than that for  $\alpha'$  martensite in such materials, it is possible to form the  $\epsilon$ -martensite phase before  $\alpha'$  martensite formation (Christian, 1979). This may be achieved by straining, applying low temperatures or both. Abrassart showed that if prestraining is to be performed to improve transformation before yield, it should be done at a temperature just above  $M_d$  (Abrassart, 1973).  $\epsilon$ -Martensite is anti-ferromagnetic and would thus be interpreted by a magnetic sensor as austenite. However, as discussed in Section 2.5,  $\epsilon$ -martensite strongly promotes the formation of  $\alpha'$  martensite.

Maxwell et al. concluded that stress-assisted  $\epsilon$ -martensite formed in some alloys with high nickel contents (Maxwell et al., 1974). As discussed in Section 2.6, this study was performed within a very narrow compositional range. Thompson studied a substantially wider group of Fe-Cr-Mn based alloys and found that  $\epsilon$ -martensite formed in alloys containing approximately 10% or more manganese (Thompson, 1986). Cina concluded that  $\epsilon$ -martensite forms in binary Fe-Mn, as well as ternary Fe-Mn alloys containing Ni, Cr, Co or C (Cina, 1958). Lower carbon contents were generally beneficial to  $\epsilon$ -martensite formation and in alloys that were not warm-worked; 0.2wt% was the maximum carbon content producing  $\epsilon$ -martensite. No  $\epsilon$ -martensite was detected in Fe-Ni alloys of 8wt% and 19wt% nickel. In Fe-Ni-Cr alloys, a combined chromium and nickel equivalent of 24wt% was required for  $\epsilon$ -martensite to form. Walters and Wells (Walters & Wells, 1936) also concluded that carbon tends to suppress  $\epsilon$ -martensite formation. Other authors found apparent  $\epsilon$ -martensite formation in relatively low nickel content Fe-Cr-Ni-Mn based alloys (Fahr, 1971) (Hedström, 2005).

### 3.5.4 Alloy design

Due to time and budgetary constraints associated with processing the hot rolled tensile alloys, and because of the substantial previous research available, as already discussed throughout this work (particularly in Sections 2.4, 2.5, 2.7 and 3.5.3), only two materials were planned for production. Warm rolling was avoided for these alloys. This was partly because a primary aim of the project was to produce low cost TRIP steel deformation sensor material for smart rock tendons. Warm rolling significantly increases the cost of producing TRIP steel alloys (fabrication costs can easily double), particularly in low quantities. Warm rolling is likely to reduce the overall transformation characteristics of most TRIP alloys, as shown in Figure 3.123 (Hedström, 2005), and also in work by Maxwell et al. and by Bhadeshia and Edmonds (Section 2.5) (Maxwell et al., 1974) (Bhadeshia & Edmonds, 1979b). Further problems are associated with warm rolled alloys. For example, although early stress-induced transformation is usually encouraged, it is often very small, with a comparatively dramatic transformation response shortly before breaking. Heavily “stepped” responses sometimes occur in these alloys (Figure 3.123) (Hedström, 2005). Warm-worked alloys also often exhibit a relatively small useable range of strain, as seen in comparing Sample A to Samples B, C and D in Figure 3.123.

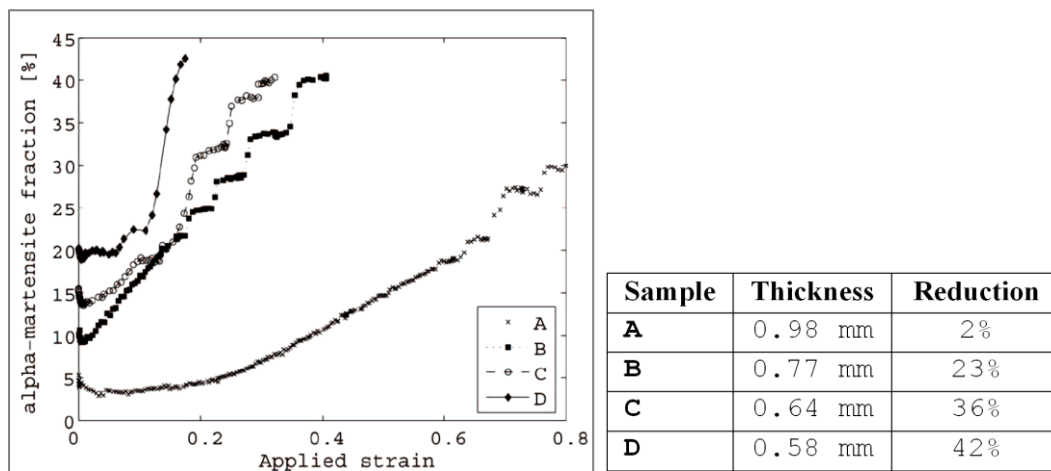


Figure 3.123: Transformation behaviour of 301 stainless steel with various amounts of warm work (Hedström, 2005).

A TRIP steel alloy optimised to form a strain-sensor element should ideally exhibit steady transformation over a broad range of strain, exhibit early transformation and be minimally sensitive to temperature and strain rate fluctuations. The compositions of the two custom-designed warm rolled TRIP steel alloys were chosen according to the literature survey, preliminary testing as described and the above analysis. The proposed alloy compositions, TRIP R and TRIP S, are shown in Table 3.21. In an effort to promote  $\epsilon$ -martensite formation and thereby reduce incubation strain and temperature and strain rate sensitivity, it was decided that they should have a manganese content of at least 10wt%. For the same reason, and in order to

keep the yield points low, it was decided that they should have carbon contents of less than 0.2wt%. Increasing the manganese content also reduces the nickel content, thus reducing the cost of the alloy, since nickel is relatively expensive. Reducing the nickel content may also decrease yield strength, since nickel also strengthens steel by solid solution strengthening.

TRIP R was designed to show somewhat lower temperature sensitivity than TRIP M, while displaying improved transformation characteristics. TRIP S was designed to show similar transformation characteristics to TRIP M, while displaying markedly reduced temperature sensitivity. Extremely low temperature sensitivity was not in fact considered a priority for the current alloy design, since the South African deep mining environment is usually relatively temperature stable within a given mine (Florides & Kalogirou, 2005) (Minnie, 2005) (Oelofse, 2005). However, it was of interest to assess the potential to reduce temperature sensitivity for other potential applications and to reduce sensitivity to strain rate.

The Schaeffler diagram and its associated equations (Schaeffler, 1949) (De Long, 1974) were also utilised extensively. After analysing the previously tested metastable alloys, as discussed in Sections 3.5.2 and 3.5.3, it was attempted to obtain large differences between the predicted  $M_s$  and  $M_{d30}$  temperatures in anticipation of stabilising the new alloys with respect to temperature and strain rate. In order to encourage more prominent transformation and in particular early transformation, the new alloys should also have relatively low chromium equivalents and low chromium-nickel equivalent averages, and thus be as near to the room temperature Schaeffler diagram martensite range as practical. Compositions were chosen so that predicted  $M_{d30}$  temperatures were well above room temperature. A small amount of nickel was added in an effort to reduce the material's yield point, high manganese contents can increase the yield point as shown in Section 2.4.1. Aluminium was not included because it may increase yield strength and has also been shown to reduce the rate of transformation in certain TRIP steels (Samek et al., 2006). A small amount of silicon was added to improve machinability. The proposed compositions (TRIP S and TRIP R) and their predicted transformation temperatures are listed in Table 3.21, along with the previously tested alloys for comparison. The compositions were also chosen so as to allow for relevant comparison between TRIP S, TRIP R and TRIP M after testing. Two other alloys, DIN 1.4567 and DIN 1.4568, were selected on similar principles for their alloy chemistry and were procured in Germany. These alloys were only available in the form of three millimetre diameter wire.



Table 3.21: Proposed and previously tested alloys with some predicted properties.

<b>Alloy:</b>	<b>1.4567</b>	<b>1.4568</b>	<b>TRIP M</b>	<b>TRIP S</b>	<b>TRIP R</b>
<b>Composition (wt%):</b>					
<b>C</b>	0.03	0.08	0.20	0.18	0.15
<b>Ni</b>	9.20	7.10	0.27	1.20	1.20
<b>Mn</b>	2.00	0.00	8.90	12.00	11.50
<b>Cr</b>	17.50	16.20	13.66	13.00	13.00
<b>Si</b>	1.00	0.00	0.56	0.00	0.10
<b>Mo</b>	0.00	0.05	0.00	0.00	0.00
<b>Al</b>	0.00	0.80	0.00	0.00	0.00
<b>Cu</b>	3.20	0.00	0.07	0.00	0.00
<b>Fe balance</b>					
<b>Cr<sub>eq</sub></b>	19.0	16.2	14.5	13.0	13.0
<b>Ni<sub>eq</sub></b>	12.7*	9.5	10.7	12.5	11.5
<b>Average [Cr<sub>eq</sub>+Ni<sub>eq</sub>]</b>	15.9	12.9	12.6	12.7	12.2
<b>M<sub>d30</sub> Pickering</b>	28.7	90.3	130.7	113.0	128.6
<b>M<sub>s</sub> Cina</b>	-135.2	58.1	72.0	-1.9	56.3
<b>M<sub>s</sub> Hull</b>	-100.0	107.7	-155.3	-266.1	-179.3
<b>M<sub>d30</sub>-M<sub>s</sub> Cina</b>	164.0	32.2	58.7	114.9	72.3
<b>M<sub>d30</sub>-M<sub>s</sub> Hull</b>	128.7	-17.4	286.0	379.0	307.9

\*Includes a nickel equivalent of 0.5 for Cu, as suggested by Crawford et al. (Crawford et al., 1982).

Figure 3.122 shows that  $M_{s \text{ Cina}}$  and  $M_{s \text{ Hull}}$  gave comparable results. However, the alloys tested by Lecroisey and Pineau (Lecroisey & Pineau, 1972) on which the analysis was based contained no manganese. In practice the equations for  $M_s$  by Cina (Cina, 1958) and Hull (Hull, 1973) vary considerably in the extent to which manganese alters their result.  $M_{s \text{ Cina}}$  places considerably less significance on the contribution of manganese to reducing  $M_s$  temperature than the other  $M_s$  equations investigated (Section 3.5.2). It is possible that  $M_{s \text{ Cina}}$  places insufficient significance on the dominance of manganese in reducing  $M_s$  temperature. Thus  $M_{s \text{ Hull}}$ , which was also found to track the experimentally measured values for  $M_s$  reasonably well, but places more significance on manganese, has been included in the analysis along with  $M_{s \text{ Cina}}$ .

TRIP S was designed to have an extremely large difference between  $M_s$  and  $M_d$ , while allowing the nickel-chromium equivalent average to remain similar to TRIP M. TRIP R was designed to have its difference between  $M_s$  and  $M_d$  slightly larger than that of TRIP M, while having a significantly lower nickel-chromium equivalent average. Thus, TRIP S is expected to exhibit similar transformation to that of TRIP M but show less temperature sensitivity, while TRIP R is expected to exhibit better transformation than TRIP M, showing slightly less temperature sensitivity. Both alloys have  $M_{d30}$  Pickering well above room temperature.

Attaining very low temperature sensitivity is not essential for TRIP steels to be utilised as sensors elements in the South African deep mining environment because this environment is usually relatively temperature stable (Florides & Kalogirou, 2005) (Minnie, 2005) (Oelofse, 2005). However, it was of interest to assess the potential to reduce temperature sensitivity because, as discussed in Section 2.5, it is believed that the effects of increased deformation strain rates are associated to those of environmental temperature fluctuation. Application to sensors in most other areas would require low temperature sensitivity.

Alloy DIN 1.4568 had a predicted  $M_s$  above operating temperature in all cases, and with  $M_s$  and  $M_{d30}$  very close together. Thus, while it may show good transformation, it is likely to be highly temperature susceptible. Alloy DIN 1.4567 has a large difference between  $M_s$  and  $M_{d30}$ , but is in the austenitic region of the Schaeffler diagram (Schaeffler, 1949).

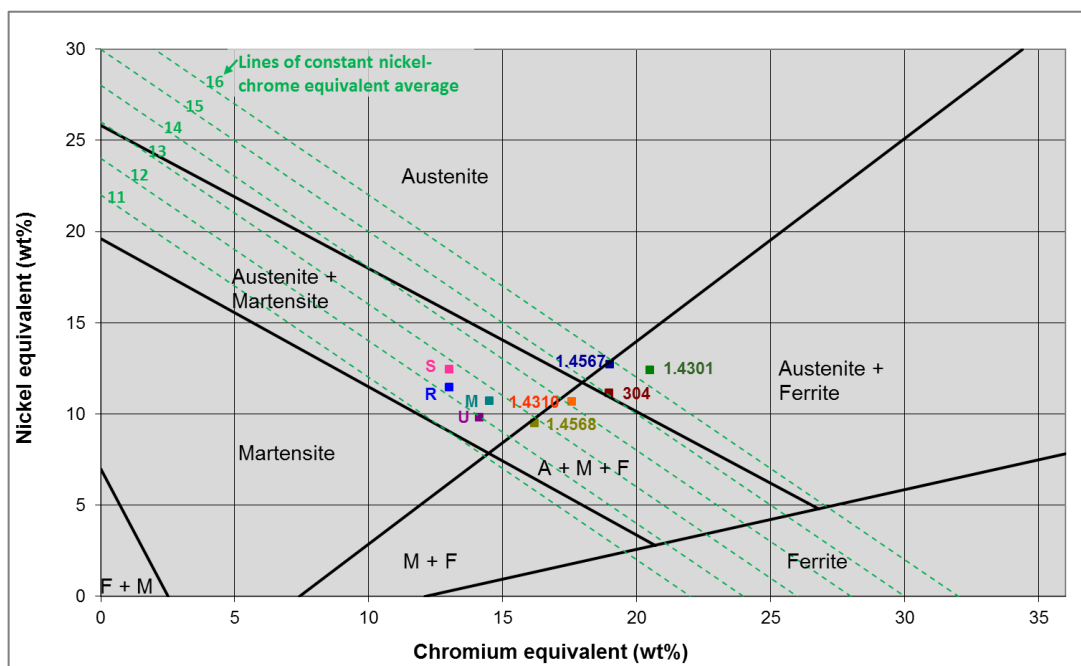


Figure 3.124: Schaeffler diagram (Schaeffler, 1949) showing the positions of the alloy compositions proposed for further investigation, as well as previously tested alloys.

### 3.5.5 Alloy fabrication

#### 3.5.5.1 Introduction

TRIP steel M was produced by Mintek specifically for the current project. The material was cast in the composition specified in Table 3.19, hot rolled and water-quenched in a relatively large quantity. Experts from Columbus Stainless assisted with practical training in the process of casting ingots in the small UKZN research inductance furnace. Melting and alloying of TRIP steels R and S was performed in an inductance furnace at UKZN.

#### 3.5.5.2 Fabrication of steels TRIP R and TRIP S

A 7 kg crucible was used and for the third set of melts a specially designed inert gas hood was also utilised (Figure 3.125). The melt was then poured into a mould. Ingots were approximately 90 mm in diameter, tapering to 70 mm diameter at the bottom. They were 200 mm long.



**Figure 3.125: UKZN inductance furnace with inert gas hood and new crucible installed.**

Three ingots each for TRIP R and TRIP S were cast. After casting, ingots were analysed using spark spectroscopy. The composition of all three TRIP S ingots and two of the TRIP R ingots were found to differ considerably from the intended composition and were scrapped. One of the TRIP R ingots had a composition close to that intended, as shown in Table 3.22. Since carbon and manganese deviated from specification the most, and since these elements are readily affected by interaction with the atmosphere, the effectiveness of the inert gas hood may have been significant in casting composition accuracy.

Table 3.22: Specified and measured compositions for TRIP R, third casting.

<b>Alloy:</b>	<b>TRIP R specified</b>	<b>TRIP R (3) measured</b>
<b>Composition (wt%):</b>		
<b>C</b>	0.15	0.16
<b>Ni</b>	1.20	1.7
<b>Mn</b>	11.50	11.1
<b>Cr</b>	13.00	12.9
<b>Si</b>	0.10	0.25
<b>Mo</b>	0.00	0.04
<b>Al</b>	0.00	0.017
<b>Cu</b>	0.00	0.08
<b>Fe balance</b>		
<b>Cr<sub>eq</sub></b>	13.0	13.3
<b>Ni<sub>eq</sub></b>	11.5	12.0
<b>eq<sub>ave</sub></b>	12.2	12.6
<b>M<sub>d30</sub> Pickering</b>	128.6	117.2
<b>M<sub>s</sub> Cina</b>	56.3	22.4
<b>M<sub>s</sub> Hull</b>	-179.3	-212.8
<b>M<sub>d30</sub>-M<sub>s</sub> Cina</b>	72.3	94.8
<b>M<sub>d30</sub>-M<sub>s</sub> Hull</b>	307.9	330.0

The ingots were then machined down to 65mm diameter. Rolling was then performed in-house using a rolling mill that was specially restored and redesigned from two previously dysfunctional rolling mills by the author for this project. Ingots were heated to 1200°C and then reduced in the rolling mill by about 5% of diameter over three to four passes, reheated for a minimum of 20 minutes and the process was repeated. Later passes reduced the diameter by a larger percentage, up to about 8% per three to four passes. The material was sectioned twice in order to keep its length manageable. In this way, the material was reduced to a 26 mm diameter over approximately 30 passes. The ingot yielded approximately 1.3 metres of 26 mm diameter bar. This bar is shown in Figure 3.126.



**Figure 3.126: Bars of newly hot rolled alloy TRIP R.**

### **3.5.5.3 Fabrication of steel TRIP MW**

In order to assist the testing of the theory developed in Section 3.3 regarding dislocation density affecting temperature sensitivity, TRIP M was warm rolled between 480°C and 350°C from 20 mm thickness to 16mm thickness, equating to 20% reduction, in nine passes and then forced-air cooled from approximately 350°C. This temperature range was selected using the charts shown in Figure 2.29 and Figure 2.5, to circumvent martensite as well as carbide formation as much as possible.

In order to assure that the material temperature did not drop below 350°C, an infra-red thermometer was used to measure the material temperature upon each exit of the rolling mill. Three passes were performed on each bar before it was placed back into the furnace and heated again to 500°C. Three such sets of reductions were performed on each bar, bringing the total number of passes to nine.

An infra-red camera was also utilised to image the process. Figure 3.127 depicts a bar before beginning the first warm rolling pass (A), after the first pass (B), the second pass (C) and the third pass (D). The outer skin of the bar cooled more rapidly than the internal metal, the temperature reading increased immediately after a pass upon brief resting outside the furnace. Since the final specimen gauge length would be of only 8.75 mm diameter, the surface temperature dropping briefly below 350°C was not of concern.

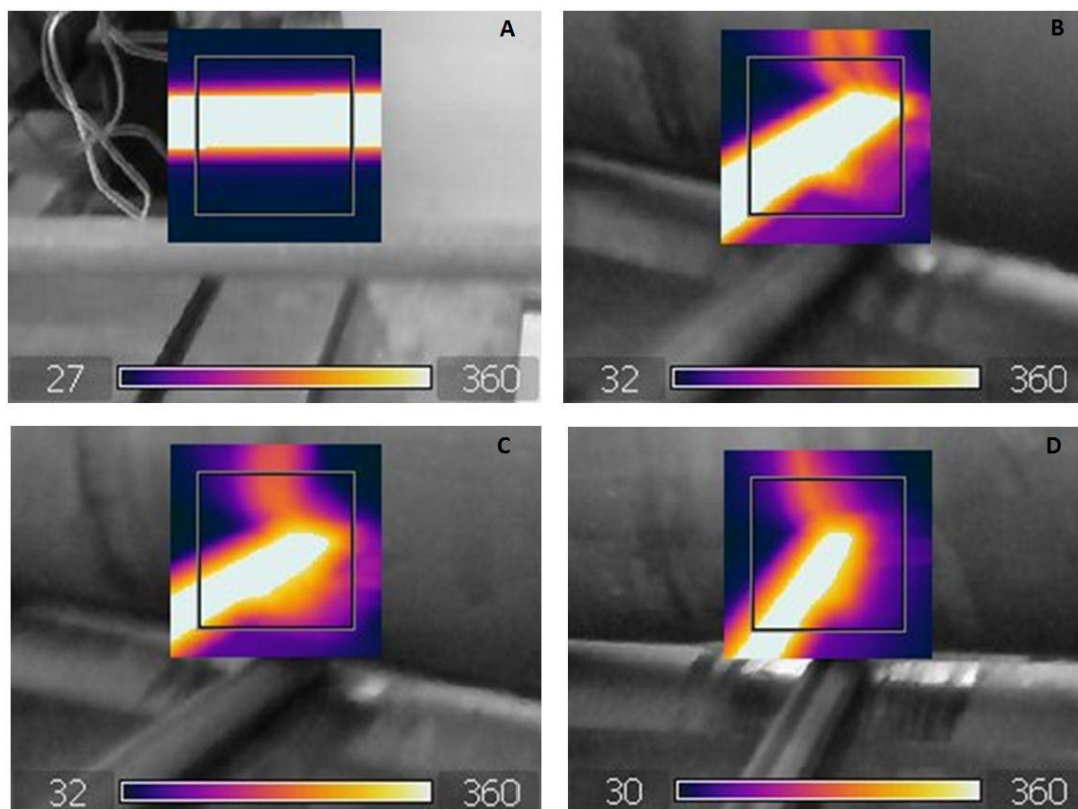


**Figure 3.127:** Images showing the surface temperature of a bar of TRIP M while being warm rolled before pass one (A), after pass one (B), after pass two (C), after pass three (D).

### 3.5.6 Experimental equipment and method

TRIP M was widely utilised in these experiments due to it being the only purpose-designed alloy available in large quantities of uniform composition and processing. A comparison was made of the basic stress versus transformation curves for all the different tensile alloys examined under quasi-static loading conditions. The total amount of transformation, the lowest load from which it was estimated that the transformation could be detected, and the level of repeatability and associated resolution of the alloys were of primary importance. The effects of heat treatment and of deformation at different temperatures on transformation characteristics was investigated. Strain rate testing was planned but was never performed due to equipment failure.

An Instron 5500R universal mechanical testing machine was used for quasi-static tensile testing. To characterise transformation during deformation, this machine was used in conjunction with an inductance meter (Tecpel LCR 612) with inductance coils. Both types of meters digitally logged data to the Instron PC.

Tensile deformation of some larger specimens was carried out using an Avery hydraulic universal testing machine, while utilising the inductance monitoring system. Cyclic loading and high-speed tensile testing were planned on an MTS 312.2 hydraulic universal testing machine, with 100 l/min power pack and hydraulic accumulators. However, due to controller breakdown during similar testing performed on compression specimens in this work (Section 3.4.10), this testing had to be abandoned.

When testing for magnetic susceptibility or inductance, readings were also taken before and after placing a specimen in the tensile testing machine, as well as once the specimen was removed. This was done for comparative purposes and to gauge the effect of the machine's structural elements on the readings. These effects were found to vary little between specimens. Specimens were always placed in similar locations in the apparatus. Coils were wound using a specially modified lathe, and the coils for any particular set of tests were identical (usually the same coil on a coil-former used repeatedly, as shown in Figure 3.133).

### 3.5.7 Alloy TRIP R comparison

Alloy TRIP R was initially tested under quasi-static conditions at an ambient temperature of 23°C for comparison to the alloys tested in Section 3.5.2. The results are shown in Figure 3.128. Specimens had a gauge length of 50 mm and 12 mm diameter. A coil of 4000 turns was used to monitor the transformation with the Tecpel LCR 612 inductance meter.

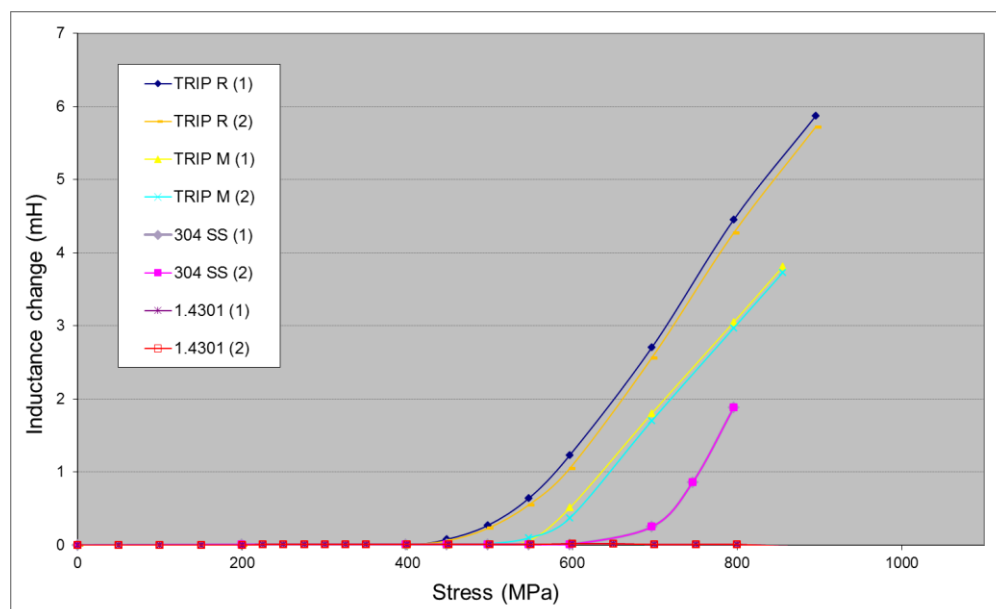


**Figure 3.128: Room temperature stress versus transformation results for alloy TRIP R compared to previously tested alloys as listed.**



Alloy TRIP R showed earlier and more prominent transformation relative to the hot rolled alloys previously tested as in Section 3.5.2. None of the previously tested alloys, other than TRIP M, were designed specifically to maximise their martensitic transformation.

### 3.5.8 Alloy DIN 1.4568

Alloy DIN 1.4568 was discovered during a search of commercial alloys. It is a specialised alloy and after considerable effort was procured in Germany in the form of 3mm wire. A small quantity of this wire was purchased and tested and found to show good transformation. The wire was tested as-received and after annealing.

Alloy DIN 1.4568 was austenitized at 1000°C for 10 min in an inert atmosphere and then air cooled. The annealed wire is referred to as DIN 1.4568a. Annealing resulted in a drastic improvement in rate of transformation, as well as a reduction in incubation period, as depicted in Figure 3.129. Since the alloy was only available in 3mm wire, it was not feasible to directly compare it to other alloys; however, DIN 1.4568a displayed extremely strong early transformation.

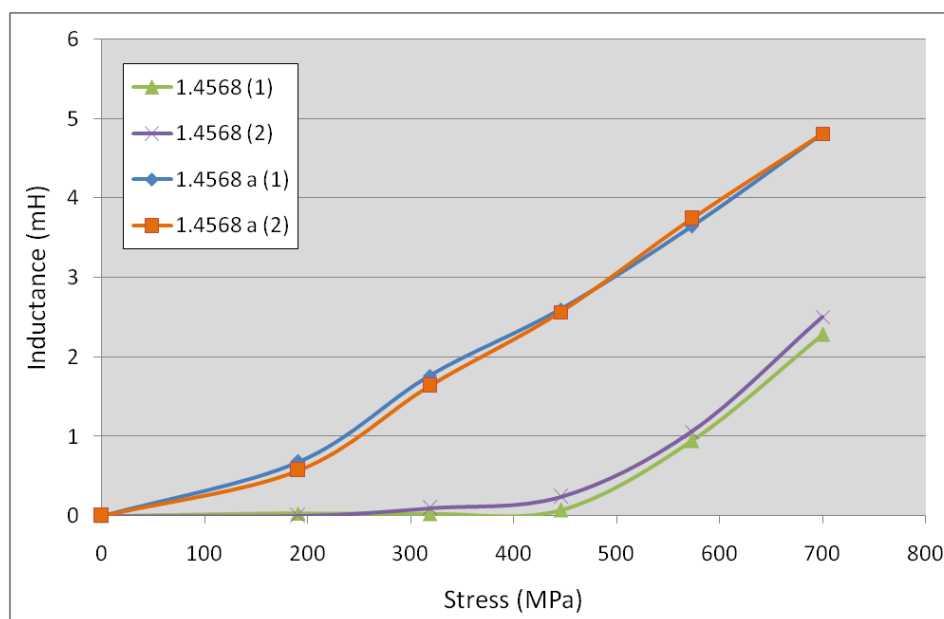


**Figure 3.129:** Graph showing inductive change versus stress for alloy DIN 1.4568 in the as-received and in the austenitized (showing “a” suffix) forms. Deformation was applied at 10 mm/min ( $0.07 \text{ min}^{-1}$ ).

Variable strain rate testing was performed on Alloy DIN 1.4568 (Figure 3.130). All strain rates were within the quasi-static range ( $0.0005$  to  $0.002 \text{ s}^{-1}$ ). Even without applying substantially high deformation speeds, a noticeably greater variation in rate of transformation was observed compared to that at constant strain rates, shown in Figure 3.129.

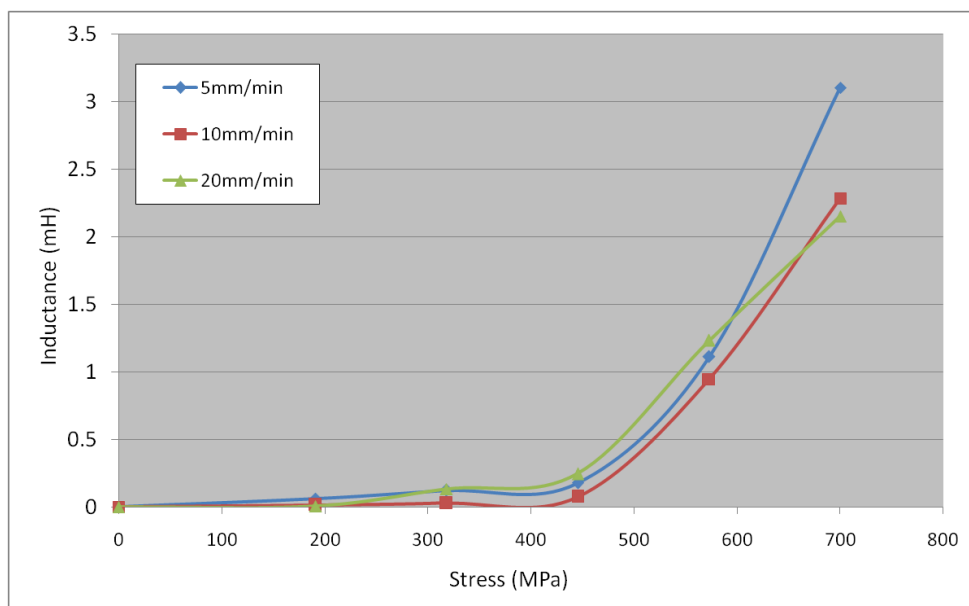


**Figure 3.130: Stress versus inductance change at different quasi-static strain rates for alloy DIN 1.4568**

Figure 3.131 and Figure 3.132 are SEM images showing the microstructure of Alloy DIN 1.4568a before and after 50% tensile deformation. Figure 3.131 shows the general effect of 50% strain on the microstructure; grains have elongated and the extent of martensite has increased. In comparing Figure 3.132 (a) and Figure 3.132 (b), which were taken at higher magnifications than Figure 3.131, Alloy DIN 1.4568 contained a large amount of martensite even before transformation. However, the majority of the microstructure in Figure 3.132 (a) shows smooth, unetched austenite. Figure 3.132 (b) shows how a considerable portion of the austenite, particularly where the austenite was present as islands within martensite, has transformed to martensite.

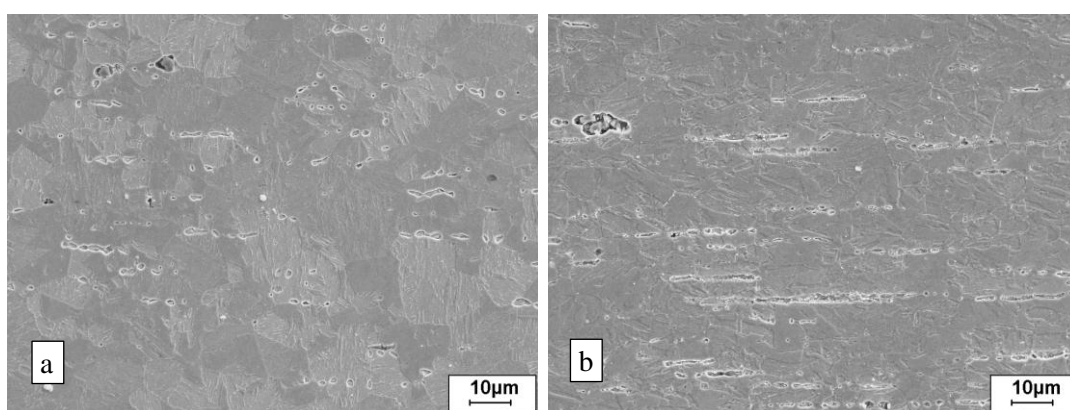


**Figure 3.131: 1.4568, longitudinal-section, SEM-SE image: (a) undeformed, smooth darker austenite, lighter coarse martensite; (b) deformed to 50% strain in tension, elongated grains, austenite grains largely fragmented by coarse martensite.**

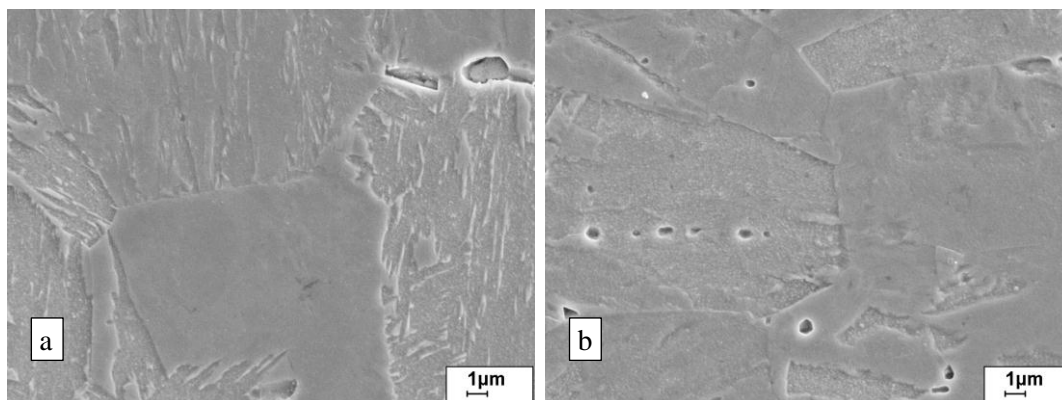


**Figure 3.132: 1.4568, longitudinal-section, SEM-SE image: (a) undeformed, smooth austenite, austenite dispersed within coarse martensite in some areas; (b) deformed to 50% strain in tension, minimal austenite remaining within martensite, most grains transformed to martensite.**

### 3.5.9 Temperature sensitivity

This section contributed to journal paper 1 (The effects of transformation temperature on the rate of transformation in TRIP steels), included in Appendix 3. A primary concern related to the utilisation of TRIP steels as sensor elements is the temperature and associated strain rate sensitivity of the transformation (Chapters 2.5, 3.3 and 3.4). A theory developed in Section 3.3 for determining the sensitivity of an alloy composition to temperature was developed. This theory was implemented in the design of alloy TRIP R in Section 3.5.4. In this section, the effect of temperature on the transformation of Alloys TRIP M and TRIP R were experimentally assessed.

In Section 3.3, it was theorised that an alloy's dislocation density also effects temperature sensitivity. A higher dislocation density was predicted to increase temperature sensitivity. Although dislocation density will be expected to increase as deformation progresses; it is expected that an alloy that begins tensile deformation with a lower dislocation density will maintain lower dislocation density until failure. This is evidenced by the well-known phenomenon that prior cold work increases tensile strength (Herbert, 1926). Alloy TRIP M was thus tested in three conditions: Annealed, hot rolled and water quenched, warm worked (Section 3.5.5.3). The material in an annealed condition was expected to have the lowest dislocation density (Singhal, 1971) (Rowcliffe & Nicholson, 1972) (Suh et al., 2002) (Okazaki, 2008). That in a warm worked condition was expected to have the highest (Williamson & Smallman, 1956) (Boswell & Smith, 1958) (Marshall, 1984) (Okazaki, 2008) (S. Murugesan et al., 2011).

The effect on hardness was assessed after warm working TRIP M to form TRIP MW, as described in Section 3.5.5.3, and after annealing TRIP M for one hour at 1150°C and furnace cooling to form TRIP MA. These results are shown in Table

**Table 3.23: Average hardness of TRIP M after warm working (TRIP MW) or annealing (TRIP MA).**

	TRIP MA	TRIP M	TRIP MW
Hardness (HRC)	21	25	38

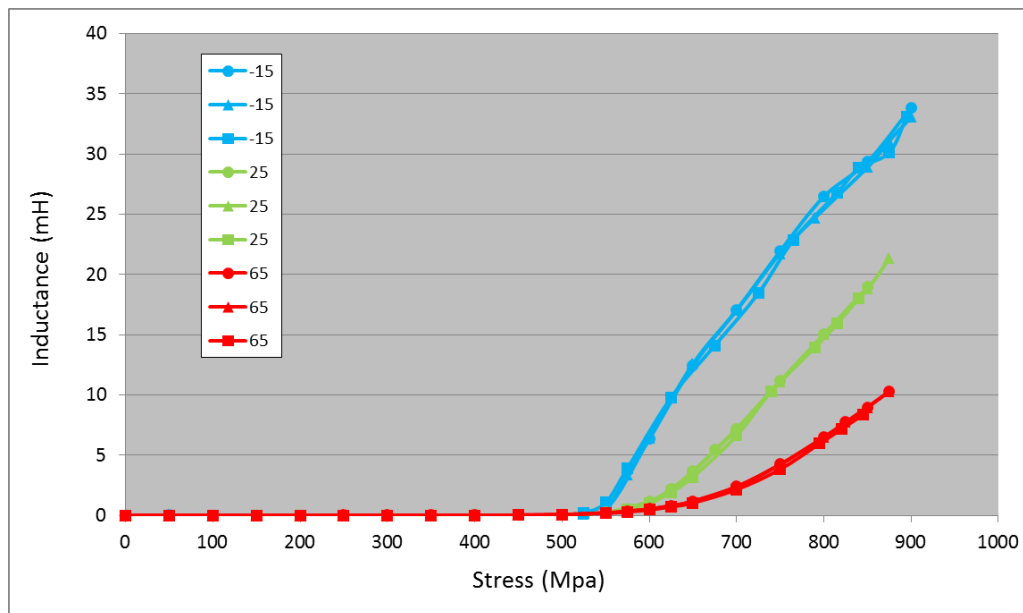
The effect of dislocation density on temperature sensitivity was assessed in relation to the theory developed in Section 3.3. Test temperatures were chosen to be -15°C, 25°C and 65°C because they were relatively easy to implement in the lab and also because they represent a range expected in many engineering structures. The custom-built coolant chamber used to perform the transformation temperature sensitivity testing is shown in Figure 3.133.



**Figure 3.133: Image (a) shows (from left to right) the coolant chamber, the loading bar with specimen and coil installed, and the next test specimen. Image (b) shows the chamber installed with specimen, cooling and instrumentation in place.**

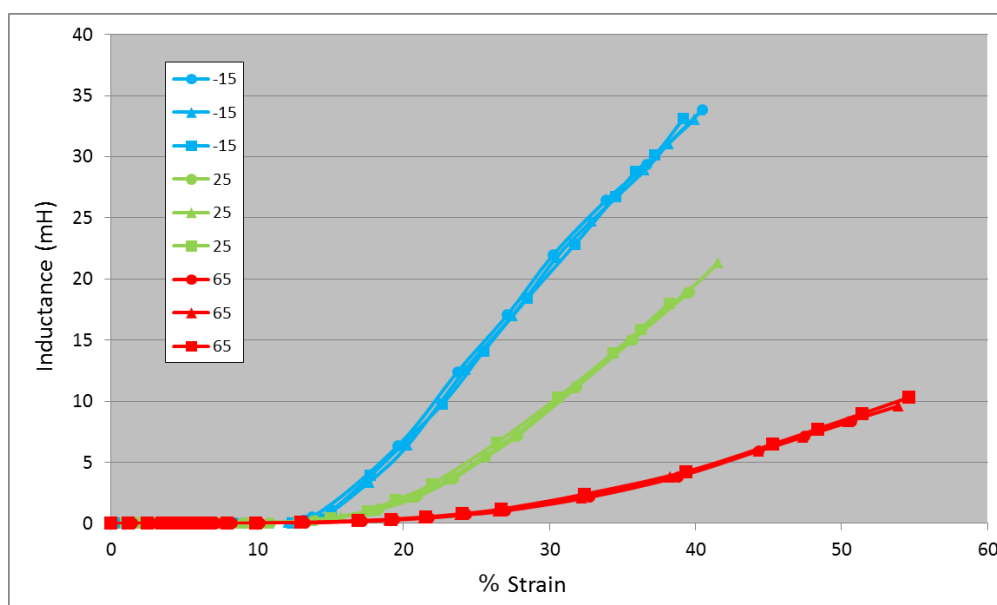
Specimens of each alloy were cooled to -30°C and held at that temperature for one hour. The magnetic susceptibility of each specimen was tested before and after cooling using a Fugro GMS-2 magnetic susceptibility meter. No detectable change in magnetic susceptibility occurred upon cooling. Thus, it was established that cooling to -15°C would not alone produce significant thermally-induced martensite in the following tests.

Figure 3.134 shows the transformation of Alloy TRIP M versus stress in a hot rolled and water-quenched state under quasi-static loading at  $-15^{\circ}\text{C}$ ,  $25^{\circ}\text{C}$  and  $65^{\circ}\text{C}$ . Three tests are shown for each temperature and the discrepancy between similar tests was insignificant, at approximately 10 MPa total error, compared to the variation due to temperature.



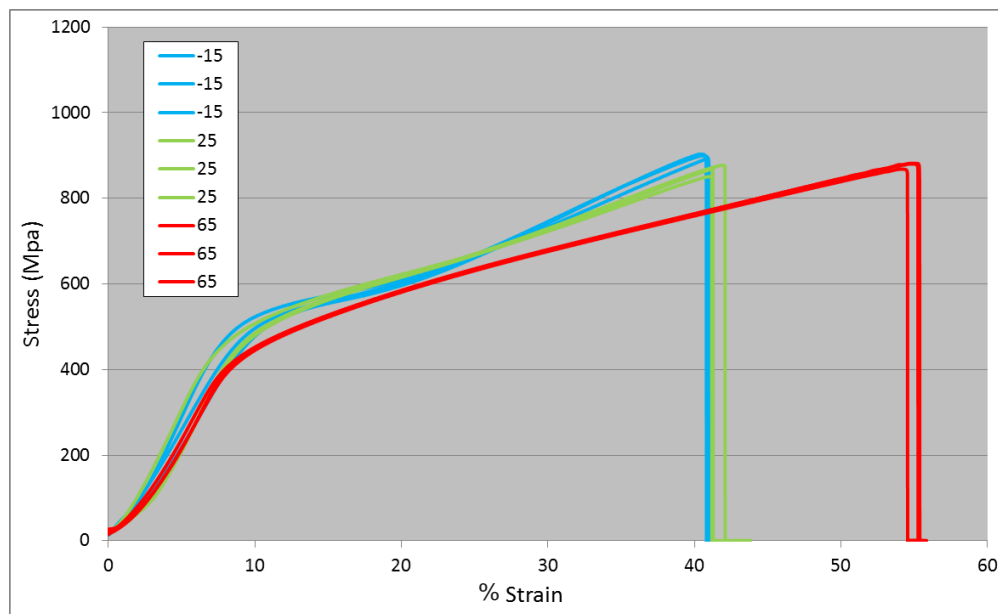
**Figure 3.134: Transformation versus stress of hot rolled TRIP M at  $-15^{\circ}\text{C}$ ,  $25^{\circ}\text{C}$  and  $65^{\circ}\text{C}$ .**

Figure 3.135 shows the transformation of Alloy TRIP M versus strain in a hot rolled and water-quenched state under quasi-static loading at  $-15^{\circ}\text{C}$ ,  $25^{\circ}\text{C}$  and  $65^{\circ}\text{C}$ . Three tests are shown for each temperature, and the discrepancy between similar tests was insignificant, at approximately 1% strain total error, compared to the variation due to environmental factors.



**Figure 3.135: Transformation versus strain of hot rolled TRIP M at  $-15^{\circ}\text{C}$ ,  $25^{\circ}\text{C}$  and  $65^{\circ}\text{C}$ .**

Figure 3.136 shows the stress versus strain curve for Alloy TRIP M in a hot rolled and water-quenched state under quasi-static loading at  $-15^{\circ}\text{C}$ ,  $25^{\circ}\text{C}$  and  $65^{\circ}\text{C}$ . Again, three tests are shown for each temperature and there was only minor discrepancy (approximately 1% strain total error above 10% strain) between similar tests. It was not possible to utilise a strain gauge during temperature testing due to the presence of the liquid coolant chamber. Thus, the strain data was derived from total extension. However, prior testing without the temperature test chamber with a strain gauge was utilised for calibration, and showed the error in frame extension data to be small when initial grip slippage was ignored by prestressing. Each specimen was also marked with a gauge length before testing, which was measured after testing, enabling a calibration adjustment and strain data verification.



**Figure 3.136: Stress versus strain for hot rolled alloy TRIP M at  $-15^{\circ}\text{C}$ ,  $25^{\circ}\text{C}$  and  $65^{\circ}\text{C}$ .**

Figure 3.137, Figure 3.138 and Figure 3.139 show stress versus strain, stress versus transformation and strain versus transformation respectively for TRIP M and TRIP R, where each curve is the average of three tests. The deviation between similar tests was insignificant compared to the effect of temperature variation. TRIP R was designed according to the empirically-based theory developed in Section 3.4 to determine the sensitivity of an alloy composition to temperature, and Figure 3.138 shows that TRIP R exhibited significantly less temperature sensitivity than TRIP M. Figure 3.139 shows that the effect of temperature on strain versus transformation is marginally less for TRIP R.

TRIP R had a more sensitive transformation with respect to stress and to strain in that the transformation starts earlier and continued for longer. This was intended by the design.

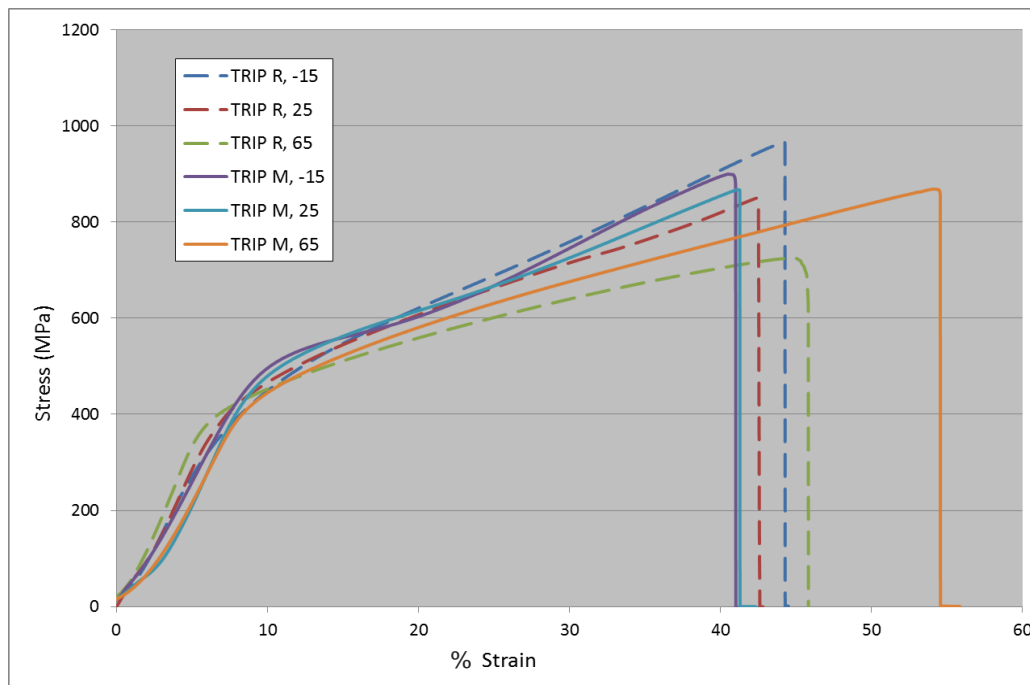


Figure 3.137: Stress versus strain for TRIP R and for TRIP M at -15°C, 25°C and 65°C.

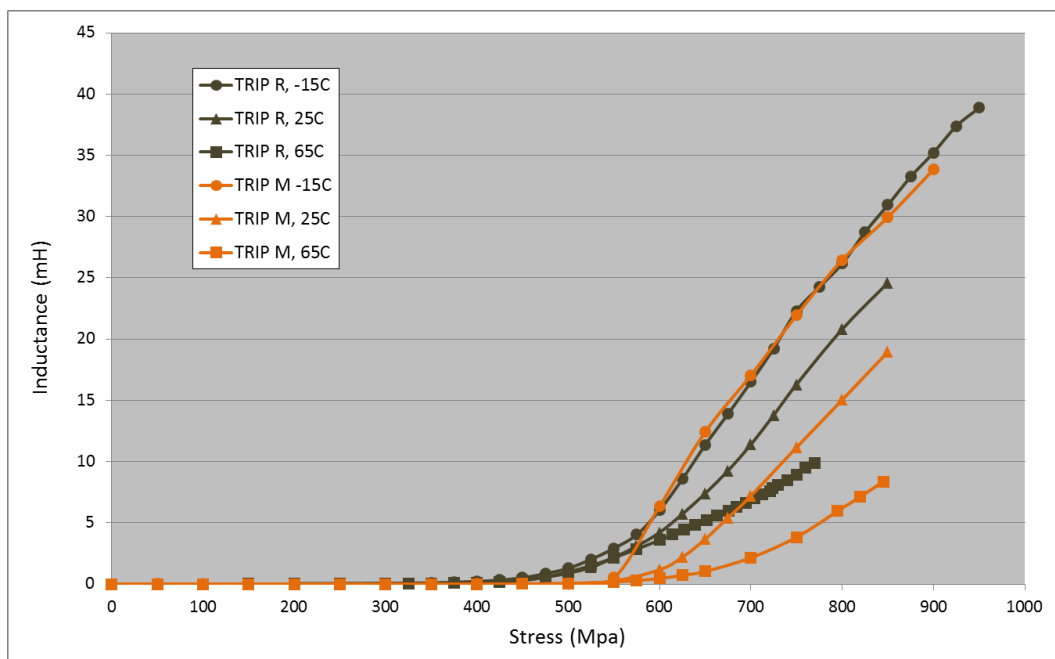
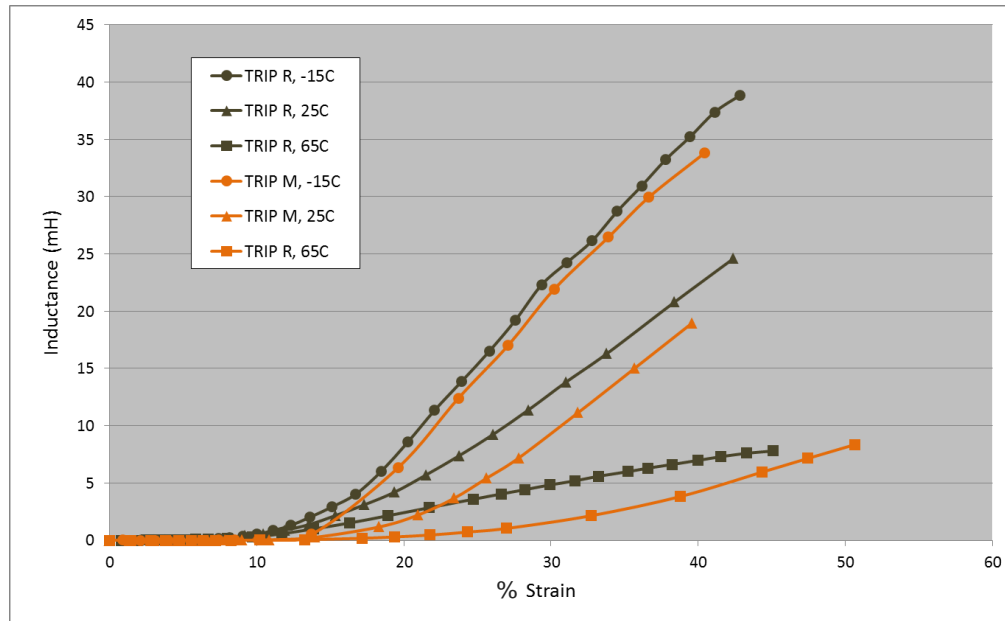


Figure 3.138: Stress versus transformation for TRIP M and TRIP R when tested at -15°C, 25°C and 65°C.





**Figure 3.139: Strain versus transformation for TRIP M and TRIP R when tested at  $-15^{\circ}\text{C}$ ,  $25^{\circ}\text{C}$  and  $65^{\circ}\text{C}$ .**

Figure 3.140 shows the effect of annealing TRIP M for one hour at  $1150^{\circ}\text{C}$  on its stress versus transformation curve at  $-15^{\circ}\text{C}$ ,  $25^{\circ}\text{C}$  and  $65^{\circ}\text{C}$ . The annealed material is referred to as TRIP MA. The annealing time and temperature were low enough not to cause a significant increase in austenitic grain size, as shown by comparing Figure 3.159 to Figure 3.171. This is significant because it was proposed that increased grain size may increase temperature sensitivity (Section 2.9). The inductance change for TRIP MA is shown amplified five times to enable relative comparison to TRIP M on the same chart.

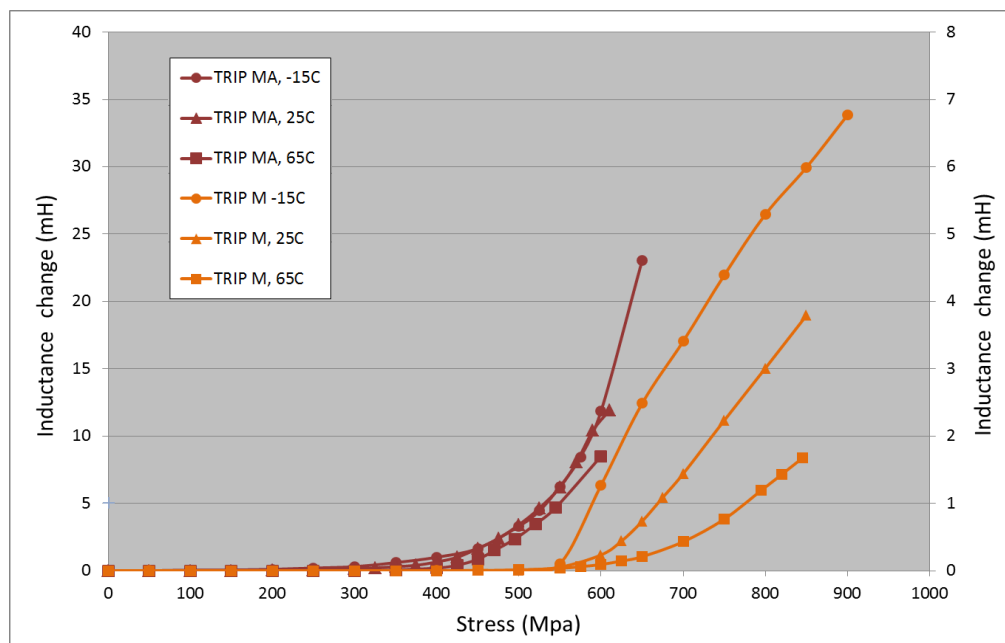


**Figure 3.140: Stress versus transformation for TRIP M and TRIP M annealed at  $1150^{\circ}\text{C}$  for one hour (TRIP MA, right axis) at  $-15^{\circ}\text{C}$ ,  $25^{\circ}\text{C}$  and  $65^{\circ}\text{C}$  (Bemont et al., 2013).**

In Chapter 3.3, it was postulated that dislocation density affects temperature sensitivity because dislocations provide martensite nucleation sites. A greater number of nucleation sites would result in a greater number of sites being activated for a particular thermal driving force, and thereby greater temperature sensitivity. It is apparent that the temperature sensitivity of TRIP M in an annealed form was substantially less than in its hot rolled and water-quenched form. The magnitude of its transformation is also significantly less. This is also expected when fewer martensite nucleation sites are present. Transformation in the annealed alloy starts earlier, consistent with lower yield strength. The UTS of the material was also lower, as expected.

Figure 3.140 shows the effect of annealing TRIP M for one hour at 1150°C on its strain versus transformation curve at -15°C, 25°C and 65°C. The inductance change for this material, TRIP MA is shown amplified five times to enable relative comparison to TRIP M on the same chart.

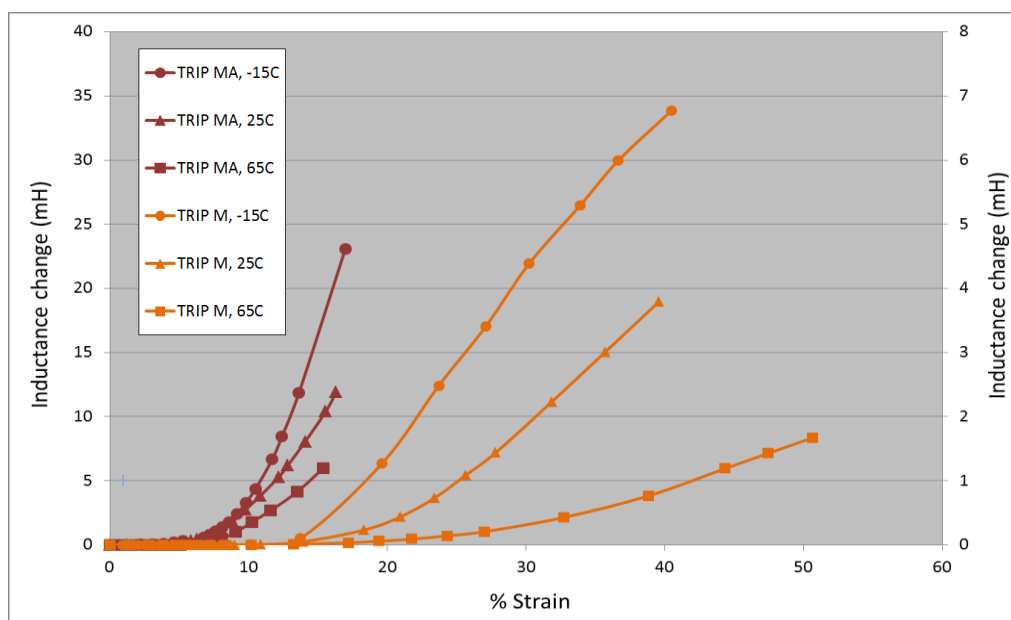


**Figure 3.141: Strain versus transformation at 15for TRIP M and TRIP M annealed at 1150°C for one hour (TRIP MA, right axis) at -15°C, 25°C and 65°C.**

The annealed form of TRIP M also showed less temperature sensitivity relative to strain. However, the reduction in temperature sensitivity was less significant than for stress. To compare the two alloys as they might be applied to a strain sensor, an inductance reading of 5 mH was considered. In the hot rolled and quenched alloy, this would imply a strain of  $31\% \pm 12\%$ . In the annealed alloy, 5mH would imply a strain of  $13\% \pm 2\%$ . This is a very significant improvement in precision, and the improvement was similar throughout the measureable range. The potential measurement range of Alloy MA would be from about 8% strain to 15% strain, whereas that of Alloy TRIP M from about 25% strain to 50% strain. However, mechanical sensor design could effect similar elongation measurements, since both materials exhibit useful transformation over about half of their total extension.

TRIP M was warm rolled to 20% reduction (Section 3.5.3) to produce TRIP MW. Figure 3.142 shows stress versus strain at  $-15^{\circ}\text{C}$ ,  $25^{\circ}\text{C}$  and  $65^{\circ}\text{C}$  for TRIP M, for TRIP MA and for TRIP MW.

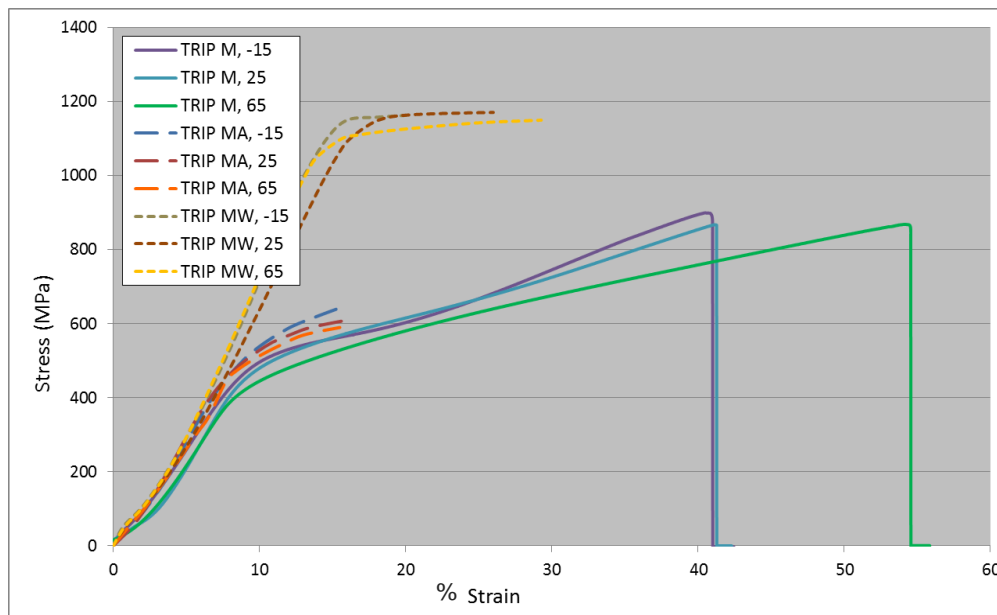


**Figure 3.142: Stress versus strain for alloys TRIP M, TRIP MA and TRIP MW at  $-15^{\circ}\text{C}$ ,  $25^{\circ}\text{C}$  and  $65^{\circ}\text{C}$ .**

Figure 3.143 shows stress versus transformation at  $-15^{\circ}\text{C}$ ,  $25^{\circ}\text{C}$  and  $65^{\circ}\text{C}$  for TRIP M and for TRIP MW. Figure 3.144 shows strain versus transformation at  $-15^{\circ}\text{C}$ ,  $25^{\circ}\text{C}$  and  $65^{\circ}\text{C}$  for TRIP M and for TRIP MW. The inductance change for TRIP MW is shown amplified twenty times to enable relative comparison to TRIP M on the same charts.

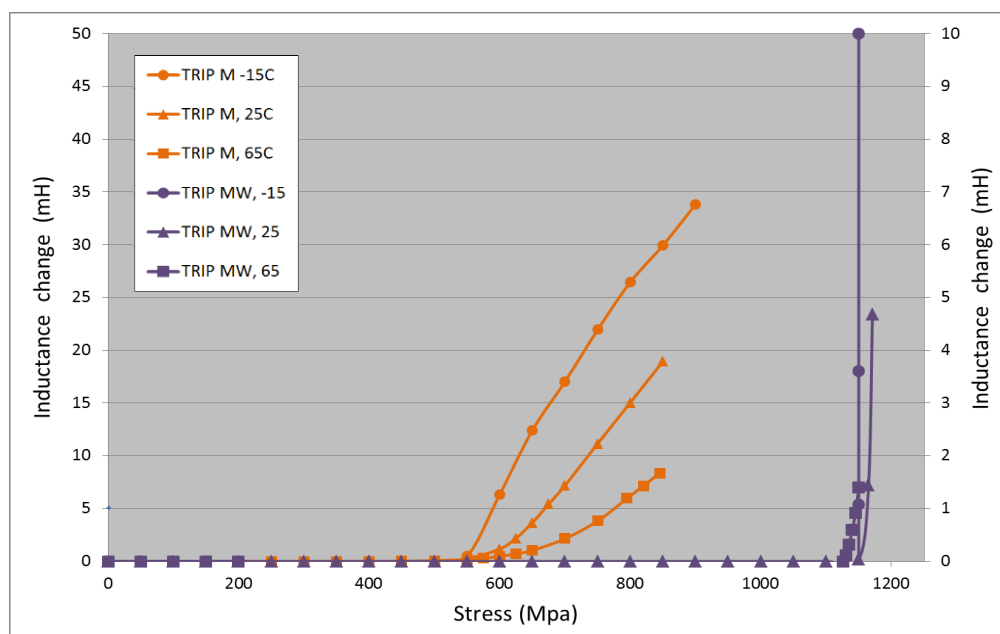


**Figure 3.143: Stress versus transformation for TRIP M and TRIP MW (right axis) at  $-15^{\circ}\text{C}$ ,  $25^{\circ}\text{C}$  and  $65^{\circ}\text{C}$  (Bemont et al., 2013).**

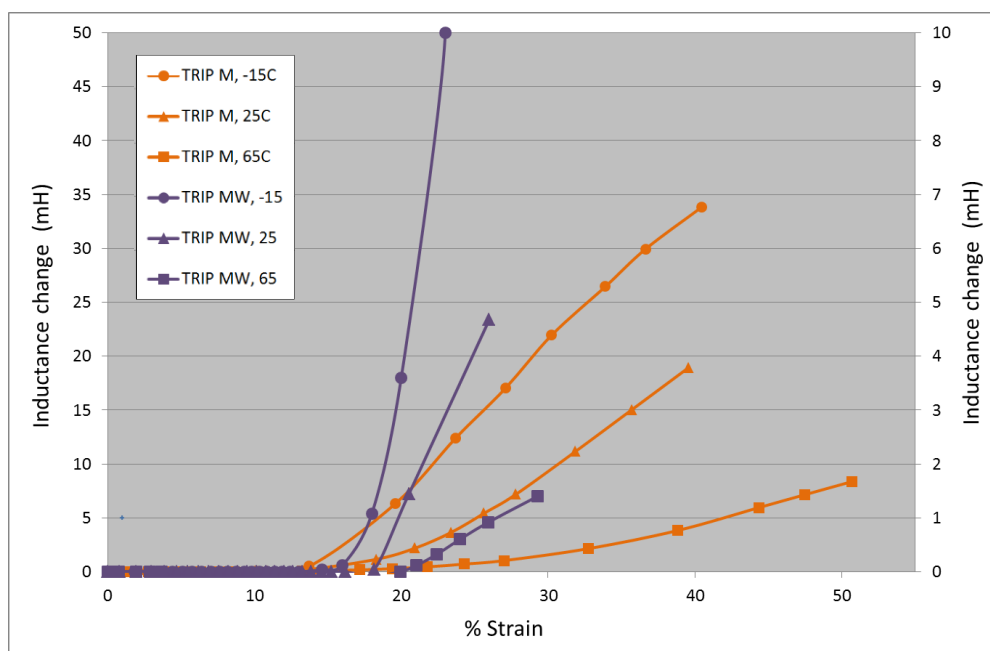


**Figure 3.144: Strain versus transformation for TRIP M and TRIP MW at -15°C, 25°C and 65°C.**

Examining Figure 3.142 and Figure 3.143, it is apparent that due to the already extremely high dislocation density in TRIP MW, significant strain hardening did not occur. The material's yield and UTS were thus almost the same. It is therefore impossible to utilise this material as a load sensor element. Temperature sensitivity of the material's transformation with increasing stress cannot be assessed, because once transformation begins, stress does not increase. However, it is clear that the material is highly temperature sensitive. Although UTS was similar at all three temperatures and the material tested at -15°C underwent considerably less strain, total transformation at -15°C was more than twenty times that at 65°C, a considerably larger difference than in any other material tested. TRIP MW would also not be practical for use as a strain measurement sensor over the temperature range investigated, because it could only be relied upon to measure strain between 20% (start of transformation at 65°C) and 23% (failure at -15°C). The error of this measurement would peak at approximately  $\pm 5\%$  strain, making the measurement useless. It is clear that the effect of temperature on extent of transformation was greatest in the warm-worked alloy and least in the annealed alloy. This corroborates the theory that dislocation density is positively related to transformation temperature sensitivity.

### 3.5.10 Metallography

#### 3.5.10.1 Sample preparation

Specimens were prepared in a similar manner and using the same equipment as described in Section 3.4.6.1 for the compressive TRIP steel alloys. However, the etchant used in Section 3.4.6, originally suggested by Olson and Azrin, was found to etch the tensile alloys poorly

(Olson & Azrin, 1978). Thus, after some experimentation with various etchants, Kalling's #1 etch was utilised, but was modified by adding an extra 7% HCl.

A standardised sectioning, grinding, polishing and etching procedure was utilised. Polishing was performed on the Struers TegraPol 11, as follows: MD-Piano 220, MD-Largo, MD-Dac, MD-Chem with OP-S suspension, MD-Nap. It was found that when OP-S was used for more than one minute, the surface of many specimens became etched in a manner that was not beneficial to final etching. Thus, MD-Chem was used with OP-S for 1 minute after which MD-Nap was used for 2.5 minutes; removing most of the OP-S etch.

After polishing, each specimen was cleaned and then submerged in the modified Kalling's #1 solution and agitated for exactly 30 seconds before being rinsed with alcohol. This means that each specimen image could be directly compared to the others because the preparation processes were identical.

### 3.5.10.2 Microstructures

The optical microscopy images were obtained using a Nikon MA200 inverted metallurgical microscope. Differential interference contrasting (DIC) was found to improve the definition of the microstructure and was utilised throughout. SEM microscopy was performed using a Zeiss Ultra FEG-SEM.

According to the ASM Speciality Handbook on Stainless Steels (Davis, 1994), Kalling's #1 solution can very lightly attack austenite, leaving it white or off-white. Ferrite is rapidly attacked and coloured (usually blue) and martensite is darkened. To enable direct metallographic comparison between the identically prepared and etched alloys, it was decided that each microstructure would be optically imaged at 100x and 500x magnification, and under SEM-SE at 10 000x. If distinguishing features were present, then other magnifications were sometimes included to portray these.

The microstructure of alloy TRIP R was shown undeformed and deformed to various extents, as specified, at -15°C, 25°C and 65°C, in Figure 3.145 to Figure 3.157. In the undeformed state, an evenly dispersed network of dark bands in somewhat twinned austenite was observed (Figure 3.145 and Figure 3.146). The bands are likely to be predominantly  $\epsilon$  martensite, since at high magnifications,  $\alpha'$  martensite is observed at band intersections (Figure 3.147). This is similar to microstructures observed by Abrassart (Figure 2.63 and Figure 2.64) (Abrassart, 1973).

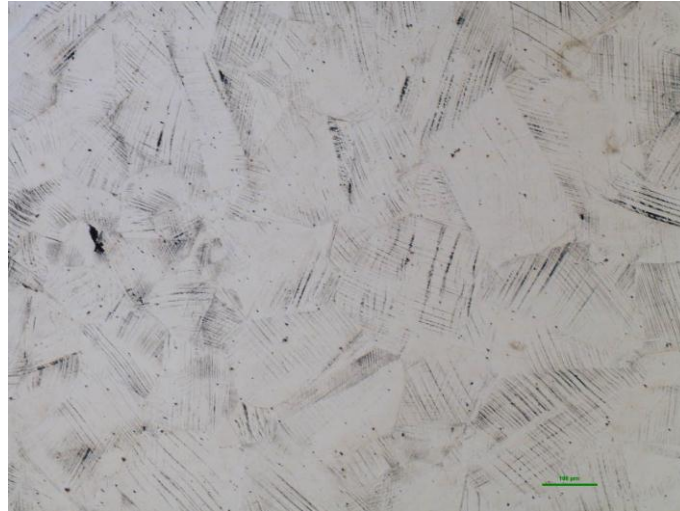


**Figure 3.145:** TRIP R, undeformed, scale bar represents 100  $\mu\text{m}$ . Optical image, light austenite, dark martensite plates.

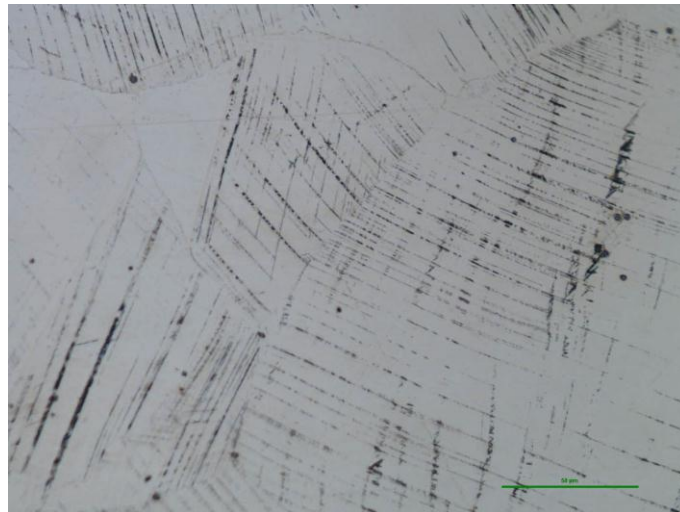


**Figure 3.146:** TRIP R, undeformed, scale bar represents 50  $\mu\text{m}$ . Optical image, light austenite, dark martensite plates.

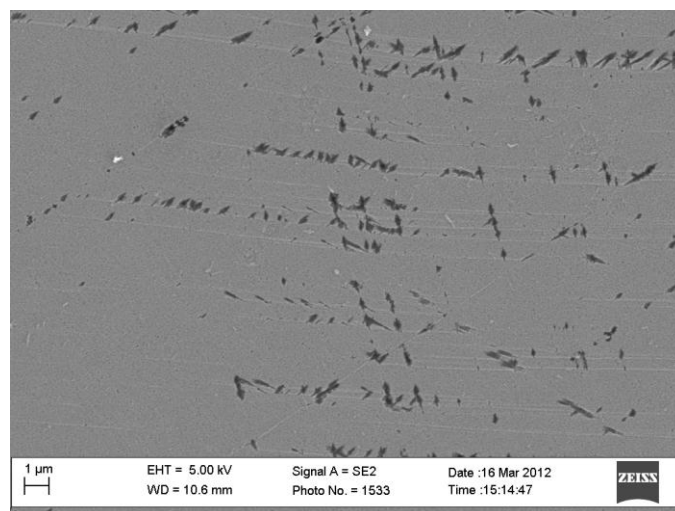


**Figure 3.147:** TRIP R undeformed. SEM-SE image at 10 000x magnification, lighter austenite, dark plate martensite.



During deformation at  $-15^{\circ}\text{C}$ , an extensive network of hatched shear bands (bands at acute angles to one another) developed by 700 MPa (Figure 3.149 (a)). Isolated regions of apparent  $\alpha'$  lath martensite were observed, most densely near to grain boundaries (Figure 3.148 (a), Figure 3.149 (a)). This may have been aided by a degree of chromium sensitisation during warm rolling, which may promote greater early transformation in areas of reduced chromium. However, the  $\alpha'$  martensite islands were also found within grains, particularly in regions of austenite twinning (Figure 3.149 (a)).

By 900 MPa, the microstructure had developed extensive  $\alpha'$  lath martensite (Figure 3.148 (b)). The  $\alpha'$  martensite was interrupted only by regions of austenite twinning and by an extensive light-coloured shear band network (Figure 3.149 (b)). Martensite plates apparently did not easily cross austenite twin boundaries (Figure 3.149 (b)). The  $\alpha'$  martensite developed here was distinct in that it grew primarily between, and not within, the shear band network (Figure 3.149 (b), Figure 3.150 (a) and (b)). Figure 3.150 (c) shows the morphology of the  $\alpha'$  martensite.

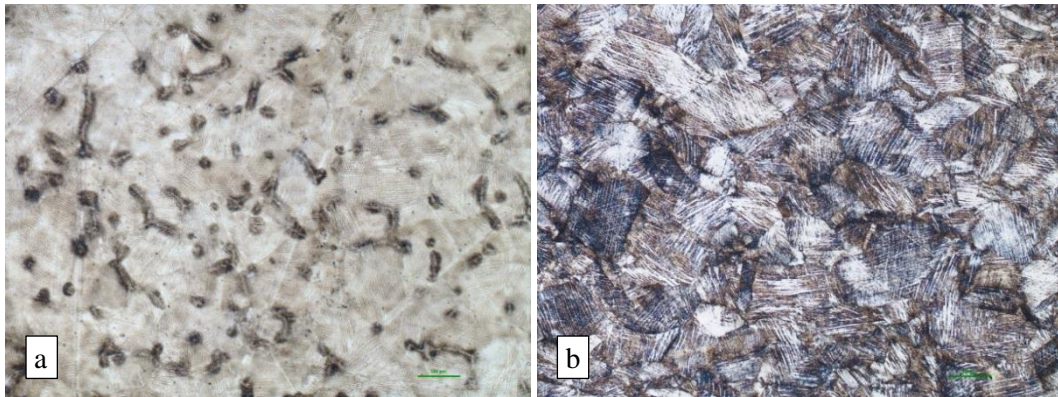


**Figure 3.148:** TRIP R, deformed at  $-15^{\circ}\text{C}$ , scale bars represent  $100\text{ }\mu\text{m}$ : (a) 700 MPa, 18 mH change in inductance, dark martensite formed predominantly on grain boundaries; (b) 966 MPa failure, 40 mH change in inductance, dark martensite uniformly distributed, light, untransformed austenitic bands.

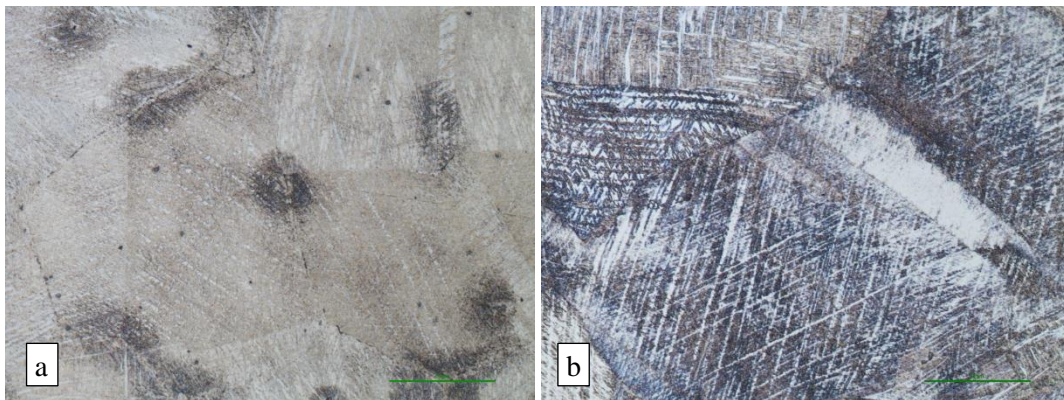


**Figure 3.149:** TRIP R, deformed at  $-15^{\circ}\text{C}$ , scale bars represent  $50\text{ }\mu\text{m}$ : (a) 700 MPa, dark martensite formed predominantly on grain and twin boundaries; (b) 966 MPa failure, lath and some plate martensite, between light, untransformed austenitic bands.



The morphology of the microstructure of TRIP R deformed at 25°C was different from that deformed at -15°C in that the banded network, while again present, appeared dark and only somewhat hatched (Figure 3.149 (b), Figure 3.151, Figure 3.152). All specimens were identically prepared and etched. Kalling's reagent is expected from literature to etch  $\epsilon$  martensite dark (Davis, 1994) (Hirsch, 2008). The shear bands formed during deformation at -15°C are thus likely to represent shear bands other than  $\epsilon$  martensite, such as slip band bundles, whereas the shear bands formed during deformation at 25°C are likely to represent  $\epsilon$  martensite.

It is possible that the white shear bands formed at -15°C are not slip bands but  $\epsilon$  martensite, and that the dark bands formed at 25°C represent  $\alpha'$  martensite that originated on shear bands. A deeper understanding of this could be obtained using EBSD on SEM or using TEM, but is not of principle importance to the current investigation.

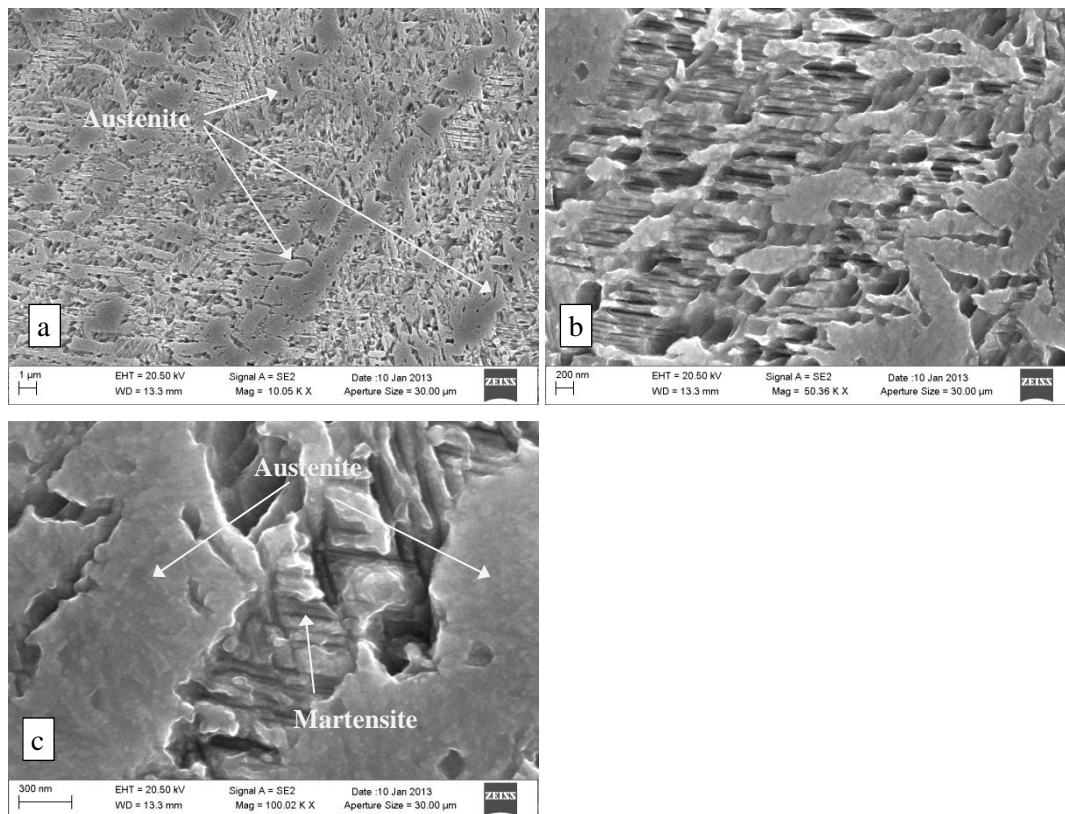


**Figure 3.150: TRIP R deformed to 966 MPa failure at -15°C, SEM-SE images, (a) 10 000x magnification, rough predominantly martensite surface, with smoother predominantly austenite bands; (b) 50 000x magnification, rough, etched martensite, smooth austenite; (c) 100 000x magnification, rough, etched martensite, smooth austenite.**

Martensite did not appear to have formed more densely at grain boundaries at 25°C, as at 15°C. This implies that the effect was either not due to sensitisation, or that the degree of sensitisation was very small. The effect of twinning is evident in Figure 3.152. While  $\alpha'$  martensite appeared equally widely spread at -15°C and 25°C deformation, its density was higher in the sample deformed at -15°C (Figure 3.148 (b), Figure 3.151 (b)). This corresponds to the considerably greater change in inductance recorded at -15°C. The martensite morphology appeared different at -15°C (Figure 3.150) and at 25°C (Figure 3.153) at high magnification, that produced at 25°C showed a more distinctly hatched appearance, possibly indicative of its origin in  $\epsilon$  martensite shear bands.

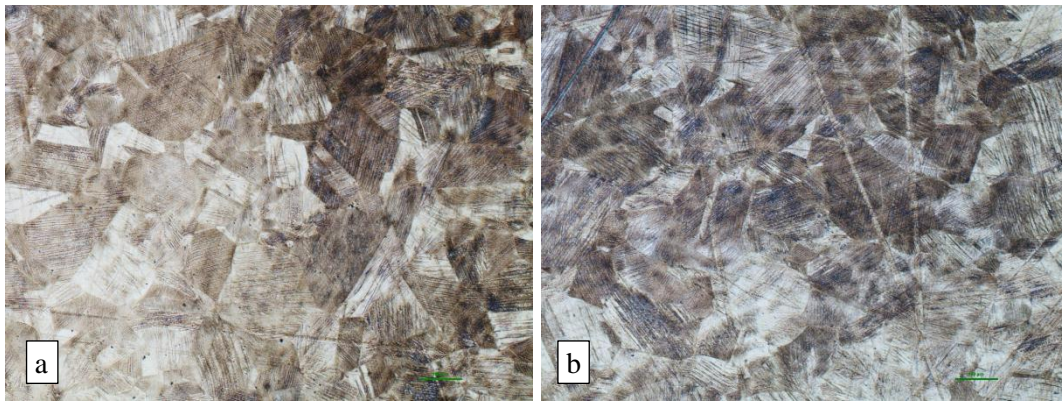


**Figure 3.151:** TRIP R, deformed at 25°C, scale bars represent 100  $\mu\text{m}$ : (a) 600 MPa, 5.5 mH change in inductance, darker, somewhat banded martensite evenly distributed in lighter austenite; (b) 850 MPa failure, 25 mH change in inductance, more dense martensite, more distinct bands.

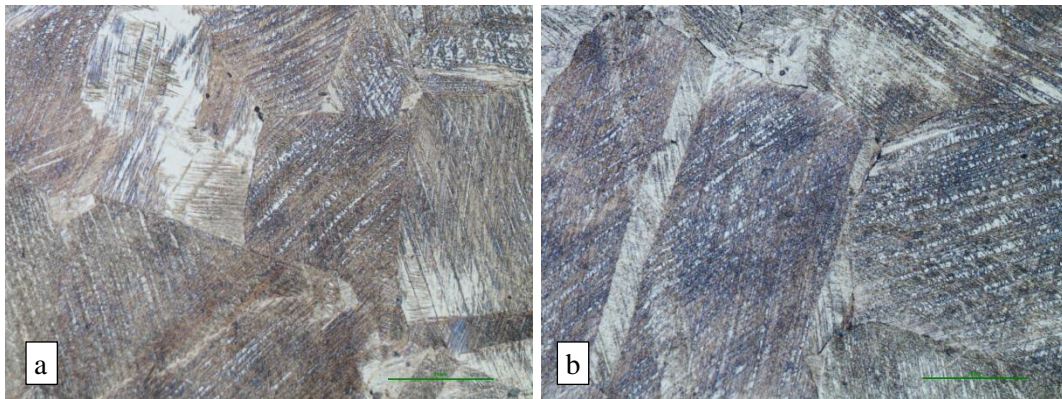


**Figure 3.152:** TRIP R, deformed at 25°C, scale bar represents 50  $\mu\text{m}$ : (a) 600 MPa, uniform darker martensite with isolated regions and broken bands of lighter austenite; (b) 850 MPa failure, darker, more dense martensite (lath and some plate), no undisturbed austenite.



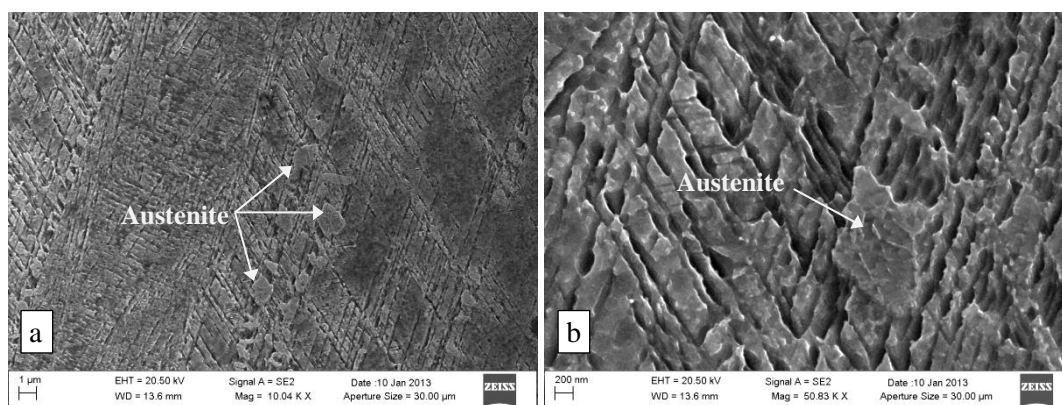


**Figure 3.153:** TRIP R deformed to 850 MPa failure at 25°C, SEM-SE image, (a) 10 000x magnification, etched martensite with very isolated regions of unetched austenite; (b) 50 000x magnification, a distinctly cross-hatched morphology, possibly related to prior-austenite slip planes.

The most distinct feature of the microstructure of TRIP R deformed at 65°C was the apparent lack of martensite near the austenite grain boundaries (Figure 3.154, Figure 3.155, Figure 3.157 (a)). This is in distinct contrast to the observation at -15°C (Figure 3.149). Again, this is likely associated to sensitisation at grain boundaries. The light regions are not believed to be ferrite because martensite could be observed growing within them (Figure 3.156) and because they were not present at lower deformation temperatures in this material. Similarly to the structure deformed at 25°C, a dark network of mostly unhatched bands had developed (Figure 3.154, Figure 3.155). Figure 3.156 provides an indication of the manner of martensite growth within the parent austenite near a grain boundary, apparently in specific crystallographic directions. The effect of austenite twins on the martensite growth was apparent, particularly at lower deformation (Figure 3.154 (a), Figure 3.155 (b), Figure 3.157 (a) and (b)). The morphology of the martensite appeared similar to that formed at 25°C (Figure 3.153 (a) and (b), Figure 3.157 (b) and (c)).

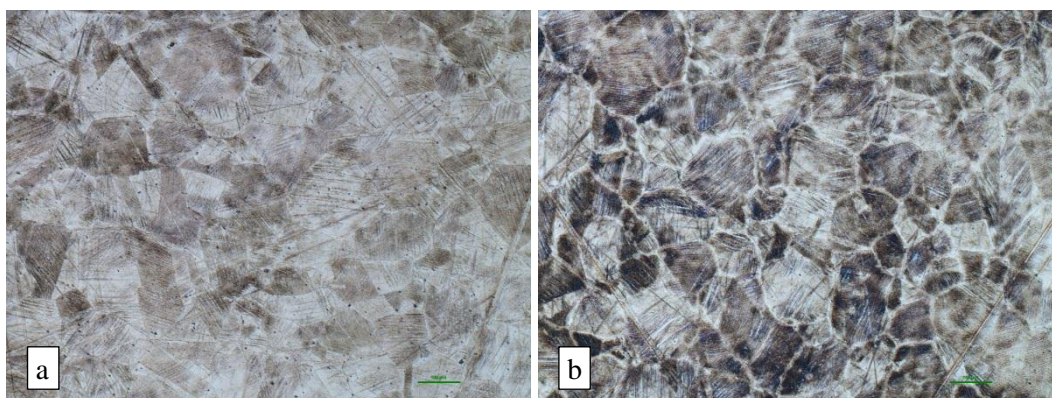


**Figure 3.154:** TRIP R, deformed at 65°C, scale bar represents 100 µm: (a) 600 MPa, 3.5 mH change in inductance, darker, uniformly distributed low density martensite in lighter austenite; (b) 770 MPa failure, 10 mH change in inductance, dense martensite within grains, less dense at grain boundaries.

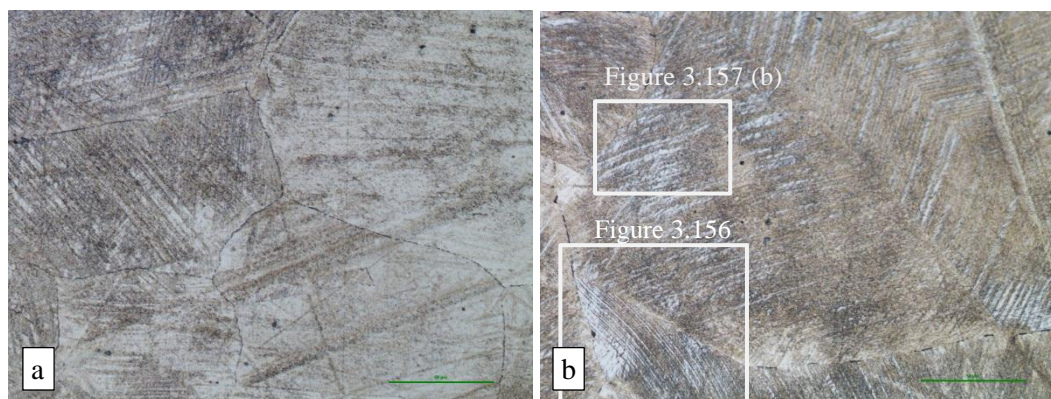


**Figure 3.155: TRIP R, deformed at 65°C, scale bar represents 50 µm: (a) 600 MPa, darker, uniformly distributed low density martensite in lighter austenite; (b) 770 MPa failure, dark martensite uniform within grains but not at grain boundaries.**



**Figure 3.156: Magnified view of region specified in Figure 3.155, showing the manner of martensite growth near a grain boundary.**

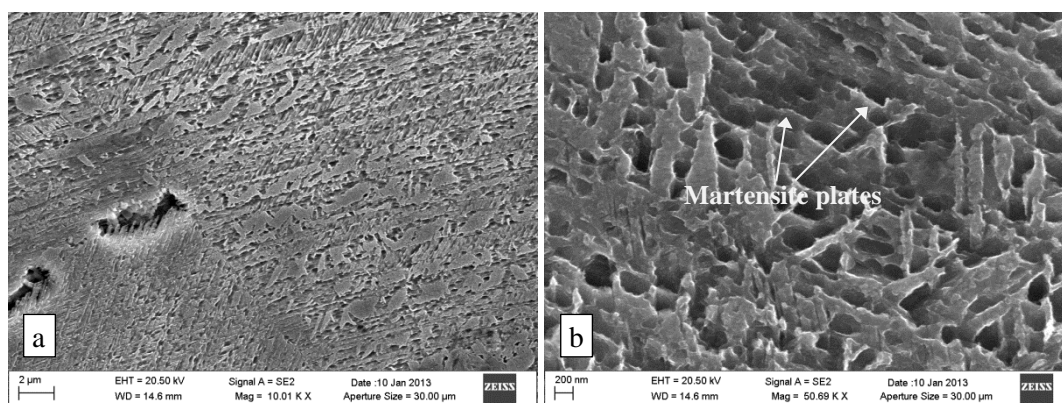


**Figure 3.157: TRIP R deformed to 770 MPa failure at 65°C, SEM-SE images, (a) 10 000x magnification, a region similar to that denoted in Figure 3.155, islands of smooth austenite within martensite; (b) 50 000x, martensite morphology was less distinct than at lower temperatures, but martensite plates are visible.**

The microstructure of alloy TRIP M is shown undeformed and deformed to various extents, as specified, at -15°C, 25°C and 65°C, in Figure 3.158 to Figure 3.169. The undeformed microstructure of TRIP M shows austenite with significant twinning and sparse martensite (Figure 3.158, Figure 3.159). High magnification SEM images revealed large networks of  $\alpha'$  lath martensite in places (Figure 3.160). Since specimens of TRIP M showed the same inductance as air, it is likely that this is surface martensite, formed during sample preparation.



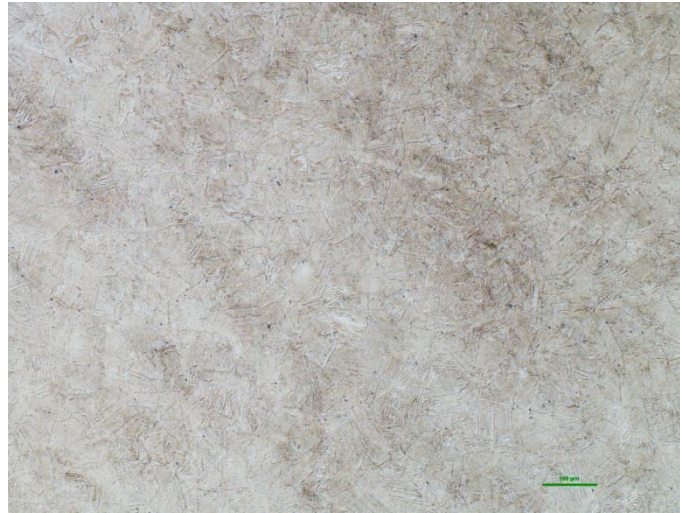


**Figure 3.158:** TRIP M, undeformed, scale bar represents 100  $\mu\text{m}$ . Sparse darker martensite in a light austenite matrix.

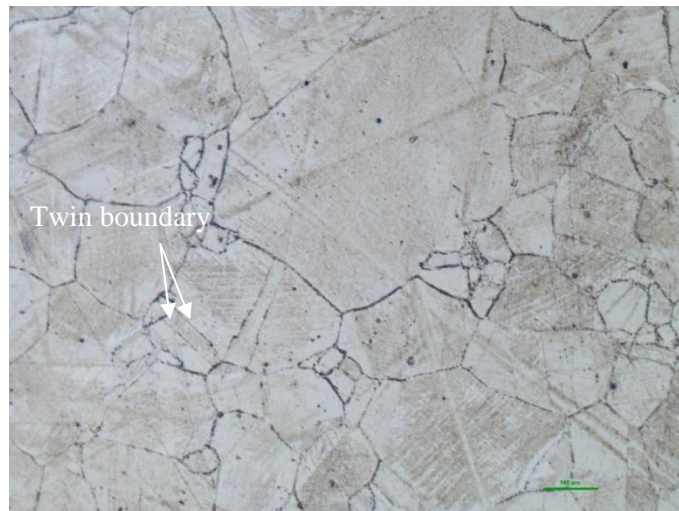


**Figure 3.159:** TRIP M, undeformed, scale bar represents 50  $\mu\text{m}$ . Sparse martensite, probably largely confined to the prepared surface, in a light austenite matrix. Signs of banding and twinning.

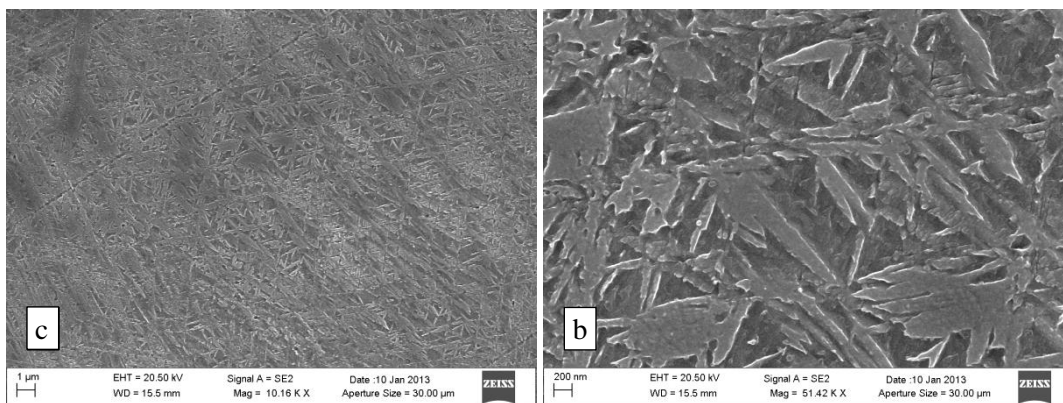


**Figure 3.160:** TRIP M undeformed, lenticular plate martensite in a relatively dense region, apparently confined to the surface: (a) 10 000x magnification; (b) 50 000x magnification.

Deformation at  $-15^{\circ}\text{C}$  developed extensive martensite by 750 MPa (Figure 3.161 (a)), with a considerable increase in the density of the martensite by 900 MPa (Figure 3.161 (b)). Martensite formed in a dark banded network, with hatching of these bands being infrequent (Figure 3.162). The dark bands are  $\alpha'$  martensite, and appeared to have grown in specific crystallographic directions. As deformation progressed, martensite appeared to concentrate in regions where it was already present (Figure 3.162). As well as growing in bands,  $\alpha'$  lath martensite also appeared to grow uniformly in some areas (Figure 3.162). As with TRIP R at  $-15^{\circ}\text{C}$ , martensite appeared to form more densely at austenite grain boundaries and twins (Figure 3.162 (b)). The martensite morphology was similar to that in the undeformed sample (Figure 3.160), but less uniformly distributed (Figure 3.163). This may be because the hard martensite already present before preparation in the deformed sample protected the remaining austenite from significant deformation and transformation to surface martensite during preparation.

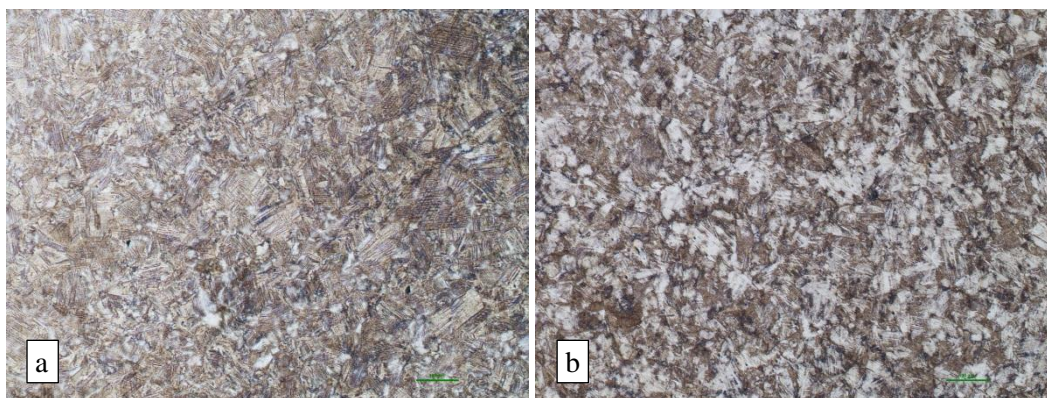


**Figure 3.161:** TRIP M deformed to failure at  $-15^{\circ}\text{C}$ , scale bars represent  $100\text{ }\mu\text{m}$ : (a) 750 MPa, 22 mH change in inductance, uniformly distributed darker martensite in light austenite; (b) 900 MPa failure, 34 mH change in inductance, dark, dense martensite with considerable regions of light austenite remaining.

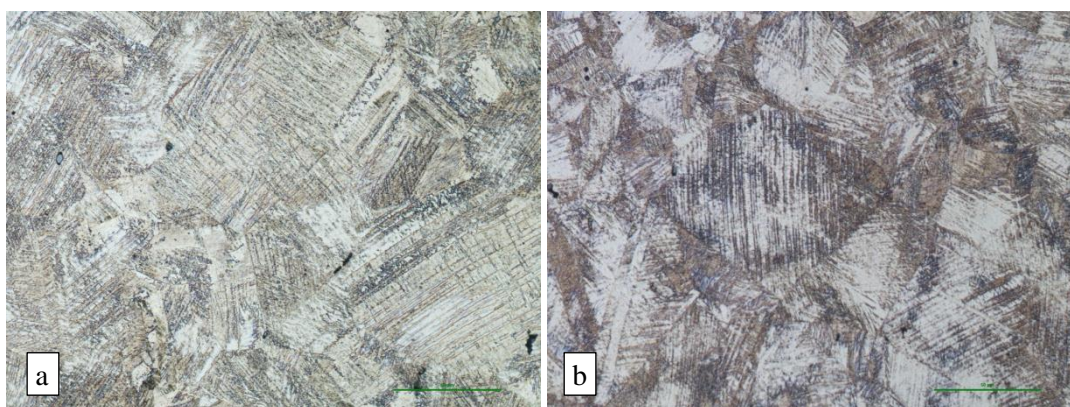


**Figure 3.162:** TRIP M deformed to failure at  $-15^{\circ}\text{C}$ , scale bars represent  $50\text{ }\mu\text{m}$ : (a) 750 MPa, sparse dark martensite, light austenite; (b) 900 MPa failure, dense martensite favouring grain boundaries in light austenite with some twinning.



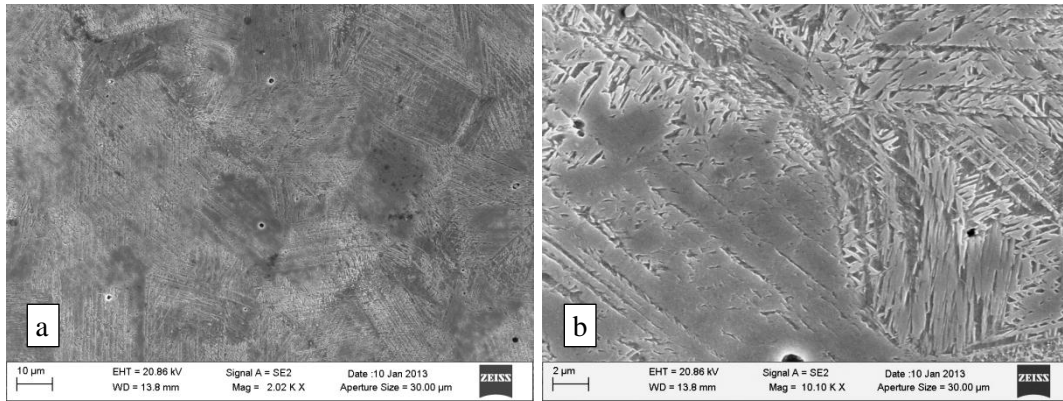


**Figure 3.163:** TRIP M deformed to 900 MPa failure at  $-15^{\circ}\text{C}$ , SEM-SE image: (a) 2 000x magnification, rough martensite surface relief surrounding islands of smoother austenite; (b) 10 000x magnification, the interface between an austenite and a martensite region.

Extensive martensite developed in TRIP M during deformation at  $25^{\circ}\text{C}$  but was noticeably less dense at a similar stress, (Figure 3.161 (a), Figure 3.164 (b)) and particularly at fracture (Figure 3.161 (b), Figure 3.162 (b), Figure 3.164 (c), Figure 3.165 (c)) compared to that formed at  $-15^{\circ}\text{C}$ . Dark martensite bands developed in a similar manner as at  $-15^{\circ}\text{C}$  (Figure 3.165). There appeared to be less propensity towards martensite growth at grain boundaries than at  $-15^{\circ}\text{C}$  (Figure 3.165). Martensite morphology was more similar to that at  $65^{\circ}\text{C}$  than that at  $-15^{\circ}\text{C}$  in that laths were less well defined (Figure 3.163, Figure 3.166, Figure 3.169).

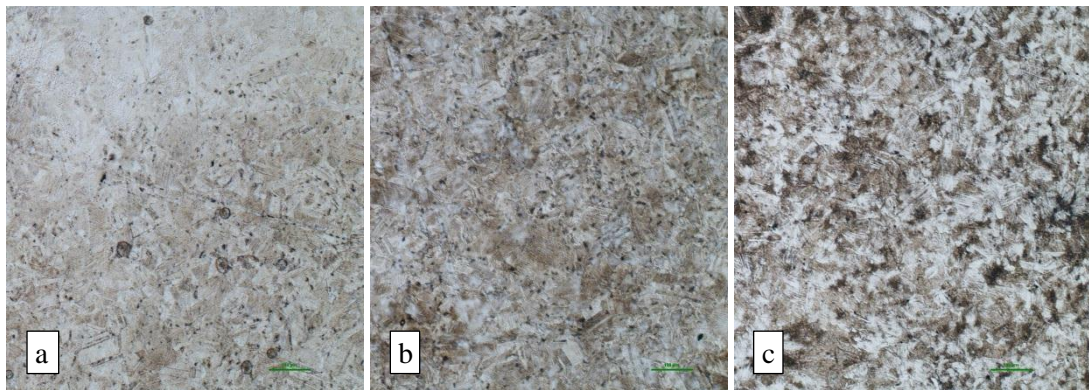


**Figure 3.164:** TRIP M deformed at  $25^{\circ}\text{C}$ , scale bars represent 100  $\mu\text{m}$ , showing progressively more dense dark martensite in the austenite matrix as the level of deformation increased: (a) 575 MPa, 0.5 mH change in inductance, (b) 750 MPa, 11 mH change in inductance (c) 870 MPa failure, 20 mH change in inductance.



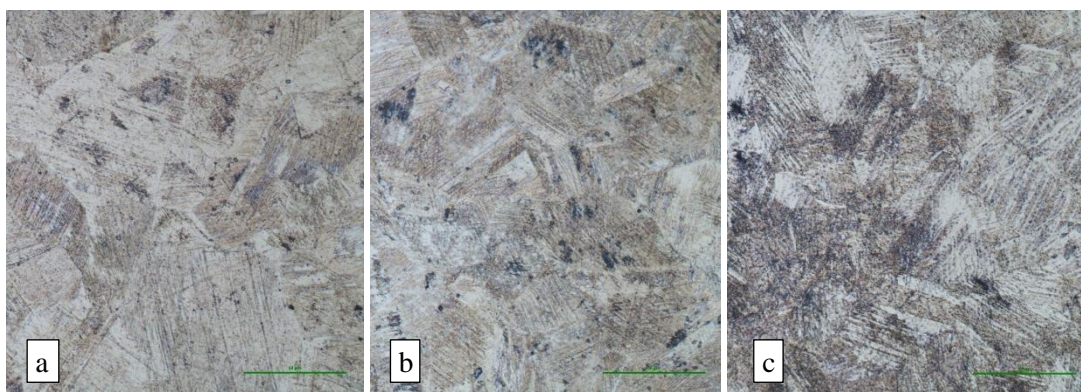


**Figure 3.165:** TRIP M deformed at 25°C, scale bars represent 50 μm, dark, banded martensite, with bands increase in apparent density with level of deformation: (a) 575 MPa (b) 750 MPa (c) 870 MPa failure.

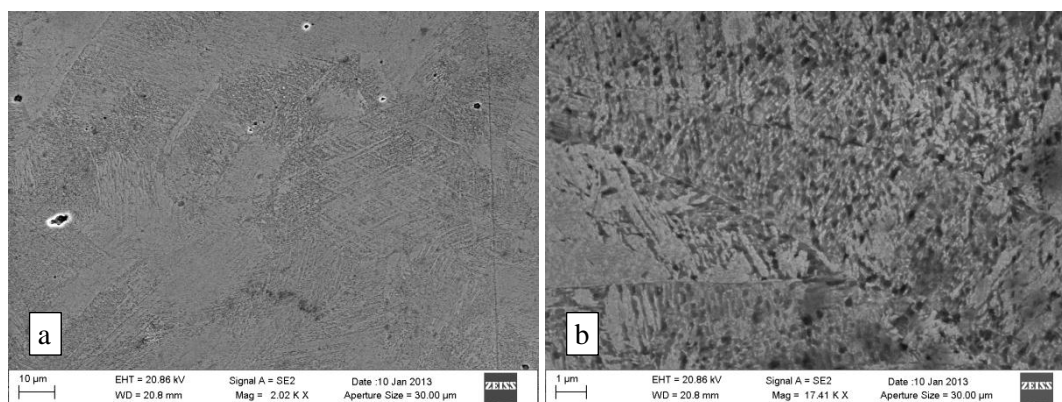


**Figure 3.166:** TRIP M deformed to 870 MPa failure at 25°C, SEM-SE image: (a) 2 000x magnification, again showing banded (hatched) martensite surface relief, as well as smoother, predominantly austenitic regions; (b) 10 000x magnification, lath martensite grown into austenite, possibly with precipitates present.

Deformation at 65°C produced noticeably less dense martensite than at 25°C at a similar stress (Figure 3.164 (c), Figure 3.165 (c), Figure 3.167 (b), Figure 3.168 (b)). In some areas, martensite again appeared slightly more dense at grain boundaries than within grains (Figure 3.168). The morphology of the martensite that developed in TRIP M during deformation at 65°C was similar to that at 25°C, with laths less clearly defined than those in the material deformed at -15°C (Figure 3.163, Figure 3.166, Figure 3.169).

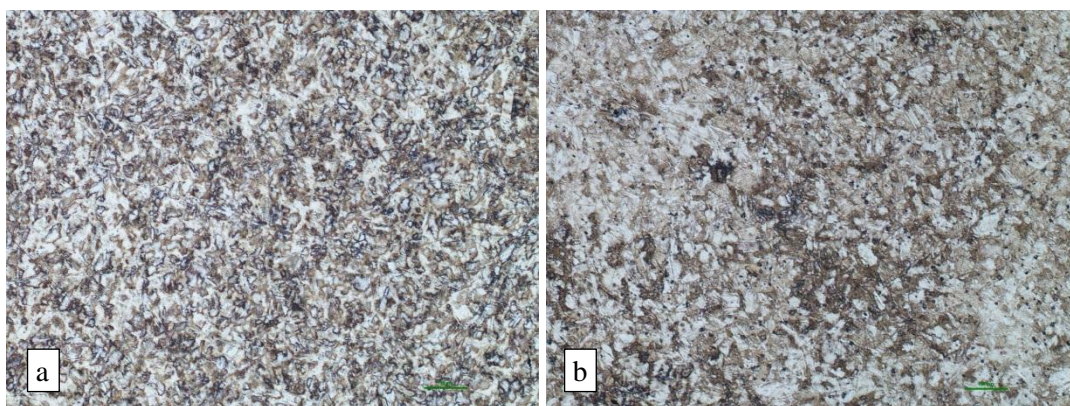


**Figure 3.167:** TRIP M deformed at 65°C, scale bars represent 100 μm, dark martensite denser after greater deformation: (a) 700 MPa, 2.2 mH change in inductance, (b) 870 MPa failure, 8.5 mH change.



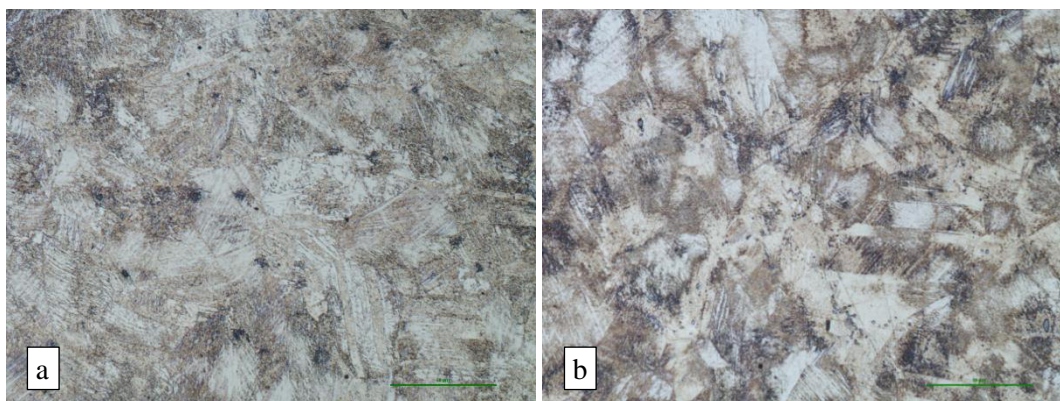


**Figure 3.168: TRIP M deformed at 65°C, scale bars represent 50 µm, bands increase in density with deformation (a) 700 MPa (b) 870 MPa failure.**

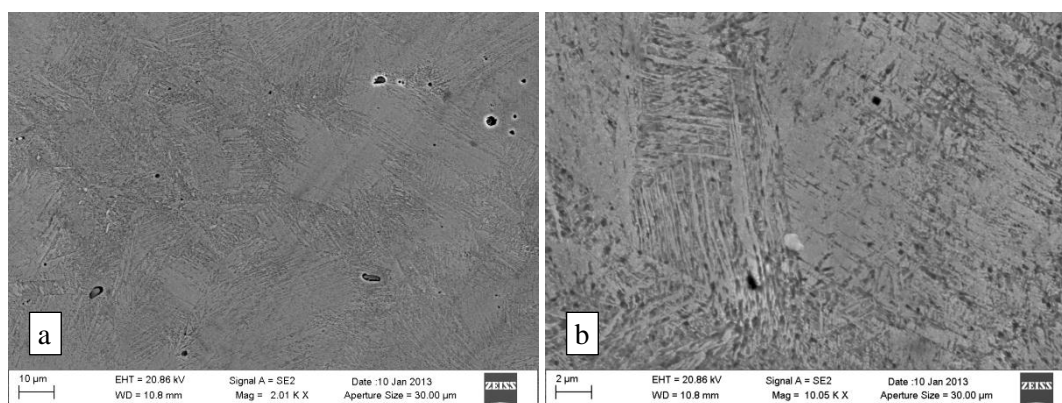


**Figure 3.169: TRIP M deformed to 870 MPa failure at 65°C, SEM-SE images, rough, banded martensite grown into smoother austenite, possible intermetallic precipitates present: (a) 2 000x magnification, (b) 10 000x magnification.**

The microstructure of Alloy TRIP MA is shown undeformed and deformed to various extents, as specified, at -15°C, 25°C and 65°C, in Figure 3.170 to Figure 3.181. The microstructure of annealed TRIP MA in its undeformed state showed the greatest degree of twinning of all the worked alloys investigated (Figure 3.170, Figure 3.171). Many grain boundaries appeared dark, they may have been somewhat sensitised, via precipitation of chromium carbides there during annealing. According to Figure 2.29, sensitisation should not have occurred, because warm rolling was performed below the carbide-forming temperatures. Slight sensitisation was not expected to significantly affect results, other than potentially producing earlier transformation in the sensitised areas, which may be beneficial.

High magnification SEM images revealed a hatched surface morphology (Figure 3.172). It is likely that this represents surface martensite developed during sample preparation. However, martensite laths were not apparent as they were for undeformed TRIP M at high magnification (Figure 3.160). Much of the surface relief may have been due to light etching of the austenite.

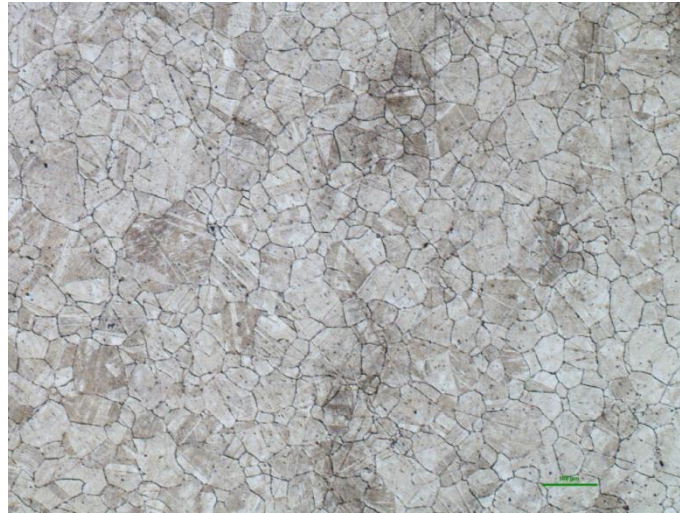


**Figure 3.170:** TRIP MA, undeformed, scale bar represents 100  $\mu\text{m}$ . Uniform, sparse martensite, likely resulting from preparation and confined to the surface, extensive twinning.

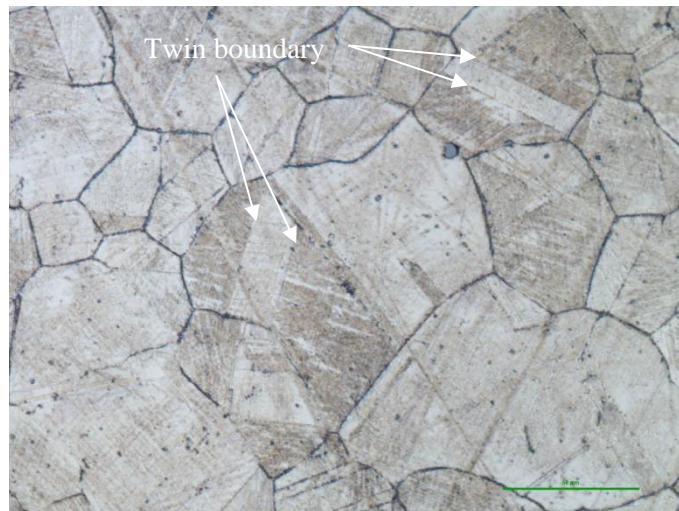


**Figure 3.171:** TRIP MA, undeformed, scale bar represents 50  $\mu\text{m}$ . Extensive twinning, slight grain boundary sensitisation.

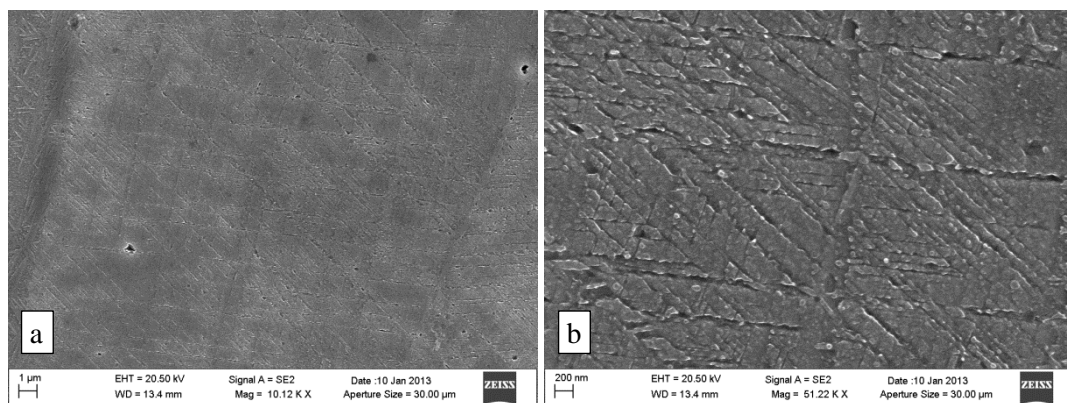


**Figure 3.172:** TRIP MA undeformed, SEM-SE images, very dispersed, hatched plate and some lath martensite grown uniformly into austenite: (a) 10 000x magnification; (b) 50 000x magnification



After deformation at  $-15^{\circ}\text{C}$ , the microstructure of TRIP MA was characterised by extensive twinning, and also by a hatched network of shear bands (Figure 3.173, Figure 3.174). TRIP MA showed a considerably greater degree of hatched shear bands than did TRIP M, or even TRIP R. The martensite growth in TRIP M was characterised by broadening parallel bands, whereas for TRIP MA the bands remained narrow and were extensively hatched. Less dense martensite also appeared to grow between the hatched bands (Figure 3.174 (b)). It was apparent that in some cases, twins and shear bands had stopped the propagation of martensite plates.

Figure 3.175 (a) shows the morphology of transformed martensite across a twin boundary as well as across a grain boundary. Figure 3.175 (b) shows a further magnified image of the twin boundary, with individual martensite plates being clearly visible.

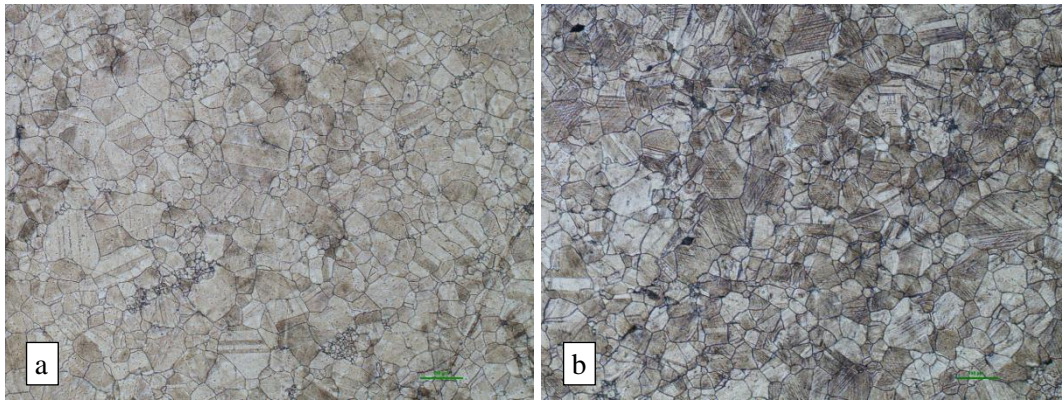


**Figure 3.173:** TRIP MA, deformed at  $-15^{\circ}\text{C}$ , scale bars represent  $100\text{ }\mu\text{m}$ , an apparent increase not in extent but in density of dark martensite with increased deformation: (a) 550 MPa, 6 mH change in inductance (b) 662 MPa failure, 25 mH change in inductance.

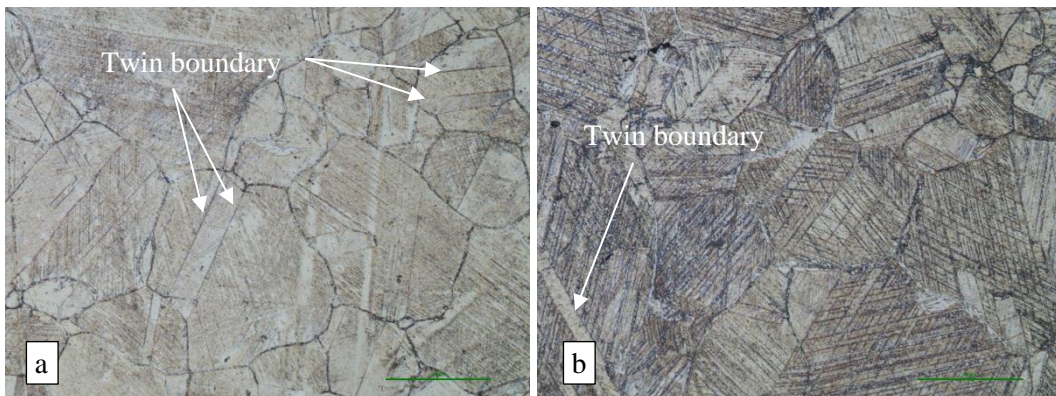


**Figure 3.174:** TRIP MA, deformed at  $-15^{\circ}\text{C}$ , 500x magnification, a banded martensite structure became distinctly cross-hatched at higher deformation: (a) 550 MPa (b) 662 MPa failure.



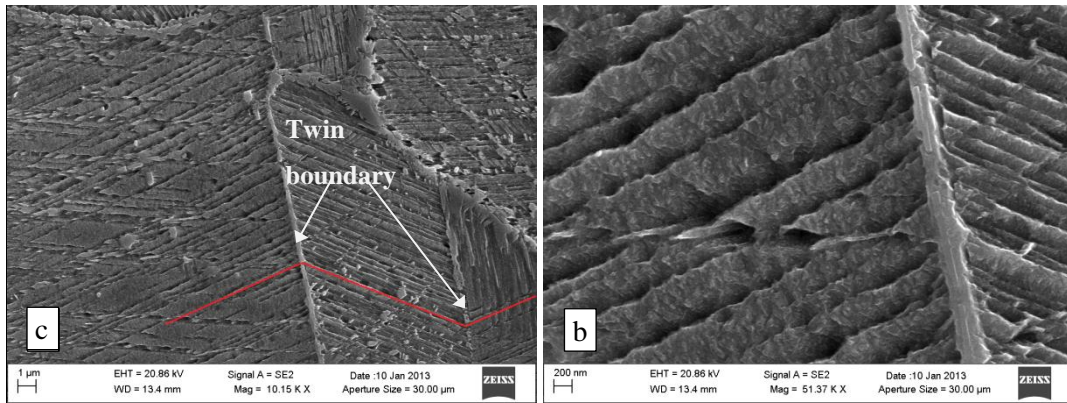


**Figure 3.175:** TRIP MA deformed to 662 MPa failure at  $-15^{\circ}\text{C}$ , SEM-SE images: (a) 10 000x magnification, martensite across twin and grain boundaries, showing plate orientation along crystallographic planes (red line); (b) 50 000x, showing very fine, discrete martensite plates.

The microstructure of TRIP MA deformed at  $25^{\circ}\text{C}$  was very similar to that at  $-15^{\circ}\text{C}$ , but with a distinctly lower density of martensite, particularly away from regions of hatched bands (Figure 3.176, Figure 3.177.). At high magnification, the morphology of the martensite away from twin boundaries appeared similar to that observed for TRIP MA deformed at  $-15^{\circ}\text{C}$  (Figure 3.178).

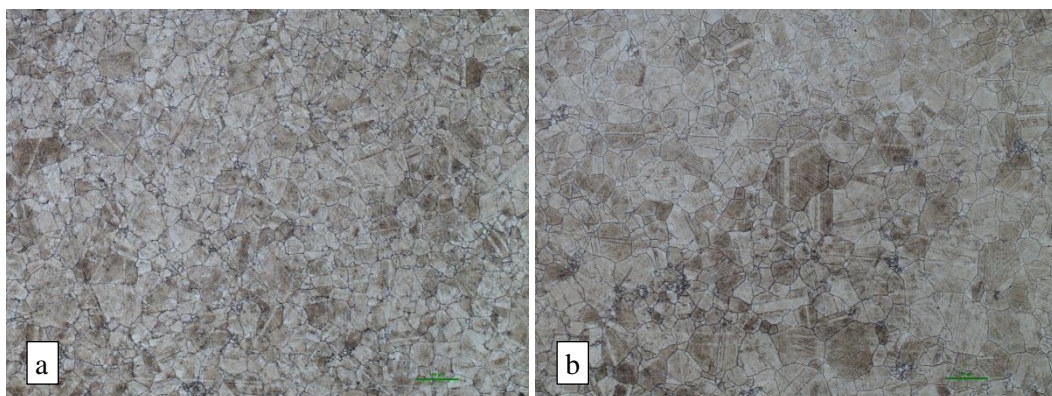


**Figure 3.176:** TRIP MA, deformed at  $25^{\circ}\text{C}$ , scale bars represent 100  $\mu\text{m}$ , marginally greater density of dark martensite after higher deformation, corresponding to marginal increase in magnetic response: (a) 550 MPa, 6 mH change in inductance; (b) 610 MPa failure, 12 mH change in inductance.

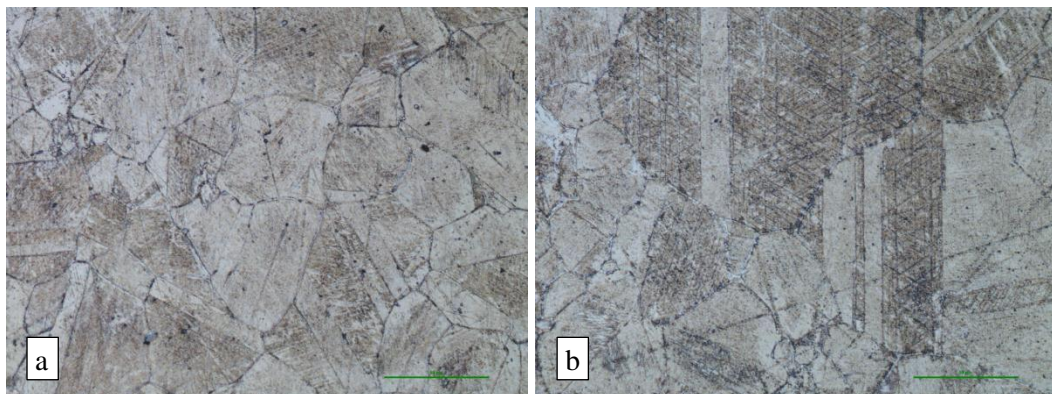


**Figure 3.177:** TRIP MA, deformed at  $25^{\circ}\text{C}$ , scale bars represent 50  $\mu\text{m}$ , dark martensite again develops primarily in a banded and hatched network, with major development after 550 MPa: (a) 550 MPa (b) 610 MPa failure.

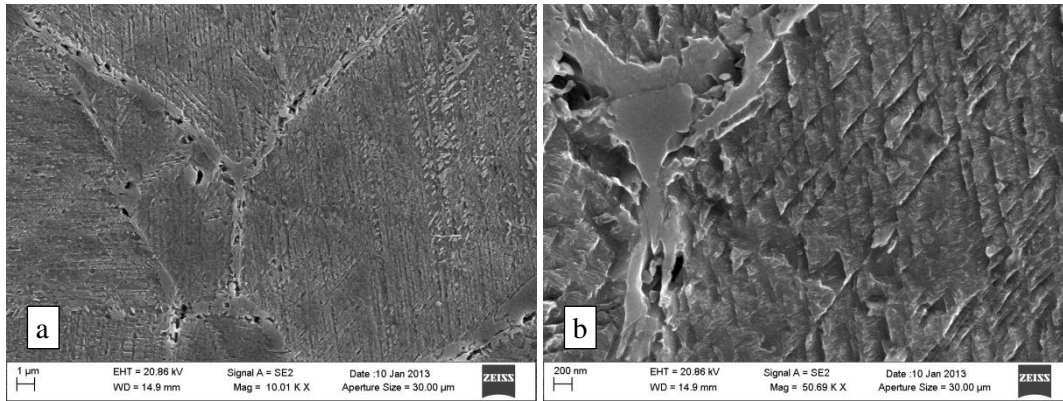


**Figure 3.178:** TRIP MA deformed to 610 MPa failure at 25°C, SEM-SE images: (a) 10 000x magnification, high martensite area with isolated austenite, martensite morphology similar to that at -15°C; (b) 50 000x magnification, with the hatched region exhibiting distinct fine, triangular martensite plates.

At 65°C, deformation of TRIP MA produced very few regions of hatched bands in the microstructure (Figure 3.179, Figure 3.180). Martensite formed in parallel plates during early deformation (Figure 3.180 (a)), and by higher loads had formed almost uniformly throughout grains (Figure 3.180 (b)). The morphology of the martensite at high magnification (Figure 3.181) appeared less ordered in many areas than for TRIP MA deformed at -15°C (Figure 3.175) and at 25°C (Figure 3.178).

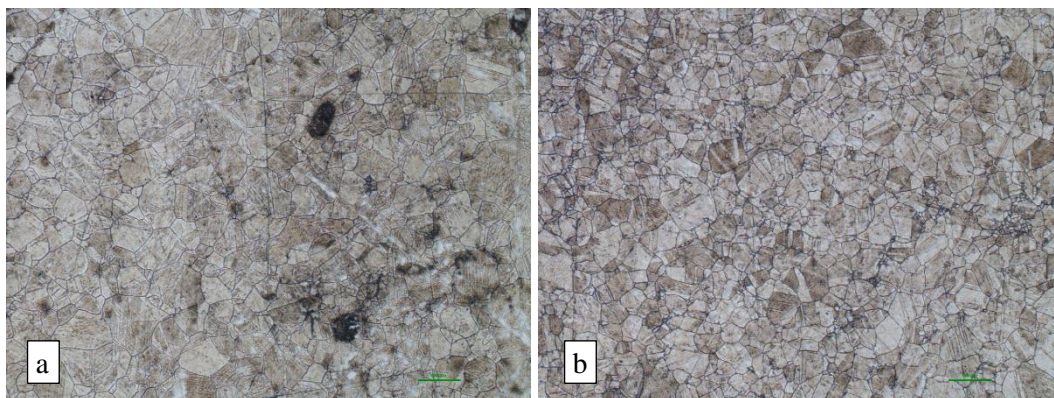


**Figure 3.179:** TRIP MA, deformed at 65°C, scale bars represent 100 µm, small increase in density of dark martensite, corresponding to the changes in magnetic response: (a) 500 MPa, 2.5 mH change in inductance (b) 600 MPa failure, 8.5 mH change in inductance.



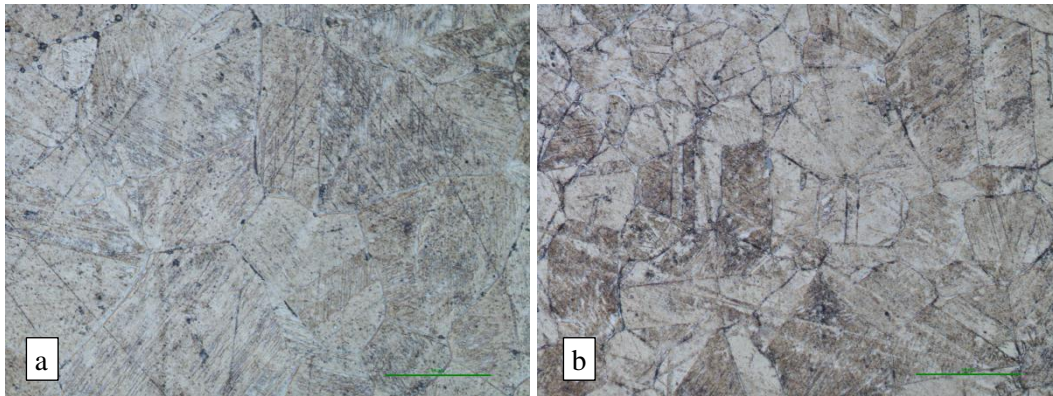


**Figure 3.180: TRIP MA, deformed at 65°C, scale bars represent 50 µm, dark martensite forming a weakly banded/hatched structure showing little development between 500 MPa and 600 MPa, with the increase in martensite appearing to come from general uniform development: (a) 500 MPa (b) 600 MPa failure.**

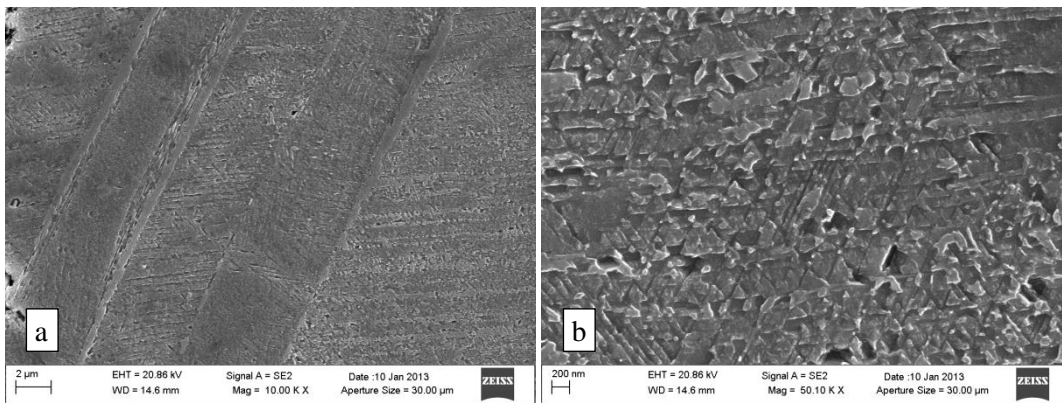


**Figure 3.181: TRIP MA deformed to 600 MPa failure at 65°C, SEM-SE images: (a) 10 000x magnification, heavily twinned area showing a hatched structure in isolated areas similar to that seen at lower temperatures, but the hatching and banding is much less prevalent; (b) 50 000x magnification, a distinct lack of discrete plates visible with only traces of a hatched structure, largely lath martensite.**

The microstructure of alloy TRIP MW is shown undeformed and deformed to various extents, as specified, at -15°C, 25°C and 65°C, in Figure 3.182 to Figure 3.193. Warm worked Alloy TRIP MW in an undeformed state showed few signs of twinning (Figure 3.182, Figure 3.183). It showed fairly distinct parallel and hatched shear bands, some of which were mechanically distorted, as expected (Figure 3.183). High magnification SEM images revealed a lightly etched surface, probably representing a combination of sparse surface martensite, developed in austenite during preparation, and lightly etched austenite, substantiated by the sample's magnetic response similar to that of air.





**Figure 3.182: TRIP MW, undeformed, scale bar represents 100  $\mu\text{m}$ . Traces of dark martensite in an austenite matrix.**

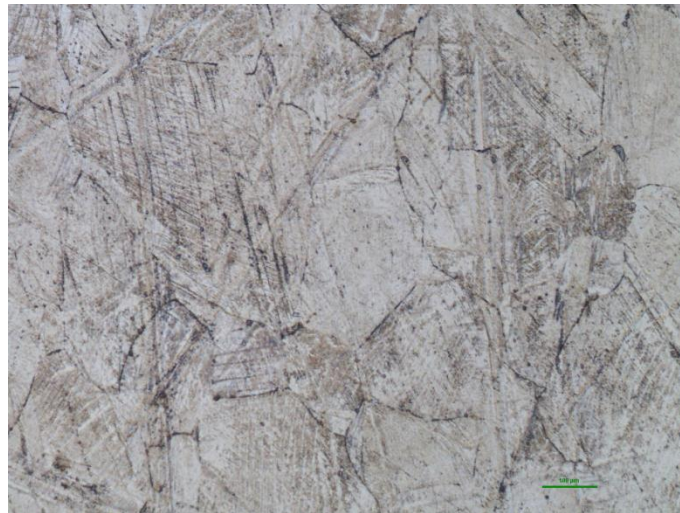


**Figure 3.183: TRIP MW, undeformed, scale bar represents 50  $\mu\text{m}$ . Martensite banding/hatching evident but not prevalent.**

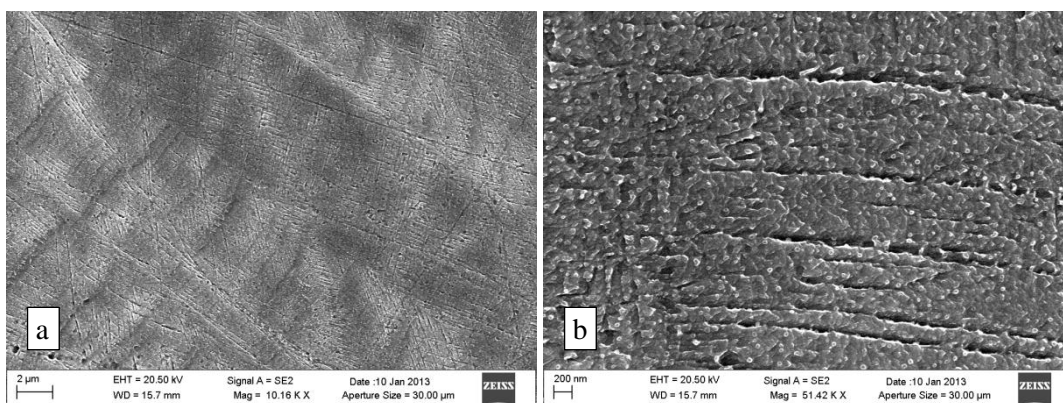


**Figure 3.184: TRIP MW undeformed, SEM-SE images, high martensite area, lath martensite developed in austenite, likely originating during preparation and confined to surface, sample magnetic response similar to air: (a) 10 000x magnification (b) 50 000x magnification.**

Isolated regions of particularly dense martensite were observed in the microstructure of TRIP MA deformed at  $-15^{\circ}\text{C}$ , while in other areas martensite was relatively sparse (Figure 3.185). White shear bands were observed in the microstructure, with martensite formed between these bands (Figure 3.186). This is similar to TRIP R deformed at  $-15^{\circ}\text{C}$  (Figure 3.149). High magnification SEM images revealed the lath martensite in the microstructure (Figure 3.187).

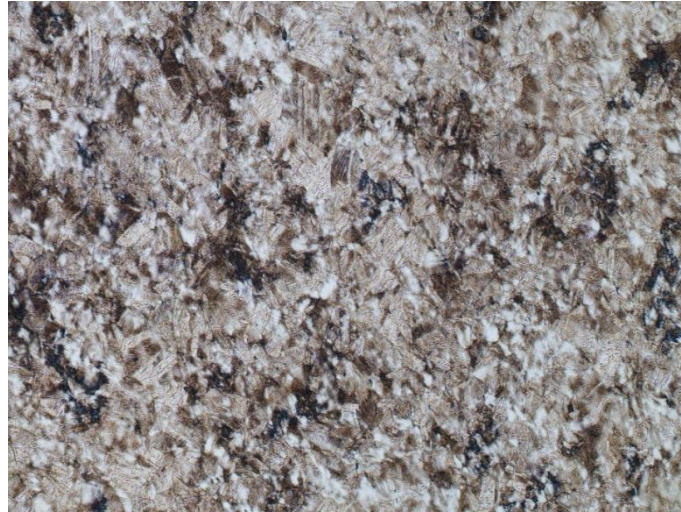


**Figure 3.185:** TRIP MW, deformed to failure at  $-15^{\circ}\text{C}$ , scale bar represents  $100\text{ }\mu\text{m}$ , 1193 MPa, 15.2 mH change in inductance. Significant dark martensite formed in the austenite, distinctly higher density regions.

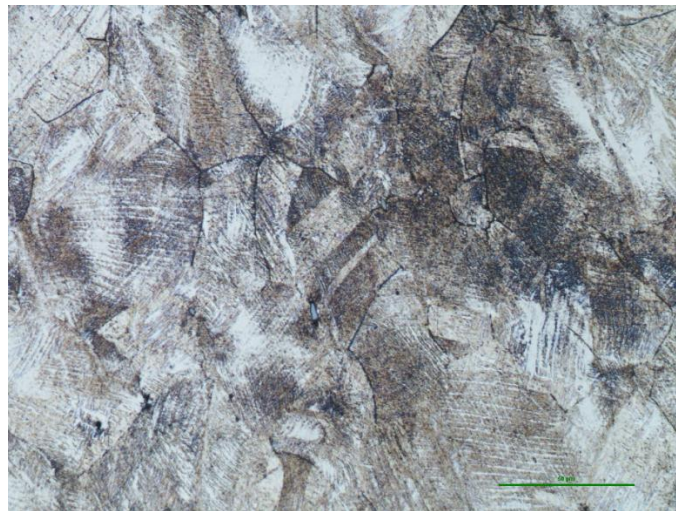


**Figure 3.186:** TRIP MW, deformed to failure at  $-15^{\circ}\text{C}$ , 1193 MPa, scale bar represents  $50\text{ }\mu\text{m}$ . Showing one region of high-density martensite. A banded/hatched structure is again present, but with light-coloured bands.



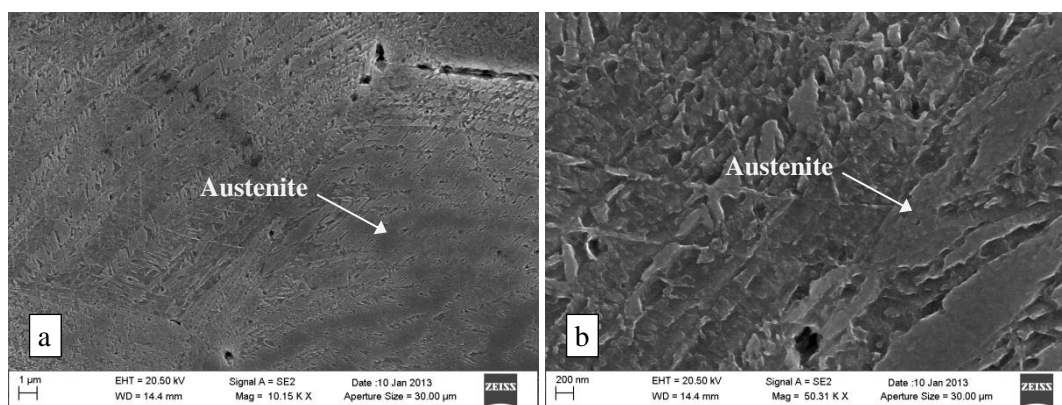


**Figure 3.187: TRIP MW deformed to 1193 MPa failure at -15°C, SEM-SE images, (a) 10 000x magnification showing a combination of smooth austenite and martensite; (b) 50 000x, primarily lath martensite with some plate martensite.**

TRIP MW deformed at 25°C revealed a similar microstructure as at -15°C, but with regions of dense martensite being more isolated, and larger regions of very sparse martensite (Figure 3.188). Higher optical magnification showed that these isolated regions of dense martensite were banded (Figure 3.189), similar to the microstructures of TRIP M deformed at -15°C and 25°C (Figure 3.162, Figure 3.165). The shear bands observed in the structure deformed at -15°C (Figure 3.186) were largely absent at 25°C (Figure 3.189).

High magnification SEM images revealed lath martensite (Figure 3.190). A small degree of grain boundary sensitisation, in the form of precipitation of chromium carbides, may have occurred during warm rolling between 350°C and 480°C (Figure 3.189, Figure 3.190 (a)), although this should not have occurred according to the theory associated to Figure 2.29, Section 2.4.6.

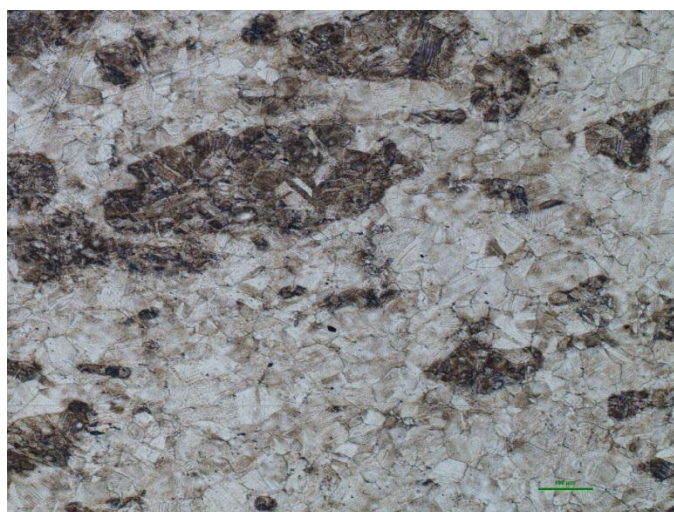


**Figure 3.188: TRIP MW, deformed to failure at 25°C, scale bar represents 100 µm, 1171 MPa, 23.5 mH change in inductance. Very isolated dark regions of considerable martensite density in austenite.**

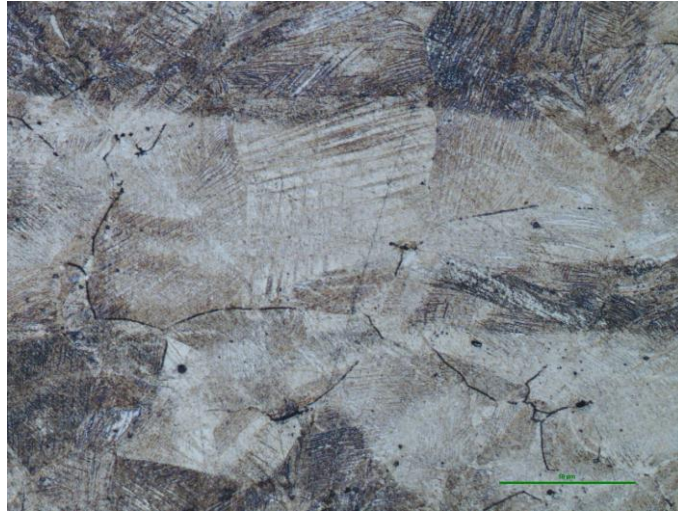


**Figure 3.189:** TRIP MW, deformed to failure at 25°C, 1171 MPa, scale bar represents 50 μm. Regions of more and of less dense martensite. Banding is extensive, particularly in more densely martensitic regions.

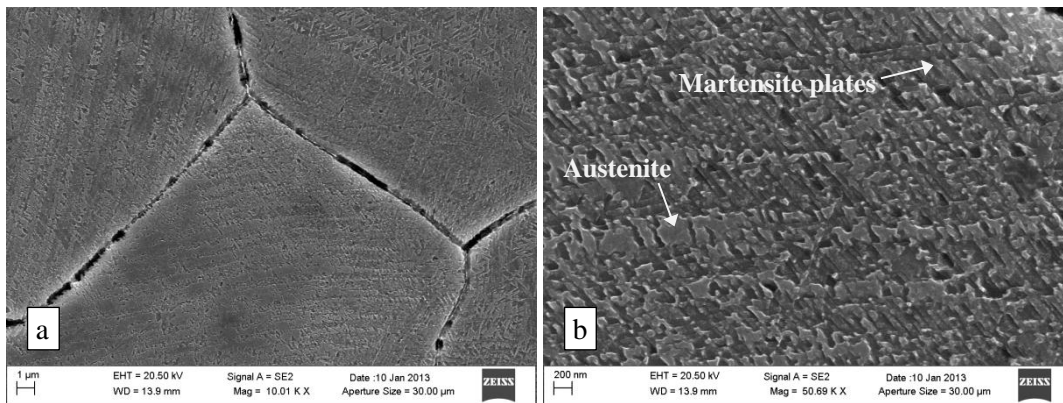


**Figure 3.190:** TRIP MW deformed to 1171 MPa failure at 25°C, SEM-SE images: (a) 10 000x magnification, possibly significant sensitisation of grain boundaries; (b) 50 000x magnification, islands of untransformed austenite (unetched), general lath martensite with areas of distinct plate martensite.

TRIP MW deformed at 65°C produced a similar microstructure to that deformed at 25°C, but with noticeably reduced martensite density. Regions of denser martensite were even more isolated (Figure 3.191), and were less dense (Figure 3.192). Martensite growth was more uniform across the microstructure than after deformation at lower temperatures. The light shear bands observed in the structure deformed at -15°C (Figure 3.186) were fewer, but were still present (Figure 3.192). Martensite morphology (Figure 3.193) was very similar to that in TRIP MW deformed at 25°C (Figure 3.190). It clearly revealed lath martensite in some areas, but generally with a less distinct structure (Figure 3.193).



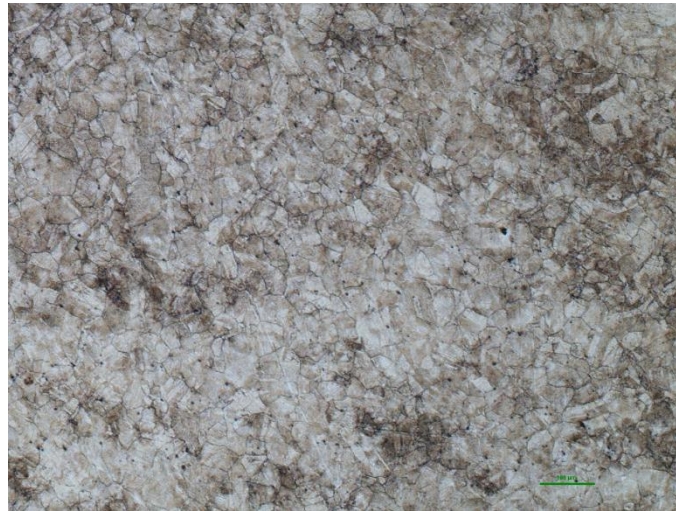


**Figure 3.191:** TRIP MW, deformed to failure at 65°C, scale bar represents 100 μm, 1148 MPa, 7 mH change in inductance. Small uniform increase in dark martensite, with isolated regions showing a greater increase.

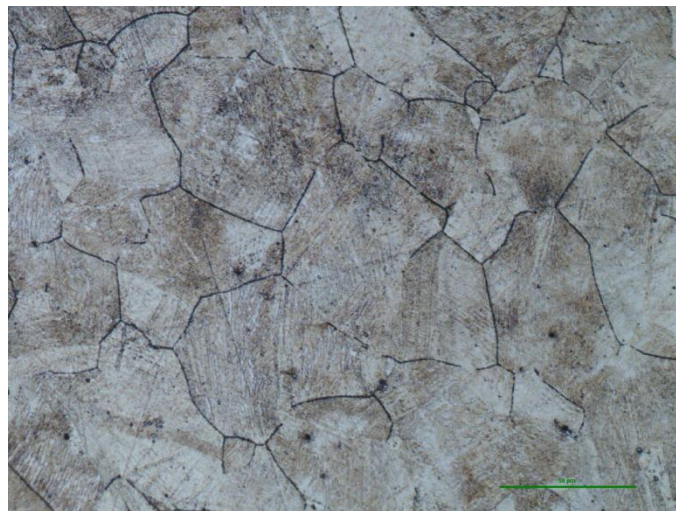


**Figure 3.192:** TRIP MW, deformed to failure at 65°C, 1148 MPa, scale bar represents 50 μm. Possibly significant sensitisation. Signs of light-coloured banding.

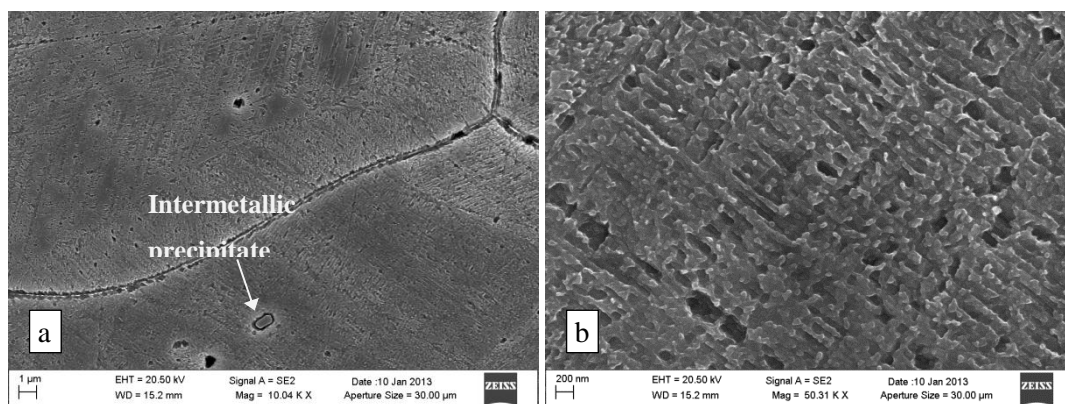


**Figure 3.193:** TRIP MW deformed to 1148 MPa failure at 65°C, SEM-SE images: (a) 10 000x magnification, austenite with a dispersion of martensite, intermetallic precipitate; (b) 50 000x, lath martensite.

### 3.5.10.3 Assessment of microstructures

The extent of martensite observed within each microstructure qualitatively corresponded to the peak inductance measured during deformation, Section 3.5.9. As expected, deformation at lower temperatures produced more inductive change and a greater density of martensite. Higher temperatures apparently encouraged  $\alpha'$  martensite to grow from slip bands and  $\epsilon$  martensite. At the lowest temperature tested ( $-15^{\circ}\text{C}$ ),  $\alpha'$  martensite was observed to grow spontaneously between shear bands.

Materials deformed at lower temperature and materials that were less heavily worked exhibited more and better defined shear bands or plate martensite. This corresponds to the theory that lower temperatures induce lower stacking fault energies in the materials (Lecroisey & Pineau, 1972), and that at lower stacking fault energies  $\epsilon$  martensite formation is a more common mode of deformation (Abrassart, 1973). As deformation temperatures and degree of work (thus inherent material defects) increases, the martensite tended more towards fine lath martensite and the martensite morphology becomes less distinct.

TRIP R produced a greater peak inductance than TRIP M upon deformation and its microstructure revealed more martensite with somewhat different morphology. A similar martensite morphology developed in the three differently processed versions of TRIP M. The extent of inductive change was again observed to qualitatively correspond to the changes in microstructure, regarding processing and deformation temperature.

Further work would be required to definitively characterise the morphology of the transforming microstructures. EBSD and TEM would be extremely useful in this. An improved electro-etching method would also be desirable.

### 3.5.11 Conclusions and further work

A TRIP steel alloy constituting the sensor element within a smart rock tendon must be cheap to produce, show transformation from the lowest load possible, show repeatable transformation that is prevalent enough to detect easily and be unsusceptible to the harsh mining environment.

Several commercial alloys, as well as Alloy TRIP M, were tested and analysed early in the project. Data from previous authors (Lecroisey & Pineau, 1972) were used to further assess the relevance of reported empirical equations for predicting  $M_{d30}$  and  $M_s$  temperatures in the current alloy composition range. The  $M_{d30}$  equation by Pickering (Pickering, 1978) and the  $M_s$  equations by Cina (Cina, 1954) and by Hull (Hull, 1973) were determined to be the most

accurate predictors. The alloys were also assessed using a Schaeffler diagram (Schaeffler, 1949) and associated equations. In this way, relevant empirical equations and Schaeffler diagram trends could be applied to further alloy design.

Two alloys (TRIP R and TRIP S) were then proposed. However, repeated attempts to produce ingots of TRIP R and TRIP S only produced one useable ingot of approximate composition TRIP R. Quasi-static tensile testing showed that TRIP R exhibited stronger transformation over a larger range than any of the previous alloys, beginning its transformation at a lower level of deformation and failing at an equivalent or greater level of deformation. Tensile deformation over a range of temperatures showed TRIP R to be less temperature susceptible than TRIP M. Both the relatively larger, earlier transformation and the slightly reduced temperature sensitivity were predicted during alloy design by the determined empirical equations for  $M_{d30}$  and  $M_s$ . That by Pickering (Pickering, 1978) was used for  $M_{d30}$  and that by Cina (Cina, 1954) and by Hull (Hull, 1973) for  $M_s$ .

Two further alloys, DIN 1.4567 and DIN 1.4568 were procured in Germany as 3mm diameter wire. Alloy DIN 1.4567 showed no transformation, but alloy DIN 1.4568 showed strong transformation as shown in Figure 3.129. Austenitizing the latter alloy at 1000°C for 10 minutes drastically improved its deformation-induced transformation response, shown in Figure 3.129. Unfortunately, the available quantity and form of this material, and the equipment did not allow for comparable temperature susceptibility testing.

Alloy TRIP M was tested for temperature susceptibility in three different conditions. These were fully annealed and furnace cooled, hot rolled and water-quenched and warm-worked. These alloys were expected to have varying dislocation densities from least to most in the order listed. According to the theory developed in Chapter 3.3, increased dislocation density should be associated to increased transformation temperature sensitivity. With respect to the degree of transformation at a given stress or at a given strain, it was found that, as expected, the annealed material TRIP MA showed the lowest temperature sensitivity and warm-worked material TRIP MW showed the highest.

High strain rate tensile testing could not be performed. The alloys were not tested in cyclic loading. High strain rate and cyclic load testing will be important for future work.



### **3.6 Warm rolled tensile alloy**

#### **3.6.1 Introduction**

This work was performed early on in the project, prior to much of the work on the hot rolled and as-cast alloys. The potential application of TRIP steels to form smart aircraft wing bolts that could behave as traditional wing bolts but also as damage sensors was investigated. A wing bolt serves to clamp the wing to the fuselage of an aircraft such as the Hercules C-130 cargo plane. Extremely costly periodic inspection of wing bolts is currently vital in guaranteeing the structural integrity of aircraft. The potential cost saving if these bolts could be made to measure and convey their level of damage is significant. TRIP steel based smart wing bolts might replace the original wing bolts with minimal, or no further, structural modification being required.

TRIP steel alloys for this application would require mechanical properties similar to those of AISI 4340, the current wing bolt material. To permit implementation in aircraft, the material and fabricated bolts would need to be fully characterised and rigorous certification would be required. However, the objective of this work was only to investigate the potential for producing TRIP steel alloys that demonstrate good transformation characteristics and tensile properties equivalent to those of AISI 4340. A batch of alloys was thus melted with the intention of warm forming them to investigate the potential to produce such high-strength TRIP steels.

Design of these alloys was not undertaken by this author, but by the co-author of journal paper 3, J. M. Vugampore, and is not included here (Vugampore & Bemont, 2012) (Appendix 3). This was included in the PhD thesis of J. M. Vugampore (Vugampore, 2006). All aspects of the work included here, including alloy characterisation and component design, manufacture and testing, were performed by this author or through collaboration between the author and co-author of journal paper 3.

The work included in this section (Section 3.6) and in Section 4.4.4 formed the basis of journal paper 3 (The design and testing of sub-scale smart aircraft wing bolts), included as submitted in Appendix 3 (Vugampore & Bemont, 2012).

#### **3.6.2 Alloy design and production**

The intention of this alloy design was to produce alloys that would attain good mechanical properties upon warm rolling, while also showing strong transformation and preferably also early transformation. The alloys were cast by Mintek. Four of the ingots that were within the target compositional range are shown in Table 3.24.

**Table 3.24: Composition of wing bolt alloys cast at Mintek.**

Alloy: Element:	W1	W2	W3	W4
Carbon	0.30	0.21	0.19	0.29
Manganese	3.86	2.57	10.5	1.13
Sulphur	0.015	0.006	0.010	0.007
Phosphorus	0.011	0.005	0.005	0.005
Silicon	0.61	0.60	0.08	0.56
Chromium	9.09	8.0	11.6	11.6
Molybdenum	-	1.91	0.03	0.01
Nickel	6.30	8.91	1.33	9.48
Iron	Bal.	Bal.	Bal.	Bal.

Each 68mm diameter ingot was then soaked at 1200°C for one hour. The ingot was then flat forged hot to 37mm thickness and soaked at 550°C for one hour. Warm rolling was then performed at 550°C with a reduction of approximately 4% per pass and a final reduction of approximately 75%.

### 3.6.3 Characterisation

Alloys were tested quasi-statically in an Instron 5500R universal testing machine with a strain gauge, in a similar manner to that described in Section 3.5.6. A Fugro GMS-2 magnetic susceptibility meter was used to monitor phase transformation via magnetic susceptibility change. Alloys W1, W2, W3 and W4 exhibited good mechanical properties, as well as showing good transformation. Stress versus strain curves of these alloys at 23°C are shown in Figure 3.194. Change in magnetic susceptibility versus Strain at 23°C is shown in Figure 3.195. These curves each represent the average of two or three tests, depending on the limited number of specimens available. Two individual tests are shown for alloy W2 in Figure 3.196.

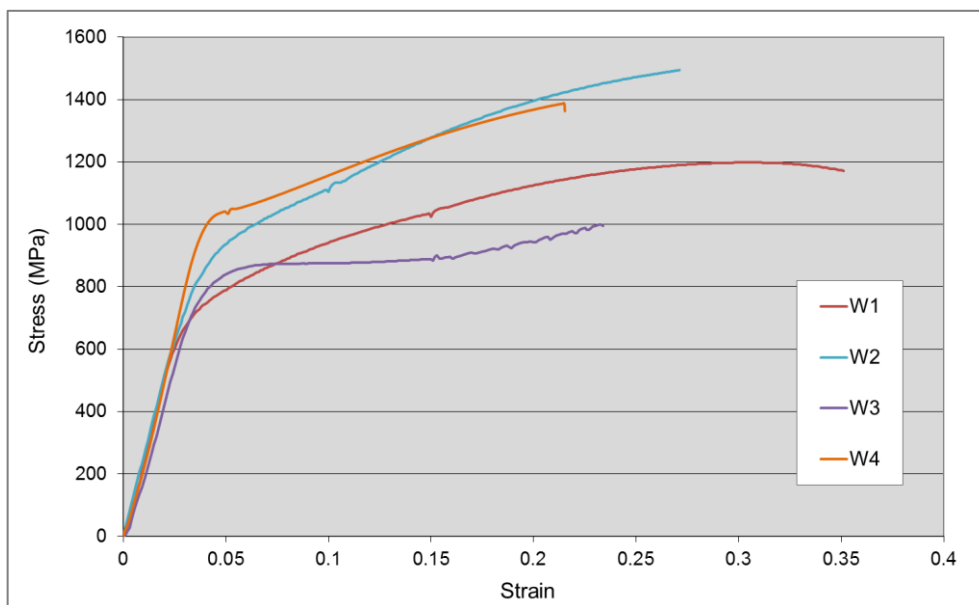


**Figure 3.194: Stress versus strain curves for warm worked alloys W1, W2, W3 and W4.**

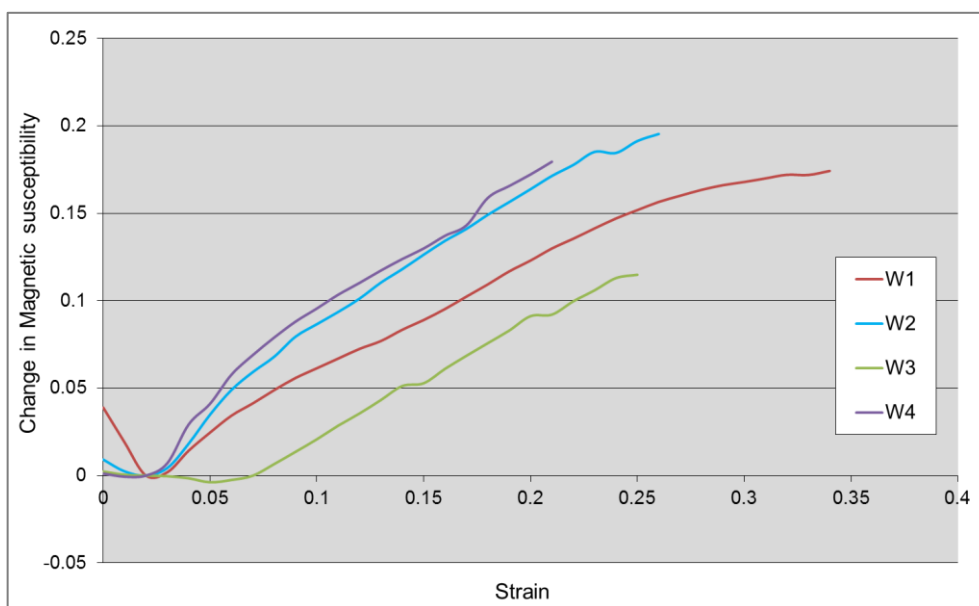


**Figure 3.195: Change in magnetic susceptibility versus strain for warm worked alloys W1, W2, W3 and W4, zeroed at 0.02 strain.**

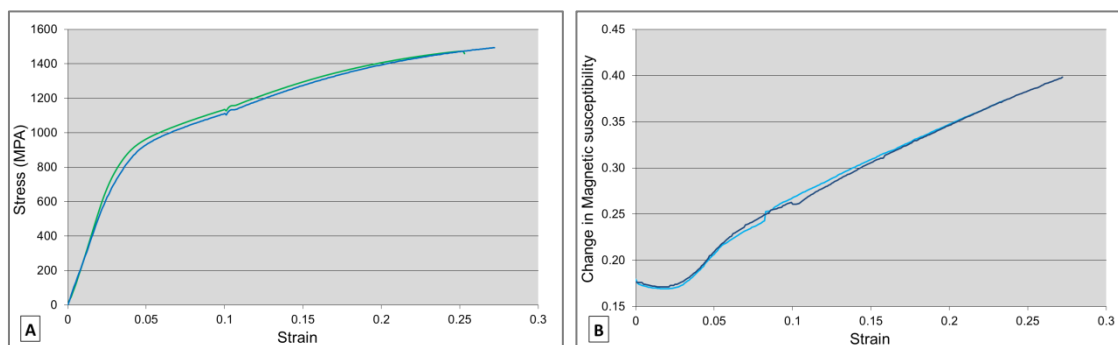


**Figure 3.196: Alloy W2, two tests, (A) stress versus strain, (B) change in magnetic susceptibility versus strain.**

Alloys W2 and W4 exhibited similarly strong transformations. Their tensile stress versus strain properties were also similar, with Alloy W2 exhibiting a marginally higher UTS and Alloy W4 a marginally higher yield strength. The mechanical properties of Alloy W4 (as an average of three tests) are compared to those of AISI 4340 in Table 3.25.

**Table 3.25: A comparison of the mechanical properties of Alloy W2 and Alloy W4 with those of AISI 4340 (Vugampore & Bemont, 2012).**

Alloy	Tempering ( $^{\circ}$ C)	Yield strength (MPa)	Tensile strength (MPa)	Elongation (%)
Alloy W2	-	880	1480	25
Alloy W4	-	1070	1360	21.5
AISI 4340	425	1368	1468	10

While the UTS of Alloy W4 is near to that of AISI 4340, its yield strength is substantially lower. However, the elongation at failure of Alloy W4 was more than double that of AISI 4340.

### 3.6.4 Metallography

Specimens were prepared in a similar manner to that described in Section 3.5.10.1. The microstructures of Alloys W2 and W4 are shown in Figure 3.197 and Figure 3.198 before deformation and after tensile fracture. They clearly show an increase in the level of dark martensite after the materials were deformed in tension.

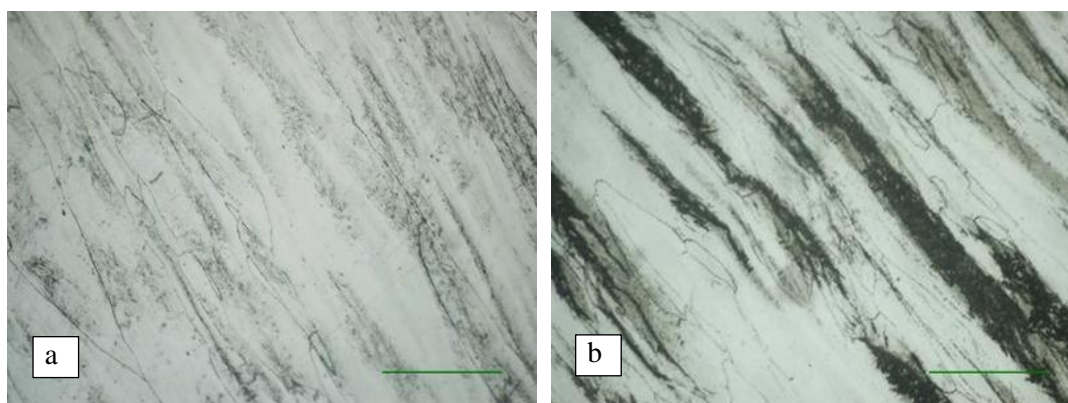


**Figure 3.197: Microstructure of Alloy W2 showing: (a) mostly light austenite before deformation and (b) a large proportion of dark martensite after tensile fracture (Vugampore & Bemont, 2012). Scale bar represents 70 $\mu$ m.**

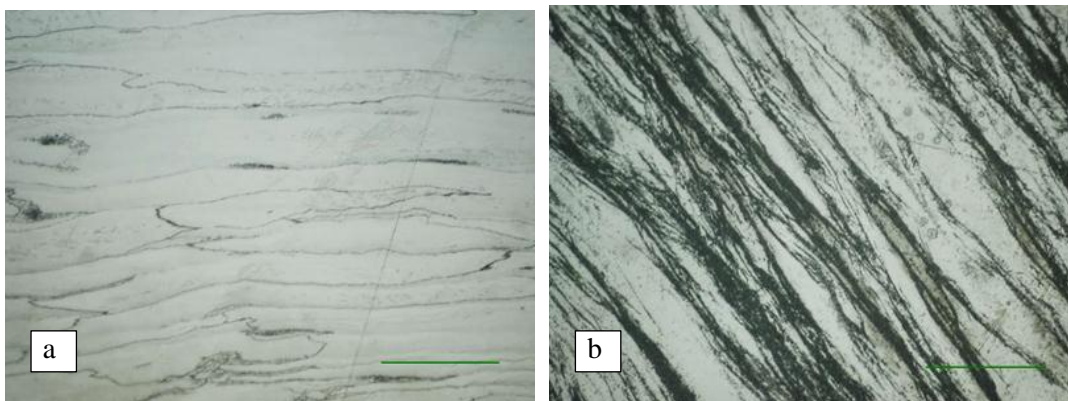


**Figure 3.198: Microstructure of Alloy W4 showing (a) mostly light austenite before deformation and (b) a large proportion of dark martensite after tensile fracture (Vugampore & Bement, 2012). Scale bar represents 70µm.**

As with the warm-worked alloy investigated in Section 3.5, the martensite formed during transformation was lath martensite. More martensite was present before deformation in Alloy W2 than in Alloy W4. The martensite forming in Alloy W2 appeared in larger, more dense and less well distributed packets than in Alloy W4.

Since aircraft are subjected to extremely low temperatures, the TRIP steel alloys might transform spontaneously upon cooling, leading to false deformation measurements. Thus, Alloys W2 and W4 were tested for spontaneously forming martensite at low temperatures. Alloy W2 exhibited transformation immediately upon cooling. Alloy W4 was cooled to  $-70^{\circ}\text{C}$  without any detected transformation.

### 3.6.5 Conclusions and further work

The aim of this portion of the work was to determine whether it was possible to produce TRIP steel alloys that matched the mechanical properties of AISI 4340 tempered at  $425^{\circ}\text{C}$ , and also showed strong transformation. The work focused on four warm-worked alloys that had good mechanical and transformation properties.

None of the alloys tested showed the target tensile or yield strengths, although Alloys W2 and W4 were close. Alloy W2 showed lower yield strength but equalled the target tensile strength. Alloy W4 was slightly below target for both yield and tensile strength. However, both of these alloys showed elongations of well over double that of AISI 4340. It is thus feasible to further warm work these alloys to attain the required tensile and yield strengths, with sufficient elongation maintained. Such further warm working is expected to alter transformation properties, but it is difficult to predict how.

The impact strength of Alloys W2 and W4 substantially surpassed those of AISI 4340, particularly at cryogenic temperatures. This again points to the potential for further warm working of these materials to increase strength.

Both Alloy W2 and Alloy W4 showed a small amount of transformation prior to the material's yield point. This is likely due to stress-induced transformation because of the extremely high dislocation densities resulting from 75% warm work. Transformation prior to yield could be highly beneficial for sensor applications.

### **3.7 Evaluating the TRIP steel transformation magnetically**

#### **3.7.1 Introduction**

In order to be certain that the change in magnetic permeability occurring within the TRIP steels would be optimally measured when utilised in sensors, it was necessary to first investigate their magnetic properties. Appendix 1 outlines some fundamental principles related to magnetism and magnetic permeability and their measurement. It can be seen from Figure 2.71, Section 2.8.2, that when the field strength in a ferromagnetic material is within the range of reversible domain alignment growth, the magnetic permeability is very low. Well before magnetic saturation, the permeability drops rapidly again. There is thus an ideal range for  $H$  where magnetic permeability ( $\mu$ ) peaks, also causing inductance to peak for constant physical parameters as expressed in Appendix A1.1. , Equation A 3.

When magnetic permeability is in its peak range, it has a greater influence over inductance, and thus a change in permeability will lead to a greater change in inductance and to increased resolution. This becomes apparent from the TRIP steel magnetisation curves in Section 3.7.3. In order to monitor in this ideal range in a ferromagnetic material, it is necessary to adjust the current through the inductor and the number of turns on the inductor to obtain a magnetic field strength correlated to peak permeability for a given set of physical parameters. When the core material is not ferromagnetic, its magnetic permeability is constant, and the above becomes irrelevant. Although it may not be practical to induce the magnetic field strength required to attain peak permeability in some sensors, particularly those that are battery powered, it is still pertinent to investigate the manner in which sensing will be effected by field strength and to optimise it as far as possible .

While most materials have fixed magnetisation curves, TRIP steels do not. As regions of the TRIP steel that forms the inductor's core transform under load from paramagnetic austenite to



ferromagnetic martensite, the shape and magnitude of the core's magnetisation curve alter. In order to observe the change, it is necessary to monitor a point on the curve, its gradient, or the change in area under a portion of the curve. If a specific point on the curve is to be monitored, some form of reference on the  $x$ -axis (field strength axis) must be used in order to detect the change. If constant field strength is chosen and flux density is monitored at this field strength in order to detect relative magnetic permeability change, then field strength in the best possible range should be chosen. In order to choose the best measurement technique and properly implement it, the change in magnetic permeability during the TRIP steel transformation should be characterised.

### 3.7.2 Determining hysteresis curves

Plotting magnetisation curves of various TRIP steels at different levels of transformation enabled proper characterisation of their shifting magnetic permeability properties. The electrical system shown in Figure 3.199 was used to detect these curves.

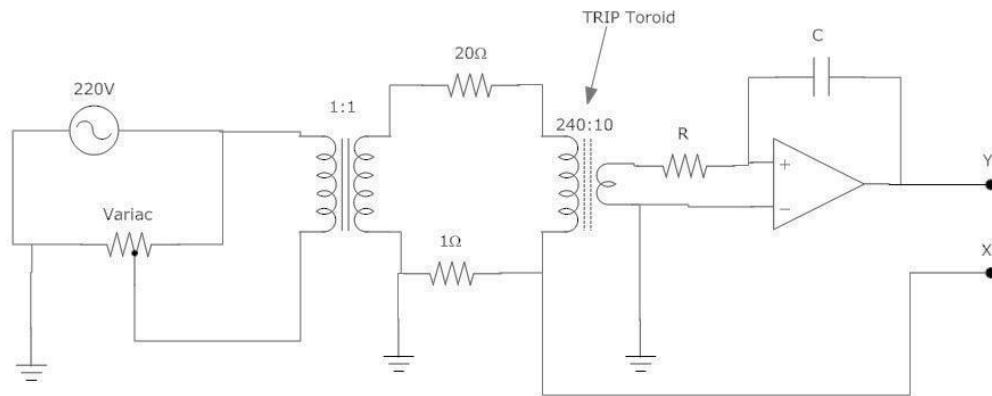


**Figure 3.199: Hysteresis curve measuring circuit, including: 230V variac, isolation transformer, primary coil driving circuit including low tolerance resistor, core, secondary winding and integrator circuit, and digital storage oscilloscope connected across X-Y.**

The voltage measured at output “X” in Figure 3.199 is proportional to current, which by Equation 3.1 (Ampere’s Law) is in turn proportional to magnetic field strength (H).

$$H = \frac{N_p \cdot I_p}{l}$$

**Equation 3.1**

where  $N_p$  is the number of turns on the primary coil,  $I_p$  is the current through the primary coil and  $l$  is the length of the inductor.

Equation 3.2 gives flux ( $\Phi$ ) and represents the integrator part of the circuit in Figure 3.199. Thus, by Equation 3.2 and Equation 3.3, flux density ( $B$ ) is proportional to the voltage measured at Y ( $V_Y$ ) since  $R$ ,  $C$ ,  $N_s$  and  $A$  represent physical constants within the circuit (Faraday, 1832).

$$\Phi = \frac{V_Y \cdot R \cdot C}{N_s}$$

Equation 3.2

where  $N_s$  is the number of turns on the secondary coil.

$$B = \frac{\Phi}{A}$$

Equation 3.3

where  $A$  is the cross-sectional area of the inductor.

The system thus plots a curve of  $Y$  versus  $X$  on an oscilloscope that is proportionate to the hysteresis curve of the inductive core material for the input peak field strength. As the primary winding current is increased (increasing the peak field strength), the tip of the curve shifts, with these consecutive curve tips tracing out a similarly proportionate magnetisation curve for the material at its current level of transformation, as shown in Figure 3.200.

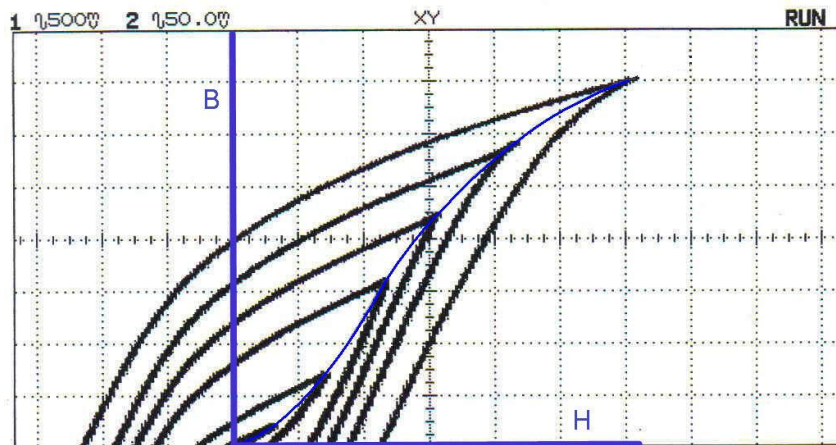


**Figure 3.200: Digital storage oscilloscope output showing consecutive proportionate hysteresis curves at different field strengths (positive  $H$  extent only). The blue curve shows how the proportionate magnetisation curve is plotted from the hysteresis curves.**

Appendix A1.3. describes how the true magnetisation curve can be readily determined from the above data when physical parameters are known.

### 3.7.3 Magnetisation curves

The above method was verified by plotting a true magnetisation curve for a sample of 27M3 silicon iron that was purchased with a specified magnetisation curve. Figure 3.201 shows that the magnetisation curve measured experimentally was very close to the specification.

Magnetisation and magnetic permeability curves were then obtained for AISI 304 stainless steel and various TRIP steels at a frequency of 50Hz. As specified in the legends, the lower curve in each plot shows the magnetisation curve for a perfect inductor core of free space.

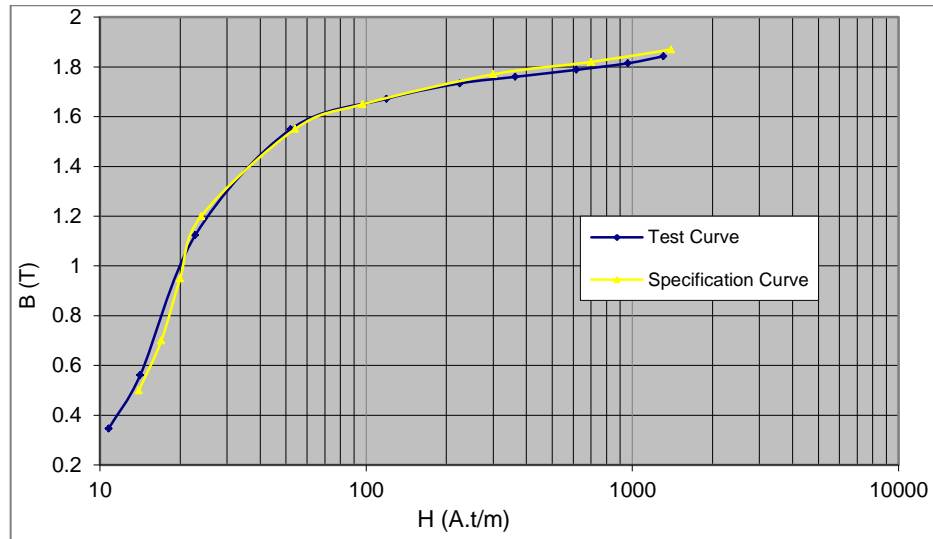


**Figure 3.201: Magnetisation curve of 27M3.** The measured curve of a standard material is compared to its specification curve in order to check the accuracy of the hysteresis curve measurement system.

According to Ashby and Jones (Ashby & Jones, 2012), annealed 304 stainless steel has an absolute magnetic permeability ( $\mu$ ) of  $1.3 \times 10^{-6} \text{ H.m}^{-1}$  at a field strength of  $4000 \text{ A.t.m}^{-1}$ . The measured absolute magnetic permeability at  $4000 \text{ A.t.m}^{-1}$  was  $1.6 \times 10^{-6} \text{ H.m}^{-1}$  for undeformed 304 stainless steel (Figure 3.202 and Figure 3.203). Since 304 stainless steel has a wide compositional tolerance and was tested in the as-purchased state, without prior annealing, this error was considered acceptable.

The true quantitative values of the magnetisation and permeability curves obtained were not in fact of key importance. Rather, their relative values compared to those of the same material deformed to different strains, and to other materials at the same strain, were of greater significance. Figure 3.203 shows that the magnetic permeability of 304 stainless steel increased strongly from about 700 MPa. Its UTS was below 750 MPa, thus substantial transformation occurred only in approximately the final 5% of the material's UTS. It is noteworthy that the difference in magnetic permeability between undeformed and deformed 304 stainless steel continuously increased with applied field strength in the range applied (Figure 3.202 and Figure 3.203).

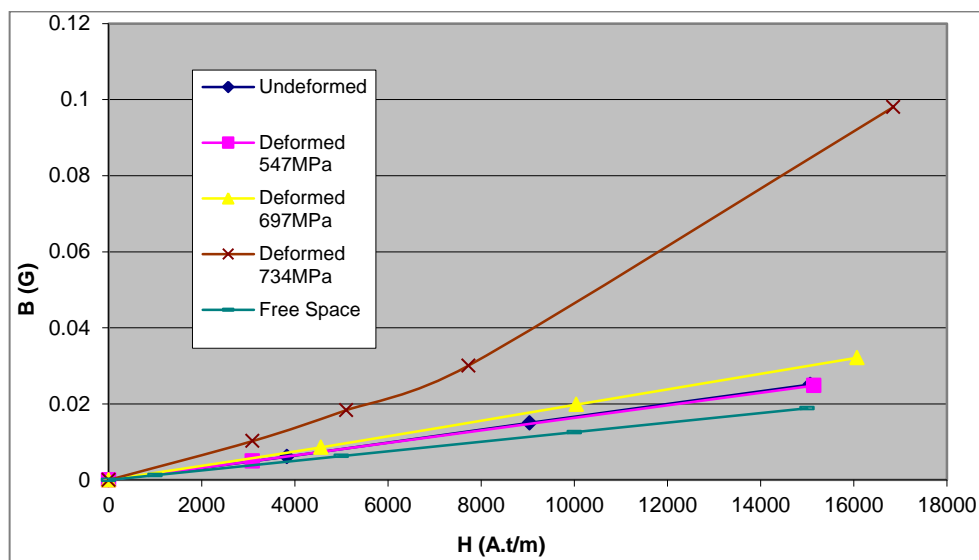


**Figure 3.202: Magnetisation curves of 304 stainless steel; undeformed and previously deformed in tension to various loads.**

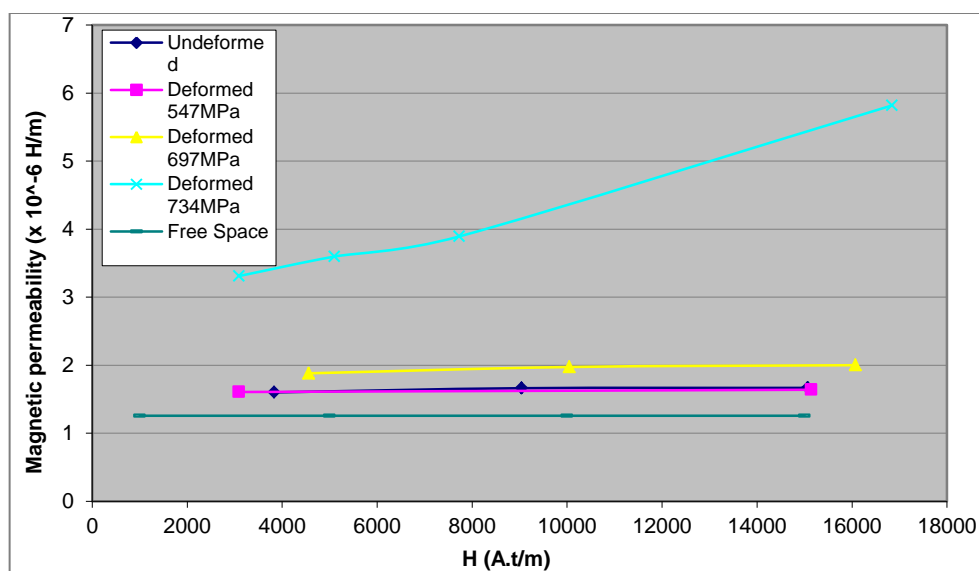


**Figure 3.203: Magnetic permeability curves of 304 stainless steel; undeformed and previously deformed in tension to various loads.**

Prior to tensile deformation, Alloy TRIP M had magnetisation and magnetic permeability curves close to those of free space (Figure 3.204 and Figure 3.205). Between 600 MPa and 700 MPa, the material showed a change in its magnetic permeability. This corresponds to data in Figure 3.138, Section 3.5.9. The UTS of TRIP M was measured to be 840 MPa (Figure 3.138), thus the material showed measureable transformation from approximately 70% of its UTS. TRIP M showed a relative increase in permeability of about 5 times from undeformed to failure.

Magnetic permeability (after transformation) peaked at a field strength of between 8000 A.t.m<sup>-1</sup> and 12000 A.t.m<sup>-1</sup> (Figure 3.205). It would be unconstructive to apply a field strength greater than 10000 A.t.m<sup>-1</sup>.

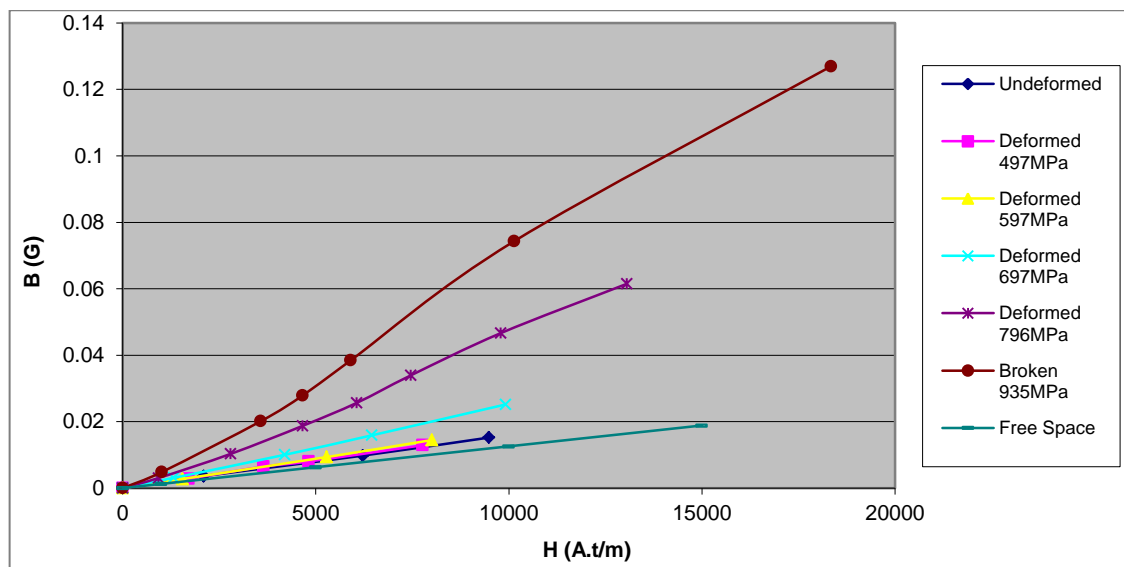


Figure 3.204: Magnetisation curve for Alloy TRIP M; undeformed and previously deformed in tension to various loads.

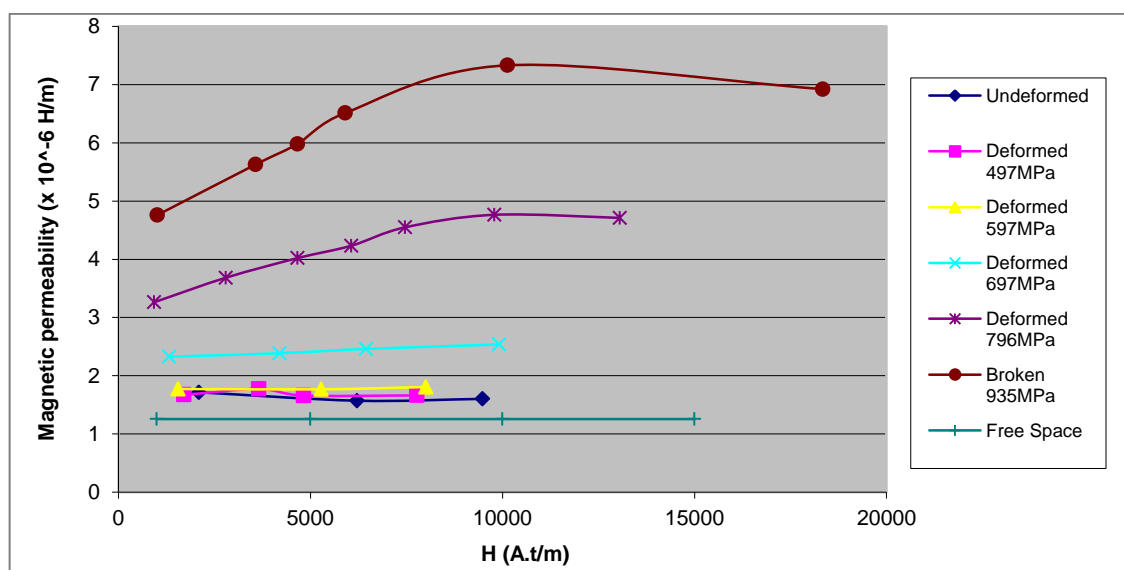


Figure 3.205: Magnetic permeability curve for Alloy TRIP M; undeformed and previously deformed in tension to various loads.

Before tensile deformation, Alloy TRIP R had a magnetisation and magnetic permeability curve close to those of free space (Figure 3.206, Figure 3.207). Between 450 MPa and 550 MPa, the material began to show a change in its magnetic permeability (Figure 3.207). This corresponds to data in Figure 3.138, Section 3.5.9.

The UTS of Alloy TRIP R was measured to be 830 MPa (Figure 3.138); the material thus transforms from approximately 55% of its UTS. TRIP R showed a relative increase in magnetic permeability of about seventeen times from undeformed to failure (Figure 3.207), by far the largest of any of the materials tested in tension, and similar to the best compressive material. This is significant, because the resolution of the sensor is directly associated to this relative change. Notably, the material's magnetic permeability (after transformation) peaked at a field strength of about 7 500 A.t.m<sup>-1</sup> (Figure 3.207).

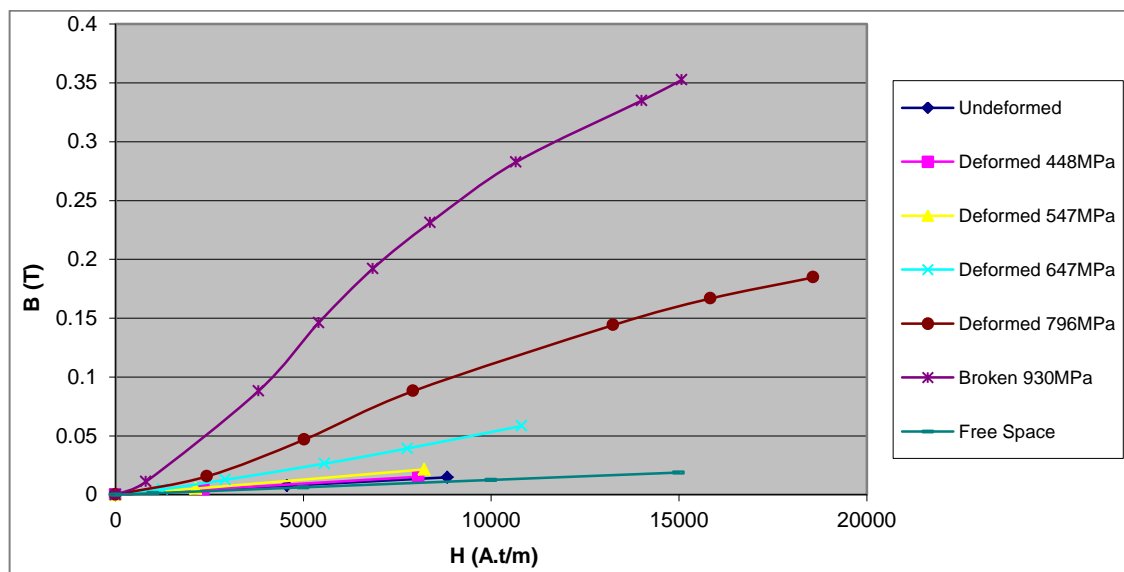


Figure 3.206: Magnetisation curve for Alloy TRIP R; undeformed and previously deformed in tension to various loads.

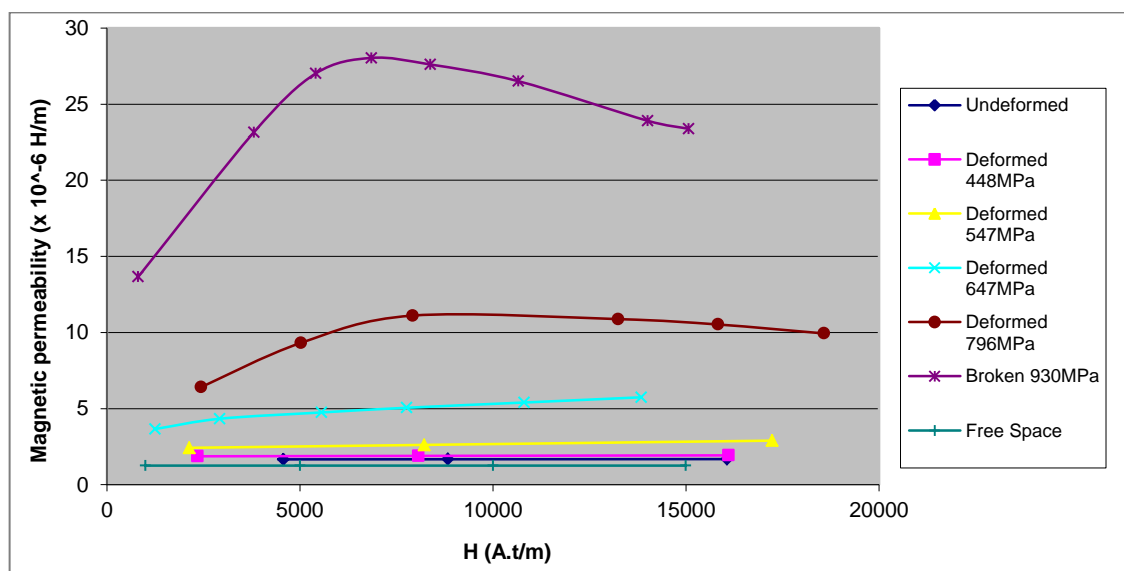
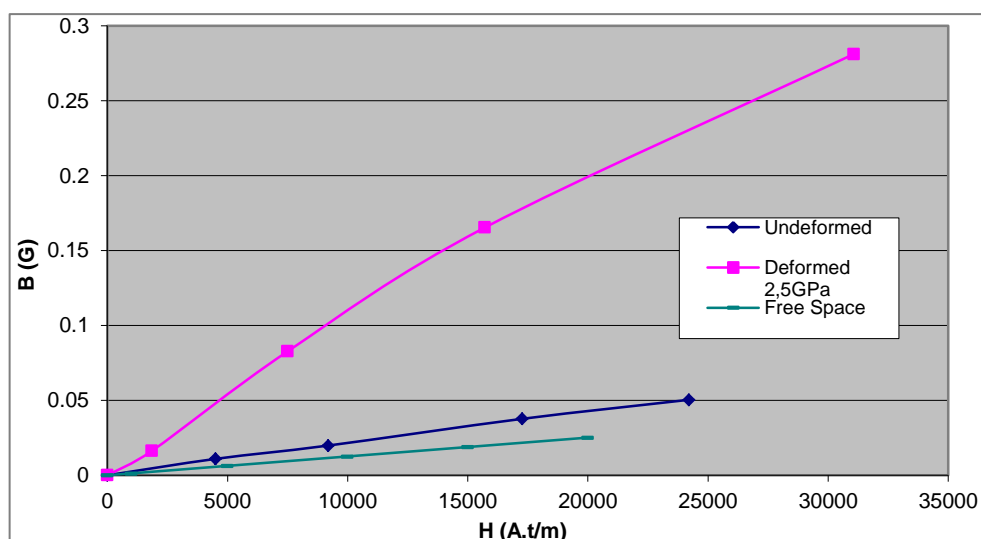


Figure 3.207: Magnetic permeability curve for Alloy TRIP R; undeformed and previously deformed in tension to various loads.



Prior to compressive deformation, Alloy TRIP V2 had a magnetisation and magnetic permeability curve slightly above those of free space (Figure 3.208 and Figure 3.209). No intermediate stress levels were measured, but a large compressive deformation of 2.5 GPa produced a strong increase in magnetic permeability (Figure 3.209). The deformed material's magnetic permeability peaked at a field strength of between 7 500 A.t.m<sup>-1</sup> and 10 000 A.t.m<sup>-1</sup> (Figure 3.209).



**Figure 3.208:** Magnetisation curve for TRIP steel V2; undeformed and previously deformed in compression to 2.5 GPa.

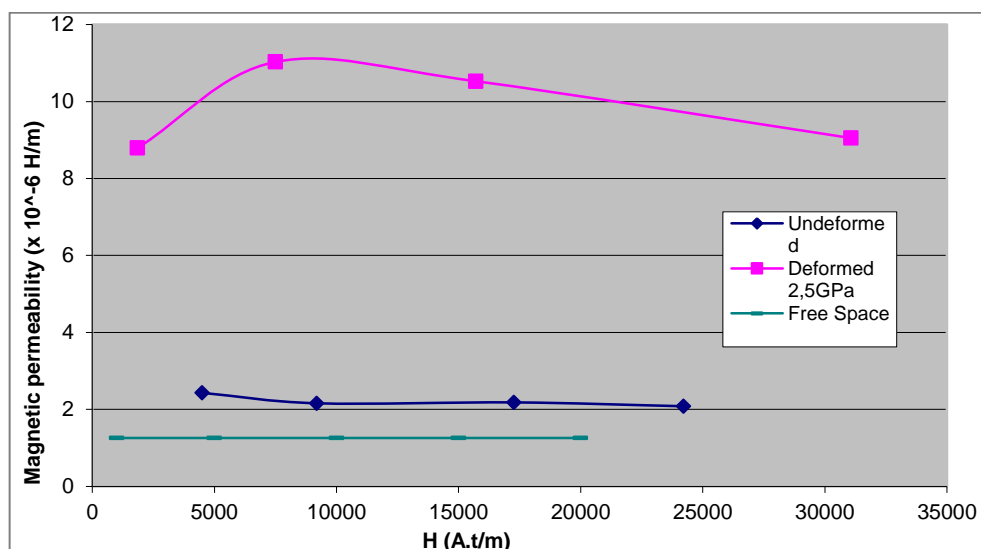


**Figure 3.209:** Magnetic permeability curve for TRIP steel V2; undeformed and previously deformed in compression to 2.5 GPa.

The magnetisation and magnetic permeability curves of Alloy TRIP V4 were well above those of free space prior to deformation (Figure 3.210, Figure 3.211). No intermediate stress levels were measured, but a large deformation of 3.5 GPa, produced a large increase in magnetic

permeability, about nineteen times that measured in the undeformed state (Figure 3.211). This was important because the smart sensor resolution is directly associated to this change. Alloy TRIP V4 was the only TRIP steel tested for which saturation of its magnetisation curve was approached within the range of applied field strengths (for the heavily deformed sample) (Figure 3.210). The deformed TRIP steel's magnetic permeability peaked at a field strength between 4 000 A.t.m<sup>-1</sup> and 8 000 A.t.m<sup>-1</sup> (Figure 3.211).

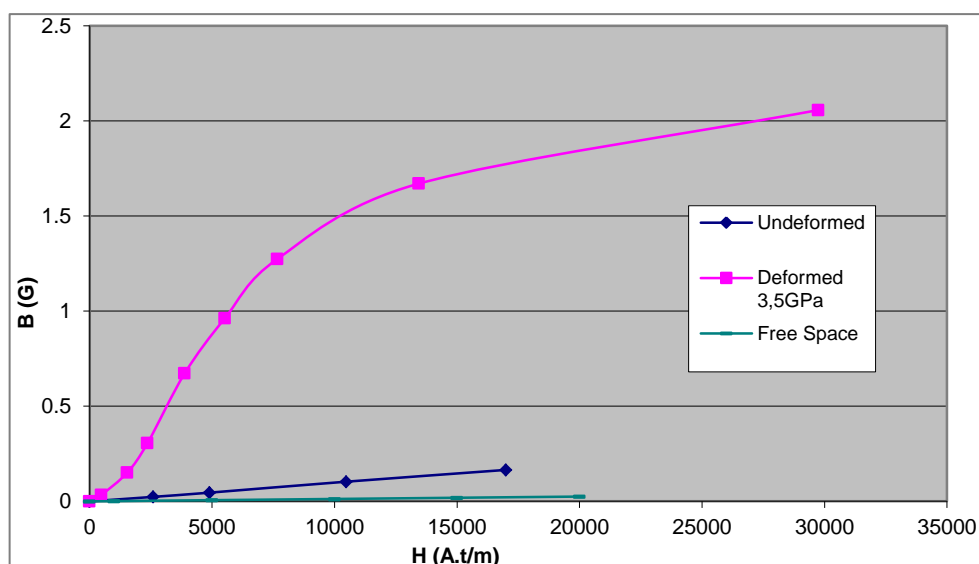


Figure 3.210: Magnetisation curve for TRIP steel V4; undeformed and previously deformed in compression to 3.5 GPa.

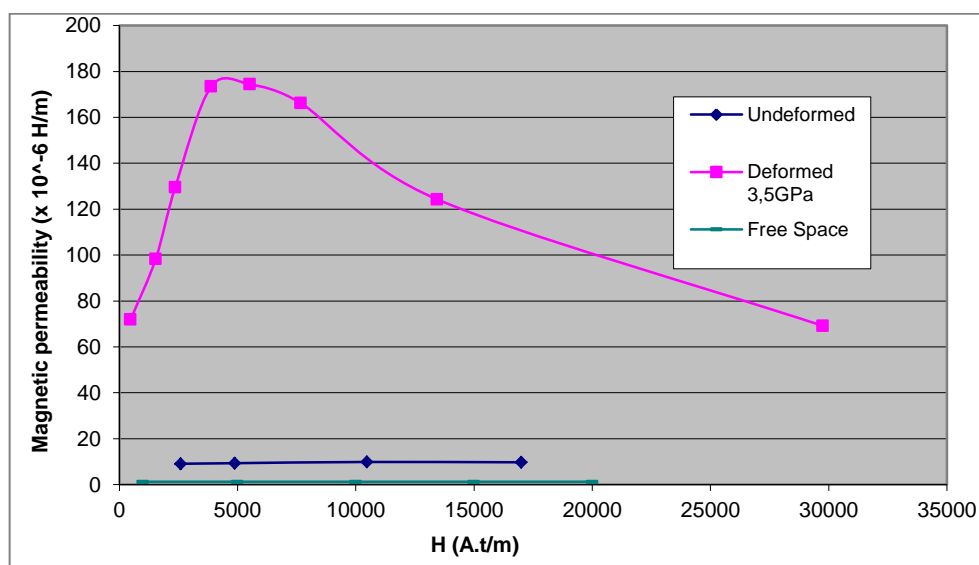
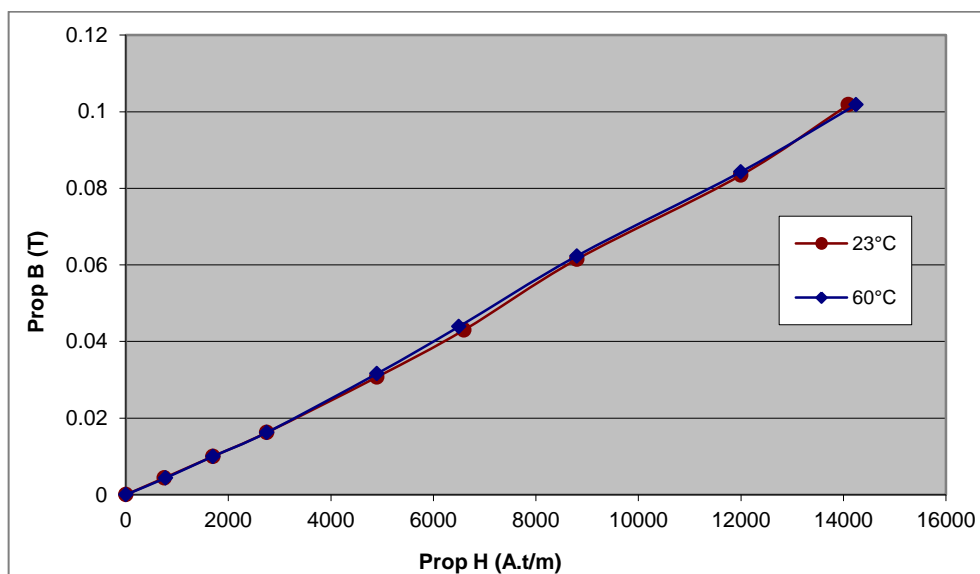


Figure 3.211: Magnetic permeability curve for TRIP steel V4; undeformed and previously deformed in compression to 3.5 GPa.

Due to possible temperature variation in the final application environment, it was also pertinent to check for changes in the magnetisation curves due to temperature variation in the coil and specimen. The above system was thus set up near a Labofurn oven and tests were repeated at

23°C and 60°C, with Alloy TRIP M in a fully deformed state. Results are shown in Figure 3.212.



**Figure 3.212: Magnetic permeability curve for Alloy TRIP M deformed to 935 MPa, at room temperature and at 60°C.**

The effect of measuring magnetic permeability at frequencies between 50 Hz and 2 500 Hz was examined, and the results are shown in Figure 3.213. A frequency fluctuation of 10 hertz at any chosen frequency was found to have an indiscernible effect on resolution compared to transformation repeatability.

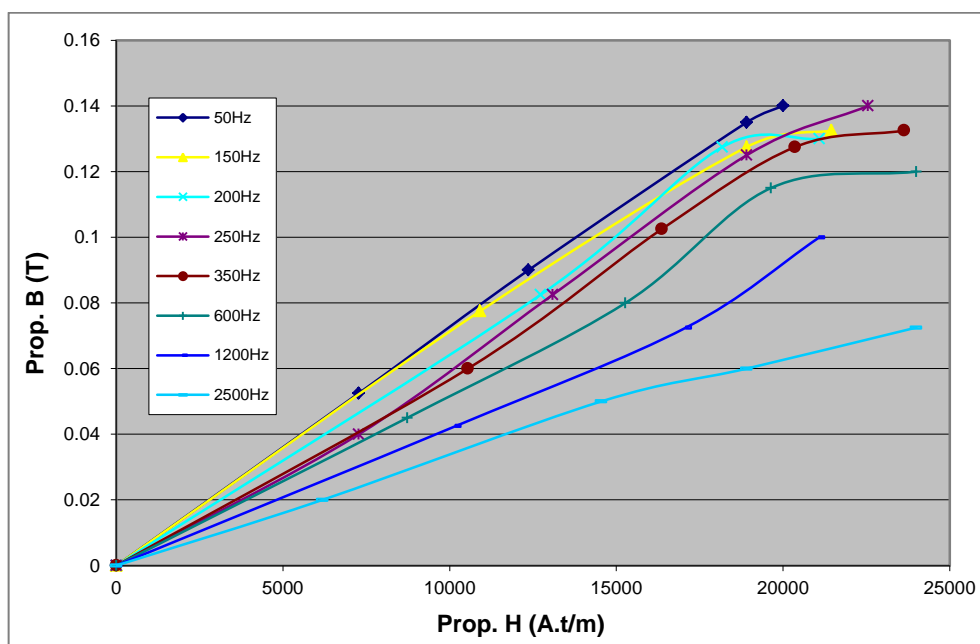


**Figure 3.213: Alloy TRIP M, deformed to approximately 800 MPa and tested at various AC frequencies to establish the effect of measurement frequency on magnetic permeability results.**

### 3.7.4 Conclusions

In order to ensure that the change in magnetic permeability occurring in the TRIP steel elements within the proposed sensors was optimally measured, it was necessary to investigate the magnetic properties of these materials. Magnetic permeability decreased rapidly well before magnetic saturation, there was thus an ideal range for field strength where permeability peaked, thus also causing inductance to peak for constant physical parameters. Therefore, simply increasing field strength via current or number of turns would not optimise permeability measurement.

When magnetic permeability was within its peak range for a given material, it had a relatively greater influence over inductance, and thus a given percentage change in permeability would lead to a greater change in inductance and increased resolution. Figure 3.202 to Figure 3.211 show that magnetic permeability can be effectively measured at any field strength from well below  $1\,000\text{ A.t.m}^{-1}$  to above  $20\,000\text{ A.t.m}^{-1}$ . However, it has also been shown that measurement above  $10\,000\text{ A.t.m}^{-1}$  is detrimental in that the magnetic permeability for a given level of transformation decreases as field strength increases. There is an ideal range where the magnetic permeability of the material is maximised; this field strength varies somewhat for different TRIP steels, but  $7\,500\text{ A.t.m}^{-1}$  is close to ideal for all of them.

Measuring the magnetic permeability (inductance) at low field strengths is possible, but, disregarding potential practical considerations, accuracy will decrease due to a smaller relative change in magnetic permeability. This was seen to be particularly pronounced in the better transforming materials, for example TRIP R and TRIP V4, where the permeability change at maximum deformation varied with field strength by nearly three times between  $500\text{ A.t.m}^{-1}$  and  $7\,500\text{ A.t.m}^{-1}$ .

Figure 3.212 shows that changes in the magnetisation curve in the measurement temperature range  $23^{\circ}\text{C}$  to  $60^{\circ}\text{C}$  were negligible. Olson and Azrin (Olson & Azrin, 1978) found that coil sensitivity to low temperature was negligible down to  $-100^{\circ}\text{C}$ . This result does not pertain to changes in the rate of paramagnetic to ferromagnetic deformation induced transformation at different temperatures, which is dealt with in Sections 3.4.8 and 3.5.9.

Figure 3.213 shows that a frequency fluctuation of a few hertz around a chosen frequency had a negligible effect on resolution. Although frequency fluctuation is unlikely, the effect was least pronounced between 50Hz and 150Hz, or above 600Hz. However, Figure 3.213 also showed that there is a 50% reduction in flux density as frequency increased from 50Hz to 2500Hz. At a

given field strength, this implies a similar reduction in relative magnetic permeability and an associated reduction in sensor resolution. It was concluded that measurement at frequencies between 50 Hz and 100 Hz was favourable, because error due to frequency fluctuation was low and flux density was maximised for a given field strength.

## 4. Developing structural health monitoring devices

### 4.1 Introduction

The primary focus of this work was to investigate the optimisation of high alloy TRIP steels for load sensor applications. However, as well as investigating TRIP steels, some complete sensor devices were also manufactured and tested. Although the development of these devices did not form a core part of this thesis, an overview of their design is provided in this chapter.

Sensor devices were targeted primarily at the mining industry and the aviation industry. Two separate channels of early project funding originated for mining load sensor devices and for aircraft wing-bolt damage sensors, and these industries showed the most interest in the technology. Several different structural health monitoring devices were developed for the mining industry and one for aircraft. The devices for mines can be divided into those utilising TRIP steel in compression and those utilising it in tension. All devices utilised TRIP steels produced for this project and investigated in Chapter 3.

The first structural health monitoring device produced is referred to as a smart rock tendon. Mining bolts are used in mines to reinforce the mined-out stope and tunnel rock by creating a self-supporting, steel reinforced arch or lintel. The bolts extend from one to several metres into the rock and are usually tightened in tension to place the surrounding rock in compression. The objective was to produce a mining bolt that would be capable of bearing the required tensile load, while also monitoring the peak level of load to which it was subjected, and by extension, any movement within the rock. This was achieved by incorporating a TRIP steel element into the bolt, and monitoring its magnetic permeability change upon deformation. It has been proposed that by monitoring bolt load and rock movement, the frequency of unpredicted rock falls may be reduced (Herron, 1983) (Hutchinson & Diederichs, 1996) (Hudson & Harrison, 2000) (Moema & Paton, 2005) (Buys, 2008). The smart rock tendon would also indicate the point at which correct bolt tension is attained during installation; incorrect tensioning at installation is often a cause of later failure.

The second structural health monitoring device produced is referred to as a smart load cell. This device was designed after the smart rock tendon. It was intended as a cheap device with broad application. The smart load cell measures load in compression in a manner similar to an ordinary load cell. It utilises a TRIP steel element that is deformed in compression as the load is



applied. Since the martensitic transformation that occurs as the TRIP steel element is deformed never reverts, the load cell always memorises peak load. The smart load cell is extremely cheap and robust in comparison to traditional load cells, and can easily be manufactured in a range of sizes and to cope with a range of loads. The primary applications of the smart load cell were also intended for the mining sector. These include monitoring overload stresses in mechanical jacks and in roof support props, which are usually visually monitored with very little accuracy or consistency. Similar applications would be expected in the civil engineering industry.

The smart load cell was also adapted into a device referred to as the smart face plate. This device is identical to the smart load cell, but incorporates a central hole to allow a shaft to pass through and some minor internal modifications to accommodate this. The smart face plate is intended to perform the same functions as the smart load cell, while also being capable of measuring the load in an ordinary mining bolt or steel tie rod or tendon. It achieves this by being located as a washer between the bolt head and the bolted surface. It is thus loaded in compression as the bolt is tensioned, allowing a standard mining bolt to be monitored in a similar fashion to the smart rock tendon. The smart face plate was designed for broad application, capable of measuring peak load between two surfaces or in any large tendon, bolt or cable.

The mining sector is a very insular industry. In order to appropriately innovate and adapt products intended for the mining industry, it was necessary to gain a deeper understanding of mining. To this end an extensive literature survey was carried out regarding mine types, mine layout, safety in mines and mine support methods. A brief summary of this is included in Section 4.2.3. Coal, gold and platinum mines were visited and their roof support structures examined. Rock engineers and mine managers, such as Mr. Minnie of Anglo Coal, Mr. Oelofse of Anglo Gold, Mr. Holder of Anglo Platinum and Mr. Coetzer of CSIR Miningtek were interviewed. The information gathered from these visits was invaluable in the attempt to design monitoring systems that would conform to industry needs.

Finally, a smart bolt was designed for use as an aircraft wing bolt. Presently, costly periodic inspection is vital in guaranteeing the structural integrity of aircraft. The intention is to reduce aircraft maintenance costs without modification of aircraft structures by implementing smart wing bolts, manufactured from TRIP steel, which can be monitored for damage *in situ*. Signs of damage within the TRIP steel bolt material are monitored via special washers incorporating embedded inductance-coils, which are able to detect the martensitic transformation that occurs in the TRIP steel bolt during deformation.

## **4.2 Structural health monitoring**

### **4.2.1 Introduction and objectives**

Dependable information concerning the health of a structure will lead to the reliable, speedy discovery and quantification of damage within the structure. This in turn will save time and money and ensure safe and consistent operation. It will allow for appropriate measures, such as support and repair or evacuation to be executed before disastrous safety or structural issues arise.

A true picture regarding the behaviour of a structure is only available once the structure is in service (Worden & Duijveland, 2004). Traditional methods are often beset with problems related to cost, reliability, accuracy and accessibility, as well as inspection down-time and human error, when inspecting and maintaining structures. This leads to over-designed structures, unnecessary replacement or repair of structures, extremely time-consuming and costly inspections, or at the other extreme, unnecessary damage or even catastrophic failure. If smart structural health monitoring systems are to be adopted, they should improve the reliability and efficiency of inspecting the structure, while saving money and reducing environmental impact in the long term.

### **4.2.2 Smart structural health monitoring technology**

Traditional methods for evaluating structural damage include non-destructive testing (NDT) techniques. NDT methods usually involve removing a structure from service for inspection; they rely on discrete, direct measurement to determine the health of a structure. Comparative historical data are not usually required, and thus resolution and calibration of equipment as well as operator competency must be heavily relied upon. Structural health monitoring (SHM) techniques are performed via permanent sensors while the structure is in service (Inman, 2002). They use comparative measurements, taken at two different times, to determine the present condition of the structure. Thus, NDT relies primarily on equipment and skill, while SHM relies more on data interpretation.

The implementation of SHM technology should lead to the monitored structure ideally never being removed from service until the end of its working life (Apsey, 2003). However, such systems usually need to be developed by dedicated multidisciplinary teams, must be accepted by designers, operators, customers or the authorities and must then be appropriately integrated into the structure.

### 4.2.3 Smart SHM for South African mines

Underground mining has for centuries been among the more intrinsically hazardous and technically challenging activities of mankind, and it remains so today. In South Africa, a country having the world's richest deposits of gold, platinum, chromium and manganese, enormous magnitudes of ore are removed from mines up to four kilometres below the earth's surface every day. Structural integrity is of fundamental importance with respect to ensuring the safe and efficient operation of these mining facilities. Billions of Rands per annum are invested for tunnel and stope development alone (Oelofse, 2005).

A rock-burst is an explosive release of energy that propagates as a high energy wave travelling through the rock, like an ultra-low intensity earthquake (Kaiser & Cai, 2012). A rock fall is simply a fall of ground that may occur for several reasons, including association with a rock-burst event. In an effort to prevent rock falls and rock-bursts from occurring in mines, as many as twenty thousand rock-bolts may be installed monthly in a single mine (Maleki, 1992) (Minnie, 2005) (Oelofse, 2005); 100 million per year in the USA alone (Jalalifar, 2006). This process accounts for a significant portion of the cost of developing tunnels and stopes (Oelofse, 2005).

Naturally-occurring rock is the intrinsic material from which tunnels and stopes must be constructed. The properties and imperfections of the rock-mass are never well defined, and it is primarily this that makes the safe engineering of mining structures so difficult. Although considerable effort and expense is made on the structural integrity of tunnels and stopes, rock-falls and rock-bursts continue to account for too many deaths. This is illustrated by Figure 4.1, which categorises the recorded fatalities in 30 South African gold mines between 1996 and 2001 by cause (SIMRAC, 2003). Figure 4.2 categorises fatalities by permanent ground support type and shows that the great majority of fatalities are caused in regions supported by rock bolts. Furthermore, an analysis by Jager and Ryder (Jager & Ryder, 1999) showed that as gold and platinum mines became deeper, fatalities due to falls of ground became more common.

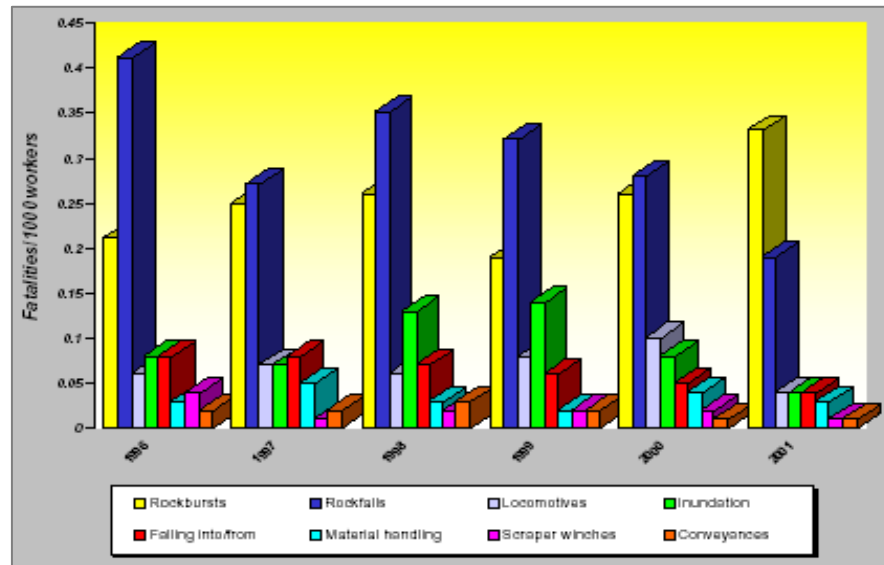


Figure 4.1: Fatality rates categorised by the eight most significant contributors in the gold mining sector (SIMRAC, 2003).

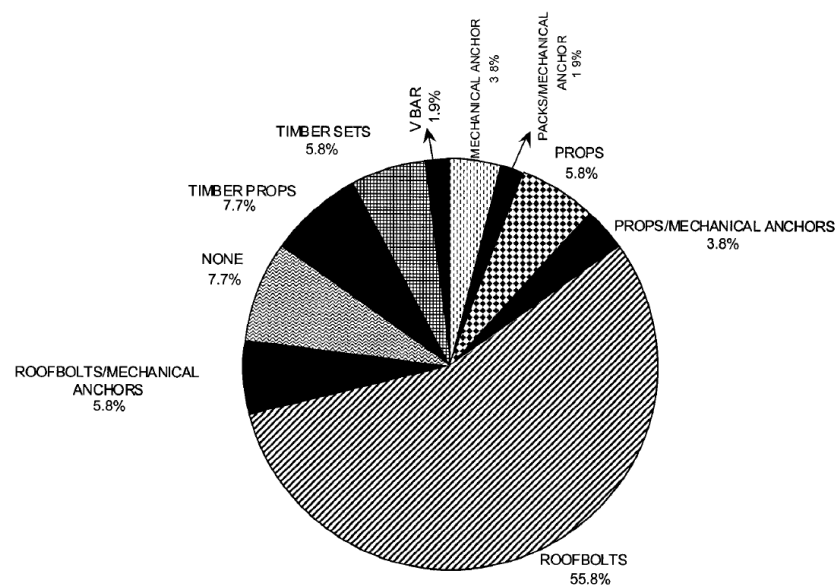


Figure 4.2: Distribution of fatalities with respect to permanent support type (Canbulat & Jack, 1999).

Rock engineers rely almost entirely upon their experience and discretion to select and inspect the support systems for the many varying rock mass conditions existing in South African mines (Daehnke et al., 2000). The notion of monitoring the integrity of this rock mass in order to make more informed decisions is not new, although all but a few proposed methods have failed to gain acceptance and none are widely utilised (Stacey, 1995) (Buys, 2008). It is generally accepted by experts that, especially in deep gold mines, most methods of *in situ* stress measurement are not applicable (Stacey, 1995) (Daehnke et al., 2000) (Buys, 2008). Reasons for this include their cost, their requirements for significant assistance from the mines in terms

of services and personnel, and their reliability under the harsh conditions experienced in the mines (Bemont et al., 2001). An Australian and a Swedish company have both developed instruments that can determine the strain within certain reinforcing rock bolts using ultrasonic methods. However, the equipment is not only expensive and cumbersome, but also requires considerable effort by qualified and skilled personnel to perform the interrogation of a bolt. Through extensive experience and interaction with the gold mining industry in South Africa, the CSIR (South African Council of Scientific and Industrial Research), Mining Technology Division, identified the following requirements for a reliable, cost effective technique with broad application to *in situ* stress measurement in deep gold mines (Stacey, 1995):

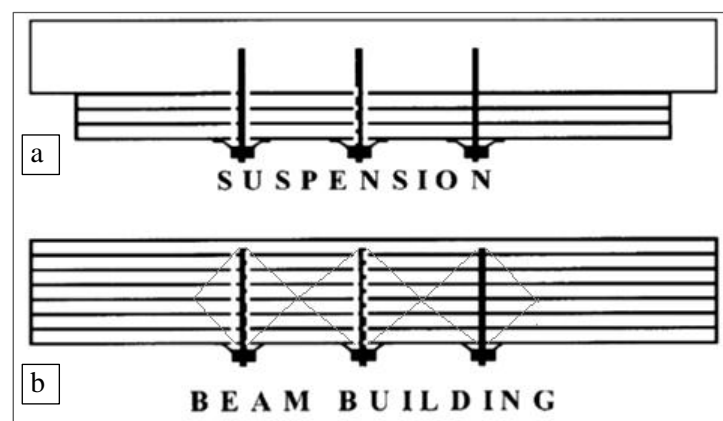
- The technique should be undemanding on the requirements for services provided by the mines. It should not require water or cable fed power and should require minimal input from mining personnel. It should impact as little as possible on all other mining operations.
- The technique should be low cost with regard to all aspects; cost of preparation, cost of installation, cost of instrumentation, cost per measurement, and economical in terms of time requirements.
- It should be possible to make many measurements during a single shift; this is preferable to a few high accuracy measurements.
- The technique should not be significantly susceptible to high stress effects, such as spalling and micro-cracking but should be sensitive to rock mass stress changes.
- The technique should be flexible, possible to implement at very short notice, at excavations of varied size and differing location. It should not require continuous measurement, but rather be implementable on a “stop-start basis”.
- The technique should not require the retrieval of rock cores and laboratory testing.
- The technique should not be susceptible to any of the harsh conditions encountered in the mining environment.

Sensor distribution in a structural health monitoring system should be optimal and the smallest number of sensors giving the required resolution should be utilised (Worden & Dulieu-Barton, 2004). In the mining environment, it is difficult to apply this practice because of the extreme uncertainty of the rock system. Sensor distribution would need to be decided according to the particular rock structure but should be as sparse as reasonably possible in order to minimise costs.

In order to design structural health monitoring sensors for the mining industry, it was necessary to become familiar with mining layouts, processes, jargon and devices. Mine types, mine layout, safety in mines and mine support methods were all investigated. Coal, gold and platinum mines were visited and their structures and support closely examined. Rock engineers and mine managers were interviewed (Minnie, 2005) (Oelofse, 2005). The information gathered from these visits enabled a much better understanding of the industry, the support devices and

their associated shortfalls. It was hoped that this would lead to the design of devices more likely to fulfil industry needs and conform to industry requirements.

A brief outline of support techniques used in South African mines completes this section. Figure 4.3 shows two distinct methodologies regarding hanging-wall (roof) support using rock reinforcing-bar or cable bolts (tendons). In (a), loose, jointed or discontinuous rock is suspended through the use of tendons to the continuous, structurally sound rock above. In (b), there is no reliance on structurally sound rock away from the excavated region. Instead, a reinforced beam is formed from the discontinuous rock when the clamping forces within the rock due to tendon pre-tensioning converge and overlap with one another, as represented by the grey lines in (b).

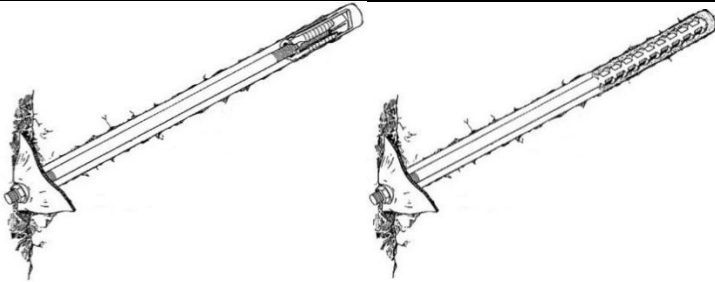
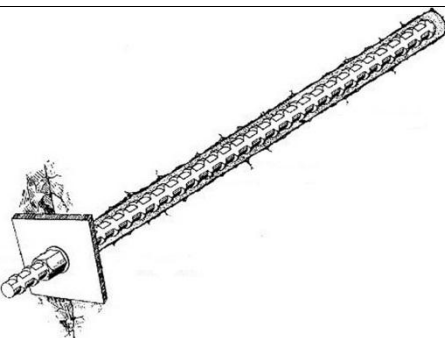
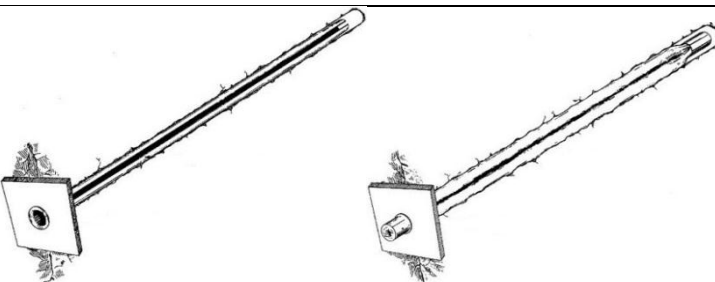


**Figure 4.3: Rock reinforcing methodologies (Canbulat & Jack, 1999): (a) Suspension, (b) beam building.**

Rock reinforcement tendons are listed by category and type in Table 4.1 (Roberts, 1995). Three broad categories of rock tendon include discretely mechanically or friction coupled (DMFC), continuously mechanically coupled (CMC) and continuously friction coupled (CFC). The first two categories may include cable as well as reinforcing bar based systems. DMFC tendons include the friction coupled variety, which utilise an expanding mechanical anchor to transmit load to the rock, and the mechanically coupled variety, which utilise a resin cartridge to bond the inmost portion of the tendon to the rock. CMC tendons utilise grout or resin along the full length of the tendon. CFC tendons are found as either split-sets or Swellex types. Split-sets utilise the spring effect of driving a hollow steel tube that is slit along one side into a hole drilled smaller than the tube. Swellex tendons are sealed steel tubes, crimped along their length, which upon insertion into the drilled hole are expanded into it, using very high pressure pumped water.



**Table 4.1: Rock reinforcing elements by category and type (images from Roberts (Roberts, 1995)):**

Category	Tendon types	Representative diagram
Discretely mechanically or friction coupled (DMFC)	Mechanically anchored or resin end-anchored bars and cables	
Continuously mechanically coupled (CMC)	All types of fully grouted bars and cables	
Continuously friction coupled (CFC)	Split sets and Swellex bolts	

### 4.3 The smart rock tendon

#### 4.3.1 Introduction and objectives

Many methods have previously been proposed for rock movement monitoring, but none have been especially successful, particularly in deep mines (Stacey, 1995) (Coetzer, 1998) (du Plessis, 2000) (Brady, 2004) (Cai & Wang, 2011). This lack of success has been due chiefly to the expense of these devices, their lack of robustness, the complexity and reliability of their installation and maintenance, and the level of training and responsibility required to monitor such systems (Buys, 2008) (Moema & Paton, 2005). The smart rock tendon (SRT) has been designed to overcome these pitfalls through the use of an integrated TRIP steel sensor element.

The SRT was designed to be used as a sensor in mines for detecting rock movements and thereby combating rock-falls and rock-bursts by warning engineers and mine managers of such

movement prior to a hazardous event, while also acting as a traditional reinforcing tendon. This dual purpose posed some difficulties because the enhancement or refining of one function often adversely affects the other.

As previously discussed in Section 4.2.3, current rock-mass support systems are typically selected by intuition and the actual capacity of a support system is seldom quantified (Minnie, 2005). This is in part due to uncertainties in quantifying the expected stress regime, and in part due to difficulties in measuring the existing stresses within the support system (Brady, 2004). Another shortcoming of current support systems is that the contributions of individual elements towards the performance of the integrated system are not known. By utilising SRT sensors, it will be possible to assess tendon loading and elongation in specific tendons as well as to track the appearance and propagation of cracks and rock movement in sidewalls and hanging walls (ceilings). This is expected to assist with design optimisation of the entire rock-tendon systems.

Another major downfall of traditional tendons is that one of the most common types, pre-tensioned DMFC tendons are often not correctly pre-tensioned at installation, they are then rendered largely useless. This occurs primarily due to difficult conditions and lack of training. It is a major headache to mine captains and is a common reason for moving to other more expensive types of support (Oelofse, 2005) (Minnie, 2005). The SRT can eliminate this problem by alerting personnel as to whether or not the bolt is pre-tensioned to the specified load. While the SRT was developed primarily for the mining industry, it is clear that it may find other applications with little or no modification in, for example, underground excavations and structures in the civil engineering industry.

The SRT has the potential to offer an accurate and immediate warning, enabling an area under stress to be reinforced before collapse or evacuated before any lives are lost. This benefit has immeasurable ethical and public relations implications, as well as direct and indirect financial implications such as remuneration to deceased miners' families, medical and disability expenses and the huge expense involved in reopening tunnels, shafts and stopes, not to mention loss of man-hours and production time while an operation is shut down. The SRT is also extremely robust, relatively cheap, maintenance-free and easy to install and use.

#### **4.3.2 Mechanical design**

In designing the SRT, factors such as cost, sensitivity, repeatability, robustness, load capacity, functionality, simplicity and familiarity were considered. Initially, a tendon manufactured entirely from TRIP steel was envisaged, although it soon became clear that the entire length of the tendon should not act as a sensor. Since high alloy TRIP steels are considerably more

expensive than HSLA steel, manufacturing the entire length of the tendon from TRIP steel would drastically increase material costs. Tendon elongation and associated rock movement would be larger than ideal at high loads, because TRIP steel has a yield point relatively lower than its tensile strength compared to HSLA steel. Except in very exceptional circumstances, DMFC tendons carry a uniform load along their length. Thus, a DMFC type smart sensor tendon only requires a short TRIP steel element to measure this load and the associated elongation occurring in the tendon.

In order to reduce unit costs, the specially-developed TRIP steel element is incorporated into any standard reinforcing rock tendon by inserting it between two off-the-shelf tendon couplings (usually used to extend a tendon), or by screwing it onto the end of a standard tendon. Friction welding was also considered for joining the high alloy TRIP steel element to the low alloy tendon.

The strain or stress in the bolt is then measured via a hand-held unit that plugs into a socket in the protruding end of the reinforcing tendon. A standard reinforcing bolt thus becomes a strain and stress sensor without losing its robustness or load bearing ability. A wireless communication system was also incorporated into one bolt, allowing it to be monitored by a remote PC and alert relevant personnel via mobile phone or alarm in event of predefined stress or strain levels being reached.

As discussed extensively in Sections 3.5 and 3.6, TRIP steels are relatively strong, even compared to HSLA steel. This means that a TRIP steel element that forms part of a tendon can be of smaller diameter than the HSLA tendon, while still imparting the same failure strength. Since the TRIP steel utilised has relatively lower yield strength compared to its tensile strength, this means that the TRIP steel will yield well before the HSLA tendon, allowing monitoring from lower stresses and elongations than otherwise possible. Since the TRIP steel element only comprises a very short portion of the tendon length, its elongation after yield will not substantially affect the total tendon elongation. Figure 4.4 shows a schematic diagram of the DMFC tendon-based smart rock tendon design, the relative total tendon length would be much greater than shown.

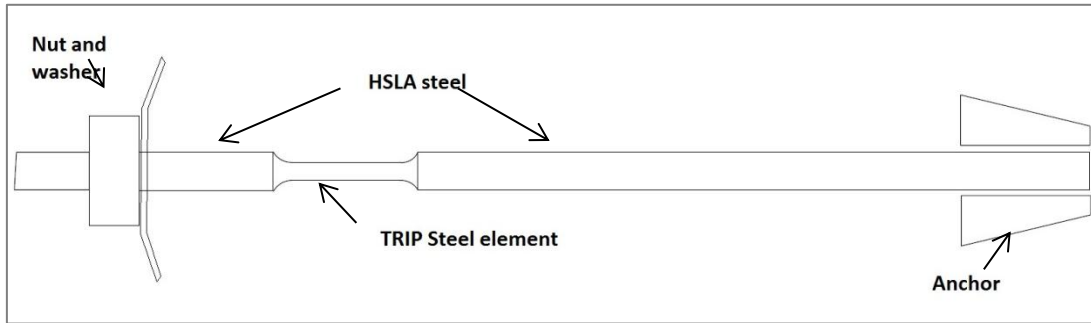


**Figure 4.4: Schematic diagram of the smart DMFC tendon design showing the TRIP steel element.**

A copper inductance coil of several hundred turns is wrapped around the TRIP steel element and the leads are lead through the hollow lower shaft tendon to its base in which a jack is located. The TRIP steel element may be joined to the HSLA part of the tendon by using a standard mechanical coupling or by friction welding. The couplings are standard items and are able to fit comfortably into the hole-size drilled into the rock for the tendon. The insulated copper coil is protected by a mild steel sheath (not shown in Figure 4.4). This sheath also serves to close the magnetic flux path around the TRIP steel element and to shield the winding from interference. This setup is shown in Figure 4.5, showing a shortened version of the smart rock tendon. In practice, a DMFC tendon may be several metres long.



**Figure 4.5: A complete, but shortened, smart rock tendon.**

#### 4.3.3 Inductive coil design

A higher number of turns on an inductor will result in an exponentially greater inductance when other factors remain unchanged. This is shown by Equation 4.1, where  $L$  is inductance,  $N$  is number of turns,  $\mu_0$  is the magnetic permeability of a vacuum,  $\mu_r$  is the relative magnetic permeability of the inductor core and is considered constant here,  $A$  is the cross-sectional area of the coil and  $l$  is the coil length (Maxwell, 1865) (Cottingham & Greenwood, 1991). Thus, as the relative magnetic permeability of the TRIP steel core changes due to the martensitic transformation, the absolute change in inductance for a given transformation will significantly increase with a greater number of turns and thus give greater sensitivity. This phenomenon is separate from that examined in Section 3.7 which characterises the manner in which increasing field strength alters a material's magnetic permeability.

$$L = \mu_0 \cdot \mu_r \cdot N^2 \cdot A / l$$

**Equation 4.1**

The more turns the coil has, the greater its impedance is for a given frequency and wire diameter and thus, for a given voltage the current will decrease since  $V = I.Z$ . Thus, when  $N$  increases,  $I$  decreases approximately proportionately and so field strength will remain approximately unchanged according to Equation 4.2, while inductance increases.

$$H = N.I$$

**Equation 4.2**

In this respect, the number of turns should thus always be maximised, but this may be constrained by other parameters. For example, constraints may simply be lack of physical space in the area surrounding the inductor, as well as the reduced effect of coils that are placed far from the centre of the solenoid as described by the Biot-Savart law (Biot & Savart, 1820). Eventually, increase in coil resistance due to the length of the coil winding may also have a negative impact, depending on circuit design.

Also of interest was the influence of the physical volume of transforming TRIP steel within the inductor on the resolution of the sensor. Increasing this volume, and thus the amount of martensite that is created under a given strain, might have the potential to increase resolution. This is verified by Equation 4.1, when the number of turns on the inductor increases linearly with inductor core length, inductance, and thus inductive change, will increase too.

The inductor with its TRIP steel core could be made longer to increase its total volume, while the stress and strain in the material would remain constant for a given load. The deformation section should thus be as long as possible when not constrained by other factors. However, in most applications, the amount of extension that may occur is limited by physical factors. Importantly, the longer the deformation section, the more extension must occur for a given level of stress, and thus for a given level of transformation to occur. The logic of longer-is-better therefore only applies unchecked in situations where extension is of no consequence and only load is of interest. Tests were performed to confirm that an increase in length with a proportional increase in number of turns resulted in a linear increase in inductance (Section 4.3.5).

It is also clear from Equation 4.1 that the inductance increases in proportion to the cross-sectional area of the inductor's core. It follows too then that this should also be maximised where no other constraints are present, for example, when only extension is to be measured and the load carried by the TRIP steel is relatively insignificant. This is not feasible with the current design, since loads to be monitored are essentially set by the strength of the standard HSLA portion of the tendon. The yield point of the TRIP steel element should be reached at as low a

load as possible in order to maximise measurement range, without compromising the tensile strength of the tendon.

#### 4.3.4 Circuit

Two circuits were specially developed for measuring the inductive change in TRIP steel sensor elements. The first was based on a transformer principle whereby two coils are wound around the TRIP steel specimen. The secondary coil is open circuit and voltage is measured across it. Due to decreasing losses in the TRIP steel core as the transformation from austenite to martensite progresses, voltage increases with the transformation. An advantage of this method was that current, and thus field strength through the primary winding, could be controlled in accordance with the results from Section 3.7. However, the output from this circuit was found to drift substantially, even with the TRIP steel core at a constant level of deformation. This significantly affected repeatability. The circuit could also not be made portable, because its power consumption was too large. This sensor circuit was therefore rejected, and another developed.

The second circuit design was based on the discharge time constant of the TRIP steel cored inductor, which varies with inductance proportionately to  $L/R$ , where  $L$  is the inductance and  $R$  is the circuit's resistance (which is constant if the winding is not changed). A Schmitt trigger based oscillator allows the TRIP steel cored inductor to be alternately charged and then discharged across a set of resistors. An integrator circuit is utilised to sum the inductor discharge times and convert them to an operational amplifier (op-amp) scaled voltage. This circuit resulted in a stable voltage output response for a given TRIP steel core deformation.

The scaled voltage outputted by the circuit is thus proportional to the inductance of the TRIP steel cored winding, which is in turn linked to the extent of martensitic transformation of the TRIP steel core. This voltage was then directed to an output jack, as well as a voltage display module, which utilises op-amps to trigger variously coloured LEDs at preset voltages corresponding to predetermined deformations. As proposed by interviewed mine rock engineers, four LEDs are utilised and can be set to trigger at specified loads corresponding to: low load or unitstalled; pre-load attained; high load; overload or failure eminent. The voltage jack provided can be utilised to determine peak load via a calibrated voltmeter. The circuit is illustrated in Appendix 2, A2.1. A complete hand-held device (Figure 4.6) based on this system was shown to trigger the LED's at preset coil inductances in a highly repeatable fashion.



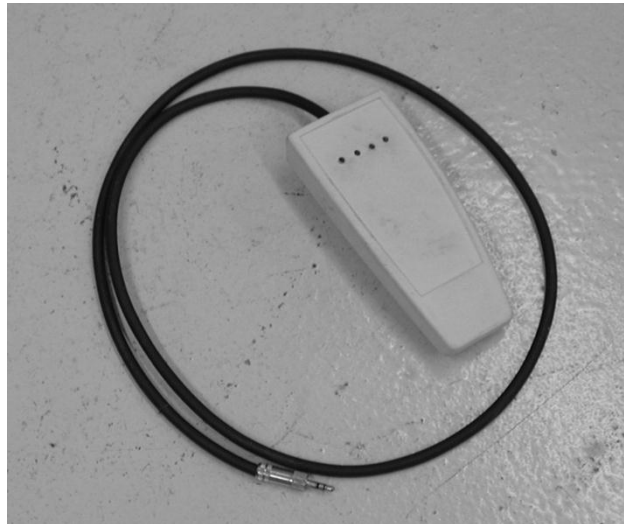


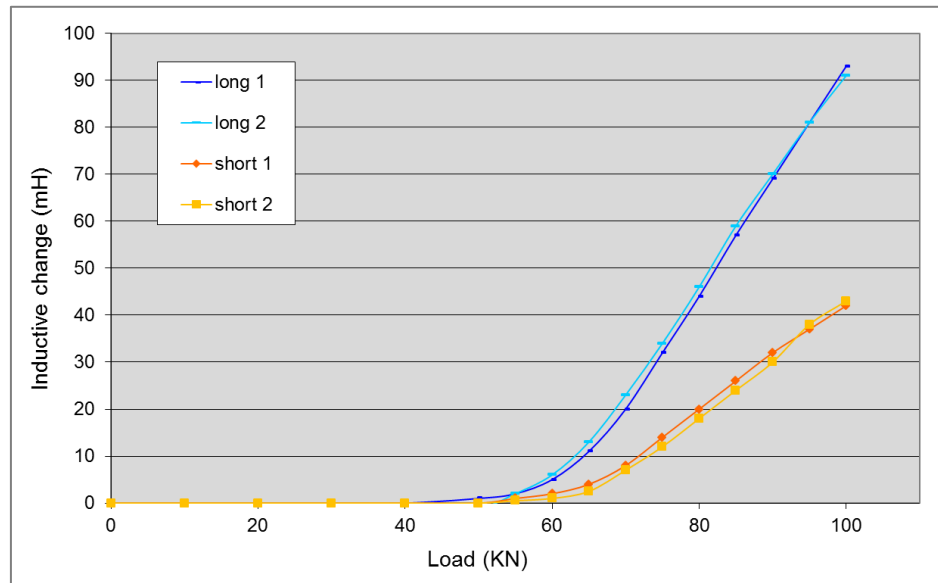
**Figure 4.6: Purpose-designed hand held device used to interrogate smart rock tendons.**

An addition to this circuit to intermittently wirelessly transmit peak load readings to a central computer or cell-phone was designed, built and tested by undergraduate students at UKZN (Heath et al., 2007). The transmitter functioned well, but in its current form used too much power to operate for extended periods from a small battery pack. It was also much too large to be integrated into a smart rock tendon, although its size could certainly be drastically reduced through revised design and construction, and through the use of surface mounted components and greater use of integrated circuits. Power consumption could be significantly reduced by using a sleep mode inbetween hourly interrogations, and only transmitting upon detection of a significant inductance change.

#### **4.3.5 Experimental**

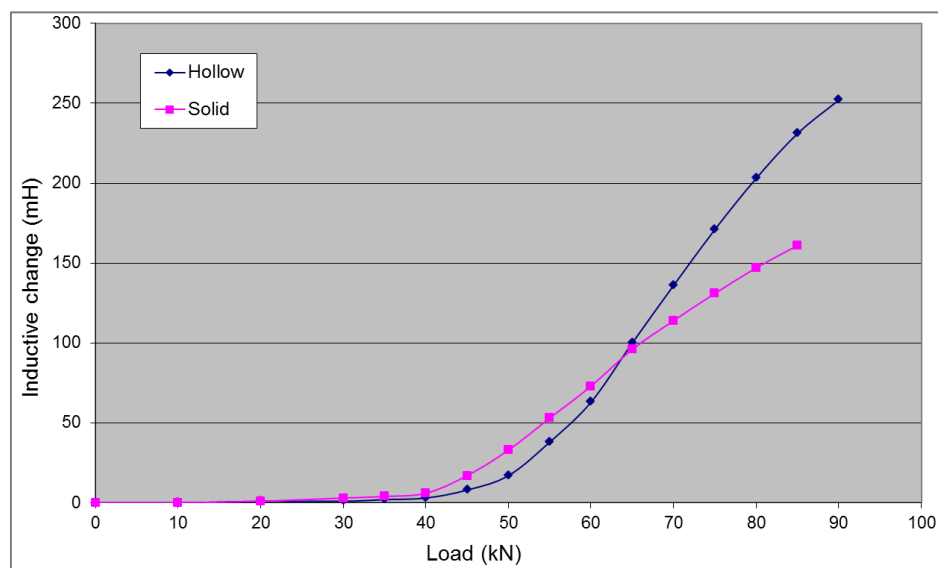
In an attempt to encourage greater sensitivity and resolution from the devices and earlier transformation, testing was performed to ascertain the effect of differently shaped specimens. As discussed in Section 4.3.3, experimental testing was also performed towards optimising the interaction of the inductance coil with the specimen. All tests were carried out at room temperature (approximately 22°C) in an air-conditioned room.

Specimens with a long gauge length were compared to those with a short gauge length (Figure 4.7). TRIP M was used for this comparison and gauge diameter was 11 mm. The short gauge length was 40 mm long and had 200 turns. The long gauge length was 80 mm long and had 400 turns. The inductance coil was wound directly onto the specimen in both cases. The gauge length that had double the number of turns and was double the length showed approximately double the inductive change at any given load.



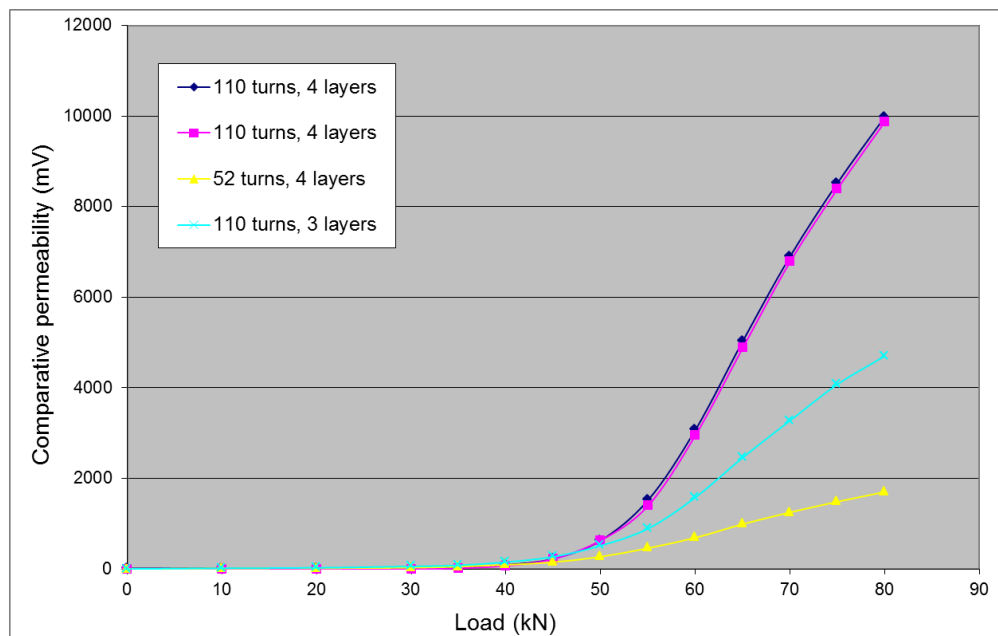
**Figure 4.7:** Comparison of the inductive change with load between a short TRIP M inductor core (40 mm) and another double its length (80 mm), with the same number of turns per unit length.

The effect of using a hollow tube, rather than a solid bar, was also investigated. It was considered that a hollow tube of the same solid cross-sectional area may result in a stronger signal from the inductance coil, because, on average, transforming inductor-core material would be nearer to the coil. TRIP R was utilised with an equivalent gauge diameter of 11 mm and gauge length of 60 mm. The hollow specimen had an outer diameter of 13.6 mm and a bore of 8 mm diameter. It was found that while the hollow tube did show a greater total signal from about half way through the transformation, the signal in the early part of the transformation was in fact lower, as illustrated in Figure 4.8. Since the low-stress portion of the transformation is of greatest significance, a solid specimen, which is also easier and cheaper to manufacture, was preferred to the hollow version.



**Figure 4.8:** Comparison of the inductive change with load between a hollow cored TRIP R inductor core and a solid one.

The number of turns on a specimen will increase inductance as shown in Equation 4.1. However, a greater number of turns also places a larger resistance and impedance across the electronic monitoring circuit and moves the coils further from the TRIP steel core. Thus, the effect of a placing a greater number of turns on a specimen by increasing the number of layers, rather than the gauge length, was investigated and the results are shown in Figure 4.9. TRIP R was utilised with a gauge length of 20 mm and a diameter of 11 mm. Copper armature wire of 0.16 mm diameter was used for the three 110 turns per layer coils and wire of 0.32 mm diameter was used for the 52 turns per layer coil. The tests were performed on a complete SRT, with a mild-steel sheath in place, and using the specially-developed circuit described in Section 4.3.4. This test setup conformed to the South African Bureau of Standards specification SANS 1408 of 1999 for the performance requirements for mechanical components for tendon based rock support systems for use in the mining industry.



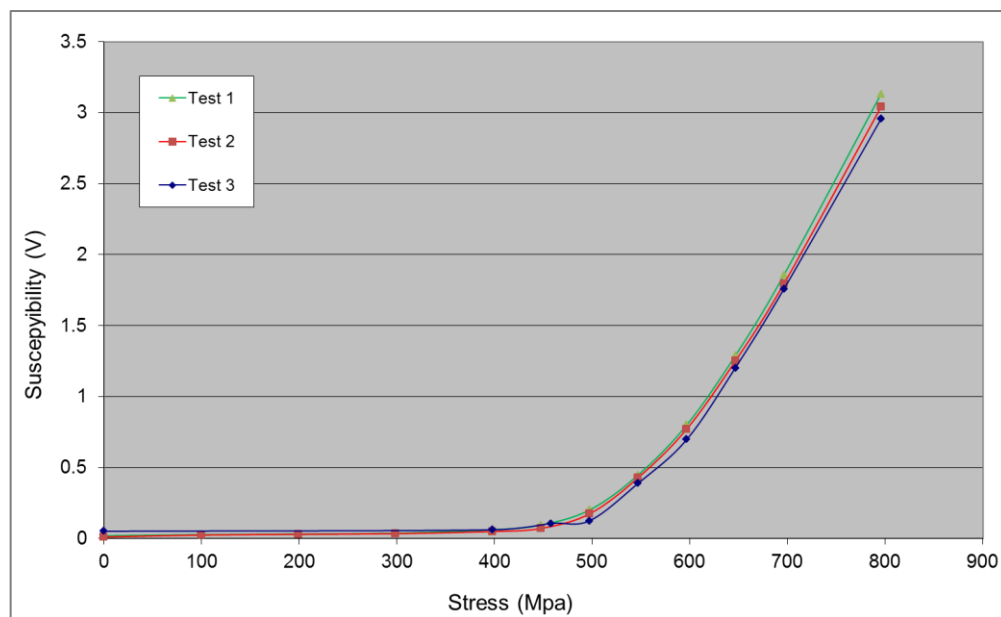
**Figure 4.9: Comparison of the inductive change with load between identical TRIP M inductor cores with different coil configurations. Number of turns are specified per layer.**

Figure 4.9 shows that three layers of 110 turns provide just over half the inductance than four layers of 110 turns at any load. This is in precise agreement with Equation 4.1. Thus, the extra impedance of extra turns does not itself significantly impact inductance, and neither is the effect of layering significant, at least in relatively few layers.

A specimen on which double thickness wire was used for the coil, with half the number of turns, would be expected to show one quarter the inductance. In practice, it showed slightly less than this, which was likely due to the circuit favouring a coil with greater resistance.

It would significantly improve the device if accurate low stress transformation could be detected, at least from immediately after yield. Of the above tests, none showed a significant improvement in measuring early transformation, although the long specimen in Figure 4.7 showed signs of a small improvement. It was considered that by introducing stress concentrations into the specimen surface slightly earlier, transformation may be initiated in these areas, and because they are adjacent to the coil, this transformation may be well detected. Thus, specimens with a helical screw-type pattern of 0.5 mm cut into the surface were tested and compared to smooth specimens. However, the results showed no significant improvement.

Testing was performed to determine repeatability of the complete smart rock tendon system, including the specially developed circuit. A gauge length of 40 mm was used so that the extra extension due to the TRIP steel element was minimised. A 15 mm diameter was used so that breaking load would approximately match 20 mm diameter HSLA tendon material. The results are shown in Figure 4.10.



**Figure 4.10: Complete smart rock tendon load versus circuit output in volts using TRIP M.**

Accurate and repeatable readings were obtained between about 100 and 160 kN. Upon installation of the TRIP element in any standard full-length DMFC tendon, association of load to a tendon elongation will be a simple matter. Since the TRIP steel transformation is irreversible, both peak historical load and elongation will be available to the rock engineer.

DMFC tendons should always be installed with pre-tension. Pre-tensions are typically 60% to 70% of tendon tensile strength, or between 96 kN and 112 kN for the 160 kN UTS tendon characterised in Figure 4.10 (Bigby et al., 2010). Thus, at a 70% preload of 112 kN, this smart

reinforcing rock tendon will be capable of alerting the installer that preload has been attained and accurately reading any further increase in load or elongation.

The tendon characterised in Figure 4.9 showed a UTS of 80 kN. Thus, a preload of 70% will be 56 kN, and this smart reinforcing rock tendon will thus also be capable of alerting the installer that preload has been attained and accurately reading any further increase in load or elongation.

#### 4.3.6 Conclusion

The SRT was the first complete TRIP steel based sensor to be designed and tested. It was designed to intermittently replace rock reinforcement tendons in mines, particularly in safety-critical areas, while also enabling the measurement of tendon load and rock movement. It was envisaged that rock engineers might thus be empowered to more accurately model a rock structure and its reinforcement system, while the tendon will also warn of an approaching failure and act as a traditional reinforcing tendon. Due to the irreversible nature of the TRIP steel transformation, the smart reinforcing rock tendon will always remember its peak load.

Under the relatively small temperature fluctuations in underground mines, measurement error due to these fluctuations is expected to be below  $\pm 5\%$ , and less in deep South African mines (see Table 3.18). The effect of strain rate fluctuation is more difficult to predict and more work needs to be done to characterise it. Rocks are known to be ejected from mine walls in two distinct types of events (Section 4.2.3). The first is a rock-fall, in which the rock simply loosens and falls, or places its mass on the reinforcing member. The second is a rock-burst which is a rapid release of stored energy in a seismic event (Kaiser & Cai, 2012). It is well known that seismic waves related to earth quakes propagate at a speed of several kilometres per second. This results from a gradual increase of fault rupture speed over an extensive fault length. However, the smart tendons are not intended to measure the utter destruction expected to result from an earthquake. Seismic wave speed also does not translate directly into rock ejection speed, since a rock must move off from a stationary position. Literature suggests that maximum rock ejection speeds are approximately 3 m/s (Hagan et al., 2001), but may reach 7.5 m/s (He et al., 2012). Since the shortest reinforcement tendons are usually around two metres, strain rates are definitely not expected to exceed  $4 \text{ s}^{-1}$ . This is extremely conservative, because these speeds were measured for relatively small rock pieces. Since the ejection is due to the propagating energy of a wave, a larger rock or structure held in place by a reinforcing tendon would be expected to move exponentially slower. From the knowledge of the link between temperature and strain rate investigated in Section 3.4.10, the extent of reduction in transformation between quasi-static speeds and  $10 \text{ s}^{-1}$  is about -10%. However, considerable further testing is required to properly characterise strain rate effects.

A purpose-built inductance measurement circuit was developed and tested and inductance coil design was investigated. Modification of various physical parameters was performed with the notion of improving the sensitivity of the electronic inductance measurement to the transformation. It was shown that increasing the length of the TRIP steel sensor element was beneficial. However, the length of the sensor is limited by its influence on tendon elongation. A hollow TRIP steel element was compared to a solid one of the same cross-sectional area. It was found that although this increased the total level of measured transformation later in the deformation, it reduced early deformation sensitivity shortly after yield, a characteristic of primary importance. The response of the purpose-designed inductance measurement circuit to the number of turns on a coil, the number of layers therein and the diameter of the wire from which it is wound was also tested. It was found that, to the extent investigated, an increased number of turns and layers increased the response.

Complete smart rock reinforcing tendons were tested utilising both TRIP M and TRIP R in an appropriate test rig conforming to the SANS standard for such equipment. It was shown that the smart tendons were capable of performing the envisaged task. They can alert personnel when a tendon is properly pre-tensioned to the specified load, be used to measure the peak level of loading and associated elongation within the tendon, and alert personnel when failure is impending.

## **4.4 The smart face plate and smart load cell**

### **4.4.1 Introduction and objectives**

The Smart load cell is a device that utilises cast TRIP steel in compression to form a very low cost and robust load cell unit that can be used to measure compressive stress or displacement. It was attempted to produce a generic device that could be easily adapted to many different applications, but a target industry was again the mining sector. Applications might include monitoring overload stresses in mechanical jacks and in roof support props in mines, which are usually visually monitored with very little accuracy or consistency. Similar potential applications exist in underground excavations and structures in the civil engineering industry.

The smart load cell was adapted into a device referred to as the smart face plate. This device is identical to the smart load cell, but incorporates a central hole through which a shaft may pass. The smart face plate is intended to be able to fulfil the same functions as the smart load cell, while also being capable of measuring the load in any ordinary rock reinforcement tendon or



steel tie-rod. It achieves this by being located as a washer between the bolt-head or nut and the bolted surface. It is loaded in compression as the bolt is tensioned, enabling the stress in the tendon, bolt or tie-rod to be monitored.

The work in Section 4.4 contributed to journal paper 2 (The development of robust structural health monitoring sensors utilising TRIP steel), which is included in Appendix 3.

#### 4.4.2 Design

The smart load cell (SLC) and smart face plate (SFP) consist of two heavy steel plates held apart by three small steel inserts (Figure 4.11 and Figure 4.12). The inserts are located in a third, thinner plate. At least one of the three inserts is made from TRIP steel. An inductive coil is situated around the TRIP steel insert(s) in order to monitor its level of irreversible martensitic transformation and thereby the associated historical peak load to which the device has been subjected.

If there is reasonable certainty regarding the manner in which the device will be loaded, as would usually be the case, then a single TRIP steel insert is sufficient. However, if the load might be applied to an unpredictable location on the load cell surface, then all three inserts should be made from TRIP steel. It is expected that this is unlikely for the SFP, since the tendon will always apply the load in a similar location.

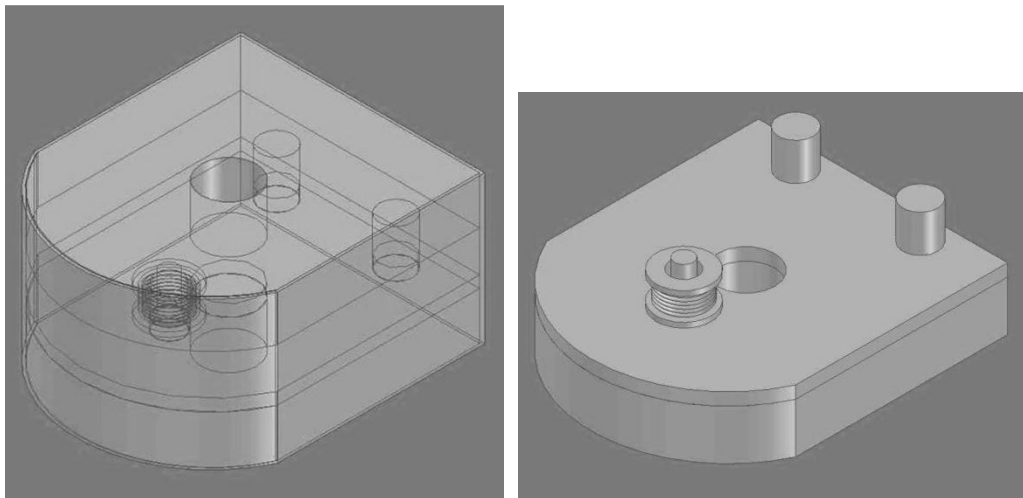


**Figure 4.11: Structure of the smart face plate (Bemont, 2009).**

The smart load cell is simply a smart face plate with a domed or flat-topped insert placed into each of its main tendon holes. The smart load cell can then be placed under a load which will be applied to these protruding inserts.

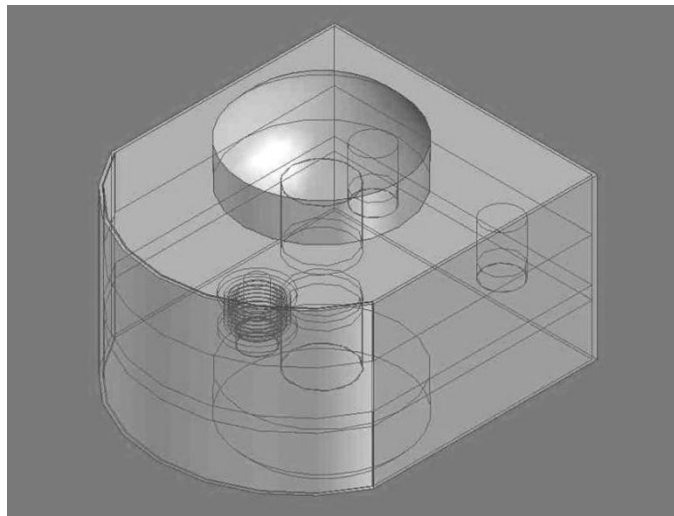


**Figure 4.12: Adaptation of a smart face plate into a smart load cell with load inserts in position.**

For ease of manufacture and assembly, it may be feasible to cast the three inserts and lower main plate in a single TRIP steel casting, removing the thin locating plate. A second mechanical component would form the top plate and side shell. Thus, the entire device would consist of just two mechanical components and two electrical components (the inductance coil and the socket located in the side shell).

The diameter of the TRIP steel insert is altered according to the desired measurement range, but measurement cannot be made before the TRIP steel insert has yielded. Thus, the device cannot be used for measuring relatively low loads. However, because cast TRIP steel alloys have a lower yield point than worked alloys, measurements can start at relatively lower loads, as shown in Section 4.4.3. Cast alloys cannot be utilised in tension because their tensile breaking strength is extremely low. They rely on the extensive *in situ* work hardening that occurs in compression to increase their compressive strength, Figure 3.5.

A coil of 2000 turns on a small coil former was placed over the TRIP steel insert, and the leads attached to the inside of the plug socket. The same circuit used for interrogating the smart rock tendon (Section 4.3.4) can be recalibrated and used to interrogate the smart face plate.

Figure 4.13 shows a prototype smart face plate. Such prototypes were designed specifically to monitor the loads in a 20 mm diameter solid bar DMFC tendon.

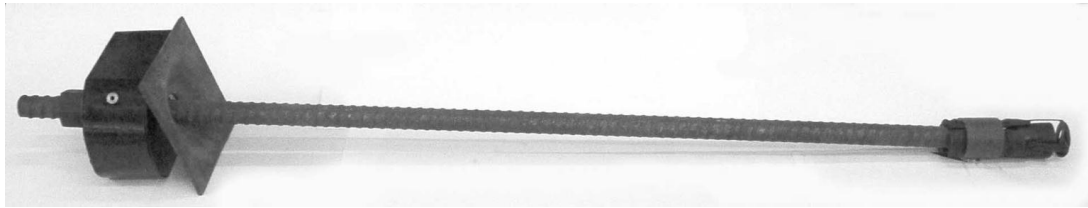


**Figure 4.13: A smart face plate installed on a complete tendon.**

It was proposed that it would be beneficial if a smart load cell or smart face plate did not require any electrical power or electronic circuitry to function. A method using a permanent magnet and magnetic viewing film was proposed. Magnetic viewing film is a plastic film that changes colour depending on the direction and intensity of a magnetic field.

Although such a device was not produced, it was modelled as shown in Figure 4.14 using an FEA magnetics program called FEMM. The model showed that through careful positioning of a strong permanent magnet and the TRIP steel element within a highly magnetically permeable iron housing, it was feasible that the concept could work. Observing the colour or shade of the side of the housing would determine the peak load experienced by the load cell.

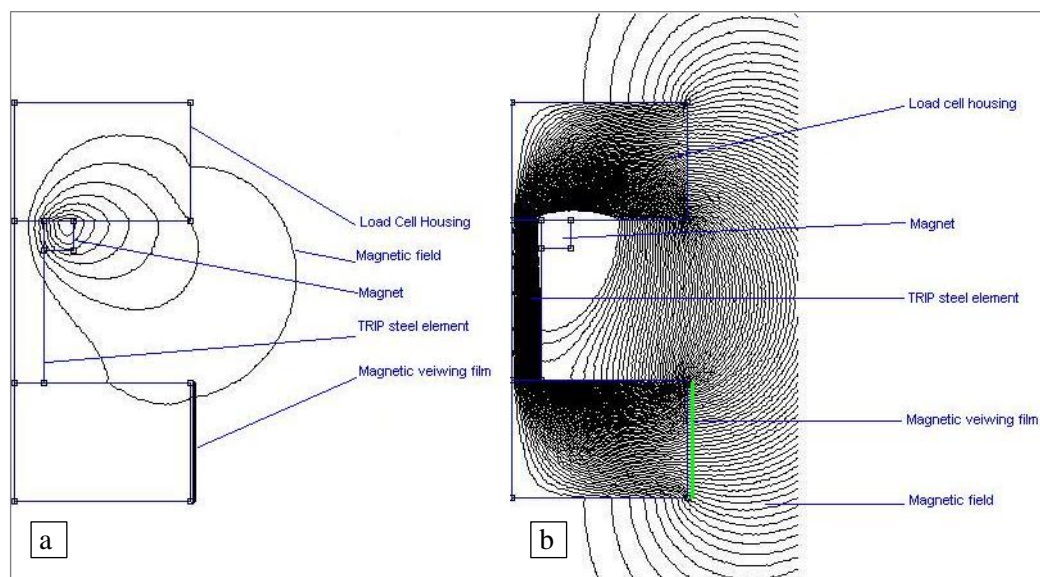


**Figure 4.14: FEMM analysis of a smart load cell utilising a permanent magnet and magnetic viewing film and not requiring any electronics or power: (a) for an undeformed TRIP steel element, (b) after the TRIP steel element has become magnetically permeable through martensitic transformation.**

FEMM was also utilised in the design of the standard smart face plate device. It showed that it would not be necessary to include a magnetically permeable solid return path for the magnetic flux in the face plate because of the large area and relatively close proximity of the two main compression plates within the device.

#### 4.4.3 Experimental testing

The smart face plate was tested in the manner shown in Figure 4.15. A 20 mm diameter tendon was secured on one side with a standard dome-nut. The tendon passed through the SFP and through a specially designed plate in the top of the Avery tensile testing machine; the other end of the tendon was gripped in the machine's tensile jaws. The setup is shown in Figure 4.15.

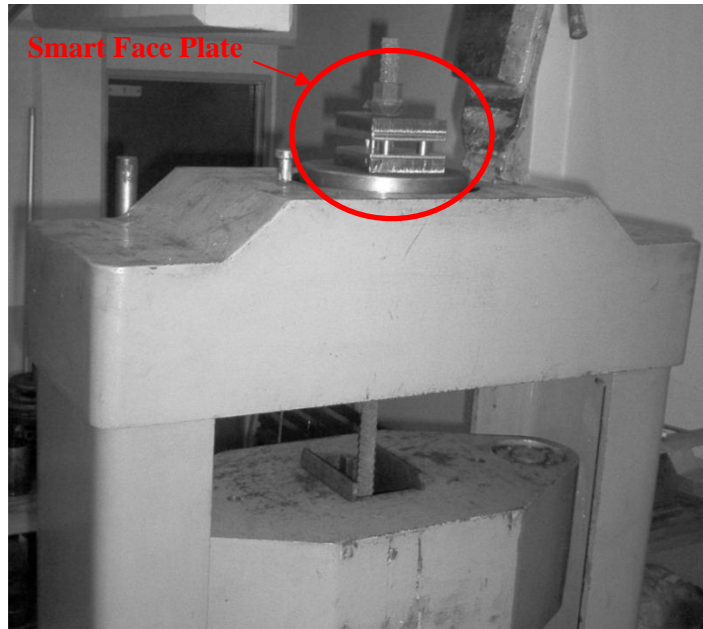


Figure 4.15: Smart face plate (at top) being tested in an Avery tensile testing machine.

Three smart face plates incorporating an 8 mm TRIP steel V4 insert (Section 3.4.3), and another three incorporating a 12.5 mm insert of the same TRIP steel, were tested under quasi-static conditions at 25°C to measure their repeatability. The results of these tests are shown in Figure 4.16 and Figure 4.17.

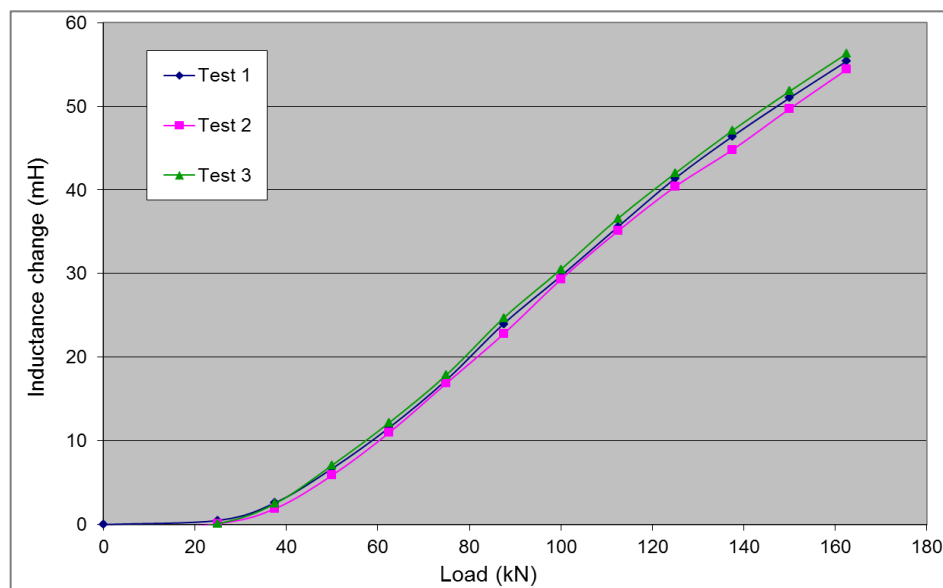
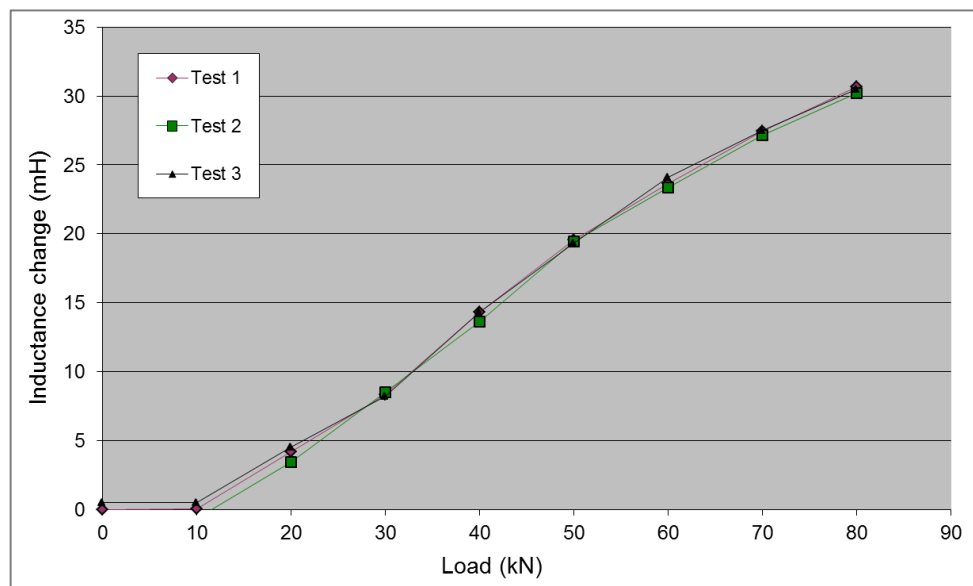


Figure 4.16: Applied load versus inductive change for a smart face plate using a 12.5 mm diameter insert of Alloy V4.



**Figure 4.17: Applied load versus inductive change for a smart face plate using an 8 mm diameter insert of Alloy V4.**

Figure 4.16 and Figure 4.17 show that the smart face plate allowed relatively much earlier load detection (relative to full-scale load) than the smart rock tendon (Figure 4.7 to Figure 4.10). This is because the cast alloy used in the smart face plate had a lower yield point of about 200 MPa compared to the worked tensile alloys, which had yield points of at least 400 MPa. As well as a lower yield point, the material could be stressed to a much greater load in compression before failure. The martensitic transformation in compression was more gradual than in tension, but continued to a much higher stress.

During testing, the inductive coil former was able to move slightly during loading. It is likely that the repeatability of the smart face plate was negatively affected by this, because the position of the TRIP steel insert relative to the inductive coil former affects inductive output. This might easily be improved in a new design.

A further experiment was performed to assess the effectiveness of measuring the transformation with deformation of a TRIP steel tube, using a coil and magnetically permeable core within the tube. Modelling in FEMM had shown that this could be effective. This might allow an even simpler single-casting smart face plate design, or might allow the design of a smart TRIP steel washer that could be used on an ordinary bolt.

Two tests utilising TRIP M were performed to this end. In one, a TRIP steel insert (in the form of a bobbin) with an inductance coil wound onto it was deformed in compression with a mild steel outer sleeve in place to transmit returning magnetic flux. This is shown after testing in

Figure 4.18 (b), note that the bobbin has been pulled slightly out of the tube to reveal the inductive coil. In the second test, a TRIP steel sleeve was deformed while a mild steel insert with an inductance coil winding was located within. This is shown after testing in Figure 4.18 (a). The cross-sectional areas of the TRIP steel and of the mild steel, as well as the number of inductor turns used, were identical, which enabled a direct comparison. The results are shown in Figure 4.19.

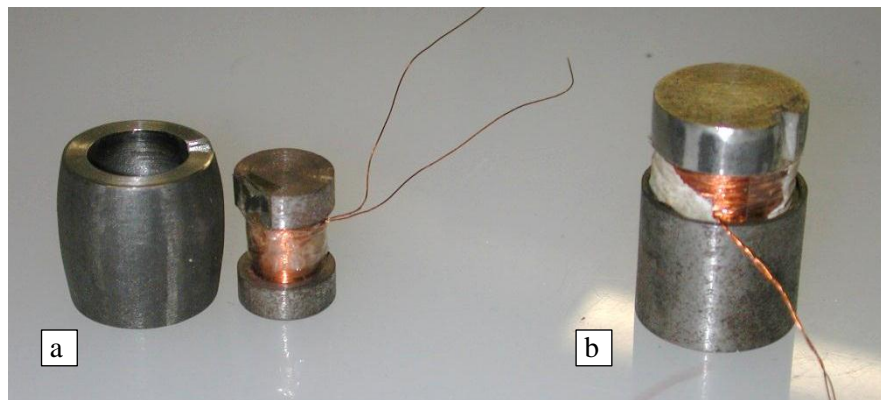


**Figure 4.18: Specimens used to compare the inductive measurement of the martensitic transformation using a TRIP steel sleeve (a) as opposed to a TRIP steel insert (b).**

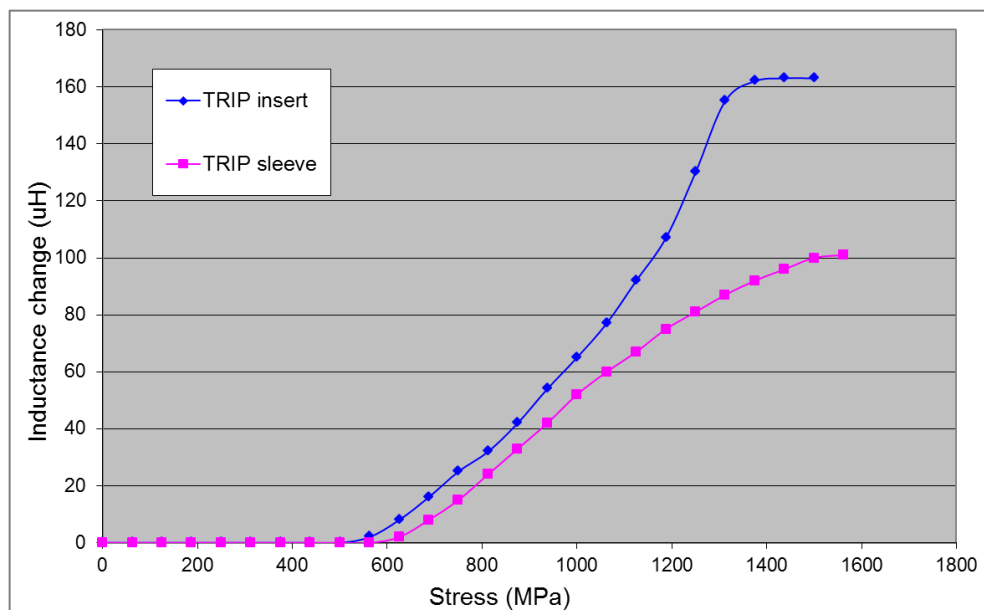


**Figure 4.19: Comparison between the inductive measurement of the martensitic transformation using a TRIP steel sleeve as opposed to a TRIP steel insert.**

Since the number of turns on the coil used was necessarily low due to the small size of the test specimens, inductance was very low. It is likely that this had a negative impact on accuracy, although the trend is clear. It is apparent that while measurement of the transformation from within results in a less pronounced change in inductance as expected, doing so is quite feasible.



#### 4.4.4 Conclusions

A peak measurement load cell was designed to be cheap and robust by employing a TRIP steel insert to detect compressive load. The smart face plate is a generic device that can be used as a peak measurement load cell, or as a load measuring washer capable of detecting the peak tensile load in any ordinary rock reinforcement tendon or steel tie rod. The smart face plate was shown to detect substantially lower loads, relative to its full-scale load, than the smart rock tendon. This was achieved by using cast TRIP steel and applying compressive instead of tensile deformation.

Testing showed that it is feasible to measure martensitic transformation using an internal inductance coil instead of an external one. Although the inductive change was not as pronounced, the response was only marginally reduced.

The smart face plate was designed to be simple to manufacture, potentially with only two cast mechanical components, or even just one utilising an internal coil, and with two electrical components. It can easily be manufactured in a range of sizes, and to cope with a range of loads. The temperature fluctuations of below 20°C (Florides & Kalogirou, 2005) (Oelofse, 2005) (Minnie, 2005) expected in the mining environment are predicted to produce an error of below  $\pm 5\%$  (Table 3.18). Further characterisation is required regarding other factors, in particular strain rate. However, preliminary data on strain rate effects (Section 3.4.10) show that, assuming a peak rock velocity of 7.5 m/s (Section 4.3.6), the associated error should not be greater than -10%.

### 4.5 Smart wing bolt

#### 4.5.1 Introduction and objectives

The potential to reduce aircraft maintenance costs without modification of aircraft structures by implementing smart TRIP steel sensor components was investigated. The possibility of replacing aircraft wing bolts with a near identical geometry smart TRIP steel sensor version was of particular interest. *In situ* warning of bolt damage would thereby be enabled, potentially reducing the costly requirement for periodic wing bolt removal and inspection and increasing safety. As seen from a summary of an analysis by Findlay and Harrison (Findlay & Harrison, 2002) in Table 4.2, the most common point of fatigue failure initiation leading to aircraft accidents is the fasteners, accounting for a quarter of all failures.

**Table 4.2: Common failure initiation sites in aircraft (Findlay & Harrison, 2002).**

Failure initiation site	Number of accidents			
	Fixed wing		Rotary wing	
Fastener	108	24%	32	26%
Fastener hole or other hole	72	16%	12	10%
Fillet, radius or notch	57	13%	22	18%
Weld	53	12%	3	2%
Corrosion	43	10%	19	15%
Thread (not on fastener)	32	7%	4	3%
Manufacturing defect or tool mark	27	6%	9	7%
Scratch, nick or dent	26	6%	2	2%
Fretting	13	3%	10	8%
Surface or subsurface flaw	6	1%	3	2%
Improper heat treatment	4	1%	2	2%
Maintenance induced crack	4	1%	-	-
Work-hardened area	2	0%	-	-
Wear	2	0%	7	6%

In aircraft such as the Hercules C-130, inspection of the wing bolts for potential overload and fatigue crack initiation requires the wings to be jacked up and removed. This process involves at least 180 man-hours of labour, and danger of damaging the wing and other components in the process (Vugampore & Bemont, 2012). Smart wing bolts might cheaply replace the original wing bolts with little or no structural modification being required.

A wing bolt serves to clamp the wing to the fuselage of an aircraft such as the C-130 cargo plane. There are two standard size wing bolts used in the C-130:  $\frac{7}{8}$ " nominal diameter, 14 threads per inch, 108 mm long and  $\frac{3}{4}$ " nominal diameter, 16 threads per inch, 94.65 mm long (Vugampore & Bemont, 2012). The  $\frac{7}{8}$ " nominal diameter bolt is shown in Figure 4.20. These are simple threaded fasteners that are currently manufactured from high strength AISI 4340 steel. These bolts are highly stressed and must be periodically inspected for damage; this is time consuming and expensive. It is proposed that these bolts might be manufactured from a TRIP steel that possesses similar mechanical properties to AISI 4340 steel but also imparts smart damage detection properties to the bolts.



**Figure 4.20: Standard  $\frac{7}{8}$ " nominal diameter bolt used in the C-130 cargo plane (Vugampore & Bemont, 2012).**

Specially alloyed warm-rolled high tensile TRIP steel could only be produced in the form of 12 mm plate and it was impractical to manufacture complete sub-scale bolts from such thin plate. The investigation of warm-rolled alloys for the aircraft wing-bolt is discussed in Section 3.6. Sub-scale smart wing-bolts were manufactured from hot-rolled alloy TRIP M and tested.

The work included in Section 3.6 and in Section 4.4.4 formed the basis of journal paper 3 (The design and testing of sub-scale smart aircraft wing bolts), included as submitted in Appendix 3 (Vugampore & Bemont, 2012).

#### **4.5.2 Design**

It is of fundamental importance to the functioning of TRIP steel based sensors that an appropriate method for monitoring the martensitic transformation of the TRIP steel element is implemented, usually via magnetic permeability detection. Magnetic permeability monitoring via inductance coils has been found to be one of the most accurate methods for monitoring the martensitic transformation, and is often also the most practical to implement (Radu et al., 2005).

The location of the inductive coils was challenging, as they must be placed near the parts of the bolt in which damage must be detectable. It is well known that the first two threads engaged by a nut are the most highly stressed region of a bolt, and thus by far the most likely to fail (Fisher et al., 1952) (American Society of Mechanical Engineers et al., 1953) (Jadon & Verma, 2010). Laboratory testing corroborated this. The region under the bolt head is the next most highly stressed region and is next most likely to fail. The smart bolts thus use an inductance coil embedded within the washer or nut that surrounds the bolt in the region of the first engaged thread, thus demanding no modification to the bolt geometry. In the case where under-head monitoring is also required, only a lengthening of the bolt-shank would be required to include a thicker washer in this location.

Scale bolts of approximately 50% of original size were manufactured, as well as similar bolts including a recess groove underneath the bolt head. This groove was placed underneath the bolt head for purposes of experimental verification. Without it, deformation occurring under the bolt head during testing was found to be nearly indiscernible, due to very low deformation relative to that at the first engaged thread. The groove thus enabled the testing of the sensitivity of the inductance coil in detecting deformation in this location, where failures are known to sometimes occur (American Society of Mechanical Engineers et al., 1953) (Jadon & Verma, 2010). The groove reduced the bolt shaft cross-section in this region, to be equal to that of the threaded cross-section. The geometry of the standard sub-scale and the grooved sub-scale smart wing

bolts tested are shown in Figure 4.21 and Figure 4.22. Figure 4.23 shows a standard geometry (ungrooved) sub-scale TRIP steel bolt with an inductance coil embedded washer, and a nut in place.

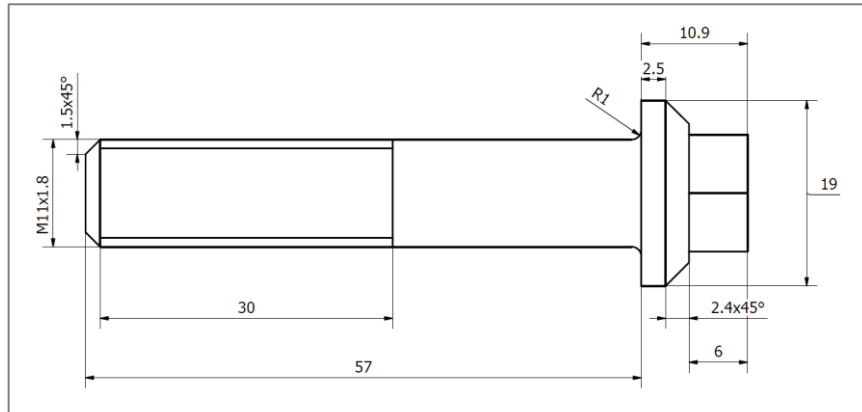


**Figure 4.21: Diagram illustrating the geometry of the sub-scale smart aircraft wing bolt (Vugampore & Bemont, 2012).**

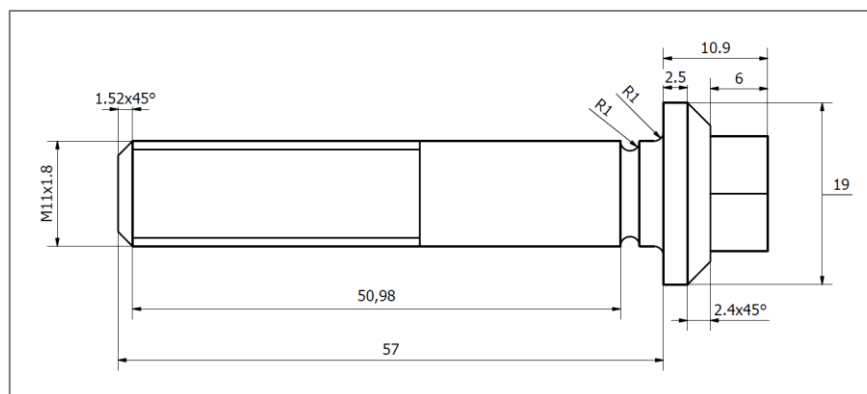


**Figure 4.22: Diagram illustrating the geometry of the grooved sub-scale smart aircraft wing bolt (Vugampore & Bemont, 2012).**



**Figure 4.23: Photograph of an assembled sub-scale TRIP steel smart aircraft wing bolt (Vugampore & Bemont, 2012).**

Figure 4.24 shows a smart washer with its embedded inductance coil. The introduction of such a sensor washer or nut will permit the bolt geometry to remain unchanged.



**Figure 4.24:** A sensor washer with an embedded coil of 149 turns and 0.019 mm diameter wire.

The embedded inductance coil in Figure 4.24 was manufactured on the spindle in Figure 4.25. The spindle was utilised in a coil-winding lathe.



**Figure 4.25:** Spindle type device used in a coil-winding lathe to produce the insert coils.

### 4.5.3 Experimental testing

The scaled-down smart wing bolt shown in Figure 4.23 was manufactured from hot rolled TRIP steel, since warm rolled TRIP steel could only be produced in thin sections due to research equipment constraints. Two digitally-logging inductance meters, one for the coil under the nut and the other for the coil under the bolt-head, were used concurrently. The data collected from these inductance meters was time-stamped and stored in the same PC that logged the tensile stress and strain applied by the Instron 5500R universal testing machine. This enabled accurate correlation of tensile strain and stress to magnetic permeability data. The standard and grooved sub-scale bolts made from hot rolled TRIP steel were quasi-statically tensile tested at 23°C using a specially designed test jig in the Instron 5500R universal tester. Results are shown in Figure 4.26 and Figure 4.27.

The inductance (magnetic permeability) measured at the first engaged thread increased gradually soon after loading, and increased much more rapidly just before failure, undoubtedly due to a similarly rapid increase in plastic deformation just before failure. The standard

geometry bolts only showed a measurable increase in under-head inductance shortly before failure on the first engaged thread. The bolts incorporating an under-head groove showed a measurable increase in inductance in this region from the material yield point. Unfortunately, different (but equivalent) coil-embedded washers had to be used on the grooved and standard geometry sub-scale bolts tested, because a washer coil was damaged on removing a bolt from the rig.

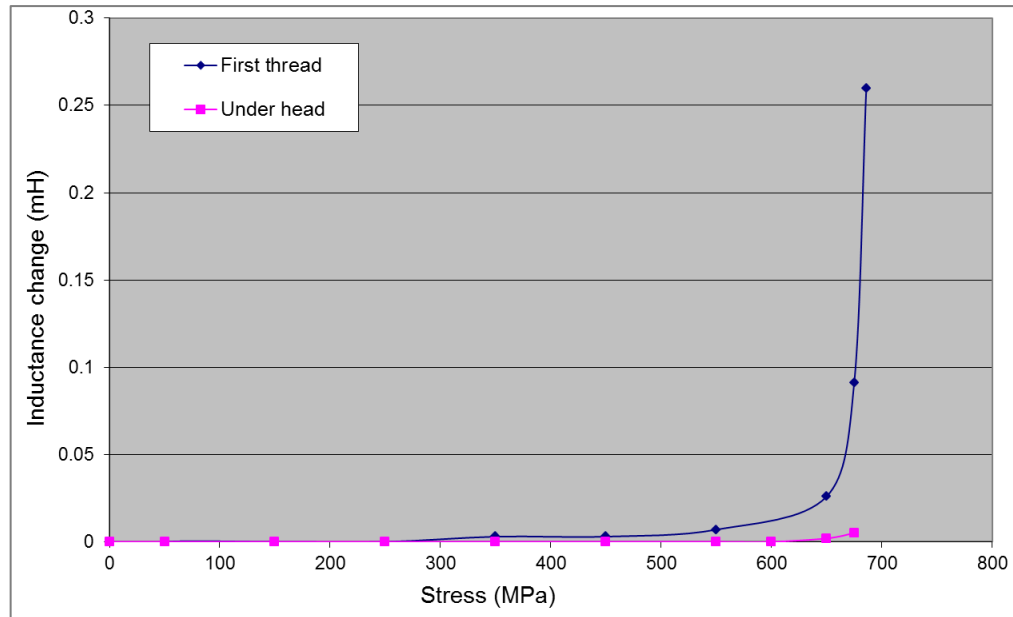


**Figure 4.26:** Inductance readings from the thread and from under the bolt-head during quasi-static tensile loading in a sub-scale bolt of standard geometry manufactured from alloy TRIP M (offset zeroed) (Vugampore & Bemont, 2012).

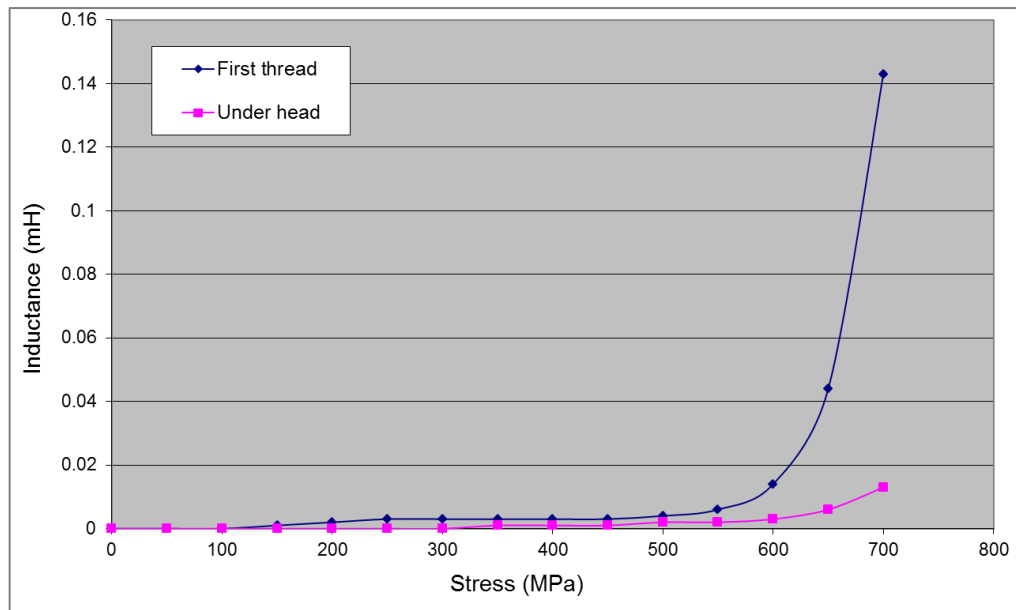


**Figure 4.27:** Inductance readings from the thread and under the bolt-head during quasi-static tensile loading in a sub-scale bolt, including a 1 mm groove under the head manufactured from alloy TRIP M (offset zeroed) (Vugampore & Bemont, 2012).



#### 4.5.4 Conclusion

Sub-scale smart aircraft wing bolts were manufactured from hot rolled TRIP steel. Transformation during quasi-static loading was monitored via inductance coils embedded within washers placed underneath each nut and the bolt-head. This arrangement allowed minimal geometric alteration to the standard wing bolt elements.

Significant martensitic transformation was detected shortly after yield, particularly at the first engaged thread. Transformation was also detected under the bolt head in both the grooved bolt, and in the standard geometry bolt. The yield point was reached not long prior to failure, which was sooner than in tensile test pieces, due to the stress concentration resulting from the thread. The principle of utilising inductance coils embedded in the wing bolt washers as sensors was successfully demonstrated.

Further work should be carried out on fatigue crack detection and environmental temperature fluctuation. Although environmental temperature fluctuation may be severe, and may severely affect the extent of the martensitic transformation, the wing bolts will not be required to display the extent of damage, because any level of damage will be cause for concern in this application. Thus, upon detection of any apparent transformation, an alert would be transmitted to the pilot or service team. Added to this, the high altitude at which the aeroplane will be loaded during flight is always low temperature, meaning that transformation will always be expected to be relatively strong and begin relatively early. If initial damage occurs during a warm take-off, such damage will be expected to propagate at altitude, or upon landing, at lower temperature. The aim is not to detect sudden catastrophic damage, but rather the progressive damage that would otherwise be detected by periodic inspections.

Sub-scale smart aircraft wing-bolts manufactured from hot rolled TRIP steel demonstrated that a washer incorporating an embedded inductance-coil can be utilised to measure the martensitic transformation occurring in a TRIP steel wing-bolt during deformation. Results in this section and in Section 3.6 suggest that *in situ* early detection of wing-bolt damage is feasible via the use of high alloy warm rolled TRIP steel in combination with magnetic sensor embedded washers.

## 5. Conclusions

TRIP steels alloys have been refined and optimised for specific load sensor applications in such a way that characteristics such as temperature sensitivity are reduced, whereas characteristics such as total transformation, low stress transformation or strength, are maximised.

Early experimental investigations and literature reviews showed that not all of the properties of available TRIP steels are ideal for sensors. In particular, the susceptibility of the martensitic transformation to environmental temperature and strain rate and lack of low stress sensitivity were issues. It was postulated that an improvement in these properties could be facilitated through composition and processing design via composition adjustments and manipulation of characteristic transformation temperatures and dislocation density. Multiple formulae by different authors, originating both empirically and theoretically, had been proposed to predict the characteristic transformation temperatures for alloys in the range under investigation. Relevant formulae were thus selected via experimentation and analysis.

Alloys inclined towards particular characteristics could then be selected or designed based on these formulae and other theories. It was verified experimentally that alloys could be designed for characteristics such as reduced temperature sensitivity, earlier transformation and considerably increased strength. While alloy transformation cannot be made free from susceptibility to temperature and strain rate, it was shown that it is possible to significantly manipulate these characteristics. Alloys were manufactured and utilised to produce a variety of practical TRIP steel based sensor prototypes.

### 5.1 Cast alloys

Cast alloys were investigated because, as well as being faster and cheaper to produce as a finished shape, they also showed relatively earlier transformation and were viable for use in compressive load sensors. A wide variety of cast TRIP steels were designed to enable the determination of the effects on transformation of certain individual alloying elements such as carbon, manganese and nickel, as well as to aid the determination of the most relevant formulae for predicting characteristic temperatures. Several cast alloys were produced, and their extent of transformation with increasing compressive deformation measured. Since an alloy's transformation is dependent on its deformation temperature relative to its characteristic transformation temperatures, it was possible to determine which of the predictive formulae for

$M_{d30}$  and  $M_s$  were most likely to be accurate for the range of high alloy TRIP steels under investigation.

It was determined that the formula for  $M_{d30}$  by Pickering was the best reported correlated predictor of the  $M_{d30}$  temperature. However, an average between two predictors of  $M_{d30}$ , that by Angel and that by Pickering, was found to be better correlated than that by Pickering alone. The best correlated formula for  $M_s$  was found to be that by Cina. It was found that these correlations were similar whether transformation at a particular strain or at a particular stress was considered.

The difference between an alloy's  $M_{d30\_Pickering}$  and  $M_{s\_Cina}$  also showed a very strong inverse correlation with its degree of transformation. The difference between other predicted  $M_{d30}$  and  $M_s$  temperatures was not as well correlated. This is relevant because, according to the theory developed in Section 3.3.2, a larger difference between an alloy's  $M_d$  and  $M_s$  temperatures should result in a more gradual transformation. Based on these results and the developed theory, certain alloys were identified as showing both high levels of transformation and being likely to show lower temperature sensitivity.

In assessing the effect of individual alloying elements on temperature sensitivity, it was determined that manganese would reduce  $M_s$  approximately 30% faster relative the  $M_{d30}$  than the other elements. Thus, an increased level of manganese should improve temperature stability. Manganese also increases austenite stability at half the speed of nickel, according to Schaeffler's formulae, meaning that more can be added before significantly retarding the martensitic transformation. Of the six alloys identified as showing high levels of transformation and being likely to show lower temperature sensitivity, five had nickel largely replaced by manganese and a low carbon content.

Transformation temperature susceptibility testing was performed on two alloys, V2 and HM. Alloy HM was predicted to be less temperature sensitive than Alloy V2 and testing proved this, with Alloy V2 showing an error of  $\pm 19\%$  between 25°C and 90°C, while Alloy HM showed an error of  $\pm 13\%$ . While both Alloys V2 and HM had significant manganese contents, Alloy HM had more, approximately 9wt%, compared to 6wt% for Alloy V2.

The effect of deformation at a high strain rate was shown, as expected, to have similar effects to increasing temperature. The effect of cyclic loading was shown to be minimal, but was not investigated in depth. The effect of circuitous loading, where a load was repeatedly increased to

a peak then released, and then increased beyond the previous peak before being released again, was found to be significant in Alloy V5, but greatly reduced in high manganese Alloy HM. The reason for this discrepancy was unclear. Strain rate, cyclic loading and circuitous loading should all be investigated in greater detail in the future.

A theory relating an alloy's transformation temperature sensitivity to its  $M_s$  and  $M_{d30}$  temperatures and to its dislocation density was developed. The deformation-induced transformation of more than twenty alloys was measured and using these data, empirical formulae to determine these temperatures were identified. Six of these alloys were identified as showing strong deformation-induced martensitic transformation, while also being likely to show low transformation temperature sensitivity. The transformation temperature sensitivity of Alloys HM and V2 were measured and found to be consistent with the theory.

## 5.2 Hot rolled alloys

Hot rolled alloys were investigated for use in tension in smart rock reinforcement tendons that would detect rock movement and tendon loading, while also acting as traditional reinforcing tendons. Hot rolled alloys were selected because they show similar mechanical properties to the HSLA steel from which rock reinforcement tendons are manufactured, while also displaying significant martensitic transformation when deformed in tension.

Hot rolled alloys were designed using a similar approach to that used for the cast alloys. Initially, the transformation curves of some available TRIP steel alloys were measured, and these data, along with data originating from the literature was used to evaluate which of the empirical formulae for the characteristic transformation temperatures was likely to be the best predictor. The same two formulae that were selected for the cast alloys, by Cina for  $M_s$  and by Pickering for  $M_{d30}$ , were found to be most reliable. Since the cast and hot rolled alloys are within a similar compositional range, this was expected. These formulae, combined with the theoretical analysis and the Schaeffler diagram, were used to design two new hot rolled alloys, TRIP R and TRIP S. These alloys were to be cast in-house in a 7kg research inductance furnace. However, after considerable effort, only a single ingot of composition close to alloy TRIP R was obtained and none for TRIP S.

After an extensive search, two commercial alloys with suitable parameters were sourced in Germany. They were only available as 3mm diameter wire. One of these alloys was substantially within the austenitic region of the Schaeffler diagram and was found on testing to

exhibit no transformation. The other exhibited very good transformation, especially after annealing. It was not possible to directly compare this alloy to other alloys due to its small diameter. However, it was predicted to show high sensitivity to transformation temperature.

Alloy TRIP R successfully exhibited earlier transformation than any previous alloys. Alloys TRIP R and TRIP M were tested for sensitivity to temperature fluctuations, and as well as exhibiting a stronger transformation, TRIP R also had lower temperature sensitivity during the transformation with respect to both stress and strain.

In order to test the hypothesis that dislocation density is positively associated to a TRIP steel's temperature sensitivity, TRIP M was tested in three conditions: annealed; hot rolled and water-quenched; warm rolled. The material's transformation temperature sensitivity with respect to both stress and to strain had a distinct positive relationship with the expected level of dislocation density in these three conditions. The annealed alloy had much less transformation temperature sensitivity, while the warm rolled alloy showed the most, with the hot rolled alloy in between.

### **5.3 Warm rolled alloys**

Warm rolled TRIP steel alloys were designed to have mechanical properties equivalent to those of AISI 4340, while also exhibiting strong deformation-induced martensitic transformation. These materials were proposed for use in smart aircraft wing bolts that would behave as traditional wing bolts, but also be damage sensors. This would alleviate an extremely labour intensive maintenance process.

Two of the alloys produced had tensile strengths near to AISI 4340. Both of these alloys exhibited yield strength significantly lower than AISI 4340 but had much greater ductility. It is thus expected that with further warm work, the yield strengths of these alloys would approach that of AISI 4340.

Both of these alloys, but in particular that with a higher yield strength, had early and easily detectable transformations. The alloys were not tested for temperature sensitivity, but being warm-worked, are expected to be relatively temperature sensitive. However, the application only requires the detection of any damage occurring in the material, as opposed to conveying the extent of damage. The martensitic transformation began before material yield at room temperature. Loading will occur at or below room temperature (at high altitude), encouraging the transformation to occur earlier, but never later. Damage occurring upon take-off at high

temperatures is expected to lead to further damage at altitude, or upon landing, while cold. The intention is not to detect sudden catastrophic failure, but rather the progressive damage that might be found during an inspection. Thus temperature fluctuation is not expected to adversely affect early damage detection.

## **5.4 Magnetics**

The magnetic properties of various cast and hot rolled TRIP steels were investigated. TRIP steels are rather unique in that their magnetisation and magnetic permeability curves are not fixed for the material at a particular frequency, but change with their degree of martensitic transformation. The magnetisation and magnetic permeability curves of these materials were characterised at different levels of transformation, which allowed insight into the substantial effect that variation in field strength induces during inductive measurement of the transformation. Field strength had considerable influence on the change in magnetic permeability perceived by an inductive sensor. A near-ideal field strength for measurement of all of the alloys characterised was 7 500 ampere turns per metre. This would maximise the magnetic permeability change perceived by an inductive sensor.

An investigation into the effect of temperature on the inductive measurement showed minimal effect. Lower frequencies resulted in increased output, but generally more absolute frequency fluctuation sensitivity. The frequency fluctuation sensitivity was determined to be lowest between 50Hz and 150Hz. Frequency fluctuation is expected to be minor using modern electronics.

## **5.5 Device development**

### **5.5.1 Smart rock tendon**

Structural health monitoring devices were developed for targeted industries. The primary focus was on the mining industry, with likely spin-offs for the civil engineering industry. The other target industry was the aviation industry.

The original concept for the mining industry was to replace selected rock reinforcement tendons with similar, but smart, versions capable of reinforcing the rock structure in the traditional manner, but also of measuring their own load and extension. Smart rock tendons were designed around the hot rolled Alloys TRIP M and later TRIP R. Several designs for the TRIP steel



element within the smart rock tendon and its associated inductive coil were investigated, with the aim of optimising them.

The smart rock tendons are able to alert the installer when correct pre-tension is attained and when certain pre-set limits are reached. They can also convey their maximum historical peak load and associated extension. Their measurement resolution will depend on the extent of temperature and strain rate fluctuation. These factors will require proper characterisation according to the particular environment, but data suggest that a resolution of better than  $\pm 15\%$  is certainly attainable. It is likely that this resolution will be acceptable for the application.

Presently, an external unit must be plugged into the smart rock tendon to obtain a load or strain reading. A similar but wireless system was implemented on an associated project, but this system must be miniaturised to make it practical.

These devices are robust, use the same accessories as ordinary reinforcement tendons, can be attached to the bottom of an ordinary tendon, and were designed to be cheap and simple to produce. Thus, they overcome many of the pitfalls encountered by previous systems. The breaking strength of the smart rock tendons is approximately equal to standard tendons. They were successfully tested in a test rig conforming to SABS standards for such components.

### **5.5.2 Smart face plate and smart load cell**

The smart face plate utilises cast TRIP steel in compression to form a very low cost and robust load cell unit that can be used to measure compressive stress or displacement in many applications, but specifically in mine roof support props and between a reinforcing rock tendon's nut and the rock face. Again, due to the irreversible nature of the martensitic transformation, the device measures historical peak load.

The device was designed to be as simple as possible, with as few components as possible. They utilise the same electronic output devices as the smart rock tendon, with altered calibration. One concept utilised magnetic viewing film to allow the unit to function in areas with good visibility without ever requiring any form of electrical power.

The devices were found to show good repeatability under quasi-static loading at room temperature. The investigations on temperature fluctuations during transformation estimated an error of  $\pm 17\%$  in outdoor applications ( $-15^{\circ}\text{C}$  to  $90^{\circ}\text{C}$ ) and  $\pm 5\%$  in underground mining environments ( $20^{\circ}\text{C}$  variation with an average between  $30^{\circ}\text{C}$  and  $50^{\circ}\text{C}$ ). Such errors are expected to be acceptable for many applications, but these errors are expected to drop

significantly upon implementation of further alloys designed on the principles developed in this work. Error due to strain rate fluctuation is expected to be negligible for the smart face plate.

### 5.5.3 Smart wing bolt

The possibility of replacing aircraft wing bolts with a near identical geometry smart TRIP steel sensor version was investigated. *In situ* warning of bolt damage would thereby be enabled, potentially reducing the costly requirement for periodic wing bolt removal and inspection, as well as increasing safety by enabling more frequent monitoring.

Scale wing bolt prototypes were manufactured from hot rolled TRIP M alloy for concept investigation. In practice, smart wing bolts would need to be made from a warm rolled TRIP steel alloy in order to attain the required mechanical properties. In order to reduce the required alterations to bolt geometry as much as possible, the inductance coil used to detect the martensitic transformation within the bolt was embedded in washers which could be placed under the nut, at the first engaged thread and, if required, under the bolt head.

Results showed that detection of damage in the first engaged threads was feasible. Damage occurring under the bolt head could also be detected. Strain rate is expected to be within a well-defined range and thus is not expected to be a major contributor to error. Error due to transformation temperature fluctuation is expected to have minimal bearing on device practicality, since the aim of the device is to detect any damage, not to convey degree of loading as in the other applications. Temperature fluctuation is expected, if anything, to aid sensor response.

## 5.6 Final conclusions

The potential for the deformation-induced martensitic transformation of TRIP steels to form the basis of smart sensors was affected by various problematic characteristics relating to environmental and loading conditions. It has been shown that TRIP steel alloys can be designed in such a way as to beneficially manipulate such characteristics.

Although there are significant limitations on the extent to which these transformation characteristics can be controlled, it has been shown that they can be manipulated to enable successful implementation of these alloys as the foundation of smart load or damage sensors. Inaccuracies are further reduced when the devices operate under well-defined environmental conditions, such as in mines. Structural health monitoring sensors based on TRIP steel alloys

have been successfully developed, built and tested. The manufacture of practical, robust, low cost structural health monitoring sensors based on the smart properties of TRIP steels has been shown to be feasible.

As TRIP and TRIP-assisted steels become more widely utilised for their excellent mechanical and smart properties, much of the theory and characterisation investigated here may find wider application in, for example, the vehicle manufacturing industry. However, further research will be required before a fundamental understanding of the complex interactions governing the martensitic transformation are properly understood. Substantial further work will be required to fully characterise the properties of this unusual material.

## 6. References

- Abrassart, F., 1973. Stress-induced  $\gamma \rightarrow \alpha'$  transformation in two carbon stainless steels. Application to TRIP steels. *Metallurgical transactions*, 4, pp.2205-16.
- Abrassart, F., Lecroisey, F. & Pineau, A., 1970. Martensitic transformations and plasticity in the Fe-Ni-Cr-C. *Centre des Materiaux de l'Ecole des Mines; RN7.*, p.905.
- Allegheny Ludlum Steel Corporation, 1959. *Stainless steel fabrication*. Pittsburgh: Allegheny Ludlum Steel Corporation.
- Ambekar, S.M., 1970. *Joining TRIP steels*. Berkeley: California Univ.
- American Society of Mechanical Engineers et al., 1953. *ASME Handbook, Metals Engineering Design*. McGraw-Hill.
- Andrade-Campos, A. et al., 2008. Effect of Strain Rate, Adiabatic Heating and Phase Transformation Phenomena on the Mechanical Behaviour of Stainless Steel. *Strain*, 46(3), pp.283-97.
- Andrews, K.W., 1965. Empirical formula for the calculation of some transformation temperatures. *Journal of the iron and steel institute*, 203(7), pp.721-27.
- Angel, T., 1954. Formation of Martensite in Austenitic Stainless Steels, Effects of Deformation, Temperature and Composition. *Journal of the Iron and Steel Institute*, 177, pp.165-74.
- Antolovich, S.D. & Singh, B., 1971. On the toughness increment associated with the austenite to martensite phase transformation in TRIP steel. *Metallurgical Transactions B*, 2(8), p.2135.
- Apsey, J., 2003. *Smart structural health monitoring of mining support units*. Durban: UKZN.
- Ashby, M.F. & Jones, D.R.H., 2012. *Engineering Materials 2: An Introduction to Microstructures and Processing*. Oxford: Butterworth-Heinemann.
- Askeland, D.R., 1988. *The Science and Engineering of Materials*. London: Van Nostrand Reinhold.
- ASM International, 2005. Bulk forming - Plastic deformation structures. In International, A. *ASM Handbook - Metalworking*. Washington: ASM International. pp.539-51.
- Baghdasarian, A. & Ravitz, S.F., 1975. Corrosion resistance of TRIP Steels. *Corrosion*, 31(5), pp.182-84.
- Bain, E.C., 1924. The nature of martensite. *Trans. AIME*, 70(1), pp.25-35.
- Bain, E.C., 1939. *The alloying elements in steel*. Cleveland: ASM International.
- Bain, E.C. & Davenport, E.S., 1930. Transformation of austenite at constant sub-critical temperatures". *Transactions of AIME*, 90, pp.117-54.
- Barrett, C.S., 1949. The crystallographic mechanisms of translation, twinning and banding. *Cold Working of Metals*, pp.65-98.

- Basuki, A. & Aernoudt, E., 1999. Influence of rolling of TRIP steel in the intercritical region on the stability of retained austenite. *Journal of Materials Processing Technology*, 89-90, pp.37-42.
- Bemont, C.P., 2009. The development of robust structural health monitoring sensors utilising TRIP steel. *IEEE Sensors Journal*, 9(11), pp.1449 - 1455.
- Bemont, C.P., Cornish, L.A. & Bright, G., 2013. The effects of transformation temperature on the rate of transformation in trip steels. *Submitted to Metallurgical Transactions*.
- Bemont, C., Gray, S., Van Wyk, D. & Vilikazi, S., 2001. *Smart strain sensor*. Report. Durban: UKZN.
- Bhadeshia, H.K.D.H., 1982. An aspect on the nucleation of burst martensite. *Journal of Material Science*, Vol. 17., pp.383-86.
- Bhadeshia, H.K.D.H., 2001a. Martensitic Transformation. In *Encyclopedia of Materials*. pp.5203-06.
- Bhadeshia, H.K.D.H., 2001b. *Geometry of Crystals*, 2nd edition. Institute of Materials.
- Bhadeshia, H.K.D.H., 2001c. *Bainite in steels*. Cambridge: Cambridge University Press.
- Bhadeshia, H.K.D.H., 2002. TRIP-assisted steels. *ISIJ International*.; Vol.42.; No.9., pp.1059-60.
- Bhadeshia, H.K.D.H., 2004. Developments in martensitic and bainitic Steels; the roll of the shape deformation. *Materials Science and Engineering*, pp.34-39.
- Bhadeshia, H.K.D.H., 2005. *Course A: Metals and Alloys; Ferrous Alloys*. Cambridge.
- Bhadeshia, H.K.D.H. & Christian, J.W., 1990. Bainite in steels. *Metallurgical Transactions A*, 21(3), pp.767-97.
- Bhadeshia, H.K.D.H. & Edmonds, D.V., 1979a. The distribution of retained austenite and martensite and the influence of inter-lath crystallography. In *Proceedings of the Third Int Conference on Martensitic Transformation, ICOMAT*. Cambridge, 1979.
- Bhadeshia, H.K.D.H. & Edmonds, D., 1979b. A direct analysis of twinning in low alloy martensite. In *Phase Transformations, Series 3*. York, 1979. The Institution of Metallurgists.
- Bhandarkar, D., Zackay, V.F. & Parker, E.R., 1972. Stability and mechanical properties of some metastable austenitic steels. *Metallurgical Transactions*, 3, p.2619.
- Bigby, D., Hurt, K., Reynolds, C. & Brown, R., 2010. *Evaluation of tensioned and non-tensioned long tendon reinforcement in UK deep mining conditions*. Burton-on-Trent: HSE Books.
- Bigdeli Karimi, M., Arabi, H., Khosravani, A. & Samei, J., 2007. Effect of rolling strain on transformation induced plasticity of austenite to martensite in a high-alloy austenitic steel. *Journal of Materials Processing Technology*, 203, pp.349-54.

- Biggs, T. & Knutsen, R.D., 1995. The effect of nitrogen on martensite formation in a Cr-Mn-Ni stainless steel. *Journal De Physique IV.; Colloque C8; Supplement au Journal de Physique III.*, 5(C8), pp.515-20.
- Biot, J.B. & Savart, F., 1820. Note on the magnetism of Volta's battery. *Annales de chimie et de physique*, 15, pp.222-23.
- Boswell, F.W.C. & Smith, E., 1958. Examination of metals by transmission electron microscopy. In *Symposium on Advances in Electron Metallography*. Baltimore, 1958. ASTM International.
- Bowles, J.S., 1951. The crystallographic mechanism of the martensite reaction in iron-carbon alloys. *Acta Crystallographica*, 4(2), pp.162-71.
- Bowles, J.S. & Wayman, C.M., 1972. The bain strain, lattice correspondences, and deformations related to martensitic transformations. *Metallurgical Transactions*, 3(5), pp.1113-21.
- Bracke, L. et al., 2006. Influence of phase transformations on the mechanical properties of high strength austenitic Fe-Mn-Cr steel. *Metallurgical and Materials Transactions A*, 37A, p.307.
- Brady, B.H.G., 2004. *Rock Mechanics: For Underground Mining*. Dordrecht: Springer.
- Brailsford, F., Oliver, D.A., Hadfield, D. & Polgreen, G.R., 1948. Magnetic materials. A review of progress. *Journal of the Institution of Electrical Engineers-Part I: General*, 95(96), pp.522-43.
- Bressanelli, J.P. & Moskowitz, A., 1966. Effects of strain rate, temperature and composition on tensile properties of metastable austenitic stainless steels. *ASM Transactions Quarterly*, 59(2), pp.223-39.
- Brito, R.M., 1981. On the dispersion hardening potential of interphase precipitation in micro-alloyed niobium steel. *Journal of Materials Science*, 16(5), pp.1257-63.
- Brooks, C.R., 1996. *Principles of the Heat Treatment of Plain Carbon and Low Alloy Steels*. ASM International.
- Brooks, J.W., Loretto, M.H. & Smallman, R.E., 1979. Direct Observations of Martensite Nuclei in Stainless Steel. *Acta Metallurgica*, 27(12), pp.1839-47.
- Bunshah, R.F., 1953. Rate of propagation of martensite. *Transactions of the AIME*, 197, p.1251.
- Buyts, B., 2008. *Rock bolt condition monitoring using ultrasonic guided waves*. MSc. Pretoria: University of Pretoria.
- Cahn, R.W., 1964. Survey of recent progress in the field of deformation twinning. In R.E. Reed-Hill, J.P. Hirth & R.H. C., eds. *Deformation Twinning*. New York: Gordon and Breech. Ch. 1.
- Cai, M. & Wang, J., 2011. *Rock Mechanics: Achievements and Ambitions*. London: CRC Press.
- Callister, W.D. & Rethwisch, D.G., 2012. *Fundamentals of Materials Science and Engineering*. Wiley.



- Canbulat, I. & Jack, B., 1999. *Review of current design methodologies to improve the safety of roof support systems, particularly in the face area in collieries*. Report. Johannesburg: CSIR Mining Technology.
- Capdevila, C., Caballero, F.G. & Garcis de Andres, C., 2002. Determination of Ms temperature in steels: A Bayesian neural network model. *ISIJ International*, 42(8), pp.894 - 902.
- Chabay, R.W. & Sherwood, B.A., 2007. *Matter and Interactions II: Electric and Magnetic Interactions*. New York: Wiley.
- Chatterjee, S., 2006. *Transformations in TRIP Assisted Steels*. PhD. Cambridge: Cambridge University.
- Chatterjee, S. & Bhadeshia, H.K.D.H., 2006. TRIP-assisted steels: cracking of high-carbon martensite. *Materials Science and Technology*, 22(6), p.645.
- Chatterjee, S., Wang, H.S., Yang, J.R. & Bhadeshia, H.K.D.H., 2006. Mechanical stabilisation of austenite. *Materials Science and Technology*, 22(6), p.641.
- Chin, G.Y., 1973. Formation of deformation twins in fcc crystals. *Acta Metallurgica*, 21, p.1353.
- Christian, J.W., 1958. Accommodation strains in martensite formation, and the use of a dilatation parameter. *Acta Metallurgica*, 6(5), pp.377-79.
- Christian, J.W., 1975. *The Theory of Transformations in Metals and Alloys, Part 1: Equilibrium and General Kinetic Theory*. 2nd ed. Oxford: Pergamon Press.
- Christian, J.W., 1979. Thermodynamics and kinetics of martensite. In *Proceedings of the international conference on martensitic transformations*. Massachusetts, 1979. ICOMAT.
- Christian, J.W. & Knowles, K.M., 1981. *Solid-Solid Phase Transformations*. Warrendale, Pennsylvania: TMS-AIME.
- ChristianXX, J.W., 1975. *The Theory of Transformations in Metals and Alloys: Equilibrium and general kinetic theory*. Oxford: Pergamon Press.
- Cina, B., 1954. Effect of cold work on the austenite-martensite transformation in some Fe-Ni-Cr alloys. *Journal of the Iron and Steel Institute*, 177, pp.406-22.
- Cina, B., 1958. A transitional hcp phase in the  $\gamma$  to  $\alpha$  transformation in certain Fe-base alloys. *Acta Metallurgica*, 6, pp.748-62.
- Clarke, R., 2008. *Magnetic properties of materials*. [Online] Available at: <http://info.ee.surrey.ac.uk/Workshop/advice/coils/mu/> [Accessed 17 March 2011].
- Coetzer, S., 1998. *Conceptual development of a method to determine the principle stress around coal mine workings, COL 326*. Johannesburg: SIMRAC.
- Cohen, M., Machlin, E.S. & Paranjpe, V.G., 1950. *Thermodynamics in Physical Metallurgy*. Cleveland, Ohio.: ASM.

- Cottingham, W.N. & Greenwood, D.A., 1991. *Electricity and Magnetism*. Cambridge: Press Syndicate, University of Cambridge.
- Cottrell, A.H., 1955. *Theoretical Structural Metallurgy*. 2nd ed. London: Edward Arnold.
- Crawford, J.D., Rohrig, K. & Bechet, S., 1982. High strength cast stainless steels with enhanced corrosion resistance. In *ASTM Stainless steel castings*. Baltimore: ASTM. pp.355 - 368.
- Creuziger, A. & Foecke, T., 2010. Transformation potential predictions for the stress-induced austenite to martensite transformation in steel. *Acta Materialia*, 58, pp.85-91.
- Cullen, J.R. & Clark, A.E., 1977. Magnetostriction and structural distortion in rare-earth intermetallics. *Physical Review B*, 15(9), pp.4510–15.
- Cullity, B.D., 1972. *Introduction to Magnetic Materials*. Reading: Addison-Wesley.
- Daehnke, A., Salamon, M.D.G. & C., R.M.K., 2000. Quantifying stable hangingwall spans between support units. *The Journal of the South African Institute of Mining and Metallurgy*, 100(6), pp.375-88.
- Dan, W.J.e.a., 2007. A model for strain-induced martensitic transformation of TRIP nsteel with strain rate. *Computational Materials Science*, 40, pp.101-07.
- Das, A. et al., 2008. Morphologies and characteristics of deformation induced martensite during tensile deformation of 304 LN stainless steel. *Materials Science and Engineering: A*, 486(1-2), pp.283-86.
- Davis, J.R., 1994. *ASM Speciality Handbook: Stainless Steels*. New York: ASM International.
- De Long, W.T., 1974. Ferrite in austenitic stainless steel weld metal. *Welding Journal*, 53(7), pp.273-86.
- De, R., 2003. Rocksmarts. *Mining Weekly*, 5 September.
- De, A.K. et al., 2004. Quantitative measurement of deformation-induced martensite in 304 stainless steel by X-ray diffraction. *Scripta Materialia*, 50(12), pp.1445-49.
- De, A.K., Speer, J.G. & Matlock, D.K., 2003. Color tint-etching for multiphase steels. *Advanced Materials & Processes*, pp.27-30.
- Dimatteo, A. et al., 2006. Microstructures and properties of TRansformation Induced Plasticity steels. *La Metallurgia Italiana*, 98(11-12), pp.37-41.
- Doitpoms, 2012. Shape Changes in a shear transformation. *Cambridge University*. Retrieved from: [http://www.doitpoms.ac.uk/ldplib/shape\\_memory/background.php](http://www.doitpoms.ac.uk/ldplib/shape_memory/background.php)
- Douthett, J., 1991. Heat treatment of stainless steels. In *ASM Handbook volume 4, Heat treating*. USA: ASM International. pp.769-92.
- du Plessis, J.A., 2000. *Pre-feasibility investigation to provide an early warning of roof falls prior to support installation, COL 703*. Johannesburg: SIMRAC.

- Dunning, J.S., 1969. *The effect of stacking fault energy on the strain induced martensite transformation and tensile characteristics in iron based alloys*. PhD Thesis. Berkley: Univ. of California Univ. of California, Berkeley, Lawrence Radiation Lab.
- Dunning, J.S. & Thompson, L.D., 1995. Development of Smart Solid State Structural Damage Assessment Systems for Underground Facilities. In *North American Conference on Smart Structures and Materials*. San Diego, 1995.
- Effenberg, G., 2008. *Selected Systems from Cu-Fe-Si to Fe-N-U, Volume 11*. Berlin: Springer.
- Elmen, G.W., 1935. Magnetic alloys of iron, nickel and cobalt. *Electrical Engineering*, 12, pp.113-35.
- Eshelby, J.D., 1957. *Proceedings of the Royal Society, A241.*, p.376.
- Fahr, D., 1971. Stress and strain induced formation of martensite and its effects on strength and ductility of metastable austenitic stainless steel. *Metallurgical Transactions*, pp.1883-92.
- Faraday, M., 1832. Experimental researches in electricity. *Philosophical Transactions of the Royal Society of London*, 122(1-2), pp.125-62.
- Findlay, J.S. & Harrison, N.D., 2002. Why aircraft fail. *Materials Today*, pp.18-25.
- Fisher, W.A.P., Cross, R.H. & Norris, G.M., 1952. Pre-tensioning for preventing fatigue failure in bolts: Simple theory and an account of experiments carried out at the RAE. *Aircraft Engineering and Aerospace Technology*, 24, pp.160-63.
- Florides, G.A. & Kalogirou, S.A., 2005. Annual ground temperature measurements at various depths. In *Proceedings of CLIMA 2005*. Limassol, 2005. Cyprus University of Technology.
- Form, G.W. & Baldwin, W.M., 1956. The Influence of Temperature on the Ductility of Austenitic Stainless Steel. *Transactions of the ASM*, 48, pp.474-85.
- Freiwillig, R., Kudrman, J. & Chráska, P., 1976. Bainite transformation in deformed austenite. *Metallurgical Transactions A*, 7(8), pp.1091-97.
- Frommeyer, G., Brüx, U. & Neumann, P., 2003. Supra-ductile and high-strength manganese-TRIP/TWIP steels for high energy absorption purposes. *ISI International*, 43(3), pp.438-46.
- Gaita, A., 2004. *Magnetic domain*. [Online] Available at: [http://en.wikipedia.org/wiki/Magnetic\\_domain](http://en.wikipedia.org/wiki/Magnetic_domain) [Accessed 17 March 2011].
- Gallagher, P.C.J., 1970. The influence of alloying, temperature, and related effects on the stacking fault energy. *Metallurgical Transactions*, 1(9), pp.2429-61.
- Gao, W. & Sammes, N., 2000. *An introduction to electronic and ionic materials*. New Jersey: World Scientific Publishing.
- Geels, K., 2007. *Metallographic and Materialographic Specimen Preparation, Light Microscopy, Image Analysis, and Hardness Testing*. West Conshohocken: ASTM International.
- Gerberich, W.W., Hemmings, P.L. & Zackay, V.F., 1971. Fracture and fractography of metastable austenites. *Metallurgical Transactions.*; Vol.2., pp.2243-53.

- Ghosh, G. & Olson, G.B., 1994. Kinetics of f.c.c.  $\rightarrow$  b.c.c. heterogeneous martensitic nucleation - II. Thermal activation. *ta Metallurgica et Materialia*, 42(10), pp.3371-79.
- Grassel, O.e.a., 1997. Phase transformations and mechanical properties of Fe-Mn-Si-Al TRIP-steels. *Journal of Physics IV*, C5, pp.383-88.
- Guenin, G., 1995. The  $\gamma \rightarrow \epsilon$  martensitic transformation: A model for stress-induced variant and its interactino with grain boundary. *Journal de Physique IV*, C8, pp.433-38.
- Guimaraes, J.R.C. & Gomes, J.C., 1978. A metallographic study of the influence of the austenite grain size on martensite kinetics. *Acta Metallurgica*, 26(10), pp.1591-96.
- Hadfield, R.A., 1888. Hadfield's Manganese Steel. *Science*, 12(306), pp.284-86.
- Hagan, T.O. et al., 2001. Simulated rockburst experiment—an overview. *The Journal of The South African Institute of Mining and Metallurgy*, 101(5), pp.217-22.
- Hall, E.O., 1951. The deformation and ageing of mild steel: III Discussion of results. *Proceedings of the Physical Society. Section B*, 64(9), pp.747-53.
- Hall, E.O., 1954. *Twinning and diffusionless transformations in metals*. London: Butterworths Scientific Publications.
- Heath, C. et al., 2007. *Smart Laminate*. Report. Durban: UKZN.
- Hedström, P., 2005. *Deformation induced martensitic transformation*. PhD. Luleå: Luleå University of Technology.
- He, M.C., Nie, W., Zhao, Z.Y. & Guo, W., 2012. Experimental investigation of bedding plane orientation on the rockburst behavior of sandstone. *Rock Mechanics and Rock Engineering*, 45(3), pp.311-26.
- Herbert, E.G., 1926. Work-Hardening Properties of Metals. *Transactions of the ASME*, 48, pp.705-48.
- Herron, L., 1983. *Rock Bolts - What we should expect from them*. Montreal: Canadian Institute of Mining and Metallurgy.
- Higgins, R.A., 1994. *Properties of Engineering Materials*. London: Edward Arnold.
- Hirsch, M.R., 2008. *Fretting behavior of aisi 301 stainless steel sheet in full hard condition*. Atlanta: Goergia Institute of Technology.
- Hirthe, J.P. & Lothe, J., 1968. *A Theory of Dislocations*. Malabar: Krieger.
- Honda, K. & Kaya, S., 1926. On the magnetization of single crystals of iron. *Scientific Reports of the Tohoku Imperial University*, 15, pp.721-53.
- Hudson, J.A. & Harrison, J.P., 2000. *Engineering rock mechanics - An introduction to the principles*. Amsterdam: Elsevier.
- Hull, F.C., 1973. Delta ferrite and martensite formation in stainless steels. *Welding Journal: Welding research supplement*, 52(5), pp.193s - 203s.

- Hutchinson, D.J. & Diederichs, M.S., 1996. *Cable bolting in underground mines*. Richmond: Bitech Publications.
- Inman, D.J., 2002. The role of smart materials in identification and structural health monitoring. In Lees, A.W., Prells, U. & Norton, J.P., eds. *Identification in Engineering Systems: Proceedings of the Third International Conference*. Swansea, 2002. University of Swansea. Keynote.
- Jadon, V.K. & Verma, S., 2010. *Analysis And Design Of Machine Elements*. New Delhi: I.K. International Publishing House Pvt. Limited.
- Jager, A.J. & Ryder, J.A., 1999. *A handbook on rock engineering practice for tubular hard rock mines*. Johannesburg: SIMRAC.
- Jalalifar, H., 2006. *The new approach for determining the load transfer mechaism in fully grouted bolts*. Wollongong: University of Wollongong.
- Jeong, W.C. & Matlock, D.K..K.G., 1993. *Material Science Engineering A*, 165, p.9.
- Jonson, D., 2003. *Finite element modelling of smart TRIP steel sensors and systems*. PhD. Durban: University of Natal.
- Kaiser, P.K. & Cai, M., 2012. Design of rock support system under rockburst condition. *Journal of Rock Mechanics and Geotechnical Engineering*, 4(3), pp.215–27.
- Kaneko, Y. et al., 2007. Material characteristics of TRIP steel with self-diagnosis and application to structural systems. *Smart Materials and Structures*, 16(6), p.2464.
- Katz, R. & Semat, H., 1958. *Physics: magnetic properties of matter*. Lincoln: University of Nebraska - Lincoln.
- Kelly, P.M., 1965. The martensite transformation in steels with low stacking fault energy. *Acta Metallurgica*, 13(6), pp.635-46.
- Kelly, P.M. & Nutting, J., 1960. The Martensite Transformation in Carbon Steels. *Proceedings of the Royal Society A*, 259(1296), pp.45-58.
- Kerr, J., Du Preez, G. & Paton, R., 1999. *Development of an economic duplex stainless steel: progress report 2*. Mintek.
- Klueh, R.L. & Mazaisz, P.J., 1990. Reduced activation austenitic stainless steels: The Fe-Mn-Cr-C system. In Klueh, R.L., Gelles, D.S., Okada, M. & Packan, M.H. *Reduced activation materials for fusion reactors, ASTM STP 1047*. Philadelphia: ASTM. pp.7-18.
- Ko, T. & Cottrell, S.A., 1952. The formation of bainite. *Journal of the Iron and Steel Institute*, 172, pp.307-13.
- Kotecki, D.J. & Siewert, T.A., 1992. WRC-1992 Constitution Diagram for stainless steel weld metals: a modification of the WRC-1988 Diagram. *Welding Journal*, 71(5), pp.171-78.
- Kouznetsovav, G. & Geers, M.G.D., 2008. A multi-scale model of transformation plasticity. *Mechanics of Materials*, 40, pp.641-57.

- Krupp, U. et al., 2001. Influence of carbon concentration on martensitic transformation in metastable austenitic steels under cyclic loading conditions. *Materials Science and Engineering A*, 319-321, pp.527-30.
- Krupp, U., West, C. & Christ, H.J., 2008. Deformation induced martensite formation during cyclic deformation of metastable austenitic steel: Influence of temperature and carbon content. *Material Science and Engineering A*, 481 - 482, pp.713 - 717.
- Kundu, S. & Bhadeshia, H.K.D.H., 2006. Transformation texture in deformed stainless steel. *Scripta Materialia*, 55, pp.779-81.
- Lampman, S., 1997. *Weld integrity and performance: a source book adapted from ASM international handbooks, conference proceedings, and technical books*. ASM International.
- Larour, P., Verleysen, P., Dahmen, K. & Bleck, W., 2013. Strain rate sensitivity of pre-strained AISI 301LN2B metastable austenitic stainless steel. *Steel Research International*, 84(1), pp.72-88.
- Leal, R.J. & Guimarães, J.R.C., 1981. Microstructure evolution during mechanically induced martensitic transformation in Fe-33% Ni-0.1% C. *Material Science Engineering*, 48(2), pp.249-54.
- Lecroisey, F. & Pineau, A., 1972. Martensitic transformations induced by plastic deformation in the Fe-Ni-Cr-C system. *Metallurgical Transactions*, 3, pp.387-96.
- Lefevre, J., Tricot, R., Gueussier, A. & Castro, R., 1974. Properties of a new family of stainless steels without nickel. *Metallurgical Transactions*, 5, p.2277.
- Li, S.H., Dan, W.J., Zhang, W.G. & Lin, Z.Q., 2007. A model for strain-induced transformation of TRIP steel with pre-strain. *Computational Materials Science*, 40(2), pp.292-99.
- Lorig, C.H., 1950. Low Temperature Properties of Ferrous Materials. *SAE Special Publication*, p.65.
- Machlin, E.S. & Cohen, M., 1951. Burst phenomenon in the martensitic transformation. *Transactions of the AIME*, 191(9), p.746.
- Machlin, E.S. & Cohen, M., 1952. Isothermal mode of the martensitic transformation. *Transactions of the AIME*, 194, pp.489-500.
- Mackenzie, J.K., 1957. A Least Squares Solution of Linear Equations with Coefficients. *Australian Journal of Physics*, 10(1), pp.103-09.
- Mahieu, J., Maki, J., de Cooman, B.C. & Claessens, S., 2002. Phase transformation and mechanical properties of Si-Free CMnAl transformation-induced plasticity-aided steel. *Metallurgical and Materials Transactions A*, 33, p.2573.
- Maleki, H., 1992. Significance of bolt tension in ground control. In Kaiser, P.K. & McCreath, D.R. *Rock Support*. Rotterdam: Balkema. pp.439-49.



- Manganon, P.L. & Thomas, G., 1970. The martensite phase in 304 stainless steel. *Metallurgical Transactions*, 1, pp.1577-86.
- Marshall, P., 1984. *Austenitic Stainless Steels: Microstructure and Mechanical Properties*. Essex: Elsevier Applied Science.
- Matsumura, O., Sakura, Y. & Takechi, H., 1987. TRIP and its kinetic aspects in austempered. 0.4C-1.5Si-0.8Mn steel. *Scripta Metallurgica*, 27, pp.1301-06.
- Maxwell, J.C., 1865. A Dynamical Theory of the Electromagnetic Field. *Philosophical Transactions of the Royal Society of London*, 155, pp.459–512.
- Maxwell, P.C., Goldberg, A. & Shyne, J.C., 1974. Influence of martensite formed during deformation on the mechanical behaviour of Fe-Ni-C alloys. *Metallurgical Transactions*, 5, pp.1319-24.
- Maxwell, P.C., Goldberg, A. & Shyne, J.C., 1974. Stress-assisted and strain-induced martensite in Fe-Ni-C alloys. *Metallurgical Transactions*, 5, pp.1305-17.
- Mayr, P. et al., 2010. Formation of delta ferrite in 9 wt.% Cr steel investigated by in-situ X-ray diffraction using synchrotron radiation. *Metallurgical and Materials Transactions A*, 41(10), pp.2462-65.
- Mazancová, E., Schindler, I. & Mazanec, K., 2009. Stacking fault energy analysis from point of view of plastic deformation response of the TWIP and triplex alloys. In *18th International Metallurgical & Materials Conference Proceedings*. Prague, 2009. ASM International.
- McCoy, R.A., Gerberich, W.W. & Zackay, V.F., 1970. On the resistance of TRIP steel to hydrogen embrittlement. *Metallurgical and Materials Transactions B*, 1(7), pp.2031-34.
- Mészáros, I., 2008. Magnetic characterization of phase transformations in TRIP steels. *Journal of Electrical Engineering*, 59(7), pp.86-89.
- Minnie, D., 2005. *Anglo Coal Mine Manager*. (Interviewer, C. P. Bemont).
- Moema, J.S., Papo, M.J. & Paton, R., 2008. Smart materials technology for roofbolting application in the mining industry. In *Proceedings of the 6th International Symposium on Ground Support in Mining and Civil Engineering Construction*. Cape Town, 2008. The Southern African Institute of Mining and Metallurgy.
- Moema, J.S. & Paton, R., 2005. *Smart materials for roofbolt application in the mining industry*. Report. Randburg: MINTEK.
- Mostafa, K.M. et al., 2007. Study of defects and phase transformation in a Fe-Mn-Si-Cr-Ni alloy by positron annihilation method. *Physica status solidi (c)*, 4(10), pp.3554-58.
- Nanga, S. et al., 2009. Strain induced martensitic transformation at high strain rate in two austenitic stainless steels. In *Proceedings of the 9th International Conference on the Mechanical and Physical Behaviour of Materials under Dynamic Loading (DYMAT)*. Brussels, 2009. DYMAT.

NDT Resource Center, 2012. *The Hysteresis Loop and Magnetic Properties*. [Online] Available at: <http://www.ndt-ed.org/EducationResources/CommunityCollege/MagParticle/Physics/HysteresisLoop.htm>

[Accessed 2 November 2012].

Nishiyama, Z., 1978. *Materials Science and Technology*. Academic Press.

Nishiyama, Z., Fine, M.E., Meshii, M. & Wayman, C.M., 1978. *Martensitic transformation*. New York: Academic Press.

Nohara, K., Ono, Y. & Ohashi, N., 1978. Composition and grain size dependencies of strain-induced martensitic transformation in metastable austenitic stainless steels. *Journal of the ISIJ*, 63(5), pp.212 - 222.

Oelofse, J., 2005. *Mine Operations Manager, AngloGold*. (Interviewer, C. P. Bemont).

Okazaki, Y., 2008. Effects of Cold Drawing and Annealing on Mechanical Properties and Microstructure of Co-Cr-Mo-Ni-Fe Alloys for Surgical Implants. *Materials Transactions*, 49(7), pp.1656-60.

Olson, G.B. & Azrin, M., 1978. Transformation behavior of TRIP steels. *Metallurgical transactions A*, 9A, pp.713-21.

Olson, G.B., Chait, R., Azrin, M. & Gagne, R.A., 1980. Fatigue Strength of TRIP Steels. *Metallurgical Transactions A*, 11(6), pp.1069-71.

Olson, G.B. & Cohen, M., 1972. A mechanism for the strain-induced nucleation of martensitic transformations. *Journal of the Less-Common Metals*, 28, pp.107-18.

Olson, G.B. & Cohen, M., 1975. Kinetics of strain induced martensitic nucleation. *Metallurgical Transactions A*, 6A, pp.791-95.

Otte, H.M., 1957. The formation of stacking faults in austenite and its relation to martensite. *Acta Metallurgica*, 5, pp.614-27.

Padilha, A.F., Machado, I.F. & Plaut, R.L., 2005. Microstructures and mechanical properties of Fe-15% Cr-15% Ni austenitic stainless steels containing different levels of niobium additions submitted to various processing stages. *Journal of Materials Processing Technology*, 170(1-2), pp.89-96.

Padilha, A.F., Plaut, R.L. & Rios, P.R., 2003. Annealing of cold-worked austenitic stainless steel. *ISIJ International*, 43(2), pp.135-43.

Parker, S.V., 1997. *Modelling of Phase Transformations in Hot-Rolled Steels*. Cambridge: University of Cambridge.

Patel, J.R. & Cohen, M., 1953. Criterion for the action of applied stress in the martensitic transformation. *Acta Metallurgica*, 1(5), pp.531-38.

Pauli, W., 1926. Über das Wasserstoffspektrum vom Standpunkt der neuen Quantenmechanik. *Zeitschrift für Physik*, 36(5), pp.336-63.

- Perepezko, J.H., Sebright, J.L., Höckel, P.G. & Wilde, G., 2002. Undercooling and solidification of atomized liquid droplets. *Materials Science and Engineering A*, 326(1), pp.144-53.
- Perlade, A., Bouaziz, O. & Furnemont, Q., 2003. A physically based model for TRIP-aided carbon steels behaviour. *Materials Science and Engineering A*, 356, pp.145-52.
- Petch, N.J., 1953. The cleavage strength of polycrystals. *Journal of the Iron and Steel Institute*, 174, pp.25-28.
- Petrov, R., Kestens, L., Wasilkowska, A. & Houbaert, Y., 2007. Microstructure and texture of a lightly deformed TRIP-assisted steel characterized by means of the EBSD technique. *Materials Science and Engineering: A*, 447(1), pp.285-97.
- Pichler, A. et al., 1998. In *40th MWSP Conference*. Warrendale, 1998.
- Pickering, F.B., 1978. *Physical metallurgy and the design of steel*. London: Applied Science Publishers.
- Pineau, A.G. & Pelloux, R.M., 1974. Influence of strain-induced martensitic transformations on fatigue crack growth rates in stainless steels. *Metallurgical and Materials Transactions B*, 5(5), pp.1103-12.
- Porter, D.A. & Easterling, K.E., 1993. *Phase Transformations in Metals and Alloys*; 2nd edition. London: Chapman and Hall.
- Porter, D.A., Easterling, K.E. & Sherif, M., 2009. *Phase transformations in metals and alloys*. London: CRC Press.
- Powell, G.W., Marshall, E.R. & Backofen, W.A., 1958. Strain hardening of austenitic stainless steel. *Transactions of the ASM*, 50, pp.478-97.
- Radu, M. et al., 2005. Continuous magnetic method for quantitative monitoring of martensitic transformation in steels containing metastable austenite. *Scripta Materialia*, 52, pp.525-30.
- Radu, M. et al., 2005. Continuous magnetic method for quantitative monitoring of martensitic transformation in steels containing metastable austenite. *Scripta Materialia*, 52, pp.525-30.
- Reed, R.P., 1989. Nitrogen in austenitic stainless steels. *JOM*, 41(3), pp.16-21.
- Remy, L., 1977. Temperature variation of the intrinsic stacking fault energy of a high manganese austenitic steel. *Acta Metallurgica*, 25(2), pp.173-79.
- Roberts, D.P., 1995. *Testing of mining tunnel support elements and systems for hard rock mines*. PhD. Durban: UKZN.
- Roser, W.R., 1963. *Stacking fault energy, ordering, and transgranular stress corrosion cracking in Fe-Cr-Ni alloys*. MSc. Berkeley: University of California, Lawrence Radiation Laboratory.
- Rowcliffe, A.F. & Nicholson, R.B., 1972. Quenching defects and precipitation in a phosphorus-containing austenitic stainless steel. *Acta Metallurgica*, 20(1), pp.143-55.

- Rowland, H.A., 1897. Electrical measurement by alternating currents. *American Journal of Science*, 24, pp.429-48.
- Ryoo, D., Kang, C. & Kang, N., 2011. Effect of Ni content on the tensile properties and strain-induced martensite transformation for 304 stainless steel. *Materials Science and Engineering: A*, 528(6), pp.2277-81.
- S. Murugesan, S., Kuppusami, P., Mohandas, E. & Vijayalakshmi M., 2011. X-ray diffraction Rietveld analysis of cold worked austenitic stainless steel. *Materials Letters*, 67, pp.173-76.
- Samek, L., De Moor, E., Penning, J. & De Cooman, B.C., 2006. Influence of alloying elements on the kinetics of strain-induced martensitic nucleation in low-alloy, multiphase high-strength steels. *Metallurgical and Materials Transactions A*, 37, p.109.
- Schaeffler, A.L., 1949. Constitution diagram for stainless steel weld metal. *Metal Progress*, 56, pp.680-680B.
- Scheil, E., 1932. Über die Umwandlung des Austenits in Martensit in Eisen-Nickellegierungen unter Belastung. *Zeitschrift für Anorganische und Allgemeine Chemie*, 207(1), pp.21-40.
- Schmid, O.E. & Knutsen, R.D., 1992. Reducing the nickel content in metastable austenitic stainless steels. In Glen, H.W., ed. *Proceedings of the 1st International Chromium Steel and Alloys Congress*, 2. Cape Town, 1992. South African Institute of Mining and Metallurgy.
- Schneider, H., 1960. Investment casting of high-hot strength 12% chrome steel. *Foundry Trade Journal*, 108, pp.562-63.
- Seens, W.B., Jensen, W.L. & Miller, O.O., 1951. Notch toughness of four alloy steels at low temperatures. *Proceedings of the ASTM*, 51, p.918.
- Sherif, M.Y., 2003. *Strain-Induced Transformation of Very Strong Metal*. PhD. Cambridge: Cambridge University.
- Sherif, M.Y., Garcia Mateo, C., Sourmail, T. & Bhadeshia, H.K.D.H., 2004. Stability of retained austenite in TRIP-assisted steels. *Materials Science and Technology*, 20, pp.319-22.
- Shibata, A. et al., 2008. The Origin of Midrib in Lenticular Martensite. *Materials Transactions*, 49(6), pp.1242-48.
- Shields, J., 2010. *Practical guidelines for the fabrication of high performance austenitic stainless steels*. London: International Molybdenum Association.
- Shockley, W., Hollomon, J.H., Maurer, R. & F., S., 1952. *Imperfections in Nearly Perfect Crystals*. New York: Wiley.
- SIMRAC, 2003. *Annual health and safety program report*. Johannesburg: SIMRAC.
- Singhal, L.K., 1971. Effect of the nature of imperfections on the precipitation of M<sub>23</sub>C<sub>6</sub> carbide in austenitic steels. *Metallurgical and Materials Transactions B*, 2(4), pp.1267-71.

- Skroc, W., 2010. *Multi Phase Twinning-Induced Plasticity (TWIP) Steel*. [Online] Available at: <http://www.keytometals.com/page.aspx?ID=CheckArticle&site=kts&LN=EN&NM=207> [Accessed 24 January 2011].
- Small, K.B., Englehart, D.A. & Christman, T.A., 2008. Guide to etching speciality alloys. *Advanced Materials and Processes*, 166(2), pp.32-37.
- Smallman, R.E. & Ngan, A.H.W., 2011. *Physical Metallurgy and Advanced Materials*. Oxford: Elsevier Science.
- Smith, W.F. & Hashemi, J., 2006. *Foundations of Materials Science and Engineering*. New York: McGraw-Hill.
- Spencer K., Vernon, M., Yu-Zhang, K. & Embury, J.D., 2009. The strain induced martensite transformation in austenitic stainless steels Part 1 – Influence of temperature and strain history. *Materials Science and Technology*, 25(1), pp.7-17.
- Spencer, K. et al., 2004. Strengthening via the formation of strain-induced martensite in stainless steels. *Materials Science and Engineering A*, 387-389, pp.873-81.
- Srinivas, K.N., 2007. *Basic Electrical Engineering*. New Delhi: I K International Publishing House.
- Stacey, T.R., 1995. *Reliable, cost effective technique for in-situ ground stress measurement in deep gold mines*, GAP 220. Johannesburg: SIMRAC.
- Stringfellow, R.G., 1991. A constitutive model for transformation plasticity accompanying strain-induced martensitic transformations in metastable austenitic steels. *Acta Metallurgica et Materialia*, 40(7), pp.1703-16.
- Stringfellow, R.G., Parks, D.M. & Olsen, G.B., 1992. A constitutive model for transformation plasticity accompanying strain induced martensitic transformation in metastable austenitic steels. *Acta Metallurgical Materials*, 40(7), pp.1703-16.
- Stuhlmann, W., 1959. Effects of alloying elements on steel. *Härterei-Technische Mitteilung*, 6, p.31.
- Stumpf, W., 2010. *Phase Transformations in Metals and Alloys*. Pretoria: University of Pretoria. Course notes.
- Sugimoto, K., Kobayashi, M. & Hashimoto, S., 1992. Metallurgical and Materials Transactions.; 23A. p.3085.
- Sugimoto, K., Misu, M., Kobayashi, M. & Hashimoto, S., 1993. Effects of second phase morphology on retained austenite morphology and tensile properties in a TRIP-aided dual-phase steel sheet. *ISIJ International*, 33, pp.775-82.
- Suh, D.W., Cho, J.Y., Oh, K.H. & Lee, H.C., 2002. Evaluation of dislocation density from the flow curves of hot deformed austenite. *ISIJ International*, 42(5), pp.564-66.

- Sumita, M., Hanawa, T. & Teoh, S.H., 2004. Development of nitrogen-containing nickel-free austenitic stainless steels for metallic biomaterials - review. *Materials Science and Engineering: C*, pp.753-60.
- Suzuki, T. et al., 1977. An Experimental Study of the Martensite Nucleation and Growth in 18/8 Stainless Steel. *Acta Metallurgica*, 25(10), pp.1151-62.
- Suzuki, T. & Wuttig, M., 1972. The triggering mechanism of the martensitic transformation. *Metallurgical Transactions*, 3, p.1555.
- Talonen, J., 2007. *Effect of strain-induced  $\alpha'$ -martensite transformation on mechanical properties of metastable austenitic stainless steels*. Helsinki: Helsinki University.
- Talonen, J., Aspegren, P. & Hänninen, H., 2004. Comparison of different methods for measuring strain induced martensite content in austenitic stainless steels. *Materials Science and Technology*, 20(12), pp.1506-12.
- Tamura, I., 1982. Deformation-induced martensitic transformation and transformation-induced plasticity in steels. *Metal Science*, 16, p.245.
- Thelning, K.E., 1984. *Steel and its Heat Treatment*. Kent: Butterworths.
- Thompson, L.D., 1986. Mechanical properties and phase transformations in engineering materials. In *The Metallurgical Society*. Warrendale, 1986.
- Thompson, L.D., 1986. The FCC to HCP to BCC phase transformation sequence in metastable Fe-Mn-Cr alloy. In *International AIME winter annual meeting, Earl R Parker Honorary Symposium*. New Orleans, 1986. AIME.
- Thompson, L.D. & Westermo, B., 1992. The Utilisation of Metastable Peak-Strain Indicating (PSI) Materials in Critical Lifeline Engineering Applications. In *ASME Pressure Vessel and Piping Conf.* New Orleans, 1992. ASME.
- Thompson, L.D. & Westermo, B.D., 1994. Applications of a New Solid-State Structural Health Monitoring Technology. In *Proceedings of the 2nd European Conference on Smart Structures and Materials*. Glasgow, 1994.
- Tisza, M., 2001. *Physical metallurgy for engineers*. Ohio: ASM International.
- Tomota, Y., Kuroki, K., Mori, T. & Tamura, I., 1976. Tensile deformation of two-ductile-phase alloys: Flow curves of  $\alpha$ - $\gamma$  Fe Cr Ni alloys. *Material Science and Engineering*, 24(1), pp.85-94.
- Totten, G.E., 2007. *Steel Heat Treatment: Metallurgy and Technologies*. Boca Raton: Taylor & Francis.
- Turteltaub, S. & Suiker, A.S.J., 2005. Transformation induced plasticity in ferrous alloys. *Journal of the Mechanics and Physics of solids*, 53, pp.1747-88.
- Vander Voort, G.F., 2004. *ASM Metals Handbook Vol. 9: Metallography and Microstructures*. New York: ASM International.



- Vander Voort, G.F. & Beuhler, L., 2004. Color Metallography. In International, A. *ASM Handbook, Volume 9: Metallography and Microstructures*. ASM International. pp.493-512.
- Verijenko, B.L., 2003. *Smart materials for structural health monitoring*. Durban: University of Natal.
- Verma, P., Gupta, P. & Tirth, V., 2006. Smart Materials - an overview. In Srivastava, R.K., Gupta, Y.K., Bhatt, A.D. & N., A.M., eds. *Proceedings Of All India Seminar On Advances In Product Development*. Delhi, 2006. New Age International Publishers Limited. Ch. 50.
- Vugampore, J.M., 2006. *Development of high strength material for a smart aircraft bolt*. PhD. Durban: UKZN.
- Vugampore, J.M. & Bemont, C.P., 2012. The design and testing of subscale smart aircraft wing bolts. *Smart Materials and Structures*, 21(7), p.075010.
- Walters, F.M. & Wells, C., 1936. Carbon-Iron-Manganese Ternary Alloy Phase Diagram. *Transactions of the ASM; Vol.24*, p.359.
- Wang, J. & van der Zwaag, S., 2001. Stabilization mechanisms of retained austenite in transformation-induced plasticity steel. *Metallurgical and Materials Transactions A*, 32(6), pp.1527-39.
- Wayman, C.M., 1965. *Physical properties of martensite and bainite*. Scarborough: British Iron and Steel Institute.
- Wen, Y.H., Dennis, S. & Gautier, E., 1996. Computer simulation of martensitic transformation under stress. *Journal de Physique IV*, C1, pp.475-83.
- Westermo, B., 1996. A passive Structural Health Monitoring System for Bridges. In *North American Smart Material and Structures Conference*. San Diego, 1996. SPIE.
- Whelan, M.J., Hirsch, P.B., Horne, R.W. & Bollmann, W., 1957. Dislocations and stacking faults in stainless steel. *Proceedings of the Royal Society of London. Series A, Mathematical and Physical Sciences*, pp.524-38.
- Whittenberger, E.J., Rosenow, E.R. & Carney, D.J., 1957. Elevated temperature phase relationships in the Cr-Ni-Mn-N system. *Transactions of the AIME*, 209, pp.889-95.
- Williamson, G.K. & Smallman, R.E., 1956. Dislocation densities in some annealed and cold-worked metals from measurements on the X-ray debye-scherrer spectrum. *Philosophical Magazine*, 1(1), pp.34-46.
- Woodcock, L.V., 1997. Entropy difference between the face-centred cubic and hexagonal close-packed crystal structures. *Nature*, 385(6612), pp.141-43.
- Worden, K. & Dulieu-Barton, J.M., 2004. An overview of intelligent fault detection systems and structures. *Structural Health Monitoring*, 3(1), pp.85-98.

- Yang, H., Zhang, J.H., Xu, Y. & Meyers, M.A., 2008. Microstructural Characterization of the Shear Bands in Fe-Cr-Ni single crystal by EBSD. *Journal of Materials Science and Technology*, 24(6), pp.819-28.
- Yardley, V.A., 2003. *Magnetic Detection of Microstructural Change in Power Plant Steels*. PhD. Cambridge.
- Zackay, V.F., 1969. *Some Anticipated Developments in Physical Metallurgy Research*. Report. Berkley: University of California, Lawrence Radiation Laboratory.
- Zackay, V.F., Justusson, M.W. & Schmatz, D.J., 1962. Strengthening by martensitic transformations. In *Strengthening mechanisms in solids: papers presented at a seminar of the American Society for Metals, 1960*. Ohio, 1962. Reinhold Publication Corporation.
- Zackay, V.F., Parker, E.R., Fahr, D. & Bush, R., 1967. The enhancement of ductility in high strength steels. *Transactions of the ASM*, 60, pp.252-59.
- Zaefferer, S., Ohlert, J. & Bleck, W., 2004. A study of microstructure, transformation mechanisms and correlation between microstructure and mechanical properties of a low alloyed TRIP steel. *Acta Materialia*, 52(9), pp.2765-78.
- Zener, C., 1946. Kinetics of the decomposition of austenite. *Transactions of the AIME*, 167, pp.550-95.
- Zhang, M.X. & Kelly, P.M., 2002. Relationship between stress-induced martensitic transformation and impact toughness in low carbon austenitic steels. *Journal of Materials Science*, 37(17), pp.3603-13.
- Zhao, L. et al., 2002. Magnetic determination of thermal stability of retained austenite in TRIP steel. In *Proceedings International Conference on TRIP-Aided High Strength Ferrous Alloys*. Ghent, 2002.

## Appendix 1

### A1.1. Magnetic permeability and magnetisation

An entire sub-branch of physics has been devoted to studying the effects that magnetic fields induce in materials. If just one parameter had to be chosen to describe this complexity then permeability would be the one to choose (Clarke, 2008). A Rowland Ring, one method used to measure magnetic permeability, is shown in Figure A 1.

Ampere's Law for an ideal solenoid, with a large length compared with its diameter and the core being a vacuum, states:

$$B_0 = \mu_0 \cdot n \cdot i$$

Equation A 1

or  $B_0 = \mu_0 \cdot H$

Equation A 2

where  $B_0$  is the flux density ( $\Phi/A$ ) in the core,  $\mu_0$  is the permeability of free space ( $4\pi \times 10^{-7}$  H.m-1),  $i$  is the current in the winding,  $n$  is the number of turns *per unit length* of the solenoid.  $H$  is the magnetic field intensity in ampere turns per metre and,

$$H = n \cdot i$$

Equation A 3

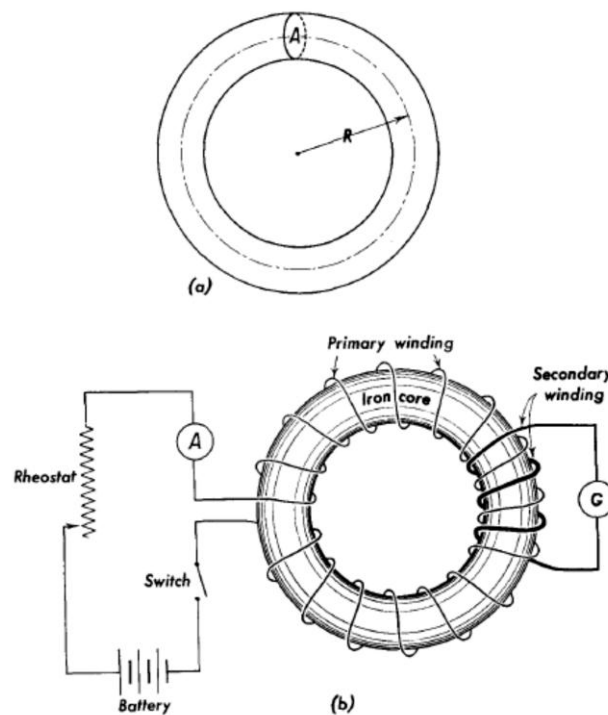


Figure A 1: A Rowland ring, used for measuring magnetic permeability, in this case incorporating a ballistic galvanometer (Katz & Semat, 1958).

In the Rowland ring (toroid) in Figure A 1 (Rowland, 1897),

$$B_0 = \mu_0 \cdot N_p \cdot i_p / 2 \cdot \pi \cdot r$$

**Equation A 4**

Or,

$$B_0 = \mu_0 \cdot H_p$$

**Equation A 5**

where  $B_0$  is the flux density that would be present in the ring if its core were a vacuum,  $N_p$  is the number of turns on the primary winding,  $i_p$  is the current in the primary winding and  $r$  is the radius of the ring.  $H_p$  is the magnetic field intensity due to the primary winding current,  $i$ .

The actual flux density,  $B$  in the Rowland ring, with a ferromagnetic core in place is greater than  $B_0$ . Thus,

$$B = B_0 + B_M$$

**Equation A 6**

where  $B_M$  is the contribution of a ferromagnetic core and usually,  $B_M \gg B_0$  and,

$$B = \mu \cdot n \cdot i \quad (\text{for a solenoid with a ferromagnetic core})$$

**Equation A 7**

Or,

$$B = \mu \cdot N_p \cdot i_p / 2 \cdot \pi \cdot r \quad (\text{for the toroid})$$

**Equation A 8**

where  $\mu$  is the material's absolute permeability and

$$\mu = \mu_0 \cdot \mu_r$$

**Equation A 9**

where  $\mu_r$  is called relative permeability and quantifies the material's permeability relative to that of free space.

$H$  is determined by currents and physical parameters only, but  $B$  also depends on the properties of the core material, they are related by

$$B = \mu \cdot H$$

**Equation A 10**

The variation of  $B$  with  $H$  is nonlinear and therefore  $\mu$  (and  $\mu_r$  but not  $\mu_0$ ) vary with  $B$  along the  $B$ - $H$  curve (also called the saturation curve for ferromagnetic materials) shown in Figure 2.71.

As seen in Section 3.7 (and also depicted in Figure 2.72), the magnetisation curves of ferromagnetic materials show hysteresis when subjected to a varying external magnetic field, as

with a coil carrying an AC current. The area within the hysteresis loop is proportional to the energy loss (as heat) per cycle. This hysteresis loss increases as the AC frequency increases. A coil carrying an AC current will also induce eddy-currents in the core material, resulting in further energy losses.

These energy losses are collectively known as core losses and can be represented by the following expressions:

$$\text{Hysteresis loss:} \quad P_h = K_h \cdot f^2 \cdot B_m^{1.5 \text{ to } 2.5} \text{ (W/kg)} \quad \text{Equation A 11}$$

$$\text{Eddy-current loss:} \quad P_e = K_e \cdot f^2 \cdot B_m^2 \text{ (W/kg)} \quad \text{Equation A 12}$$

## A1.2. Electromagnetism and Inductance

Magnetic flux is responsible for the phenomenon of electromagnetic induction. Flux ( $\Phi$ ) is a measure of the amount of magnetic field that passes through a circuit due to a vector magnetic field,  $B$ . Faraday found that a changing magnetic field induced an electro-motive force (emf) in a circuit and that the magnitude of this emf (measured in volts) equals the rate at which the flux of this magnetic field changes through the circuit (Faraday, 1832),

$$\text{emf} = -d\Phi / dt \quad (\text{Faraday's Law for a one turn coil}) \quad \text{Equation A 13}$$

Or, 
$$\text{emf} = -N \cdot d\Phi / dt \quad (\text{Faraday's Law for a multiple turn coil}) \quad \text{Equation A 14}$$

where  $N$  is the number of turns.

The minus sign in this equation is a manifestation of Lenz's law which states that "what arises is that which opposes any change in the system". The term self-inductance refers to the reaction a circuit has to a changing current within it. The flux density of a magnetic field,  $B$  is equal to the flux of the field divided by the (perpendicular) area through which it occurs,  $B = \Phi/A$ . Thus, since  $B$  is proportional to  $i$  (Equation A 7), so is  $\Phi$ . The constant of proportionality is the self-inductance of the circuit,  $L$ , as defined by the equation:

$$N \cdot \Phi = L \cdot i \quad \text{Equation A 15}$$

The term mutual inductance describes the reaction two circuits have on one another when a changing current is present (Rowland, 1897). When the magnetic field of the first circuit,  $B_1$ , passes through circuit 2, a magnetic flux,  $\Phi_{21}$ , exists in circuit 2 due to the current in circuit 1 ( $i_1$ ) and,  $\Phi_{21} = M_{21} \cdot i_1$ . Similarly, the magnetic flux induced in circuit 1 due to a current in circuit

2 is given by  $\Phi_{12} = M_{12}.i_2$ .  $M_{21}$  must always be equal to  $M_{12}$  and these terms are thus collectively referred to as  $M$  (mutual inductance). The magnitude of  $M$  in the two circuits can vary from  $+\sqrt{L_1.L_2}$  to  $-\sqrt{L_1.L_2}$ , and is determined by the flux linkage between the circuits (Chabay & Sherwood, 2007).

When the time rate of change is taken for the terms on both sides of Equation A 15,

$$N.d\Phi /dt = L.di /dt \quad \text{Equation A 16}$$

Thus, from Equation A 14,

$$\text{emf} = -L.di /dt \quad \text{Equation A 17}$$

If a long solenoid of cross-sectional area  $A$  is considered,

$$\Phi = (B.A) \quad \text{Equation A 18}$$

for a solenoid with a ferromagnetic core (from Equation A 8 and Equation A 9),

$$B = \mu_0.\mu_r.N.i / l \quad \text{Equation A 19}$$

where  $l$  is the length of the solenoid.

From Equation A 15,

$$L = N.\Phi / i \quad \text{Equation A 20}$$

Thus, from Equation A 18 and Equation A 19,

$$L = N.(\mu_0.\mu_r.N.i.A) / i.l \quad \text{Equation A 21}$$

and

$$L = \mu_0.\mu_r.N^2.A / l \quad \text{Equation A 22}$$

Thus, the inductance depends only on geometrical factors and the relative permeability of the solenoid's core. By measuring inductance, relative permeability can thus be calculated if the geometric factors are known.



### A1.3. Determining the true magnetisation curve

It will be shown that if all required parameters are precisely known or measured, then it is possible to find true B and true H and thus the core material's true magnetisation curve from the proportionate data derived as described in Section 3.7.2. Magnetic permeability can then be calculated at any point along this curve from:

$$\mu = B / H \quad \text{Equation A 23}$$

Since R, in the circuit shown in Figure 3.199 in Section 3.7.2, is precisely known, the primary current ( $I_p$ ) can be calculated from the voltage variation measured across R, shown on the oscilloscope x-axis ( $V_x$ ). From this current, the field strength, H can be found (in A.t.m-1) from:

$$H = N_p \times I_p / l \quad \text{Equation A 24}$$

where  $N_p$  is the number of turns on the primary coil,  $l$  is the length of the inductor.

or

$$H = N_p \times V_x / (R.l) \quad \text{Equation A 25}$$

In order to determine B, we begin with Faraday's law, which states:

$$V_s = -N_s \cdot (d\Phi/dt) \quad \text{Equation A 26}$$

where  $V_s$  is the voltage on the secondary winding,  $N_s$  is the number of turns on the secondary winding and  $\Phi$  is the magnetic flux in the core.

For the op-amp in the integrator circuit,

$$dV_Y/dt = -V_s / (C.R)$$

where  $V_Y$  is the output voltage of the op-amp on terminal Y in Figure 3.199, and C and R are constants in the circuit.

$$\text{Equation A 27}$$

Substituting into Equation A 28:

$$dV_Y/dt = -N_s \cdot (d\Phi/dt) / (C.R) \quad \text{Equation A 28}$$

Integrating both sides with reference to time gives:

$$V_Y = -N_s \cdot \Phi / (C.R) \quad \text{Equation A 29}$$

and

$$\Phi = -V_Y \cdot (C.R) / N_s \quad \text{Equation A 30}$$

also

$$B = \Phi / A \quad \text{Equation A 31}$$

where A is the cross-sectional area of the core.

Thus the flux density within the core material can be found:

$$B = -V_Y \cdot (C.R) / N_s \cdot A \quad \text{Equation A 32}$$

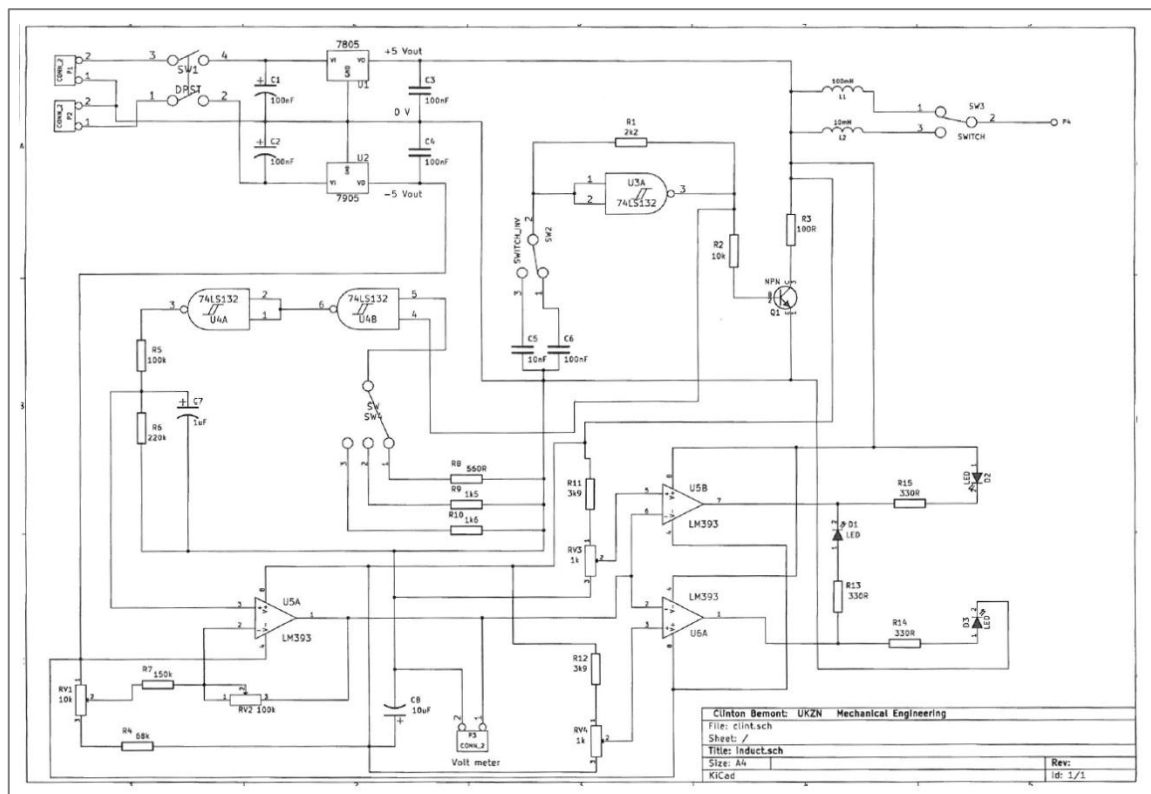
Thus, utilising Equation A 24 and Equation A 32, the magnetic permeability at any point can then be found from:

$$\mu = B / H \quad \text{Equation A 33}$$

## Appendix 2

### A2.1. Circuit used in hand-held sensor interrogation device

As described in Section 4.3.4, a hand-held device was designed and built to interrogate the degree of stress in either the smart rock tendon or smart face plate, according to calibration. The circuit was designed to have a very simple interface, with four LEDs signalling: low load or uninstalled; pre-load attained; high load; overload or failure eminent. The operating principle for the circuit was described in Section 4.3.4.



## **Appendix 3**

### **Journal papers**

Details of contribution to publications that form part and/or include research presented in this thesis follow. The actual publications, along with their reference details, are included in Appendix 3.1, 3.2 and 3.3.

#### **Journal paper 1 (to be submitted):**

All aspects of the work, conception, experimentation and writing, are the sole work of the author of this thesis.

#### **Journal paper 2 (Published in IEEE Sensors):**

All aspects of the work, conception, experimentation and writing, are the sole work of the author of this thesis. One set of experiments was operated by an undergraduate assistant.

#### **Journal paper 3 (Published in IOP Smart Materials and Structures):**

The author of this thesis played a fundamental role in conception and experimentation. Writing of the paper was done almost exclusively by this author. The co-author made a significant contribution in designing the alloys for this work and to other aspects of the experimental work. Other staff and students also aided in the experimental work.

Details of conference papers associated to this thesis are given in Appendix 3.4.

**A3.1. Journal Paper 1**

## **The Effects of Transformation Temperature on the Rate of Transformation in TRIP Steels**

**CLINTON BEMONT<sup>1\*</sup>, LESLEY CORNISH<sup>2</sup>, GLEN BRIGHT<sup>3</sup>**

<sup>1,3</sup> School of Mechanical Engineering, University of KwaZulu-Natal, Durban, South Africa, 4041  
(Email: bemontc@ukzn.ac.za)

<sup>2</sup> DST/NRF Centre of Excellence in Strong Materials and School of Chemical and Metallurgical Engineering, University of the Witwatersrand, Johannesburg, South Africa, 2050  
(Email: lesley.cornish@wits.ac.za)

\*Corresponding Author

TRIP steels undergo a phase transformation from austenite to martensite when mechanically deformed. The rate of transformation is significantly affected by the environmental temperature at the time of deformation. In applying TRIP steels or similar alloys as passive smart load monitoring sensors, or to any application where their rate of transformation is significant, it is imperative that this attribute is quantified, controlled, and if possible, minimised.

By comparing energy diagrams of diffusional and diffusionless transformations, it was hypothesised that transformation temperature sensitivity can be controlled through alloy composition and processing, specifically by controlling transformation temperatures such as the martensite start and finish temperatures. Certain empirical equations determining alloy transformation temperatures were identified as applicable to the alloys of interest.

In line with the hypothesis, experimental work showed that fully annealed material exhibited less transformation temperature sensitivity. Considerable further experimental work across different compositions will be required to further characterise the hypothesis.

### **Keywords**

TRIP steel, martensitic transformation, diffusionless transformation, transformation temperature sensitivity, martensitic transformation rate.

## 1. INTRODUCTION

The austenite to martensite transformation occurring during the deformation of TRIP steels is well known to be temperature sensitive<sup>[1]</sup>. However, the effect of transformation temperature is often not taken into account when researching new applications for TRIP steels, and it has not as yet been widely investigated or well characterised. The purpose of this investigation is to better understand this phenomenon, and if possible to uncover methods for its minimisation.

Attempts to characterise or model this effect have not been demonstrated to be successful outside of a narrow range of alloys. The current work focuses on the temperature sensitivity of high alloy stainless TRIP steels deformed in compression. The investigation stems from research into the development of TRIP steel based load sensors and the need for the minimisation of transformation temperature sensitivity in such applications<sup>[2]</sup>. However, transformation temperature sensitivity is relevant to many applications. In recent years, there has been particular interest in low-alloy TRIP-assisted steels for their potential use in applications such as vehicle bodies, due to their high-strength, high toughness and good formability<sup>[3][4]</sup>. It is hoped that a greater understanding of temperature sensitivity in high alloy, high transformation TRIP steels will aid the understanding of these characteristics in a wider range of TRIP and TRIP assisted steels.

It is well known that an austenite to martensite transformation begins in many steels upon rapidly quenching to a temperature specific to the alloy, known as  $M_s$  (martensite start temperature), and that upon reaching a lower temperature,  $M_f$  (martensite finish temperature), the transformation to martensite is complete (with some retained austenite permanently remaining). At any intermediate temperature, a specific amount of martensite is

permanently formed, and this will not increase without a further reduction in temperature. The transformation occurs extremely rapidly due to its diffusionless nature.

The martensitic transformation can be understood in terms of free energy diagrams. First, the case of a diffusional transformation is considered in Figure 1. During diffusional transformation, a phase will either develop gradually as temperature drops ( $\gamma \rightarrow \alpha$  in  $T_1 \rightarrow T_2 \rightarrow T_3$ ), or may form at one temperature such as a eutectoid temperature ( $\gamma \rightarrow \alpha + \beta$  at  $T_4$ ). In all cases, compositional change between phases via diffusion is necessary and quasi-equilibrium is ultimately thus maintained.

Diffusionless transformations occur extremely rapidly and undergo no composition change. A free energy diagram for a diffusionless austenitic to martensitic transformation is shown in Figure 2. For the composition of interest, at some temperature  $T_3$  ( $\approx T_0$ ), the austenitic and martensitic phases have the same Gibbs free energy ( $G$ ). However, in order for the transformation from austenite to martensite to proceed, it is necessary to overcome certain retarding forces associated primarily with the surface formation of the new phase and also with lattice strain. This means that further cooling to  $T_4$  ( $\approx M_s$ ) is required so that an extra driving force for the transformation,  $\Delta G^{\gamma \rightarrow \alpha'}$  is present before transformation will proceed.

Once  $M_s$  is reached, a very small amount of austenite will transform into martensite. But in order for transformation to proceed and produce more martensite, temperature must be further reduced.

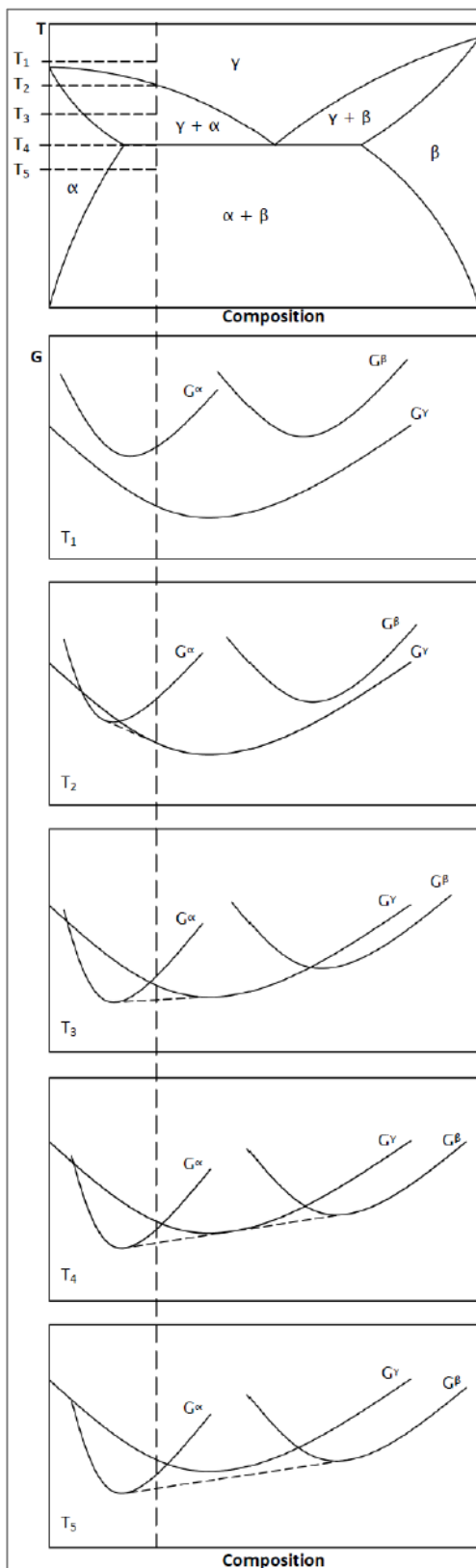


Figure 1. Gibbs free energy diagrams for a material undergoing phase change due to diffusion. Based on work by A. H. Cottrell<sup>[5]</sup>.

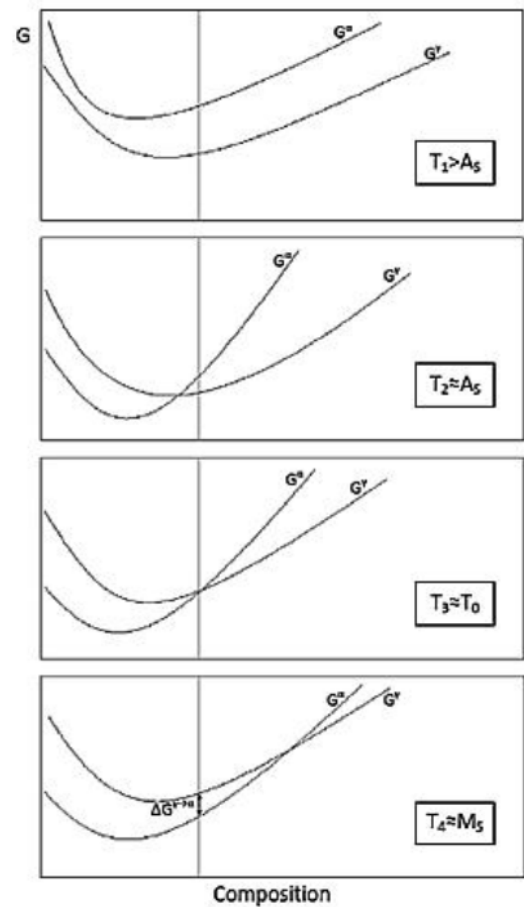


Figure 2. Gibbs free energy diagrams for a material undergoing diffusionless phase change.

The fact that the transformation does not occur entirely or even primarily at any distinct temperature, but rather over a range of temperatures, must be due to one or more of the following:

- Inherent variation in the magnitude of the driving or retarding forces in different regions of the material.
- Increasing lattice strains in the austenite lattice as martensite volume fraction increases.
- Change in magnitude of the driving or retarding forces at the austenite-martensite interface as a martensite plate grows.
- Differences in heterogeneous nucleation site potential.



If transformation occurs over a range of temperatures due to differences in heterogeneous nucleation site potential, then there must also be a mechanism preventing existing martensite grains from growing continuously larger.

In small particle experiments in which submicron single crystal particles were cooled, it was shown that even at 4K, with undercoolings of 300K, some particles remained untransformed<sup>[6]</sup>. This implies that the reason that transformation occurs over a range of temperatures is related primarily to heterogeneous nucleation, rather than to variations in surface or strain energy retarding forces.

A single plate of martensite in steels is known to grow to its full size in  $10^{-5}$  to  $10^{-7}$  s at constant temperature<sup>[7]</sup>. This implies that neither strain induced in the austenitic lattice nor changes in the austenite martensite interface are fundamentally responsible for the continually increasing driving force required. In fact, the strain induced in the austenitic lattice by the growth of a martensitic plate is even known to encourage martensitic nucleation or growth in other orientations, known as autocatalysis<sup>[8]</sup>. At any rate, the maximum growth of any martensite plate is limited by its morphology and the size of prior austenite grains.

Again, this implies that the increase in required driving force for the transformation to proceed is primarily due to a variation in heterogeneous nucleation site activation energies, rather than due to changing surface or strain energy retarding forces.

It has previously been approximated that the critical energy required to form a homogeneous martensite nucleus in austenite is too large for thermal fluctuations alone to overcome<sup>[9]</sup>. Thus, from the above argument, it is hypothesised that different driving forces (different temperatures) will be required to

activate different pre-existing or autocatalytically induced potential nucleation site configurations, depending on the activation energy required. This will then lead to transformation over a range of temperatures, as occurs in practice. The lack of increased driving force for nucleation relative to growth during diffusionless transformation is also relevant here, since otherwise wide-spread instantaneous nucleation would be expected with associated growth. This is again due to the lack of compositional change, as opposed to the diffusional case where the driving force for nucleation can be considerably greater than that for growth. Figure 3 shows the substantially increased driving force present for nucleation in diffusional transformations.

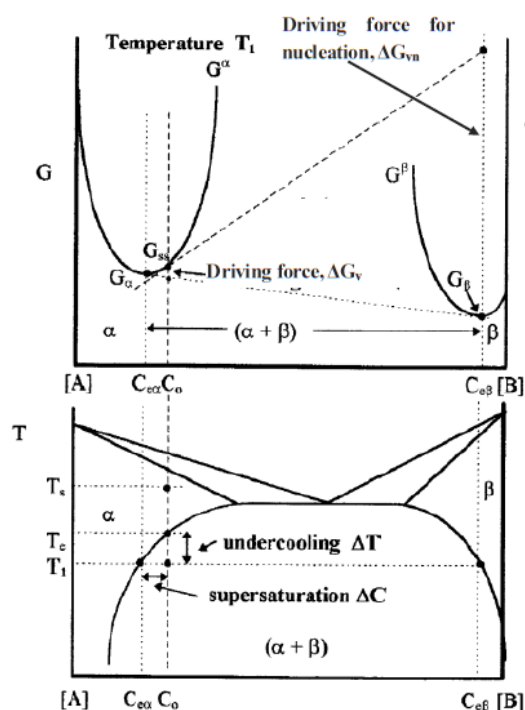


Figure 3: Schematic relationship between the driving force  $\Delta G_v$ , the supersaturation  $\Delta c$ , and the undercooling  $\Delta T$  for a diffusional transformation<sup>[9]</sup>.

This result is thus in agreement with the view that the austenite to martensite transformation is nucleation-controlled. It

corresponds more specifically with the dislocation strain energy assisted transformation nucleation theory in which the nucleation barrier to form a coherent nucleus is reduced by a favourable interaction with the elastic strain field of a dislocation, allowing a very broad range of potential favourable interactions<sup>[9]</sup>. Furthermore, new potential nucleation or autocatalysis sites may be formed during the growth of new martensite plates. The strain energy generated as the transformation progresses may contribute to controlling growth, but probably not nucleation. This is because, as already discussed, strain would be expected to actually encourage nucleation in certain orientations, at least until very large and wide-spread austenitic lattice strains occur.

Some understanding of the progression of the martensitic transformation with temperature reduction is expected to be helpful in designing alloys to be less temperature sensitive during deformation-induced transformation. If an alloy was designed such that it had large numbers of nucleation sites within a narrow range of activation energies, just below  $M_s$ , then  $M_f$  would be expected to be close to  $M_s$ . Thus, high temperature sensitivity would be expected, since a small change in temperature of deformation should result in a large change in the proportion of nuclei activated, as in Figure 4a.

In Figure 4, the deformation-induced transformation is represented as progressing from 0% to 100% between the upper and lower dotted lines respectively. These lines represent the energy contribution required from deformation for the transformation to progress to the specified level at the temperature of interest. When considering deformation-induced transformations, a deformation energy contribution that induces about 50% transformation into the alloy in Figure 4a at standard test temperature ( $T_1$ ) requires a smaller temperature change to instead attain

either zero or complete transformation than the alloy in Figure 4b, which has a lower  $M_f$  temperature, with  $M_s$  and  $T_0$  remaining unchanged.  $\Delta G_{Ms}$  remains approximately constant between alloys, as is believed to be the case<sup>[9]</sup>. This implies greater transformation temperature sensitivity for the alloy in Figure 4a. The alloy in Figure 4b is also expected to transform over a larger deformation range, more gradually. However, the maximum extent of transformation should be about the same for the two alloys represented by Figures 4a and 4b, with similar amounts of retained austenite, and a more gradual transformation is even likely to be beneficial. It is also observed that transformation should begin sooner in whichever of these two alloys has the test temperature closest to  $M_s$ .

Reducing the gradient of the difference between the free energy curves by separating  $M_f$ ,  $M_s$  and  $T_0$  should also then reduce temperature sensitivity. This is illustrated when comparing Figure 4b to Figure 4c, where only  $T_0$  moves, while  $M_s$  and  $M_f$  remain constant and  $\Delta G_{Ms}$  again remains approximately constant. The alloy in Figure 4c shows slightly less temperature sensitivity than that in Figure 4b. Figure 4d represents the most likely scenario, where the temperature differences between  $M_f$ ,  $M_s$ ,  $M_d$  and  $T_0$  all increase. Clearly, temperature sensitivity is substantially reduced for the alloy represented in Figure 4d, while rate of transformation with deformation is likely to either decrease or remain the same, but may also increase, depending of the extent of reduction in gradient.

From the above analysis of energy diagrams and dislocation nucleation theory, it is clear that no TRIP steel alloy can be made to be completely temperature insensitive during deformation-induced  $\gamma \rightarrow \alpha'$  transformation. This is because under a given deformation, at a lower temperature, a greater proportion of the nucleation sites present will be activated as martensitic nuclei since the driving force for

transformation is larger.

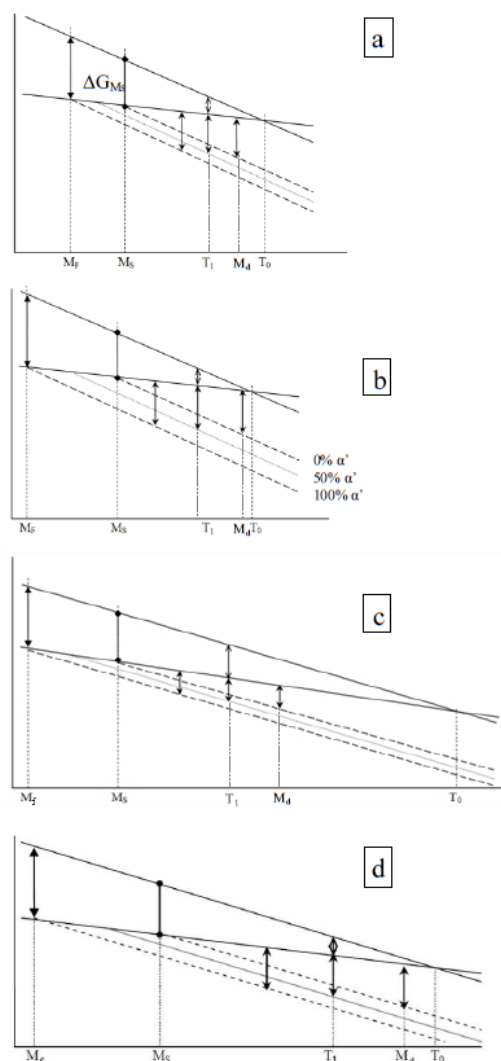


**Figure 4.** Schematic diagrams representing free energy versus temperature for the austenite to martensite transformation. Deformation induced transformation temperature sensitivity varies as  $M_f$ ,  $M_s$  and  $T_0$  change.

## 2. EXPERIMENTAL METHOD

In order to test these hypotheses in the alloys of interest, the transformation temperature sensitivity of different alloy compositions according to predicted  $M_f$ ,  $M_s$ ,  $M_d$  and  $T_0$  temperatures (or at least some of these parameters) should be tested. To do so, a range of special alloys should be designed

according to these parameters. However, no fundamental models are known that can be relied upon to predict these parameters accurately for the high alloy stainless TRIP steels of interest. All of the parameters, other than  $M_s$ , are hard to measure experimentally. However, there has been substantial experimental work done to empirically model  $M_s$  and  $M_{d30}$  (where  $M_{d30}$  is the temperature at which 50% martensite is attained at 30% strain)<sup>[10][16]</sup>. Thus, to test the hypothesis, and for the result to be useful, it will be necessary to be able to predict at least some of the alloys' characteristic temperature parameters during alloy design using empirical models.

Several empirical models for  $M_s$  and  $M_{d30}$  are found in the literature for materials close to the alloy range of interest<sup>[10][16]</sup>. However, there is significant variation between these models, and it was not known which might most accurately represent the alloys being investigated. Very little experimental work has been performed on high alloy TRIP steels in compression. Thus, several experimental alloys were cast and their transformations measured via inductive change during compressive deformation. This was done with a view to determining which of the empirical equations were most relevant, and also the manner in which alloy composition affected the rate of transformation with deformation in the alloys<sup>[2]</sup>. If specific empirical equations could be identified to be suitable predictors, then they might be used to estimate the  $M_s$  and  $M_{d30}$  of these or new alloys (at least relative to one another) and thereby be used to test the above hypotheses relating these intrinsic temperature parameters to an alloy's temperature sensitivity.

Two further sets of testing were performed to examine the effects of material condition and implicit changes in dislocation density on transformation temperature sensitivity. In the first a bar of composition TRIP M (Table 1) was utilised. One piece of



this bar was utilised in a hot-rolled (between 1000°C and 1200°C) and water quenched state, while the other was annealed at 1100°C for 2 hours in inert gas and furnace cooled. The as-rolled and water quenched samples were expected to have greater dislocation density than the annealed samples and to therefore show greater temperature sensitivity. Both materials were then deformed in compression at -15°C, 15°C and 45°C while their relative transformation was measured via inductive change.

The effect of dislocation density on transformation temperature sensitivity was also assessed in tensile deformation by comparing alloy TRIP M in an annealed form, a hot rolled and water-quenched form and a warm-worked form. The warm worked alloy, TRIP M-W was reduced 20% between 350°C and 500°C. TRIP M-A was annealed at 1150°C for one hour. These alloys were again tested at three temperatures, -15°C, 25°C and 65°C.

### 3. RESULTS

Multiple alloy compositions were cast and a selection of these are listed in Table 1. They were utilised as-cast to determine, via inductive measurement, their rate of transformation with deformation in compression (Figure 5)<sup>[2]</sup>.

**Table 1. Alloy compositions (wt %).**

Alloy	C	Si	Mn	Cr	Ni
A3a	0.044	0.45	0.23	12.8	12.8
B2	0.08	0.64	10.2	11.5	6.6
C1	0.007	0.007	0.1	15.0	14.4
C2a	0.037	0.47	0.23	14.0	10.7
C3	0.05	0.42	7.92	14.0	6.61
M1a	0.23	0.74	11.0	13.2	0.29
N1	0.13	0.65	11.8	13.5	4.13
1.4301	0.05	0.35	1.43	20.0	8.6
TRIP M	0.18	0.46	9.3	14.2	0.54

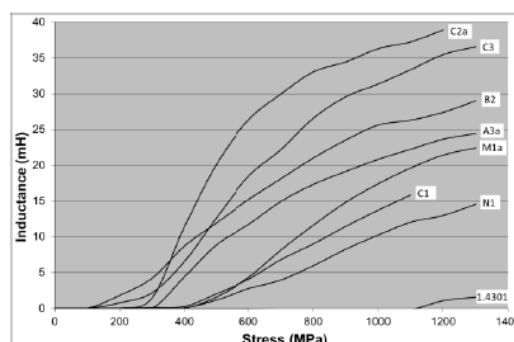


**Figure 5. Transformation characteristics of alloys in Table 1.**

These data were also used to predict which empirical equations describing  $M_s$  and  $M_{d30}$  are most suitable. This was done by plotting the level of transformation of each alloy at 25% strain against each of the relevant empirical equations predicting  $M_s$  and  $M_{d30}$  temperatures. Applying the energy diagram theory as discussed, these temperatures should closely affect rate of transformation with deformation. Thus, empirical equations that are relevant for these alloys should show an obvious trend when plotted against transformation level for each alloy at room temperature. This methodology was tested by plotting transformation level against the average of the alloy's Schaeffler nickel equivalent ( $Ni_{eq}$ ) and chromium equivalents ( $Cr_{eq}$ )<sup>[17]</sup>. The average of  $Ni_{eq}$  and  $Cr_{eq}$  is representative of an alloy's propensity to form austenite or martensite at room temperature, as per the widely accepted Schaeffler diagram<sup>[17]</sup>. The transformation level of each alloy was also plotted against the average of its nickel and chromium content, for comparison. Figure 6b shows that there was a clear relationship between the level of an alloy's transformation and the average of its  $Ni_{eq}$  and  $Cr_{eq}$ , while no apparent relationship was observed for the average of its nickel and chromium content.

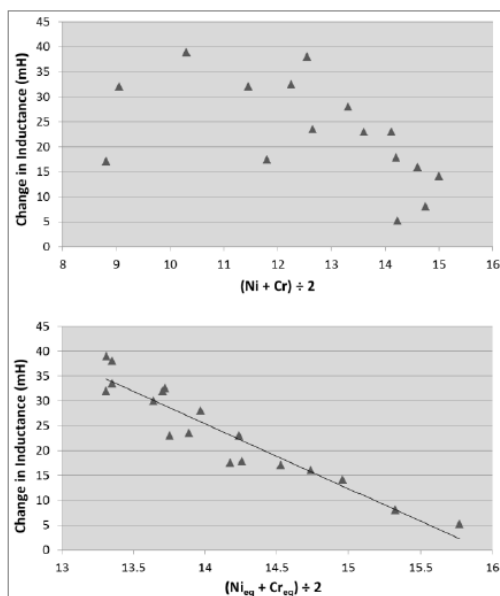


**Figure 6.** The relationship between alloy inductance at 25% deformation and (a) average of Ni and Cr content, (b) average of  $Ni_{eq}$  and  $Cr_{eq}$  average.

This method was then applied to the empirical equations for  $M_s$  and  $M_{d30}$  or the difference between those equations, an example of which is shown in Figure 7 for the Cina equation<sup>[11]</sup>. The results of these plots showed that  $M_s$  and  $M_{d30}$  were best predicted by the Cina and Pickering equations respectively<sup>[10][11]</sup>. The coefficient of correlation for the Cina equation for  $M_s$  was 0.81 and for the Pickering equation for  $M_{d30}$ , 0.66. It was noted that the average of two equations for  $M_{d30}$  (that by Pickering and that by Angel) showed a coefficient of correlation of 0.9, substantially better than any single equation.

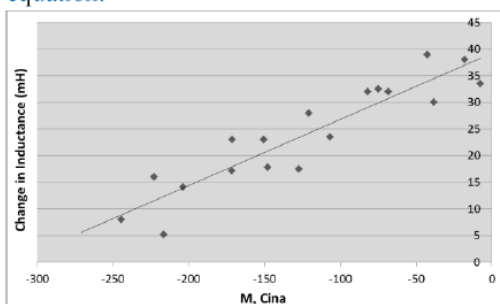


**Figure 7.** Alloy inductance at 25% deformation vs.  $M_s$  Cina.

The plot of the difference between  $M_{d30}$  Pickering and  $M_s$  Cina ( $M_{d30}$  Pickering -  $M_s$  Cina) versus transformation also showed a better coefficient of correlation (0.84) than any equation did on its own (Figure 8). Although this plot is heavily influenced by  $M_s$  temperature, it supports the hypothesis that a lower gradient difference between the  $\gamma$  and  $\alpha'$  free energy curves (corresponding to a larger difference between  $M_{d30}$  and  $M_s$ ) should result in reduced transformation for a given amount of deformation at a constant temperature.

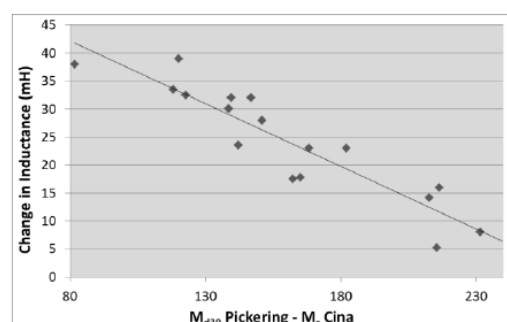


**Figure 8.** Difference between  $M_{d30}$  Pickering and  $M_s$  Cina plotted against alloy inductance in selected alloys at 25% deformation.

Finally, the effects of material condition on transformation temperature sensitivity were examined. Warm work is expected to increase the dislocation density of hot worked, water-quenched material<sup>[18][19]</sup>. Annealing is expected to reduce the dislocation density of hot worked, water-quenched material<sup>[19][20]</sup>. Increased dislocation density is expected to increase  $M_f$  temperature due to the greater number of available nucleation sites, thereby increasing temperature sensitivity. Although dislocation density will be expected to increase as deformation progresses, it is expected that an alloy that begins tensile deformation with a lower dislocation density will tend to maintain that lower dislocation density. This is evidenced by the well-known phenomenon that prior cold work increases tensile strength<sup>[19][21]</sup>.

This was investigated first by comparing the transformation of hot-rolled and water

quenched TRIP M to the same material in an annealed state. The results are shown in Figure 9, and each curve is the average of three tests.

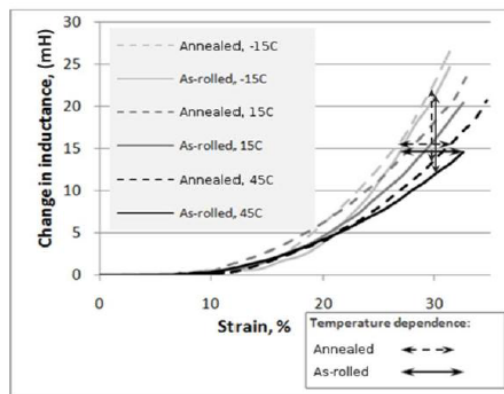


**Figure 9.** Strain vs. Transformation curves for alloy M in an as-rolled and water quenched state and in an annealed state at different deformation temperatures. Arrows show temperature sensitivity.

In all cases, the variation between similar tests was found to be small compared to the results of temperature variation. The annealed material shows a slightly more rapid transformation with deformation. This is probably due to a larger austenite grain size. Slightly less temperature sensitivity was exhibited by the annealed material. At 30% strain, the difference in temperature sensitivity between the two materials was about 2 mH change in inductance over 60°C (9% for the annealed material and 10% for the as-rolled material), this was statistically significant at the  $p = 0.05$  level, compared to the test repeatability error. The difference in temperature sensitivity at 15 mH was 1% strain over 60°C, also statistically significant at  $p = 0.05$ . This correlates with the hypothesis that a higher dislocation density is expected to increase  $M_f$  and thereby increase temperature sensitivity, as discussed.

The effect of material condition on transformation temperature sensitivity was also assessed by tensile deformation in comparing alloy TRIP M in an annealed form, a hot rolled and water-quenched form and a warm-worked form. The warm-worked alloy, TRIP M-W was

reduced 20% between 350°C and 500°C. TRIP M-A was annealed at 1150°C for one hour. The hardness of TRIP M in the three conditions is shown in Table 2.

**Table 2.** Hardness of alloy TRIP M in three conditions (M-A - annealed, M - hot-rolled, M-W - warm worked).

	TRIP M-A	TRIP M	TRIP M-W
Hardness (HRC)	21	25	38

Figure 10 shows the result of testing these materials at -15°C, 25°C and 65°C. The plots for each material were scaled to enable relative transformation temperature sensitivity comparison on the same axes.

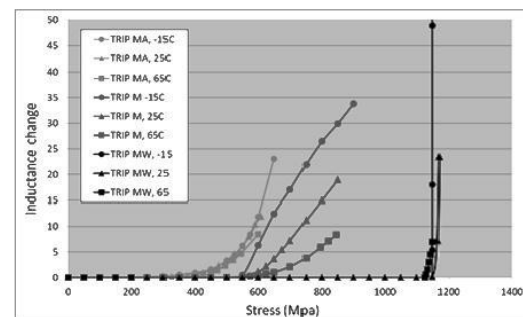


**Figure 10.** TRIP M tensile tested in different deformation states at different temperatures.

Figure 10 shows that the temperature sensitivity of the annealed alloy was significantly lower than the hot worked alloy. It was apparent that due to the already high dislocation density in TRIP M-W, significant strain hardening did not occur. The material's yield and UTS were thus almost the same and it was therefore impossible to utilise this material as a load sensor element. Transformation temperature sensitivity of TRIP M-W with increasing stress cannot be assessed because once transformation begins, stress does not increase significantly. However, it is clear that the material was highly temperature sensitive. Although ultimate tensile stress was similar at all three temperatures and the material tested at -15°C



underwent considerably less strain (23% compared to 40% for TRIP M), total transformation in the material tested at  $-15^{\circ}\text{C}$  was more than twenty times that of the material tested at  $65^{\circ}\text{C}$ , a considerably larger difference than in the annealed and the hot-worked materials.

#### 4. CONCLUSION

An energy diagram approach has been used to reach the hypothesis that the transformation temperature sensitivity of TRIP steel alloys can be minimised by manipulating  $M_f$ ,  $M_s$  and  $M_d$  by alloy composition and processing control. In order to allow the design of alloy compositions of interest according to the above hypothesis, a number of published empirical equations to determine  $M_s$  and  $M_{d30}$  were tested, and two were identified to be most promising. In future,  $M_s$  and  $M_{d30}$  temperatures might be directly measured to determine the accuracy of the empirical equations, and also to properly test the hypothesis that alloys with greater differences between  $M_s$  and  $M_{d30}$  will show less transformation temperature sensitivity.

The effect of full annealing on an alloy's transformation temperature sensitivity was also investigated. Full annealing was shown to reduce the alloy's temperature sensitivity, in line with the hypothesis that it would reduce dislocation density, thereby reducing  $M_f$  and temperature sensitivity.

Significant experimental work will be required to confirm whether the identified empirical equations are accurate predictors of the relevant temperatures in the alloy range of interest. Further experimental work will also be required to determine whether the above approach can be utilised to reduce transformation temperature sensitivity without severely compromising the extent of transformation.

#### Acknowledgments

The authors would like to acknowledge research assistant Shikar Nunkissor for his contributed experimental work.

#### References

- [1] Bressanelli, J.P., Moskowitz, A. (1966), Effects of Strain Rate, Temperature and Composition on Tensile Properties of Austenitic Stainless Steels, *Transactions of the ASM*, 59, 223 – 229.
- [2] Bemont, C.P. (2009), The development of robust structural health monitoring sensors utilising TRIP steel, *IEEE Sensors Journal*, 9 (11), 1449 – 1455.
- [3] Timokhina, B., Hodgson, P. D., Pereloma, E. V. (2004), Effect of microstructure on the stability of retained austenite in transformation-induced-plasticity steels. *Metallurgical and Materials Transactions A*, 35 (8), 2331-2341.
- [4] Adamczyk, J. (2006), Development of the microalloyed constructional steels. *Journal of Achievements in Materials and Manufacturing Engineering*, 14, 9-20.
- [5] Cottrell, A. H. (1955), Theoretical Structural Metallurgy, 2<sup>nd</sup> ed., London, Edward Arnold
- [6] Perepezko, J., Sebright, J., Höckel, P., & Wilde, G. (2002). Undercooling and solidification of atomized liquid droplets. *Materials Science and Engineering A*, 326 (1), 144-153.
- [7] Nishiyama, Z., Fine, M., Meshii, M., & Wayman, C. (1978). *Martensitic transformation*. Michigan Academic Press.
- [8] Olson, G.B., Cohen, M (1972), A mechanism for the strain-induced nucleation of martensitic transformations, *Journal of the Less-Common Metals*, 28, 107 – 118.



- [9] Porter, A.D., Easterling, K.E., Sherif, M. (2009), *Phase Transformations in Metals and Alloys*. CRC Press, Boca Raton, USA.
- [10] Pickering, F.B. (1978), *Physical metallurgy and the design of steel*, Applied Science Publishers, London, UK.
- [11] Cina, U., West, C., Christ, H.J. (2008), Deformation-induced martensite formation during cyclic deformation of metastable austenitic steel: Influence of temperature and carbon content, *Materials Science and Engineering A*, 481-482, 713 - 717.
- [12] Hull, F.C. (1973), Delta ferrite and martensite formation in stainless steels, *Welding Journal: Welding Research Supplement*, 52 (5) 193-203.
- [13] Andrew, K.W. (1965), Empirical formula for the calculation of some transformation temperatures, *Journal of the Iron and Steel Institute*, 203 (7), 721-727.
- [14] Capdevila, C., Caballero F.G., Garcis de Andres, C. (2002), Determination of  $M_s$  temperature in steels: A Bayesian neural network model, *ISIJ International*, 42 (8), 894-902.
- [15] Angel, T. (1954), Formation of Martensite in Austenitic Stainless Steels, Effects of Deformation, Temperature and Composition, *Journal of the Iron and Steel Institute*, 177, 165-174.
- [16] Nohara, K., Ono, Y., Ohashi, N. (1978), Composition and grain size dependencies of strain-induced martensitic transformation in metastable austenitic stainless steels, *Journal of the ISIJ*, 63 (5), 212-222.
- [17] Schaeffler, A.L. (1949), Constitution diagram for stainless steel weld metal, *Metal Progress*, 56, 680-680B.
- [18] Boswell, F. W. C., Smith, E. (1958), Examination of metals by transmission electron microscopy, In Symposium on Advances in Electron Metallography, Baltimore, 31-42.
- [19] Okazaki, Y. (2008), Effects of Cold Drawing and Annealing on Mechanical Properties and Microstructure of Co-Cr-Mo-Ni-Fe Alloys for Surgical Implants, *Materials Transactions*, 49 (7), 1656-1660.
- [20] Rowcliffe, A.F., Nicholson, R.B. (1972), Quenching defects and precipitation in a phosphorus-containing austenitic stainless steel, *Acta Metallurgica*, 20 (1), 143-155.
- [21] Herbert, E. G., Work-Hardening Properties of Metals (1926), Transactions of the ASME, 48, 705-748.

## A3.2. Journal Paper 2

Sensors-02875

1

# The development of robust structural health monitoring sensors utilizing TRIP steel

C. P. Bemont

**Abstract**—The feasibility of using the inherently smart properties of transformation induced plasticity (TRIP) steels as a basis for low cost, robust smart structural health monitoring sensors has been investigated. These steels undergo an irreversible strain-induced phase transformation from paramagnetic austenite to ferromagnetic martensite. Specific needs were identified in the geotechnical industry and a primary aim of the project was the development of a load cell based on this technology. Cast TRIP steel alloys were designed and tested for their transformation performance during deformation. The response of the phase transformation was also studied under various environmental and loading conditions. The inaccuracies accumulated under unknown environmental and loading conditions were found to be substantial but not excessive for some applications where other characteristics such as cost and reliability are more important. Results point to potential methods for the reduction of the inaccuracies. Prototype load cells were built and tested and one variation was installed in a suspension bridge.

**Index Terms**— Structural health monitoring, Smart Load Cell, Smart sensor, Meta-stable steel, TRIP steel

## I. INTRODUCTION

THE meta-stable alloys known as TRIP steels undergo an irreversible strain-induced phase transformation. The inherently smart properties of TRIP steel have been applied in attempting to find solutions for situations where robust, low cost structural health monitoring without great precision is required.

A need was identified in the geotechnical industry for strain and load sensors that are low-cost, low maintenance and robust but do not necessarily exhibit good resolution. For such sensors to be successfully implemented they must also function in a variety of harsh environments, be easy to install, simple to operate and usually be tamper and theft proof too. It was envisaged that a good solution for such situations might come in the form of a smart material such as TRIP steel.

The extent of a TRIP steel alloy's crystal structure transformation from austenite to martensite has been shown to be approximately proportional to the historical peak strain mechanically induced in it [1]. The transformation, and thus the associated peak strain, can be monitored using several different methods to detect various physical property changes between the austenitic and martensitic phases. Because the parent austenitic phase is paramagnetic while the generated martensitic phase is ferromagnetic, one such method is to monitor the level of ferromagnetism within the material. A correlation has been shown to exist between the strain induced in the material and its magnetic permeability [2].

The relationship between the level of induced strain and the level of phase transformation in a TRIP steel depends on the stability of the metastable parent austenite and therefore on its elemental composition and its microstructural condition [3]. A number of empirical relations have previously been formulated to assist in prediction of the transformation behaviour of meta-stable alloy steels. Some of these were employed and evaluated for their applicability to the range of TRIP steels of interest, with a view towards improving future alloy design.

It was recognised that it may be beneficial to utilise a TRIP steel element in compression rather than in tension. This has potential advantages for the envisaged applications, for example during complete failure of the TRIP steel element a device would hold load with minimal deflection. Also, experimentation showed that it is thereby possible to reduce the effect of incubation strain (low load insensitivity) and thus attain acceptable resolution at a lower load than would be possible in tension.

## II. EXPERIMENTAL PROCESS AND MATERIALS

It was anticipated that as-cast alloys would be cheapest to implement and may also result in a still smaller incubation period due to having a lower yield point. It was found to be impossible to obtain as-cast material of the desired compositional range from suppliers and thus the casting of this material was undertaken in-house.

TRIP steel alloys comprise a broad range of elemental compositions exhibiting distinct characteristics. Alloy composition affects the chemical free energy difference between the phases and thus the stability of the austenitic phase [4]. The Schaeffler diagram with its associated nickel and chromium equivalent equations ( $Ni_{eq}$  and  $Cr_{eq}$

Manuscript received September 30, 2008. An earlier version of this paper was presented at the ISSS 2008 conference. This work was supported in part by Technische Universität Chemnitz, Germany and MINTEK, South Africa.

C. P. Bemont is with the University of KwaZulu-Natal, Durban, South Africa, 4041 (tel: +2731-260-3207; fax: +2731-260-3217; e-mail: bemontc@ukzn.ac.za).

respectively) is commonly used to assist in prediction of the stability of austenite in high alloy steels from their elemental composition.

Other empirical relations, for example for  $M_s$  (the temperature at which martensitic transformation begins spontaneously on cooling) or  $M_{d50}$  (the temperature at which the material will exhibit 50% martensite after 30% deformation) are also used to assist in predicting austenite stability and phase transformation characteristics of metastable alloy stainless steels and TRIP steels from composition and microstructure properties [5]. There are several empirical equations claimed to be applicable within the alloy composition range of interest that have been developed to approximate  $M_s$  and  $M_{d50}$ . These formulas were found to give substantially varying results and it was unknown which of these empirical relations would be most compatible with the alloy groups of interest. Alloy compositions were thus designed in such a way so as to assist in determining this, as well as the effectiveness of the Schaeffler diagram and the influence of individual alloying elements. Some alloys of similar elemental composition were designed to fall into separate regions of the Schaeffler diagram and some alloys of different elemental compositions were designed to fall into the same regions (figure 1). Table 1 lists the compositions of eight of the alloys that were produced as well as that of the DIN 1.4301 material that was also tested.

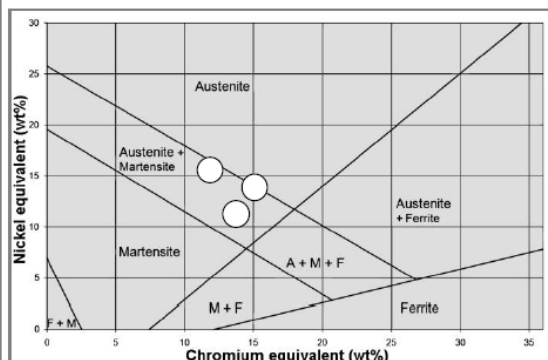


Fig. 1. Schaeffler Diagram showing the proposed alloy groupings [modified from [3], originating from: A. Schaeffler, "Constitution diagram for stainless steel", *Metal Progress*, Vol.56, pp. 680, 1949].

Twenty alloys were designed and produced primarily within the range of nickel and chromium equivalents from 11 to 16 and 11 to 15.5 respectively.

$$Ni_{eq} = Ni + 30(C + N) + 0.5Mn + 0.5(Cu + Co) \quad (1)$$

$$Cr_{eq} = Cr + 1.5 Si + Mo + 2Ti + 0.5Nb \quad (2)$$

An inductance meter (Volcraft LCR 4080) was chosen and inductive measurement coils designed according to trends observed in the results of experiments performed on several alloys to characterise their B-H curves. The resulting device was then utilised to plot the dependence of each TRIP steels' magnetic permeability on applied compressive strain and load. The TRIP steel specimen of interest was placed within the

inductive pickup coil in the compressive testing rig (Instron 5500R, 100kN), enabling results to be collected continuously during compressive deformation.

In service these materials may need to behave with repeatable accuracy while subjected to a variety of environments and loading conditions. High speed testing, fatigue testing, circuitous load testing (loading in a non-continuous manner) and temperature testing were therefore carried out. A complete load cell with inductive pickup coil was also shown to be immune to the magnetic interference of a large electric motor. It was attempted to simulate and analyse most scenarios that might occur in practical applications.

Alloy:	C	Si	Mn	Cr	Ni
C2	0.037	0.47	0.2	14.0	10.7
A3	0.067	0.49	0.22	13.0	11.5
B2	0.08	0.64	10.2	11.5	6.6
V4	0.179	0.77	5.67	12.71	3.16
V5	0.189	0.63	4.88	12.33	3.24
N1	0.13	0.65	11.8	13.5	4.13
V2	0.15	0.81	6.12	12.2	3.59
HM*	0.18	0.46	9.3	14.2	0.54
1.4301	0.057	0.65	1.8	18.0	8.51

Table 1. Weight percentage composition is shown for eight of the alloys that were produced and of the DIN 1.4301 material that was also tested. \*Alloy HM was hot-rolled and annealed for one hour at 1150°C.

Finally tests were performed on prototype Smart Load Cell devices and a set of such devices was installed on a suspension bridge as a pilot project.

### III. EXPERIMENTAL RESULTS AND DISCUSSION

#### A. General Magnetic Characterisation

In order to measure the change in magnetic permeability and thereby the associated transformation of the material with the best viable precision, it was necessary to first characterize the nature of the changes in magnetic permeability that occur in the alloys during transformation [6]. The magnetic permeability curves of several purchased and in-house TRIP steels were measured before and after being deformed to different loads. The material described in figure 2 is an in-house cast TRIP steel showing good transformation properties.

It can be seen that after a very large compressive deformation of 3.5GPa the material shows a very large increase in magnetic permeability, up to nineteen times that of its undeformed state. This is important because the smart sensor resolution is directly associated to this change. It can be seen that the deformed material's magnetic permeability peaks at a field strength of between 4000 A/m and 8000 A/m. It is important to take measurements in this peak range to attain the greatest possible resolution from the sensor.

This ideal field strength varies somewhat for the different TRIP steels tested but 7500 A/m was observed to be close to ideal for all the cast materials studied. The graph shows that using a field strength outside of the region where magnetic



permeability peaks can be very detrimental to the perceived magnetic permeability change.

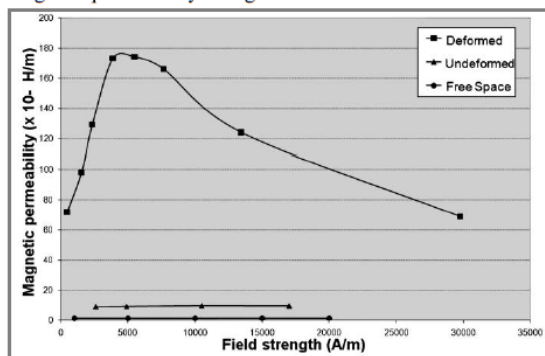


Fig. 2. Characteristic magnetic permeability curves for a cast TRIP steel (alloy V5) showing good transformation. The line denoted with round markers shows the magnetic permeability of free space, the line with triangular markers that of an undeformed TRIP steel specimen and the line with square markers that of a deformed specimen.

#### B. Alloy Comparison, Continuous Quasi-Static Loading

Quantitative X-ray diffraction phase analysis as well as optical and SEM micrographs of the specimens in unloaded and loaded conditions confirmed a correlation of the residual austenite content with the measured inductance.

A comparison of the transformation performance of the alloys produced showed considerable composition dependence (figure 3). When the alloy compositions were plotted on a Schaeffler diagram according to their inductive change at 10% strain and at 28% strain, the only pattern observed was a generally superior transformation in those alloy compositions closer to the martensitic region of the diagram. When the inductance change in the specimens at 28% strain is plotted against the average of  $Ni_{eq}$  and  $Cr_{eq}$ , there is a definite trend. As seen in figure 4, a reduced  $Ni_{eq}-Cr_{eq}$  average generally leads to better transformation performance within the alloy range investigated.

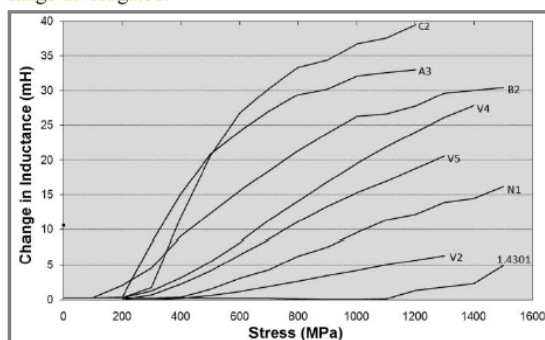


Fig. 3. A comparison of the transformation performance of some of the alloys that were cast in-house (offsets are zeroed and alloy DIN 1.4301 is included for comparative purposes).

Empirical formulas previously proposed to describe either  $M_s$  temperature or  $M_{d30}$  temperature within the alloy range of

interest were tested against experimentally measured transformation characteristics. Results from  $M_s$  formulas by Andrew, Krupp, Hull, Stuhlmann and Capdevila (neural network) for each alloy were plotted against initial inductance and total inductance change [7, 8, 9]. It is proposed that since  $M_s$  is a predictor of austenite stability, the empirical relations most relevant to the alloy group of interest would show a more apparent graphical trend when plotted against certain measured transformation characteristics, such as rate of transformation and total change in inductance [10]. It was found that of the  $M_s$  formulas, that developed by Krupp showed the most distinct trend (figure 5). It was also found that alloys with predicted  $M_{s\_Krupp}$  temperatures above  $-120^\circ\text{C}$  performed very well.

$$M_{s\_Krupp} = 1305 - 61(\%Ni) - 42(\%Cr) - 33(\%Mn) - 28(\%Si) - 1667(\%C + \%N)$$

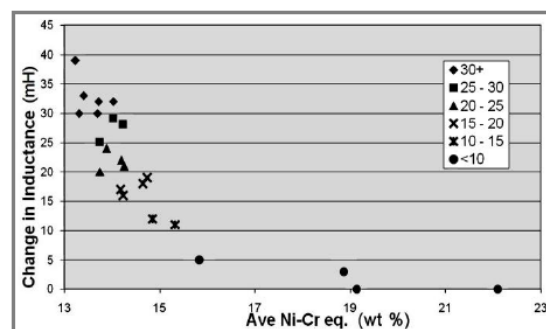


Fig. 4. A lower  $Ni_{eq}-Cr_{eq}$  average generally leads to improved transformation (a greater change in inductance).

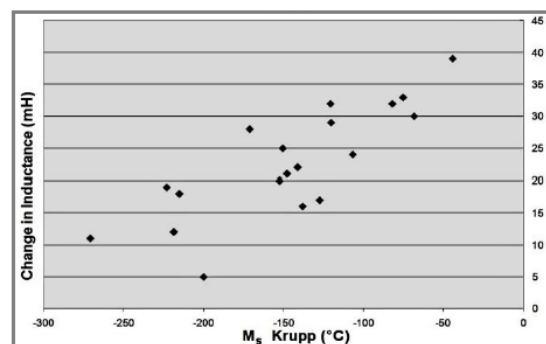


Fig. 5. The empirical formula for  $M_s$  Krupp shows a trend when compared to the total change in inductance for the alloy group investigated.

Empirical relations by Angel, Pickering and Nohara for  $M_{d30}$  were analysed in a similar manner [11, 12, 13]. That developed by Pickering was found to show the most distinct trend. It was found that alloys with predicted  $M_{d30\_Pickering}$  temperatures above  $10^\circ\text{C}$  performed well.

$$M_{d30\_Pickering} = 497 - 462(\%C + \%N) - 8.1(\%Mn) - 20(\%Ni) - 13.7(\%Cr) - 18.75(\%Mo) - 9.2(\%Si)$$

While sizeable changes in individual alloying elements have well documented effects on transformation, little association has been perceived between transformation performance and

precise levels of individual alloying elements. This is probably due to their complicated inter-relationships, with one often substituting for another, as signified by the empirical equations referred to [14].

#### C. Repeatability under Continuous Quasi-Static Loading

For a number of alloys the repeatability of the inductance measured at particular loads on different specimens was investigated under continuous quasi-static loading conditions. This parameter is instrumental in determining the accuracy of a final device. While a relatively small change in stress or strain produces an evident change in inductance on any specimen, there is an evident difference in inductive reading from one specimen to the next at an identical stress.

The three curves shown on the graph in figure 6 were plotted by measuring inductive change during the quasi-static, continuous, constant temperature loading of three different specimens of alloy V5. The graph implies that an error in outputted load readings of less than  $\pm 3\%$  would be expected beyond incubation. While this result is typical, testing on some alloys showed larger deviations. This may be due to material inhomogeneity or variation in experimental testing conditions. When fully incorporated into a complete load cell fabricated to relatively low tolerances and utilising a TRIP steel alloy produced in large batches, the repeatability under constant temperature, continuous, quasi-static loading conditions is expected to be similar to or better than the result depicted.

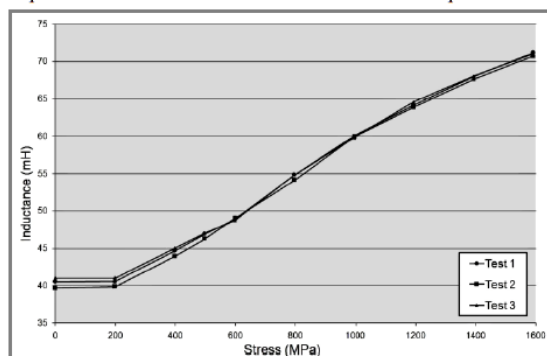


Fig. 6. This graph illustrates three tests conducted on alloy V5 under constant temperature, continuous, quasi-static loading conditions.

#### D. Strain Rate Effect

High strain rate testing was performed on alloy HM. In the most extreme case, a stress of 1300 MPa was attained at a strain rate of 10 /s and held for only 4ms (MTS 312.2 frame with hydraulic accumulators). Using a quasi-static strain rate (0.001 /s) calibration curve to convert the material's transformation to a load reading, this scenario would result in an output reading 20% below the true peak load.

In less extreme scenarios the error is considerably smaller. At the same strain rate of 10 /s but with the maximum load held, an output of approximately 12% below the true load would be measured by correlation to the quasi-static

calibration curve. The effect of varying the strain rate between 0.001 /s and 0.1 /s was shown to be negligible considering the quasi-static loading resolution, discussed above.

Strain rate will therefore have a substantial effect on a device's effective resolution in an environment where the strain rate is completely unpredictable. However, when the strain rate is known to be within a limited range, the potential error has been shown to be relatively small.

#### E. Cyclic Loading

No change in inductance was detected during cyclic loading within the full elastic zone for more than 10 000 cycles. This test was conducted on alloys N1 and HM, with the same result. During cyclic loading into the plastic zone, the inductance measured at peak load was observed to be within the same range measured during quasi-static continuous loading.

#### F. Circuitous Loading

Applying load cycles other than continuously increasing lead to unexpected results. In figure 7 shown below, a specimen of alloy V5 was repeatedly loaded to a local peak stress, unloaded to no load and then reloaded to a higher local peak stress. This loading regime is referred to as circuitous loading.

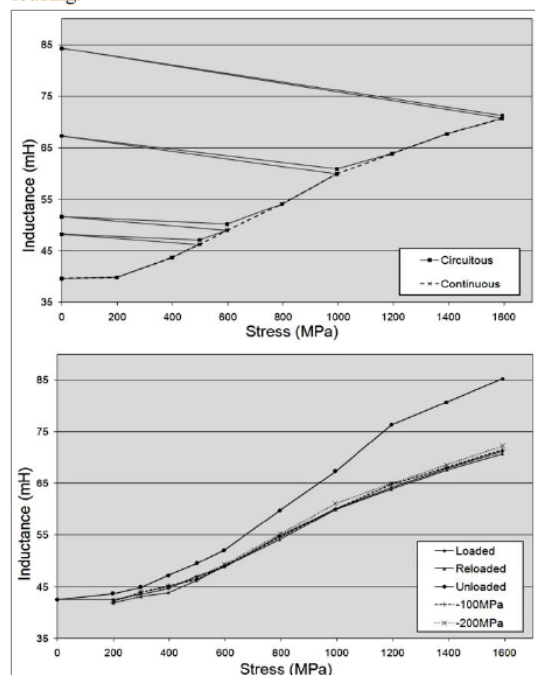


Fig. 7. The two graphs above describe the same data. Using alloy V5, the inductive output is plotted against load during circuitous loading (the load is applied to a peak, removed and then reapplied to a higher peak with inductance measured at peak loads as well as when reduced and removed). The first graph also includes a plot of a continuously loaded specimen, for comparison. The second plot clarifies the phenomenon's effect on resolution by more clearly depicting the potential range of implied stress for a particular measured inductive output.

It is notable that the profile of the transformation curve is very close to that of its continuously loaded counterpart (plotted in figure 6). However, the process of releasing the load is seen to increase the inductance reading, thus mimicking an increase in load from the standpoint of the inductance measurement. It has been found that this effect is not as prominent in tension as it is in compression. This increase in inductance is contrary to what is expected when the magnetic path length of an inductor increases and the magnetically permeable volume within the inductive coil decreases (due to the regaining of the specimen's elastic strain). It is possible that the reason for this phenomenon is a small change in the lattice parameters within the material's crystal structure.

According to the circuitous loading curve shown for alloy V5, at 500MPa the additional error due to this phenomenon is 10%, at 650MPa it is 13% and by 1000MPa it is over 25%. The inaccuracies due to this phenomenon are in one direction only; the load interpreted from the proposed device may register above the true peak historical load, but never below.

The second graph of figure 7 depicts the same set of data but illustrates more clearly how the resolution of the device is affected by more clearly depicting the potential range of implied stress for a particular measured inductive output. It is notable that up to 30% of the load can be released with little effect on the output; only drastically reduced loads substantially affect output readings.

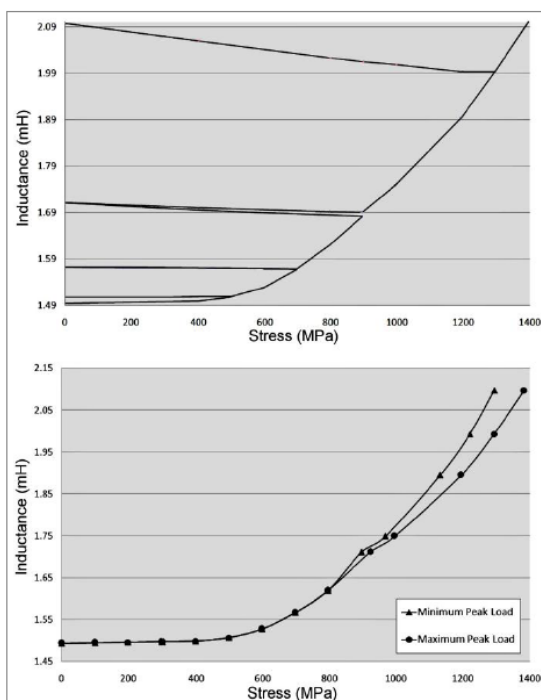


Fig. 8. The inductive output of alloy HM is plotted against load during circuitous loading in a similar manner as was done using alloy V5 in figure 7.

It can be seen from figure 8 that hot worked alloy HM is considerably less susceptible to this phenomenon. Up to 700MPa there is almost no error and at 1000MPa it produces less than 5% error, in a single direction only. Only well beyond 1000MPa, where it is unlikely to be utilised, does the error become significant. It is currently inconclusive whether this is due to microstructural condition, composition or a combination of both. However the material shows bad early load sensitivity (it has a large incubation period) and has a relatively small useful range.

#### G. Temperature Sensitivity

Temperature at time of measurement has been shown to have no significant effect on results. This was verified between  $-20^{\circ}\text{C}$  and  $120^{\circ}\text{C}$ . Cyclic temperature change at constant stress has also been shown to have no significant effect. Specimens were cycled between  $-50^{\circ}\text{C}$  and  $80^{\circ}\text{C}$  for approximately 100 cycles with no observable change in inductive output. However temperature at time of deformation has been shown to have a significant effect.

Compressive temperature testing was conducted on cast alloy V2. As seen in figure 9, this alloy would produce a total error of up to  $\pm 18\%$  at 800MPa when transformation occurs between  $24^{\circ}\text{C}$  and  $90^{\circ}\text{C}$ . However this temperature range is unlikely to be encountered in many practical applications. If necessary, it would also be possible to utilise such devices in temperature stable environments, such as mines. Over a transformation temperature variation between  $24^{\circ}\text{C}$  and  $40^{\circ}\text{C}$  this alloy would produce up to  $\pm 7\%$  error at 800 MPa.

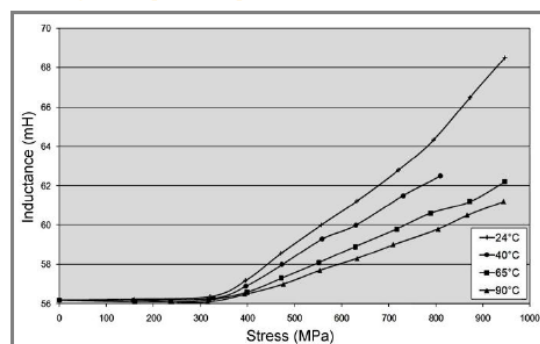


Fig. 9. Change in transformation levels due to transformation temperature variation for alloy V2.

A registered output will always predict a lower load than the true historical peak load when the temperature was higher than expected at the time of deformation. A higher load will always be predicted when the temperature during deformation was below that expected.

There can be little doubt that alloy composition will affect transformation temperature sensitivity; more alloys must be tested. It is hypothesised that the magnitude of the difference between each alloy's  $M_s$  and  $M_d$  temperature will affect transformation temperature sensitivity. The larger the temperature difference between  $M_s$  and  $M_d$  is, the lower the



gradient of the free energy vs. temperature curve and thus the less influence an absolute change in temperature will have on the contribution of mechanical deformation to the rate of transformation. The magnitude of the difference between each of these temperatures and the temperature range in which the alloy operates is also likely to affect transformation temperature sensitivity. In particular, if the operating temperature is very close to  $M_s$  or  $M_d$  then it is expected that the rate of transformation will be severely affected. Selecting an alloy with  $M_{d30}$  well above operating temperature and  $M_s$  well below should therefore cause its transformation to be less susceptible to temperature at deformation.

Empirical formulas intended to approximate such temperatures within the alloy range of interest, based on chemical composition and microstructure, did not give consistent results. However, as discussed, some of these empirical formulas showed trends with measured transformation characteristics of this as-cast alloy group (see subsection B) and are thus considered likely to be more accurate predictors than the others. While further testing on current alloys may help to clarify this, new alloys will have to be designed, produced and tested to properly analyse this phenomenon.

Alloy V2 showed an  $M_{sKrupp}$  of 99°C and a  $M_{d30Pickering}$  of 128°C. These two formulas were only shown to have relevance after the transformation temperature testing was already conducted. It is notable that the gap between the two temperatures is small, only 29°C and that the testing temperatures were below or closely approaching  $M_s$ . Most of the other alloys exhibiting good transformation performance had considerably larger differences between their  $M_{sKrupp}$  and  $M_{d30Pickering}$  of 100°C to 170°C. For some of those alloys an operating range of -5°C to 40°C would fall in the middle of their  $M_s - M_{d30}$  range. These predicted values may well imply considerably less temperature sensitivity than alloy V2. It is thus possible that one of the most temperature sensitive alloys was inadvertently chosen for this testing.

It has been proposed that strain rate sensitivity is related to transformation temperature sensitivity. Higher strain rates are believed to cause microscopic heating, which does not have time to dissipate, within the highly strained regions of the material's crystal structure. It is proposed that the reduced transformation at higher strain rates is thus due to the influence of this temperature increase [15]. It is thus hoped that an alloy with lower temperature transformation sensitivity will also exhibit less strain rate sensitivity.

Preliminary deformation temperature testing was also carried out on alloy HM at 0°C and 40°C. With calibration at 22°C, a margin of error of about  $\pm 5\%$  was deduced at 650MPa, significantly lower than alloy V2.

#### IV. PROTOTYPES

##### A. Smart Load Cell and Smart Face Plate

More than one type of Smart Load Cell prototype has been constructed. The version shown below was designed for use in

mines. It includes a hole through the centre so that it can also serve as a load monitoring face-plate (or washer) for rock-bolts. The output of such a Smart Load Cell utilising as-cast alloy V2 is shown in figure 10. These devices have not yet been tested in-situ but have passed testing in a South African Bureau of Standards grade test rig for such mining components.

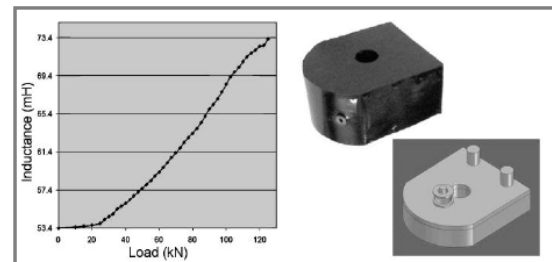


Fig. 10. The output of a complete prototype Smart Load Cell is shown, along with a photograph of the device and a 3D rendering with the top plate removed.

##### B. Smart Bridge Load Cell

Another variation of the Smart Load Cell, called the Smart Bridge Load Cell, was designed for use in monitoring the wire ropes within the anchor piles of a new suspension bridge being erected in KwaZulu-Natal, South Africa. A newly installed Smart Bridge Load Cell is shown in figure 11. Excessive ground movement can cause overloading in the wire ropes. So far data has only been assessed up to the stage of anchor settlement, not since the anchors have been fully loaded into their working range. Output data thus far shows peak loading similar to that predicted and the Smart Bridge Load Cells are functioning as expected.



Fig. 11. A photograph of a Smart Bridge Load Cell immediately after installation on suspension bridge anchors.

#### V. CONCLUSION

The smart properties of TRIP steels have been utilised to produce low-cost, low maintenance, robust deflection and load sensors. Various types of smart load cells have been brought to



prototype stage and one has been installed in-situ.

The accuracy of these sensors is currently very low under entirely unknown environmental and loading conditions. When all possible errors are accumulated, an estimated worst-case accuracy of approximately  $\pm 16\%$  is currently attainable beyond incubation strain utilizing tested alloys, with the only constraint being a maximum temperature variation of about  $40^\circ\text{C}$ . Some errors are not accumulative, for example the error due to a released load is always positive but error due to a high strain-rate is always negative.

When certain environmental or loading conditions can be excluded, this accuracy increases considerably to a minimum of less than  $\pm 5\%$ .

Numerous TRIP steel alloys were produced, tested and analysed. Several different aspects of the phase transformation and its consistency under varying environmental and loading conditions were examined. It is likely that it will be possible to considerably improve the accuracy of the devices through further alloy refinement utilising the current results.

#### ACKNOWLEDGMENT

The author would like to thank G. Bright for his guidance. B.L. Verijenko and V.E. Verijenko are acknowledged for previous work leading to this research.

#### REFERENCES

- [1] L. D. Thompson, B. D. Westermo, D. B. Crum, W. Law, R. Trombi, R. Waldbusser, "Smart structural fasteners for the aircraft and construction industries", *Proceedings of SPIE*, Vol. 3668, No. 1, pp. 143-152, 1999
- [2] B. Verijenko, V.E. Verijenko, C. Bement, "Smart rock anchors for increased safety in deep mines", *II ECCOMAS Thematic Conference on Smart Structures and Materials*, pp. 11.4-11.14, 2005
- [3] M. Radu, J. Valy, A.F. Gourgues, F. Le Strat, A. Pineau, "Continuous magnetic method for quantitative monitoring of martensitic transformation in steels containing metastable austenite", *Scripta Materialia*, vol. 52, pp. 525-530, 2005
- [4] J. S. Meoma, R. Paton, S. Roberts, D. Adams, "Smartbolt technology and methods of monitoring to assess the condition of mining roof support systems", *7<sup>th</sup> international colloquium on asset management of aged plant and materials assessment methods*, Cape Town, South Africa, pp. 153 – 167, 2003
- [5] M. Y. Sherif, C. Garcia Mateo, T. Sourmail and H. K. D. H. Bhadeshia, "Stability of retained austenite in TRIP-assisted steels", *Materials Science and Technology*, Vol. 20, pp. 319-322, 2004
- [6] J. Talonen, P. Aspegren, H. Hänninen, "Comparison of Different Methods for Measuring Strain Induced  $\alpha$ -Martensite Content in Austenitic Stainless Steels", *Materials Science and Technology*, Vol. 20, pp. 1506-1512, 2004
- [7] U. Krupp, C. West, H.-J. Christ, "Deformation-induced martensite formation during cyclic deformation of metastable austenitic steel: Influence of temperature and carbon content", *Materials Science and Engineering A*, Vol. 481-482, pp. 713-717, 2008
- [8] F. C. Hull, "Delta ferrite and martensite formation in stainless steels", *Welding Research Supplement: Welding Journal*, Vol. 52(5), pp. 193s-203s, 1973
- [9] C. Capdevila, F. G. Caballero, C. Garcis de Andres, "Determination of  $M_s$  temperature in steels: A Bayesian neural network model", *ISIJ International*, Vol. 42, No. 8, pp. 894-902, 2002
- [10] C. Capdevila, F. G. Caballero, C. Garcis de Andres, "Analysis of effect of alloying elements on martensite start temperature of steels", *Materials Science and Technology*, Vol. 19, pp. 581-586, 2003
- [11] T. Angel, "Formation of Martensite in Austenitic Stainless Steels, Effects of Deformation, Temperature and Composition", *Journal of the Iron and Steel Institute*, Vol. 177, pp. 165-174, 1954
- [12] F. B. Pickering, *Physical metallurgy and the design of steel*, Applied Science Publishers, London, 1978, pp. 229
- [13] K. Nohara, Y. Ono, N. Ohashi, "Composition and grain size dependencies of strain-induced martensitic transformation in metastable austenitic stainless steels", *Journal of the ISIJ*, Vol. 63, No. 5, pp. 212-222, 1978
- [14] L. Bracke, G. Mertens, J. Penning, B. C. De Cooman, M. Liebeheer, N. Akdut, "Influence of phase transformations on the mechanical properties of high-strength austenitic Fe-Mn-Cr steel", *Metallurgical and Materials Transactions A*, Vol. 37A, pp. 307-316, 2006
- [15] J. P. Bressanelli, A. Moskowitz, "Effects of Strain Rate, Temperature and Composition on Tensile Properties of Austenitic Stainless Steels", *Transactions of the ASM*, Vol. 59, pp. 223-239, 1966

#### The Development of Robust Structural Health Monitoring Sensors Utilizing TRIP Steel

Bement, C.P.  
Vol. 9, issue 11  
Page(s): 1449-1455  
Digital Object Identifier 10.1109/JSEN.2009.2021801  
IEEE SENSORS JOURNAL

## A3.3. Journal Paper 3

IOP PUBLISHING

SMART MATERIALS AND STRUCTURES

Smart Mater. Struct. 21 (2012) 075010 (8pp)

doi:10.1088/0964-1726/21/7/075010

# The design and testing of subscale smart aircraft wing bolts

J M V Vugampore<sup>1</sup> and C Bemont<sup>2,3</sup><sup>1</sup> Department of Mechanical Engineering, Mangosuthu University of Technology, PO Box 12363, Jacobs, 4026, South Africa<sup>2</sup> School of Mechanical Engineering, University of KwaZulu-Natal, South AfricaE-mail: [vugampor@mut.ac.za](mailto:vugampor@mut.ac.za) and [bemontc@ukzn.ac.za](mailto:bemontc@ukzn.ac.za)

Received 19 October 2011, in final form 13 April 2012

Published 13 June 2012

Online at [stacks.iop.org/SMS/21/075010](http://stacks.iop.org/SMS/21/075010)

## Abstract

Presently costly periodic inspection is vital in guaranteeing the structural integrity of aircraft. This investigation assesses the potential for significantly reducing aircraft maintenance costs without modification of aircraft structures by implementing smart wing bolts, manufactured from TRIP steel, which can be monitored for damage *in situ*. TRIP steels undergo a transformation from paramagnetic austenite to ferromagnetic martensite during deformation. Subscale smart aircraft wing bolts were manufactured from hot rolled TRIP steel. These wing bolts were used to demonstrate that washers incorporating embedded inductance coils can be utilized to measure the martensitic transformation occurring in the TRIP steel during bolt deformation. Early *in situ* warning of a critical bolt stress level was thereby facilitated, potentially reducing the costly requirement for periodic wing bolt removal and inspection. The hot rolled TRIP steels that were utilized in these subscale bolts do not however exhibit the mechanical properties required of wing bolt material. Thus warm rolled TRIP steel alloys were also investigated. The mechanical properties of the best warm rolled TRIP steel alloy tested almost matched those of AISI 4340. The warm rolled alloys were also shown to exhibit transformation before yield, allowing for earlier warning when overload occurs. Further work will be required relating to fatigue crack detection, environmental temperature fluctuation and more thorough material characterization. However, present results show that *in situ* early detection of wing bolt overload is feasible via the use of high alloy warm rolled TRIP steel wing bolts in combination with inductive sensor embedded washers.

## 1. Introduction

Periodic inspection is vital in guaranteeing the structural integrity of aircraft. However, in aircraft such as the Hercules C-130, inspection of the wing bolts for potential overload and fatigue cracking requires the wings to be jacked up and removed, a process that involves at least 180 man-hours of labor and the danger of damaging the wing in the process. There is the potential to significantly reduce costs if these bolts could be made to measure and convey their level of damage *in situ*. This investigation assesses the potential for reducing aircraft maintenance costs by implementing smart damage monitoring wing bolts in the C-130 aircraft.

Structural health monitoring (SHM) is of growing importance in the area of maintenance, inspection and repair of engineering infrastructure. Many different technologies are employed for damage monitoring in a wide variety of structures. Various SHM technologies have previously been applied or proposed for C-130 and similar aircraft structures. These include strain gauges, embedded fiber optic sensors, ultrasonic transducers, natural frequency assessment and acoustic emission [1]. While such damage monitoring systems may add to the safety and longevity of the infrastructure and reduce maintenance expenses, they are likely to add significantly to its complexity and capital expense. Such systems are usually also sensitive to severe environmental conditions, such as those experienced in aircraft, unless special precautions are taken. In the case of aircraft wing

<sup>3</sup> Author to whom any correspondence should be addressed.

bolts, there are further constraints associated with bolt geometry, accessibility and the relatively large number of bolts (52 altogether).

It was proposed that the damage status of C-130 wing bolts might be reliably monitored with minimal additional complexity or cost by manufacturing these bolts from TRIP (transformation induced plasticity) steels and implementing associated passive sensor systems [2]. Such smart wing bolts might replace the original wing bolts with no further structural modification being required.

Any damage occurring within an engineering structure (due to overload, corrosion, fatigue or crack propagation) will result in the weakening of the structure, leading to an increase in structural stress. This imposed stress will result in elastic or plastic deformation of the structure. Mechanical testing will enable correlation between stress and strain within the smart wing bolts. Warning limits may be set to trigger when particular stress or strain levels are reached. In many potential applications, including the C-130 wing bolts, the historic peak stress or strain undergone in the structure, even after loads have dropped, is of primary interest. Memorization of historic peak deformation is inherent when utilizing a TRIP steel smart structural sensor element.

These materials possess the distinctive property of recording the peak deformation undergone by the material via an irreversible deformation induced phase transformation from paramagnetic austenite to ferromagnetic martensite [3, 4]. Thus, if TRIP steel is incorporated within key elements of a structure, these elements may be made to provide useful feedback information in assessing the damage state of the structure. Any deformation occurring within the TRIP steel sensor element leads to a correlated degree of permanent austenitic to martensitic transformation, which in turn increases the element's ferromagnetic response. There is no reverse transformation upon unloading. High alloy TRIP steels are austenitic stainless steels with excellent mechanical properties (high strength, ductility and toughness) and are thus excellent structural materials [5–7].

It is known that TRIP steels do not usually exhibit substantial martensitic transformation before yield at room temperature [8]. The kinetics of isothermal martensitic transformations in steels are considered to be nucleation controlled [9]. In order for substantial transformation to occur, it is usually necessary to plastically strain the material in order to produce martensite nucleation sites [10, 11]. Martensite formed due to such plastic deformation is usually referred to as strain induced martensite. TRIP steels deformed at room temperature may also exhibit transformation prior to yield, though usually in insignificant amounts. A stress that is applied below yield may add the energy required for the transformation to proceed at a pre-existing nucleation site; thus this type of transformation is commonly referred to as stress assisted. Stress assisted nucleation is believed to occur at the same nucleation sites where spontaneous cooling transformation would occur [9].

TRIP steels formed in the temperature range where austenite is stable, above their upper deformation transformation temperature ( $M_d$ ) but below recrystallization temperature,



Figure 1. Image showing a standard 7/8" nominal diameter bolt used in the C-130 cargo plane.

are known to be more likely to exhibit measurable transformation before yield over a broad range of temperatures [12]. These materials are referred to as warm formed TRIP steels. It is believed that they exhibit better transformation before yield because martensite nucleation sites produced during the forming process remain within the material, encouraging stress assisted transformation. Specifically, the range of temperatures over which substantial transformation occurs at or before yield has been found to be considerably broader in these warm formed materials [8]. For the current application it would be beneficial to use a warm formed alloy that exhibits early (stress assisted) transformation in order to enable deformation measurement in the smart wing bolts at the lowest possible intensities.

It is possible to increase the transformation range of a TRIP steel alloy by varying alloy composition. While alloy compositions were carefully selected according to the literature, the effects of the numerous alloying elements on the transformation are not yet properly understood and have not been fully characterized [13–15]. The alloy used in this application will also be required to display very good mechanical properties, thus again restricting alloy design to high tensile warm rolled alloys.

## 2. Subscale smart aircraft wing bolt design

A wing bolt serves to clamp the wing to the fuselage of an aircraft such as the C-130 cargo plane. There are two standard size wing bolts used in the C-130: 7/8" nominal diameter, 14 threads per inch, 108 mm long and 3/4" nominal diameter, 16 threads per inch, 94.65 mm long. The 7/8" nominal diameter bolt is shown in figure 1. These are simple threaded fasteners that are currently manufactured from high strength AISI 4340 steel. These bolts are highly stressed and must be periodically inspected for wear and crack propagation. This is a time consuming and expensive procedure. It is proposed that these bolts might be manufactured from a TRIP steel that possesses similar mechanical properties to AISI 4340 steel and also imparts smart properties to the bolts.

It is of fundamental importance to the functioning of TRIP steel based sensors that an appropriate method for monitoring the crystal phase transformation of the TRIP steel element is implemented, usually via magnetic permeability detection. Neither the smart aircraft wing bolt nor its associated magnetic measurement device should significantly alter the mechanical structure of the aircraft. There are many methods for measuring the level of magnetic permeability of



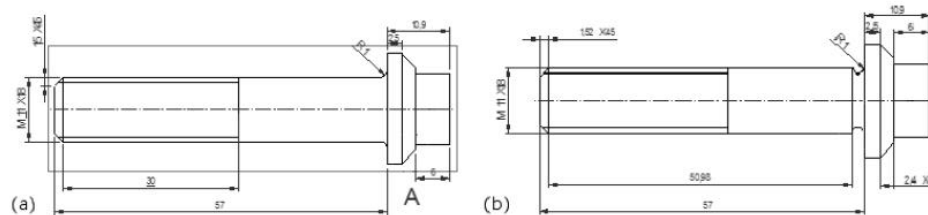


Figure 2. Diagrams illustrating the geometry of the subscale (a) and grooved subscale (b) smart aircraft wing bolts tested.



Figure 3. Photo of an assembled subscale TRIP steel smart aircraft wing bolt.



Figure 4. A sensor nut for a subscale smart wing bolt, before the inductance coil has been embedded.



Figure 5. A sensor washer with an embedded coil of 149 turns and 0.019 mm diameter wire.

materials. Magnetic susceptibility monitoring via inductance coils has been found to be one of the most accurate methods for monitoring the martensitic transformation, and is typically the most practical to implement [16]. Any accurate method of inductance measurement may be applied to an inductance coil wound around the relevant section of the TRIP steel specimen in order to monitor the associated change in magnetic permeability as deformation occurs.

The location of the strain sensor coil or coils was a challenging matter, as they must be placed near the parts of the bolt in which failure will occur. It is well known that the first thread engaged by a nut is the most highly stressed region of a bolt and thus the most likely to fail; and that the region under the bolt head is the next most highly stressed region and is next most likely to fail. This has also been verified for the aircraft bolts in question by using finite element analysis data [17] as well as service data from the aircraft company. Later laboratory testing also corroborated this.

Scale bolts of approximately 50% of original size were manufactured, as well as similar bolts including a recess groove located underneath the bolt head. This groove was placed underneath the bolt head for purposes of experimental verification. Without it, deformation occurring under the bolt head during testing was found to be nearly indiscernible due to very low deformation relative to that at the first engaged thread. The groove thus enabled the testing of the sensitivity of the inductance coil in detecting deformation in this location, where failures are known to sometimes occur in practice. The groove reduced the bolt shaft cross-section in this region to be equal to that of the threaded cross-section.

Diagrams illustrating the geometry of the standard subscale and the grooved subscale smart wing bolts tested are shown in figure 2. Figure 3 shows a photo of a standard

geometry (ungrooved) subscale TRIP steel bolt. The bolts use the principle of an inductance coil embedded within the washer or nut that surrounds the bolt in the region of the first engaged thread, thus demanding no modification to the bolt geometry, or in the case where under-head monitoring is also required, only a lengthening of the bolt-shank to include a washer in this location would be required.

Figure 4 shows a smart nut and figure 5 a smart washer. The small recess that houses the inductance coil is visible in figure 4. The small inductance coil embedded in the washer is shown in figure 5. The introduction of such a sensor washer or nut permits the bolt geometry to remain unchanged.

**Table 1.** Actual chemical compositions in mass per cent for the eight alloys after processing (75% warm reduction at 550 °C). (Note: all other elements detected in quantities less than 0.03 mass per cent.)

Element	Alloy							
	1/2	1/3	2/2	2/3	3/2	3/3	4/2	4/3
Carbon	0.16	0.30	0.21	0.33	0.19	0.20	0.29	0.35
Manganese	4.00	3.86	2.57	2.63	10.5	10.14	1.13	1.64
Sulfur	0.007	0.015	0.006	0.016	0.010	0.014	0.007	0.012
Phosphorus	0.005	0.011	0.005	0.013	0.005	0.011	0.005	0.011
Silicon	0.53	0.61	0.60	0.44	0.08	0.068	0.56	0.58
Chromium	8.14	9.09	8.0	8.75	11.6	9.66	11.6	11.95
Molybdenum	0.03	—	1.91	1.70	0.03	0.013	0.01	0.002
Nickel	8.31	6.30	8.91	8.49	1.33	1.86	9.48	8.89
Iron	Bal.	Bal.	Bal.	Bal.	Bal.	Bal.	Bal.	Bal.

### 3. Experimental method

In order to manufacture a smart bolt that will give accurate information about its damage state, a magnetic sensor (in this case a washer or nut with an embedded coil) must be located near the highly stressed regions in which failure would occur. It was decided that instead of using coil-embedded nuts, standard nuts would be utilized and inductance coils would be embedded within the washers that are placed underneath the nut (very near the first thread). Thus, one sensor coil washer was located underneath the nut, near the first engaged thread, and in some cases another was also placed under the bolt head.

The scaled down smart wing bolt shown in figure 3 was manufactured from hot rolled TRIP steel since warm rolled TRIP steel could only be produced in thin sections due to research equipment constraints. Two digitally logging inductance meters, one for each coil, were used concurrently. The data collected from these inductance meters were time-stamped and stored in the same PC that logged the tensile stress and strain applied by the Instron 5500R universal testing machine. This enabled accurate correlation of tensile strain and stress to magnetic permeability data.

Warm rolled high strength TRIP steel could only be produced in the form of 12 mm plate and it was thus impractical to manufacture subscale bolts from this thin plate. However a threaded bar was manufactured from this plate, thus simulating the most highly stressed threaded region of the bolt on both ends. The geometry of the double threaded bar in an assembled state with nuts and coil-embedded washers is shown schematically in figure 6. A photograph of an assembled double threaded bar made from warm rolled TRIP steel is shown in figure 7. Before the testing of the warm rolled TRIP steel threaded bar was performed, various warm rolled TRIP steel alloys were tested as traditional tensile specimens.

Eight different alloys in four groups were produced for warm rolling. These alloy compositions are shown in table 1. The objective of the alloy formulation and processing was to obtain TRIP steel alloys that showed good deformation induced transformation characteristics and also displayed mechanical properties similar to those of the 4340 material currently used in the aircraft wing bolts. All eight of the alloys were warm rolled 75% at 550 °C in a flat rolling mill and the tensile specimens were then cut from the resulting flat plate.

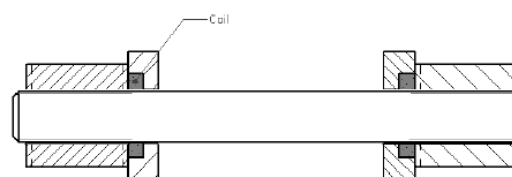


**Figure 6.** Schematic of the double threaded bar, made from warm rolled high strength TRIP steel 12 mm plate, shown in assembly with nuts and coil-embedded washers on both ends.

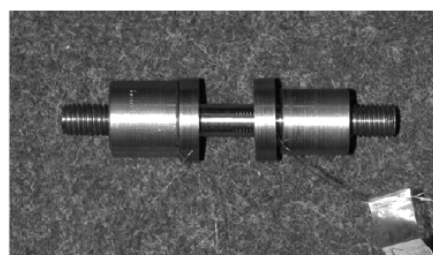


**Figure 7.** Photo of a double threaded bar, showing nuts and coil-embedded washers on both ends.

Monitoring of the change in magnetic permeability during tensile testing was achieved by using a magnetic permeability meter instead of an inductance coil, as shown in figure 8.

### 4. Experimental results

#### 4.1. Subscale bolts manufactured from hot rolled TRIP steel

The standard and grooved subscale bolts made from hot rolled TRIP steel were quasi-statically tensile tested while being monitored for deformation induced phase transformation, as described above. Results are shown in figure 9. The inductance (magnetic permeability) measured at the first engaged thread was found to increase gradually soon after load was applied and to increase much more rapidly in the period before failure. The bolts incorporating an under-head groove showed a measurable increase in inductance in this region from shortly after yield. The standard geometry bolts only showed a measurable increase in under-head inductance



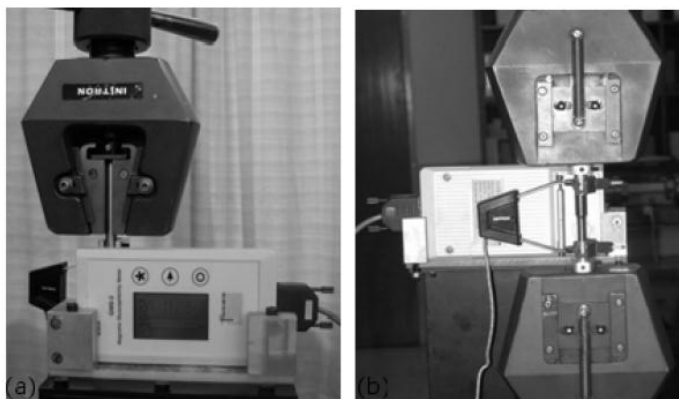


Figure 8. Front and back view of the tensile testing test rig. A magnetic susceptibility meter is used to measure the change in magnetic permeability and an extensometer is used to record the specimen strain.

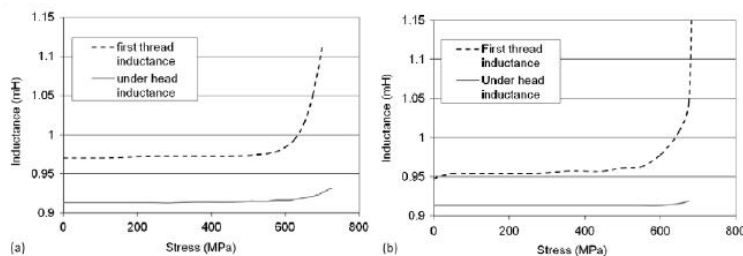


Figure 9. Inductance readings from the thread and under the bolt head during quasi-static tensile loading in a subscale bolt with a 1 mm groove under the head (a) and a subscale bolt of standard geometry (b).

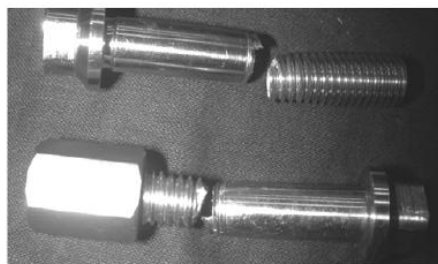


Figure 10. Two of the overloaded subscale smart bolts. Both failed at the first engaged thread.

shortly before failure occurred in the first engaged thread. The above tests were each repeated three times, resulting in comparable data on each occasion. Unfortunately different (but equivalent) coil-embedded washers had to be used on the grooved and standard geometry subscale bolts. Figure 10 shows two failed bolts after testing.

#### 4.2. Quasi-static tensile testing of warm rolled alloys

The eight warm rolled high tensile TRIP steel alloys shown in table 1 were quasi-statically tensile tested to failure while monitoring magnetic permeability using a magnetic

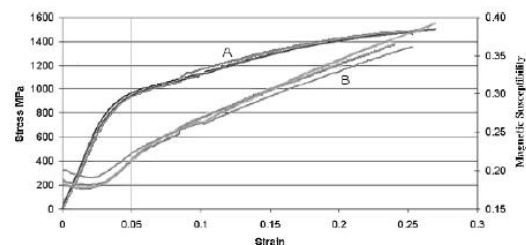
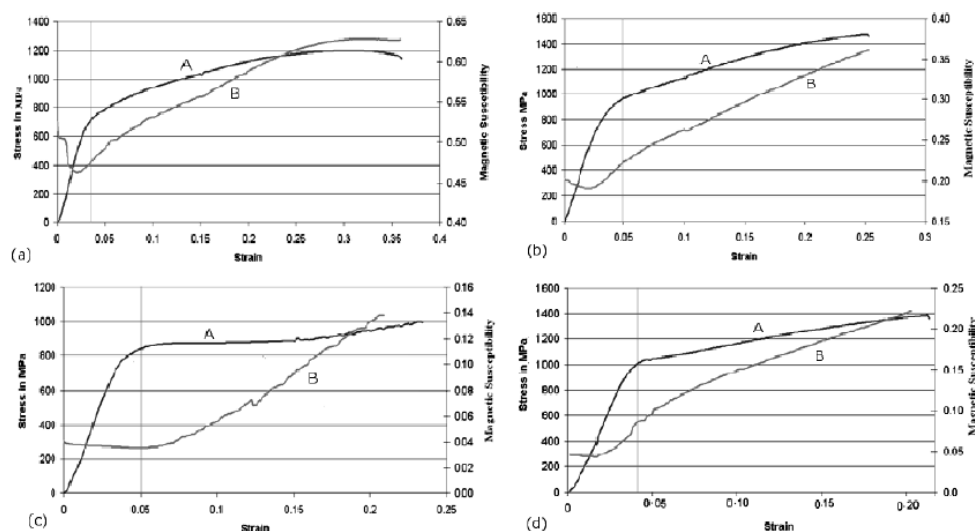


Figure 11. Stress versus strain (A) and strain versus magnetic susceptibility (B) results for three tensile specimens of alloy 2/2.

susceptibility meter. Three specimens of each alloy were tested and generally showed repeatable results. Although care was taken to build a rig to accurately position the magnetic susceptibility meter relative to the Instron testing machine, deviations in strain–transformation data between tests is considered to be due at least partly to slight position or orientation variation and other interference related to this sensitive device. Deviations in strain–transformation data may also result from material inhomogeneity, though care was taken to avoid this during pre-rolling heat treatments.

Stress–strain and strain–transformation data are plotted in figure 11 for all three alloy 2/2 tensile specimens tested. Figure 12 shows one characteristic set of stress–strain and



**Figure 12.** Typical stress versus strain (A) and strain versus magnetic susceptibility (B) results for: (a) alloy 1/2, (b) alloy 2/2, (c) alloy 3/2 and (d) alloy 4/2.

**Table 2.** Room temperature tensile properties of alloy 4/2 compared to quenched and tempered nickel–chromium–molybdenum alloy steel (AISI 4340) currently used in Hercules C-130 wing bolts.

Alloy	Tempering (°C)	Yield strength (MPa)	Tensile strength (MPa)	Elongation (%)
Alloy 4/2	—	1100	1390	24
AISI 4340	427	1368	1468	10

**Table 3.** Impact test results for alloy 4/2.

Alloy	Lateral expansion		Shear %		Charpy impact resistance (J)	
	20 °C	−50 °C	20 °C	−50 °C	20 °C	−50 °C
Alloy 4/2	0.24	0.22	100	100	90	106
	0.21	0.12	100	100	98	144
	0.16	0.28	100	100	70	118
AISI 4340	42 min					

strain–transformation curves each for alloys 1/2, 2/2, 3/2 and 4/2. Alloy 2/2 exhibited the highest tensile strength and the second highest yield strength. Alloy 4/2 exhibited the highest yield strength and the second highest tensile strength. Alloy 2/2 and alloy 4/2 exhibited similarly good transformation.

The mechanical properties of alloy 4/2, determined from an average of three tensile tests, is shown in table 2 and compared to those of the AISI 4340 material (quenched and tempered at 427 °C) currently used for the Hercules C-130 wing bolts. The yield strength of alloy 4/2 is significantly below that of the AISI 4340 material. The ultimate tensile strength of alloy 4/2 is near to that of AISI 4340. The elongation at break of alloy 4/2 is more than double that of AISI 4340.

Toughness is also of great significance for the aircraft wing bolts. Charpy impact testing was carried out on alloy 4/2 and results are shown in table 3. Alloy 4/2 absorbed an average of 86 J at 20 °C, where AISI 4340 should exhibit a minimum of just 42 J at 20 °C according to specification. Low temperature impact toughness of alloy 4/2 proved to be even more impressive. The magnetic susceptibility of the alloy 4/2 Charpy impact specimens was measured before and after

impact. Results showed that significant transformation does occur even at high rates of loading.

The change in the microstructure of alloy 4/2 from before deformation to after deformation is depicted in figure 13. Before deformation the microstructure is seen to consist of light-colored austenitic grains that have been elongated during warm rolling. Very little martensite is apparent. After deformation a significant proportion of the microstructure is seen to have transformed to dark-colored martensite.

TRIP steels undergo transformation not only during deformation but also spontaneously upon their temperature dropping below some predefined level (denoted as  $M_s$  temperature), in a fashion similar to all steels. The effect of temperature fluctuation alone (without any associated loading) on alloy 2/2 and alloy 4/2 was thus measured. It was found that while transformation was detected in alloy 2/2 immediately upon cooling, no transformation was detected in alloy 4/2 at above −70 °C.

## 5. Discussion

Subscale wing bolts manufactured from hot rolled TRIP steel displayed significant martensitic transformation in the region



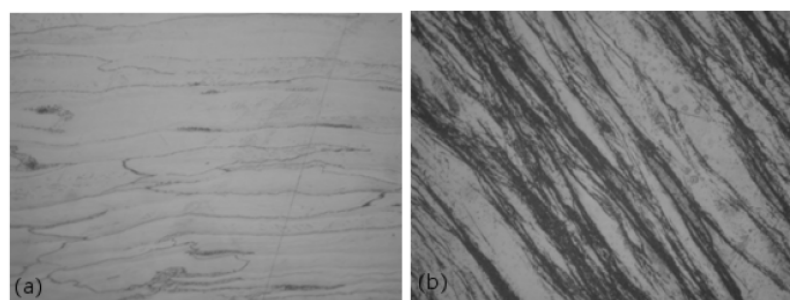


**Figure 13.** Microstructure of warm worked alloy 4/2 before (a) and after (b) tensile testing. The image to the left shows elongated austenitic grains with little or no martensite present. The image to the right shows that significant levels of martensite developed during tensile testing.

of the first engaged thread from the material's yield point on. The yield point is however reached not long prior to failure. The principle of utilizing inductance coils embedded in the wing bolt washers as sensors was successfully demonstrated. Transformation was detected in the first engaged thread and under the bolt head in the scale bolts including an under-head groove as well as in the standard geometry bolts.

As discussed, warm rolled alloys are favored for the application because they possess superior mechanical properties as well as exhibiting relatively earlier measurable martensitic transformation over a broad range of temperatures. All warm rolled alloys displayed similarities in their mechanical properties but showed substantially different levels of deformation induced transformation. Alloy 4/2 in particular displayed significant (stress assisted) transformation prior to its yield point. Alloy 2/2 also displayed transformation prior to its yield point. These two alloys also displayed the greatest yield and ultimate tensile strengths of all eight alloys. Their superior mechanical properties may thus be linked to the elevated level of stress assisted transformation they undergo before yield.

Alloy 4/2 is considered to have displayed the best mechanical properties of the alloys tested. The yield strength of alloy 4/2 is however substantially below that of the AISI 4340 material currently used for the Hercules C-130 wing bolts. The ultimate tensile strength of alloy 4/2 is near to that of AISI 4340. However, alloy 4/2 shows an elongation at break of more than double that of the AISI 4340 material. Further warm working reduction to increase the yield point and also the ultimate tensile strength of alloy 4/2, while maintaining good ductility, is therefore considered quite feasible. Such further warm working may be expected to alter transformation sensitivity somewhat, but it is difficult to predict just how.

Charpy impact testing results for alloy 4/2 are better than those of AISI 4340, particularly at low temperature ( $-50^{\circ}\text{C}$ ). Magnetic susceptibility measurement of impact specimens before and after testing showed that significant martensitic transformation does occur even at high rates of loading. The improved impact toughness of alloy 4/2 at  $-50^{\circ}\text{C}$  compared to  $20^{\circ}\text{C}$  is probably due to the effects of a more rapid transformation at low temperature. It was not possible to

compare absolute levels of transformation to those measured during quasi-static tensile testing because of the different specimen geometry and the impracticality of implementing continuous magnetic susceptibility monitoring during Charpy impact testing.

Considerable further investigations will be required to assess the potential for implementing high strength TRIP steels as smart aircraft wing bolts. Resistance to fatigue failure in TRIP steels is expected to be better than that occurring in materials with comparable mechanical properties because fatigue crack propagation is retarded through the austenite to martensite transformation occurring in the vicinity of the crack tip [18]. Cyclic testing should however be implemented to assess the potential to detect fatigue crack propagation via changes in magnetic susceptibility.

Variations in environmental conditions during loading are also known to affect the transformation characteristics as well as the mechanical properties of TRIP steels [19]. In particular, material temperature at the time of loading is known to directly affect the level of transformation occurring in TRIP steels. It may however be possible to minimize these effects within a given temperature range [20, 21]. It was shown that in alloy 4/2, temperature fluctuation alone does not result in martensitic transformation above  $-70^{\circ}\text{C}$ , which is below the temperature range under which the Hercules C-130 aircraft operates.

## 6. Conclusion

Subscale smart aircraft wing bolts were manufactured from hot rolled TRIP steel. Transformation during quasi-static loading was monitored via inductance coils embedded within washers placed underneath the nut and the bolt head. This arrangement results in minimal geometric alteration to the standard wing bolt elements. In the hot rolled material, significant martensitic transformation was observed shortly after yield via an increase in magnetic permeability.

It was expected that warm rolled TRIP steels would exhibit substantially increased yield and tensile strengths compared to the hot rolled TRIP steels from which the subscale wing bolts were produced. Warm rolled TRIP steels

are also known to exhibit earlier transformation over a broader temperature range than hot rolled TRIP steels.

Eight warm rolled high strength TRIP steel alloys were produced and tested, though scale wing bolts could not be manufactured from these alloys. These materials clearly exhibited transformation before yield at room temperature, allowing for significantly earlier warning when overload occurs as compared to the hot rolled variety. The mechanical properties of the best alloy tested almost matched those of AISI 4340. Yield strength was however appreciably below that of AISI 4340, while ductility and toughness were appreciably higher. It is thus expected that a greater degree of warm rolling reduction will result in mechanical properties more closely matched to AISI 4340.

Further work will need to be carried out relating to fatigue crack detection and also to environmental temperature fluctuation. A more thorough characterization of a range of warm rolled TRIP steels would be beneficial. However, present results show that *in situ* early detection of wing bolt overload is feasible via the use of high alloy warm rolled TRIP steel wing bolts in combination with magnetic sensor embedded washers.

### Acknowledgments

This work was partly funded by the South African National Research Foundation via the Innovation Fund under project number 32402. The authors would like to thank Sheleni Mukosa for contributing to the drafting of some of the graphs and figures included in this paper. The authors would also like to acknowledge Victor and Belinda Verijenko and Rob Bodger's supervisory roles in parts of this work.

### References

- [1] Banks J, Moose C, Conlon S and Reichard K 2008 Air force C-130 rainbow fitting diagnostic technology development *J. Reliab. Inf. Anal. Center* **16** 2–7
- [2] Tominaga M, Thompson L and Westermo B 1999 *Current and Future Trends in Bridge Design, Construction and Maintenance* ed P C Das, D M Frangopol and A S Nowak (London: Thomas Telford) pp 482–93
- [3] Lecroisey F and Pineau A 1972 Martensitic transformation induced by plastic deformation in the Fe–Ni–Cr–C system *Metall. Trans.* **3** 387–96
- [4] Zackay V F, Parker E R, Fahr D and Bush R 1967 The enhancement of ductility in high-strength steels *Trans. ASM* **60** 252–9
- [5] Zakay V F, Bhandarkar M D and Parker E R 1978 The role of deformation-induced phase transformation in the plasticity of some iron base alloys *Metall. Trans.* **41** 351–403
- [6] Webster D 1971 Development of a high strength stainless steel with improved toughness and ductility *Metall. Trans.* **2** 2097–104
- [7] Parker E R and Zackay V F 1973 Enhancement of fracture toughness in high strength steel by microstructural control *Eng. Fract. Mech.* **5** 147–65
- [8] Olson G B and Azrin M 1978 Transformation behavior of TRIP steels *Metall. Trans. A* **9** 713–21
- [9] Olson G B and Cohen M 1982 Stress-assisted isothermal martensitic transformation: application to TRIP Steels *Metall. Trans. A* **13A** 1907–14
- [10] Maxwell P C, Goldberg A and Shyne J C 1974 Stress-assisted and strain induced martensites in Fe–Ni–C alloys *Metallurg. Trans.* **5** 1305–17
- [11] Tsakiris V and Edmonds D V 1999 Martensite and deformation twinning in austenitic steels *Mater. Sci. Eng. A* **273–275** 430–6
- [12] Goldberg A and Hoge K G 1974 Effect of strain rate on tension and compression stress–strain behavior in a TRIP alloy *Mater. Sci. Eng.* **13** 211–22
- [13] Porter D A, Easterling K E and Sherif M Y 2009 *Phase Transformations in Metals and Alloys* 3rd edn (Boca Raton, FL: CRC) pp 397–415
- [14] Capdevila C, Caballero F G and García De Andrés C 2003 Analysis of effect of alloying elements on martensite start temperature of steels *Mater. Sci. Technol.* **19** 581–6
- [15] Gutkin M Yu, Mikaelyan K N, Verijenko V E and Thompson L D 2002 Dislocation–disclination model of heterogeneous martensite nucleation in transformation-induced-plasticity steels *Metall. Mater. Trans. A* **33** 1351–62
- [16] Radu M, Valy J, Gourgues A F, Le Strat F and Pineau A 2005 Continuous magnetic method for quantitative monitoring of martensitic transformation in steels containing metastable austenite *Scr. Mater.* **52** 525–30
- [17] Jonson D 2003 Finite element modelling of smart trip steel sensors and systems *PhD Thesis* University of Natal, Durban, South Africa
- [18] Hennessy D, Steckel G and Alstetter C 1976 Phase transformation of stainless steel during fatigue *Metall. Trans. A* **7** 415–24
- [19] Park S U, Yoo S W, Kim M H and Lee J M 2010 Strain-rate effects on the mechanical behavior of the AISI 300 series of austenitic stainless steel under cryogenic environments *Mater. Des.* **31** 3630–40
- [20] Bemont C 2009 The development of robust structural health monitoring sensors utilizing trip steel *IEEE Sensors J.* **9** 1449–55
- [21] Krupp U, West C and Christ H J 2008 Deformation-induced martensite formation during cyclic deformation of metastable austenitic steel: influence of temperature and carbon content *Mater. Sci. Eng. A* **481/482** 713–7

#### **A3.4. List of associated conference papers**

All conference papers other than 1 and 3 were almost exclusively the work of the author of this thesis. The experimental work for paper 1 was the sole work of this author, while the writing of the paper had substantial contribution from the co-authors. A small part of the experimental work for paper 3 was performed by the co-authors, while the paper was written principally by this author.

- A3.4.1.** II Eccomas thematic conference on smart structures and materials, July 2005: “Smart rock anchors for increased safety in deep mines“, B. Verijenko, V. Verijenko, C. Bemont.
- A3.4.2.** SACEA Symposium, April 2007, “The use of strain memory alloys in structural health monitoring systems“, C. Bemont, V. Verijenko.
- A3.4.3.** KMCM, August 2007, “Promising materials for embedded sensors dedicated to the health monitoring of fibre reinforced polymer matrix composites“, C. Bemont, D. Ragusch, H. Mucha, T. Schurig, B. Wielage, B. Verijenko.
- A3.4.4.** International Conference on Smart Materials Structures and Systems, July 2008, “The development of robust structural health monitoring systems utilizing TRIP steel“, C. Bemont, G. Bright and R. Bodger.
- A3.4.5.** International Conference on Advances and Trends in Engineering Materials and their Applications, July 2011, “The effects of transformation temperature on the rate of transformation in trip steels“, C. Bemont, L. A. Cornish, G. Bright.